Design of Luminescent Polypyridyl-Imidazole based Ruthenium Complexes for Construction of Sensors, Switches and Logic Devices

A Thesis

Submitted for the Degree of

Doctor of Philosophy (Science)

of

Jadavpur University

by

Sourav Deb

DEPARTMENT OF CHEMISTRY

JADAVPUR UNIVERSITY

JADAVPUR, KOLKATA 700032

INDIA

2022

Dr. Sujoy Baitalik
Professor
Department of Chemistry
Inorganic Chemistry Section

JADAVPUR UNIVERSITY
KOLKATA – 700 032, INDIA
Telephone: 91-033-2414-6666
Facsimile : 91-033-2414-6584
E-mail: sbaitalik@hotmail.com

CERTIFICATE FROM THE SUPERVISOR

This is to certify that **Mr. Sourav Deb** who got his name registered on 25.04.2017 and having index No. 08/17/Chem./25, has submitted his thesis entitled "**Design of Luminescent Polypyridyl-Imidazole based Ruthenium Complexes for Construction of Sensors, Switches and Logic Devices**" on 12/12/2022 for the award of Ph.D. (Science) degree of Jadavpur University. The work embodied in the thesis is absolutely based upon his own work under my supervision and that neither this thesis nor any part of it has been submitted for any degree/diploma or any other academic award anywhere before.

Sujoy Baitalik 12/12/2022
(SUJOY BAITALIK)
Signature of the Supervisor
& Date with official seal

Professor Sujoy Baitalik
Department of Chemistry
Jadavpur University
Kolkata- 700 032, India

Dedicated
to
My Family

Nothing in life is to be feared, it is only to be understood. Now is the time to understand more, so that we may fear less.

…………. **Marie Curie**

PREFACE

The work embodied in the thesis entitled “Design of Luminescent Polypyridyl-Imidazole based Ruthenium Complexes for Construction of Sensors, Switches and Logic Devices” have been carried out in the Department of Chemistry of Jadavpur University during the period between 2016 and 2022. The thesis is composed of six chapters.

Chapter 1 describes an overview of the photophysical and electrochemical properties of Ru(II) complexes derived from polypyridine ligands. A brief review has been presented on Ru(II) complexes incorporating various polyheterocyclic ligands with special emphasis on their design and photophysical properties. The switching of photophysical properties in presence of different external stimuli has been discussed. Moreover, diverse Boolean logic operations exhibited by the complexes based on their optical and electrochemical responses in presence of a large variety of activating inputs were also reviewed. Finally, objective and scope of this dissertation has been discussed at the end of the chapter.

In **Chapter 2**, synthesis and characterization of a new array of Ru (II)-terpyridine complexes derived from a terpyridyl-imidazole ligand (tpy-HImzPh$_3$Me$_2$) have been reported. Acid and anions induced modulation of absorption and emission spectral characteristics of the complexes were thoroughly studied by multiple optical channels and spectroscopic techniques. DFT and TD-DFT studies were carried out to understand the electronic structures of the complexes and also for appropriate assignment of the spectral bands.

Chapter 3 reports the synthesis, characterization and photo-redox behaviors of three homo- and heteroleptic Ru(II)-complexes based on fluoro-substituted terpyridyl-imidazole ligand (tpy-HImzPh$_3$F$_2$). The major focus of this chapter is pH and temperature induced modulation of absorption and emission spectral behaviors as well as electrochemical properties. DFT and TD-DFT studies were carried out to compare the experimental and theoretical spectra of the complexes. Finally, the spectral signatures of the complexes upon the influence of temperature, acid and bases were employed to construct multiple Boolean logic gates.

Chapter 4 describes synthesis, characterization and photophysical properties of a series Ru(II) complexes based on dimethylamino-substituted terpyridyl-imidazole ligand [(tpy-HImzPh$_3$(NMe$_2$)$_2$]. Anion and temperature responsive behaviours of the complexes were thoroughly investigated. Additionally, the anion and temperature responsive behaviours of the complexes were utilized to fabricate multiple Boolean (BL) and Fuzzy logic (FL) operations. Finally, Artificial Neural Networks (ANNs), Fuzzy-logic and Adaptive Neuro-Fuzzy Inference System (ANFIS) were employed to fully understand as well as to forecast the complete sensing behaviors of the complexes.

Chapter 5 deals with anion-responsive conduct of a Ru(II) complex of the type [(bpy)$_2$Ru(H$_3$pzbzim)] (ClO$_4$)$_2$ (**1**), where bpy = 2,2'-bipyridine and H$_3$pzbzim = pyrazole-3,5-bis(benzimidazole) in acetonitrile and water via absorption, and emission spectroscopy as well as by square-wave voltammetry (SWV). Alteration of the photophysical and electrochemical behavior of the complex in presence of the selected anions were predicted computationally by implementing Neural network based deep learning methodologies such as ANNs and ANFIS.

In **Chapter 6,** multi-channel anion sensing behavior of a Ru(II) complex of the form [(bpy)$_2$Ru(Hpzbzth)] (ClO$_4$)$_2$ (**1**) {bpy=2,2'-bipyridine and Hpzbzth=3,5-bis (benzthiazol-2-yl)pyrazole} is carried out and also analyzed through multiple machine learning tools.

ACKNOWLEDGEMENTS

I want to acknowledge those people who played a role directly or indirectly for the successful completion of my thesis.

First and foremost, I would like to express my gratitude and thanks to my supervisor Professor Sujoy Baitalik. It was impossible to complete this journey successfully without his continuous help and support. I am greatly benefitted by his resourceful insight on my analysis and numerous revisions. His hard work and positive energy has always been an inspiration for me.

I am very much thankful to the Department of Chemistry of Jadavpur University for giving me the scope to carry out my research work. I would like to thank the present Dean, Faculty Council of Science, Prof. Subenoy Chakraborty and the Head of the department, Prof. Swapan Kumar Bhattacharya, and the Section-in-charge, Prof. Saurabh Das for providing the departmental and laboratory facilities. I also extend my heartfelt gratitude to all the faculty members and non-teaching staffs of this department for their help and supportive cooperation.

I would specially like to acknowledge Prof. Samaresh Bhattacharya, Prof. Nitin Chattopadhyay, Prof. Chittaranjan Sinha, Prof. Subrata Mukhopadhayay, Prof. Jnan Prakash Naskar, Prof. Mahammad Ali, Dr. Tapan Kumar Mondal, Dr. Bibhuti Bhusan Shaw, and Dr. Partha Mahata for their kind cooperation and constant encouragement throughout my journey of research.

I am thankful to DST-INSPIRE for awarding me JRF and SRF fellowship for the last five years to carry out my research work smoothly.

I would like to acknowledge DST for providing single crystal X-ray diffractometer in FIST and Time-Resolved Nanosecond Spectrofluorimeter in PURSE programme to the Department of Chemistry, Jadavpur University.

I also want to express my heartfelt regards and a lot of thanks to my former lab-mates Dr. Dinesh Maity, Dr. Srikanta Karmakar, Dr. Sourav Mardanya, Dr. Debiprasad Mondal, Dr. Manoranjan Bar, Dr. Poulami Pal, Dr. Shruti Mukherjee, Dr. Animesh Paul for their continuous help and support. An extensive help from my present lab-mate Dr. Amit Chakraborty, Tanusree Ganguly, Anik Sahoo, Toushique Ahmed, Soumi Das and Sohini Bhattacharya is very much praiseworthy and deserves my heartfelt acknowledgement. All the moments we spent together during the research activities and others became a memory for the whole life. I think I am fortunate enough to get an opportunity to work with this helpful and friendly research group.

It was really impossible to complete this journey without the unconditional love, support and encouragement from my family members, especially from my parents. I want to express a heartfelt gratitude to all my family members who always kept me in their prayers. I am also thankful to my brother Saikat for his support.

I am also eager to acknowledge all of my friends and seniors for their mental support during the phase of different ups and downs *in these years. Especially, I want to give a heartfelt thank to joydeep da, my ex-roommate and a real friend of mine, who helped me a lot. I am indebted to my friend Manish for helping me with data analysis of my research work. Now I am expressing my apology since I have failed to mention personally each and everyone.*

Finally I would like to thank the almighty for his blessing to journey of completion of my thesis.

Sourav Deb 12/12/2022

(Sourav Deb)

Department of Chemistry,
Inorganic Chemistry Section,
Jadavpur University,
Kolkata-700032, India

CONTENTS

Chapter 1

General Introduction and Brief Review on Luminescent Ru (II)-Polypyridine Complexes

and

Objective and Scope of the Present Work

1.1. General Introduction

Ru(II) complexes of polypyridine ligands play promising role in the diverse field of research such as artificial photosynthesis, dye-sensitized solar cell, photocatalysis, molecular electronic devices and chemosensors because of their excellent photophysical and redox characteristics.[1-10] More interestingly, their optoelectic properties can be tuned by incorporating different chromophores in the ligand moiety or upon interaction with different external stimuli such as anion, cation, pH, temperature.[11-21] The enormous advancement in this branch of photochemistry was originated upon incorporation of $[Ru(bpy)_3]^{2+}$ moiety which exhibits excellent photosensitizing properties.[22-28] Latter on, numerous polypyridine ligands involving either bidentate 2,2'-bipyridine (bpy) type or tridentate 2,2':6',2"-terpyridine (tpy)-type chelating sites were designed to modulate the photo-redox properties in the resulting complexes. Ru(II) complexes based on bpy types of ligands exhibit strong and long-lived luminescence at room temperature (RT) whereas $[Ru(tpy)_2]^{2+}$ does not emit at RT with a very low excited state lifetime of $\tau = 250$ ps.[25-28] In addition, bpy-type ligands give rise to diasteromeric mixtures in resulting octahedral complexes which are often difficult to separate. On the other hand, $[Ru(tpy)_2]^{2+}$-type complexes produce achiral rodlike structures.[22-24] The major objective of this dissertation is to design terpyridine complexes of Ru(II) exhibiting strong and long-lived emission at RT. Additionally, we synthesized some Ru(II) complexes incorporating bpy-type chelating units functionalized with imidazole and thiazole moieties.

Another important focus of this dissertation is to modulate photophysical and redox behaviors of the complexes via exploitation of their second coordination sphere with external stimuli. Synthetic protocol offers a number of azole moieties in their secondary coordination sphere which upon interaction with anions can lead to substantial modulation of photo-redox properties of the complexes. Upon inducing extensive delocalization and/or incorporating electron-donating and electron withdrawing unit in the ligand framework, the RT emission characteristics of the Ru(II)-terpyridine complexes have been substantially improved by adjusting their ^{3}MLCT-^{3}MC energy barrier. As temperature also plays a crucial role on the emission characteristics of the complexes through adjustment of their ^{3}MLCT-^{3}MC energy barrier, we performed temperature-dependent emission spectral measurements to explore the efficacy of the complexes to act as temperature-triggered molecular switches. Theoretical calculation using density functional theory (DFT) and time-dependent DFT are also executed to get better knowledge about the structural and spectral aspects of the complexes.

The spectral and electrochemical outputs of the complexes in response to different stimuli are also employed for construction of multiple Boolean Logic (BL) as well as Fuzzy Logic (FL) functions. In BL, the output signal varies between two extremes, "0" or "1".[29-48] But the practical systems often consist of innumerable number of intermediate states. To address the in-between states, the FL is an appropriate choice.[49-55] Herein, we applied FL to provide an infinite-valued logic algorithm upon utilizing spectral output of the complexes in presence of the stimuli.[56-68] Execution of very detailed sensing studies upon varying the analyte concentration within a wide domain is very tedious, time-consuming and expensive. In order to overcome the lacuna, we implemented soft computing tools such as Artificial Neural Network (ANNs), Fuzzy Logic (FL) and Adaptive Neuro-Fuzzy Inference System (ANFIS) to analyze as well as to predict the experimental sensing data of the complexes.

1.2. Overview of Photophysical Behaviors of Ru(II) Complexes Based on Polypyridine Ligands

In the previous section, we have already discussed that Ru(II) complexes of polypyridyl ligands are potential building blocks for light harvesting applications because of their unique combination of photphysical, photochemical, and electrochemical properties.[23-27] The complexes strongly absorb in the visible (between 420 and 500 nm), display strong RT luminescence in the red and decay to the ground state via primarily ^{3}MLCT state with lifetimes that vary between a few nanoseconds to a few microseconds.[23-27,69-71] Photophysical properties of parent $[Ru(bpy)_3]^{2+}$ and $[Ru(tpy)_2]^{2+}$ are presented in Table 1.1 and Figure 1.1. It is observed that absorption spectral profile of complexes consist of metal-to-ligand charge transfer (MLCT), metal-centered (MC) and ligand-centered (LC) bands, the position of which depends upon the electronic nature of ligand environment (Figure 1.1.). Literature survey shows that $[Ru(bpy)_3]^{2+}$-type complexes exhibit superior luminescence properties in comparison with $[Ru(tpy)_2]^{2+}$-type analogues.[23-29.70-75] Whereas both types of complexes display intense absorption bands in the visible region due to MLCT transition(s) as well as very strong bands in the UV region due to ligand-centered transitions.[23-29,72-80]

Table 1.1. Photophysical parameters of the Parent Ru(II) complexes in Deaerated CH_3CN at RT.

Complex	λ_{max}^{abs} (MLCT), nm	λ_{max}^{em}, nm	τ_{exst}, 298 K, ns	Ref.
$Ru(bpy)_3^{2+}$	454	620	800	23,28
$Ru(tpy)_2^{2+}$	475	628	< 5	23,28

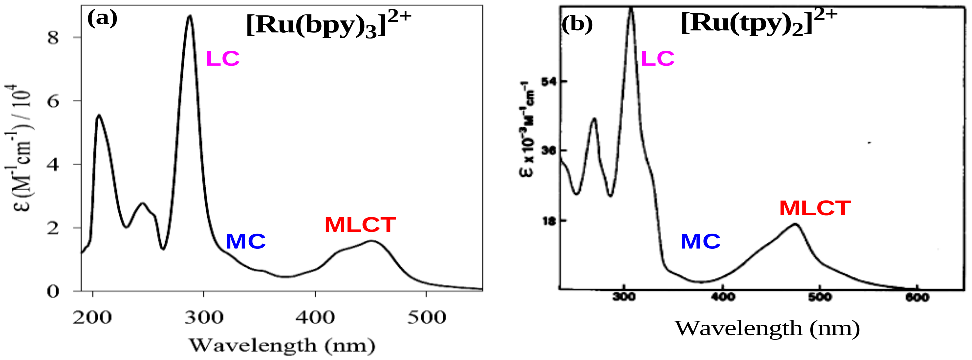

Figure 1.1. Uv-vis absorption profile of parent $[Ru(bpy)_3]^{2+}$ (a) and $[Ru(tpy)_2]^{2+}$ (b) in MeCN solution.

Upon excitation at MLCT bands, the complexes first promoted to excited state(s) and undergo very fast intersystem crossing to either ^{3}MC or ^{3}MLCT states or both and eventually deactivates to ground state either through radiative or non-radiative decay process.[23-29] The deactivation process mainly depends on the energetic relationship amongst ^{3}MLCT, ^{3}MC as well as ^{3}LC states. For complexes incorporating $[Ru(bpy)_3]^{2+}$ moiety, the lowest lying excited state is predominantly ^{3}MLCT which undergo radiative deactivation with reasonably long lifetime. By contrast, the complexes incorporating $[Ru(tpy)_2]^{2+}$ motif are usually non-emissive or very weakly emissive because of close proximity of their emitting ^{3}MLCT and non-emitting ^{3}MC states at RT (**Figure 1.2**).

1.3. Electrochemical Behaviors of Ru(II) Complexes Based on Polypyridine Ligands

Electrochemical properties of Ru(II) complexes of polypyridine are quite interesting because of their reversible nature. Highest occupied molecular orbital (HOMO) of the complexes predominantly situated on the metal site, that means on oxidation Ru(II) gets converted to Ru(III), whereas the lowest unoccupied molecular orbital (LUMO) is localized over the pyridine rings and upon reduction, the electrons are accumulated on the LUMO of the polypyridine ligands.[72-75] It is observed that mono-metallic complexes usually display one reversible oxidation in the positive window and many reduction peaks in the negative potential window.

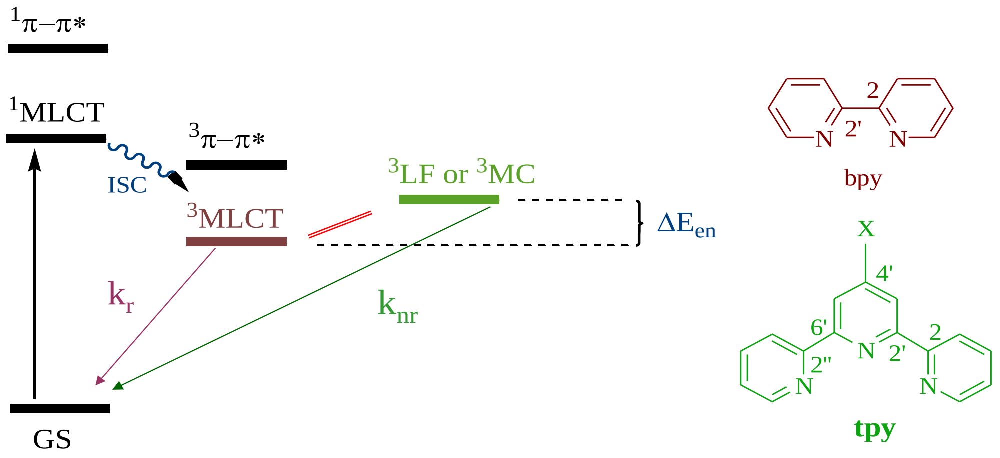

Figure 1.2. Simplfied energy profile diagram

1.4. Fabrication of Logic Functions

Electronic devices play a crucial role in our daily life which has reformed the world through communication, sharing information, storing and processing of data.[30-45] The working principle of these digital electronic devices are based on few logics of Boolean algebra. In real scenario, Boolean algebra deals with two binary codes “On-state (1)” and “Off- State (0)”. The data processing was depended upon the logic operation of single or multiple logic inputs which gives a single output in each case. Usually, eight fundamental logic operation are used for this purpose. They are OR, AND, XOR, NOR, NAND, XNOR, INHIBIT (INH) and IMPLICATION (IMP). Several complicated combinational logic operations are also possible based on the fundamental logic systems. The fundamental circuits undergo arithmetic and other complicated operation and give rise to different complicated circuits, such as half-adder/subtractor, [81-85] keypad-lock, [84-86] set-reset-flip-flop,[86-89] memory-device,[88-90] multiplexer/demultiplexer/exciplex,[91-93] and encoder/decoder[34] etc.

Silicon based technology are very efficient for modern integrated circuits but the only limitation is its size. Molecular computation is superior in comparison with silicon-based devices as it can deals with the information upto nanometer scale. Hence, molecular mimicry of logic gates has considered as potential alternative which is proposed by a de Silva in 1993.[30-31] Thus, deigning of stimuli responsive molecules are important in term of molecular level computation. Output signal of these molecules upon interaction of various external stimuli (such as temperature, anion, cation, pH, light, etc) are often utilized to fabricate different binary logic functions.

1.5 A Brief Review of Ruthenium (II) Complexes Derived from Poly-Pyridine Ligands

Different research group across the world has published various notable reviews and papers pointing out the photophysical, photochemical and electrochemical properties of Ru(II) complexes based on polypyridine ligands (mainly bpy or tpy).[23-29,69-75] The optoelectic properties of the complexes can also be tuned either by altering the electronic distribution in ligand backbone or by interaction with various external guests such as anion, cation, temperature, pH, solvent and light. Some relevant literature similar to our present study will be reviewed in this dissertation.

Balzani and co-workers have reported a series of complexes of the type $[Ru(tpy\text{-}X)(tpy\text{-}Y)]^{2+}$, where X and Y represent electron-donating and withdrawing groups at the 4′-position of the terpyridine moiety (Scheme 1.1).[26,94] It is observed that electron withdrawing groups give more stability to lowest unoccupied molecular orbital (LUMO) which is mainly located in the ligand moiety in comparison to metal-based highest occupied molecular orbital (HOMO), So the complexes absorb at lower energy. Incorporation of electron withdrawing group, on the other hand, lowered the energy of ^{3}MLCT state with a reduction of thermal population of the ^{3}MC state. As consequence, the excited properties of the complexes improved substantially (X = H, Y = SO_2Me: λ_{max} = 679 nm, τ = 36 ns; X = SO_2Me, Y = SO_2Me: λ_{max} = 666 nm, τ = 25 ns). By contrast, the electron-donating group destabilized the metal-based HOMO more than ligand-based LUMO, keeping the ^{3}MC state unaltered. A mixture of electron-donating and electron-withdrawing groups, improves the luminescent properties of the complexes substantially and the longest excited lifetime was observed for X = OH, Y = SO_2Me (λ_{max} = 706 nm, τ = 50 ns).[94]

Indelli et al. reported the solvent-dependent photophysics of a new series of tricyano-terpyridine complexes (Scheme 1.2).[95] The luminescence properties of the complexes strongly depend upon the second-sphere donor-acceptor (SSDA) mechanism of cyanide moiety and the solvent. With the increase of the acceptor nature of the solvent, the MLCT band energy increases. An enormous improvement of excited-state lifetime of complexes was observed. This is a classic example demonstrating proper usage of ancillary ligands could substantially enrich the luminescence characteristics of Ru(II)-tpy complexes.

	X	**Y**
1.	**$MeSO_2$**	**$MeSO_2$**
2.	**Cl**	**Cl**
3.	**H**	**H**
4.	**Ph**	**Ph**
5.	**EtO**	**EtO**
6.	**OH**	**OH**
7.	**Me_2N**	**Me_2N**
8.	**H**	**$MeSO_2$**
9.	**OH**	**$MeSO_2$**
10.	**Cl**	**EtO**
11.	**OH**	**Ph**
12.	**$MeSO_2$**	**Me_2N**
13.	**Cl**	**Me_2N**
14.	**OH**	**Me_2N**

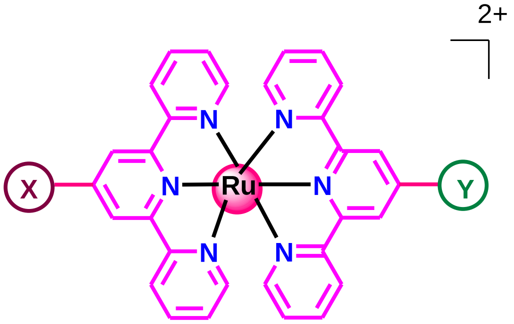

Scheme 1.1

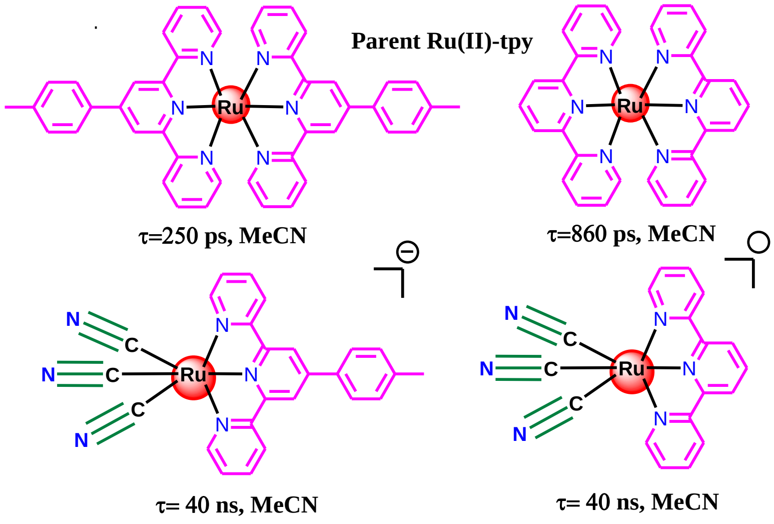

Scheme 1.2

Incorporation of π-conjugated aromatic rings in the ligand moiety is also an important strategy for improving the RT emission characteristics (Scheme 1.3).[96] It is observed that introduction of pyrimidine ring in the 4′-position of a terpyridine can improve the luminescence property quite substantially.[97] π-conjugation can be further increased by introduction of a second conjugated rings (pyrimidine, phenyl, pentafluorophenyl) in the para-position of the first pyrimidine ring. As a consequence, the triplet MC-MLCT energy gap increases and leads to good emission properties in the complexes with enhancement of lifetime values up to 200 ns.

Hanan and co-workers reported a new array of Ru(II)-terpyridine complexes where different heterocyclic units (triazines, pyrimidines or N-heterocyclic carbenes pyridine) have been introduced in the pyridine rings of the terpyridine moiety (Scheme 1.4).[98] Incorporation of additional N-atoms stabilize the ligand centered LUMO whereas the metal center becomes electron deficient. As a result, the absorption and emission spectra show a bathochromic shift compared to their analogues derivative with lesser number of N-atom (Table 1.2). This behavior is also reflected in their MC-MLCT energy gap which in turn improved the luminescence properties of the complexes substantially. Presence of extra N-atom in complex backbone increases the probability of hydrogen bonding and the complex structure becomes planner which facilitates delocalization of π-electron through aromatic moieties.

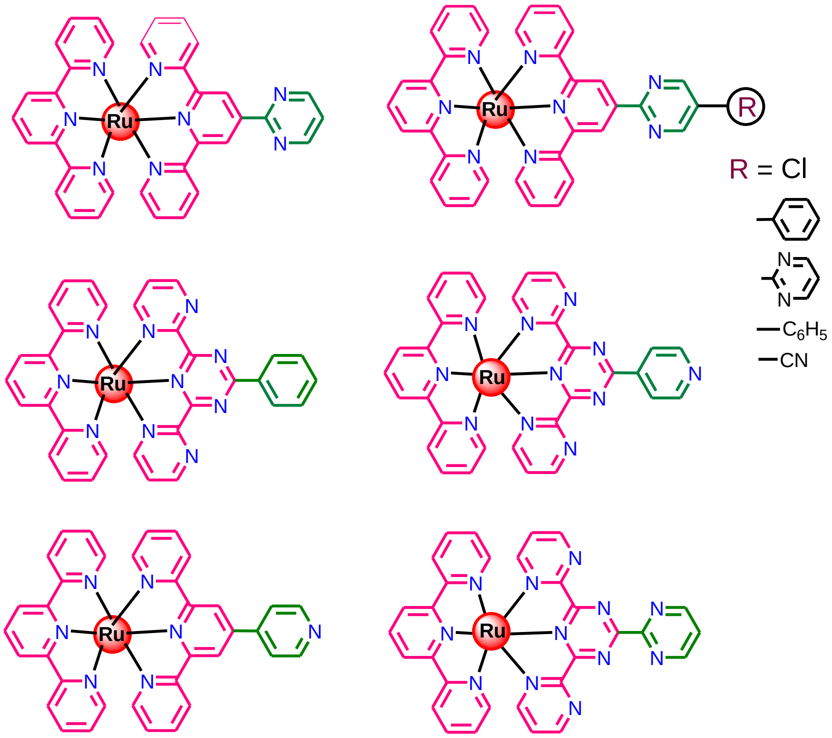

Scheme 1.3

Table 1.2. Photophysical and Electrochemical Data of Complexes in MeCN at RT as presented in Scheme 1.4

Complex	λ_{abs}/nm	$\varepsilon/10^4\ M^{-1}cm^{-1}$	λ_{em}/nm	τ/ns	ϕ	E_{ox}/V	Ref
A	492	1.33	646	3.6	1×10^{-4}	1.22	98
B	500	1.46	716	8.4	3×10^{-5}	1.56	
C	497	3.4	658	3.8	74×10^{-5}	0.89	
D	490	2.3	738	30	17.5×10^{-4}	1.36	

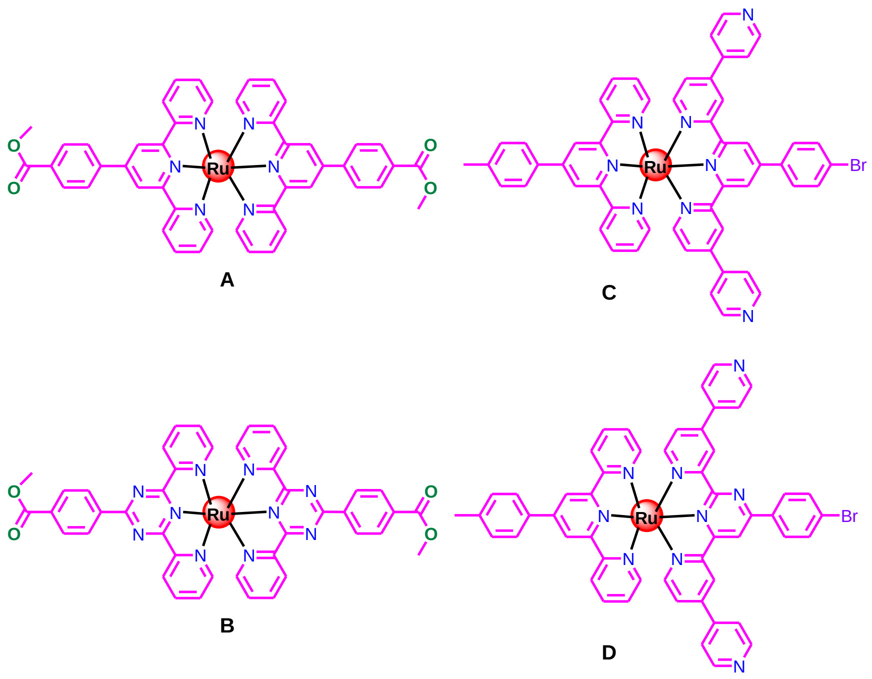

Scheme 1.4

Incorporation of fused aromatic unit into the terpyridine unit could also improve the emission properties of Ru(II)-tpy complexes. Constable and co-worker incorporated an anthracene moiety in the 4′-position of terpyridine unit of a Ru(II)-tpy moiety.[99] A metal centered emission is observed at 650 nm. Another literature is found where a pyrene unit is introduced in 4′-position of terpyridine (Scheme 1.5).[100]

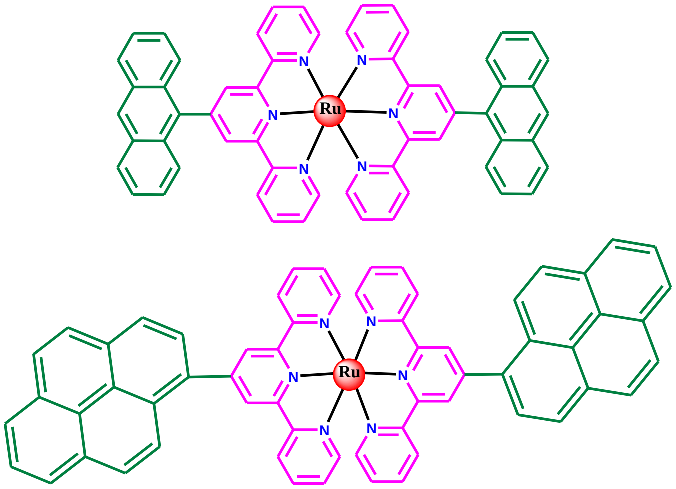

Scheme 1.5

Campagna and Hanan group reported homo- and hereoleptic complexes of Ru(II) derived from tridentate polypyridine ligands where terpyridine unit is connected to anthracene moiety through a pyrimidyl spacer (Scheme 1.6 a,b).[101] It is observed that the incorporation of polyaromatic unit has improved the excited state luminescence properties significantly. This group beautifully demonstrated another important work highlighting the application of Ru(II) complexes as excited state storage element.[102] In the reported complexes, the Ru(II) metal is sandwiched between a pyrimyl-tpy and an anthryl-tpy unit (Scheme 1.6c). Complexes exhibit impressive emission characteristics with bi-exponential decay profile. It is clear from the emission data that energy of the emissive ^{3}MLCT state gets lower in comparison with non-emissive triplet of anthracene (^{3}An). The shorter component arises from the initially formed ^{3}MLCT whereas the long component generated from the equilibrated state of ^{3}MLCT and ^{3}An. (τ_1 varies from 10-28 ns, τ_2 varies from 698-1040 ns).

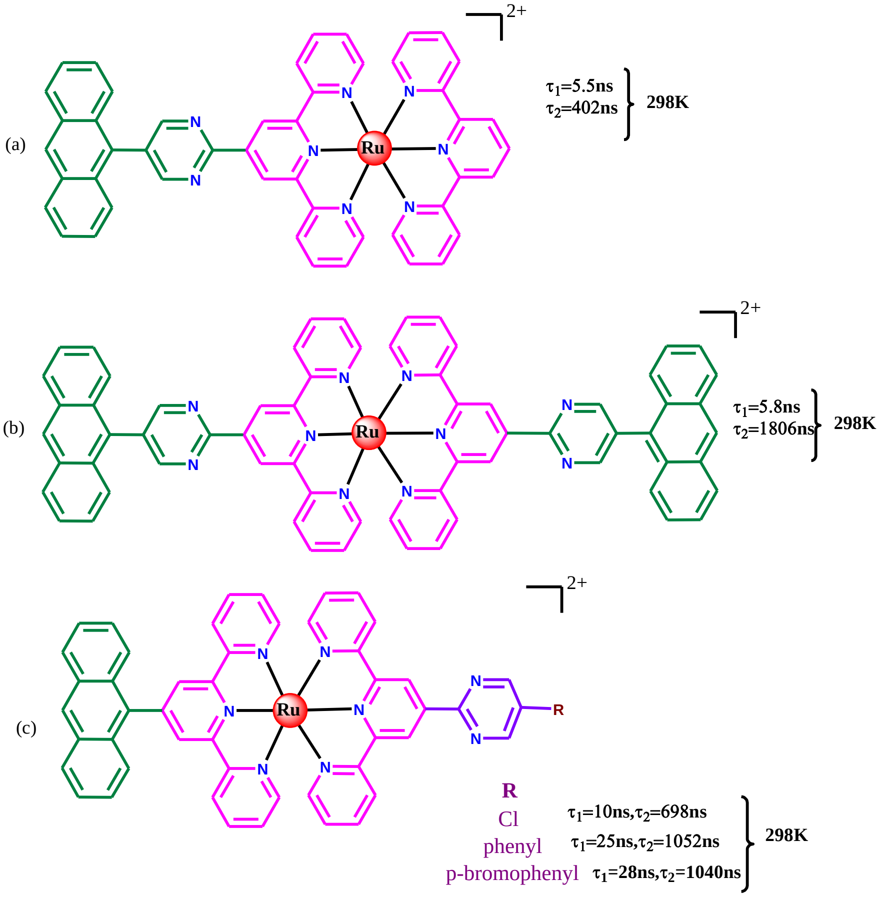

Scheme 1.6

Baley and co-worker found that introduction of different heterocyclic ring (such as furyl, pyrrolyl, thienyl and bithienyl groups) into the terpyridine moiety can effectively enhance the excited state emission properties (Scheme 1.7).[103] The heterocyclic rings increase the extent of delocalization and the ^{3}MLCT gets stabilized. As a result, triplet MC-MLCT energy gap increased and consequently improvement of luminescence properties was observed. Emission quantam yield is found to be quite high in comparison to the parent $[Ru(tpy)_2]^{2+}$, notably the bithienyl substituted complex shows 100 times higher emission quantum yield. The electron-donating effect of the heterocyclic unit destabilizes the metal centered HOMO and a bathochromic shift is reflected in the absorption and emission profile of the complexes.

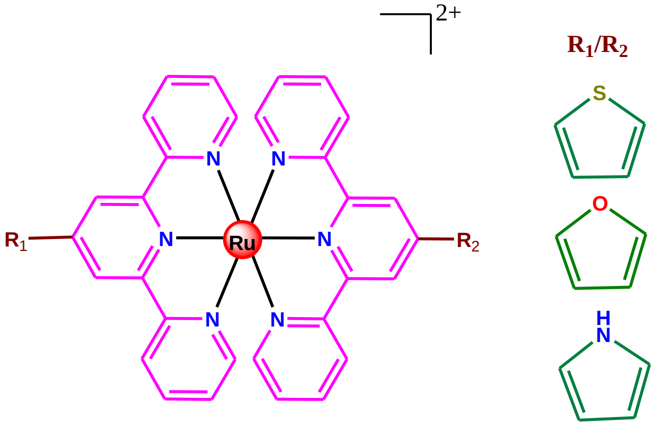

Scheme 1.7

Siemeling's group demonstrated the photophysics of a series of Ru(II)-tpy complexes where 4′ position of terpyridine moiety is connected with either a ferrocenyl (Fc) or octamethyl ferrocenyl substituent (Fc$^{\#}$) (Scheme 1.8).[104] The reported complexes show a ^{1}MLCT band in region of 489-505 nm. The ferrocene derivatives of Ru-tpy display poor emission properties due to the presence of Fc-unit which quench the emissive ^{3}MLCT either by energy transfer or by reductive electron transfer pathway. The length of the spacer plays a crucial role in emission properties of the complexes. The longest spacer exhibits maximum luminescence properties. Improvement of luminescence characteristics is also observed upon oxidation of the ferrocenyl moiety.

Schubert et. al. reported Ru(II)-terpyridine complex based on long chain polymeric π-conjugated system which exhibits its potential to act as white light emitter (Scheme 1.9).[105] The complex displays a strong absorption band at ~500 nm and a emission band at 640 nm. The ^{3}MLCT state gets stabilized via enhanced π-conjugation of the ligand and plausible equilibrium between ^{3}MLCT and ^{3}LC states is responsible for the observed room temperature phosphorescence with lifetime (τ_P) of 36.5 ns.

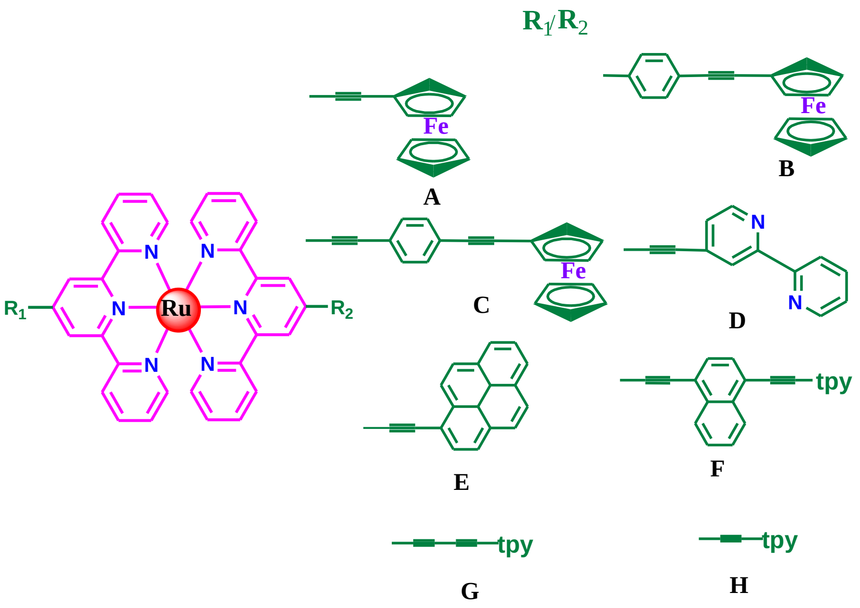

R_1	R_2	τ/ns
H	A	260
A	A	260
H	B	< 20
B	B	< 20
H	C	120
C	C	110
H	D	75
H	E	580
H	F	415
H	G	170
H	H	55

Scheme 1.8

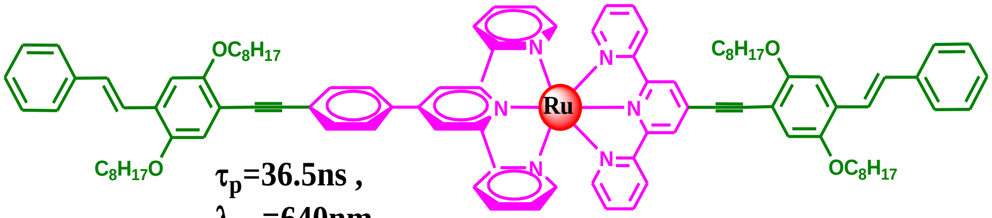

τ_p=36.5ns ,
λ_{em}=640nm

Scheme 1.9

Vos's group reported a series of Ru(II)-terpyridine complexes connected with triazole/tetrazole motifs (Scheme 1.10).[106-107] All of them display intense absorption band near 480 nm and emission band near 700 nm at RT. Their lifetimes vary between 20 and 80 ns. σ-donor characteristics of ligands increased upon deprotonation which in turn enhances the energy of the ^{3}MC state. As a consequence, deprotonation of the triazole/tetrazole moiety leads to enhancement of the lifetime almost double in comparison with parent Ru(tpy)$_2$. By contrast, the emission intensity gets quenched upon protonation.

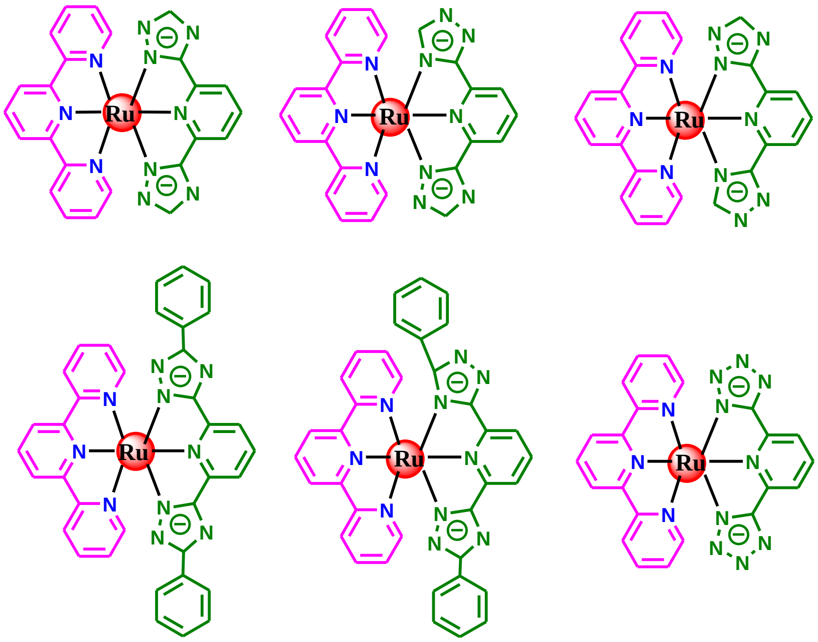

Scheme 1.10

Harriman and co-worker reported Ru(II)-terpyridine complexes incorporating an ethynylene substituent and studied their temperature-responsive emission characteristics (Scheme 1.11a).[108] The complexes display a strong absorption peak at ~490 nm due to MLCT transition and emission near 680 nm at RT in butyronitrile. It is observed that with lowering of temperature both the luminescence intensity and quantum yield increases.

In a separate work, they introduced hydroquinone unit into the R(II)-tpy-phenylethynyl moiety to tune their luminescence properties (Scheme 1.11b,c).[109]

Excitation on the MLCT band in the complexes generates a triplet state which in turn delocalized onto the tpy-phenylethynyl moiety. The excited state lifetime of the complex is ~46 ns which enhanced remarkably on lowering of temperature. Upon oxidation of hydroquinone to benzoquinone, promotion of an electron takes place from the ^{3}MLCT to the quinone moiety and subsequently the excited lifetime decreases to 190 ps together with quenching of emission.

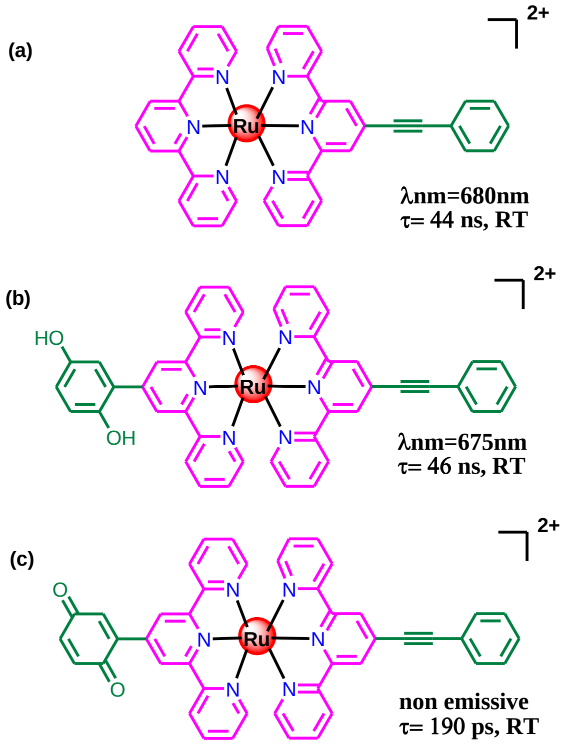

Scheme 1.11

Cyclometallation is also an effective synthetic strategy for improvement of RT luminescence properties of Ru(II)-terpyridine type complexes and the literature on this topic is quite exhaustive.[27,110-111] Sauvage and co-workers reported a series of cyclometallated Ru(II)-tpy complex coupled with phenyl-phenanthroline type unit (Scheme 1.12).[110] A huge increase in excited state lifetime was reported for cyclometallated complex in comparison with non-cyclometalled. Lifetime is found to be in the range of 70 to 130 ns. The emission maxima of cyclometallated complexes are also red-shifted. This happens because the σ-donation power increases upon cyclometallation which in turn populates electron density in metal centre and effectively increases the ^{3}MLCT-^{3}MC energy gap.

Berlinguette and co-worker reported a new array of Ru(II) cyclometalated complexes based on different substituted terpyridine-triazole unit (Scheme 1.13).[111] The complexes exhibit excited state lifetime in the microsecond range and steady state emission maximum varies in the range of 643-694 nm. The introduction of triazole motif is the main reason behind such a remarkable improvement of excited state properties because it has a strongly σ-donating and weakly π-accepting tendency. It actually increases the energy separation between ^{3}MLCT and MC states. It is observed the incorporation of electron-donating and electron-withdrawing group in the ligand moiety further increase the MLCT-MC energy gap which is reflected in their excited-state lifetimes.

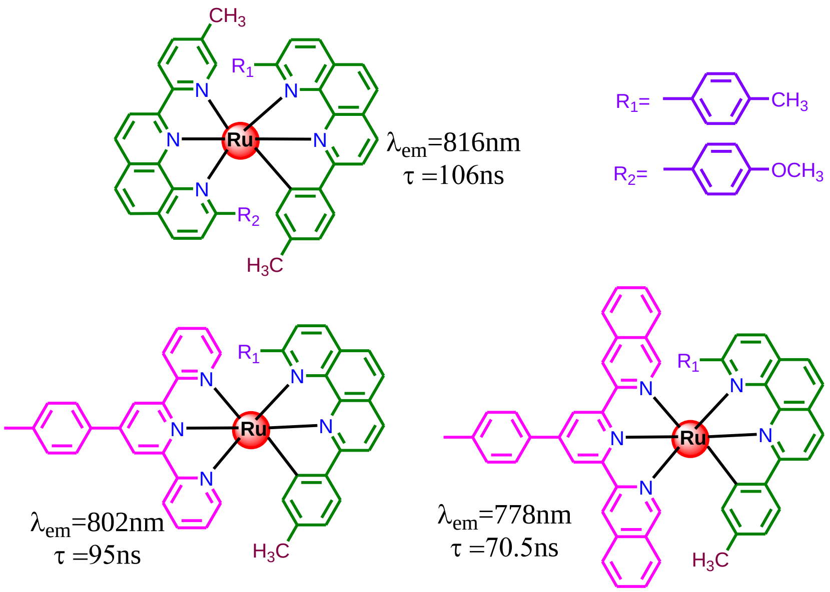

Scheme 1.12

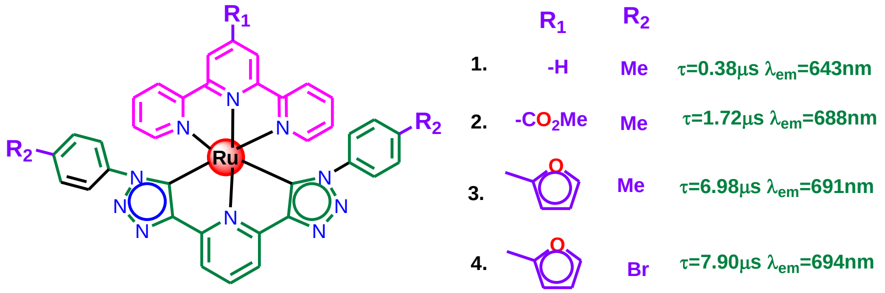

Scheme 1.13

1.6. Switching of Photophysical and Electrochemical Properties Ruthenium (II) Complexes Derived From Poly-pyridine Ligands

In the previous section, several strategies for improvement of excited state characteristics of Ru(II)-terpyridine type complexes have been discussed. The researchers across the globe are also interested to systematically tuned photo-redox behaviors of Ru(II)-polypyridine complexes upon the action of different external stimuli for making these complexes as useful building blocks for a large variety of applications. A brief review of the stimuli-responsive photophysical and electrochemical behaviors of Ru(II)-polypyridine complexes will be done in the next section.

Sessler and co-workers demonstrated the anion sensing studies of Ru(II)-polypyridyl complexes of dipyrrolylquinoxaline (DPQ) phenanthroline derivatives (Scheme 1.14).[112-113] It is observed that on coordination with Ru^{2+}, the NH protons of the pyrrole moiety becomes more acidic in comparison of free ligand. The complex strongly interacts with F^- in DMSO with a value of binding constant being 1.2×10^4 M^{-1}, which is almost 30 times higher than that of free ligand. This group reported another similar type Ru(II) complex (**2**), where the change of emission characteristics with $H_2PO_4^-$ is taken under consideration. The emission intensity at 630 nm gets quenched with incremental addition of $H_2PO_4^-$ with a binding constant of 1.0×10^5 M^{-1}. It is evident from Jobs-plot that a 1:1 complex is formed with $H_2PO_4^-$.

Later, Anzenbacher and co-workers studied a luminescence-lifetime based sensor of related Ru(II)-complex (**3**).[114] In this case, both the emission intensity and excited state lifetime decreases with addition F^- and CN^- in MeCN medium and binding constant values are found in the range of 4.3×10^5 M^{-1} to 6.4×10^5 M^{-1}.

Ye and co-worker synthesized a series of Ru(II)-complexes based on bis-imidazole derivatives (**4-7**) and studied their anion-induced modulation of photophysical and electrochemical properties (Scheme 1.15).[115-118] The complexes posses two NH-protons in their secondary co-ordination sphere. Depending upon the basicity of the anion and acidity of NH proton, the complexes exhibit three types interaction between imidazole NH protons and the anions (anion-NH hydrogen bonding, mono-deprotonation, and double-deprotonation) (Figure 1.3). It is observed that Cl^-, Br^-, I^-, NO_3^-, HSO_4^-, $H_2PO_4^-$, and OAc^- anions forms H-bonding adduct with complex **4** and excess addition of OAc^- gives the mono-deprotonated complex with a visual color change from yellow to orange. But in presence F^-, double-deprotonation occurs in two consecutive steps and finally the color of the solution turns violet.

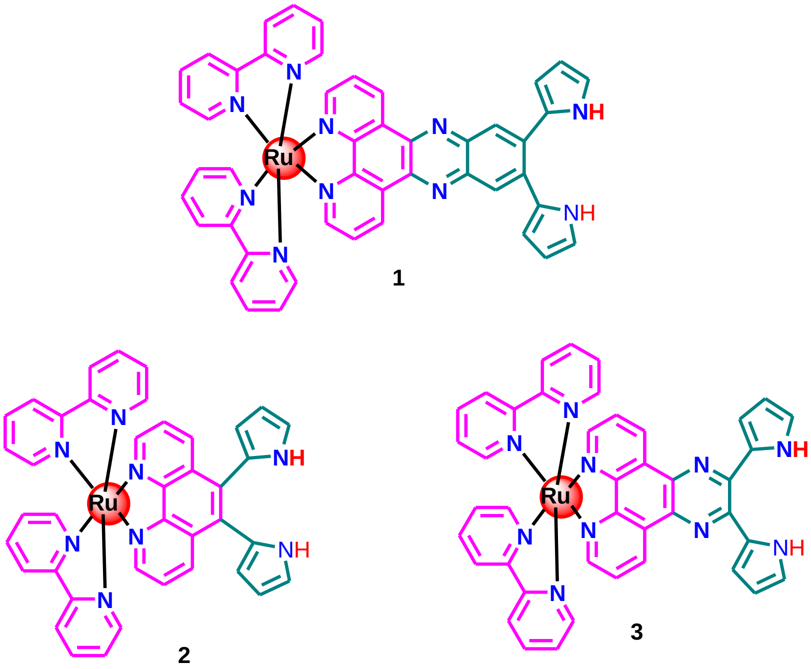

Scheme 1.14

In case of bis-benzimidazole complex (**5**), a similar trend is observed for both F^{-} and OAc^{-}**.**[115] First step deprotonation is observed with low concentration of anion (F^{-} and OAc^{-}) but excess anion leads to complete deprotonation of the complex. Two different types of binding nature of **4** and **5** with anions could be attributed to difference in their pK_a values (7.2 for **4** and 5.7 for **5**).

The methyl-substituent bis-benzimidazole complex **(6)** exhibits a p*K*a value of 6.2 which is in-between the p*K*a values of complex **4** and **5.**[116-118] In presence of weakly basic anion, complex **6** displays an increase in photoluminescence intensity at 617 nm with a slight bathochromic shift. The main reason is the rigidity of the complex-anion adduct due to strong H-bond with weakly basic anion which actually diminishes the non-radiative deactivation of ^{3}MLCT state. But in presence of strongly basic anions (F^{-} and AcO^{-}), the emission intensity decreases due to complete deprotonation of the imidazole NH protons.

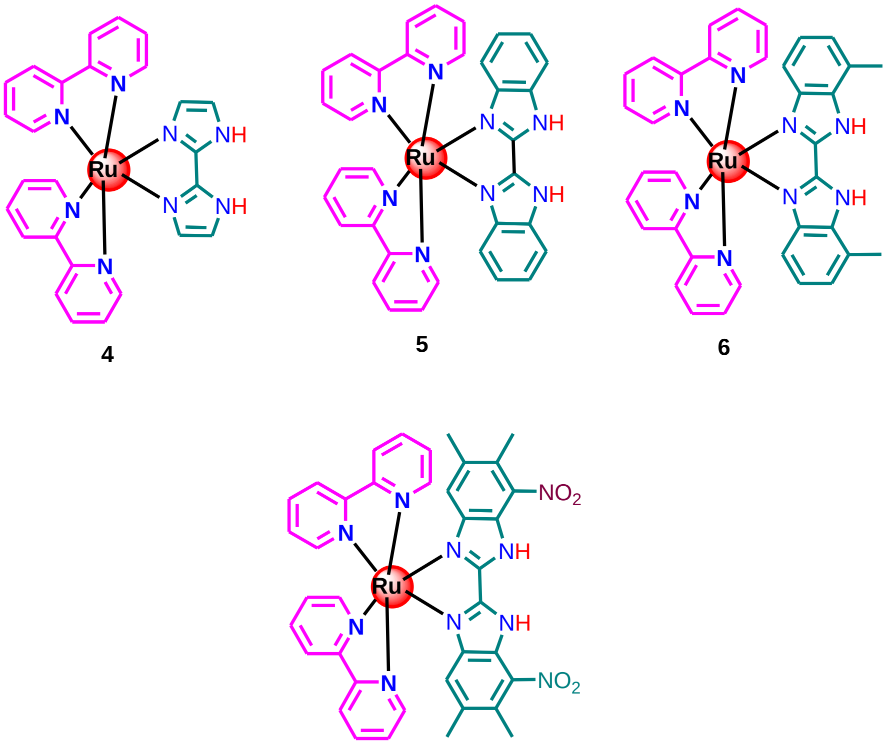

4 **5** **6**

7

Scheme 1.15

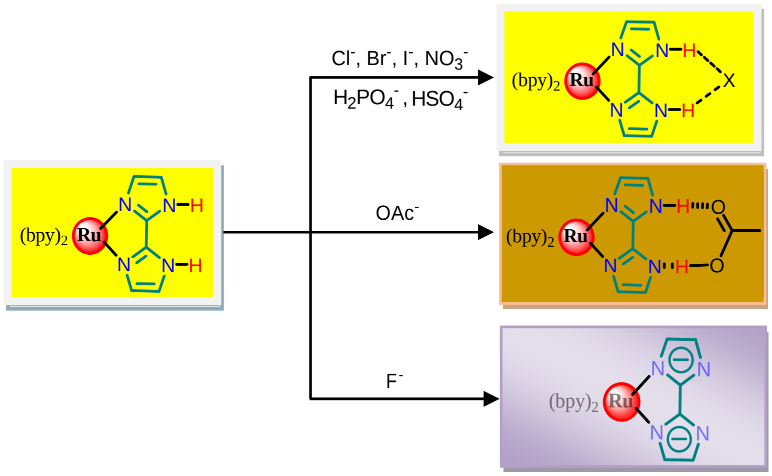

Figure 1.3. The interaction mode of complex 4 with different anion.

The nitro-derivative of bis-benzimidazole complex **(7)** displays different behavior with weakly basic anions.[118] The metalloreceptor exhibits strong affinity for Cl^- and Br^-, a weak affinity for I^- and no such effect for NO_3^- and HSO_4^-. In essence, Ye and co-worker beautifully demonstrated the effect of variation of peripheral unit of the metallo receptor on their anion sensing characteristics.

Molina and co-workers designed a Ru-complex derived from a ferrocene appended phenanthroline-imidazole ligand (Scheme 1.16).[119] The complex **(8)** posses sensing selectivity for Cl^-. A significant increase in luminescence intensity is observed with gradual addition Cl^- (almost 30 times). Additionally, the cathodic shift of Fe(II)/Fe(III) couple is also observed without alteration of Ru(II)/Ru(III).

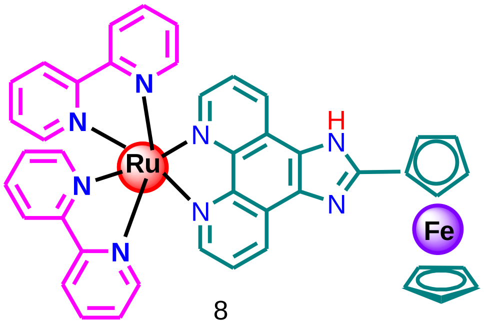

8

Scheme 1.16

Baitalik and co-worker reported Ru(II) and Os(II)-bpy complexes (**9** and **10**) incorporating a pyrenylimidazole-10-pyridin-2-yl-9H-9,11-diazacyclopenta[e]pyrene (HImzPPy) ligand (Scheme 1.17).[120] DNA and anion binding studies of complexes were investigated via absorption, steady sate and time-resolved emission as well as by circular dichroism spectroscopy. In presence of excess F^- and OAc^- ions, the imidazole NH proton gets deprotonated which induces marked reduction in emission intensity and leads to the "Off-state". But a different scenario is observed in case of H-bond interaction with $H_2PO_4^-$ which induces enhancement of emission intensity and represents to the "On-state". The binding constant of these systems were found to be in the order of 10^6, while the detection limit in the order of 10^{-9}(M).

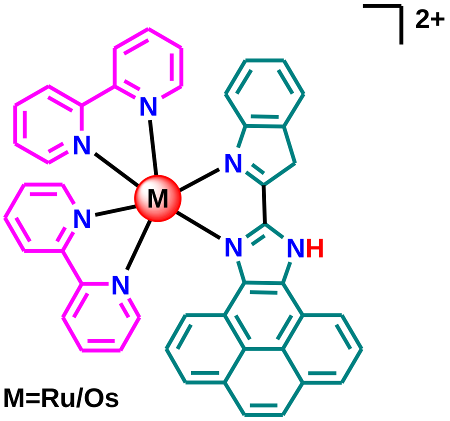

9/10

Scheme 1.17

Baitalik and coworkers also designed a Ru(II) monometallic complex based on a heteroditopic bpy-tpy type ligand of composition, $(bpy)_2Ru(tpy\text{-}Hbzim\text{-}dipy)] (ClO4)_2$ (**11**) (Scheme 1.18).[121] The complex (**11)** exhibits an absorption peak near 470 due to MLCT transition. The complex also displays solvent-dependent emission spectrum with its maximum lying between 628 and 649 nm with excited state lifetime in the range 116-257 ns. Both anion and cation sensing ability the complex was investigated through different optical channels. It is observed that in presence of $H_2PO_4^-$ and HSO_4^-, the emission intensity increases designating the "On-state", whereas presence of more basic anions (F^- and AcO^-) , gives rise to reduction in emission intensity representing the "Off-state". The cation sensing aspect of the complex was also studied by taking advantage of its free terpyridine motif. Fe^{2+} among the other bivalent 3d cation exhibits visual color of the complex from yellow to violet and thus act as a suitable colorimetric senor for Fe^{2+}.

Later, this same group reported an array of Ru(II)-terpyridine complexes (**12-14**) coupled with an anthraquinone unit (Scheme 1.19).[122] Complexes exhibit excellent luminescence properties at RT. The RT lifetime of the complexes varies in the range of 1.5-52.8 ns, depending upon solvent as well the ligand architecture. Presence of electron withdrawing anthraquinone unit enhanced the acidity of NH protons. Taking advantage of it, anion induced tuning of photophysical properties of the complexes were performed in both organic as well as aqueous solutions. It is found that the complexes has an admirable selectivity towards CN^{-} in aqueous solution with limit of detection values in the order 10^{-8} M.

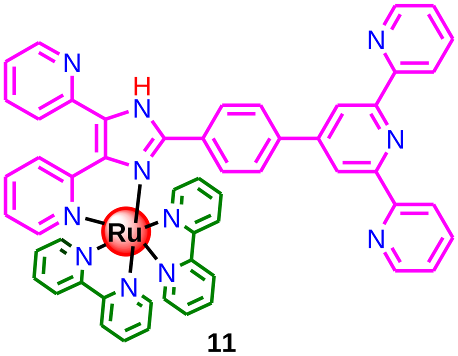

11

Scheme 1.18

Das and co-worker designed a series of Ru(II)-bpy monomers (**15-17**) based on dipyridylamine ligand moiety (Scheme 1.20).[123] Anion sensing behavior of the complexes were thoroughly investigated via. absorption, emission and cyclic voltametry. It is observed that complexes can act as potential sensor for selected anions such as F^{-} and CN^{-}, which is also reflected in their visual color change.

Schmittel and co-worker designed two Ru(II)-complexes (**18-19**) based on bypyridine and phenanthroline unit containing free -CHO group in their second co-ordination sphere (Scheme 1.21).[124] The complexes display high selectivity towards CN^{-} via formation of cyanohydrins intermediate. It is observed that the emission intensity of the complexes enhanced with a blue shift of ~100 nm with gradual addition of CN^{-}. A change of visual color from red to orange is also noticed.

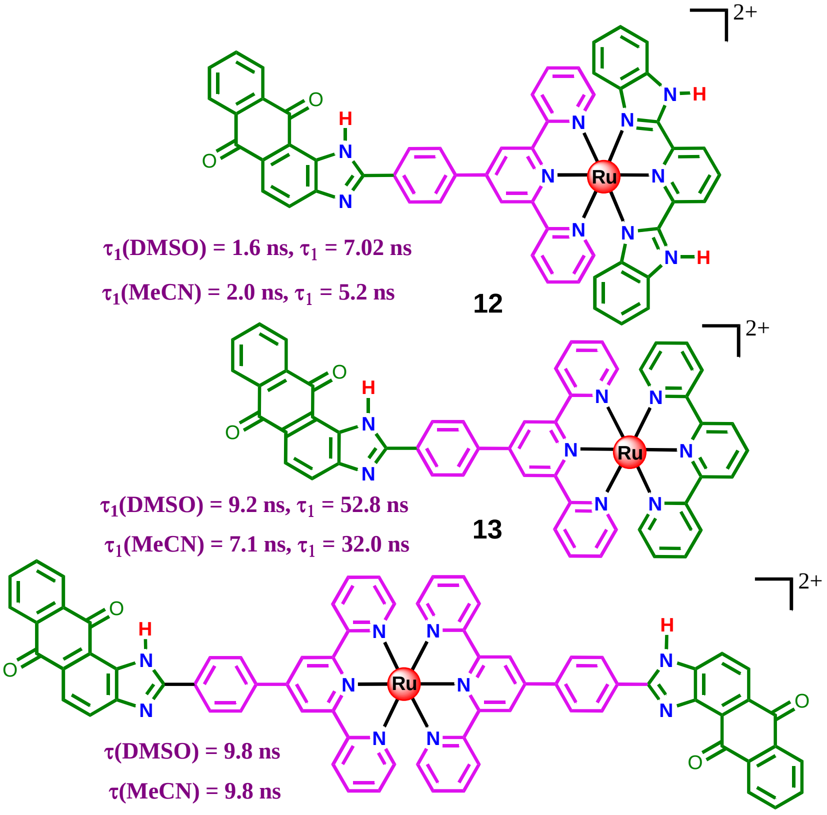

τ_1(DMSO) = 1.6 ns, τ_1 = 7.02 ns

τ_1(MeCN) = 2.0 ns, τ_1 = 5.2 ns

12

τ_1(DMSO) = 9.2 ns, τ_1 = 52.8 ns

τ_1(MeCN) = 7.1 ns, τ_1 = 32.0 ns

13

τ(DMSO) = 9.8 ns

τ(MeCN) = 9.8 ns

14

Scheme 1.19

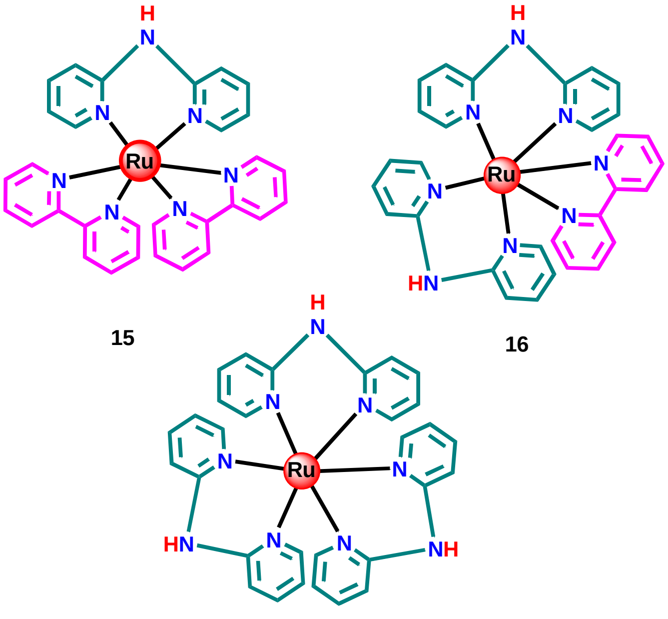

15

16

17

Scheme 1.20

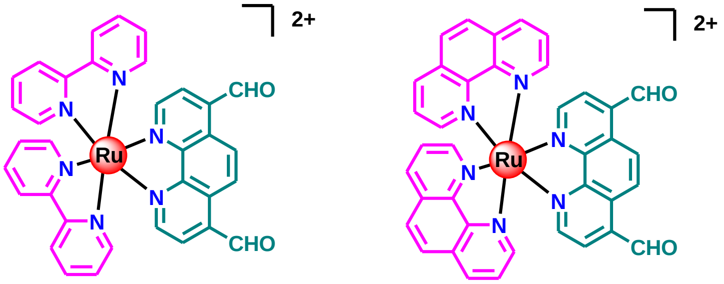

18

19

Scheme 1.21

1.7. A Brief Review on Logic Gates

Computer has emerged as an inevitable tool during last few decades with regard to high level calculations, data processing, communication or sharing information.[29-48] The consciousness of information processing and computation at the molecular level was first recognized by De Silva in1993. The motivation was to construct very small size as well as powerful computers which could not be fabricated with traditional silicon based technology. Logic gates are the devices used to perform binary arithmetic and logical operations which actually constitute the basis of modern computers. The computation at the molecular level is possible only with molecular logic gate, which is capable of integrating simple logic gates into combinational circuits and thus have the potential for computation on a nanometer scale that silicon-based devices cannot address. The whole process is carried out through some encrypted data in the form of binary digit. The binary actually deals with two extremes, either 0 or 1. Different basic logic gates together with their outputs are represented in Table 1.3. A brief literature survey on selected molecular logic gates are discussed below.

Table 1.3. Truth Table of Different Binary Logic Gates

Output / Input		IMPLICATION	INHIBIT	OR	XOR	NOR	XNOR	AND	NAND
0	0	1	0	0	0	1	1	0	1
0	1	1	1	1	1	0	0	0	1
1	0	0	0	1	1	0	0	0	1
1	1	1	0	1	0	0	1	1	0

Redmond and co-worker reported the construction of two input NOR logical behavior of a Ru(II) complex (Scheme 1.22).[125] They choose applied electric field as input 1 and Cu^{2+} ion as the input 2. In presence of any of the two inputs, the luminescence intensity at 668 nm gets quenched and corresponds to the “Off- state”. The “On-state” is only feasible when no input is applied. Thus, the system can mimic the function of NOR-gate.

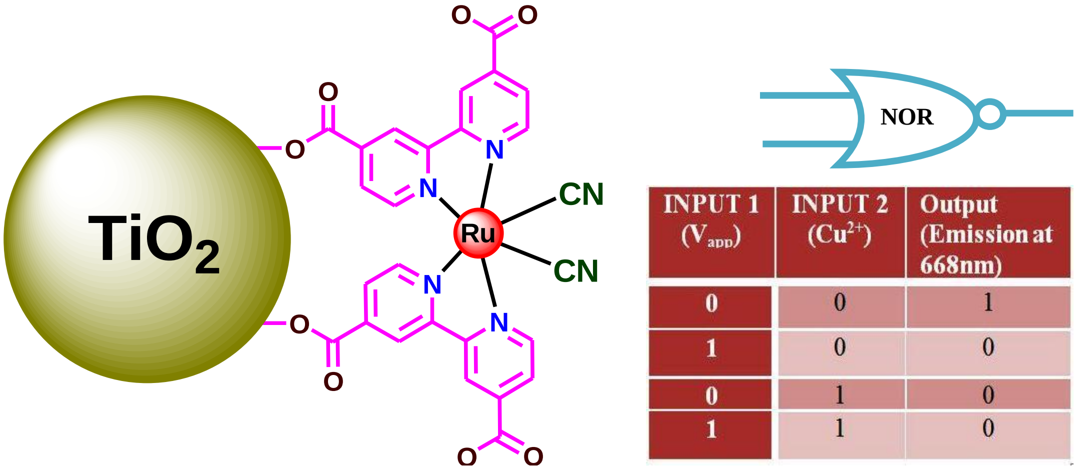

INPUT 1 (V_{app})	INPUT 2 (Cu^{2+})	Output (Emission at 668nm)
0	0	1
1	0	0
0	1	0
1	1	0

Scheme 1.22. NOR logic gate in presence of electric field and Cu^{2+} ion.

Li and co-worker developed Ir(III)-based chemosensor which can mimic the function of AND and INHIBIT logic gate in presence of Hg^{2+} and histidine (Scheme 1.23).[126] It is observed that the complex is non-luminescent in its free form but in presence of histidine, the emission intensity increases slightly whereas a huge increase in emission intensity is observed in presence of both histidine and Hg^{2+}. Thus, the Ir(III)-based receptor demonstrates the function of two input AND and INHIBIT logic gate as shown in Scheme 1.23.

Kumar and co-worker designed an optical chemosensor derived from pyrene-thiacalix[4]arene of 1,3-*alternate* conformer (Scheme 1.24).[127] It is observed that the receptor demonstrates the function of XNOR gate in presence of Fe^{3+} and F^- ions. They have monitored the emission intensity at 386 nm as the output signal. In presence or absence of both inputs (Fe^{3+} and F^{-}), the output signal is in “on-state”, whereas in presence of any of the inputs, the output signal is in “off -state”.

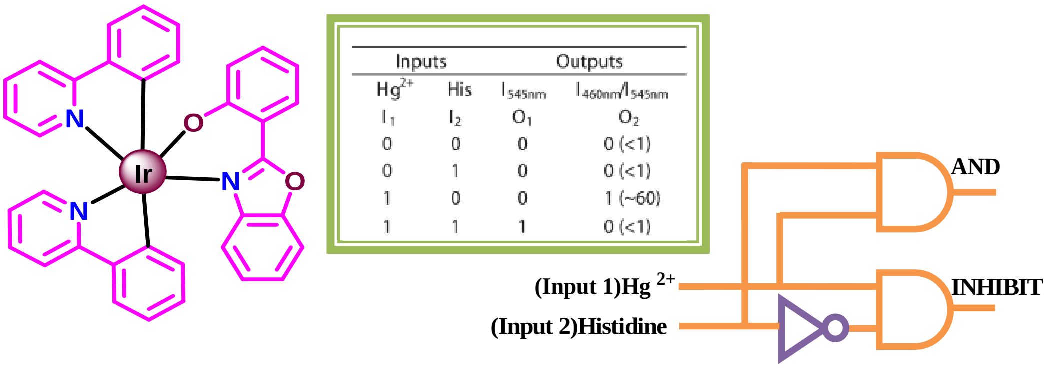

Inputs		Outputs	
Hg^{2+}	His	I_{545nm}	I_{460nm}/I_{545nm}
I_1	I_2	O_1	O_2
0	0	0	0 (<1)
0	1	0	0 (<1)
1	0	0	1 (~60)
1	1	1	0 (<1)

Scheme 1.23. AND and INHIBIT logic gate in presence of histidine and Hg^{2+}.

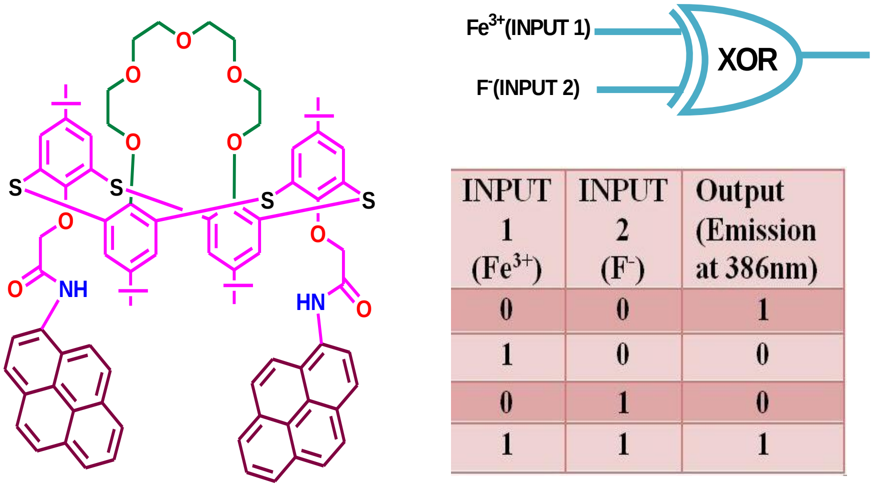

INPUT 1 (Fe^{3+})	INPUT 2 (F^{-})	Output (Emission at 386nm)
0	0	1
1	0	0
0	1	0
1	1	1

Scheme 1.24. XOR logic gate in presence of $F^{-}$and Fe^{3+}.

Yen and co-worker designed a receptor incorporating oxygen and sulfur donor atoms which can mimic the functions of several logic gates as shown in Scheme 1.25.[128] The emission intensity at 473 nm was utilized as the output signal in presence of Fe^{2+} and $NOBF_4$ inputs for the construction of NAND gate. Addition of any one of the two inputs does not alter emission spectral behavior of the receptor, whereas simultaneous addition of the inputs leads to quenching of emission intensity and thereby mimic the function of a NAND gate.

Secondly, alteration of emission intensity at 473 nm under the influence of $[(NH_4)_2Ce(NO_3)_6]$ and CF_3COOH was utilized for the construction of AND gate. In presence of any of the two inputs (Ce^{4+}/H^+), the emission intensity remains below threshold level, whereas the presence of both of the inputs raises the emission signal above the threshold level. In essence, the function of an AND gate is mimicked.

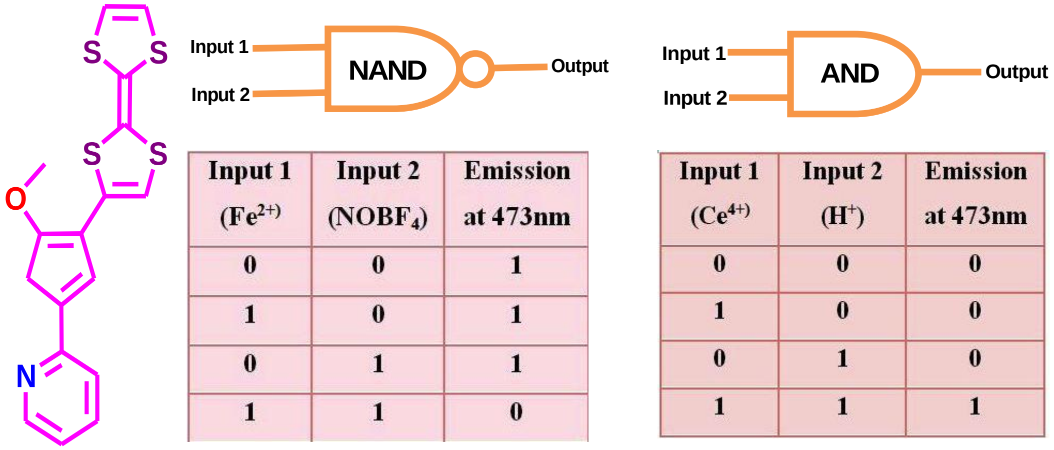

Input 1 (Fe^{2+})	Input 2 ($NOBF_4$)	Emission at 473nm
0	0	1
1	0	1
0	1	1
1	1	0

Input 1 (Ce^{4+})	Input 2 (H^+)	Emission at 473nm
0	0	0
1	0	0
0	1	0
1	1	1

Scheme 1.25. Molecular system mimics the function of NAND and AND logic gate.

Awasthi and co-worker designed an imidazole-carboxylate based Os(II)-bpy complex which can mimic the function of combinational logic (Scheme 1.26).[129] It is observed that the brown color of the complex turns to colorless in presence of Cu^{2+} while upon addition of H_2O the complex regains its original brown color. Cu^{2+} and H_2O were utilized as two inputs and absorption at 509 and 293 nm were monitored as the output signals. Absorption signal at 509 nm leads to fabrication of an INHIBIT logic whereas the signal at 293 nm gives rise to construction of an IMPLICATION logic gate.

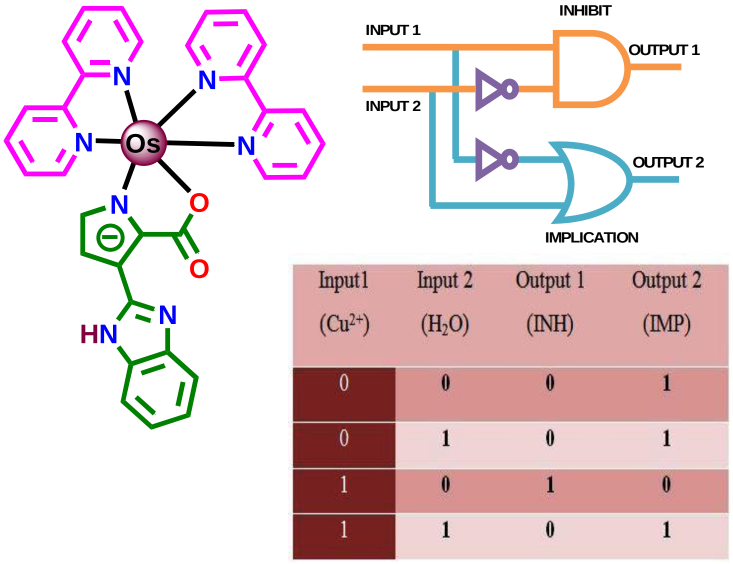

Input1 (Cu^{2+})	Input 2 (H_2O)	Output 1 (INH)	Output 2 (IMP)
0	0	0	1
0	1	0	1
1	0	1	0
1	1	0	1

Scheme 1.26. Molecular system mimic the function of combined logic circuits of INHIBIT and IMPLICATION logic gate.

Zharnikov and co-worker employed the terpyridine ligand based triads incorporating Fe(II), Ru(II), and Os(II) metals onto the solid SiO_x surface connected via Cu^{2+} for mimicking different combinational Boolean logic functions in the solid state (Scheme 1.27).[130] It is observed that absorption band at 577 nm for the triad gets red-shifted upon addition of NO^+ which can be restored again by adding deionizer water. They have constructed a combination logic gate utilizing NO^+, H_2O, and Et_3N as three different inputs and absorbance at 577 nm as the output signal.

They also fabricated another combination logic upon considering the oxidation of Os^{2+} center in the triad which is very much time dependent. In this case, NO^+, H_2O, Et_3N and time (t) were considered as 4 different inputs and absorption signal at 501 nm was utilized as the output. Furthermore, they beautifully demonstrated the write-read-erase-read cycle. The absorption signal at 501 nm can be shifted to 508 nm in presence of H_2O while initial position can be restored by using NO^+ . This reversible cycle can be repeated many times.

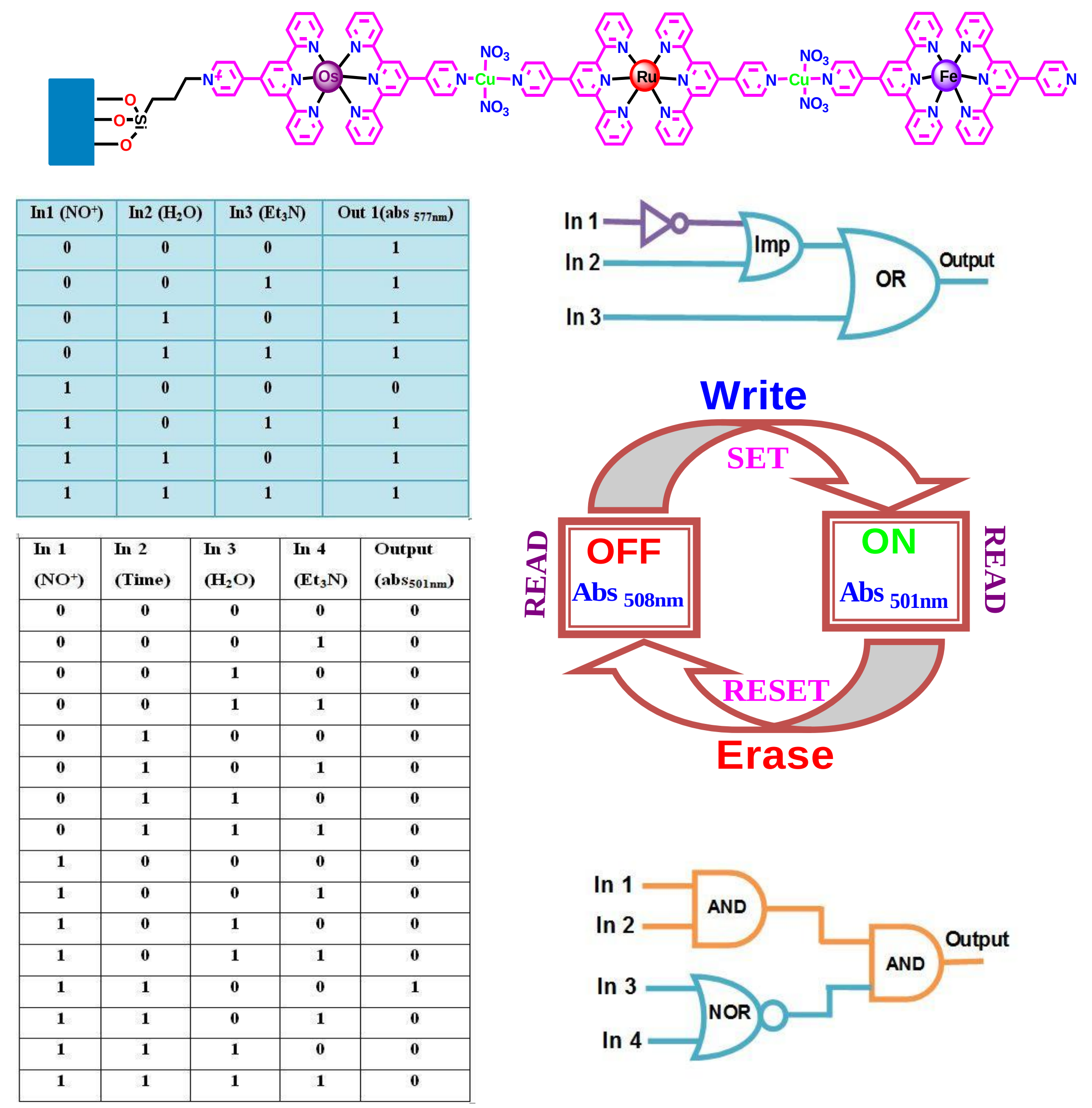

In1 (NO⁺)	In2 (H_2O)	In3 (Et_3N)	Out 1(abs $_{577nm}$)
0	0	0	1
0	0	1	1
0	1	0	1
0	1	1	1
1	0	0	0
1	0	1	1
1	1	0	1
1	1	1	1

In 1 (NO⁺)	In 2 (Time)	In 3 (H_2O)	In 4 (Et_3N)	Output (abs$_{501nm}$)
0	0	0	0	0
0	0	0	1	0
0	0	1	0	0
0	0	1	1	0
0	1	0	0	0
0	1	0	1	0
0	1	1	0	0
0	1	1	1	0
1	0	0	0	0
1	0	0	1	0
1	0	1	0	0
1	0	1	1	0
1	1	0	0	1
1	1	0	1	0
1	1	1	0	0
1	1	1	1	0

Scheme 1.27. Molecular system mimic the function of different combination logic gates

Molecular system can also be employed for mimicking the operation of keypad lock by sequential addition of different inputs. Shanzer and co-workers first induced such logic operation.[85] Thereafter, several molecular systems are utilized by different research group for the construction of keypad lock.

Baitalik and co-worker recently developed such keypad lock (Scheme 1.28).[131] The absorption spectral signal at 535 nm of a Ru(II) complex based on stilbene appended terpyridyl-imidazole ligand was utilized in presence of different external stimuli such as OH^- and light (λ_{ex}=334 nm). Two inputs OH^- and light (λ_{ex}=334 nm) are labeled as "A" and "C" respectively while "ON-state" and "OFF-state" are designated as "T" and "E". In absence of any input, the absorption signal at 535 nm is in the "OFF-state. Sequential action of light (λ_{ex}=334 nm) followed by OH^- indicate "OFF-state. Thus a secret code "ACE" was generated as keypad lock.

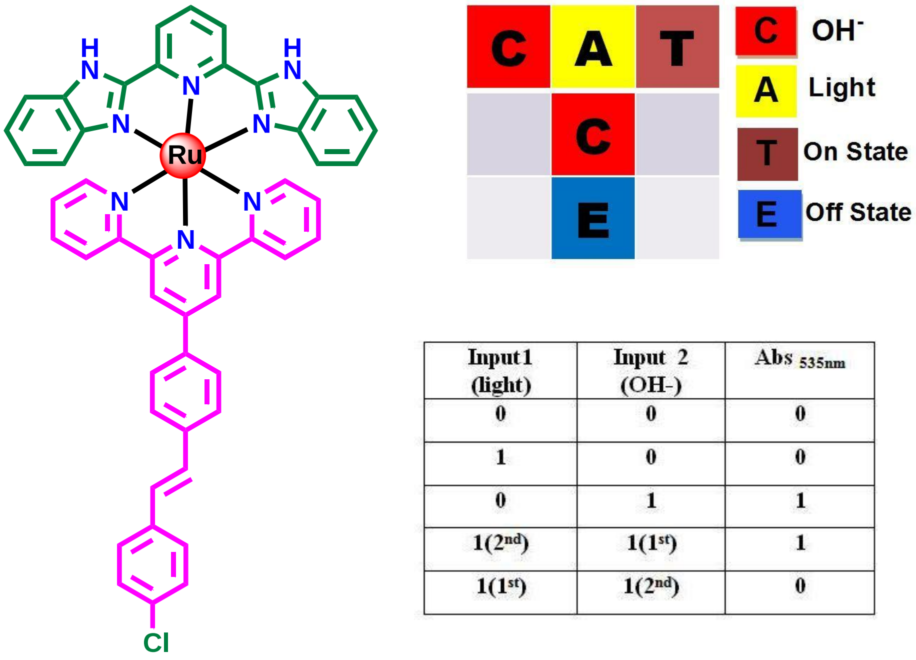

Input1 (light)	Input 2 (OH-)	Abs $_{535nm}$
0	0	0
1	0	0
0	1	1
1(2nd)	1(1st)	1
1(1st)	1(2nd)	0

Scheme 1.28. Molecular system mimic the function of Keypad lock

1.8. Objectives and Scope of the Present Work

Upon brief review of literature it appears that coordination complexes of ruthenium(II) metal based on polypyridine type ligands play crucial roles for the fabrication of photochemical molecular devices by utilizing their outstanding photophysical and electrochemical properties. Among the polypyridines, usually bipyridine (bpy) or terpyridine (tpy) type chelating units covalently coupled with a variety of aromatic and heteroaromatic units or electron-attracting or electron-releasing groups are commonly employed. The tpy-type ligands always generate achiral and rod-like architectures in the resulting octahedral complexes, whereas the analogous bpy-type ligands yield complexes with isomeric mixtures and the separation of which are extremely tedious. But the major drawbacks of Ru(II)-tpy type complexes is their poor room temperature luminescence properties and short excited state lifetime compared with their bpy-type analogues. Hence, the major objective of the present dissertation is to design terpyridine complexes of Ru(II) with enhanced RT emission characteristics as well as lifetime so that the complexes can act useful building blocks for the construction of light harvesting materials.

In order to achieve our objective, we have synthesized a series of terpyridyl-imidazole ligand (tpy-HImzPh$_3$X$_2$), wherein a terpyridine motif is covalently connected with a substituted benzil unit via a phenylimidazole spacer. The benzil unit is decorated with both electron-donating as well as electron-withdrawing group to fine tune the photophysical and redox properties in the resulting Ru(II) complexes. The desired ligand are synthesized upon condensation of 4,4'-substituted benzil and tpy-PhCHO in 1:1 molar ratio in refluxing acetic acid in presence of excess NH$_4$OAc (Scheme 1.30).

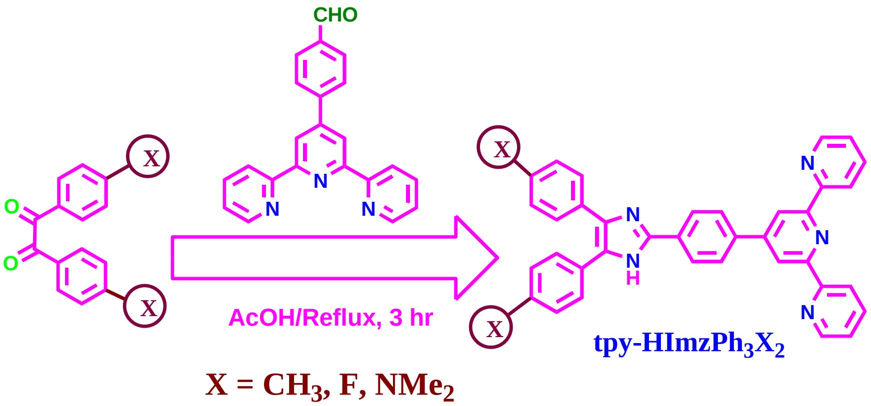

Scheme 1.30

The scope of formation of various homo- and heteroleptic Ru(II) complexes with the proposed terpyridyl-imidazole ligand (tpy-HImzPh$_3$X$_2$) are summarized in Scheme 1.31.

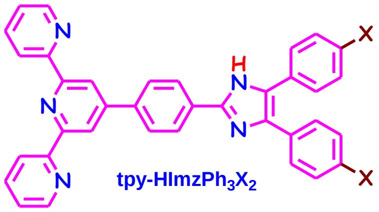

tpy-HImzPh$_3$X$_2$

X= CH$_3$, F , NMe$_2$

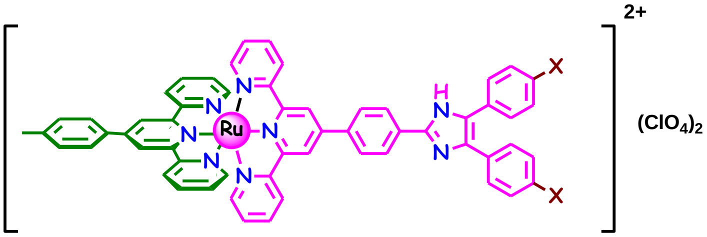

[(tpy-PhCH$_3$)Ru(tpy-HImzPh$_3$(X)$_2$)](ClO$_4$)$_2$

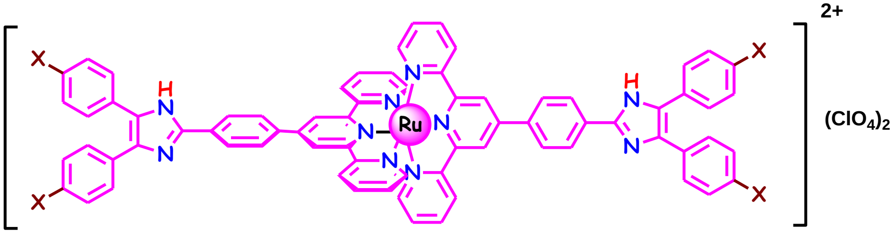

[Ru(tpy-HImzPh$_3$(X$_2$)$_2$](ClO$_4$)$_2$

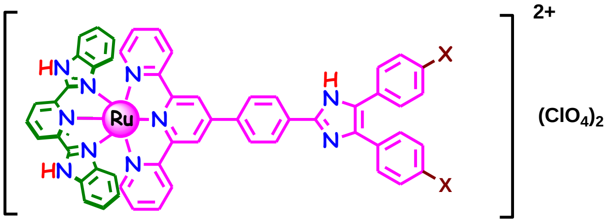

[(H$_2$pbbzim) Ru(tpy-HImzPh$_3$(X$_2$)](ClO$_4$)$_2$

Scheme 1.31

Subsequent to the synthesis of the ligands and their Ru(II) complexes, they will be carefully characterized by standard analytical tools and spectroscopic techniques such as elemental analysis, Electrospray ionization (ESI) mass spectra as well as NMR spectroscopic methods. Efforts will be given to determine X-ray crystal structures of selected complexes. Absorption and emission spectral properties of the metal complexes together with the ligands will be systematically investigated. The excited state lifetime of the complexes along with the ligands will be measured by time-correlated single photon counting experiments. The electrochemical properties of the compounds will be investigated by cyclic and square wave voltammetry.

In conjunction with the experimental measurements, theoretical calculations employing density functional theory (DFT) as well as time-dependent (TD)-DFT methods will be carried out to gain knowledge about their electronic structures and to appropriately assign the origin of the experimentally observed absorption and emission spectral bands.

Another important objective of this dissertation is to modulate the photo-redox properties of the complexes upon exploiting their secondary coordination sphere with the aid of different external stimuli for the fabrication of potential molecular sensors and switches. All the metal complexes possess acidic imidazole NH proton(s) in the second coordination sphere. Taking benefit of the NH motif(s), anion-induced modulation of the photophysical and electrochemical properties will be explored via different optical channel (absorption, emission and lifetime) as well as cyclic voltammetry (CV) and square wave voltammetry (SWV) (Scheme 1.32-1.33). The extent of interaction between the complexes and anions will be accessed through absorption and emission titration experiments. The variation of excited state lifetime of the complexes in presence of anions will also be explored be performed to check the potentiality as to act as lifetime-based anion sensors.

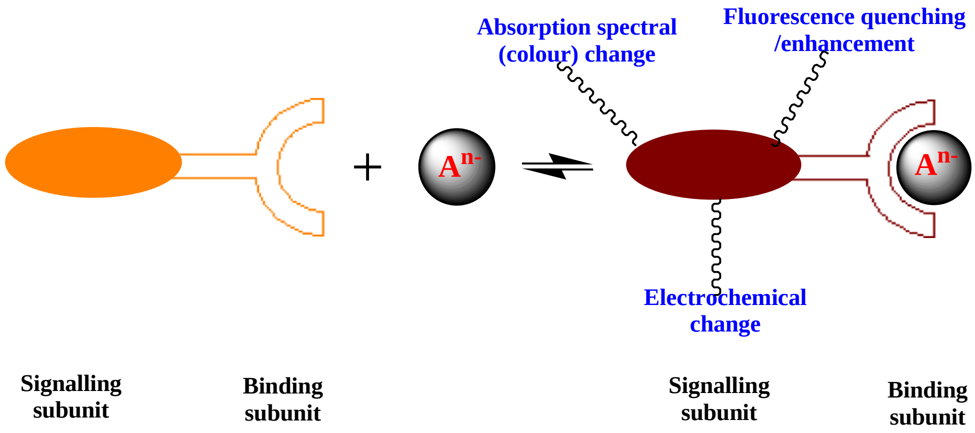

Scheme 1.32

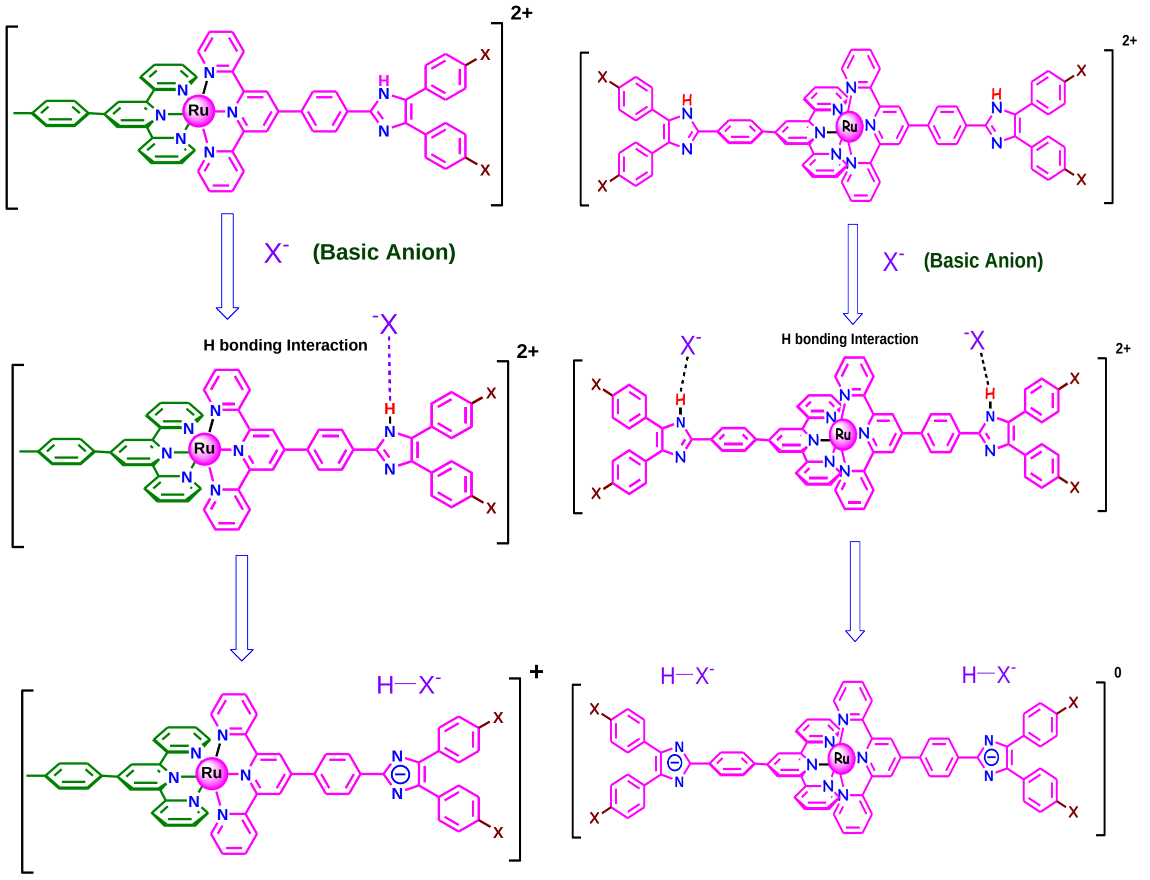

Scheme 1.33

Taking advantage of their NH motif(s), we will also be interested to investigate the effect of pH on the photo-redox behaviors of the complexes. Systematic change in the absorption and emission spectra as well as in the lifetime of the complexes will also be explored upon gradual change in the pH within the domain of 2.0-12.0 (Scheme 1.34). The titration profiles will be utilized for the estimation of both the ground and excited state pK_a values of the complexes. Proton-coupled oxidative electrochemical measurement could also be feasible upon measuring half wave potential of Ru^{2+}/Ru^{3+} couple by varying the pH of the medium. The $E_{1/2}$ *vs.* pH profiles will allow the evaluation of the acid dissociation constants of the complexes in both of Ru^{2+} and Ru^{3+} states (Scheme 1.35).

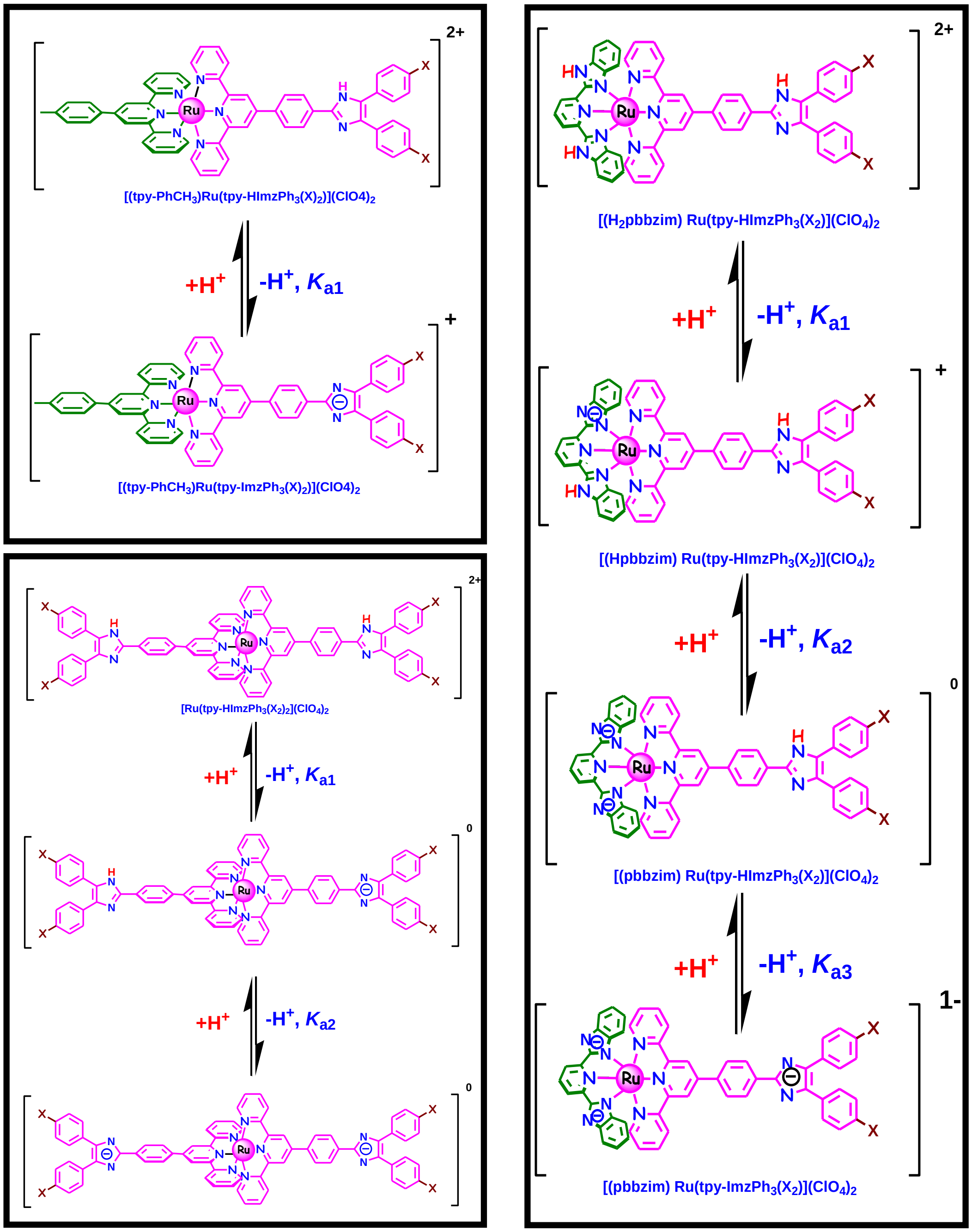

2+
[(tpy-PhCH$_3$)Ru(tpy-HImzPh$_3$(X)$_2$)](ClO4)$_2$
+H$^+$
-H$^+$, K_{a1}
+
[(tpy-PhCH$_3$)Ru(tpy-ImzPh$_3$(X)$_2$)](ClO4)$_2$
2+
[Ru(tpy-HImzPh$_3$(X$_2$)$_2$](ClO$_4$)$_2$
+H$^+$
-H$^+$, K_{a1}
0
+H$^+$
-H$^+$, K_{a2}
0
2+
[(H$_2$pbbzim) Ru(tpy-HImzPh$_3$(X$_2$)](ClO$_4$)$_2$
+H$^+$
-H$^+$, K_{a1}
+
[(Hpbbzim) Ru(tpy-HImzPh$_3$(X$_2$)](ClO$_4$)$_2$
+H$^+$
-H$^+$, K_{a2}
0
[(pbbzim) Ru(tpy-HImzPh$_3$(X$_2$)](ClO$_4$)$_2$
+H$^+$
-H$^+$, K_{a3}
1-
[(pbbzim) Ru(tpy-ImzPh$_3$(X$_2$)](ClO$_4$)$_2$

Scheme 1.34

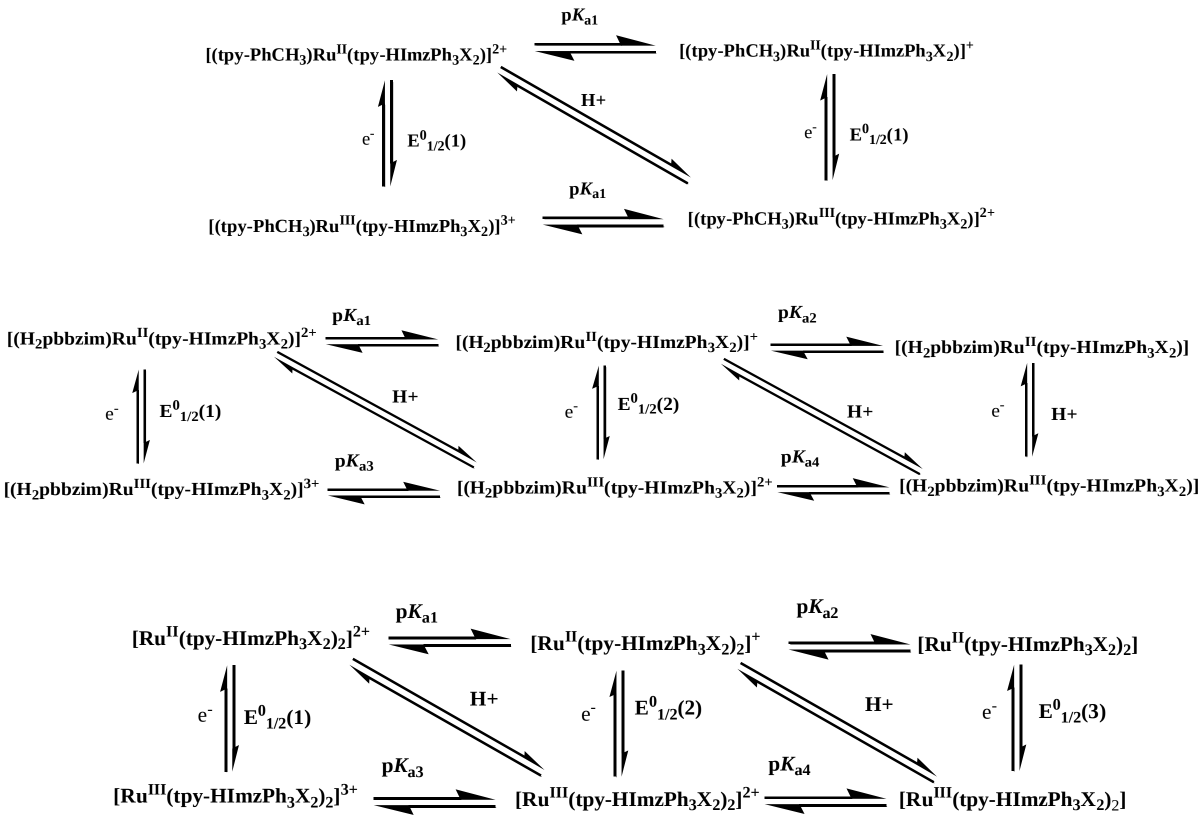

Scheme 1.35. Probable square schemes of electro-protic equilibria for the complexes.

The luminescence properties of the Ru(II)-tpy complexes dependent upon energy difference between emitting ^{3}MLCT and non-emitting ^{3}MC levels which in turn critically dependent on temperature. Hence, temperature-dependent emission spectral measurement will be thoroughly investigated to check the variation of emission intensity, quantum yield and lifetime of the complexes as a function of temperature.

Thus, substantial alteration of the photo-redox behaviors of the complexes could be expected upon the action of different external stimuli (anion, acid, pH and temperature). By the use of spectral outputs of as a function of the said stimuli in appropriate sequence, the possibility of mimicking advanced Boolean and Fuzzy logic operations will be also explored (Scheme 1.36). Additionally, diverse soft computing tools such as artificial neural network (ANN) and adopted neuro fuzzy inference system

(ANFIS) could also be implemented to analyze and predict the detailed sensing behaviors of the complexes (Scheme 1.37-1.39).

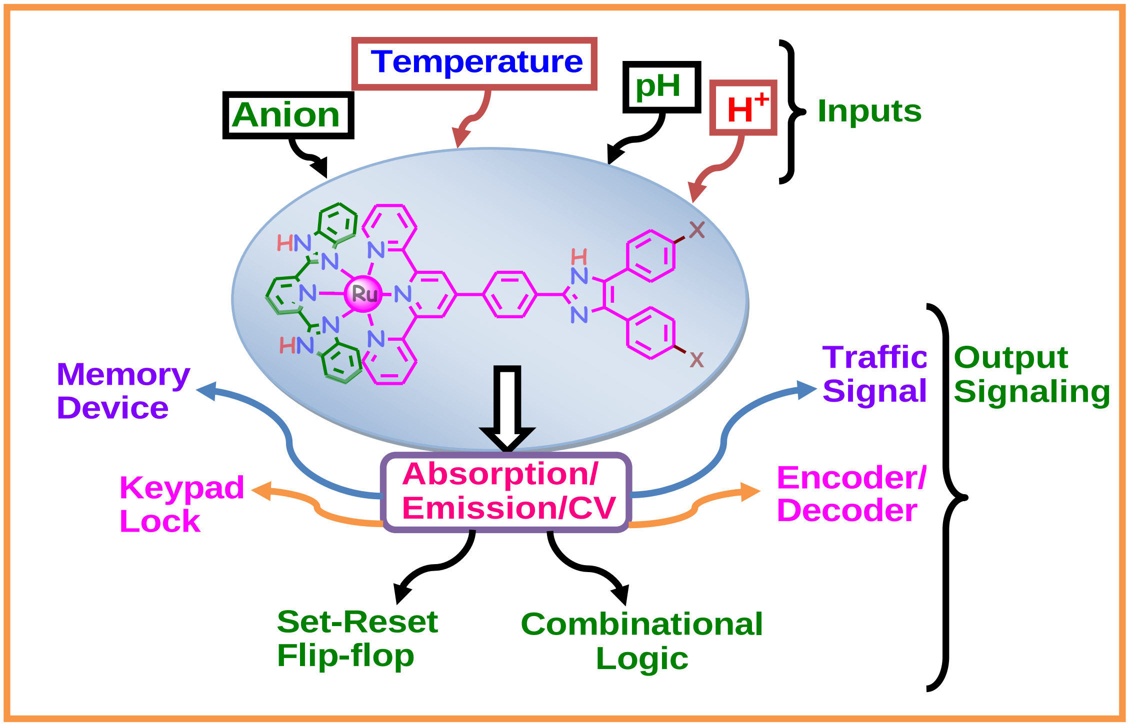

Scheme 1.36

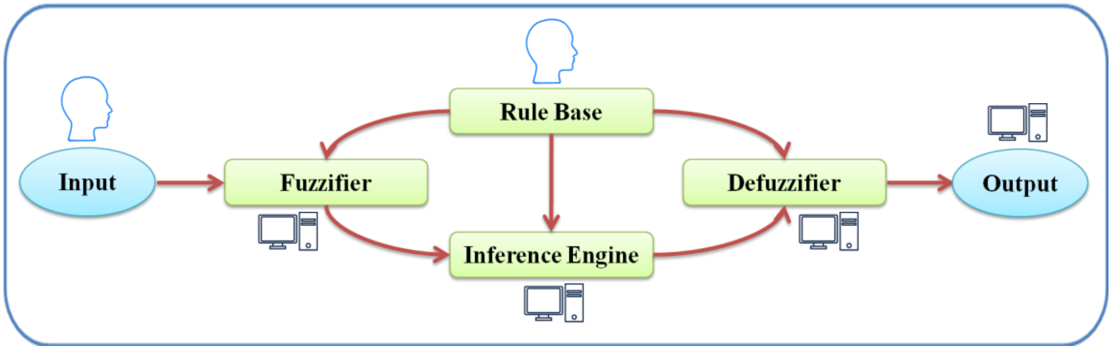

Fuzzy Logic Scheme

Scheme 1.37

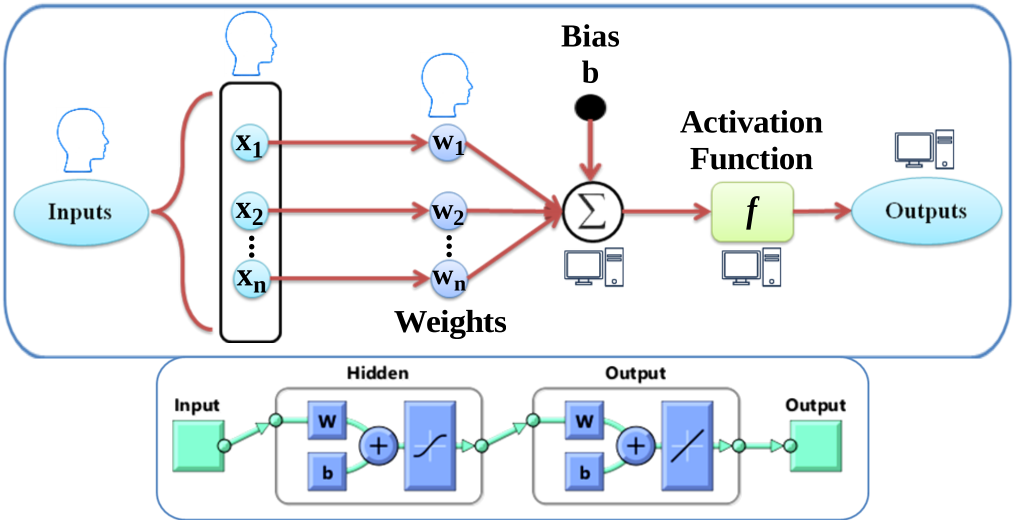

ANN Scheme

Scheme 1.37

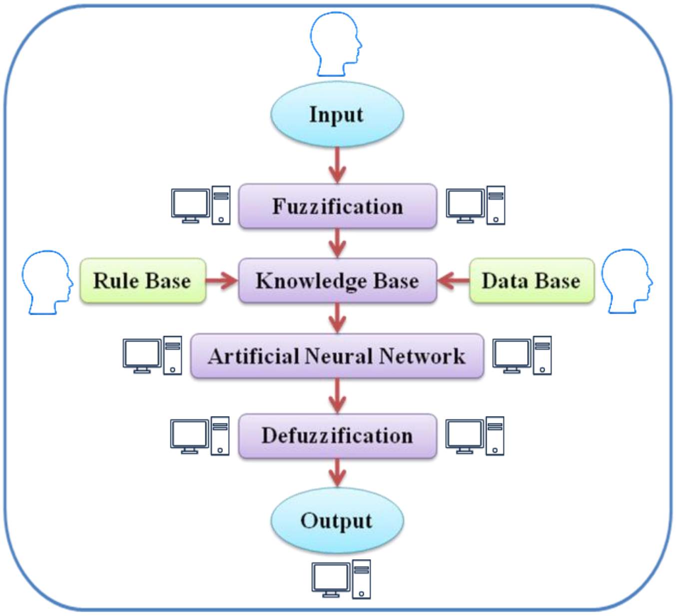

ANFIS Scheme

Scheme 1.37

The execution of diverse scopes together with relevant investigations will be presented in chapters 2-6. Chapter 2 deals with the synthesis, characterization, and photophysical behaviors of three Ru(II)-terpyridine complexes derived from a terpyridyl-imidazole ligand (tpy-HImzPh$_3$Me$_2$), wherein a terpyridine moiety has been coupled with dimethybenzil unit through phenylimidazole spacer. Characterization studies include elemental analysis, ESI mass spectrometry and NMR spectroscopy. Acid and anion induced modulation of absorption and emission spectral characteristics of the complexes will be thoroughly studied by multiple optical channels and spectroscopic techniques. Binding constant and detection limit of the complexes towards selected anions will be evaluated from the spectral titration data in both aqueous and organic media. In conjunction with the experimental investigation, DFT and TD-DFT studies will be carried out to understand the electronic structures of the complexes and also for appropriate assignment of the spectral bands.

Synthesis, characterization and detailed photophysical as well as redox behaviors of a series of homo- and heteroleptic Ru(II)-complexes based on fluoro-substituted terpyridyl-imidazole ligand (tpy-HImzPh$_3$F$_2$) are reported in chapter 3. Electron-withdrawing fluoro group has been incorporated in the ligand backbone to modulate the photo-redox behaviours in the resulting complexes. Temperature dependent emission spectral measurements are executed to acquire knowledge about deactivation dynamics of the complexes. pH-induced modulation of the absorption and emission spectral behaviors as well as electrochemical properties are thoroughly investigated and associated pK_a values of the complexes are determined. Interestingly, the spectral signatures of the complexes upon the influence of temperature, acid and bases will be employed to construct multiple Boolean logic gates. Finally, DFT and TD-DFT studies will be carried out to compare the experimental and theoretical spectra of the complexes.

Chapter 4 deals with the synthesis, characterization and photophysical properties a series of Ru(II) complexes based on dimethylamino-substituted terpyridyl-imidazole ligand [(tpy-HImzPh$_3$(NMe$_2$)$_2$]. Anion and temperature responsive behaviours of the complexes are thoroughly studied. The absorption and emission spectral response upon the influence of anion, acid and temperature will be used to fabricate multiple Boolean (BL) and Fuzzy logic (FL) operations. Finally, soft computing techniques {Artificial

Neural Networks (ANNs), Fuzzy-logic and Adaptive Neuro-Fuzzy Inference System (ANFIS)} will be employed to fully understand as well as to forecast the complete sensing behaviors of the complexes.

The scope of investigation reported in Chapter 4 and 5 slightly differs from the preceding chapters. Chapter 5 deals with detailed anion responsive conduct of one of our previously reported Ru(II) complex of the type $[(bpy)_2Ru(H_3pzbzim)] (ClO_4)_2$ (**1**), where bpy = 2,2'-bipyridine and $H_3pzbzim$ = pyrazole-3,5-bis(benzimidazole) in acetonitrile and water via absorption, and emission spectroscopy as well as by square-wave voltammetry (SWV). Alteration of the photophysical and electrochemical behavior of the complex in presence of the selected anions is reported. In essence, the complex acts as anion- and acid-responsive molecular switches. Neural network based deep learning methodologies such as ANNs and ANFIS are also employed to compare the models outputs with those of the experimentally observed values.

Multi-channel anion sensing behavior of a Ru(II) complex of the form $[(bpy)_2Ru(Hpzbzth)] (ClO_4)_2$ (**1**) {bpy=2,2'-bipyridine and Hpzbzth=3,5-bis(benzthiazol-2-yl)pyrazole} is carried out in chapter 6 and also analyzed through multiple machine learning tools. The absorption, emission and electrochemical outputs of the complex in presence of anions and acid are employed to mimic different types of Boolean and FL operations. To overcome the shortcomings associated with carrying out very detailed sensing experiment, we also implemented different deep learning tools such as FL, ANNs and ANFIS to envisage the full anion sensing aspects of the complex. The outcomes of the three models are compared and also tallied with the experimental parameters.

1.9. References

1. Beaujuge, P.; Fréchet, J. Molecular Design and Ordering Effects in π-Functional Materials for Transistor and Solar Cell Applications. *J. Am. Chem. Soc.* **2011**, *133*, 20009-20029.
2. Ray, D.; Liang, C. K.; McClenaghan, N.; Bassani, D. Organic and Supramolecular Materials for LED and Photovoltaic Applications. *Curr. Phys. Chem.* **2011**, *1*, 169-180.

3. Song, W.; Chen, Z.; Brennaman, M.; Concepcion, J.; Patrocinio, A.; Murakami Iha, N.; Meyer, T. Making Solar Fuels by Artificial Photosynthesis. *Pure Appl. Chem.* **2011**, *83*, 749-768.
4. Swierk, J. R.; Mallouk, T. E. Design and Development of Photoanodes for Water-Splitting Dye-Sensitized Photoelectrochemical Cells. *Chem. Soc. Rev.* **2013**, *42*, 2357-2387.
5. Wasielewski, M. R. Self-Assembly Strategies for Integrating Light Harvesting and Charge Separation in Artificial Photosynthetic Systems. *Acc. Chem. Res.* **2009**, *42* , 1910-1921.
6. Nocera, D. G. Chemistry of Personalized Solar Energy. *Inorg. Chem.* **2009**, *48*, 10001-10017.
7. Gust, D.; Moore, T. A.; Moore, A. L. Realizing Artificial Photosynthesis. *Acc. Chem. Res.* **2009**, *42*, 1890 -1898.
8. Sumida, K.; Rogow, D. L.; Mason, J. A.; McDonald, T. M.; Bloch, E. D.; Herm, Z. R.; Bae, T. H.; Long, J. R. Carbon Dioxide Capture in Metal-Organic Frameworks. *Chem. Rev.* **2012**, *112*, 724-781.
9. Frischmann, P. D.; Mahata, K.; Würthner, F. Powering the Future of Molecular Artificial Photosynthesis with Light-Harvesting Metallosupramolecular Dye Assemblies. *Chem. Soc. Rev.* **2013**, *42*, 1847-1870.
10. Beaujuge, P.; Fréchet, J. Molecular Design and Ordering Effects in π-Functional Materials for Transistor and Solar Cell Applications. *J. Am. Chem. Soc.* **2011**, *133*, 20009-20029.
11. McConnell, A. J.; Wood, C. S.; Neelakandan, P. P.; Nitschke, J. R. Stimuli-Responsive Metal-Ligand Assemblies. *Chem. Rev.* **2015**, *115*, 7729-7793.
12. Intelligent Stimuli-Responsive Materials; Li, Q., Ed.; John Wiley & Sons, Inc.: Hoboken, Nj, **2013**.
13. Manez, R. M.; Sancenon, F. Fluorogenic and Chromogenic Chemosensors and Reagents for Anions. *Chem. Rev.* **2003,** *103*, 4419-4476.
14. De Silva, A. P.; Gunaratne, H. Q. N.; Gunnlaugsson, T.; Huxley, A. J. M.; McCoy, C. P.; Rademacher, J. T.; Rice, T. E. Signaling Recognition Events with Fluorescent Sensors and Switches. *Chem. Rev.* **1997**, *97*, 1515-1566.

15. Ko, C. C.; Yam, V. W. W. Coordination Compounds with Photochromic Ligands: Ready Tunability and Visible Light-Sensitized Photochromism. *Acc. Chem. Res.* **2018**, *51*, 149-159.
16. Kurihara, M.; Nishihara, H. Azo- and Quinone-Conjugated Redox Complexes-Photo- and Proton-Coupled Intramolecular Reactions Based on d-π Interaction. *Coord. Chem. Rev.* **2002**, *226*,125-135.
17. Cui, B-B.; Zhong, Y-W.; Yao, J. Three-State Near-Infrared Electrochromism at the Molecular Scale. *J. Am. Chem. Soc.* **2015**, *137*, 4058-4061.
18. Jia, C.; Wang, J.; Yao, C.; Cao, Y.; Zhong, Y.; Liu, Z.; Liu, Z.; Guo, X. Conductance Switching and Mechanisms in Single-Molecule Junctions. *Angew. Chem. Int. Ed.* **2013**, *52*, 8666 -8670.
19. Haga, M.; Ali, M. M.; Maegawa, H. Nozaki, K. Yoshimura, A.; Ohno, T. Photoexcited States of Dinuclear Ru Complexes Bridged by Proton-Dissociable Benzimidazole Derivatives. *Coord. Chem. Rev.* **1994**, *132*, 99-104.
20. Motoyama, D.; Yoshikawa, K.; Ozawa, H.; Tadokoro, M.; Haga, M. Energy-Storage Applications for a pH Gradient between Two Benzimidazole-Ligated Ruthenium Complexes That Engage in Proton-Coupled Electron-Transfer Reactions in Solution. *Inorg. Chem.* **2017**, *56*, 6419-6428.
21. Huynh, M. H. V.; Meyer, T. J. Proton-Coupled Electron Transfer. *Chem. Rev.* **2007**, *107,* 5004-5064.
22. Ali, C.; Banaszak, M.; Astumian, R. D.; Stoddart, J. F.; Grzybowski, B. A. Great Expectations: Can Artificial Molecular Machines Deliver on Their Promise? *Chem. Soc. Rev.* **2012**, *41*, 19-30.
23. Juris, A.; Balzani, V.; Barigelletti, F.; Campagna, S.; Belser, P.; Von Zelewsky, A. Ru (II) Polypyridine Complexes: Photophysics, Photochemistry, Eletrochemistry, and Chemiluminescence. *Coord. Chem. Rev.* **1988**, *84,* 85-277.
24. Balzani, V.; Juris, A.; Venturi, M.; Campagna, S.; Serroni, S. Luminescent and Redox-Active Polynuclear Transition Metal Complexes. *Chem. Rev.* **1996**, *96*, 759-833.
25. Sauvage, J.-P.; Collin, J. P.; Chambron, J. C.; Guillerez, S.; Coudret, C.; Balzani, V.; Barigelletti, F.; De Cola, L.; Flamigni, L. Ruthenium(II) and Osmium(II)

Bis(terpyridine) Complexes in Covalently-Linked Multicomponent Systems: Synthesis, Electrochemical Behavior, Absorption Spectra, and Photochemical and Photophysical Properties. *Chem. Rev*. **1994**, *94*, 993-1019.

26. Medlycott, E. A.; Hanan, G. S. Designing Tridentate Ligands for Ruthenium (II) Complexes with Prolonged Room Temperature Luminescence Lifetimes**.** *Chem. Soc. Rev*. **2005**, *34*, 133-142.
27. Medlycott, E. A.; Hanan, G. S. Synthesis and Properties of Mono- and Oligo-Nuclear Ru (II) Complexes of Tridentate Ligands: The Quest for Long-Lived Excited States at Room Temperature. *Coord. Chem. Rev.* **2006**, *250*, 1763-1782.
28. Wang, X.; Guerzo, A.; Baitalik, S.; Simon, G.; Shaw, G. B.; Chen, L. X.; Schmehl, R. H. The Influence of Bridging Ligand Electronic Structure on the Photophysical Properties of Noble Metal Diimine and Triimine Light Harvesting Systems. *Photosynth. Res.* **2006**, *87*, 83-103.
29. Schubert, U. S.; Eschbaumer, C. Macromolecules Containing Bipyridine and Terpyridine Metal Complexes: Towards Metallosupramolecular Polymers. *Angew. Chem. Int. Ed.* **2002**, *41*, 2892-2896.
30. De Silva, A. P.; Gunaratne, H.Q.N.; McCoy, C.P. A Molecular Photoionic AND Gate Based on Fluorescent Signaling. *Nature*. **1993**, *364*, 42-44.
31. De Silva, A. P.; Fox, D. P.; Huxley, A. J. M.; Moody, T. S. Combining Luminescence, Coordination and Electron Transfer for Signaling Purposes. *Coord. Chem. Rev*., **2000**, *205*, 41-57.
32. Ling, J.; Daly, B.; Silverson, V. A. D.; de Silva, A. P. Taking Baby Steps in Molecular Logic-Based Computation. *Chem. Commun.,* **2015**, *51*, 8403-8409.
33. Daly, B.; Ling, J.; de Silva, A. P. Current Developments in Fluorescent PET (Photoinduced Electron Transfer) Sensors and Switches. *Chem. Soc. Rev.,* **2015**, *44*, 4203-4211.
34. Andréasson, J.; Pischel, U. Smart Molecules at Work Mimicking Advanced Logic Operations. *Chem. Soc. Rev.,* **2010**, *39*, 174-188.
35. Carvalho, C. P.; Dominguez, Z.; Da Silva, J. P.; Pischel, U. A Supramolecular Keypad Lock. *Chem. Commun.*, **2015**, *51*, 2698-2701.

36. Andreasson, J.; Pischel, U. Molecules with a Sense of Logic: A Progress Report. *Chem. Soc. Rev*., **2015**, *44*, 1053-1069.
37. Schmittel, M.; Mal, P.; de los Rios, A. Multiport Logic Operations Triggered by Protonation-a Trisphenanthroline as a 3-input AND-NOR-OR Circuit, *Chem. Commun*., **2010**, *46*, 2031-2033.
38. Biswas, P. K.; Saha, S.; Gaikwad, S.; Schmittel, M. Reversible Multicomponent AND Gate Triggered by Stoichiometric Chemical Pulses Commands the Self-Assembly and Actuation of Catalytic Machinery. *J. Am. Chem. Soc.,* **2020**, *142*, 7889-7897.
39. Szaciłowski, K. Digital Information Processing in Molecular Systems. *Chem. Rev*., **2008,** *108*, 3481-3548.
40. Szaciłowski, K.; Macyk, W.; Stochel, G.; Light-Driven OR and XOR Programmable Chemical Logic Gates. *J. Am. Chem. Soc*., **2006**, *128*, 4550-4551.
41. Said, A. I.; Georgiev, N. I.; Bojinov, V. B. A Fluorescent Bichromophoric "Off-On-Off" pH Probe as a Molecular Logic Device (Half-Subtractor and Digital Comparator) Operating by Controlled PET and ICT Processes. *Dyes and Pigments*, **2019**, *162*, 377-384.
42. Georgiev, N. I.; Yaneva, I. S.; Surleva, A. R.; Asiri, A. M.; Bojinov, V. B. Synthesis, Sensor Activity and Logic Behavior of a Highly Water-Soluble Naphthalimide Derivative. *Sensors and Actuators B*, **2013**, 54-63.
43. Georgiev, N. I.; Sakr, A. R. Bojinov, V. B. Design and Synthesis of a Novel PET and ICT Based 1,8-Naphthalimide FRET Bichromophore as a Four-Input Disabled-Enabled-OR Logic Gate. *Sensors and Actuators B*, **2015**, *221*, 625-634.
44. Magri, D. C.; Spiteri, J. C. Proof of Principle of A Three-Input AND–INHIBIT–OR Combinatorial Logic Gate Array. *Org. Biomol. Chem*. **2017**, *15*, 6706-6709.
45. Mardanya, S.; Mondal, D.; Karmakar, S.; Baitalik, S. Smart Ruthenium and Osmium Complexes Mimic the Complicated Functions of Traffic Signal and Memory Device. *Sens. Actuators B: Chem*. **2017**, *239*, 635-641.
46. Cui, B. B.; Tang, J. H.; Yao, J.; Zhong, Y. W. A Molecular Platform For Multistate Near-Infrared Electrochromism and Flip-Flop, Flip-Flap-Flop, and Ternary Memory. Angew. Chem. Int. Ed. **2015**, *54*, 9192-9197.

47. Shao, J. Y.; Yao, C. J.; Cui, B. B.; Gong, Z. L.; Zhong, Y. W. Electropolymerized Films of Redox-Active Ruthenium Complexes for Multistate Near-Infrared Electrochromism, Ion Sensing, and Information Storage. *Chin. Chem. Lett*. **2016**, *27*, 1105-1114.
48. Szaciłowski, K. Molecular Logic Gates Based on Pentacyanoferrate Complexes: From Simple Gates to Three-Dimensional Logic Systems. *Chem. Eur. J.* **2004**, *10*, 2520-2528.
49. Artrith, N.; Butler, K. T.; Coudert, F. X.; Han, S.; Isayev, O.; Jain, A.; Walsh, A. Best Practices in Machine Learning for Chemistry. *Nat. Chem*. **2021**, *13*, 505-508.
50. Mater, A. C.; Coote, M. L. Deep Learning in Chemistry. *J. Chem. Inf. Model*. **2019**, *59*, 2545-2559.
51. Pflüger, P. M.; Glorius, F. Molecular Machine Learning: the Future of Synthetic Chemistry? *Angew. Chem. Int. Ed.* **2020**, *59*, 18860-18865.
52. He, L.; Bai, L.; Dionysiou, D. D.; Wei, Z.; Spinney, R.; Chu, C.; Xiao, R. Applications of Computational Chemistry, Artificial Intelligence, and Machine Learning in Aquatic Chemistry Research. *Chem. Eng. J.* **2021**, *426*, 131810.
53. Gentili, P. L. A Strategy to Face Complexity: The Development of Chemical Artificial Intelligence. In Advances in Artificial Life, Evolutionary Computation, and Systems Chemistry; Rossi, F., Piotto, S., Concilio, S., Eds.; *Springer: Cham*, Switzerland; New York, NY, USA. **2017**, *708*, 151-160.
54. Zadeh, L. A. Toward Human Level Machine Intelligence-is It Achievable? the Need for a Paradigm Shift. *IEEE Comput. Intell. Mag*. **2008**, *3*, 11-22.
55. Zadeh, L.A. Outline of a New Approach to the Analysis of Complex Systems and Decision Processes. *IEEE Trans. Syst. Man Cyb*. **1973**, *3*, 28-44.
56. Conrad, M. Molecular Computing. *Adv. Comput*. **1990**, *31*, 235-324.
57. Zadeh, L. A. Fuzzy sets. In Fuzzy Sets, Fuzzy Logic, and Fuzzy Systems: Selected Papers by Lotfi A Zadeh, pp. *394-432*. **1996.**
58. Gentili, P. L. Boolean and Fuzzy Logic Gates Based on The Interaction of Flindersine with Bovine Serum Albumin and Tryptophan. *J. Phys. Chem. A*. **2008**, *112*, 11992-11997.

59. Gentili, P. L. The Fuzziness of the Molecular World and Its Perspectives. *Molecules.* **2018**, *23*, 2074.
60. Gentili, P.L. The Fundamental Fuzzy Logic Operators and Some Complex Boolean Logic Circuits Implemented by the Chromogenism of a Spirooxazine. *Phys. Chem. Chem. Phys.* **2011**, *13*, 20335-20344.
61. Gentili, P.L.; Giubila, M.S.; Heron, B.M. Processing Binary and Fuzzy Logic by Chaotic Time Series Generated by a Hydrodynamic Photochemical Oscillator. *Chem Phys Chem.* **2017**, *18*, 1831-1841.
62. Gentili, P.L.; Giubila, M.S.; Germani, R.; Romani, A.; Nicoziani, A.; Spalletti, A.; Heron; B.M. Optical Communication Among Oscillatory Reactions and Photo-Excitable Systems: Uv and Visible Radiation Can Synchronize Artificial Neuron Models. *Angew. Chem. Int. Ed.* **2017**, *56*, 7535-7540.
63. Schumann, A.; Adamatzky, A. The Double-Slit Experiment with Physarum Polycephalum and P-adic Valued Probabilities and Fuzziness. *Int J Gen Syst.* **2015**, *44*, 392-408.
64. Giri Nandagopal, M. S.; Selvaraju, N. Prediction of Liquid-Liquid Flow Patterns in a Y-junction Circular Microchannel Using Advanced Neural Network Techniques. *Ind. Eng. Chem. Res.* **2016**, *55*, 11346-11362.
65. Bingöl, D.; Inal, M.; Çetintaş, S. Evaluation of Copper Biosorption Onto Date Palm (Phoenix Dactylifera L.) Seeds with MLR and ANFIS Models. *Ind. Eng. Chem.Res* **2013**, *52*, 4429-4435.
66. İnal, M. Predicting the Conversion Ratio for the Leaching of Celestite in Sodium Carbonate Solution Using An Adaptive Neuro-Fuzzy Inference System. *Ind. Eng. Chem.Res* **2014**, *53*, 4975-4980.
67. Jang, J. S. R.; Sun, C. T. Neuro-Fuzzy Modeling and Control. *Proc. IEEE.* **1995**, *83,* 378-405.
68. Sugeno, M.; Yasukhiro, T. A Fuzzy-Logic-Based Approach to Qualitative Modeling. *IEEE Trans. Fuzzy Syst.* **1993**, *1*, 7-31.
69. Kalyanasundaram, K. Photophysics, Photochemistry and Solar Energy Conversion with Tris (bipyridyl) Ruthenium (II) and Its Analogs.*Coord. Chem. Rev.* **1982**, *46,* 159.

70. Scandola, F.; Indelli M. T. Second Sphere Donor Acceptor Interactions in Excited States of Coordination Compounds. Ruthenium (II) Bipyridine Cyano Complexes. *Pure Appl. Chem.* **1988**, *60*, 973.
71. Endicott, J. F.; Schlegel, H. B.; Uddin, M.J.; Seniveratne, D.S. MLCT excited states and charge delocalization in some ruthenium–ammine–polypyridyl complexes. *Coord.Chem. Rev.* 2002, *229*, 95-106.
72. Bar, M.; Pal, P.; Maity, D.; Baitalik, S. Heterobimetallic Ru-Os Complexes Function as Multichannel Sensors for Selected Anions by Taking Profit of Metal-Ligand Interaction. *Sensors and Actuators* B, **2018**, *266*, 493-505.
73. Bhaumik, C.; Maity, D.; Das, S.; Dutta, S.; Baitalik, S. Anion Sensing Studies of Luminescent Bis-tridentate Ruthenium (II) and Osmium (II) Complexes Based on Terpyridyl-Imidazole Ligand Through Different Channels. *Polyhedron* **2013**, *52*, 890-899.
74. Maity, D.; Bhaumik, C.; Mondal, D.; Baitalik, S. Ru (II) and Os(II) Complexes Based on Terpyridyl-Imidazole Ligand Rigidly Linked to Pyrene: Synthesis, Structure, Photophysics, Electrochemistry, and Anion-Sensing Studies. *Inorg. Chem.*, **2013**, *52*, 13941-13955.
75. Mardanya, S.; Karmakar, S.; Maity, D.; Baitalik, S. Multichromophoric Bimetallic Ru (II) Terpyridine Complexes Based on Pyrenyl-bis-phenylimidazole Spacer: Synthesis, Photophysics, Spectroelectrochemistry, and TD-DFT Calculations. *Inorg. Chem.*, **2014**, *53*, 12036-12049.
76. Kober, E.M.; Caspar, J.V.; Lumpkin, R. S.; Meyer, T. J. Application of the Energy gap Law to Excited-state Decay of Osmium (II)-Polypyridine Complexes: Calculation of Relative Nonradiative Decay Rates from Emission Spectral Profiles. *J. Phys. Chem.*, **1986**, *90*, 3722-3734.
77. Caspar, J. V.; Meyer, T. J. Application of the Energy Gap Law to Nonradiative, Excited-State Decay. *J. Phys. Chem.*, **1983**, *87*, 6-10.
78. Amini, A.; Harriman, A.; Mayeux, A. The Triplet Excited State of Ruthenium (II) Bis(2,2′:6′,2″-terpyridine): Comparison Between Experiment and Theory. *Phys. Chem. Chem. Phys.* **2004**, *6*, 1157-1164.

79. Gu, J.; Yan, Y.; Helbig, B. J.; Huang, Z.; Lian, T.; Schmehl, R. H. The Influence of Ligand Localized Excited States on the Photophysics of Second Row and Third Row Transition Metal Terpyridyl Complexes: Recent Examples and a Case Study. *Coord. Chem rev,* **2015**, *222-283*, 100-109.
80. Hammarström, L.; Barigelletti, F.; Flamigni, L.; Indelli, M. T.; Armaroli, N.; Calogero, G.; Guardigli, M.; Sour, A.; Collin, J.-P. ; Sauvage, J.-P. A Study on Delocalization of MLCT Excited States by Rigid Bridging Ligands in Homometallic Dinuclear Complexes of Ruthenium (II). *J. Phys. Chem. A* **1997**, *101*, 9061-9069.
81. Suresh, M.; Jose D. A.; Das, A. 2,2'-Bipyridyl-3,3'-diol as a Molecular Half-Subtractor. *Org. Lett*., **2007**, *9*, 441-444.
82. Coskun, A.; Deniz, E.; Akkaya, E. U. Effective PET and ICT Switching of Boradiazaindacene Emission: A Unimolecular, Emission-Mode, Molecular Half-Subtractor with Reconfigurable Logic Gates. *Org. Lett*., **2005**, *7*, 5187-5189.
83. Langford, S. J.; Yann, T. Molecular Logic: A Half-Subtractor Based on Tetraphenylporphyrin. *J. Am. Chem. Soc*., **2003**, *125*, 11198-11199.
84. Kumar, S.; Luxami, V.; Saini, R.; Kaur, D. Superimposed Molecular Keypad Lock and Half-Subtractor Implications in a Single Fluorophore. *Chem. Commun*., **2009**, 3044-3046.
85. Margulies, D.; Melman G.; Shanzer, A. A Molecular Full-Adder and Full-Subtractor, an Additional Step toward a Moleculator. *J. Am. Chem. Soc*., **2006**, *128*, 4865-4871.
86. Kaur, N.; Kumar, S. Aminoanthraquinone-Based Chemosensors: Colorimetric Molecular Logic Mimicking Molecular Trafficking and a Set-Reset Memorized Device. *Dalton Trans*., **2012**, *41*, 5217-5224.
87. MacVittie, K.; Halamek, J.; Katz, E. Enzyme-Based D-Flip-Flop Memory System *Chem. Commun*., **2012**, *48*, 11742-11744.
88. Zhuang, H.; Zhou, Q.; Zhang, Q.; Li, H.; Li, N.; Xu, Q.; Lu, J. Effects of Aromatic Spacers on Film Morphology and Device Memory Performance Based on Imidazole-π–Triphenylamine Derivatives. *J. Mater. Chem. C*, **2015**, *3*, 416-422.
89. Mardanya, S. ; Karmakar, S. ; Mondal, D. ; Baitalik, S. An Imidazolyl-Pyreno-Imidazole Conjugate As A Cyanide Sensor and a Set-Reset Memorized Sequential Logic Device. *Dalton Trans*., **2015**, *44*, 15994-16012.

90. Karmakar, S.; Mardanya, S.; Das, S.; Baitalik, S. Efficient Deep-Blue Emittier and Molecular-Scale Memory Device Based on Dipyridyl-Phenylimidazole-Terpyridine Assembly. *J. Phys. Chem. C.*, **2015**, *119*, 6793-6805.
91. Andrasson, J.; Straight, S. D.; Bandyopadhyay, S.; Mitchell, R. H.; Moore, T. A.; Moore A. L.; Gust, D. Molecular 2:1 Digital Multiplexer. *Angew. Chem. Int. Ed*., **2007**, *46*, 958-961.
92. Erbas-Cakmak, S.; Bozdemir, O. A.; Cakmak Y.; Akkaya, E. U. Proof of Principle for a Molecular 1 : 2 Demultiplexer to Function as an Autonomously Switching Theranostic Device. *Chem. Sci.*, **2013**, *4*, 858-862.
93. Xu, S.; Hao, Y.-X.; Sun, W.; Fang, C.-J.; Lu, X.; Li, M.-N.; Zhao, M.; Peng, S.Q.; Yan, C.-H. 2:1 Multiplexing Function in a Simple Molecular System. *Sensors* **2012**, *12*, 4421-4430.
94. Maestri, M.; Armaroli, N.; Balzani, V.; Constable, E. C.; Thompson, A. M. W. C. Complexes of the Ruthenium(II)-2,2':6',2"-terpyridine Family. Effect of Electron-Accepting and -Donating Substituents on the Photophysical and Electrochemical Properties**.** *Inorg. Chem.*, **1995**, *34*, 2759
95. Indelli, M. T.; Bignozzi, C. A.; Scandola, F. Design of Long-Lived Ru(II)-Terpyridine MLCT States. Tricyano Terpyridine Complexes. *Inorg. Chem.* **1998**, *37*, 6084-6089.
96. Hofmeier, H.; Schubert, U. S. Recent Developments in the Supramolecular Chemistry of Terpyridine-Metal Complexes. *Chem. Soc. Rev*. **2004**, *33*, 373-399.
97. Fang, Y.-Q.; Taylor, N. J.; Hanan, G. S.; Loiseau, F.; Passalacqua, R.; Campagna, S.; Nierengarten, H.; van Dorsselaer, A. A Strategy for Improving the Room-Temperature Luminescence Properties of Ru (II) Complexes with Tridentate Ligands. *J. Am. Chem. Soc.*, **2002**, *124*, 7912.
98. Rupp, M. T.; Shevchenko, N.; Hanan, G.S.; Kurth, D. G. Enhance the Photophysical Properties of Ru (II) Complexes by Specific Design of Terpyridine Ligands. *Coord. Chem. Rev.* **2021**, *446*, 214127(1-16).
99. Constable, E. C.; Smith, D. R. 4'4(9-Anthryl)-2,2':6',2"-Terpyridine a Novel Luminescent Component for Metallosupramolecular Systems. *Supramol. Chem.*, **1994**, *4*, 5-7.

100. Harriman, A.; Khatyr A.; Ziessel, R. Intramolecular Triplet Energy Transfer in Pyrene Metal Polypyridine Dyads: A Strategy for Extending the Triplet Lifetime of the Metal Complex. *Chem. Eur. J.*, **1999**, *5*, 3366-3381.
101. Passalacqua, R.; Loiseau, F.; Campagna, S.; Fang, Y.-Q.; Hanan, G.S. In Search of Ruthenium(II) Complexes Based on Tridentate Polypyridine Ligands that Feature Long-Lived Room-Temperature Luminescence: The Multichromophore Approach. *Angew. Chem. Int. Ed.* **2003**, *42*, 1607-1611.
102. Wang, J.; Hanan, G. S.; Loiseau, F.; Campagna, S. Prolonged Luminescence Lifetimes of Ru (II) Complexes via the Multichromophore Approach: The Excited-State Storage Element can be on a Ligand Not Involved in the MLCT Emitting State. *Chem. Commun.* **2004.** 2068-2069.
103. Beley, M.; Delabouglise, D.; Houppy, G.; Husson, J.; Petit, J.-P. Preparation and Properties of Ruthenium (II) Complexes of 2,2':6',2''-Terpyridines Substituted at the 4'-Position with Heterocyclic Groups. *Inorg. Chim. Acta.* **2005**, *358*, 3075-3083.
104. Siemeling, U.; Vor der Brueggen, J.; Vorfeld, U.; Neumann, B.; Stammler, A.; Stammler, H.-G.; Brockhinke, A.; Plessow, R.; Zanello, P.; Laschi, F.; Fabrizi de Biani, F.; Fontani, M.; Steenken, S.; Stapper, M.; Gurzadyan, G. Ferrocenyl-Functionalised Terpyridines and Their Transition-Metal Complexes: Syntheses, Structures and Spectroscopic and Electrochemical Properties. *Chem.-Eur. J.*, **2003**, *9*, 2819-2833
105. Siebert, R.; Winter, A.; Dietzek, B.; Schubert, U. S.; Popp. J .Dual Emission from Highly Conjugated 2,2': 6:2''-Terpyridine Complexes-A Potential Route to White Emitters. *Macromol. Rapid Commun.* **2010**, *31*, 883-888.
106. Duati, M.; Tasca, S.; Lynch, F. C.; Bohlen, H.; Vos, J. G.; Stagni, S.; Ward, M. D. Enhancement of Luminescence Lifetimes of Mononuclear Ruthenium(II)-Terpyridine Complexes by Manipulation of the σ-Donor Strength of Ligands. *Inorg. Chem.*, **2003**, *42*, 8377-8384.
107. Duati, M.; Fanni, S.; Vos, J. G. A New Luminescent Ru (Terpy) Complex Incorporating a 1,2,4-Triazole Based σ -Donor ligand*Inorg. Chem. Commun.*, **2000**, *3*, 68-70.

108. Benniston, A. C.; Chapman, G.; Harriman, A.; Mehrabi, M.; Sams. C. A. Electron Delocalization in a Ruthenium (II) Bis(2,2′:6′,2″-terpyridyl) Complex. *Inorg. Chem.* **2004**, *43*, 4227-4233.
109. Benniston, A. C.; Chapman, G.; Harriman, A.; Rostron, S. A.; Reversible Luminescence Switching in a Ruthenium(II) Bis(2,2′:6′,2″-terpyridine)-Benzoquinone Dyad. *Inorg. Chem.* **2005**, *44*, 4097-4036.
110. Barigelletti, F.; Ventura, B.; Collin, J.P.; Kayhanian, R.; Gavina, P.; Sauvage, J.P. Electrochemical and Spectroscopic Properties of Cyclometallated and Non-Cyclometallated Ruthenium (II) Complexes Containing Sterically Hindering Ligands of the Phenanthroline and Terpyridine Families. *Eur. J. Inorg. Chem.* **2000**, 113-119.
111. Brown, D. G. Sanguantrakun, N.; Schulze, B.; Schubert, U. S. Berlinguette, C. P. Bis (tridentate) Ruthenium-Terpyridine Complexes Featuring Microsecond Excited-State Lifetimes. *J. Am. Chem. Soc.* **2012**, *134*, 12354-12357.
112. Chang, K. C.; Sun, S. S.; Odago, M. O.; Lees. A. J. Anion Recongnition and Sensing By Transitiom-Metal Complexes with polarized NH recongnition motif. *Coord. Chem. Rev.* **2015**, *284*,111-123.
113. Mizuno, T.; Wei, W.H.; Eller, L.R.; Sessler, J.L. Phenanthroline Complexes Bearing Fused Dipyrrolylquinoxaline Anion Recognition Sites: Efficient Fluoride Anion Receptors. *J. Am. Chem. Soc.* **2002**, *124*, 1134-1135.
114. Anzenbacher Jr, P.; Tyson, D.S.; Jursiková, K.; Castellano, F.N. Luminescence Lifetime-Based Sensor for Cyanide and Related Anions. *J. Am. Chem. Soc.* **2002**, *124*, 1134-1135.
115. Cui, Y.; Mo, H.J.; Chen, J.C.; Niu, Y.L.; Zhong, Y.R.; Zheng K. C., Ye, B.H. Anion-Selective Interaction and Colorimeter by an Optical Metalloreceptor Based on Ruthenium(II) 2,2′-Biimidazole: Hydrogen Bonding and Proton Transfer. *Inorg. Chem.* **2007**, *46*, 6427-6436.
116. Cui, Y.; Niu, Y.L.; Cao, M.L.; Wang, K.; Mo, H. J.; Zhong, Y. R.; Ye, B.H. Ruthenium(II) 2,2′-Bibenzimidazole Complex as a Second-Sphere Receptor for Anions Interaction and colorimeter. Inorg. Chem. **2008**. *47*,5616-5624.

117. Mo, H.J.; Niu, Y. L.; Zhang, M.; Qiao, Z.P.; Ye, B.H. Photophysical, Electrochemical and Anion Sensing Properties of Ru(II) Bipyridine Complexes with 2,2'-Biimidazole-Like Ligand. *Dalton Trans.* **2011**, *40, 8218*-8225.

118. Mo, H.J.; Chao, H. Y.; Ye, B. H. A Ruthenium Biimidazole-Like Anion Receptor with Two Chelating NH···O Intramolecular Hydrogen Bonds. *Inorg. Chem. Commun.* **2013**, *35*,100-103.

119. Zapata, F.; Caballero, A.; Espinosa, A.; Tárraga, A.; Molina, P. Cation Coordination Induced Modulation of the Anion Sensing Properties of a Ferrocene-Imidazophenanthroline Dyad. *J. Org. Chem*. **2008**, *73*, 4034-4044.

120. Mardanya, S.; Karmakar, S.; Maity, D.; Baitalik, S. Ruthenium (II) and Osmium (II) Mixed Chelates Based on Pyrenyl-Pyridylimidazole and 2,2′-Bipyridine Ligands as Efficient DNA Intercalators and Anion Sensors. *Inorg. Chem.* **2015**, *54*, 513-526.

121. Das, S.; Karmakar, S.; Mardanya, S.; Baitalik. Synthesis, Structural Characterization, and Multichannel Anion and Cation Sensing Studies of a Bifunctional Ru (II) Polypyridyl-Imidazole Based Receptor. *Dalton Trans.*, **2014**, *43*, 3767-3782.

122. Mondal, D.; Bar, M.; Mukherjee, S.; Baitalik, S. Design of Ru (II) Complexes Based on Anthraimidazoledione-Functionalized Terpyridine Ligand for Improvement of Room-Temperature Luminescence Characteristics and Recognition of Selective Anions: Experimental and DFT/TD-DFT Study. *Inorg. Chem.* **2016**, *55*, 9707-9724.

123. Patil, S. K.; Ghosh, R.; Kennedy, P.; Mobin, S. M.; Das, D. Potential Anion Sensing Properties By a Redox and Substitution Series of $[Ru(bpy)_{3-n}(Hdpa)_n]^{2+,}$ n = 1-3; Hdpa = 2,2’ -Dipyridylamine: Selective Recognition and Stoichiometric Binding Cyanide and Fluoride Ions. *RSC Adv.*, **2016**, *6*, 62310-62319.

124. Khatua, S.; Samanta, D.; Bats, J. W.; Schmittel, M. Rapid and Highly Sensitive Dual-Channel Detection of Cyanide by Bis-heteroleptic Ruthenium (II) Complexes. *Inorg. Chem.* **2012**, *51*, 7075-7086.

125. Biancardo, M.; Bignozzi, C.; Doyle, H.; Redmond Gareth. A Potential and Ion Switched Molecular Photonic Logic Gate. *Chem. Commun.*, **2005**, 3918-3920.

126. Liu, Y.; Li, M.; Zhao, Q.; Wu, H.; Huang, K.; Li. F. Phosphorescent Iridium (III) Complex with an N^O Ligand as a Hg^{2+}-Selective Chemodosimeter and Logic Gate *Inorg. Chem.* 2011, *50*, 5969-5977.

127. Bhalla, V.; Kumar, R.; Kumar, M. On-Off' Reversible Switch for Fe^{3+} and F^- Mimicking XNOR Logic Function. *Tetrahedron Lett.* **2010**, *51*, 5559-5562.

128. Fang, C. J.; Zhu, Z.; Sun, W.; Xu, C. H.; Yan, C. H. New TTF Derivatives: Several Molecular Logic Gates Based on Their Switchable Fluorescent Emissions. *New J. Chem.*, **2007**, *31*, 580-586.

129. Kumar, A.; Chhatwal, M.; Gupta, R. D.; Awasthi S. K. Chemically-Driven "Molecular Logic Circuit" Based on Osmium Chromophore with a Resettable Multiple Readout. *RSC Adv.*, **2015**, *5*, 5217-5220.

130. Mondal, P. C.; Singh, V.; Jeyachandran, Y. L.; Zharnikov, M. Surface-Confined Heterometallic Triads on the Basis of Terpyridyl Complexes and Design of Molecular Logic Gates. *ACS Appl. Mater. Interfaces* **2015**, *7*, 8677-8686.

131. Pal, P.; Sahoo, A.; Paul, A.; Baitalik, S. Anion and Light Responsive Molecular Switches Based on Stilbene-Appended Ru (II) Terpyridyl-Imidazole Complexes That Mimic Advanced Boolean and Fuzzy Logic Operations. *Eur. J. Inorg. Chem.* **2022**, e202200219 (1-10).

****

Chapter 2

Exploitation of Second Coordination Sphere to Promote Significant Increase of Room Temperature Luminescence Lifetime and Anion Sensing in Ruthenium-Terpyridine Complexes

2.1. Introduction

Atoms or groups which are situated at the outskirts of ligands and not directly coordinated to a particular metal, often play a pivotal role on the physicochemical behaviours of complexes.[1-4] This type of secondary coordination sphere effect is operative in many proteins, but usually difficult to reproduce in synthetically designed systems.[5-7] We are interested in modulating the photophysical properties of Ru(II) complexes because of their promising roles in diverse fields of research such as photochemical conversion of solar energy, molecular electronic devices, and multichannel optical sensors, arising out of their outstanding photo-redox behaviors.[8-11] Many ruthenium(II) complexes derived from bipyridine-type ligands are particularly important in this regard as they absorb light throughout the entire visible region, have excited-state lifetimes of about 1µs at room temperature, are stable upon one-electron oxidation and reduction, and display remarkable photo-stability. However, bpy-type ligands give rise to diasteromeric mixtures in resulting octahedral complexes which are often difficult to separate. On the other hand, $[Ru(tpy)_2]^{2+}$ type complexes produce achiral rod-like structures.[12-17] But their shortcomings are non-luminescence characteristics and very short excited state lifetimes at RT (τ=0.25 ns for $[Ru(tpy)_2]^{2+}$).[18] Therefore, improvement of RT emission behaviors of Ru(II)-terpyridine complexes are necessary to utilize them as effective visible light photo-sensitizers. Enormous efforts have already been exercised to design terpyridine complexes of Ru(II) with improved RT luminescence characteristics and longer excited-state lifetimes by adopting various synthetic protocols such as incorporation of electron-donating or -accepting groups[19-22] and polyaromatic moieties[23-27] onto the terpyridine ring. Most of these approaches were involved in modulating the energy of ^{3}MLCT and ^{3}MC states. Cyclometalated ligands have the ability to increase the energy of ^{3}MC state.[28-30] Change of pyridine moiety by other heterocyclic rings sometimes produce less distorted octahedral geometry.[31-35] Important point is to extend electron delocalization in the excited state to minimize non-radiative deactivation channels.[36-44] During last few years, our group also designed a variety of Ru(II)-terpyridine complexes by incorporating different aromatic and heteroaromatic moieties at the 4'-position of terpyridine motif which are capable of displaying RT luminescence with reasonably long lifetimes.[45-51]

In this work, our objective is to modulate RT emission characteristics of Ru(II)-terpyridine complexes through exploitation of their secondary coordination spheres. In order to achieve this, we have synthesized a terpyridyl-imidazole ligand, 2-(6-pyridin-2-yl)-4-(4-(4,5-di*p*-tolyl-1*H*-imidazol-2-yl)phenyl)pyridin-2-yl)pyridine(**tpyHImzPh$_3$Me$_2$**), in which the terpyridine moiety has been coupled with dimethybenzil unit through phenyl-imidazole spacer. This ligand has been employed for the preparation of three Ru (II) complexes (both homo- and heteroleptic types) for fine tuning their emission spectral properties (**Chart 2.1**). All these complexes display luminescence with relatively long lifetime at RT. Additionally, the complexes possess imidazole ring(s) in their second coordination sphere whose NH proton(s) can be subjected to protonation by acid and deprotonation by base or selected anions. Accordingly, we have thoroughly investigated the photophysical behaviors of these complexes as a function of both acid and anions.

Previously, we reported an array of Ru(II) and Os(II) complexes based on similar terpyridyl-imidazole motif differing by peripheral methyl groups and investigated their photophysical behaviors and anion sensing properties in MeCN and it was seen that the complexes act as sensors for F^-, AcO^-, CN^-, and $H_2PO_4^-$ without selectivity.[52-53] The incorporation of peripheral methyl group in the present ligand induces an enormous effect on the emission characteristics of the complexes with regard to protonation of the imidazole nitrogen atom(s). Most importantly, protonation induces augmentation of emission lifetime by 80-fold with respect to their free forms. Anion sensing behaviours of the present complexes studied both in organic and aqueous media via multiple optical channels showed that while the complexes are highly sensitive probes for F^-, CN^-, and AcO^- in MeCN, they lack selectivity. In sharp contrast, the complexes act as very selective probes for CN^- in H_2O having limit of detection as low as 10^{-8} M. Again, while remarkable improvement of emission characteristics occur in the presence of acid, selected anions induce substantial quenching of emission intensity and lifetime of the complexes.

A large body of reports are available in literature, particularly by the research groups of Rau[54,55] and Vos[56,57], concerning the effect of solution acidity on the emission characteristics of polypyridine complexes of Ru(II) along with various azole-based ligands. However, studied made with tridentate ligands are sparse compared with bidentate ligands.[25,54-57] A sizeable number of reports are also available from our group[45-48] as well as from the research groups of Rau,[58-61] Ye,[62-65] Fabrizzi,[66] Lees,[67] to name a few, on Ru(II)-polypyridine complexes coupled with azole functionalities for recognition of anions.

We have also carried out computation studies employing DFT and TD-DFT methods on free-, protonated- and deprotonated forms of the complexes in order to gain better understanding of their electronic structures and for appropriate assignment of absorption and emission spectral bands.

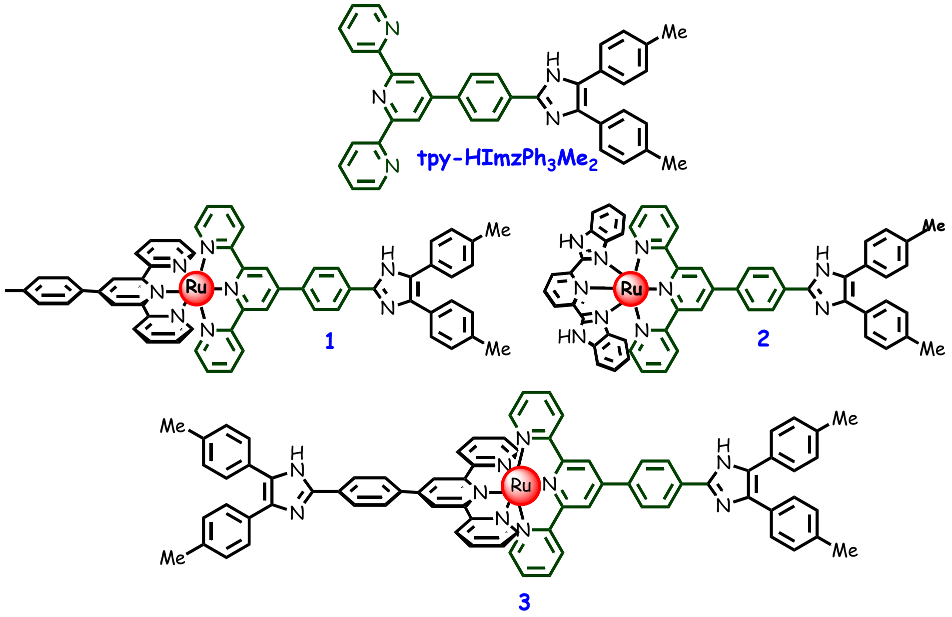

Chart 2.1. Molecular structures of the complex cations **1**$^{2+}$, **2**$^{2+}$, and **3**$^{2+}$ under present investigation.

2.2 Experimental Section

2.2.1. Materials. Chemicals and solvents were purchased from local suppliers. 4-formyl-2,2':6',2"-terpyridine (tpy-PhCHO)[68] and 2,6-bis(benzimidazole-2-yl)pyridine (H_2pbbzim) were prepared following reported procedures.[69] [(tpy-$PhCH_3$)$RuCl_3$] and [(H_2pbbzim)$RuCl_3$] were synthesized by treating $RuCl_3·3H_2O$ with tpy-$PhCH_3$ and H_2pbbzim, respectively in 1:1 molar ratio in refluxing EtOH.

2.2.2. Synthesis of the Ligand. [2-(6-pyridin-2-yl)-4-(4-(4,5-di*p*-tolyl-1*H*-imidazol-2-yl)phenyl)pyridin-2-yl)pyridine(tpy-HImzPh$_3$Me$_2$)]. Dimethylbenzil (1.7g, 2.97 mmol), tpy-PhCHO (1.00 g, 2.97 mmol), and NH_4OAc (2.3 g, 30 mmol) were dissolved in CH_3COOH (20 mL) and refluxed for 2h. After cool down to RT, the resulting solution was poured into crushed ice (300 mL) and upon stirring an off-white compound that deposited was filtered. The residue was dispersed in water (*ca.* 100 mL) and neutralized with Na_2CO_3 solution. The resulting solid was filtered and thoroughly washed with water. Purification of the compounds were performed through silica gel column chromatography using $CHCl_3$ as the eluting solvent and finally through recrystallization from $CHCl_3$-MeOH (1:1) mixture. Yield, 1.24 g, 74%). ^1H NMR (400 MHz, DMSO-d_6, δ/ppm): 11.90 (s, 1H, NH(imidazole)), 8.81-8.79 (m, 4H, $2H_{3'}+2H_6$), 8.71 (d, 2H, *J*=8.0 Hz, H_3), 8.32 (d, 2H, *J*=8.4 Hz, H_8), 8.14 (d, 2H, *J*=8.0 Hz, H_7), 8.07 (t, 2H, *J*=7.8 Hz, H_4), 7.46-7.42 (m, 6H, $2H_5+4H_{10}$), 7.24 (d, 4H, *J*=7.4 Hz H_9), 2.51 (s, 6H, Me). ESI-MS: *m/z* 556.24 ($[L+H]^+$). Anal. Calcd for $C_{38}H_{29}N_5$: C, 82.14; H, 5.26; N, 12.60. Found: C, 82.07; H, 5.32; N, 12.55.

2.2.3.Synthesis of the Metal Complexes. The complexes were prepared under oxygen and moisture free dinitrogen using standard Schlenk techniques.

$[(tpy\text{-}PhCH_3)Ru(tpy\text{-}HImzPh_3Me_2)](ClO_4)_2\cdot H_2O$ (1). Ru(tpy-$PhCH_3$)Cl_3 (80 mg, 0.15 mmol) and tpy-$HImzPh_3Me_2$ (84 mg, 0.15 mmol) were added to 10 mL ethylene glycol and refluxed for 2h under Ar protection. The resulting solution was cooled to RT and upon spilling into an aqueous solution of $NaClO_4$ an orange-red compound deposited. The compound was collected and purified by silica-gel column chromatography eluting with CH_3CN. Recrystallization from CH_3CN-MeOH (1:1, v/v) mixture afforded a red microcrystalline compound. Yield: 98 mg (55%). Anal. Calcd. for $C_{60}H_{48}N_8Cl_2O_9Ru$: C, 60.17; H, 3.87; N, 9.36. Found: C, 60.11; H, 3.94; N, 9.29. ^1H NMR (400 MHz, DMSO-d_6, δ/ppm): 12.40 (s, 1H, NH imidazole), 9.57 (s, 2H, $H_{3'}$), 9.45 (d, *J*=8.0Hz, 2H, $H_{3'''}$), 9.11 (d, 4H, *J*=8.0 Hz, $2H_6+2H_{6'}$), 8.75 (d, 2H, *J*=8.8 Hz, H_8), 8.51 (d, 2H, *J*=8.40 Hz, H_7), 8.36 (d, 2H, *J*=8.40 Hz, $H_{8'}$) 8.10-8.07 (m, 4H, $H_4+H_{4'}$), 7.58 (d, 4H, *J* = 5.6 Hz, $2H_3+2H_{3''}$), 7.53 (d, 2H, *J*=5.6 Hz, $H_{7'}$), 7.50 (d, 4H, *J*=8.0 Hz, H_9), 7.36 (d, 4H, *J*=7.2 Hz, H_{10}), 7.28 (m, 4H, $2H_5+2H_{5'}$), 2.48 {(s, 6H, CH_3 (tpy-$HImzPh_3Me_2$)}, 2.39 (s, 3H, CH_3 (tpy-$PhCH_3$)}. ESI-MS (positive, CH_3CN) *m/z* = 490.18 (100 %) $[(tpy\text{-}PhCH_3)Ru\ (tpy\text{-}HImzPh_3Me_2)]^{2+}$.

[(H_2pbbzim)Ru(tpy-HImzPh$_3$Me$_2$)](ClO$_4$)$_2$·H_2O (2). Complex **2** was prepared by following the same procedure as **1**. In this case [(H_2pbbzim)RuCl$_3$] (78 mg, 0.15 mmol) was used in place of Ru(tpy-PhCH$_3$)Cl$_3$ and recrystallization was carried out in CH_3CN-H_2O (2:1, v/v) mixture under weakly acidic condition. Yield: 96 mg (54%). Calcd. for $C_{57}H_{44}N_{10}Cl_2O_9Ru$: C, 57.70; H, 3.74; N,11.81. Found: C, 57.63; H, 3.80; N, 10.93. ^{1}H NMR data (400 MHz, DMSO-d_6, δ/ppm): 15.08 (s, 2H, NH imidazole), 12.13 (s, 1H, NH imidazole), 9.68 (s, 2H, $H_{3'}$), 9.05 (d, 2H, J=8.0 Hz, H_6), 8.87 (d, 2H, J =8.0 Hz, H_8), 8.81(d, 2H, J=8.0 Hz, H_{15}), 8.66 (t, 1H, J=8.0 Hz, H_{16}), 8.56 (d, 2H, J=8.0 Hz, H_7), 7.99 (t, 2H, J= 7.8 Hz, H_4), 7.68 (d, 2H, J=8.0 Hz, H_{14}), 7.53 (d, 4H, J=7.6 Hz 2H_3 +2H_{10}), 7.37 (d, 4H, J= 7.6 Hz, H_9), 7.28 (m, 4H, 2H_{13}+2H_5), 7.03 (t, 2H, J=7.8 Hz, H_{12}), 6.10 (d, 2H, J=8.4 Hz, H_{11}), 2.50 {s, 6H, CH_3 (tpy-HImzPh$_3$Me$_2$)}. ESI-MS (positive, CH_3CN) m/z = 484.09 (100 %) [(H_2pbbzim)Ru(tpy-HImzPh$_3$Me$_2$)]$^{2+}$.

[Ru(tpy-HImzPh$_3$Me$_2$)$_2$](ClO$_4$)$_2$·2H_2O (3). Synthetic protocol for **3** is basically similar to that of **1**. In this case Ru(DMSO)$_4$Cl$_2$ (72 mg, 0.15 mmol) and tpy-HImzPh$_3$Me$_2$ (167 mg, 0.30 mmol) were taken in 1:2 molar ratio in ethylene glycol and refluxed for 3h. The compound was purified successively by silica gel column chromatography as well as recrystallization from MeCN-MeOH (1:1, v/v) in weakly acidic condition. Yield: 113 mg (52 %). Anal. Calcd. for $C_{76}H_{62}N_{10}Cl_2O_{10}Ru$: C, 63.04; H, 4.32; N, 9.67. Found: C, 62.97; H, 4.37; N, 9.62. ^{1}H NMR data (400 MHz, DMSO-d_6, δ/ppm): 12.20 (s, 2H, NH imidazole), 9.61 (s, 4H, $H_{3'}$), 9.15 (d, 4H, J=8.4 Hz, H_6), 8.75 (d, 4H, J=7.6 Hz, H_8), 8.53 (d, 4H, J=8.0 Hz, H_7), 8.12(t, 4H, J=7.6 Hz, H_4), 7.59 (d, 4H, J=5.6, H_3), 7.59 (d, 8H, J=7.6, H_{10}), 7.34 (m, 12H, 4H_5+8H_9), 2.51 {s, 12H, CH_3 (tpy-HImzPh$_3$Me$_2$)}. ESI-MS(positive,CH_3CN) m/z=606.16(100%)[Ru(tpy-HImzPh$_3$Me$_2$)$_2$]$^{2+}$.

Caution! Perchlorate salts of the metal complexes are explosive and should be handled in small amount with extreme care.

2.2.4. Physical Measurements. Elemental analyses of the compounds were performed with a Vario-Micro V2.0.11 elemental (CHNSO) analyzer. NMR spectra were collected on a Bruker 400 MHz spectrometer in DMSO-d_6 for both the ligand and metal complexes. High resolution mass spectroscopy was performed on a Waters Xevo G2 QTOf mass spectrometer. The UV-vis absorption spectra were recorded with a Shimadzu

UV 1800 spectrometer. Steady state luminescence spectra were obtained by a Horiba Fluoromax-4 spectrometer. Luminescence quantum yields were determined by using literature method taking $[Ru(bpy)_3]^{2+}$as the standard. Luminescence lifetime measurements were carried out by using time-correlated single photon counting set up from Horiba Jobin-Yvon. The luminescence decay data were collected on a Hamamatsu MCP photomultiplier (R3809) and were analyzed by using IBH DAS6 software. For a typical absorption and emission titration experiment, aliquots of $HClO_4$ (0.1 M) were added incrementally to a 2.5 mL solution of the complexes (1.0×10^{-5} M).

Experimental uncertainties are as follows: absorption maxima, ±2 nm; molar absorption coefficients, 10%; emission maxima, ±5 nm; excited–state lifetimes, 10%; luminescence quantum yields, 20%.

The binding/equilibrium constants were evaluated from absorption/emission titration data using equation (1).[70,71]

$$\Delta A = \frac{\Delta\varepsilon b([\mathrm{H}] + [\mathrm{G}] + (1/K)) \pm \sqrt{\Delta\varepsilon^2 b^2([\mathrm{H}] + [\mathrm{G}] + (1/K))^2 - 4\Delta\varepsilon^2 b^2[\mathrm{H}][\mathrm{G}]}}{2} \qquad \mathbf{1}$$

where ΔA is the change in absorbance, [H] and [G] is the concentration of metal complex and added anion, respectively. Δε is the change in molar extinction coefficient, b is the absorption path length, and K is the binding constant. Non-linear regression analysis of absorption/emission spectral data as a function of anion concentration lead to the value of binding constants. Binding constants were performed in duplicate, and the average value is reported.

Detection limits of complexes were determined by utilizing their absorption/emission titration profiles. The curves plotted between normalized absorbance or luminescence intensity *vs*. Log[anion]. Linear regression curves as fitted to the intermediate values are also shown in the said figures. The point at which the line crossed the ordinate axis was taken as the detection limit of the anion.

2.2.5. Computational Methods. All calculations were performed with the Gaussian 09 program [72] employing the DFT method with Becke's three-parameter hybrid functional and Lee-Yang-Parr's gradient corrected correlation functional B3LYP level of theory.[73-74] 6-31G* and $6\text{-}311G^*$ basis sets were employed for the C, H, N, and O while SDD basis set was used for Ru atom.[75] Geometries were fully optimized using the criteria of the respective programs. TD-DFT[76-79] calculations of the singlet-singlet excitations were performed in acetonitrile simulated by the CPCM model[80] by using the so-called nonequilibrium approach, which has been designed for the study of the absorption process.[81-82] Orbital analysis was completed with Gauss View[83] and Gauss sum 2.2.[84]

2.3. Results and Discussion

2.3.1. Synthesis and Characterization. The ligand tpy-HImzPh$_3$Me$_2$ was prepared by refluxing equimolar mixture of dimethylbenzil and tpy-PhCHO in CH_3COOH with excess NH_4OAc. The heteroleptic complexes (**1** and **2**) were synthesized by reacting tpy-HImzPh$_3$Me$_2$ with the precursor complexes, [(tpy-PhCH$_3$)RuCl$_3$] and [(H$_2$pbbzim) RuCl$_3$], respectively in 1:1 molar ratio in ethylene glycol at an elevated temperature. The homoleptic complex (**3**), on the other hand, was obtained by refluxing Ru(DMSO)$_4$Cl$_2$ with 2 equiv of tpy-HImzPh$_3$Me$_2$ in ethylene glycol. In all cases, the reactions were followed by counter anion exchange with $NaClO_4$. The perchlorate salts of the metal complexes are potentially explosive and should be handled in small amount with extreme care. Column chromatography and recrystallization techniques were employed for purification and all the complexes were obtained in fairly good yields (~55%). The complexes were characterized by elemental analyses, ESI mass, and NMR spectroscopic investigations. Details of synthesis and characterization data are already provided in the previous experimental Section.

ESI mass spectra of **1** and **3** in conjunction with their computed isotopic patterns are delineated in Figure 2.1. The complexes display intense peaks with m/z values between 484.09 and 606.16, corresponding to bi-positive cation. Good correspondence between experimental and computed isotopic pattern was observed in all cases. Proton NMR spectra of the complexes including the ligand, are exhibited in Figure 2.2. The spectrum of **3** is relatively simple due to the symmetrical ligand environment around the Ru(II) center, whereas the spectra of the heteroleptic analogues (**1** and **2**) are more complex because of overlapping resonances associated with two types of ligands.

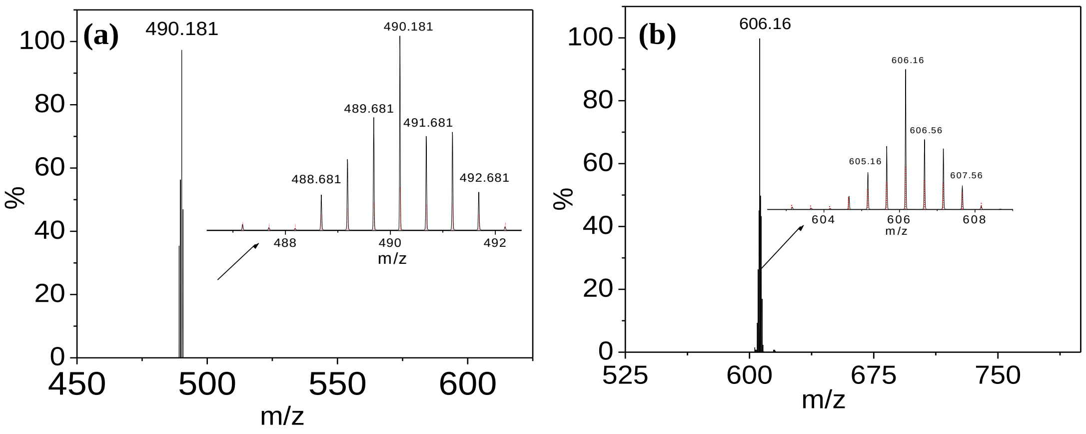

Figure 2.1. ESI (positive) mass spectrum for the complex cation of **1** [(tpy-PhCH$_3$)Ru(tpy-HImzPh$_3$Me$_2$]$^{2+}$ (m/z = 490.18) (a) and **3** [(Ru(tpy-HImzPh$_3$Me$_2$)$_2$]$^{2+}$ (m/z = 606.16) (b) in MeCN showing both observed and simulated isotopic distribution patterns.

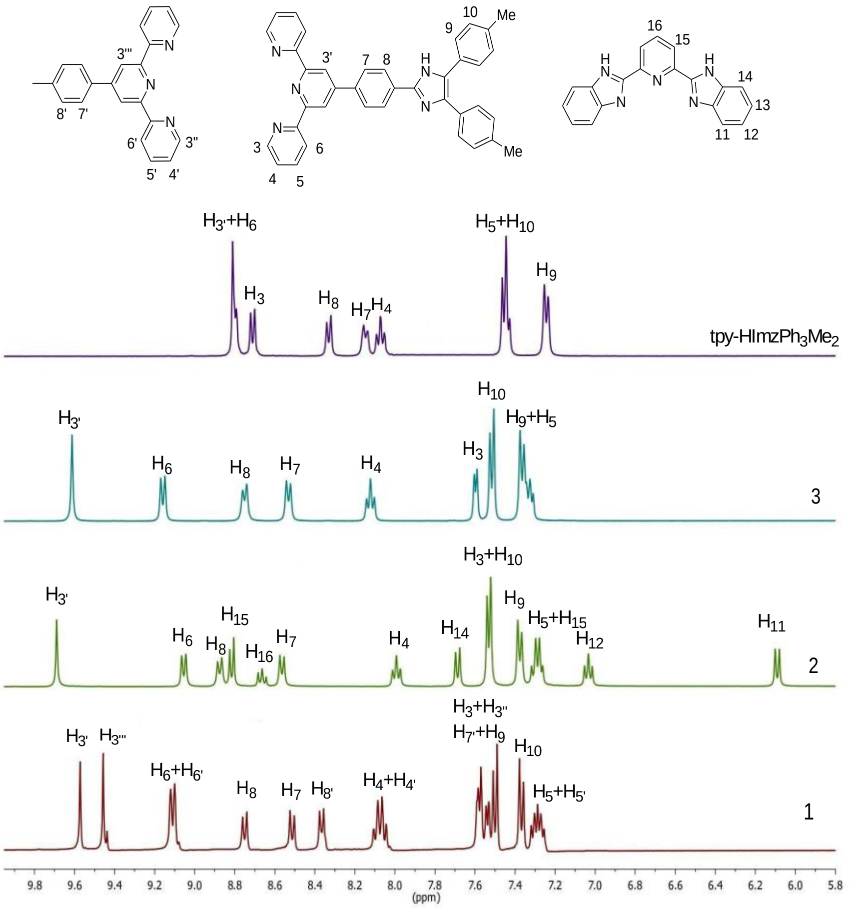

Figure 2.2. ^{1}H NMR spectra of **1-3** together with **tpy-HImzPh$_3$Me$_2$** in DMSO-d_6.

2.3.2. DFT and TD-DFT Studies. Gaussian 09 software was used to optimize the geometries of complexes (using B3LYP functional and 6-31G* basis set for C, H, N, O and SDD basis set for Ru) in their free-, protonated- and deprotonated forms (**Chart 2.2**). Optimized geometries are displayed in Figure 2.3. Structural parameters are tabulated in Table 2.1. Diversion from perfect octahedral geometry is observed in all cases. Ru-N distances vary over the range of 1.963 Å and 2.116 Å, which are in agreement with the values reported in literature for structurally characterized related Ru (II)-terpyridine complexes.[45-52] Frontier molecular orbitals and their compositions are presented in Figures 2.4-2.5 and in Table 2.2-2.3. Electronic charge density allocation in complexes **1-3** and their reallocation on protonation (**1a-3a**) and deprotonation (**1b-3b**) can be envisaged from their electrostatic surface potential (ESP) plots (Figure 2.6). Green color symbolizes electron rich region, while blue color implies electron deficient region. It may be noted that the phenyl-imidazole portion of the complexes became more electron deficient on protonaton and electron-rich zone upon deprotonation.

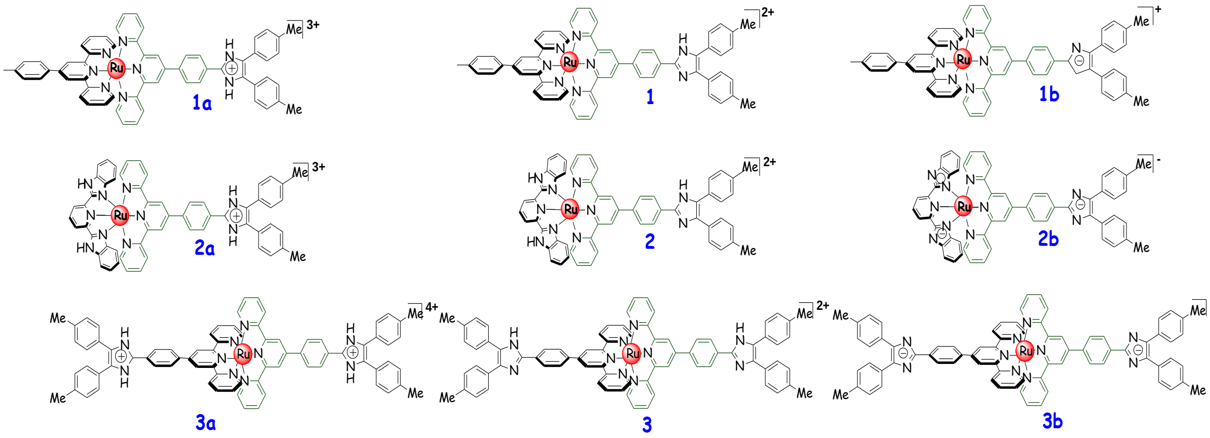

Chart 2.2. Molecular structures of the complexes in their free- **(1-3)**, protonated-(**1a-3a**) and deprotonated (**1b-3b**) forms.

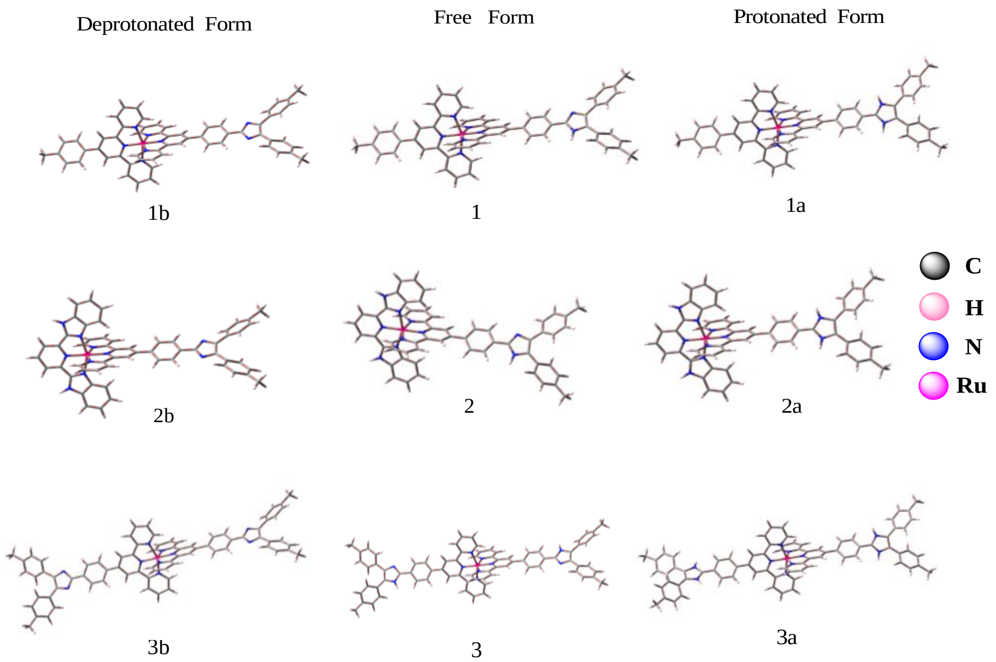

Figure 2.3. Ground state optimized geometries of complexes in their free- (**1-3**), protonated- (**1a-3a**) and deprotonated (**1b-3b**) forms in MeCN.

Table 2.1. Selected Calculated Bond Distances and Angles for **1-3**.

	1	
	Ground State	Excited State
	Bond length/Å	
Ru1-N1	2.112	2.116
Ru1-N6	2.006	2.111
Ru1-N4	2.112	2.111
Ru1-N3	2.112	2.116
Ru1-N5	2.007	2.033
Ru1-N2	2.112	1.963
Bond angle/°		
N1-Ru1-N6	92.2	92.3
N1-Ru1-N4	92.4	92.3
N6-Ru1-N4	156.7	155.3
N1-Ru1-N3	156.8	157.8
N6-Ru1-N3	92.4	92.3
N4-Ru1-N3	92.2	92.4
N1-Ru1-N5	101.6	101.0
N6-Ru1-N5	78.4	77.6
N4-Ru1-N5	78.3	77.6
N3-Ru1-N5	101.5	101.1
N1-Ru1-N2	78.0	79.0
N6-Ru1-N2	101.6	102.2
N4-Ru1-N2	101.6	102.4
N3-Ru1-N2	78.4	79.0
N5-Ru1-N2	179.9	179.9

	2	
	Ground State	Excited State
	Bond length/Å	
Ru1-N1	2.101	2.115
Ru1-N6	2.001	2.114
Ru1-N4	2.107	2.115
Ru1-N3	2.120	2.115
Ru1-N5	2.041	2.076
Ru1-N2	2.120	1.964
Bond angle/°		
N1-Ru1-N6	92.1	92.4
N1-Ru1-N4	92.7	92.6
N6-Ru1-N4	154.9	153.3
N1-Ru1-N3	157.0	158.2
N6-Ru1-N3	92.7	92.6
N4-Ru1-N3	92.1	92.4
N1-Ru1-N5	101.5	100.8
N6-Ru1-N5	77.4	76.6
N4-Ru1-N5	77.4	76.6
N3-Ru1-N5	101.4	100.9
N1-Ru1-N2	78.5	79.1
N6-Ru1-N2	102.5	103.3
N4-Ru1-N2	102.5	103.3
N3-Ru1-N2	78.5	79.1
N5-Ru1-N2	179.9	179.9

	3	
	Ground State	Excited State
	Bond length/Å	
Ru1-N1	2.111	2.115
Ru1-N6	2.112	2.114
Ru1-N4	2.112	2.116
Ru1-N3	2.112	2.115
Ru1-N5	2.007	2.017
Ru1-N2	2.007	1.947
Bond angle/°		
N1-Ru1-N6	92.3	92.5
N1-Ru1-N4	92.3	92.4
N6-Ru1-N4	156.7	155.1
N1-Ru1-N3	156.7	157.9
N6-Ru1-N3	92.3	92.1
N4-Ru1-N3	92.3	92.5
N1-Ru1-N5	101.5	100.7
N6-Ru1-N5	78.4	77.2
N4-Ru1-N5	78.4	77.6
N3-Ru1-N5	101.7	100.8
N1-Ru1-N2	78.4	79.5
N6-Ru1-N2	101.7	102.7
N4-Ru1-N2	101.5	102.4
N3-Ru1-N2	78.4	79.3
N5-Ru1-N2	179.9	179.9

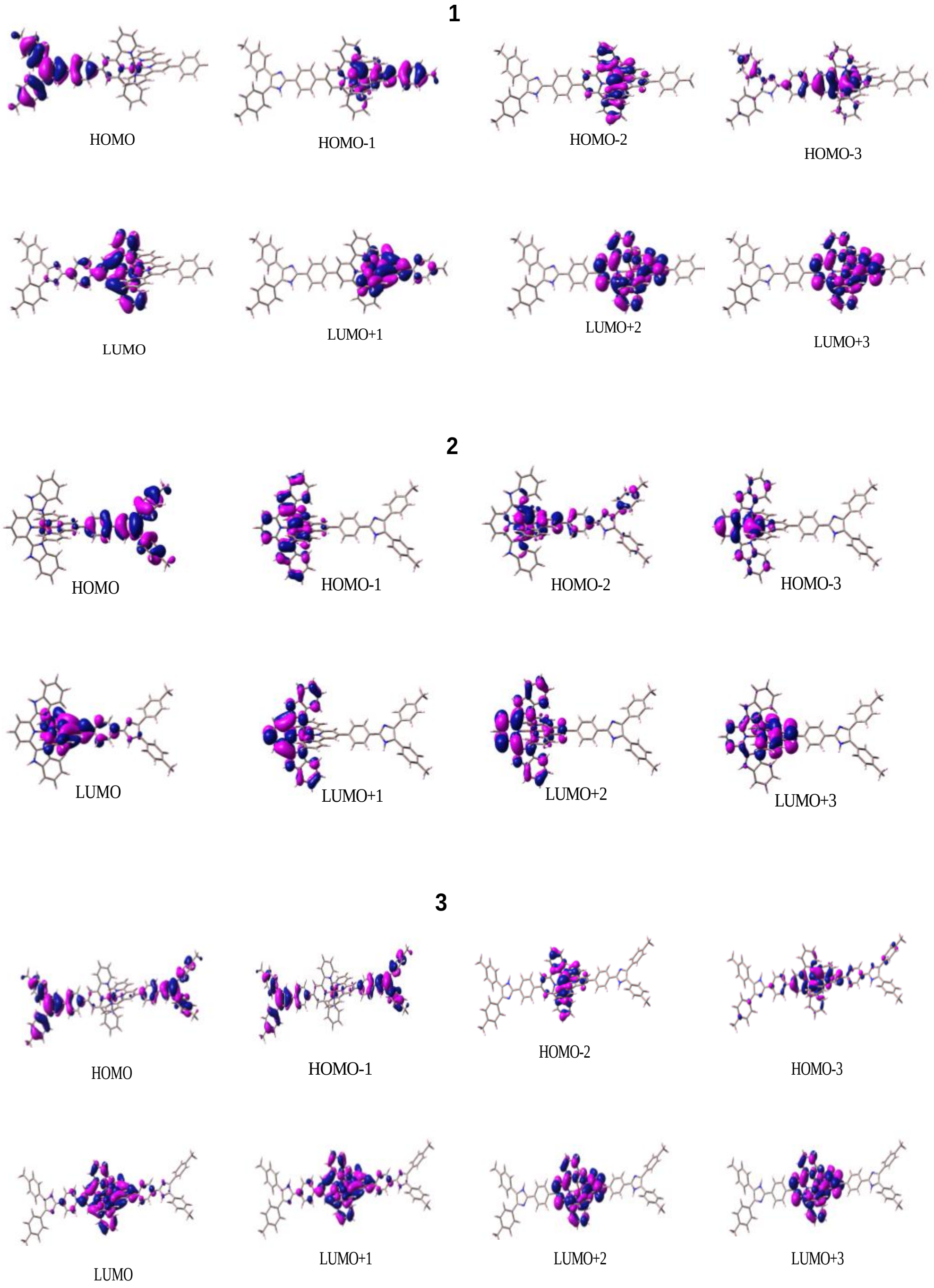

Figure 2.4. Schematic drawings of the selective frontier molecular orbitals of free forms **1-3** in MeCN.

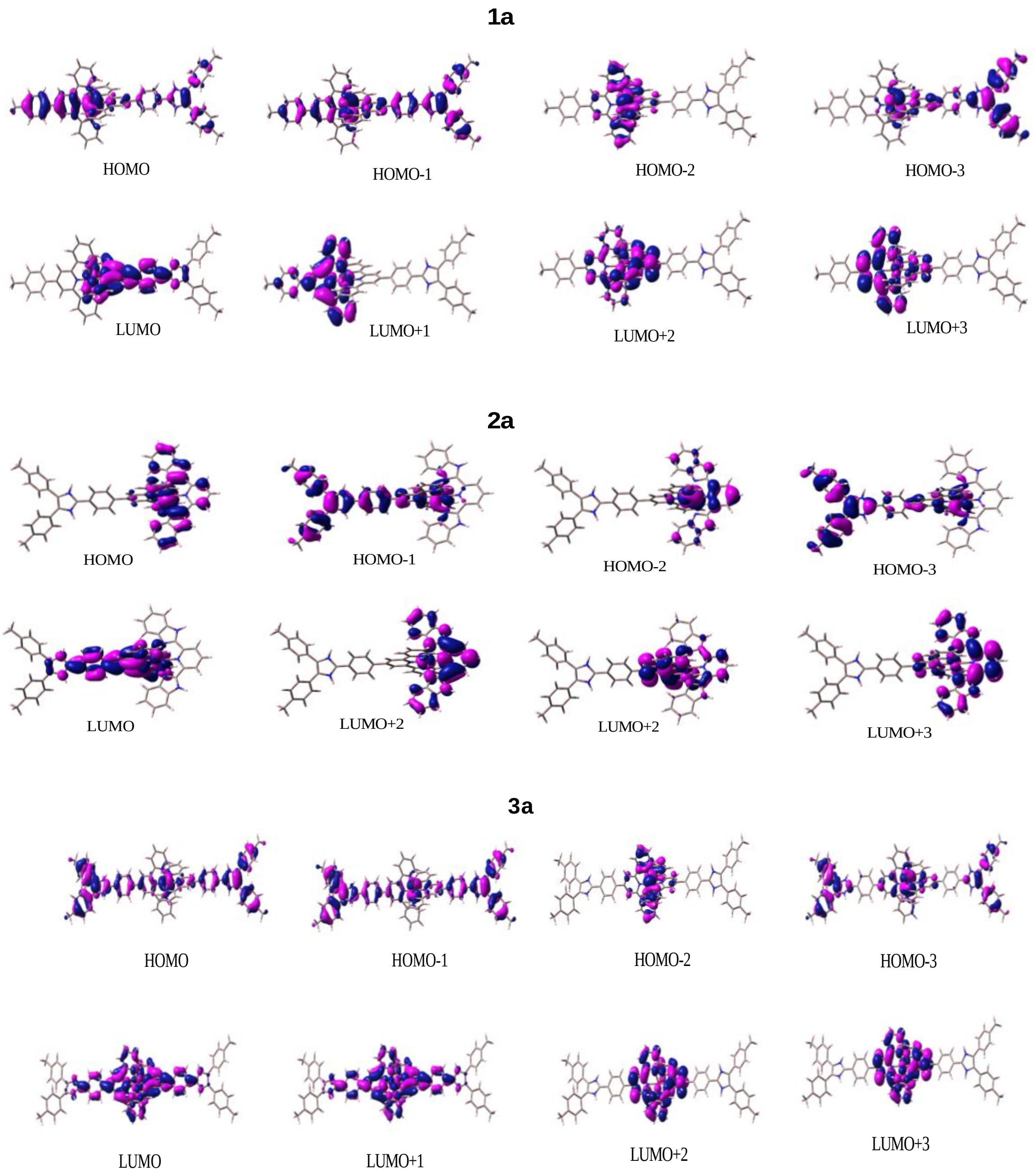

Figure 2.5. Schematic drawings of the selective frontier molecular orbitals of protonated form of complexes **1a-3a** in MeCN.

Table 2.2 Selected MOs along with their Energies and Compositions in the Ground State of the Complex in its Free (**1**), Protonated (**1a**) and Deprotonated (**1b**) Forms in MeCN.

M O	Energy/eV			% Compositions											
	1b	**1**	**1a**	**1b**				**1**				**1a**			
				Ru	imzph	tpy	PhMe	Ru	imzph	tpy	PhMe	Ru	imzph	tpy	PhMe
LUMO+5	-1.5	-1.59	-1.64	1.5	0.0	90.3	8.1	0.0	0.0	99.9	0.0	0.0	0.0	99.9	0.0
LUMO+4	-1.52	-1.69	-2.23	0.0	0.0	99.9	0.0	1.1	40.3	59.2	0.0	1.2	59.9	38.9	0.0
LUMO+3	-2.31	-2.42	-2.48	2.8	0.6	96.5	0.1	2.7	0.3	96.3	0.4	2.6	0.1	96.7	0.5
LUMO+2	-2.42	-2.5	-2.59	0.4	0.1	98.9	0.5	0.4	0.4	99.3	0.3	0.4	0.6	98.9	0.1
LUMO+1	-2.54	-2.66	-2.71	7.3	8.0	84.7	0.0	7.6	0.1	86.4	5.6	7.6	0.0	86.6	5.7
LUMO	-2.6	-2.7	-2.90	8.2	0.0	86.0	5.7	7.4	9.6	82.5	0.1	7.4	24.5	66.1	0.0
HOMO	-4.39	-5.39	-6.15	1.1	95.1	3.8	0.0	50.7	95.5	2.5	0.0	50.7	17.6	21.7	9.9
HOMO-1	-5.77	-6.08	-6.16	0.0	99.9	0.0	0.0	45.1	0.0	25.3	14.3	45.1	30.4	18.8	5.8
HOMO-2	-5.95	-6.14	-6.21	47.9	31.3	20.8	0.00	69.9	0.01	29.9	0.0	69.9	0.0	30.0	0.0
HOMO-3	-5.99	-6.15	-6.36	61.8	0.0	25.5	12.6	32.2	12.4	24.9	0.0	32.2	54.9	12.8	0.0
HOMO-4	-6.04	-6.62	-6.95	69.9	0.0	29.9	0.0	13.7	96.3	1.4	0.0	13.6	0.0	14.6	71.7
HOMO-5	-6.16	-6.82	-7.20	6.9	90.5	2.7	0.0	0.1	99.7	0.1	0.0	0.1	0.0	3.9	96.1

Table 2.3. Selected MOs along with their Energies and Compositions in the Ground State of the Complex in its Free (**2**), Protonated (**2a**) and Deprotonated (**2b**) Forms in MeCN.

M O	Energy/eV			% Compositions											
	2b	**2**	**2a**	**2b**				**2**				**2a**			
				Ru	imzph	tpy	Hbzim	Ru	imzph	tpy	Hbzim	Ru	imzph	tpy	Hbzim
LUMO+5	-1.34	-1.42	-1.55	3.4	0.0	96.1	0.5	3.4	0.0	96.1	0.5	0.0	99.9	0.0	0.0
LUMO+4	-1.46	-1.67	-2.21	1.6	10.9	87.6	0.0	0.6	40.2	59.1	0.0	1.2	59.5	39.1	0.2
LUMO+3	-2.3	-2.44	-2.52	1.2	0.7	95.9	1.5	2.4	0.5	84.9	12.1	2.4	0.1	12.4	85.1
LUMO+2	-2.42	-2.48	-2.56	1.2	0.0	1.8	96.9	0.5	0.1	12.9	86.5	0.5	0.6	85.5	13.5
LUMO+1	-2.51	-2.59	-2.65	7.3	8.0	82.9	1.6	7.8	0.0	1.7	90.5	7.5	0.0	1.3	91.1
LUMO	-2.53	-2.67	-2.89	8.1	0.0	1.7	90.1	7.9	9.4	81.0	1.7	7.4	26.9	64.5	1.2
HOMO	-4.39	-5.38	-5.93	1.1	95.1	3.6	0.1	2.0	95.6	2.1	0.2	59.0	0.0	10.9	30.0
HOMO-1	-5.76	-5.86	-6.14	0.7	98.8	0.1	0.3	59.6	0.0	11.2	29.2	39.1	44.8	12.2	3.9
HOMO-2	-5.77	-6.14	-6.27	59.8	1.2	0.3	27.7	63.3	12.0	18.4	6.3	69.7	0.0	8.0	22.2
HOMO-3	-5.93	-6.19	-6.35	49.1	29.9	11.3	4.8	69.7	0.0	7.9	22.1	30.1	58.2	8.6	2.9
HOMO-4	-6.08	-6.61	-6.81	70.1	0.1	7.9	21.9	2.2	96.5	1.1	0.2	3.5	0.0	1.3	95.2
HOMO-5	-6.16	-6.76	-6.98	6.4	91.1	1.8	0.6	3.4	0.0	1.4	95.2	0.8	0.0	0.1	99.1

Calculated UV-vis absorption spectra were obtained by carrying out TD-DFT calculations. Spectral parameters along with assignment of bands are presented in Table 2.4-2.6. MOs associated with lowest energy absorption in three different forms of the complexes are demonstrated in Figure 2.7 (for **2** and **3**). Calculated lowest energy band that shows up at 506 nm for **1**, at 501 nm for **2** and at 510 nm for **3** is due to combined Ru(II)→terpyridine and phenyl-imidazole→terpyridine (tpy-HImzPh$_3$Me$_2$) charge transfer transitions. Calculated data indicate that the lowest energy band gets blue-shifted on protonation, while red-shifted on deprotonation of the imidazole moiety (Figure 2.7). It is observed that protonation leads to stabilization of HOMOs, while deprotonation gives rise to destabilization relative to their free forms. LUMOs, on the other hand,

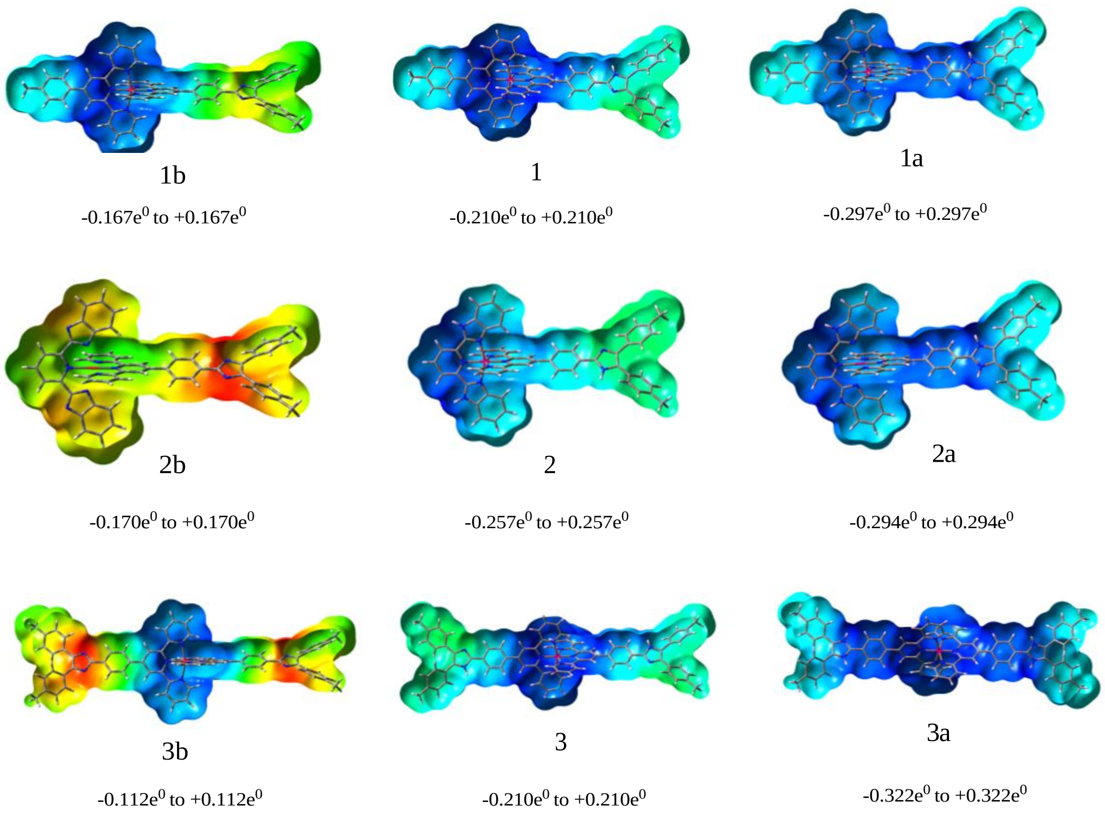

1b

$-0.167e^0$ to $+0.167e^0$

1

$-0.210e^0$ to $+0.210e^0$

1a

$-0.297e^0$ to $+0.297e^0$

2b

$-0.170e^0$ to $+0.170e^0$

2

$-0.257e^0$ to $+0.257e^0$

2a

$-0.294e^0$ to $+0.294e^0$

3b

$-0.112e^0$ to $+0.112e^0$

3

$-0.210e^0$ to $+0.210e^0$

3a

$-0.322e^0$ to $+0.322e^0$

Figure 2.6. Electrostatic surface potential (ESP) plots of the complexes in their free- (**1-3**), protonated- (**1a-3a**) and deprotonated (**1b-3b**) forms in MeCN.

remain less perturbed by protonation/deprotonation. The extent of shift depends upon the number of protonation/deprotonation sites and overall electronic nature of complexes.

To get guidance for appropriate assignment of bands, EDDM and NTO plots[85] associated with lowest energy band of free (S_1 for **1** and **3**; S_3 for **2**), protonated (S_5 for **1a** and **3a**; S_7 for **2a**) and deprotonated (S_2 for **1b** and **2b**; S_1 for **3b**) forms of the complexes are portrayed in Figure 2.8-2.9. NTOs associated with lowest-energy absorption lines all show considerable MLCT character. The geometries in their lowest triplet-state (T1) were also optimized and the singlet-triplet excitation energies were obtained from TD-DFT calculations by using the same functional, pseudopotential, and basis set. Dominant transitions involved in the lowest lying triplet excited states of complexes are presented in Figure 2.10 and and the singlet-triplet excitation energies at the lowest triplet state are presented in Table 2.7. Upon inspection of the dominant configurations, the lowest lying triplet excited states is expected to be predominantly ^{3}MLCT state featuring singly occupied molecular orbitals (SOMOs) located on the metal center/tpy-HImMe$_2$ or tpy-ImMe$_2^-$ and the tpy ligand. UKS calculations were also carried out directly on the triplet state of the complexes and the comparison of the experimental and calculated emission data are provided in Table 2.8. Calculated results show that protonation leads to blue-shift, whereas deprotonation induces red-shift of the original emission maxima.

Table 2.4. Selected UV-vis Energy Transitions at the TD-DFT/B3LYP Level of **1**, **1a**, and **1b** in MeCN.

Excited state	λ_{cal}/nm	Oscillator strength(f)	λ_{expt}/nm	Key transitions	Character
			1		
S_1	506	0.6	492	H→L (94%)	MLCT,ILCT
S_{17}	356	0.7	356	H→L+4 (94%)	MLCT, ILCT, π-π*
S_{25}	314	0.2	330	H-6→L+1 (82%), H-2→L+5 (10%)	ILCT, MLCT
S_{41}	298	0.2	311	H→L+10 (88%) H-7→L (7%)	π-π*, ILCT
S_{81}	262	0.8	281	H-11→L+2 (21%), H-10→L+3 (38%), H-8→L+3 (10%), H→L+9 (8%)	π-π*, ILCT
			1a		
S_5	487	0.7	491	H-3→L (11%), H-1→L (33%), H-1→L+1 (13%), H→L (22%), H→L+1 (12%),H-2→L+2 (5%)	MLCT, ILCT
S_{22}	352	0.3	350	H-4→L+1 (14%), H-3→L+4 (75%)	MLCT, ILCT, π-π*
S_{45}	324	0.3	329	H-9→L+1 (10%), H-8→L+1 (60%), H-2→L+6 (21%)	MLCT, ILCT, π-π*
S_{51}	312	0.5	310	H-11→L (63%), H-2→L+9 (16%),H-9→L+2 (6%)	π-π*, ILCT
S_{68}	298	0.8	280	H-9→L+2 (16%), H-8→L+3 (58%), H→L+10 (8%)	π-π*, ILCT
			1b		
S_2	474	0.6	500	H→L+1 (98%)	MLCT,ILCT
S_{17}	423	0.5	394	H-4→L+2 (49%), H-4→L+3 (10%), H→L+8 (37%)	MLCT, ILCT, π-π*
S_{32}	354	0.25	335	H→L+12 (96%)	ILCT, MLCT
S_{76}	303	0.42	316	H-14→L (71%), H-4→L+5 (16%)	π-π*
S_{106}	277	0.77	287	H-14→L+2 (45%), H-14→L+3 (15%), H-12→L+3 (25%)	π-π*, ILCT
S_{162}	242	0.17	235	H-17→L+3 (51%), H-12→L+6 (25%), H-7→L+7 (11%)	π-π*, ILCT

Table 2.5. Selected UV-vis Energy Transitions at the TD-DFT/B3LYP Level of **2**, **2a**, and **2b** in MeCN.

Excited state	λ_{cal}/nm	Oscillator strength(f)	λ_{expt}/nm	Key transitions	Character
2					
S_3	501	0.5	491	H→L (94%)	MLCT,ILCT
S_{18}	353	0.7	347	H→L+4 (94%)	MLCT,ILCT , π-π*
S_{58}	328	0.5	333	H-10→L (10%), H-1→L+11 (37%), H→L+10 (36%) H-9→L+1 (8%)	MLCT, ILCT, ,π-π*
S_{43}	298	0.53	315	H→L+7 (86%)	π-π*, ILCT
S_{50}	290	0.3	282	H-14→L+2 (25%), H-13→L+3 (43%), H-16→L+2 (7%), H-6→L+5 (5%), H-5→L+4 (5%)	π-π*, ILCT
S_{76}	263	0.4	240	H-12→L+3 (64%),H-13→L+3 (5%), H-12→L+2 (7%), H-10→L+3 (7%), H-4→L+4 (5%)	π-π*, ILCT
2a					
S_7	478	0.6	489	H-1→L (33%), H→L+2 (52%) H-2→L+1 (9%)	MLCT,ILCT
S_{23}	376	0.5	346	H-4→L+1 (96%)	ILCT ,π-π*
S_{38}	343	0.2	333	H-10→L (36%), H-2→L+7 (10%), H-1→L+7 (24%) H-5→L+3 (2%), H-3→L+7 (8%), H-2→L+19 (4%), H→L+6 (8%)	ILCT ,π-π*,MLCT
S_{50}	310	0.4	313	H-3→L+5 (26%), H-1→L+5 (72%)	π-π*, ILCT,MLCT
2b					
S_2	472	0.37	520	H→L+1 (99%)	MLCT,ILCT
S_{18}	416	0.40	395(br)	H→L+6 (91%)	MLCT, ILCT, π-π*
S_{33}	345	0.48	356	H-9→LUMO (96%)	MLCT, ILCT, π-π*
S_{57}	315	0.13	316	H-9→L+2 (30%), H-9→L+3 (48%)H-14→L(8%), H-2→L+5 (8%)	π-π*, ILCT
S_{102}	277	0.24	282	H-16→L (22%), H-15→L+3 (42%) H-13→L+3 (8%), H-2→L+17 (8%)	π-π*, ILCT
S_{126}	252	0.31	242	H-6→L+6 (31%), H-1→L+10 (48%)	π-π*, ILCT

Table 2.6. Selected UV-vis Energy Transitions at the TD-DFT/B3LYP Level of **3**, **3a**, and **3b** in MeCN.

Excited state	λ_{cal}/nm	Oscillator strength(f)	λ_{expt}/nm	Key transitions	Character
3					
S_1	510	1.2	497	H-1→L+1 (39%), H→L (53%)	MLCT,ILCT
S_{15}	400	0.3	356	H-2→L+2 (88%) H-4→LUMO (5%),H-3→L+1 (5%)	MLCT,ILCT
S_{21}	354	1.4	334	H-1→L+4 (47%), H→L+5 (46%)	ILCT ,π-π*
S_{58}	293	0.5	312	H-10→L (10%), H-1→L+11 (37%), H→L+10 (36%), H-9→L+1 (8%)	π-π*, ILCT
S_{106}	260	0.9	280	H-14→L+2 (25%), H-13→L+3 (43%), H-16→L+2 (7%), H-6→L+5 (5%), H-5→L+4 (5%)	ILCT ,π-π*
3a					
S_5	490	1.1	495	H-4→L (12%), H-3→L+1 (14%), H-1→L+1 (35%), H→L (33%)	MLCT,ILCT
S_{13}	420	0.3	354	H-4→L (36%), H-3→L+1 (31%), H-1→L+1 (10%), H→L (12%), H-2→L+2 (7%)	MLCT,ILCT
S_{20}	375	0.8	333	H-1→L+4 (43%), H→L+5 (43%)	MLCT, ILCT, π-π*
S_{62}	310	1.0	312	H-14→L (48%), H-13→L+1 (43%)	π-π*, ILCT
S_{147}	271	0.2	280	H-14→L+5 (18%), H-13→L+4 (19%)H-11→L+9 (8%), H-10→L+10 (7%), H-4→L+14 (6%), H-3→L+15 (6%)	π-π*, ILCT
3b					
S_1	473	1.10	507	H-1→L+1 (38%), HOMO→LUMO (61%)	MLCT,ILCT
S_{25}	424	0.76	390(br)	H-6→L+2 (62%), H-1→L+9 (17%), H→L+8 (17%)	MLCT, ILCT
S_{49}	355	0.47	350	H-1→L+12 (47%), H→L+11 (47%)	π-π* , ILCT
S_{112}	301	0.10	310	H-20→L+1 (41%), H-12→L+3 (14%), H-3→L+6 (13%), H-2→L+5 (11%), H-15→L(7%)	π-π*, ILCT
S_{160}	277	0.85	278	H-20→L+2 (28%), H-19→L+3 (46%)	π-π*, ILCT

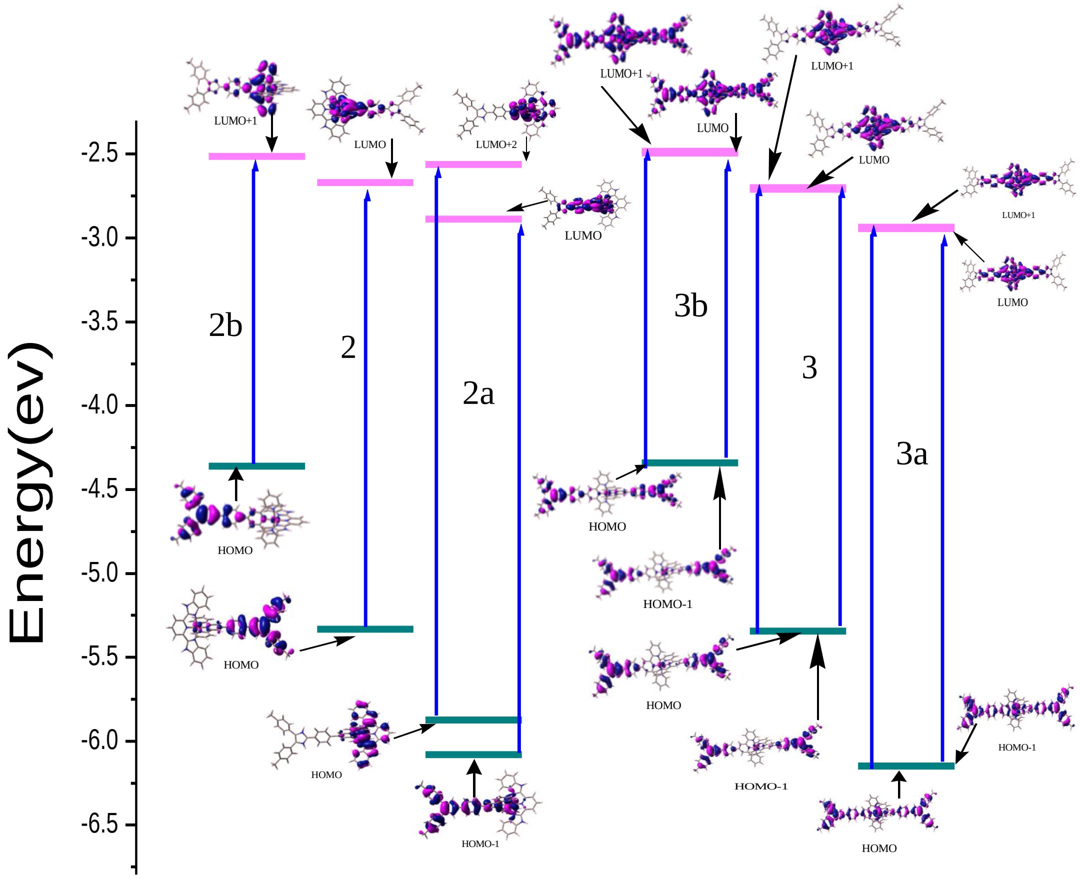

Figure 2.7. Calculated energy level diagram showing major transitions that comprise the lowest-energy absorption band for **2**, **2a**, **2b** and **3**, **3a**, **3b** in MeCN.

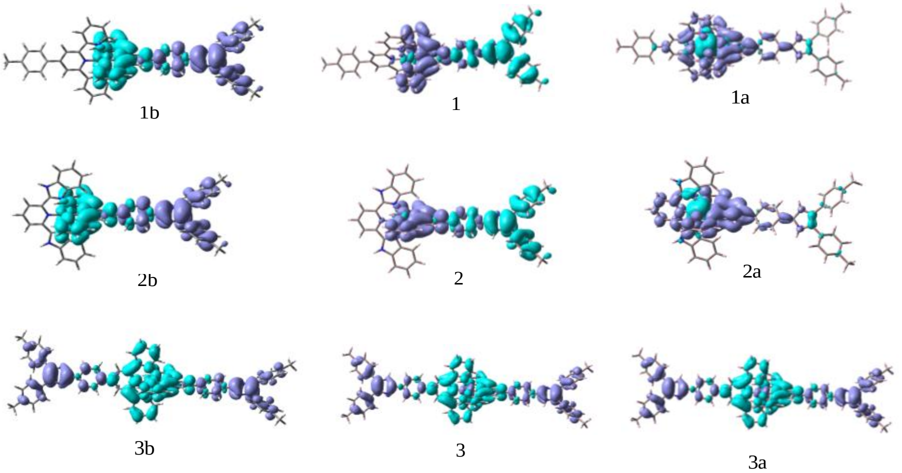

Figure 2.8. Difference in electron density upon excitation from the ground S_0 state to the lowest energy singlet excited state in free (**1-3**), protonated (**1a-3a**) and deprotonated (**1b-3b**) forms. Purple and cyan color shows regions of increasing and decreasing electron density, respectively.

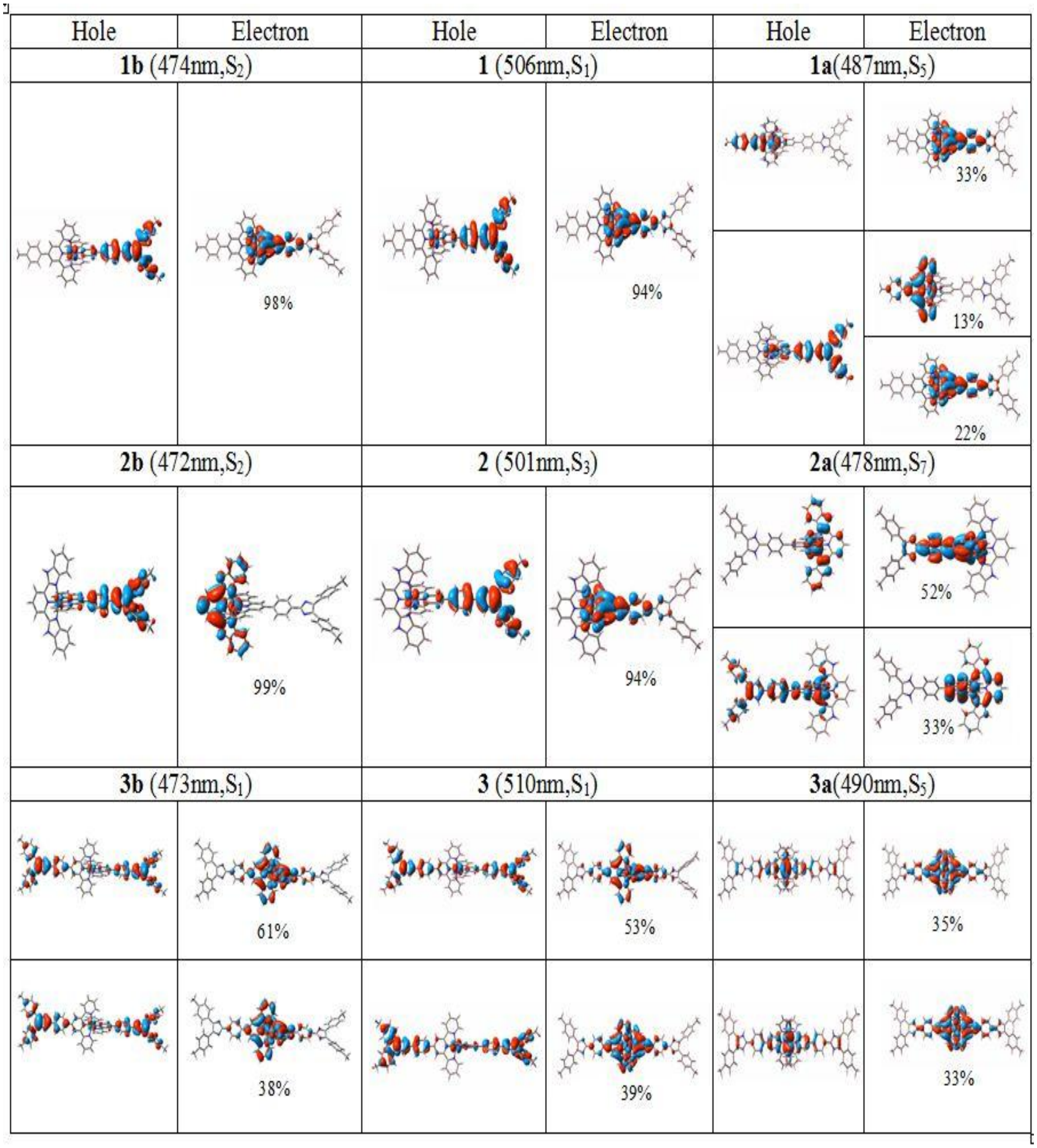

Figure 2.9. NTOs illustrating the nature of optically active lowest energy singlet excited states in the absorption bands of the complexes in their free (**1-3**), protonated (**1a-3a**), and deprotonated (**1b-3b**) forms. The occupied (holes) and unoccupied (electrons) NTO pairs that contribute more than 10% to each excited state are only represented. All transitions comprise of mixed ^{1}MLCT/^{1}ILCT characters.

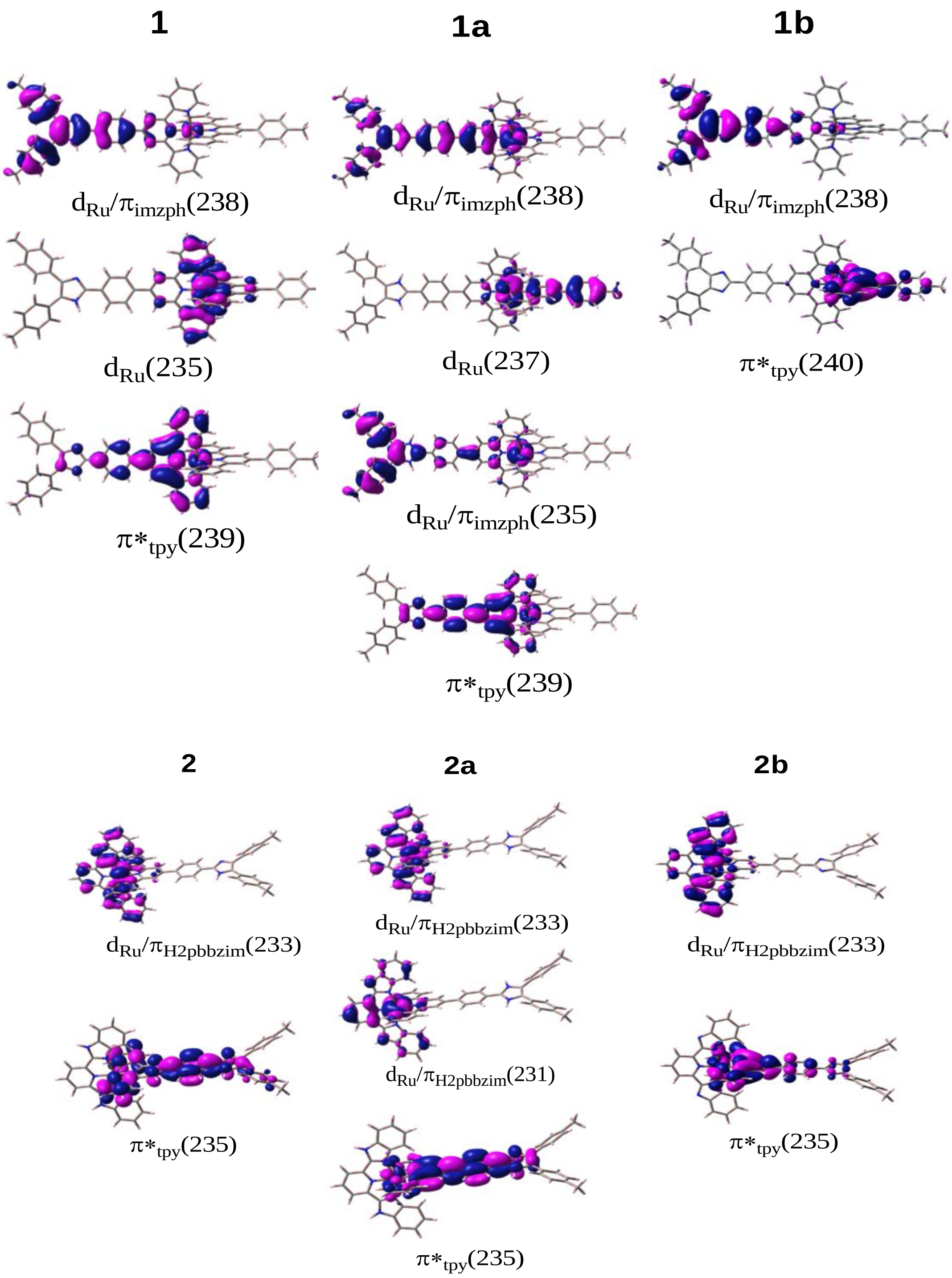

Figure 2.10 Schematic drawings of the MOs that participate in the dominant configurations of the lowest lying triplet excited states of **1** and **2** in MeCN.

Table 2.7. Singlet-Triplet Excitation Energies at the Lowest Triplet State (T_1) along with Key Transition of Complexes in Their Free- (**1-3**), Protonated- (**1a-3a**), and Deprotonated (**1b-3b**) Forms in MeCN.

Compounds	Key transitions	*E* (cm^{-1})
1	$d_{Ru}/\pi_{imzph}(238)\rightarrow\pi^*_{tpy}(239)$ (47%) $d_{Ru}(235)\rightarrow\pi^*_{tpy}(239)$ (41%)	16367
1a	$d_{Ru}(237)\rightarrow\pi^*_{tpy}(239)$ (41%) $d_{Ru}/\pi_{imzph}(238)\rightarrow\pi^*_{tpy}(239)$ (23%) $d_{Ru}/\pi_{imzph}(235)\rightarrow\pi^*_{tpy}(239)$ (23%)	16639
1b	$d_{Ru}/\pi_{imzph}(238)\rightarrow\pi^*_{tpy}(240)$ (94%)	12019
2	$d_{Ru}/\pi_{H2pbbzim}(233)\rightarrow\pi^*_{tpy}(235)$ (94%)	16287
2a	$d_{Ru}/\pi_{H2pbbzim}(233)\rightarrow\pi^*_{tpy}(235)$ (67%) $d_{Ru}/\pi_{H2pbbzim}(231)\rightarrow\pi^*_{tpy}(235)$ (22%)	16611
2b	$d_{Ru}/\pi_{H2pbbzim}(233)\rightarrow\pi^*_{tpy}(235)$ (95%)	12469
3	$d_{Ru}/\pi_{imzph}(298)\rightarrow\pi^*_{tpy}(300)$ (24%) $d_{Ru}/\pi_{imzph}(299)\rightarrow\pi^*_{tpy}(301)$ (23%) $d_{Ru}(296)\rightarrow\pi^*_{tpy}(300)$ (22%)	16207
3a	$d_{Ru}/\pi_{imzph}(299)\rightarrow\pi^*_{tpy}(301)$ (27%) $d_{Ru}/\pi_{imzph}(298)\rightarrow\pi^*_{tpy}(300)$ (27%) $d_{Ru}/\pi_{imzph}(296)\rightarrow\pi^*_{tpy}(300)$ (20%)	16779
3b	$d_{Ru}/\pi_{imzph}(298)\rightarrow\pi^*_{tpy}(300)$ (48%) $d_{Ru}/\pi_{imzph}(299)\rightarrow\pi^*_{tpy}(301)$ (45%)	12195

imzph = imidazole-phenyl moieties, H_2pbbzim = 2,6-bis(benzimidazole-2-yl)pyridine, tpy=terpyridine

Table 2.8. Emissions Data of the Complexes in Their Free- (**1-3**), Protonated- (**1a-3a**), and Deprotonated (**1b-3b**) Forms According to TD-DFT and UKS Calculations and Associated Experimental Values in MeCN

Compounds	Theoretical		Experimental
	TD-DFT	UKS	
1	611	613	660
1a	601	605	660
1b	832	1011	662
2	614	640	680
2a	602	625	680
2b	802	996	746
3	617	638	655
3a	596	610	650
3b	820	987	657

2.3.3. Electronic Absorption Spectra. UV-vis absorption spectra of complexes **1-3** were recorded in a few selected solvents (MeCN, MeOH, DMSO and H_2O) and that in DMSO are displayed in Figure 2.11. Pertinent spectral data are summarized in Table 2.9. Assignment of the observed bands have been made by comparing with the spectra observed for analogous Ru(II)-terpyridine complexes as well as by considering the results of TD-DFT calculations. The strong peak observed at 490-500 nm is attributed to

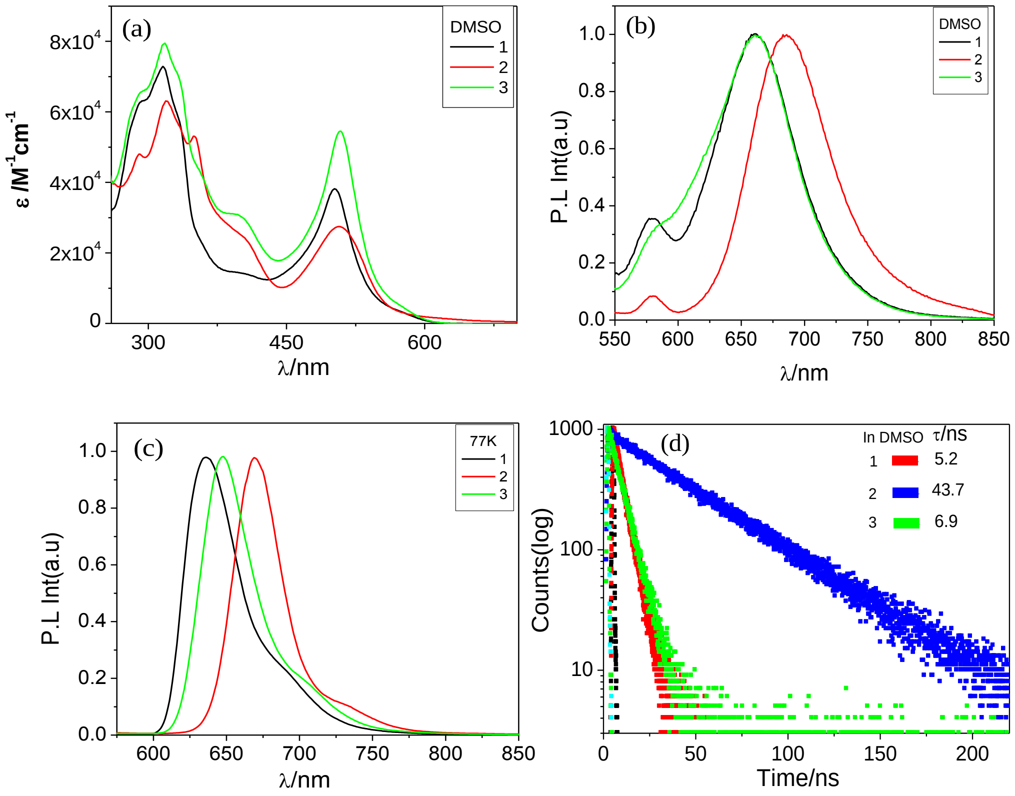

Figure 2.11. UV-vis absorption (a) and normalized emission (λ_{ex} = 490 nm) spectra (b) for complexes **1-3** at RT. Normalized emission spectra of **1-3** in EtOH-MeOH (4:1, v/v) glass at 77 K (c) and excited state decay profiles following pulsed excitation at 450 nm in DMSO at RT (d).

$^1[Ru^{II}(d\pi)^6] \rightarrow {}^1[Ru^{II}(d\pi)^5$tpy- $HImzPh_3Me_2(\pi^*)^1]$ MLCT transition with contribution of intraligand charge transfer (ILCT) transition from phenyl-imidazole to terpyridine. Two very strong bands at ~280 and ~315 nm are due to π-π* ligand centered transitions, while the peaks occurring between 330 and 350 nm arise as a result of intra-ligand charge transfer transitions among the coordinated ligands. The ^{1}MLCT peak in **1**-**3** is found to be red-shifted relative to $[Ru(tpy)_2]^{2+}$ (474 nm) and $[Ru(H_2pbbzim)_2]^{2+}$ (475 nm) which may be correlated with increased conjugation at the 4'-position of terpyridine unit of the present ligand.[18,48,53] Interestingly, all the complexes exhibit considerably stronger absorptivity (ε) in the visible region relative to that of $[Ru(tpy)_2]^{2+}$ and therefore should be good candidates for light-harvesting.

Table 2.9. Photophysical Data for Complexes **1-3** in Different Solvents.

Compounds		Absorption λ_{max}/ nm (ε,$M^{-1}cm^{-1}$)	Luminescence				
			λ_{max} / nm	τ/ ns	Φ	k_r/s^{-1a}	k_{nr}/s^{-1b}
1	MeCN(298K)	493(36100),355(sh)(32900),332(sh)(57900),311(72300),283(71600)	660	τ_1=0.4(8%) τ_2=5.2(92%)	0.50×10^{-3}	—	—
2		490(25500),348(58200),332(56300),314(59200),284(50000)	680	32	1.61×10^{-3}	5.0×10^{4}	3.1×10^{7}
3		496(49500),352(sh)(61800),332(76300),312(77000),282(78600)	655	5.4	0.60×10^{-3}	1.1×10^{5}	1.85×10^{8}
1	DMSO(298K)	503(38300),402(br)(14400),335(sh)(57000),316(72800)	660	5.2	1.01×10^{-3}	1.9×10^{5}	1.9×10^{8}
2		507(27700),405(br)(24300),350(53200),320(63100),290(48300)	685	43.7	4.11×10^{-3}	9.4×10^{4}	2.3×10^{7}
3		508(54500),403(br)(30000),337(br)(67500),318(79600)	661	6.9	1.03×10^{-3}	1.5×10^{5}	1.4×10^{8}
1	H_2O(298K)	493(19600),334(br)(33300),312(42500),283(39900),238(br)(32400)	655	τ_1=0.2(22%) τ_2=7.3(78%)	4.91×10^{-3}	—	—
2		494(36500),410(br)(37200),356(98800),318(95000),291(sh)(82400),230(114500)	680	40.0	4.25×10^{-3}	1.0×10^{5}	2.5×10^{7}
3		510(37500),409(17600),360(br)(30300),336(br)(44700),313(53200),235(br)(47300)	660	τ_1=0.2(20%) τ_2=4.7(80%)	1.23×10^{-3}	—	—
1	MeOH(298K)	495(24000),394(br)(7276),331(sh)(33900),311(48700),285(42410)	647	τ_1=1.2(25%) τ_2=2.3(75%)	2.84×10^{-3}	—	—
2		513(19100),352(37200),316(43500),285(36900)	682	τ_1=9.1(15%) τ_2=35.4(85%)	1.97×10^{-3}	—	—
3		500(39300),395(br)(21100),332(br)(47700),311(61100),285(50700)	655	τ_1=2.6(25%) τ_2=4.4(75%)	2.95×10^{-3}	—	—
1	EtOH-MeOH (4:1) (77K)		635	15.5μs	0.205	1.32×10^{4}	5.13×10^{4}
2			668	9.8μs	0.252	2.57×10^{4}	7.63×10^{4}
3			645	15.5μs	0.192	1.24×10^{4}	5.21×10^{4}

[a,b] k_r and k_{nr} were estimated by using the relation, $k_r = \phi/\tau$ and $k_{nr} = (1-\phi)/\tau$; separation of k_r and k_{nr} is meaningful for mono-exponential decay kinetics.

2.3.4. Emission Spectral Behaviors. Emission spectra of the complexes were acquired in the above-mentioned solvents at RT, as well as in EtOH-MeOH (4:1, v/v) at 77 K and related data are summarized in Table 2.9. On excitation at the MLCT band, all the complexes display one broad emission band within the range of 647-685 nm at RT. This band originates from radiative deactivation of the lowest energy triplet excited state. By comparing the TDDFT calculated results and the literature data of similar Ru (II)-terpyridine complexes, we can assign the lowest excited state to be $Ru^{II}(d\pi)\rightarrow tpy(\pi^*)$ triplet (^{3}MLCT) state. Of particular interest to note, while the complexes are luminescent in fluid solutions at RT, $[Ru(tpy/tpy\text{-}PhCH_3)_2]^{2+}$ or $[Ru(H_2pbbzim)_2]^{2+}$ are non-luminescent. As shown in Figure 2.11(d), the emission lifetime of the complexes in DMSO at RT increases in the order **1** (5.2 ns) < **3** (6.9 ns) < **2** (43.7 ns). On the other hand, these values lie between 9.8 μs (**2**) and 15.5 μs (**1**, **3**) in EtOH-MeOH (4:1) glass at 77K (Figure 2.12). It may be noted that RT emission lifetime of the present complexes are far longer than $[Ru(tpy)_2]^{2+}$ (0.25 ns). On lowering of temperature to 77K, the

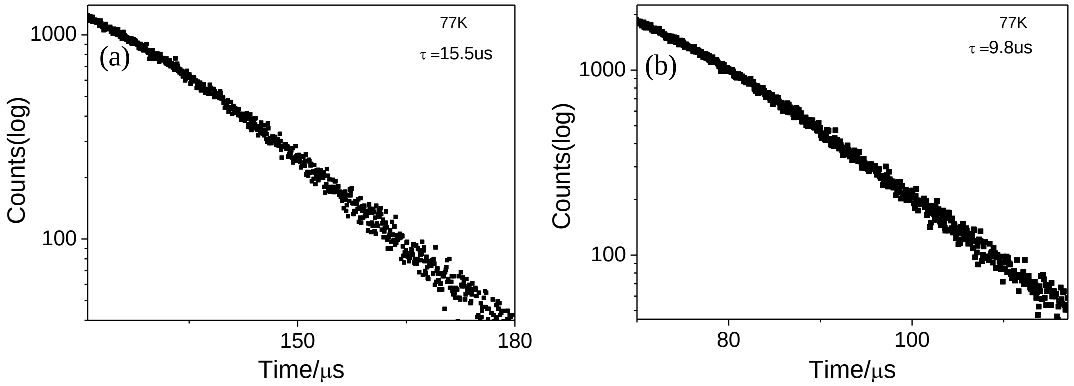

Figure 2.12. Excited state decay profiles together with the lifetime of **1** (a) and **2** (b), EtOH-MeOH (4:1, v/v) glass at 77 K in MCS mode.

emission band moves to shorter wavelength region with enormous increase in emission intensity, quantum yield and lifetime, the features common to ^{3}MLCT emitters (Table 2.9). Zero-zero excitation energy (E_{00}) for ^{3}MLCT state of **1-3** were evaluated from their emission maximum at 77 K and the estimated values are 1.95 eV for **1**, 1.85 eV for **2**, and 1.92 eV for **3**. 77K emission spectra also display vibronic progression in lower energy region. Vibrational spacing was calculated by deconvolution of 77K spectra and the estimated values are 842 cm^{-1} for **1**, 781 cm^{-1} for **2**, and 834 cm^{-1} for **3** (Figure 2.13). The observed vibronic spacing is about 30% less than expected for aromatic ring stretching frequencies.[9,12-14]

Excited-state lifetime of Ru(II)-polypyridine complexes are dominated by nonradiative decay and in this limit the decay is usually related by the following equation.[8,9]

$$k_{nr} = k_{nr}^{0} + k^{'}_{nr} \qquad (1)$$

where k_{nr}^{0} corresponds to decay from the ^{3}MLCT state to the ground state and $k^{'}_{nr}$ is related to thermally stimulated process involving a surface-crossing from ^{3}MLCT state to closely situated ^{3}MC state. Due to small energy gap between ^{3}MLCT and ^{3}MC states,

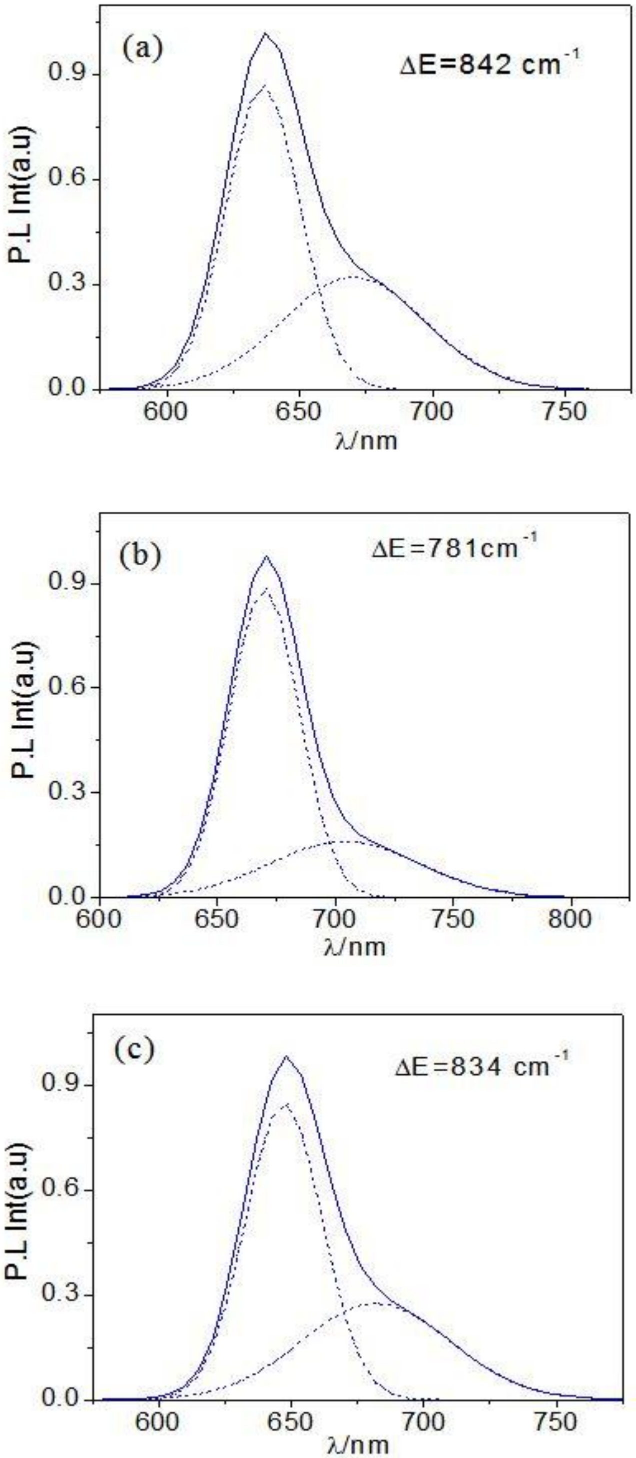

Figure 2.13. Experimental (solid line) and deconvoluted (dotted line) emission spectra of **1** (a), **2** (b), and **3** (c) in EtOH-MeOH (4:1v/v) at 77 K. The insets show the values of vibrational spacing.

terpyridine complexes of Ru(II) usually exhibit poor RT emission behaviours. However, as a consequence of increased pi-electron conjugation at the 4'-position of the terpyridine unit of the present ligand, it is expected that the energy of ^{3}MLCT state will be lowered, which, in turn, will assist to decouple MLCT triplet from higher-energy MC states.[16,23,44] We have investigated the effect of temperature on quantum yield and lifetime of complexes **1-3** in MeCN at varying temperatures (between 283K and 333K). As may be noted, with increase of temperature, the emission intensity (Figure 2.14), quantum yield (Table 2.10), and lifetime (Figure 2.15) of the complexes decrease gradually, albeit to

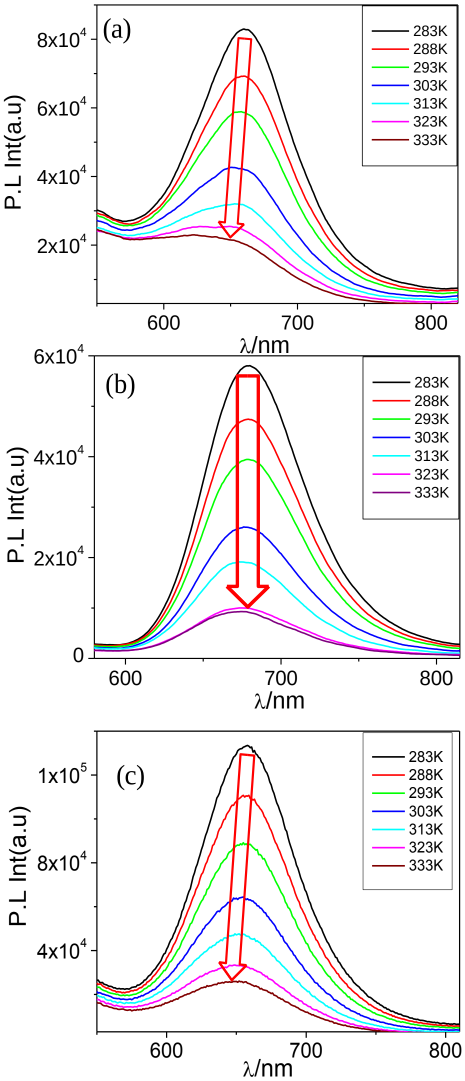

Figure 2.14. Change in emission spectral profile of **1** (a), **2** (b), and **3** (c) in MeCN as a function of temperature in the range of 283K and 333K.

Table 2.10. Quantum Yield (Φ) of the Complexes **1-3** with Variation of Temperature in the Range of 283K-333K.

Temperature/K	Quantum Yield(Φ)×10^{-3}		
	1	**2**	**3**
283	0.78	2.80	1.00
288	0.68	2.30	0.86
293	0.60	1.96	0.71
303	0.47	1.33	0.53
313	0.38	1.00	0.41
323	0.32	0.56	0.30
333	0.28	0.52	0.25

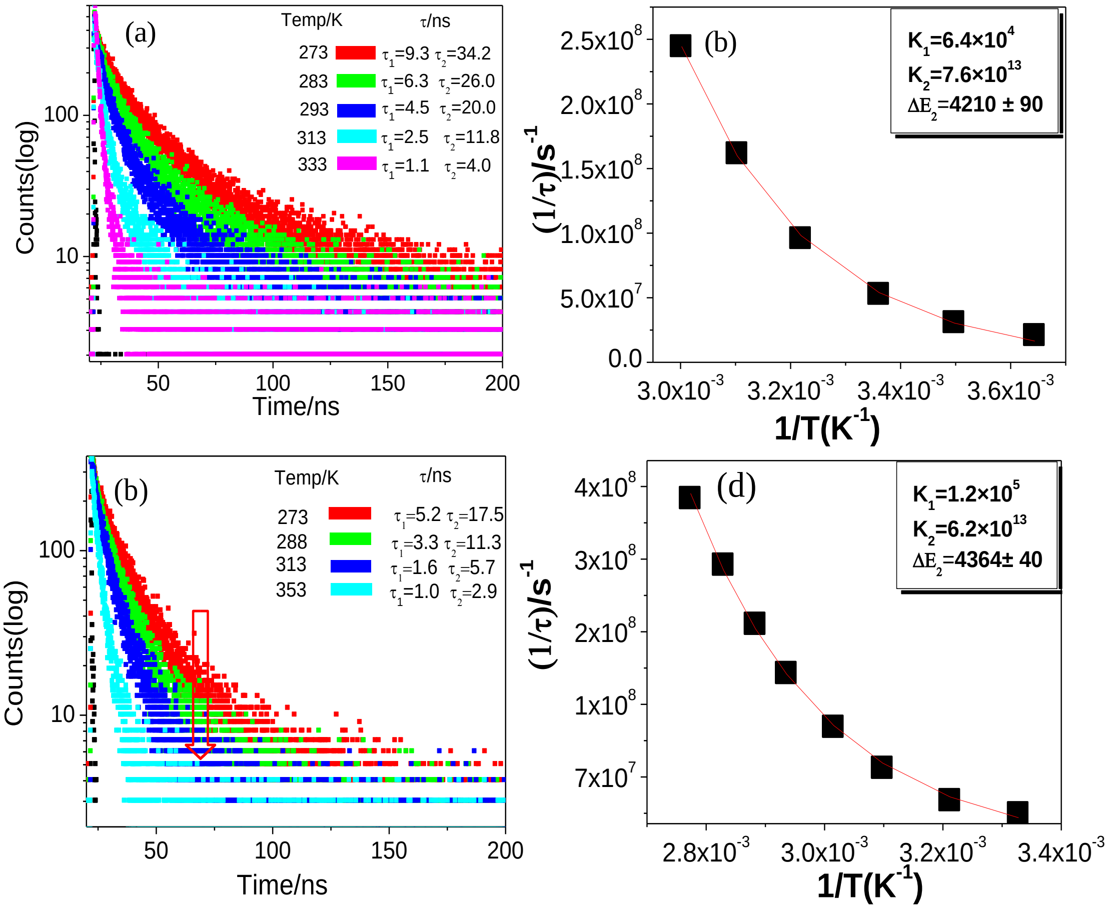

Figure 2.15. The decay profile for **1** (a) upon variation of temperature in acetonitrile. Nonlinear fitting of temperature dependent lifetime data together with the values of different parameters are presented in (b).

different extent. Lifetime *vs.* temperature data of the complexes were fitted by non-linear regression analysis to equation (2).[8,9]

$$[\tau(T)]^{-1} = (k_1 + k_2 \exp[-\Delta E_2/RT])/(1+\exp[-\Delta E_2/RT]) \qquad (2)$$

where k_1 corresponds to temperature-independent rate constant which is aggregate of both radiative (k_r), and non-radiative (k_{nr}) rate constants from ^{3}MLCT state at 77K and the values of k_1 lie in the range of 6.4×10^4-1.2×10^5 s^{-1}, depending upon the complexes and their protonation states. It is commonly proposed that the temperature dependent rate constant, k_2 corresponds to the rate of surface crossing from ^{3}MLCT to ^{3}MC state and ΔE_2 is the activation energy for the said surface crossing process. We would like to mention here that the previous statement is a hypothesis based on several assumptions and there is no actual experimental or theoretical support for such a correlation in a variety of related compounds. We obtained the values of k_2 and ΔE_2 by the non-linear regression analysis using equation 2, keeping k_1 as constant throughout the fitting process (Table 2.11 and Figure 2.15). While the values of ΔE_2 are 4210±90, 4435±34, and 4364±40 cm^{-1} for **1**, **2**, and **3**, respectively, the values of k_2 vary between 6.0×10^{13} and 4.4×10^{14} s^{-1}. As the present complexes are well emissive at RT, the equation 2 holds good for our systems in the limiting conditions of $\Delta E_2 >>0$ and $k_2 >> k_1$. The agreement between these values and those reported for related Ru(II)-terpyridine complexes is quite good.[9,12-16] Considerable increase of ΔE_2 value is evident for all the three complexes relative to that of $[Ru(tpy)_2]^{2+}$ (ΔE_2=1500 cm^{-1}) and $[Ru(tpy\text{-}PhCH_3)_2]^{2+}$ (ΔE_2=1800 cm^{-1}). The boost in ΔE_2 values occurs presumably due to augmented π-electron cloud

Table 2.11. Temperature Dependent Luminescence Spectral Parameters of Free Form (**1-3**) and Their Protonated Forms (**1a-3a**) in Acetonitrile.

Complex	$^a k_1$/s^{-1}	k_2/s^{-1}	ΔE_2/cm^{-1}
1	6.4×10^4	7.6×10^{13}	4210±90
1a	6.5×10^4	4.4×10^{14}	5221±70
2	1.0×10^5	6.0×10^{13}	4435±34
2a	1.0×10^5	3.9×10^{14}	6023±34
3	1.2×10^5	6.2×10^{13}	4364±40
3a	6.5×10^4	1.4×10^{14}	6111±40

$^a k_1 = k_r + k_{nr}$ (k_r and k_{nr} are obtained from emission quantum yield and lifetime data at 77K) delocalization of tpy-HImzPh$_3$Me$_2$ frame in the excited state.[16,19,23,34,40] The important outcome is the substantial increased lifetimes of the present complexes at RT. Thus, suitable absorption and emission spectral characteristics particularly in the visible region along with moderately long RT lifetimes are the key features of the present complexes for their probable use as light-harvesting building blocks.

2.3.5. Acid-Induced Changes of the Emission Spectral Characteristics of Complexes. The heteroleptic complexes **1** and **2** having one imidazole ring and the homoleptic complex **3** with two such rings can be subjected to protonation by treating with acid. The effect of incremental addition of acid on photophysical behavior of the complexes in MeCN and aqueous medium was investigated through absorption, steady state and time-resolved emission spectral measurements.

The spectral changes that occurred in aqueous solution for **1** and **2** in water upon incremental addition of 0.1 M HClO$_4$ are displayed in Figure 2.16 and Figure 2.17. One-step change is noticed for both **1** and **2** (Figure 2.16), whereas two-step changes are observed in the case of **3** (Figure 2.17). Substantial increase of emission intensity occurred in all the three complexes, albeit to different extent. While for **1** and **2**, maximization of emission took place on addition of 20 equiv of acid, 40 equiv of acid was required to reach the end point for **3**. The extent of enhancement of emission is 2-, 8-, and 12-fold for **1**, **2**, and **3**, respectively. It appears that complexes **1** and **2** undergo one protonation process, while two successive proton transfer processes occur in the case **3**. Although it was expected that absorption band energy would increase upon protonation, no such shift actually occurred. Lifetimes of the complexes have been determined in water as a function of the amount acid added (Figure 2.18). In agreement with their steady state spectra, lifetime of all the three complexes increased to a significant extent. Remarkably, the lifetime increases from 7.3 ns to 122.0 ns for **1**, from 40.0 ns to 371.0 ns for **2**, and from 4.7 ns to 338.0 ns for **3**. During the course of this study, we also checked the influence of acid on luminescence characteristics of our previously reported complexes based on similar terpyridyl-imidazole motif differing by peripheral methyl groups (**Chart 2.3**).[52] It needs to be mentioned here that the lifetime of those complexes

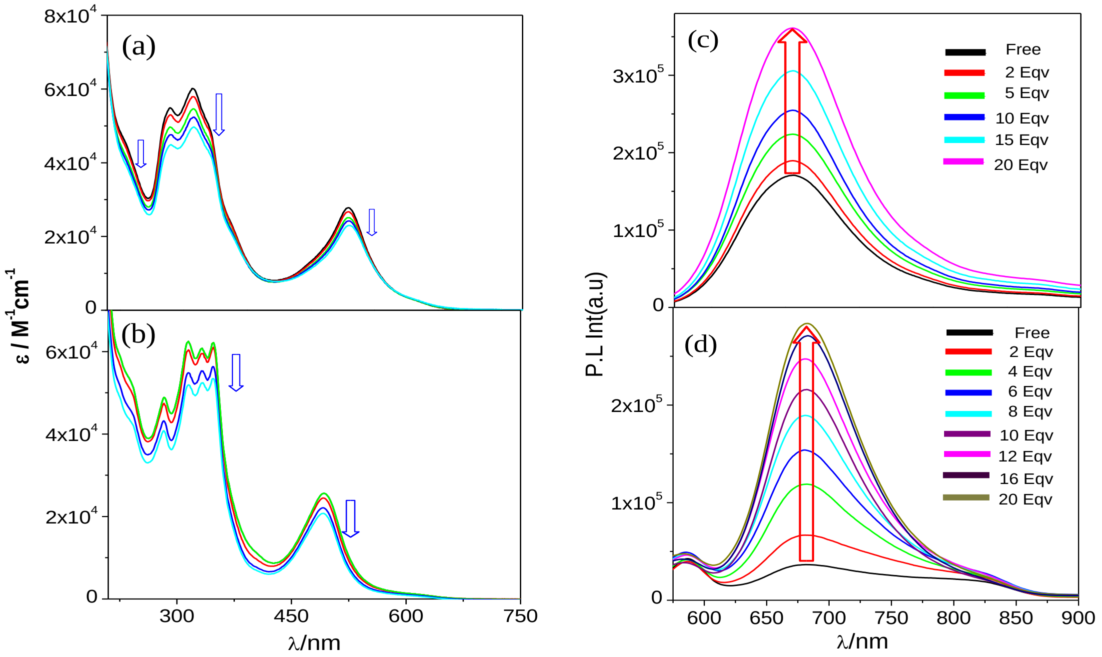

Figure 2.16. Absorption and emission spectral changes of **1** (a and c, respectively) and **2** (b and d, respectively) in water upon gradual addition of 0.1(M) $HClO_4$.

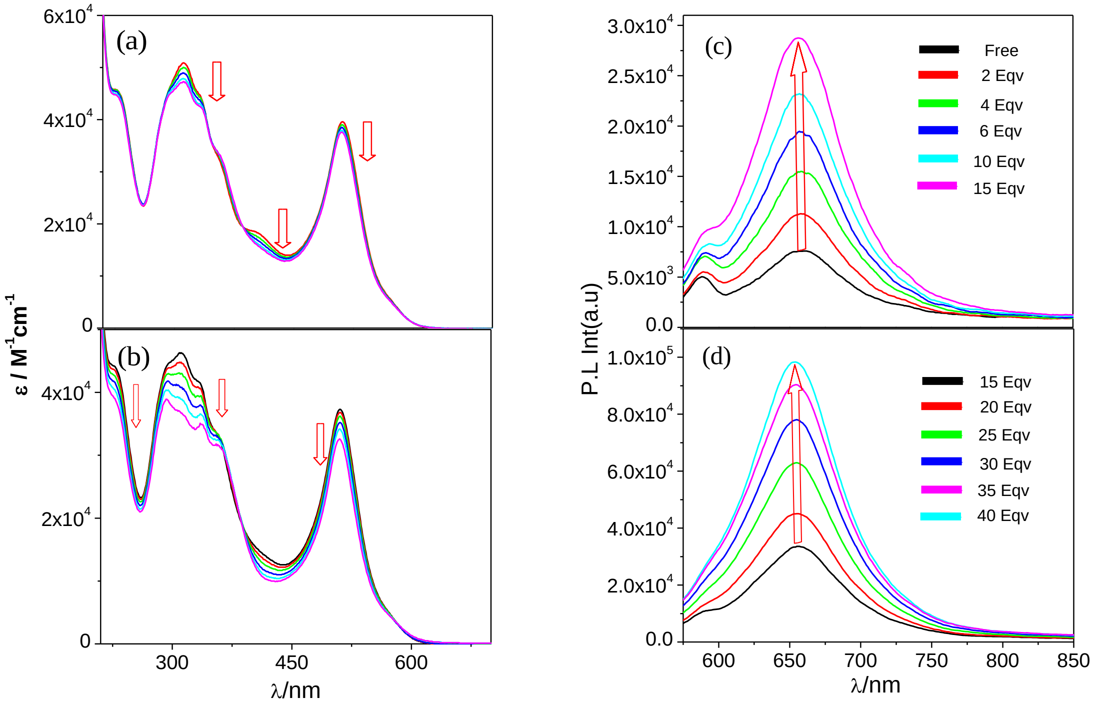

Figure 2.17. UV-vis absorption (a and b) and luminescence (c and d) spectral changes of **3** in water upon gradual addition of 0.1(M) $HClO_4$.

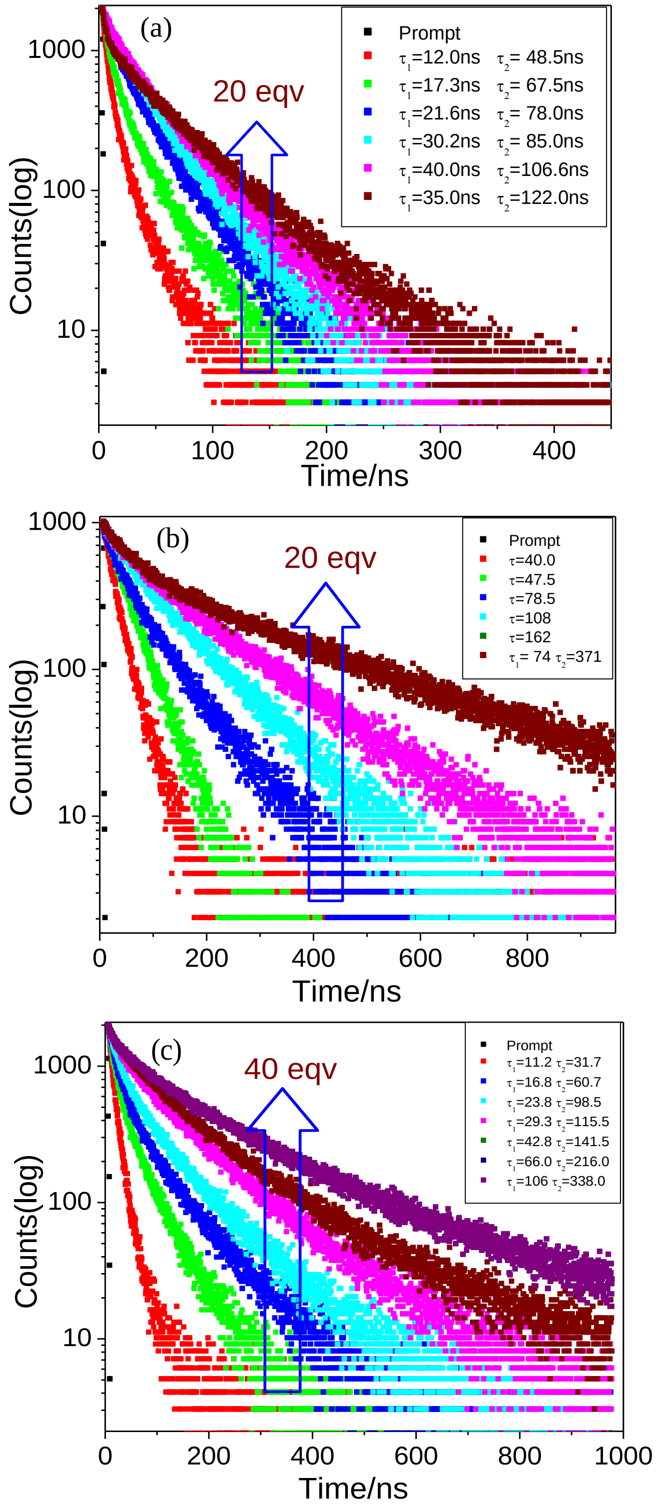

Figure 2.18. Change of luminescence decays of **1** (a) **2** (b) and **3** (c) in water upon gradual addition of 0.1(M) $HClO_4$. Inset shows the lifetime values.

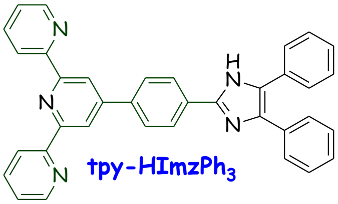

Chart 2.3. Chemdraw structure of our previously reported ligand.[52]

were reported in MeCN and the values obtained were 6.8 ns for tpy-PhCH_3, 35.0 ns for H_2pbbzim, and 8.5 ns for the homoleptic bis-complex of tpy-HImzPh$_3$. For the sake of comparison, we have determined lifetime of the previous complexes in water and observed that the values are slightly less compared with those observed in MeCN (3.7 ns for tpy-PhCH_3, 30.0 ns for H_2pbbzim, and 5.5 ns for homoleptic bis-complex of tpy-HImzPh$_3$) than MeCN. Again, with the addition of acid, the lifetime increased from 3.7 ns to16.4 ns for tpy-PhCH_3, 30.0 ns to 80.0 ns for H_2pbbzim, and 5.5 ns to 17.3 ns for the homoleptic complex of tpy-HImzPh$_3$) (Figure 2.19). It is evident that the extent of enhancement of lifetime is remarkably higher for the present series of complexes than the previous series. Clearly, the incorporation of peripheral methyl group in the present ligand has induced an enormous effect on the emission characteristics of complexes **1-3** with regard to protonation of imidazole nitrogen atom(s). Of particular interest to note, in the case of **3** the lifetime has increased 80-fold due to protonation. The effect of protonation on photophysics of the complexes is not clear at this stage. We surmise a possible reason could be due to electrostatic effect.

The spectral changes that occur in MeCN for complexes **1-3** upon gradual addition of acid are displayed in Figure 2.20. The extent of change observed is far less relative to that in water. In consonance with this, the increase of lifetime on protonation in MeCN is also much less compared to water. The observed difference seems to be due to large difference of dielectric constant between the two solvents. In highly polar aqueous solution, extensive intermolecular hydrogen bonding of the protonated species via surrounding water molecules probably leads to aggregation of the species and augmentation of lifetime.

It would be of interest to compare the effect of protonation on emission characteristics of present complexes with those of related systems.

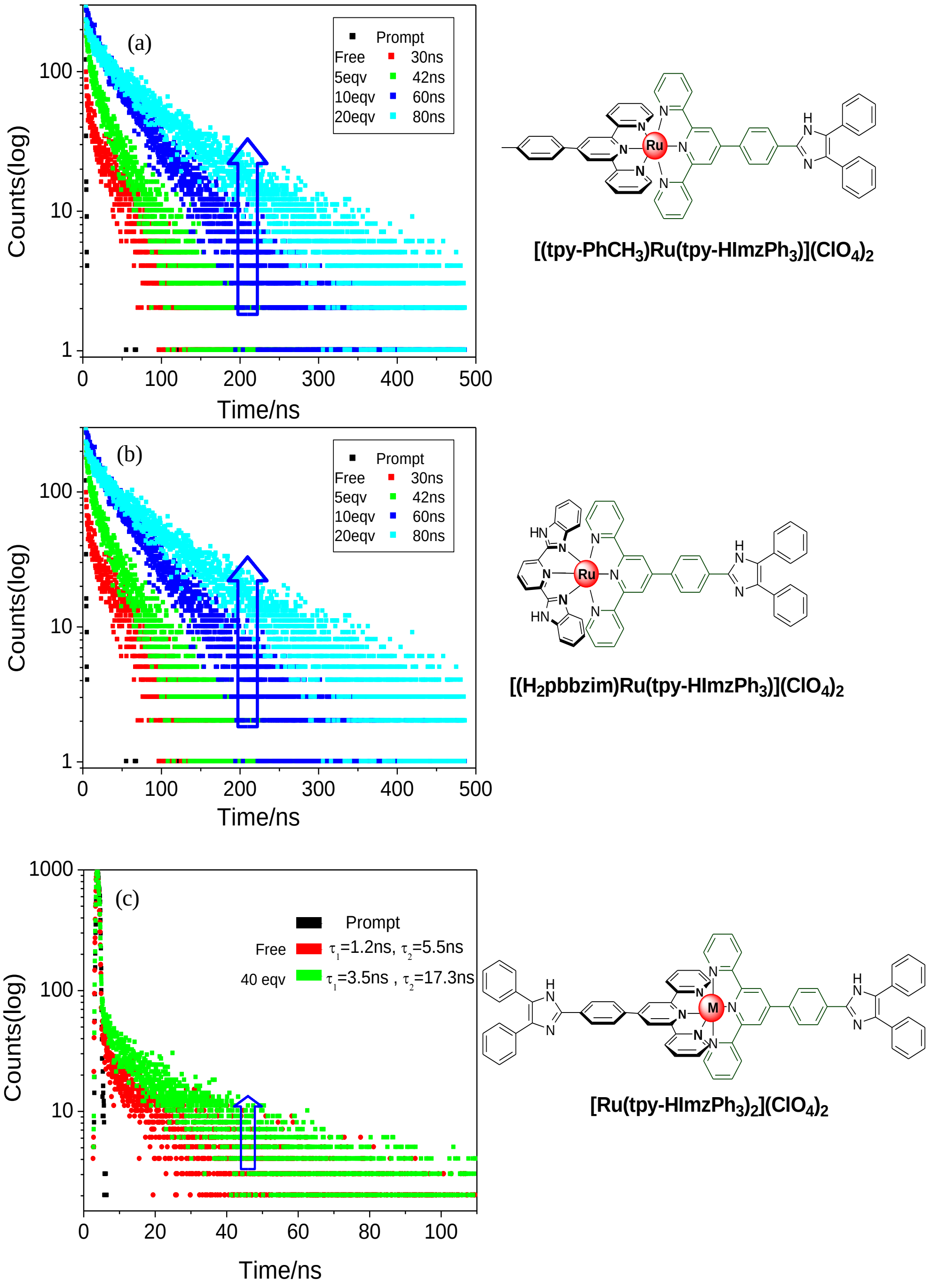

Figure 2.19. Change of luminescence decay profiles of our previously reported [(tpy-PhCH$_3$)Ru(tpy-HImzPh$_3$)](ClO$_4$)$_2$ (a) [(H$_2$pbbzim)Ru(tpy-HImzPh$_3$)](ClO$_4$)$_2$ (b) and [Ru(tpy-HImzPh$_3$)$_2$](ClO$_4$)$_2$ (c) complexes without peripheral methyl group in the ligand in water upon gradual addition of 0.1(M) HClO$_4$. Inset shows the lifetime values.

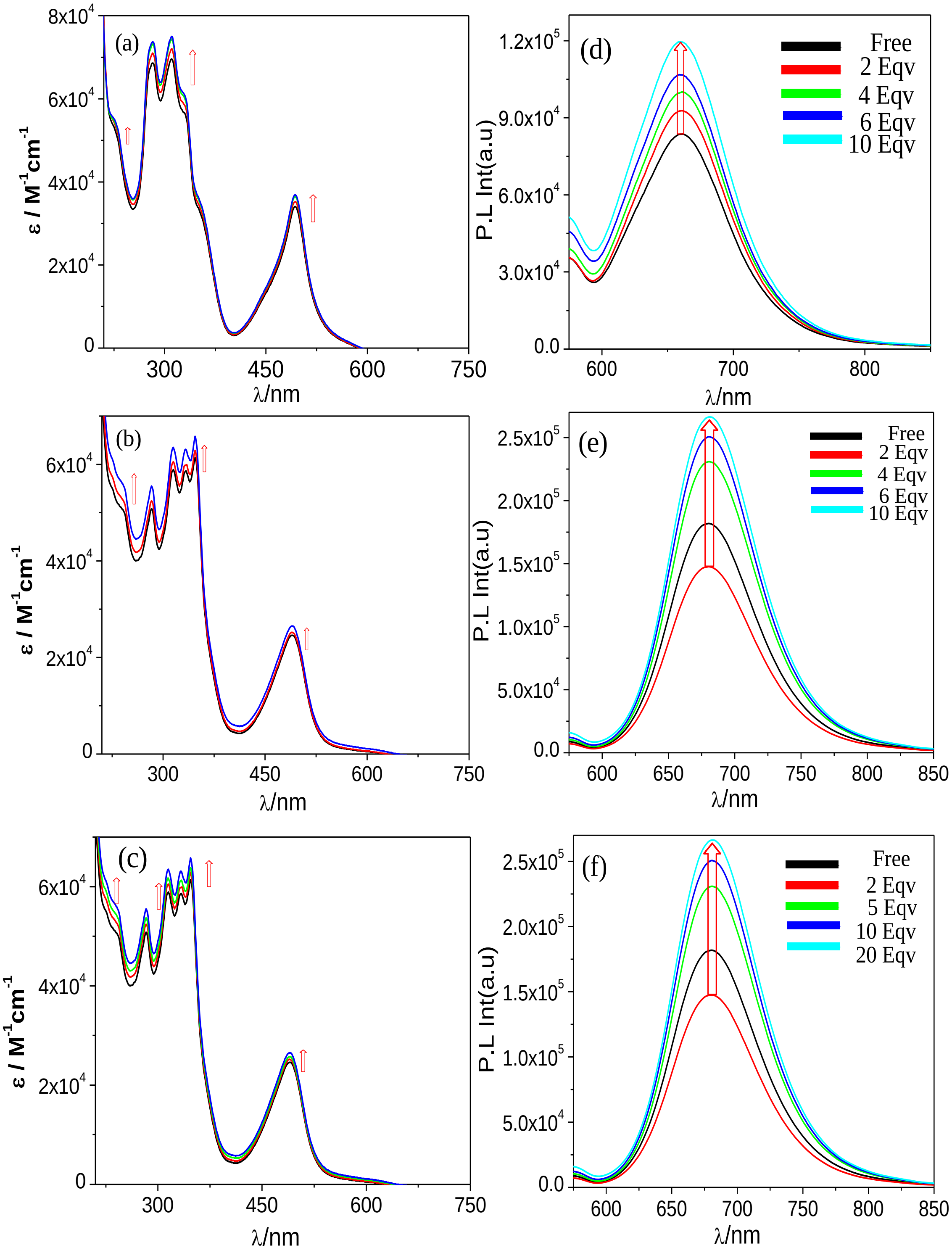

Figure 2.20. UV-vis absorption (a-c) and luminescence (d-f) spectral changes of **1**, **2** and **3** respectively in MeCN upon gradual addition of 0.1(M) $HClO_4$.

Dietzek, Rau and co-workers thoroughly studied protonation-deprotonation behaviors of ruthenium dye containing 5,5',6,6'-tetramethyl-2,2'-bibenzimidazole and 4'-di-tert-butyl-2,2'-bipyridine moieties and observed an overall increase in lifetime up to 8 times (from <1 ns to 8 ns) on protonation.[55] Vos and co-workers studied protonation-deprotonation effect of two binuclear Ru(II)-polypyridine complexes based on bridging 5,5'-bis(pyridin-2''-yl)-3,3'-bis(1H-1,2,4-triazole) (bpbt) and 5,5'-bis(pyrazin-2''-yl)-3,3'-bis(1H-1,2,4-triazole) (bpzbt) ligands and of their monomeric precursors. Both the complexes underwent two successive protonation processes in aqueous buffered solution. The emission maximum of $[(bpy)_2Ru(bpbt)Ru(bpy)_2]^{2+}$ gets blue-shifted from 690 to 660 nm with concomitant increase of lifetime from 102 to 344 ns (~3 times) in the first step which is in sharp contrast to the protonation behavior of corresponding monomeric precursor. An additional blue-shift from 660 to 630 nm together with remarkable decrease of lifetime from 344 to <5 ns was observed in the second step, which is in-line with the behavior of monomeric precursor in terms of emission energy and emission lifetime. For the pyrazine-triazole based dimer, $[(bpy)_2Ru(bpzbt)Ru(bpy)_2]^{2+}$, protonation also occurs in two successive steps but here a small red shift in emission (~10 nm) was observed which is in agreement with similar pyrazine based complexes. As compared to pyridine-triazole based dimer **(**$[(bpy)_2Ru(bpbt)Ru(bpy)_2]^{2+}$), the change in emission energy was much smaller, but the lifetime increased to greater extent (214→ 764 ns in the first step and 764 →1000 ns in the second step). Overall increase of lifetime is ~5 times compared with its free form.[56]

In a separate work, Vos and co-workers reported heteroleptic terpyridine complexes of Ru(II) incorporating 2,6-bis-([1,2,4]triazol-3-yl)pyridine, 2,6-bis(5-phenyl-[1,2,4]triazol-3-yl)pyridine, and 2,6-bis([1,2,3,4]tetrazol-5-yl)pyridine and studied their emission characteristics as a function of both acid and base.[25] A series of bis(tridentate) Ru(II) complexes featuring anionic 1,2,3-triazolate-based tridentate ligands and 2,2':6',2''-terpyridine was also reported by Berlinguette and coworkers.[31] They observed that deprotonation of triazole/tetrazole moiety led to significant enhancement of emission intensity and excited-state lifetime. By contrast, protonation of one or both of the azole rings induced almost complete emission quenching together with increase in emission energy. Upon deprotonation, enhanced σ-donor strength of the azolate ligands raise the ligand field stabilization Ru(e_g) energy and consequently led to increase ^{3}MLCT-^{3}MC energy gap. In our case, the situation is reverse, protonation of imidazole nitrogen(s) gives rise to substantial enhancement of emission intensity and lifetime of the complexes. From the survey of literature, it appears that the extent of increase in lifetime of the present complexes on protonation is remarkably higher (up to 80 times) compared with previously reported systems.

In order to figure out the decay dynamics of ^{3}MLCT state, both steady state emission spectra and lifetime of acid saturated solutions of **1a-3a** (in MeCN) were acquired by varying temperature between 283K and 333 K. Representative experimental results are displayed in Figure 2.21-2.22. Emission intensity and lifetime gradually decreased in all cases, albeit to different extent, upon increase of temperature. Fitting of the experimental lifetime *vs.* temperature data to equation 2 gives rise to the values of k_1, k_2 and ΔE_2. The obtained ΔE_2 values are 5221±70 (for **1a**), 6023±34 (for **2a**), and 6111±40 cm^{-1} for **3a** (Table 2.11). While temperature-dependant lifetime measurement of the free form of the complexes at room temperature show considerable enhancement of ΔE_2 (^{3}MLCT and ^{3}MC energy gap) relative to $[Ru(tpy)_2]^{2+}$ (ΔE=1500 cm^{-1}), further increase of ΔE_2 take place on protonation of the complexes.

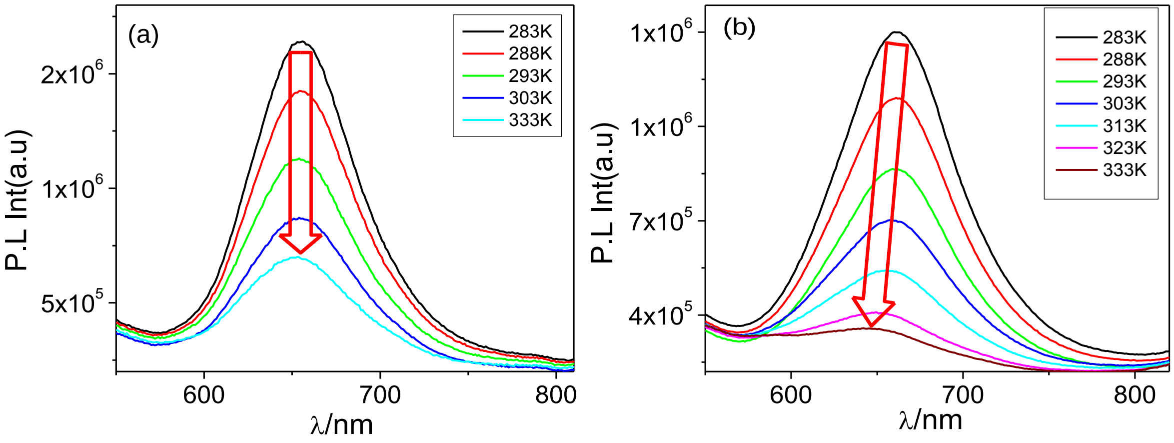

Figure 2.21. Emission spectral changes (λ_{ex}= 490 nm) of **1a** (a) and **3a** (b)) in MeCN as a function of temperature in the range of 283K and 333K.

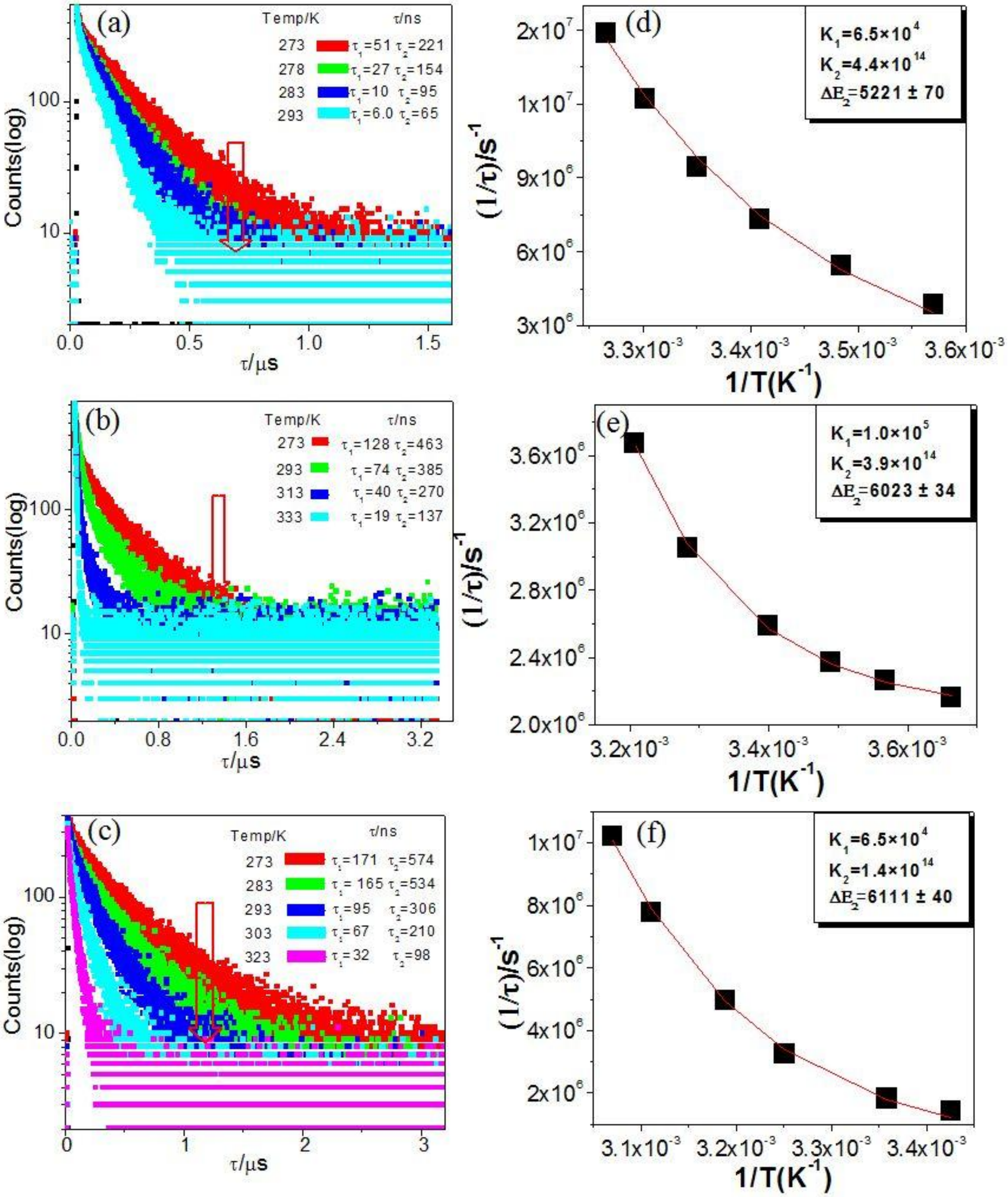

Figure 2.22. Change in decay profiles for **1a** (a), **2a** (b), and **3a** (c) as a function of temperature in MeCN. Temperature-dependent lifetime data along with the values of different parameters and the corresponding nonlinear fits are shown in (d), (e), and (f) for **1a**, **2a**, and **3a**, respectively.

2.3.6. Anion-Induced Changes in the Photophysical Properties of the Complexes. The polarizable NH group(s) of the imidazole unit has been exploited, to modulate the photophysical properties of the complexes during their interaction with various anions in MeCN and H_2O. Tetrabutylammonium salts of F^-, Cl^-, Br^-, I^-, CN^-, HSO_4^-, AcO^-, NO_3^-, and $H_2PO_4^-$ were used for this study. For carrying out studies in water, we used HEPES buffer solution at pH 7.2 to exclude the interference of OH^- ion. Representative UV-vis absorption and emission spectra in the presence of the above-mentioned anions are presented in Figure 2.23. Considerable changes in their spectral profiles as well as visual change of color in MeCN were observed with F^-, AcO^- and CN^- and to a smaller extent with $H_2PO_4^-$. By contrast, the color change in aqueous solution was observed only with CN^-. MLCT and ILCT bands are mostly affected by anions and red-shift of MLCT band with significant alteration of its intensity was observed in most cases. Red-shift of MLCT band resulted due to second coordination sphere interaction (hydrogen-bonding and/or anion-induced deprotonation) between the polarized NH

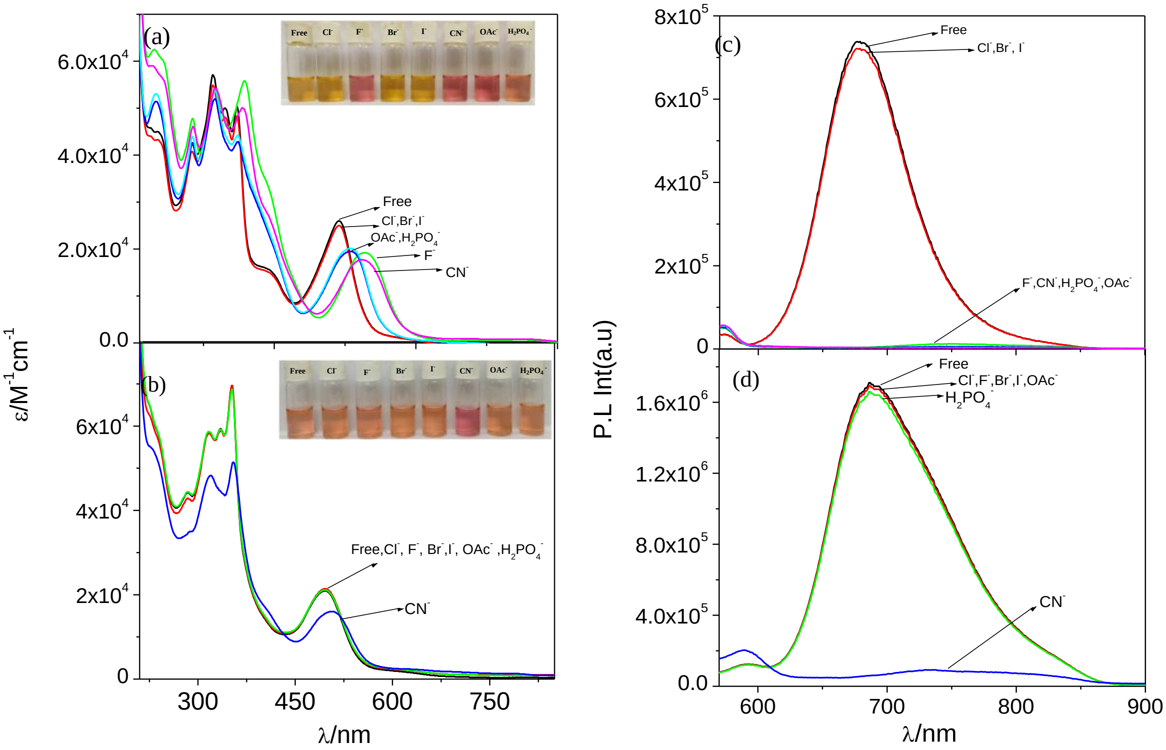

Figure 2.23. Absorption and emission spectral profile of **2** in MeCN (a and c, respectively) and water-HEPES (pH = 7.2) (b and d, respectively) as a function of various anions. Insets of (a) and (b) show the visual color changes.

motif(s) and anions. The extent of spectral change depends upon the type of the complex and number of NH motifs in the second coordination sphere. Substantial quenching of emission occurs for all the three complexes and the quenching effect is again dependent upon the type of the complex, nature of anions, and solvent medium. It is of interest to note that while all the three complexes are capable of sensing CN^- selectively in aqueous solution, they lack selectivity for sensing F^-, CN^-, and AcO^- in MeCN.

In order to obtain quantitative information regarding receptor-anion interaction, absorption and emission spectral titrations experiments were carried out. For complexes **1** and **3**, the spectral changes observed as a function of anion concentration in MeCN are displayed in Figure 2.24-2.25. Complex **1** interacts with F^-, CN^-, and AcO^- in a single step, whereas for **2** and **3,** two-step interactions are involved. Spectral change exhibited by $H_2PO_4^-$ differs slightly from the rest. In all the cases, the UV-vis titration profiles are associated with several clear-cut isosbestic points. The luminescence spectroscopic titrations in all cases show gradual decrease of luminescence intensity, although the extent of decrease varies with the complex and the anions used. In the case of **1** and **3**, no shift of emission band is noticed during quenching, while for **2** two-step quenching processes are accompanied by remarkable red-shift of the emission bands (680→745 nm for 1st step and 745→765 nm for 2nd step).

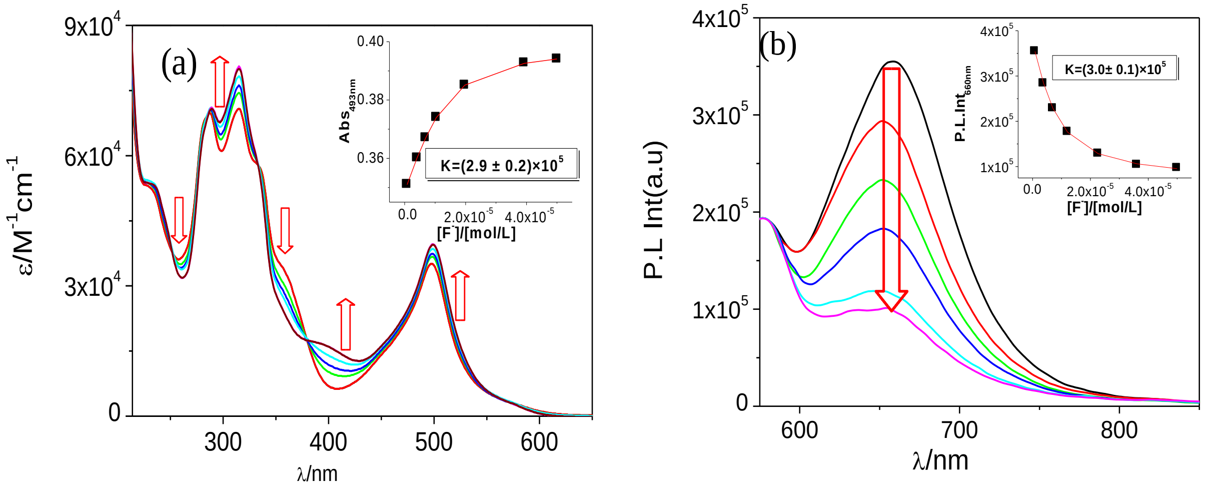

Figure 2.24. Changes in UV-vis absorption and luminescence spectra of **1** in acetonitrile upon incremental addition of F^- (a and b, respectively). Insets show the fit of the experimental absorbance and luminescence data to a 1:1 binding profile.

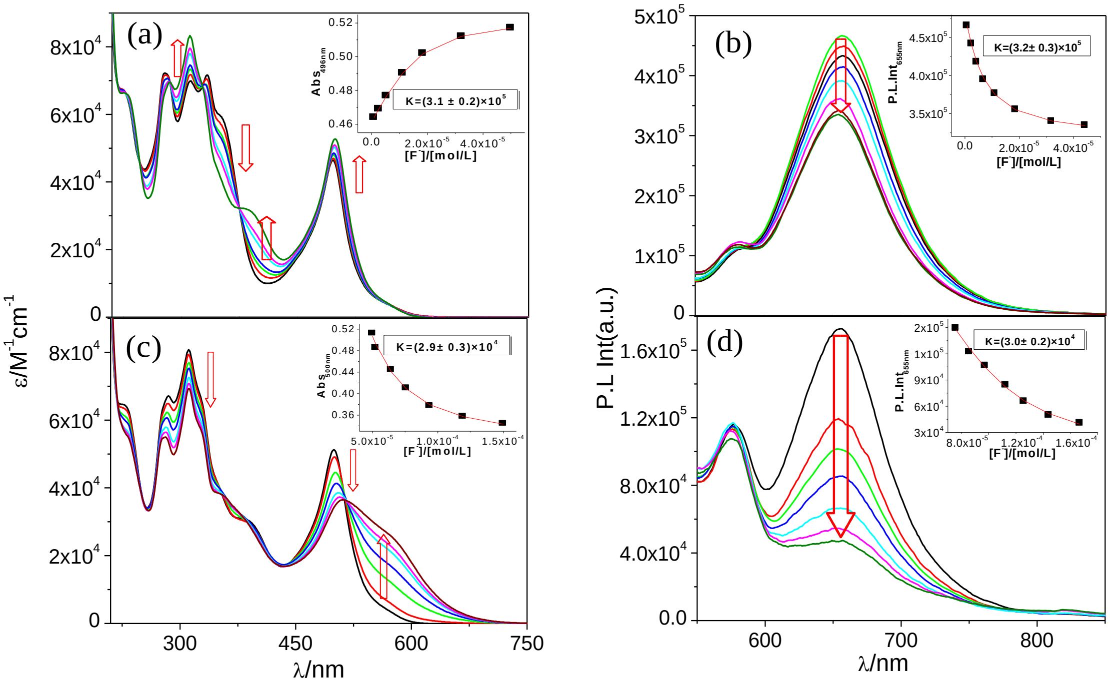

Figure 2.25. Change in UV-vis absorption (a and c) and luminescence (b and d) spectrum of **3** in acetonitrile upon incremental addition of F^-. Insets display the fit of the experimental data to a 1:1 binding profile.

Absorption and emission spectral titrations were also executed in water-HEPES buffer solution with incremental addition of CN^-. The spectral profiles of the complexes in the buffer solution resemble closely to that in MeCN with small variation of peak position and intensity. Again, complex **2** displays a two-stage change (Figure 2.27), whereas **1** and **3** show one-step change in their spectral profiles (Figure 2.26 and 2.28). CN^- induces minor red-shift of MLCT band in **1** (493 nm→496 nm) and **3** (510 → 515 nm) with diminution of band intensity. Emission quenching with no shift of band maximum is observed for both complexes **1** and **3**, although the extent of quenching is relatively less in water compared with MeCN. On the other hand, CN^- induces two-stage changes in **2** with gradual red-shift of MLCT band from 494 to 505 nm in first step (up to 4 equiv) and eventually to 510 nm in the second stage in presence of excess CN^-.

Luminescence lifetime was also measured in MeCN and H_2O as a function of added anions (Figure 2.29). **1** and **3** exhibit bi-exponential decay, while **2** shows almost mono-exponential decay in MeCN. Inclusion of specific anion (such as F^- or CN^-)

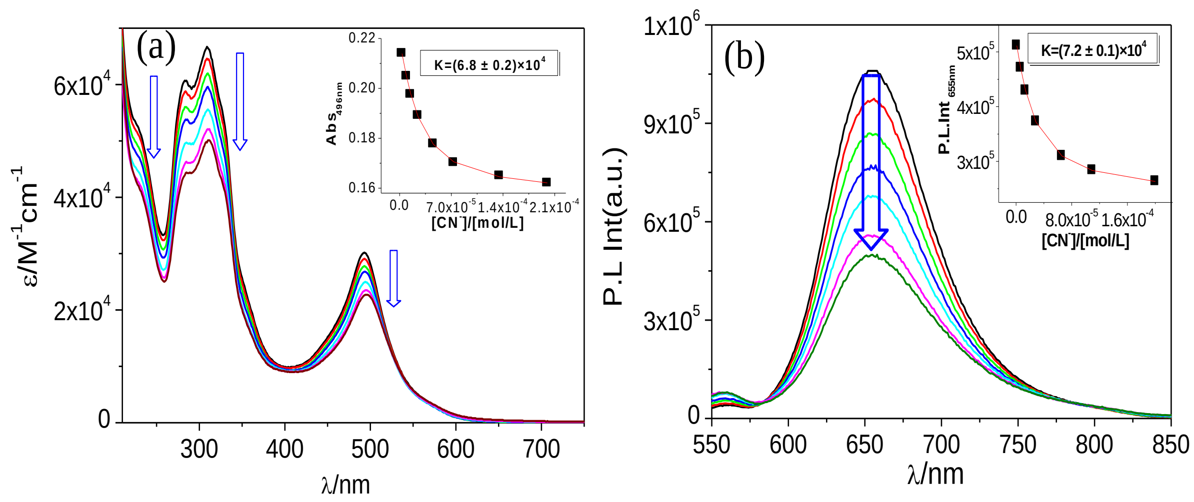

Figure 2.26. Changes in UV-vis absorption and luminescence spectra of **1** in water-HEPES buffer mixture upon incremental addition of CN$^-$ (a and b, respectively). Insets show the fit of the experimental absorbance and luminescence data to a 1:1 binding profile.

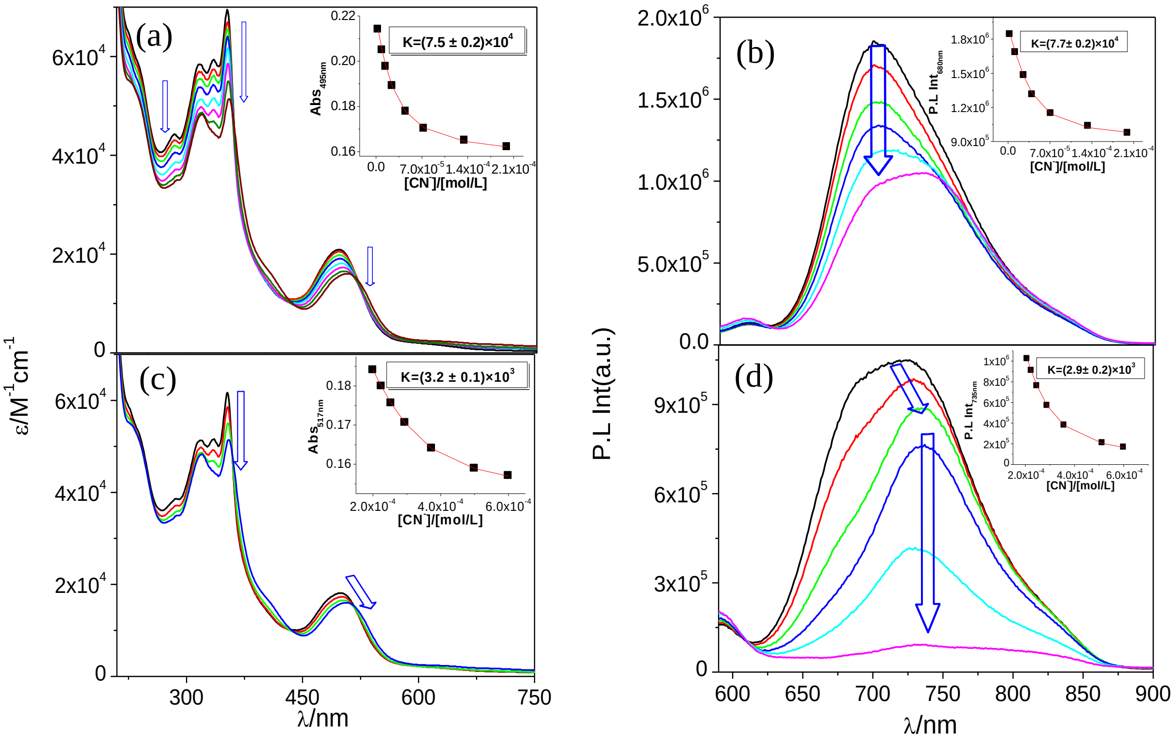

Figure 2.27. Change in UV-vis absorption (a and c) and luminescence (b and d) spectrum of **2** in water-HEPES buffer (pH = 7.2) upon incremental addition of CN$^-$. Insets show the fit of the experimental data to a 1:1 binding profile.

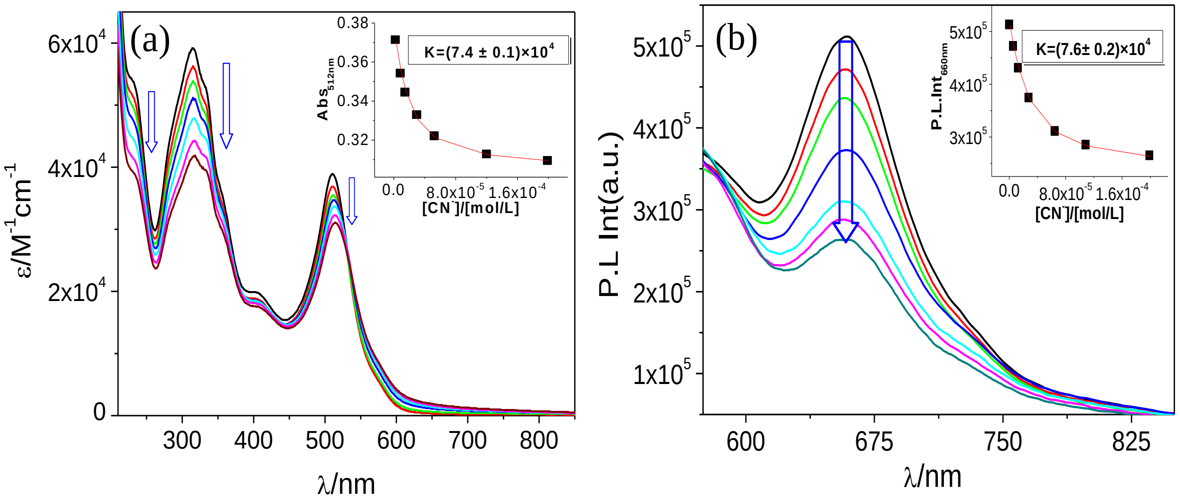

Figure 2.28. Change in UV-vis absorption (a) and luminescence (b) spectrum of **3** in water-HEPES buffer mixture upon incremental addition of CN^-. Insets show the fit of the experimental absorbance and luminescence data to a 1:1 binding profile.

brings about progressive reduction of lifetime. Similar to the steady-state method, extent of lifetime reduction is much higher (32 ns → 3.5 ns) for **2** than that of **1** (5.2 ns → 1.7 ns) and **3** (5.4 ns→ 3.8 ns). Again, in contrast to the behaviour in MeCN, lifetime reduction of the complexes occurs only with CN^- in water. Moreover, the magnitude of change is much higher for **2** (40.0 ns →11.6 ns) compared with **1** and **3**. Thus, significant alteration of emission and lifetime behaviours of the complexes upon interaction with selected anions help us to visualize the anion recognition event.

The equilibrium constants involving association with anions have been determined from the absorption and emission titration data and the values obtained are given in Table 2.12. The values of K_1 in MeCN are grossly of the order of 10^5, while the K_2 values are one order of magnitude less. Both K_1 and K_2 values decrease by one order of magnitude on going from MeCN to H_2O. Detection limit of CN^- in water for the three complexes ranges between 0.01 and 0.064 μM (Table 2.13 and Figure 2.30-2.33).

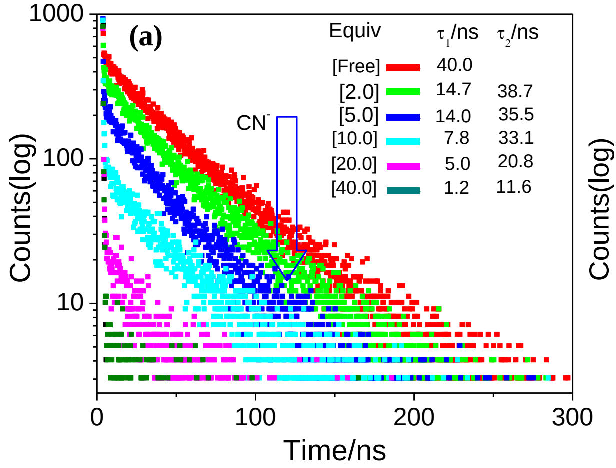

Figure 2.29. Change of luminescence decay profiles of **2** in (a) water-HEPES buffer mixture upon gradual addition of CN^- (b) acetonitrile upon gradual addition of F^- .Inset shows the lifetime values.

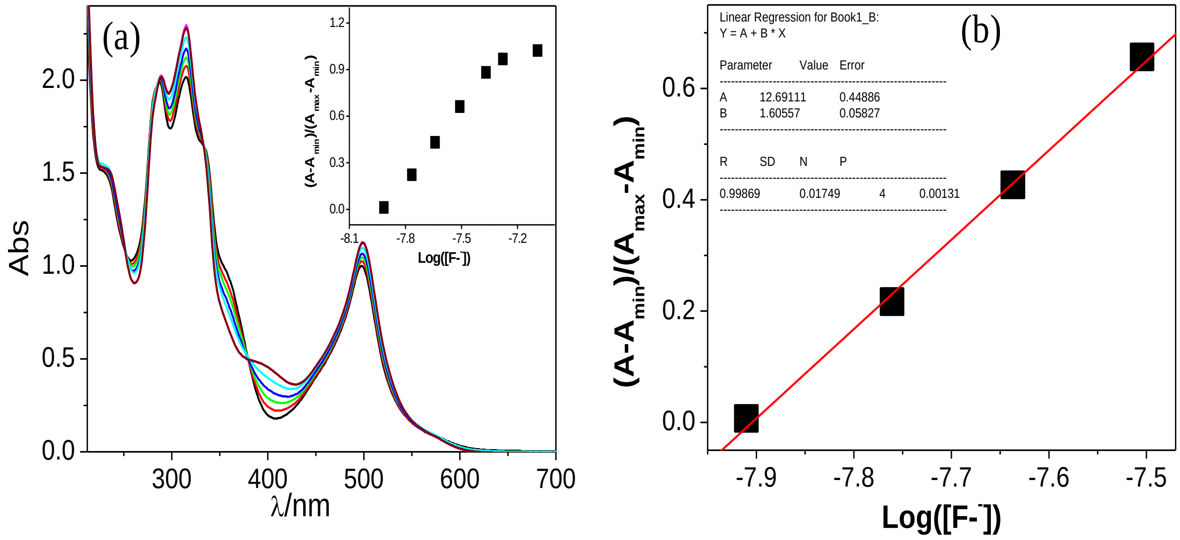

Figure 2.30. (a) Absorption spectral changes during the titration of the receptor **1** (1.0×10^{-5} M) with F^- in acetonitrile, inset: Normalized absorbance between the minimum absorbance and the maximum absorbance. (b) A plot of $(A-A_{min})/(A_{max}-A_{min})$ vs. Log ($[F^-]$), the calculated detection limit of receptor is 1.1×10^{-8} M.

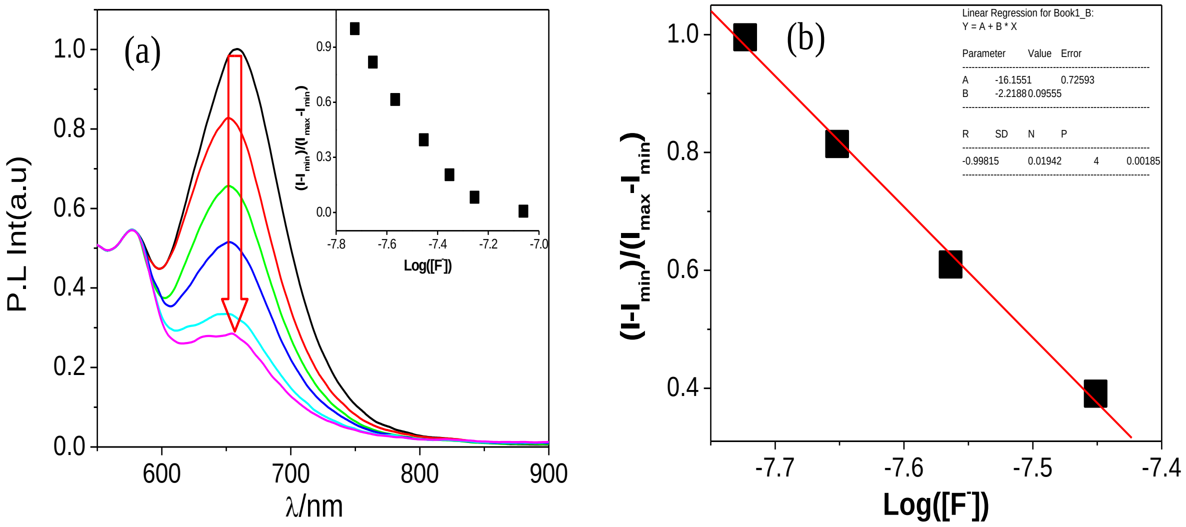

Figure 2.31. (a) Emission spectral changes during the titration of the receptor **1** (1.0×10^{-5} M) with F^- in acetonitrile, inset: Normalized intensity between the minimum intensity and the maximum intensity. (b) A plot of $(I\text{-}I_{min})/(I_{max}\text{-}I_{min})$ vs Log ($[F^-]$), the calculated detection limit of receptor is 3.8×10^{-8} M.

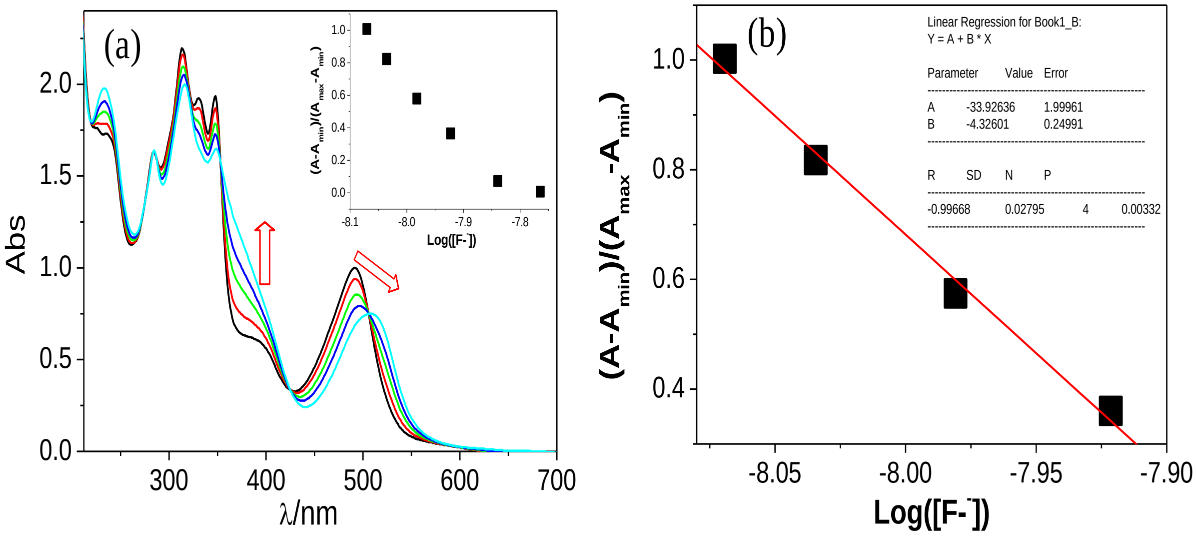

Figure 2.32. (a) Absorption spectral changes during the titration of the receptor **2** (1.0×10^{-5} M) with F^- in acetonitrile, inset: Normalized absorbance between the minimum absorbance and the maximum absorbance. (b) A plot of $(A\text{-}A_{min})/(A_{max}\text{-}A_{min})$ vs. Log ($[F^-]$), the calculated detection limit of receptor is 1.2×10^{-8} M.

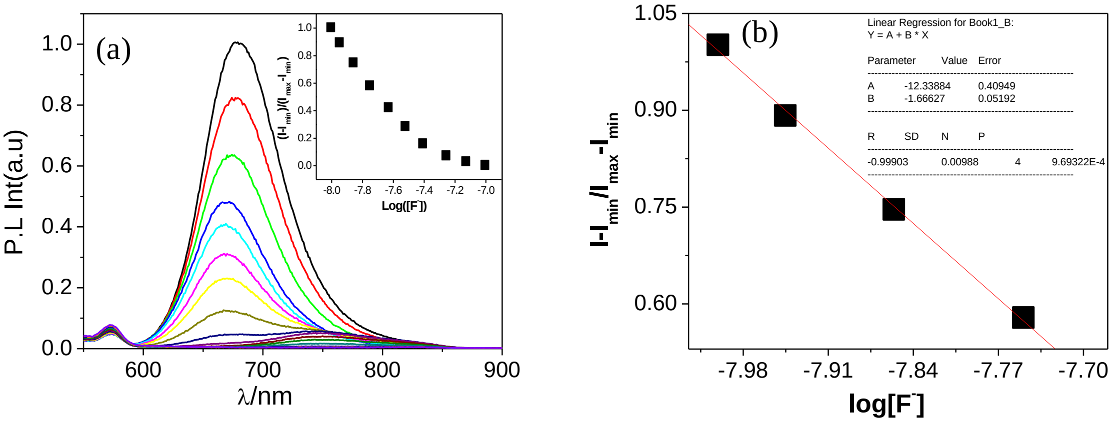

Figure 2.33. (a) Emission spectral changes during the titration of the receptor **2** (1.0×10^{-5} M) with F$^-$ in acetonitrile, inset: Normalized intensity between the minimum intensity and the maximum intensity. (b) A plot of (I-I$_{min}$)/(I$_{max}$-I$_{min}$) vs. Log ([F$^-$]), the calculated detection limit of receptor is 2.0×10^{-8} M.

As already mentioned, anion sensing behaviour of several Ru(II) complexes based on polypyridyl-imidazole ligands were reported by different research groups.[45-47,58-67,86,87] Selected results are summarized in Table 2.13 for the sake of comparison in the context of present study. It may be noted that among various Ru(II)-based chemosensors, only a few have the abilities to recognize CN$^-$ in water, most of them can detect CN$^-$ either in non aqueous solvent or in aqueous-organic medium with low detection limit. Moreover, their detection limit is not sufficiently low for practical applications. The detection limit of the present complexes for CN$^-$, which is of the order of 10^{-8} M, lies below the allowable level (0.2 ppm) for drinking water approved by Environment Protection Agency (EPA)[88] and makes them encouraging contenders for detecting CN$^-$ in water. Greater selectivity of CN$^-$ in water can be related to its lower free energy of hydration ($\Delta G_h°$= -295 kJ/mol) as well as higher pK_a value of HCN (9.0) compared to the greater free energy of hydration for F$^-$ ($\Delta G_h°$= -465 kJ/mol) or AcO$^-$ ($\Delta G_h°$= -365 kJ/mol) and lower pK_a values of their corresponding acids HF (pKa = 3.17) and AcOH (pKa =4.76).[89]

Table 2.12. Equilibrium/Binding Constants[a,b] (*K*) for **1-3** towards Various Anions in Acetonitrile and Water at 298 K

<table>
<tr><td colspan="7">From Absorption spectra (acetonitrile medium)</td></tr>
<tr><td>Anions</td><td colspan="2">1</td><td colspan="2">2</td><td colspan="2">3</td></tr>
<tr><td></td><td>K_1</td><td>K_2</td><td>K_1</td><td>K_2</td><td>K_1</td><td>K_2</td></tr>
<tr><td>F^-</td><td>2.9×10^5</td><td>-</td><td>3.5×10^5</td><td>2.7×10^4</td><td>3.1×10^5</td><td>2.9×10^4</td></tr>
<tr><td></td><td colspan="6">From Absorption spectra (aqueous medium)</td></tr>
<tr><td>CN^-</td><td>6.8×10^4</td><td></td><td>7.5×10^4</td><td>3.2×10^3</td><td>7.4×10^4</td><td>-</td></tr>
<tr><td colspan="7">From Emission spectra (acetonitrile medium)</td></tr>
<tr><td>Anions</td><td colspan="2">1</td><td colspan="2">2</td><td colspan="2">3</td></tr>
<tr><td></td><td>K_1</td><td>K_2</td><td>K_1</td><td>K_2</td><td>K_1</td><td>K_2</td></tr>
<tr><td>F^-</td><td>3.0×10^5</td><td>-</td><td>3.8×10^5</td><td>3.2×10^4</td><td>3.2×10^5</td><td>3.0×10^4</td></tr>
<tr><td colspan="7">From Emission spectra (aqueous medium)</td></tr>
<tr><td>CN^-</td><td>7.2×10^4</td><td>-</td><td>7.7×10^4</td><td>2.9×10^3</td><td>7.6×10^4</td><td>-</td></tr>
</table>

[a]t-Butyl salts of the respective anions were used for the studies. [b]Estimated errors were < 15 %.

Table 2.13. Representative Anion Sensors based on Ru(II)-Polyheterocyclic Complexes

Complex	Solvent/Anion	Emission	Binding Parameter/K	Detection Limit(μM)	Reference
$[(tpyPhCH_3)Ru(tpyHImzPh_3Me_2)](ClO_4)_2$(**1**) $[(H_2pbbzim)Ru(tpyHImzPh_3Me_2)](ClO_4)_2$(**2**) $[Ru(tpy\text{-}HImzPh_3Me_2)_2](ClO_4)_2$(**3**)	CH_3CN/ F^- H_2O-HEPES buffer $/CN^-$	Turn Off	2.9×10^3 to 3.8×10^5	0.01-0.064	Present work
$[Ru(bpy)_2(mpipH)](ClO4)_2$ $[Ru_2(bpy)_4(mbpibH_2)](ClO4)_4$	HEPES buffer/CN^- F^-	Turn-off Turn-off	3.45×10^2 8.78×10^2	100 5	65
$Ru(bpy)_2(H_2biim)(PF_6)_2$	CH_3CN /F^-	Turn-off	1.94×10^5		63
$[Ru(bpy_{)2}(DMBbimH_2)](PF_6)_2$	CD_3CN/NO_3^- $CD_3CN/H_2PO_4^-$	Turn-On	2.09×10^4 1.71×10^4		64
$Ru(bipy)_2(calixarene)](PF_6)$	$H_2O\text{-}CH_3CN/CN^-$	Turn Off	2.50×10^4	0.07	86
$[Ru(bpy)_2(DPQ\text{-}phen)](PF_6)_3$	$CH_2Cl_2\text{-}CH_3CN$ $/CN^-$ F^-	Turn Off	6.40×10^5 4.28×10^5		87
4,4′,5,5′-Tetramethyl-2,2′-Bibenzimidazole Bis(4,4′-di-*tert*-butyl-2,2′bipyridine)Ruthenium(II) 4,4′-di(*p* anisyl)-2,2′-Bibenzimidazole Bis(4,4′-di-*tert*-butyl-2,2′bipyridine)Ruthenium(II) 4,4′-Di(*o*,*o*′-dimethyl-*p*anisyl)-2,2′-Bibenzimidazole Bis(4,4′-di-*tert*-butyl-2,2′bipyridine)Ruthenium(II)	CH_3CN/Br^-	Turn On	2.04×10^5 4.26×10^5 4.26×10^5		60,61
$[(tpy)Ru(tpy\text{-}HPhImz\text{-}Anq)](ClO_4)_2$ $[Ru(tpy\text{-}HPhImz\text{-}Anq)_2](ClO_4)_2$	CH_3CN/ F^- $CH_3CN\text{-}H_2O/CN^-$	Turn Off	1.01×10^6 to 1.48×10^6	0.006-0.007 0.02	45
$[(tpy\text{-}NaPh)Ru(tpy\text{-}HImzPy)](ClO_4)_2$ $[(H_2pbbzim)Ru(tpy\text{-}HImzPy)](ClO_4)_2$	$DMSO\text{-}CH_3CN/F^-$	Turn Off	2.86×10^5 to 3.62×10^6	0.001-0.01	46
$[(H_2pbbzim)Ru(tpy\text{-}Ar)](ClO_4)_2$	$CH_3CN/CH_2Cl_2/F^-$	Turn Off	3.56×10^6	0.004-0.005	47

mpipH = 2-(4-methylphenyl)-imidazo[4,5-f]-1,10-phenanthroline) and $mbpibH_2$ = 1,3-bis([1,10]-phenanthroline-[5,6-d]imidazol-2-yl)-benzene)[65], bpy = 2, 2′-bipyridine and H_2biim =2,2′-biimidazole [63], $DMBbimH_2$ = 7, 7’-dimethyl-2, 2’-bibenzimidazole [64], DPQ-phen= 2,3-di(1*H*-2-pyrrolyl)quinoxaline [70], tpy-HPhImz-Anq = 2-(4-(2,6-di (pyridine-4-yl)phenyl)-1H-anthra[1,2-d]imidazole-6,11-dione [45], tpy-HImzPy = 10-(4-[2,2':6',2''-terpyridine]terpyridin-4'-ylphenyl)-9H-9,11-diaza-cyclopenta pyrene) [46], tpy-Ar = 4′-substituted terpyridine ligands with Ar = phenyl, 2-naphthyl, 9-anthryl, and 1-pyrenyl [47]

2.4. Conclusion

Herein we have reported three Ru(II)-terpyridine complexes (**1-3**) derived from a terpyridyl-imidazole ligand (tpy-HImzPh$_3$Me$_2$) which are luminescent at room temperature with lifetimes spanning the range of 2.3-43.7 ns, depending upon the coligand and solvent used. In contrast to our previous study dealing with Ru(II) complexes derived from similar terpyridyl imidazole motif differing by peripheral methyl groups, significant enhancement of RT emission intensity, quantum yield and remarkable increase of emission lifetime of the present complexes have been observed to take place upon protonation of the imidazole nitrogen(s) with perchloric acid. The most important observation in this study is that protonation has induced augmentation of emission lifetime by as much as 80 times with respect to their free forms. The enhanced luminescence characteristic of the complexes on protonation seems to be due to the increase of thermal barrier for relaxation. Complexes **1-3** are luminescent at RT because of increased energy gap (in the range of 4210-4435 cm^{-1}) between emitting ^{3}MLCT and non-emitting ^{3}MC states relative to that of non-luminescent [Ru(tpy)$_2$]$^{2+}$ (1500 cm^{-1}) Temperature dependent emission measurements suggest further increase of energy separation between ^{3}MLCT and ^{3}MC states (in the range of 5221- 6111 cm^{-1}) in presence of acid.

We have also looked into anion recognition aspects of the complexes in MeCN and aqueous solution. Although the complexes are sensitive for detection of F$^-$, CN$^-$, and AcO$^-$ in acetonitrile, they lack selectivity. The highlight of the study is that the complexes selectively recognize CN$^-$ in water and the detection limit is as low as 10^{-8} M. In conclusion, the objective of significantly modulating the absorption, emission, quantum yield, and emission lifetime of complexes **1-3** by perturbing the second coordination sphere imidazole group of the terpyridyl-imidazole ligand has been largely achieved.

2.5. References

1. Pannwitz, A.; Poirier, S., Desmarais, N. B.; Prescimone, A.; Wenger, O. S.; Reber. C. Controlling Second Coordination Sphere Effects in Luminescent Ruthenium Complexes by Means of External Pressure. *Chem. Eur. J.* **2018**, *24*, 7830-7833.

2. Hull, J. F.; Himeda, Y.; Wang, W.H.; Hashiguchi, B.; Periana, R.; Szalda, D. J.; Muckerman, J. T.; Fujita, E. Reversible Hydrogen Storage Using CO_2 and a Proton-Switchable Iridium Catalyst in Aqueous Media Under Mild Temperatures and Pressures. *Nat. Chem.* **2013**, *5*, 228-233.
3. Yang, J. Y.; Smith, S. E.; Liu, T.; Dougherty, W. G.; Hoffert, W. A.; Kassel, W. S.; Dubois, M. R.; DuBois, D. L.; Bullock. R. M. Two Pathways for Electrocatalytic Oxidation of Hydrogen by a Nickel Bis (Diphosphine) Complex with Pendant Amines in the Second Coordination Sphere. *J. Am. Chem. Soc*. **2013**, *135*, 9700-9712.
4. Rauchfuss T. B. Diiron Azadithiolates as Models for the [FeFe]-Hydrogenase Active Site and Paradigm for the role of the Second Coordination sphere. *Acc. Chem. Res*. **2015**, *48*, 2107-2116.
5. Hyster, T. K.; Knörr, L.; Ward, T. R.; Rovis, T. Biotinylated Rh (III) Complexes in Engineered Streptavidin for Accelerated Asymmetric C-H Activation. *Science*. **2012**, *338*, 500-503.
6. Ward, T. R. Artificial Metalloenzymes Based on the Biotin-Avidin Technology: Enantioselective Catalysis and Beyond. *Acc. Chem. Res.* **2011**, *44*, 47-57.
7. Key, H. M.; Dydio, P.; Clark, D. S.; Hartwig, J. F. Abiological Catalysis by Artificial Haem Proteins Containing Noble Metals in Place of Iron. *Nature* **2016**, *534*, 534-537.
8. Juris, A.; Balzani, V.; Barigelletti, F.; Campagna, S.; Beleser, P.; Zelewsky, A. V. Ru(II) Polypyridine Complexes: Photophysics, Photochemistry, Electrochemistry, and Chemiluminescence. *Coord. Chem. Rev*. **1988**, *84,* 85-277.
9. Sauvage, J.-P. ; Collin, J. P. J. ; Chambron, C. ; Guillerez, S. ; Coudret, C. ; Balzani, V.; Barigelletti, F.; De Cola, L. ; Flamigni, L. Ruthenium(II) and Osmium(II) Bis (Terpyridine) Complexes in Covalently-Linked Multicomponent Systems: Synthesis, Electrochemical Behavior, Absorption spectra, and Photochemical and Photophysical Properties. *Chem. Rev*. **1994**, *94*, 993-1019.

10. Browne, W. R.; O'Boyle, N. M.; McGarvey, J. J.; Vos, J. G. Elucidating Excited State Electronic Structure and Intercomponent Interactions in Multicomponent and Supramolecular Systems. *Chem. Soc. Rev.* **2005**, *34*, 641-663.
11. Williams, J. A. G. The Coordination Chemistry of Dipyridylbenzene: N-deficient Terpyridine or Panacea for Brightly Luminescent Metal Complexes. *Chem. Soc. Rev.* **2009**, *38*, 1783-1801.
12. Pal, A. K.; Hanan, G. S. Design, Synthesis and Excited-State Properties of Mononuclear Ru (II) Complexes of Tridentate Heterocyclic Ligands. *Chem. Soc. Rev.* **2014**, *43*, 6184-6197.
13. Medlycott, E. A.; Hanan, G. S. Synthesis and Properties of Mono and Oligo-Nuclear Ru (II) Complexes of Tridentate Ligands: the Quest for Long-Lived Excited States at Room Temperature. Coord. *Chem. Rev.* **2006**, *250*, 1763-1782.
14. Hofmeier, H.; Schubert, U. S. Recent Developments in the Supramolecular Chemistry of Terpyridine-Metal Complexes. *Chem. Soc. Rev.* **2004**, *33*, 373-399.
15. Constable, E. C. 2,2′:6′,2″-Terpyridines: from Chemical Obscurity to Common Supramolecular Motifs. *Chem. Soc. Rev*. **2007**, *33*, 246-253.
16. Harriman, A.; Ziessel, R. Making Photoactive, Molecular-Scale Wires. *Chem. Commun*. **1996**, 1707-1716.
17. Breivogel, A.; Kreitner, C.; Heinze, K. Redox and Photochemistry of Bis (Terpyridine) Ruthenium (II) Amino Acids and Their Amide Conjugates-From Understanding to Applications. *Eur. J. Inorg. Chem.* **2014**, 5468-5490.
18. Winkler, J. R.; Netzel, T.; Creutz, C.; Sutin, N. Direct Observation of Metal-to-Ligand Charge-Transfer (MLCT) Excited States of Pentaammineruthenium (II) Complex. *J. Am. Chem. Soc*. **1987**, *109*, 2381-2392.
19. Wang, J.; Fang, Y. Q. ; Hanan, G. S. ; Loiseau F. ; Campagna, S. Synthesis and Properties of the Elusive Ruthenium(II) Complexes of 4'-cyano-2,2':6',2''-Terpyridine. *Inorg. Chem*. **2005**, *44*, 5-7.
20. Kubel, J.; Schroot, R.; Wachtler, M.; Schubert, U. S.; Dietzek, B.; Jager, M. Photoredox-Active Dyads Based on a Ru(II) Photosensitizer Equipped with

Electron Donor or Acceptor Polymer Chains: a Spectroscopic Study of Light-Induced Processes Toward Efficient Charge Separation. *J. Phys. Chem. C*. **2015**, *119*, 4742-4751.

21. Maestri, M.; Armaroli, N.; Balzani, V.; Constable, E. C.; Thompson, A. M. W. C. Complexes of the Ruthenium (II)-2, 2':6',2''-Terpyridine Family. Effect of Electron-Accepting and Donating Substituents on the Photophysical and Electrochemical properties**.** *Inorg. Chem.* **1995**, *34*, 2759-2767.
22. Santoni, M.P.; Hanan, G. S.; Hasenknopf, B.; Proust, A.; Nastasi, F.; Serroni, S.; Campagna. S. Dinuclear Ru (II) Complexes of Bis-(dipyrid-2′-yl) Triazine (bis-dpt) Ligands as Efficient Electron Reservoirs**.** *Chem. Commun.* **2011**, *47*, 3586-3588.
23. Fang, Y. Q.; Taylor, N. J. ; Hanan, G. S.; Loiseau, F.; Passalacqua, R.; Campagna, S. ; Nierengarten, H.; Dorsselaer, A. V. A Strategy for Improving the Room-Temperature Luminescence Properties of Ru(II) Complexes with Tridentate Ligands. *J. Am. Chem. Soc.* **2002**, *124*, 7912-7913.
24. Encinas, S.; Flamigni, L.; Barigelletti, F.; Constable, E. C.; Housecroft, C. E. ; Schofield, E. R.; Figgemeier, E.; Fenske, D.; Neuburger, M.; Vos, J. G.; Zehnder, M. Electronic Energy Transfer and Collection in Luminescent Molecular Rods Containing Ruthenium(II) and Osmium(II) 2,2′:6′,2″-Terpyridine Complexes Linked by Thiophene-2,5-diyl Spacers. *Chem. Eur. J.* **2002**, *8*, 137-150.
25. Duati, M.; Tasca, S.; Lynch, F. C.; Bohlen, H.; Vos, J. G.; Stagni, S.; Ward, M. D. Enhancement of Luminescence Lifetimes of Mononuclear Ruthenium(II)-Terpyridine Complexes by Manipulation of the Sigma-donor Strength of Ligands**.** *Inorg. Chem.* **2003**, *42*, 8377-8384.
26. Polson, M. I. J.; Loiseau, F.; Campagna, S.; Hanan.G. S. Bridging Ligand Planarity as a Route to Long-Lived, Near Infrared Emitting Dinuclear Ruthenium (II) Complexes. *Chem. Commun*. **2006**, 1301–1303.
27. Loiseau, F.; Passalacqua, R.; Campagna, S.; Polson, M. I. J.; Fang, Y.Q.; Hanan, G. S. New Dinuclear Ru (II) Complexes Containing Free Chelating Polypyridine Sites Within the Bridging Ligands: Absorption Spectra,

Luminescence Properties, Redox Behavior and Sensing Properties *Photochem. Photobiol. Sci.* **2002**, *1*, 982-990.

28. Dietrich, J.; Thorenz, U.; Forster, C.; Heinze, K. Effects of Sequence, Connectivity, and Counter Ions in New Amide-Linked Ru(tpy)$_2$-Re(bpy) Chromophores on Redox Chemistry and Photophysics. *Inorg. Chem*. **2013**, *52*, 1248-1264.
29. Wadman, S. H.; Lutz, M.; Tooke, D. M.; Spek, A. L.; Hartl, F.; Havenith, R.W. A.; van Klink G. P. M.; van Koten, G. Consequences of *N*,*C*,*N′*- and *C*,*N*,*N′*-Coordination Modes on Electronic and Photophysical Properties of Cyclometalated Aryl Ruthenium(II) Complexes. *Inorg. Chem*. **2009**, *48*, 1887-1900.
30. Kreitner, C.; Erdmann, E.; Seidel; W. W. Heinze, K. Understanding the Excited State Behavior of Cyclometalated Bis (Tridentate) Ruthenium (II) Complexes: a Combined Experimental and Theoretical Study. *Inorg. Chem*. **2015**, *54*, 11088.
31. Sinn, S.; Schulze, B.; Friebe, C.; Brown, D. G.; Jäger, M.; Kübel, J.; Dietzek, B.; Berlinguette, C. P.; Schubert, U. S. A Heteroleptic Bis (Tridentate) Ruthenium (II) Platform Featuring an Anionic 1, 2, 3-Triazolate-Based Ligand for Application in the Dye-Sensitized Solar Cell. *Inorg. Chem*. **2014**, *53*, 1637-1645.
32. Brown, D. G.; Sanguantrakun, N.; Schulze, B.; Schubert, U. S.; Berlinguette, C. P. Bis (Tridentate) Ruthenium-Terpyridine Complexes Featuring Microsecond Excited-State Lifetimes. *J. Am. Chem. Soc.* **2012**, *134*, 12354-12357.
33. Fang, Y. Q.; Taylor, N. J.; Laverdiere, F.; Hanan, G. S.; Loiseau, F.; Nastasi, F.; Campagna, S.; Nierengarten, H.; Leize Wagner, E.; Van Dorsselaer, A. Ruthenium(II) Complexes with Improved Photophysical Properties Based on Planar 4'-(2-Pyrimidinyl)-2,2':6',2"-Terpyridine Ligands. *Inorg. Chem*. **2007**, *46,* 2854-2863.
34. Passalacqua, R. ; Loiseau, F. ; Campagna, S. ; Fang, Y. Q. ; Hanan, G. S. In Search of Ruthenium(II) Complexes Based on Tridentate Polypyridine Ligands

that Feature Long-Lived Room-Temperature Luminescence: the Multichromophore Approach. *Angew. Chem. Int. Ed.* **2003**, *42*, 1608-1611.

35. Schlotthauer, T.; Suchland, B.; Gorls, H.; Parada, G. A.; Hammarstrom, L.; Schubert, U. S.; Jager, M. Aryl-decorated Ru^{II} Polypyridyl-type Photosensitizer Approaching NIR Emission with Microsecond Excited State Lifetimes**.** *Inorg. Chem.* **2016**, *55*, 5405-5416.
36. Abrahamsson, M.; Jäger, M.; Kumar, R. J.; Österman, T.; Persson, P.; Becker, H.-C.; Johansson, O.; Hammarström, L. Bistridentate Ruthenium(II) Polypyridyl-Type Complexes with Microsecond ^{3}MLCT State Lifetimes: Sensitizers for Rod-like Molecular Arrays. *J. Am. Chem. Soc*. **2008**, *130*, 15533-15542.
37. Wang, X-Y.; Del Guerzo, A.; Tunuguntla, H.; Schmehl, R. H. Photophysical Behavior of Ru(II) and Os(II) Terpyridyl Phenylene Vinylene Complexes: Perturbation of MLCT State by Intra-Ligand Charge-Transfer State**.** *Res. Chem. Intermed.* **2007**, *33*, 63-77.
38. Siebert, R.; Winter, A.; Schubert, U. S.; Dietzek, B.; Poppa, J. The Molecular Mechanism of Dual Emission in Terpyridine Transition Metal Complexes-Ultrafast Investigations of Photoinduced Dynamics. *Phys. Chem. Chem. Phys.* **2011**, *13*, 1606-1617.
39. Preiß, J.; Jger, M.; Rau, S.; Dietzek, B.; Popp, J.; Martnez; T.; Presselt, M. How does Peripheral Functionalization of Ruthenium (II)-Terpyridine Complexes Affect Spatial Charge Redistribution after Photoexcitation at the Franck-Condon Point? *ChemPhysChem.* **2015**, *16*, 1395-1404.
40. Hissler, M.; El-ghayoury, A.; Harriman, A.; Ziessel, R. Fine-Tuning the Electronic Properties of Binuclear Bis (Terpyridyl) Ruthenium (II) Complexes. *Angew. Chem. Int. Ed.* **1998**, *37*, 1717-1720.
41. Breivogel, A.; Förster, C.; Heinze, K.; A Heteroleptic Bis (Tridentate) Ruthenium (II) Polypyridine Complex with Improved Photophysical Properties and Integrated Functionalizability. *Inorg. Chem*. **2010**, *49*, 7052-7056.
42. Leslie, W.; Batsanov, A. S.; Howard , J. A. K.; Williams, J. A. G. Cross-Couplings in the Elaboration of Luminescent Bis-Terpyridyl Iridium

Complexes: the Effect of Extended or Inhibited Conjugation on Emission. *Dalton Trans.* **2004**, 623- 631.

43. Arm, K. J.; Williams, J. A. G. A Cross-Coupling Strategy for the Synthesis of Dimetallic Assemblies Containing Mixed Bipyridine–Terpyridine Bridging Ligands: Luminescence and Energy Transfer Properties. *Dalton Trans.* **2006**, 2172–2174.
44. Benniston, A. C.; Chapman, G.; Harriman, A.; Mehrabi, M.; Sams, C. A. Electron Delocalization in a Ruthenium (II) Bis (2,2′:6′,2″-terpyridyl) Complex. *Inorg. Chem*. **2004**, *43*, 4227-4233.
45. Mondal, D.; Bar, M.; Mukherjee, S.; Baitalik, S. Design of Ru (II) Complexes Based on Anthraimidazoledione-Functionalized Terpyridine Ligand for Improvement of Room-Temperature Luminescence Characteristics and Recognition of Selective Anions: Experimental and DFT/TD-DFT Study. *Inorg. Chem*. **2016**, *55*, 9707-9724.
46. Maity, D.; Bhaumik, C.; Mondal, D.; Baitalik, S. Ru (II) and Os(II) Complexes Based on Terpyridyl-Imidazole Ligand Rigidly Linked to Pyrene: Synthesis, Structure, Photophysics, Electrochemistry, and Anion-Sensing Studies. *Inorg. Chem*. **2013**, *52*, 13941-13955.
47. Maity, D.; Das, S.; Mardanya, S.; Baitalik, S. Synthesis, Structural Characterization, and Photophysical, Spectroelectrochemical and Anion-Sensing Studies of H0eteroleptic Ruthenium(II) Complexes Derived from 4′-Polyaromatic-Substituted Terpyridine Derivatives and 2,6-Bis(Benzimidazol-2-yl)Pyridine. *Inorg. Chem*. **2013**, *52*, 6820-6838.
48. Bhaumik, C.; Saha, D.; Das, S.; Baitalik, S. Synthesis, Structural Characterization, Photophysical, Electrochemical and Anion-Sensing Studies of Luminescent Homo- and Heteroleptic Ruthenium(II) and Osmium(II) Complexes Based on Terpyridyl-Imidazole Ligand. *Inorg. Chem.* **2011**, *50*, 12586-12600.
49. Karmakar, S.; Mardanya, S.; Das S.; Baitalik, S.; Efficient Deep-Blue Emitter and Molecular-Scale Memory Device Based on Dipyridyl-Phenylimidazole-Terpyridine Assembly. *J. Phys. Chem. C*. **2015**, *119*, 6793-6805.

50. Mondal, D.; Biswas, S.; Paul, A.; Baitalik, S. Luminescent Dinuclear Ruthenium Terpyridine Complexes with a Bis-Phenylbenzimidazole Spacer. *Inorg. Chem*, **2017**, *56*, 7624-7641.
51. Bhaumik, C.; Das, S.; Saha, D.; Dutta, S.; Baitalik, S. Synthesis, Characterization, Photophysical and Anion-Binding Studies of Luminescent Heteroleptic Bis-Tridentate Ruthenium(II) Complexes Based on 2,6-Bis(Benzimidazole-2-yl)Pyridine and 4'-Substituted 2,2':6',2" Terpyridine Derivatives. *Inorg. Chem.* **2010,** *49*, 5049-5062.
52. Bhaumik, C.; Das, S.; Maity, D.; Baitalik, S. Luminescent Bis-Tridentate Ruthenium (II) and Osmium (II) Complexes Based on Terpyridyl-Imidazole Ligand: synthesis, Structural Characterization, Photophysical, Electrochemical and Solvent Dependence Studies. *Dalton Trans.* **2012**, *41*, 2427-2438.
53. Bhaumik, C.; Maity, D.; Das, S.; Dutta, S.; Baitalik, S. Anion Sensing Studies of Luminescent Bis-Tridentate Ruthenium (II) and Osmium (II) Complexes Based on Terpyridyl-Imidazole Ligand Through Different Channels. *Polyhedron.* **2013**, *52*, 890-899.
54. Wachtler, M.; Kupfer, S.; Guthmuller, J.; Rau, S.; González, L.; Dietzek, B. Structural Control of Photoinduced Dynamics in 4H‑ImidazoleRuthenium Dyes. *J. Phys. Chem. C* **2012**, *116*, 25664−25676.
55. Brautigam, M.; Wachtler, M.; Rau, S.; Popp, J.; Dietzek, B Photophysical Dynamics of a Ruthenium Polypyridine Dye Controlled by Solvent pH. *J. Phys. Chem. C* **2012**, *116*, 1274–1281
56. Pietro, C.D.; Serroni, S.; Campagna, S.; Gandolfi, M. T.; Ballardini, R.; Fanni, S.; Browne, W.R.; Vos, J. G. Proton Controlled Intramolecular Communication in Dinuclear Ruthenium(II) Polypyridine Complexes. *Inorg. Chem.* **2002**, *41*, 2871-2878.
57. Brennan, C.; Draksharapu, A.; Browne,W.R.; McGarvey, J. J.; Vos, J.G.; Pryce, M. T. Unexpected Reversible Pyrazine Based Methylation in a Ru(II) Complex Bearing a Pyrazin-2'-yl-1,2,4-Triazolato Ligand and Its Effect on Acid/Base and Photophysical Properties. *Dalton Trans.* **2013**, *42*, 2546–2555.

58. Petermann, L.; Staehle, R.; Pilz, T. D.; Sorsche, D.; Görls, H.; Rau, S. Synthetic Strategies for Variably Substituted Ruthenium-Imidazophenanthrolinium Complexes. *Eur. J. Inorg. Chem*. **2015**, *2015*, 750-762.
59. Staehle, R.; Reichardt, C.; Popp, J.; Sorsche, D.; Petermann, L.; Kastner, K.; Streb, C.; Dietzek, B.; Rau, S. Ruthenium Imidazophenanthrolinium Complexes with Prolonged Eexcited-State Lifetimes. *Eur. J. Inorg. Chem*. **2015**, *2015*, 3932-3939.
60. Sorsche, D.; Rommel, S.A.; Rau S. Functional Dimming of Pincer-Shaped Bibenzimidazole-Ruthenium (II) Complexes with Improved Anion-Sensitive Luminescence. *Eur. J. Inorg. Chem.* **2016**, 1503–1513.
61. Rommel S. A.; Sorsche, D.; Fleischmann, M.; Rau, S. Optical Sensing of Anions via Supramolecular Recognition with Biimidazole Complexes. *Chem. Eur. J.* **2017**, *23*, 18101 -18119.
62. Cui, Y.; Niu, Y. L.; Cao, M. L.; Wang, K.; Mo, H. J.; Zhong, Y. R.; Ye, B.-H. Ruthenium (II) 2,2′-Bibenzimidazole Complex as a Second-Sphere Receptor for Anion Interaction and Colorimeter. *Inorg. Chem.* **2008**, *47*, 5616-5624.
63. Cui, Y.; Mo, H.-J.; Chen, J.-C.; Niu, Y.-L.; Zhong, Y.-R.; Zheng, K. C.; Ye, B. H. Anion-Selective Interaction and Colorimeter by an Optical Metalloreceptor Based on Ruthenium (II) 2,2'-Biimidazole: Hydrogen Bonding and Proton Transfer. *Inorg. Chem*. **2007**, *46*,6427-6436
64. Mo, H.-J.; Niu, Y.L.; Zhang, M.; Qiao, Z.P.; Ye, B. H. Photophysical, Electrochemical and Anion Sensing Properties of Ru(II) Bipyridine Complexes with 2,2′-Biimidazole-Like Ligand. *Dalton Trans*. **2011**, *40*, 8218-8225.
65. Mo, H.J.; Shen, Y.; Ye, B.-H. Selective Recognition of Cyanide Anion Via Formation of Multipoint NH and Phenyl CH Hydrogen Bonding with Acyclic Ruthenium Bipyridine Imidazole Receptors in Water. *Inorg. Chem*. **2012**, *51*, 7174-7184.
66. Amendola, V.; Fabbrizzi, L. Anion Receptors That Contain Metals as Structural Units. *Chem*. *Commun*. **2009**, 513-531.

67. Chang, K. C.; Sun, S. S.; Odago, M. O.; Lees, A. J. Anion Recognition and Sensing by Transition-Metal Complexes with Polarized N-H Recognition Motifs. *Coord. Chem. Rev.* **2015**, *284*, 111-123.
68. Pott, K. T.; Usifer, D. A.; Abruna, H. D. 4-Vinyl-, 6-Vinyl-, and 4'-Vinyl-2,2':6',2"-Terpyridinyl Ligands: Their Synthesis and the Electrochemistry of Their Transition-Metal Coordination Complexes. *J. Am. Chem. Soc.* **1987**,*109*, 3961-3967
69. Haga, M.; Takasugi, T.; Tomie, A.; Ishizuya, M.; Yamada, T.; M. Hossain, D.; Inoue, M. Molecular Design of a Proton-Induced Molecular Switch Based on Rod-Shaped Ru Dinuclear Complexes with Bis-Tridentate 2,6-Bis(Benzimidazol-2-yl)Pyridine Derivatives. *Dalton Trans.* **2003**, *10*, 2069-2079.
70. Schneider, H.-J.; Yatsimirsky, A. Principles and Methods in Supramolecular Chemistry. *John Wiley & Sons, England*, **2000**, pp. p.142.
71. Mo, H-J.; Wu, J-J.; Qiao, Z-P.; Ye, B-H. Interaction Between Biimidazole Complexes of Ruthenium and Acetate Hydrogen Bonding and Proton Transfer. *Dalton Trans.,* **2012**, *41*, 7026-7036.
72. Frisch, M. J.; Trucks, G. W.; Schlegel, H. B.; Scuseria, G. E.; Robb, M. A.; Cheeseman, J. R.; Scalmani, G.; Barone, V.; Mennucci, B.; Petersson, G. A., et al. Gaussian 09, revision A.02; Gaussian Inc.: Wallingford, CT, **2009**
73. Becke, A. D. Density Functional Thermo Chemistry. III. The Role of Exact Exchange. *J. Chem. Phys.* **1993**, *98,* 5648-5652.
74. Lee, C. T.; Yang, W. T.; Parr, R. G. Development of the Colle-Salvetti Correlation-Energy Formula into a Functional of the Electron Density. *Phys. Rev. B* **1988**, *37*, 785-789.
75. (a) Andrae, D.; Haeussermann, U.; Dolg, M.; Stoll, H.; Preuss, H. Energy-Adjusted ab Initio Pseudo Potentials for the Second and Third Row Transition Elements. *Theor. Chim. Acta.* **1990**, *77*, 123-141. (b) Fuentealba, P.; Preuss, H.; Stoll, H.; Szentpaly, L. V. A Proper Account of Core-Polarization with

Pseudopotentials: Single Valence-Electron Alkali Compounds. *Chem. Phys. Lett*. **1989**, *89*, 418-422.

76. Hay, P. J.; Wadt, W. R. Ab Initio Effective Core Potentials for Molecular Calculations. Potentials for K to Au Including the Outermost Core Orbitals. *J. Chem. Phys.* **1985**, *82*, 299-310.
77. Casida, M. E.; Jamorski, C.; Casida, K. C.; Salahub, D. R. Molecular Excitation Energy to High-Lying Bound State from Time-Dependent Density Functional Response Theory: Charecterization and Correction of the Time Dependent Local Density Approximation Ionization Threshold. *J. Chem. Phys.* **1998**, *108*, 4439-4449.
78. Stratmann, R. E.; Scuseria, G. E.; Frisch, M. J. An Efficient Implementation of Time-Dependent Density-Functional Theory for the Calculation of Excitation Energies of Large Molecules. *J. Chem. Phys.* **1998**, *109*, 8218-8224.
79. Walters, V. A.; Hadad, C. M.; Thiel, Y.; Colson, S. D.; Wiberg, K. B.; Johnson, P. M.; Foresman, J. B. Assignment of the A State in Bicyclobutane. The Multiphoton ionization spectrum and calculations of transition energies *J. Am. Chem. Soc.* **1991**, *113*, 4782-4791.
80. (a) Tomasi, J.; Mennucci, B.; Cammi, R. Quantum Mechanical Continuum Solvation Models. *Chem. Rev*. **2005**, *105*, 2999-3094. (b) Cossi, M.; Scalmani, G.; Rega, N.; Barone, V. New Developments in the Polarizable Continuum Model for Quantum Mechanical and Classical Calculations on Molecules in Solution. *J. Chem. Phys*. **2002**, *117*, 43-54.
81. Caricato, M.; Mennucci, B.; Tomasi, J.; Ingrosso, F.; Cammi, R.; Corni, S.; Scalmani, G. Formation and Relaxation of Excited States in Solution: A New Time Dependent Polarizable Continuum Model Based on Time Dependent Density Functional Theory. *J. Chem. Phys*. **2006**, *124*, 124520-124530.
82. Mennucci, B.; Cappelli, C.; Guido, C. A.; Cammi, R.; Tomasi, J. Structures and Properties of Electronically Excited Chromophores in Solution from the Polarizable Continuum Model Coupled to the Time-Dependent Density Functional Theory. *J. Phys. Chem. A* **2009**, *113*, 3009.

83. Dennington, R. II.; Keith T.; Millam, J. *Gauss View 3*; Semichem, Inc.: Shawnee Mission, KS, **2007**.
84. O Boyle, N. M.; Tenderholt, A. L.; Langner, K. M. cclib: A Library for Package-Independent Computational Chemistry Algorithms. *J. Comput. Chem*. **2008**, *29*, 839.
85. Martin, R. L. Natural Transition Orbitals. *J. Chem. Phys.* **2003**, *118*, 4775–4777.
86. Maity, D.; Vyas, G.; Bhatta, M.; Paul; P. Detection of NaCN in Aqueous Media Using a Calixarene-Based Fluoroionophore Containing Ruthenium(II)-Bipyridine as the Fluorogenic Unit. *RSC Adv*. **2015**, *5*, 6151–6159.
87. Anzenbacher, P. Jr., Tyson, D. S.; Jursikova, K.; and Castellano F. N. Luminescence Lifetime-Based Sensor for Cyanide and Related Anions. *J. Chem. Soc* **2002**, *124*, 6232-6233.
88. The US Environmental Protection Agency (EPA) Has Set the so Called Maximum Contaminant Level Goals For Cyanide in Drinking Water to 0.2 ppm, and Fluorideto be 2 ppm. http://ecfr.gpoaccess.gov (last Accessed 1st March, 2006).
89. Marcus, Y. *J*. Thermodynamics of Solvation of Ions. *J. Chem. Soc. Faraday Trans*. **1991**, *87*, 2995-2999.

****

Chapter 3

Stimuli-Responsive Molecular Switches and Logic Devices Based on Ru(II)-Terpyridyl-Imidazole Coordination Motif

3.1. Introduction

Emission of light is a very powerful tool to carry out information at the molecular-scale.[1-7] For the development of artificial molecular sensors and switches, the emission of light should be alternately turned-on and turned-off between two or more states upon the action of different stimuli, viz. temperature, ionic guests and pH.[8-16] Stimuli-responsiveness is of particular interest to expand the efficacy and functionality of various materials ranging from sensors to molecular switches and machines. Appropriate assembly of metal and ligand could give rise to potential stimuli-responsive luminophores. Heavy metals in combination with suitable ligand framework often give rise to strong and long-lived luminescence, useful for signal detection.[5-7] Additionally, one or more stimuli-responsive units (viz. protonable/deprotonable motifs) could be judiciously introduced in the ligand moiety that could facilitate the use of pH stimulus to be operative and can show their promise to function as potential sensors and switches.[17-28]

Our main objective here is to show how the photophysical and redox behaviors of the metal-ligand luminophores could be changed in a systematic manner upon incorporation of appropriate ligand framework and how the properties of the resulting complexes would be switched by changing the temperature and pH as the stimuli. Our interest is focused on the coordination complexes of Ru^{2+} metal in combination with polypyridine ligands because of their outstanding photo-redox behaviors and because of their participation as active component in wide range of applications such as dye-sensitized solar cells, light-emitting diodes, photochemical molecular devices, luminescence sensors, and antitumor agents.[29-33] Among the various types of pyridine-based ligands, the complexes based on bipyridine-type of ligands (such as $[Ru(bpy)_3]^{2+}$, bpy = 2, 2´-bipyridine) constitute an important class as they absorb strongly and emit intensely with long lifetimes (around 1μs) in visible spectrum, are stable following oxidation and reduction, and are photo-stable. But the inherent problem is the generation of different isomers during the synthesis of $Ru(bpy)_3$-type complexes. By contrast, complexes based on terpyridine-type ligands yield achiral linear structures but the most important drawback is their non-luminescent character at RT together with very short excited-state lifetime ($[Ru(tpy)_2]^{2+}$, $\tau = 0.25$ ns).[34-40] Thus, it would be good to improve their RT emission characteristics and to lengthen their lifetime so that they can function as effective luminophores. Obviously, various studies were carried out by different research groups for improving their RT emission characteristics. These include insertion of electron accepting or releasing groups,[41-44] polyaromatic hydrocarbons[45-49] onto the terpyridine moiety as well the use of strongly electron donating cyclometalated ligands.[50-54] In majority of the adopted strategies, the important point is to increase the effective energy gap between emitting triplet metal-to-ligand charge-transfer transition (^{3}MLCT) and non-emitting triplet metal-centered (^{3}MC) excited states.[55-59] Our group also designed several Ru(II) complexes upon covalent coupling of aromatic and/or heteroaromatic units onto the terpyridine moiety which exhibit moderately strong emission with reasonably long lifetime at RT.[60-66]

The main focus of this work is to investigate the stimuli-responsive behaviors on the optical (particularly the luminescence) and redox properties of the terpyridine complexes of Ru(II) towards the design of molecular switches. To fulfil our objective, we prepared a terpyridyl-imidazole ligand (**tpy-HImzPh$_3$F$_2$**) wherein the terpyridine unit is covalently coupled with difluorobenzil unit via phenyl-imidazole spacer and used the ligand to synthesize three Ru(II) complexes (**Chart 3.1**). In the design strategy of the ligand, we incorporated electron withdrawing fluoro units in order to get enhanced luminescence property in the resulting complexes by tuning the ^{3}MLCT-^{3}MC energy gap. The energy gap between ^{3}MLCT and ^{3}MC states plays crucial role on the luminescence behaviours of Ru(II)-terpyridine complexes and temperature plays an important role to tune ^{3}MLCT-^{3}MC energy gap. In this regard, we investigated the effect of temperature on the emission spectral behaviors of the complexes to look over their usefulness as temperature-dependent molecular switches. In practice, remarkable alteration of luminescence intensity, quantum yield and lifetime takes place upon variation of temperature.

In addition, secondary coordination sphere of the complexes possesses acidic imidazole NH protons which may be removed upon the increase of pH. To this end, we also studied in detail the impact of pH on the photo-redox behaviors of the complexes. In the present work, our target is also to tune the extent of change of the photo-redox properties as a function of number of NH protons. To this end, we have systematically increase the number of imidazole NH proton from one (for complex **1**), to two (complex

3) to three (for complex **2**) as shown in **Chart 3.1**. In essence, the complexes have the potentiality to act as molecular switches based on significant alteration of their absorption, emission and redox behaviors as function of both pH and temperature.[67-74] In addition, the optical spectral responses of the complexes as function of pH and temperature were utilized for the fabrication of two-input binary logic gates. Information processing at the molecular scale is now a very active area of research and judicious utilization of sequential logic operations exhibited by molecular and supramolecular species is a huge task in the field of information technology.[75-80] Finally, computational studies using DFT and TD-DFT are executed to understand their structures and for appropriate interpretation of the spectral bands.

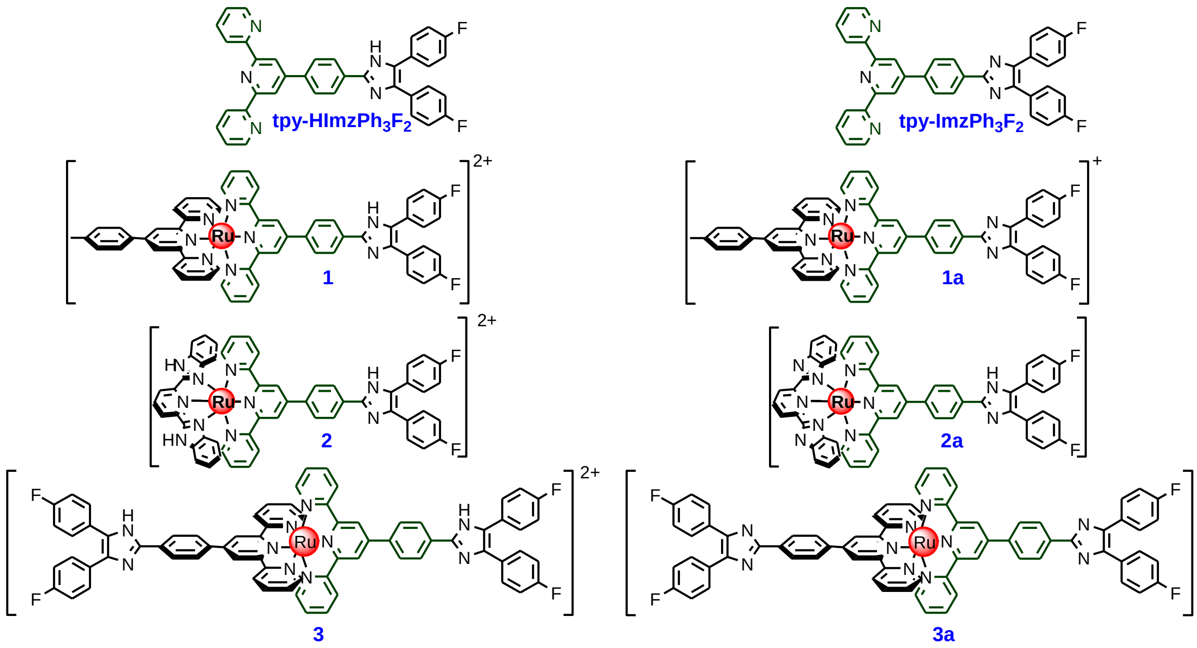

Chart 3.1. Free- (left panel) and deprotonated forms (right panel) of the complexes.

3.2 Experimental Section

3.2.1 Materials. Chemicals and solvents were purchased from local suppliers. 4-formyl-2,2':6',2"-terpyridine(tpy-PhCHO)[81] and 2,6-bis(benzimidazole-2-yl)pyridine (H_2pbbzim) were prepared following reported procedures.[82] [(tpy-PhCH$_3$)RuCl$_3$] and

[(H_2pbbzim)RuCl_3] were synthesized by treating $RuCl_3 \cdot 3H_2O$ with tpy-PhCH_3 and H_2pbbzim, respectively in 1:1 molar ratio in refluxing EtOH.

3.2.2. Synthesis of the Ligand. 2-(4-(4-(4,5-bis(4-fluorophenyl)-1H-imidazol-2-yl)phenyl)-6-(pyridin-2-yl) pyridin-2-yl)pyridine (tpy-HImzPh$_3$F$_2$). Difluorolbenzil (1.7g, 2.97 mmol), tpy-PhCHO (1.00 g, 2.97 mmol), and NH_4OAc (2.3 g, 30 mmol) were dissolved in CH_3COOH (20 mL) and refluxed for 2h. After cool down to RT, the resulting solution was poured into crushed ice (300 mL) and upon stirring an off-white compound that deposited was filtered. The residue was dispersed in water (*ca.* 100 mL) and neutralized with Na_2CO_3 solution. The resulting solid was filtered and thoroughly washed with water. Purification of the compounds were performed through silica gel column chromatography using $CHCl_3$ as the eluting solvent and finally through recrystallization from $CHCl_3$-MeOH (1:1) mixture (370 mg, 0.70 mmol, yield 66%). ^{1}H NMR {400 MHz, DMSO–d_6, δ(ppm)}: 13.60 (s, 1H, NH imidazole), 8.80 (s, 4H, 2H3$'$+2H6), 8.71 (d, 2H, *J*= 7.2, 2H3), 8.32 (d, 2H, *J* = 7.2 Hz, H8), 8.12 (m, 4H, 2H7+2H4), 7.57 (s, 6H, 2H5+4H10), 7.27 (s, 4H, H9), ESI-MS: *m/z* 564.17 ([L+H]$^+$). Anal.Calcd for $C_{36}H_{23}F_2N_5$: C, 77.15; H, 4.31; N, 13.02. Found: C, 76.98; H, 4.13; N, 12.49.

3.2.3. Synthesis of the Metal Complexes. [(tpy-PhCH$_3$)Ru(tpy-HImzPh$_3$F$_2$)] (ClO$_4$)$_2$·H$_2$O (1). Ru(tpy-PhCH_3)Cl_3 (80 mg, 0.15 mmol) and tpy-HImzPh$_3$F$_2$ (84 mg, 0.15 mmol) were added to 10 mL ethylene glycol and refluxed for 2h under Ar protection. The resulting solution was cooled to RT and upon spilling into an aqueous solution of $NaClO_4$ an orange-red compound deposited. The compound was collected and purified by silica-gel column chromatography eluting with CH_3CN. Recrystallization from CH_3CN-MeOH (1:1, v/v) mixture afforded a red microcrystalline compound. (110 mg, Yield: 61%). Anal.Calcd.for $C_{58}H_{42}N_8Cl_2O_9F_2Ru$: C, 57.81; H, 3.51; N, 9.30. Found: C, 56.76; H, 3.45; N, 9.25. ^{1}H NMR (400 MHz, DMSO-d_6, δ/ppm): 12.40 (s, 1H, NH imidazole), 9.56 (s, 2H, $H_{3'}$), 9.46 (s, 2H, $H_{3'''}$), 9.12-9.09 (m, 4H, 2H_6 +2$H_{6'}$), 8.71(d, 2H, *J*=8.4 Hz, H_8), 8.51 (d, 2H, *J*=8.49 Hz, H_7), 8.37 (d, 2H, *J*=8.4 Hz, $H_{8'}$), 8.10-8.04 (m, 8H, 2H_4+2$H_{4'}$+2H_3+2$H_{3''}$), 7.65-7.53 (m, 6H,2 $H_{7'}$+4H_9), 7.40 (t, 4H, *J*= 8.8 Hz, H_{10}), 7.31-7.25 (m, 4H, 2H_5+2$H_{5'}$), 2.39 (s, 3H, CH_3 (tpy-PhCH_3)}. ESI-MS (positive, CH_3CN) *m/z* = 494.17 (100 %) [(tpy-PhCH_3) Ru (tpy-HImzPh$_3$F$_2$)]$^{2+}$.

[(H_2pbbzim)Ru(tpy-HImzPh$_3$F$_2$)](ClO$_4$)$_2$·H$_2$O (2). Complex **2** was prepared by following the same procedure as **1**. In this case [(H_2pbbzim)RuCl$_3$] (78 mg, 0.15 mmol) was used in place of Ru(tpy-PhCH$_3$)Cl$_3$ and recrystallization was carried out in CH$_3$CN-H$_2$O (2:1, v/v) mixture under weakly acidic condition. (125 mg, Yield: 70%). Calcd.for $C_{55}H_{38}N_8Cl_2O_9F_2Ru$: C, 55.38; H, 3.21; N, 11.74. Found: C, 55.18; H, 3.04; N, 11.55. ^{1}H NMR data (400 MHz, DMSO-*d*$_6$, δ/ppm): 15.08 (s, 2H, NH imidazole), 12.13 (s, 1H, NH imidazole), 9.67 (s, 2H, $H_{3'}$), 9.06 (d, 2H, *J*=8.0 Hz, H_6), 8.82 (d, 2H, *J* =8.0 Hz, H_8), 8.67(t, 1H, *J*=8.0 Hz, H_{16}), 8.54 (d, 2H, *J*=8.4 Hz, H_7), 8.00 (t, 2H, *J*=7.8 Hz, H_4), 7.69-7.64 (m, 2H, H_{14}), 7.53 (d, 6H, *J*=5.2 Hz, $2H_3$+$2H_{10}$), 7.40 (t, 4H, *J*=8.6 Hz, $2H_9$), 7.31-7.25(m, 4H, $2H_5$+$2H_{15}$), 7.06 (t, 2H, *J*=7.8 Hz, H_{12}), 6.10 (d, 2H, *J*=8.4 Hz, H_{11}), 6.10 (d, 2H, *J*=8.4 Hz, H_{11}). ESI-MS (positive, CH$_3$CN) *m/z* = 488.07 (100%) [(H_2pbbzim) Ru(tpy-HImzPh$_3$F$_2$)]$^{2+}$.

[Ru(tpy-HImzPh$_3$F$_2$)$_2$](ClO$_4$)$_2$·2H$_2$O (3). Synthetic protocol for **3** is basically similar to that of **1**. In this case Ru (DMSO)$_4$Cl$_2$ (72 mg, 0.15 mmol) and tpy-HImzPh$_3$F$_2$ (169 mg, 0.30 mmol) were taken in 1:2 molar ratio in ethylene glycol and refluxed for 3h. The compound was purified successively by silica gel column chromatography as well as recrystallization from MeCN-MeOH (1:1, v/v) in weakly acidic condition (78 mg, Yield: 55 %). Anal.Calcd.for $C_{72}H_{54}N_{10}Cl_2O_{10}F_4Ru$: C, 63.30; H, 3.98; N, 10.25. Found: C, 63.04; H, 3.57; N, 9.85. ^{1}H NMR data (400 MHz, DMSO-*d*$_6$, δ/ppm): 12.20 (s, 2H, NH imidazole), 9.60 (s, 4H, $H_{3'}$), 9.17 (d, 4H, *J*=8.0 Hz, H_6), 8.72 (d, 4H, *J*=8.0 Hz, H_8), 8.51 (d, 4H, *J*=8.0 Hz, H_7), 8.13 (t, 4H, *J*=7.6 Hz, H_4), 7.66-7.63 (m, 4H, H_3), 7.60 (d, 8H, *J*=5.2, H_{10}), 7.41 (t, 8H, *J*=5.2, H_9), 7.33 (t, 4H, *J*=6.4, H_5). ESI-MS (positive, CH$_3$CN) *m/z* = 614.11 (100%) [Ru(tpy-HImzPh$_3$F$_2$)$_2$]$^{2+}$.

Caution! Perchlorate salts of the metal complexes are explosive and should be handled in small amount with extreme care.

3.2.4. Physical Measurements. The details of different equipments used and experimental process to measure absorption and luminescence spectral behaviors, and computational studies using DFT and TD-DFT methods have been discussed in chapter 2.

Spectrophotometric titrations were carried out with a series of acetonitrile-water (3:2 v/v) solutions containing the same amount of complex (10^{-5} M) and pH adjusted in the range of 2.0-12. Robinson-Britton buffer was used in the study. The pH measurements were made with a Beckman Research Model pH meter.

Electrochemical measurements were carried out in deaerated acetonitrile with a BAS epsilon electrochemistry system and a three-electrode set up consisting of a platinum or glassy carbon working electrode, a platinum counter electrode, and Ag/AgCl reference electrode. In all the experiments, tetraethylammonium perchlorate (TEAP) was used as background electrolyte. The potentials reported in this study were referenced against the Ag/AgCl electrode, which under the given experimental conditions gave a value of 0.36 V for the Fc/Fc+ couple.

3.3. Results and Discussion

3.3.1. Synthesis and Characterization. Tpy-HImzPh$_3$F$_2$ was synthesized by refluxing difluorobenzil and tpy-PhCHO in 1:1 proportion in acetic acid with ammonium acetate. The heteroleptic compounds (**1** and **2**) were obtained by refluxing tpy-HImzPh$_3$F$_2$ with [(tpy-PhCH$_3$)RuCl$_3$] and [(H$_2$pbbzim)RuCl$_3$, respectively (1:1 ratio), while complex **3** was obtained upon refluxing Ru(DMSO)$_4$Cl$_2$ and tpy-HImzPh$_3$F$_2$ (2:1 ratio) in ethylene glycol and anion exchange was done with NaClO$_4$. The perchlorate salts of the complexes are explosive and must be carefully treated with small quantity. Purifications were performed via chromatography and recrystallization techniques under acidic condition and were characterized through ESI mass and NMR spectroscopy

The ESI mass of the complexes in MeCN are provided in Figure 3.1-3.3.The correlation between experimental and calculated isotopic pattern is found to be good. The most abundant peak spanning within the m/z range of 488.07-614.11 is due to bi-positive complex cation. ^{1}H NMR spectra of tpy-HImzPh$_3$F$_2$ and the complexes together with the tentative assignment of the peaks are provided in Figure 3.4.

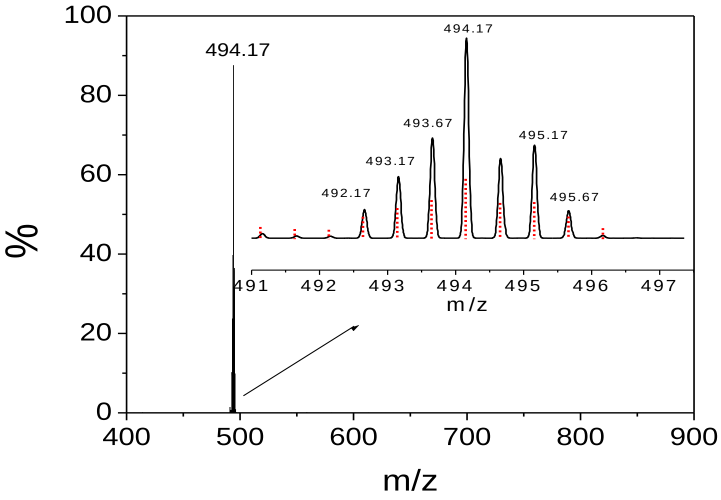

Figure 3.1. ESI (positive) mass spectrum for the complex cation of **1** [(tpy-PhCH$_3$)Ru (tpy-HImzPh$_3$F$_2$]$^{2+}$ (m/z = 494.17) in MeCN showing both observed and simulated isotopic distribution patterns.

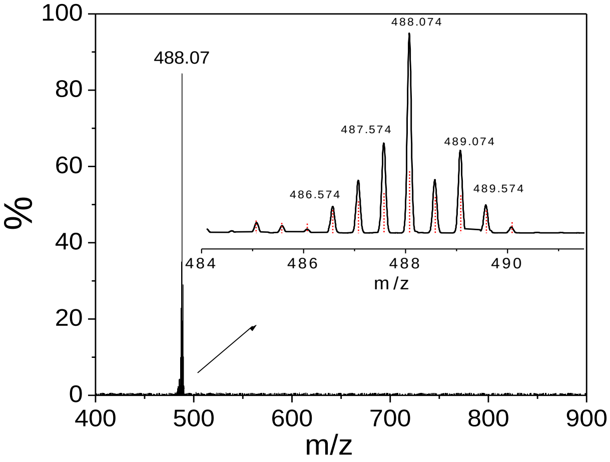

Figure 3.2. ESI (positive) mass spectrum for the complex cation of **2** [(H$_2$pbbzim)Ru (tpy-HImzPh$_3$F$_2$)]$^{2+}$ (m/z = 488.07) in MeCN showing both observed and simulated isotopic distribution patterns.

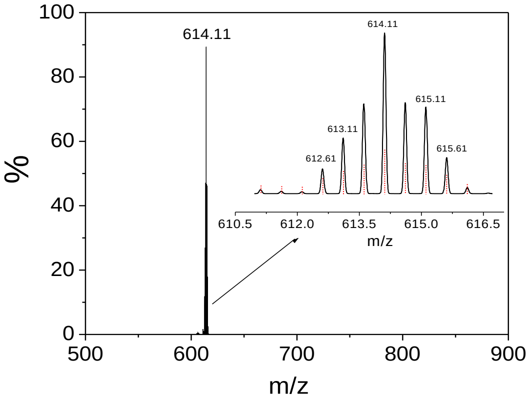

Figure 3.3. ESI (positive) mass spectrum for the complex cation of **3** [(Ru(tpy-HImzPh$_3$F$_2$)$_2$]$^{2+}$ (m/z = 614.11) in MeCN showing both observed and simulated isotopic distribution pattern

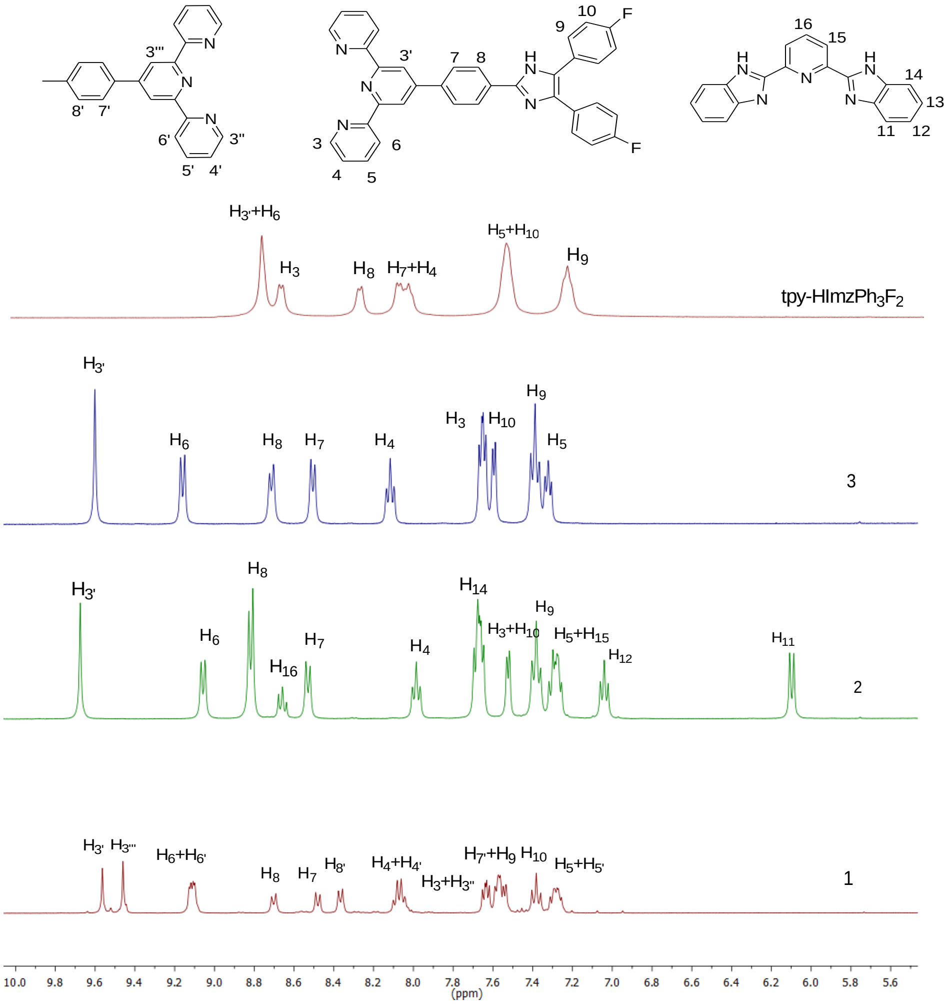

Figure 3.4. ^{1}H NMR spectra of **1-3** together with **tpy-HImzPh$_3$F$_2$** in DMSO-d_6.

3.3.2. Absorption and Emission Spectra. The absorption and emission spectra of the complexes are acquired in few solvents and pertinent spectral data are tabulated in Table 3.1, while their spectra in MeCN are shown in Figure 3.5a-3.5c Assignment of the bands are done by correlating the spectra of similar Ru(II)-terpyridine complexes and taking into consideration the outcome of TD-DFT computations. Geometry optimization is performed with Gaussian 09 programme and TD-DFT calculations are carried out in MeCN to obtain their calculated absorption spectra. The details of the optimized structures and their metrical parameters are provided in Figures 3.6-3.10 and Tables 3.2-3.7.

Table 3.1. Absorption and Emission Spectral Data for **1-3** in Different Solvents

Compounds		Absorption λ_{max}/ nm (ε,M^{-1}cm^{-1})	Luminescence				
			λ_{max} /nm	τ/ns	Φ	k_r/s^{-1}	$k_{nr,}$ /s^{-1}
1	MeCN(298K)	493(36400),354(sh)(27700),332(sh)(57500),310 (75800),283(68500)	658	τ_1=2.7 (33%), τ_2=5.6 (67%)	9.2×10^{-3}		
2		490(33100),395(sh)(16000),348(73400),332(70400),318(75300),283(57300)	676	τ_1=10 (15%), τ_2=35 (85%)	14.1×10^{-3}		
3		496(37900),354(sh)(45500),333(60700),311(60900), 277(53100)	658	τ_1=3.0 (10%), τ_2=6.8 (90%)	1.2×10^{-3}		
1	DMSO (298K)	499(27800),338(sh)(40900),316 (54700),290(50200)	658	τ_1=1.5 (26%), τ_2=5.8 (74%)	3.2×10^{-3}		
2		536(13700),396(sh)(21400),362(35200),319(33700),287(28800)	687	42.8	9.0×10^{-3}	2.1×10^{5}	2.3×10^{7}
3		506(49000),391(sh)(33100),334(sh)(63400),316(72800),290(66800)	661	6.5	1.8×10^{-3}	2.7×10^{5}	1.5×10^{8}
1	H_2O (298K)	492(33137),332(sh)(51119), 310(72747),283(70903)	656	τ_1=1.4(8%), τ_2=6.0(92%)	25.1×10^{-3}		
2		498(26500),353(90677), 324(82315),281(sh)(79500)	682	τ_1=10.5(10%), τ_2=49 (90%)	35.9×10^{-3}		
3		504(25100),395(br)(14600),334(sh)(38300),315(45800),284(86300)	660	τ_1=0.4(15%), τ_2=13.4 (85%)	21.8×10^{-3}		
1	MeOH(298K)	492(23400),328(sh)(36500),309 (49500),284(45000)	650	τ_1=1.4(15%), τ_2=6.5 (85%)	4.6×10^{-3}		
2		512(14600),356(32800),316(34600),283(29000)	660	13.8	7.1×10^{-3}	5.1×10^{5}	7.2×10^{7}
3		497(37500),380(sh)(26300),330(sh)(49000),311(59900),283(52200)	656	τ_1=2.4(25%), τ_2=4.5 (75%)	5.7×10^{-3}		
1	EtOH-MeOH (4:1) (77K)		647	12.5μs	0.35	2.8×10^{4}	5.2×10^{4}
2			670	8.7μs	0.28	3.2×10^{4}	8.2×10^{4}
3			653	13.3μs	0.42	3.1×10^{4}	4.3×10^{4}

The overlay of the experimental and calculated spectra is also presented in Figure 3.5a-3.5c. The origin of the intense band within 490-500 nm is due to charge transfer from Ru(II)→terpyridine (MLCT) and phenyl-imidazole→terpyridine (ILCT) transitions. The mixed MLCT and ILCT characters of the band (S_1 for **1** and **3**, and S_3 for **2**) in the complexes was also confirmed by electron density difference map (EDDM) and natural transition orbital analysis (NTO) plots (Figure 3.9 and 3.10). The peaks in the range of 330-350 nm are mainly due to phenyl-imidazole→terpyridine (ILCT) electron transitions, whereas the very intense peaks at ~280 and ~315 nm arise because of π→π* electronic transition within the ligand.

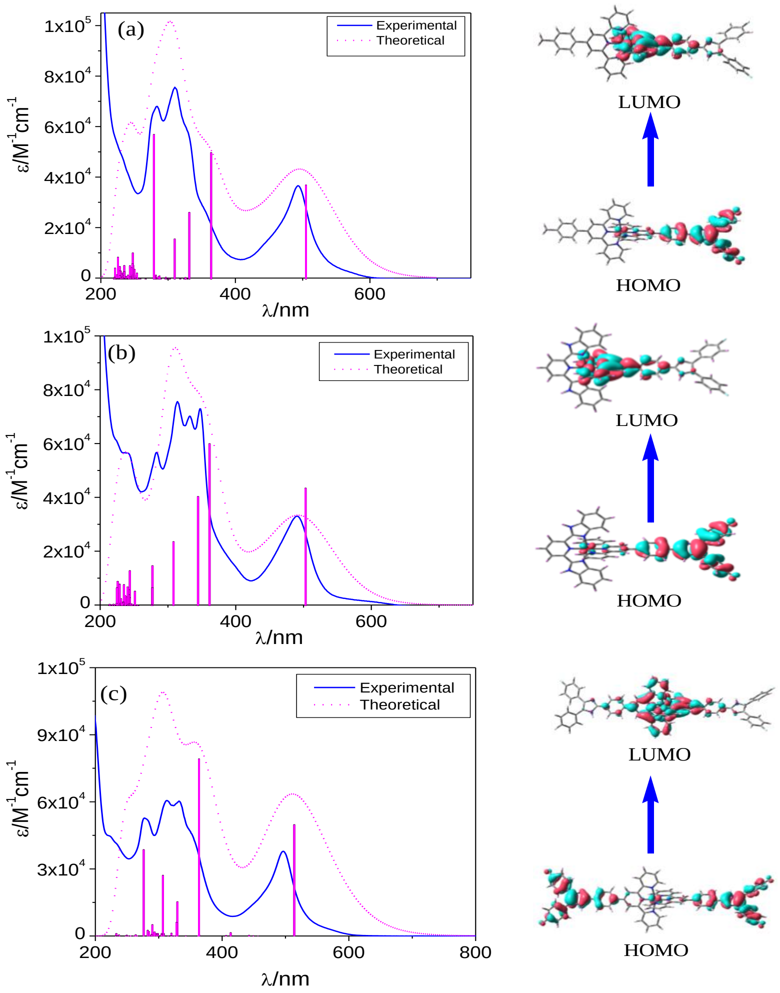

Figure 3.5. Overlay of the experimental (blue solid line) and calculated (pink dotted line) absorption spectra along with stick form of the complexes **1** (a), **2** (b), and **3** (c) in

MeCN. The right panel shows the HOMO and LUMO that takes part in the lowest energy band

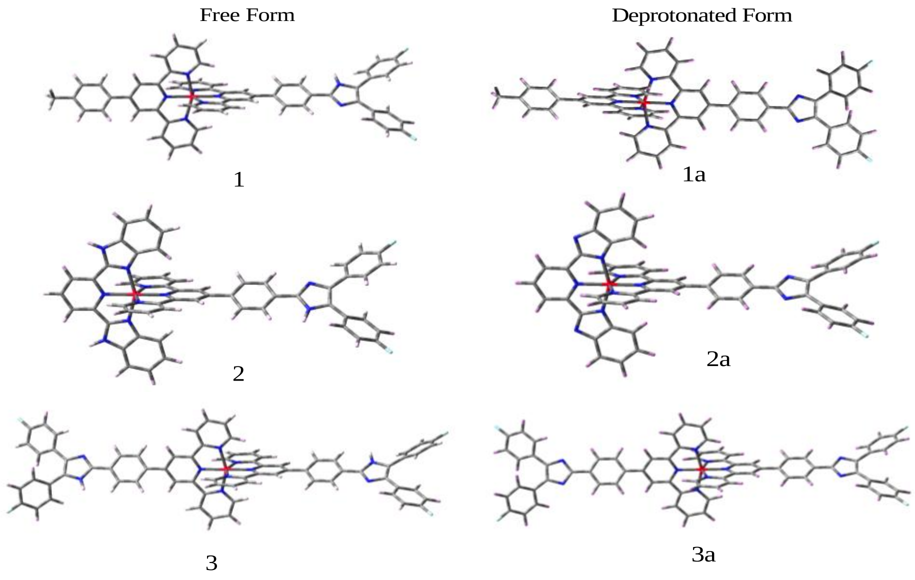

Figure 3.6. Ground state optimized geometries of complexes in their free (**1-3**) and deprotonated (**1a-3a**) forms in MeCN.

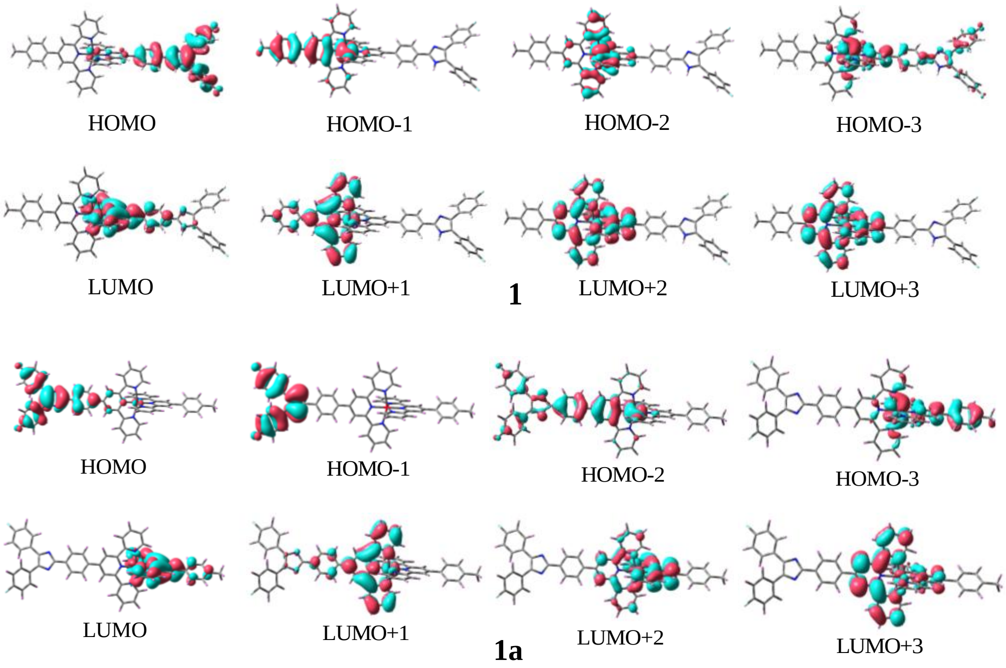

Figure 3.7. Schematic drawings of the selective frontier molecular orbitals of free (**1**) and deprotonated (**1a**) forms in MeCN.

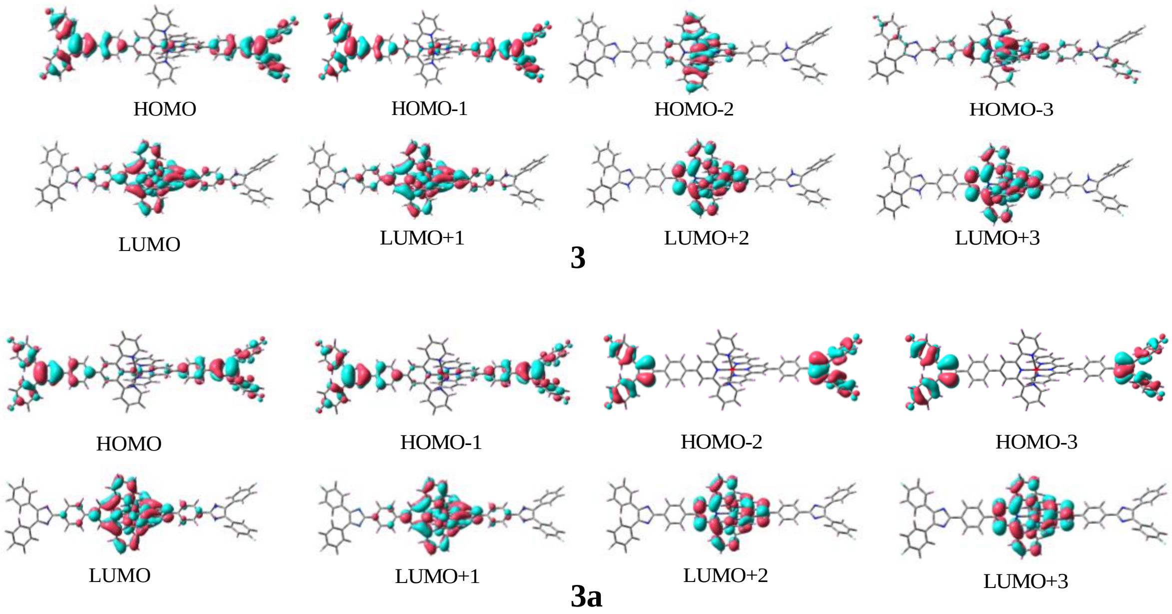

Figure 3. 8. Schematic drawings of the selective frontier molecular orbitals of free (**3**) and deprotonated (**3a**) forms in MeCN.

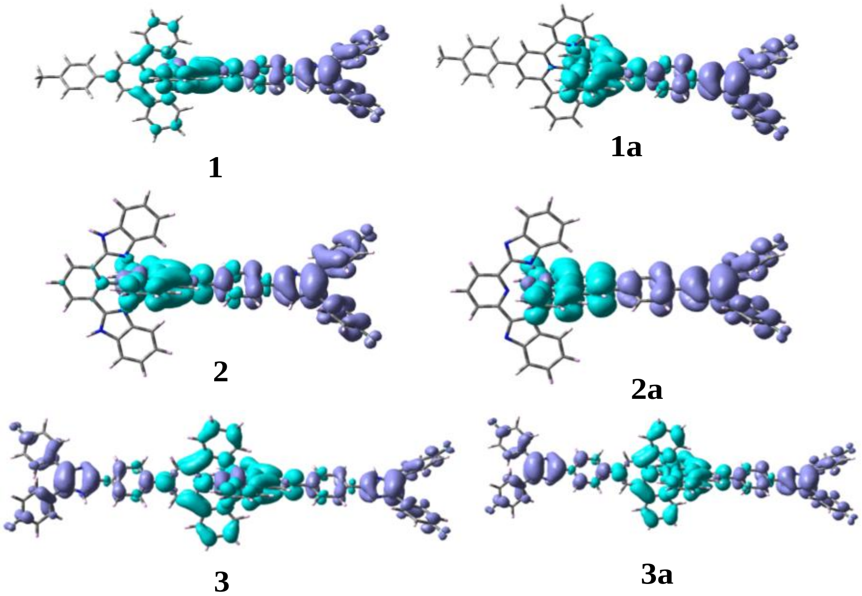

Figure 3.9. Difference in electron density upon excitation from the ground S_0 state to the lowest energy singlet excited state in free (**1-3**) and deprotonated (**1a-3a**) forms. Purple and cyan color shows regions of increasing and decreasing electron density, respectively.

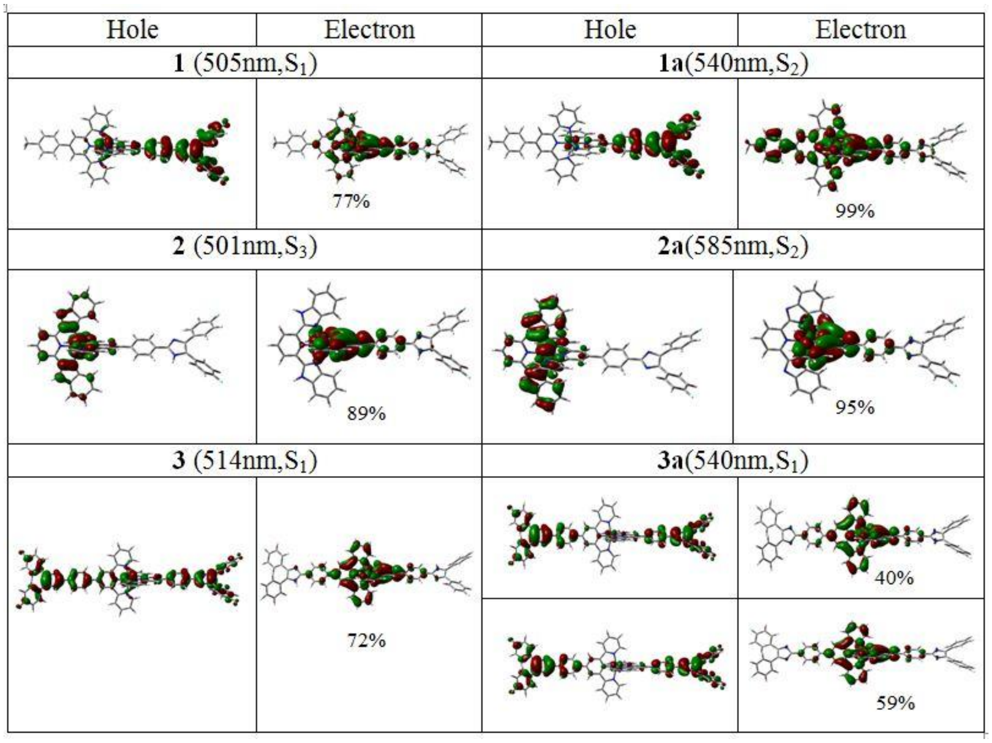

Figure 3.10. NTOs illustrating the nature of optically active lowest energy singlet excited states in the absorption bands of the complexes in their free (**1-3**) and deprotonated (**1a-3a**) forms. The occupied (holes) and unoccupied (electrons) NTO pairs that contribute more than 10% to each excited state are only represented.

Table 3.2. Selected MOs along with their Energies and Compositions in the Ground State of the Complex in its Free (**1**) and Deprotonated (**1a**) forms in MeCN.

MO	Energy/ev		% Compositions							
	1	**1a**	**1**				**1a**			
			Ru	Fimzph	tpy	PhMe	Ru	Fimzph	tpy	PhMe
LUMO+5	-1.59	-1.50	0.0	0.0	99.9	0.0	1.5	0.0	90.3	8.2
LUMO+4	-1.71	-1.53	0.5	41.9	57.5	0.0	0.0	0.0	99.9	0.0
LUMO+3	-2.42	-2.32	3.1	0.3	96.3	0.4	2.8	0.5	96.5	0.1
LUMO+2	-2.50	-2.42	0.0	0.4	99.3	0.2	0.4	0.1	98.9	0.5
LUMO+1	-2.66	-2.54	7.9	0.1	86.4	5.6	7.4	7.5	85.0	0.0
LUMO	-2.70	-2.60	7.9	9.8	82.3	0.0	8.1	0.0	86.1	5.7
HOMO	-5.49	-4.47	2.2	94.3	2.8	0.0	1.1	95.3	3.6	0.0
HOMO-1	-6.09	-5.86	60.4	0.0	25.2	14.3	0.0	99.9	0.0	0.0
HOMO-2	-6.14	-5.98	70.0	0.0	29.9	0.0	53.3	24.0	22.3	0.0
HOMO-3	-6.17	-5.99	63.1	11.9	24.9	0.0	61.7	0.1	25.5	12.7
HOMO-4	-6.76	-6.05	2.1	96.1	1.8	0.0	70.0	0.0	30.0	0.0
HOMO-5	-6.92	-6.22	12.4	0.0	14.5	73.2	4.7	93.4	1.9	0.0

Table 3.3. Selected MOs along with their Energies and Compositions in the Ground State of the Complex in its Free (**2**) and Deprotonated (**2a**) forms in MeCN.

MO	Energy/ev		% Compositions							
	2	**2a**	**2**				**2a**			
			Ru	Fimzph	tpy	Hbzim	Ru	Fimzph	tpy	Hbzim
LUMO+5	-1.42	-1.00	3.4	0.0	96.1	0.5	4.4	0.0	94.7	0.8
LUMO+4	-1.68	-1.17	0.5	42.4	56.9	0.0	1.3	14.9	83.8	0.0
LUMO+3	-2.44	-1.30	2.5	0.5	83.5	13.5	1.0	0.0	0.3	98.7
LUMO+2	-2.48	-1.43	0.5	0.0	14.3	85.1	5.7	0.0	0.1	93.3
LUMO+1	-2.60	-2.00	7.8	0.0	1.6	90.6	2.0	0.7	97.1	0.2
LUMO	-2.68	-2.13	8.0	9.7	80.8	1.6	10.9	7.5	79.7	1.9
HOMO	-5.49	-4.36	2.8	94.3	2.5	0.3	2.8	93.9	2.9	0.3
HOMO-1	-5.86	-4.79	59.6	0.0	11.2	29.2	47.7	0.0	8.6	43.1
HOMO-2	-6.15	-5.25	63.6	11.7	18.3	6.4	55.9	0.0	6.9	37.1
HOMO-3	-6.19	-5.29	69.9	0.0	8.0	22.1	62.5	9.8	20.6	7.0
HOMO-4	-6.76	-5.45	2.1	93.9	1.5	2.5	0.5	0.0	0.0	99.4
HOMO-5	-6.76	-5.72	3.3	2.3	1.4	92.9	1.0	0.0	0.0	99.0

Table 3.4. Selected MOs along with their Energies and Compositions in the Ground State of the Complex in its Free (**3**) and Deprotonated (**3a**) forms in MeCN.

MO	Energy/ev		% Compositions					
	3	**3a**	**3**			**3a**		
			Ru	FimzPh	tpy	Ru	Fimzph	tpy
LUMO+5	-1.72	-1.44	0.5	42.1	57.4	1.5	50.8	47.6
LUMO+4	-1.72	-1.47	0.5	42.1	57.3	0.0	63.2	36.7
LUMO+3	-2.43	-2.25	3.1	0.7	96.2	3.2	46.0	50.7
LUMO+2	-2.51	-2.33	0.0	0.7	99.3	0.0	49.3	50.7
LUMO+1	-2.71	-2.49	7.9	10.2	81.9	7.6	36.7	55.5
LUMO	-2.72	-2.50	7.8	10.3	81.9	7.5	36.6	55.8
HOMO	-5.50	-4.45	2.8	94.1	3.0	1.2	5.8	92.9
HOMO-1	-5.50	-4.45	2.8	94.2	2.9	1.2	5.8	92.9
HOMO-2	-6.15	-5.85	70.0	0.0	29.9	0.0	0.0	99.9
HOMO-3	-6.18	-5.85	62.9	12.4	24.7	0.0	0.0	99.9
HOMO-4	-6.18	-5.91	62.5	12.5	24.9	55.8	9.8	34.3
HOMO-5	-6.76	-5.91	2.3	95.8	1.9	56.4	9.8	33.8

Table 3.5. Selected UV-vis Energy Transitions at the TD-DFT/B3LYP Level of **1** and **1a** in MeCN

Excited state	λ_{cal}/nm	Oscillator strength(f)	λ_{expt}/nm	Key transitions	Character
			1		
S_1	505	0.5	494	H→L (77%)	MLCT,ILCT
S_{18}	363	0.7	356(sh)	H→L+4 (94%)	MLCT, ILCT, π-π*
S_{23}	331	0.4	332	H-5→L+1 (54%), H-4→L(16%),	ILCT, MLCT
S_{42}	309	0.2	307	H-8→L+1 (92%)	π-π*
S_{78}	278	0.8	282	H-10→L+2 (23%), H-9→L+3 (49%)	π-π*, ILCT
			1a		
S_2	570	0.5	540(sh)	H→L+1 (99%)	MLCT, ILCT
S_{40}	329	0.2	330(sh)	H-8→L(47%), H-4→L+4 (17%), H-2→L+4 (23%)	ILCT , MLCT, π-π*
S_{64}	305	0.4	313	H-12→L+1 (60%), H-4→L+6 (20%)	π-π*, ILCT
S_{102}	277	0.8	282	H-14→L+2 (41%), H-14→L+3 (23%), H-12→L+3 (16%)	π-π*, ILCT

Table 3.6. Selected UV-vis Energy Transitions at the TD-DFT/B3LYP Level of **2** and **2a** in MeCN

Excited state	λ_{cal}/nm	Oscillator strength(f)	λ_{expt}/nm	Key transitions	Character
			2		
S_3	501	0.5	490	H→L (89%)	MLCT,ILCT
S_{18}	361	0.7	378	H→L+4 (94%)	MLCT, ILCT, π-π*
S_{20}	344	0.5	347	H-5→L+1 (93%)	MLCT, ILCT, π-π*
S_{43}	309	0.3	314	H→L+7 (91%)	π-π*, ILCT
S_{69}	278	0.2	282	H-11→L+3 (35%), H→L+8 (31%)	π-π*, ILCT
			2a		
S_2	585	0.4	552(br)	H→L (95%)	MLCT,ILCT
S_{13}	435	0.5	415(sh)	H→L+4 (95%)	ILCT, π-π*
S_{36}	356	0.4	357	H-4→L+2 (59%), H-2→L+5 (26%)	ILCT, π-π*, MLCT
S_{51}	319	0.2	318	H-5→L+3 (65%)	π-π*, ILCT, MLCT
S_{85}	274	0.2	282	H-13→L+1 (37%), H-8→L+4 (27%)	π-π*, ILCT

Upon excitation at the MLCT band, a broad luminescence band is observed at 658 (for **1** and **3**) and at 676 nm for **2** in MeCN (Figure 3.11). It is to be noted in the Table 3.1 that the lowest energy absorption (MLCT) and emission maximum of the complexes undergo a small bathochromic shift upon increase of polarity and hydrogen bonding ability of the solvents. On passing from RT to 77K, a small blue-shift of the band takes place accompanied with increase in luminescence intensity and quantum yield (Figure 3.11). The origin of band is mainly due to radiative deactivation of ^{3}MLCT $\{Ru^{II}(d\pi)\rightarrow tpy\text{-}HImzPh_3F_2(\pi^*)\}$ excited state. The emission energies of the complexes are also calculated by taking the difference in energy between lowest triplet excited state (T_1) and ground singlet state (S_0) through UKS calculations and correlate well with the experimental data (Table 3.7). The notable outcome is to observe RT emission of the complexes relative to non-luminescent parents ($[Ru(tpy)_2]^{2+}$ or $[Ru(H_2pbbzim)_2]^{2+}$}. Luminescence lifetime of the complexes vary between 5.6 (**1**) and 35 ns (**2**) in MeCN at RT and between 8.7 (**2**) and 13.3 (**3**) μs at 77 K (Figure 3.11c-3.11d). Thus, the enhancement of lifetime is almost two order of magnitudes higher relative to $[Ru(tpy)_2]^{2+}$ (0.25 ns). The E_{00} values of the complexes are also calculated from their 77K spectra (Figure 3.12a-3.12c). The complexes display double-exponential decay in most of the solvents at RT. The initial short-lived component is probably due to deactivation of the ^{3}MLCT state, while the long-lived second component takes into account the radiative deactivation of the equilibrated state of ^{3}MLCT and ^{3}ILCT (difluorobenzil conjugated phenyl-imidazole spacer). The luminescence spectra at 77 K display vibrational structure with their spacing ~800 cm^{-1} suggesting the involvement of triplet ligand-centered emission (Figure 3.12a-3.12c).

The excited-state decay of the polypyridine compounds of Ru(II) is usually expressed by equation 1.[29,31]

$$k_{nr} = k_{nr}^{0} + k'_{nr} \qquad (1)$$

The radiationless deactivation consists of two terms. k_{nr}^{0} denotes the decay directly from ^{3}MLCT to the ground state, while k'_{nr} corresponds to the thermally activated process from ^{3}MLCT to the ^{3}MC state and depends on their energy gap (ΔE). k'_{nr} is usually plays a dominant role for the terpyridine complexes because of lower ΔE value. In the present case, it is assumed that the energy of the MC state remains almost invariant, whereas the energy of MLCT state is lowered because of pi-electron conjugation in the tpy-$HImzPh_3F_2$ motif. The increased energy gap in turn reduces the efficiency of the MLCT-to-MC surface-crossing pathway.

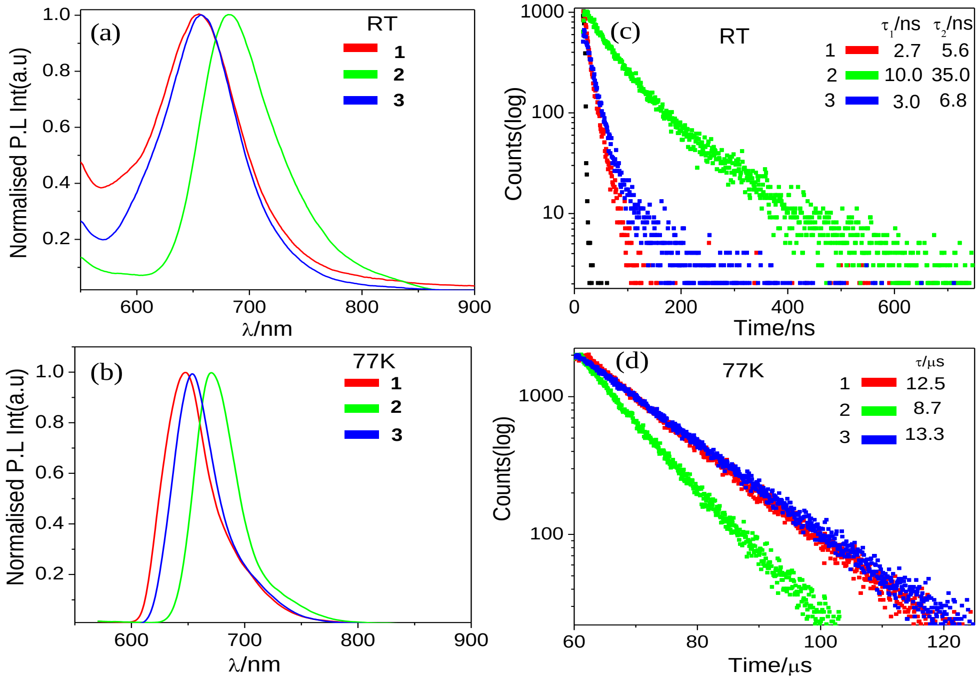

Figure 3.11. Normalized emission (λ_{ex} = 490 nm) spectra of **1-3** in MeCN at RT (a) and in EtOH-MeOH (4:1, v/v) glass at 77 K (b). The decay profiles and corresponding lifetimes are presented in (c) at RT and (d) at 77K.

Table 3.7. Phosphorescent Emissions of the Complexes in Their Free-(**1-3**), Deprotonated (**1a-3a**) Forms in MeCN According UKS Calculations and Associated Experimental Values

Compn^d	Theoretical UKS/nm	Experimental /nm
1	613	658
1a	795	657
2	636	676
2a	837	752
3	633	658
3a	838	660

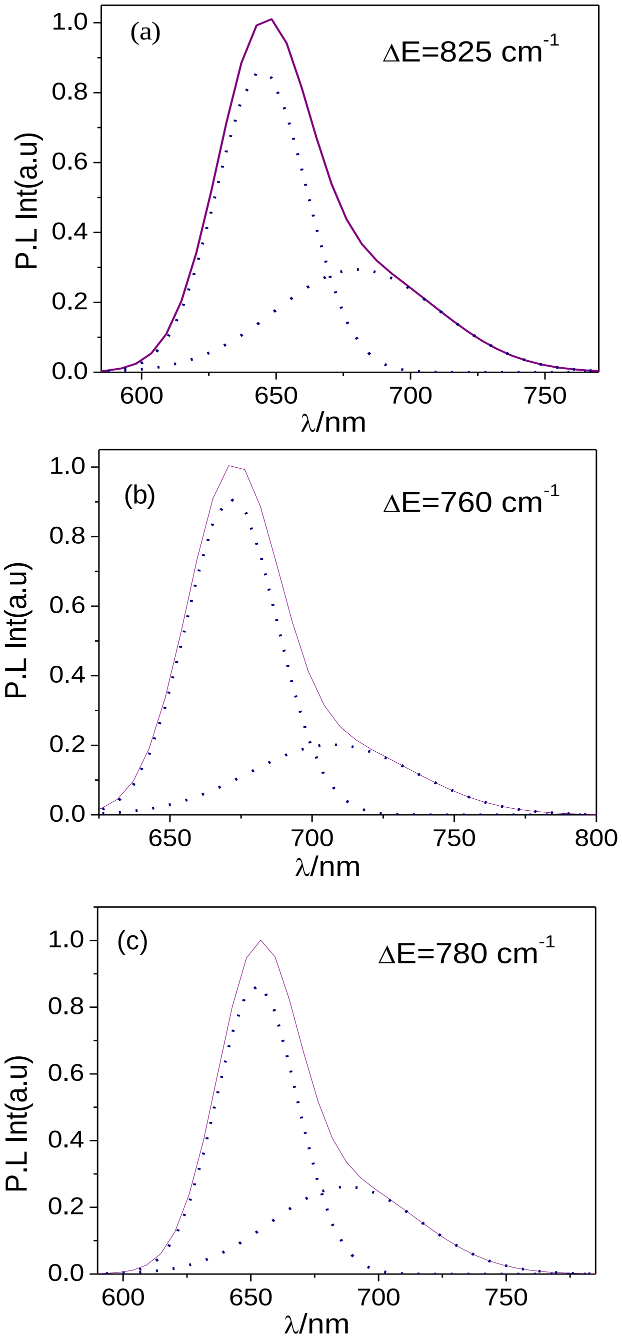

Figure 3.12. Experimental (solid line) and deconvoluted (dotted line) emission spectra of **1** (a), **2** (b), and **3** (c) in EtOH-MeOH (4:1v/v) at 77 K. The insets show the values of vibrational spacing.

3.3.3. Temperature-Induced Switching of Emission Spectral Behaviors. We use the temperature as an external stimulus to modulate the emission spectral aspects of the complexes. We acquired emission spectra and lifetime of the complexes **1-3** within the temperature domain of 263K and 333K and the experimental results are delineated in Figure 3.13a-3.13c, Table 3.8 and Figure 3.14. When temperature is lowered, the emission intensity and lifetime is enhanced demonstrating the “on-state”, while the

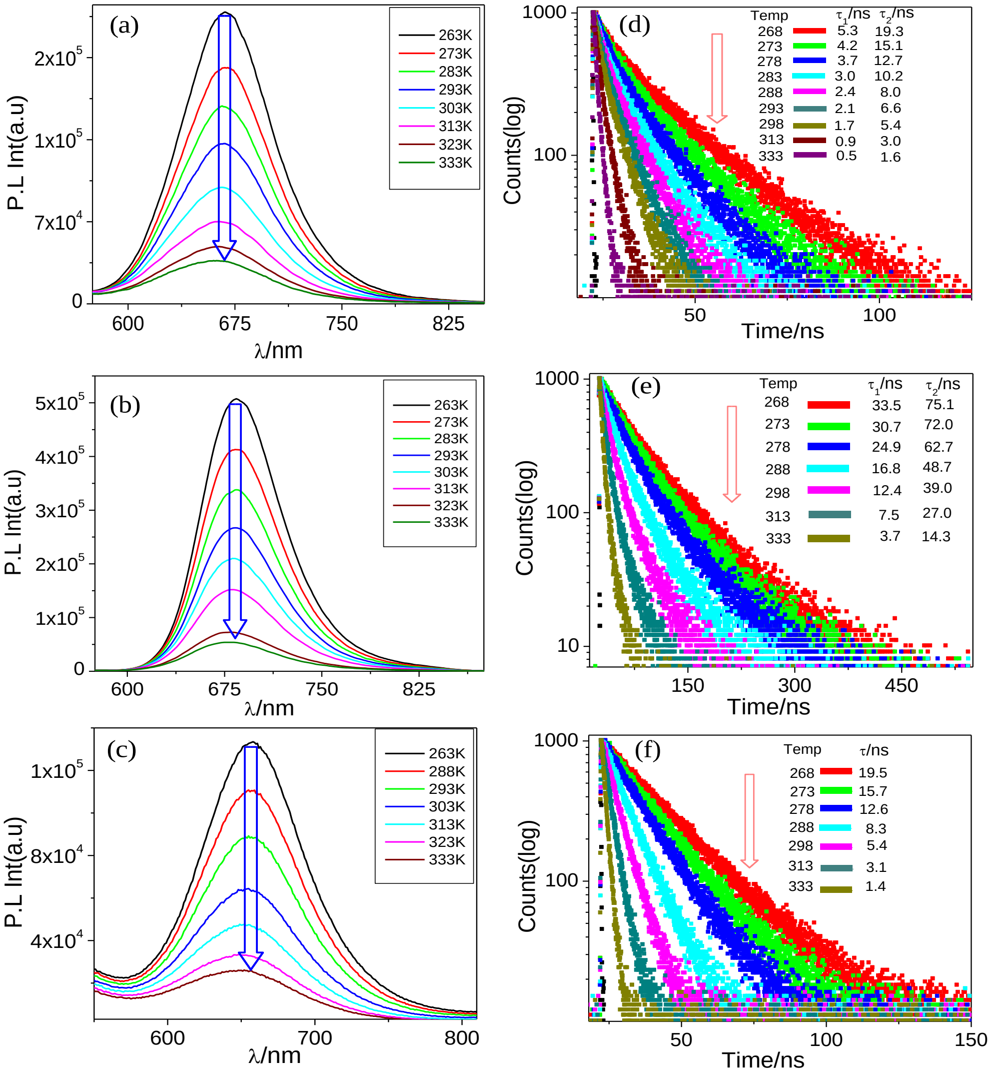

Figure 3.13. Change in the steady state emission (λ_{ex} = 490 nm) and decay profiles for complexes of **1** (a and d, respectively), **2** (b and e, respectively), and **3** (c and f, respectively) upon variation of temperature in MeCN in the range of 263K and 333K.

increase of temperature leads to quenching of emission intensity and lifetime designating the “off- state”. This "on-off" and "off-on" emission switching is fully reversible and can be repeated many times upon alternate heating and cooling.

We also explored the reason for emission switching as a function of temperature and try to understand the relaxation dynamics of the excited states. To this end, we fitted lifetime *versus* temperature data using equation (2).[29,31]

$$(\tau(\mathrm{T}))^{-1} = (k_1 + k_2 \exp[-\Delta \mathrm{E}_2/\mathrm{RT}])/(1+ \exp[-\Delta \mathrm{E}_2/\mathrm{RT}] \qquad (2)$$

where k_1→temperature-independent rate constant {sum of both radiative (k_r), and non-radiative (k_{nr}) rate constants from ^{3}MLCT at 77K}, k_2→temperature dependent rate constant (taking account of population of ^{3}MC from ^{3}MLCT state) and ΔE_2 → activation energy for this surface crossing process. Non-linear regression analysis of τ *vs*. T data yields k_2 and ΔE_2 values (Figure 3.13a-3.13c, Table 3.8 and Figure 3.14). The calculated ΔE_2 value is 4381±40, 4017±44, and 4049±40 cm^{-1} for **1**, **2**, and **3**, respectively. The magnitude of k_1 lies in the domain of 1.0×10^5–8.0×10^5 s^{-1}, while that of k_2 varies between 1×10^{13} and 2.9×10^{14} s^{-1}. The estimated ΔE_2 values of the present complexes are substantially higher than [Ru(tpy)$_2$]$^{2+}$ (ΔE_2=1500 cm^{-1}).

Table 3.8. Temperature Dependent Emission Spectral Data of **1-3**

Complex	k_1/s^{-1}	k_2/s^{-1}	ΔE_2/cm^{-1}
1	8.0×10^5	2.9×10^{14}	4381±40
2	1.0×10^5	1.0×10^{13}	4017±44
3	7.5×10^5	1.2×10^{14}	4049±40

The substantial increase in ΔE_2 value is probably because of enhanced electron delocalization in the excited state induced by pi-conjugated backbone of tpy-HImzPh$_3$F$_2$ motif in the complexes. The decrease of temperature induces larger energy separation between ^{3}MLCT and ^{3}MC state and enhances emission intensity and lifetime, while the increase of temperature enhances the thermal equilibrium between ^{3}MLCT and ^{3}MC state and gives rise to reduction of emission intensity and lifetime. Thus, alternative heating and cooling leads to "off-on" and "on-off" emission switching by modulating the effective energy gap between ^{3}MLCT and ^{3}MC state.

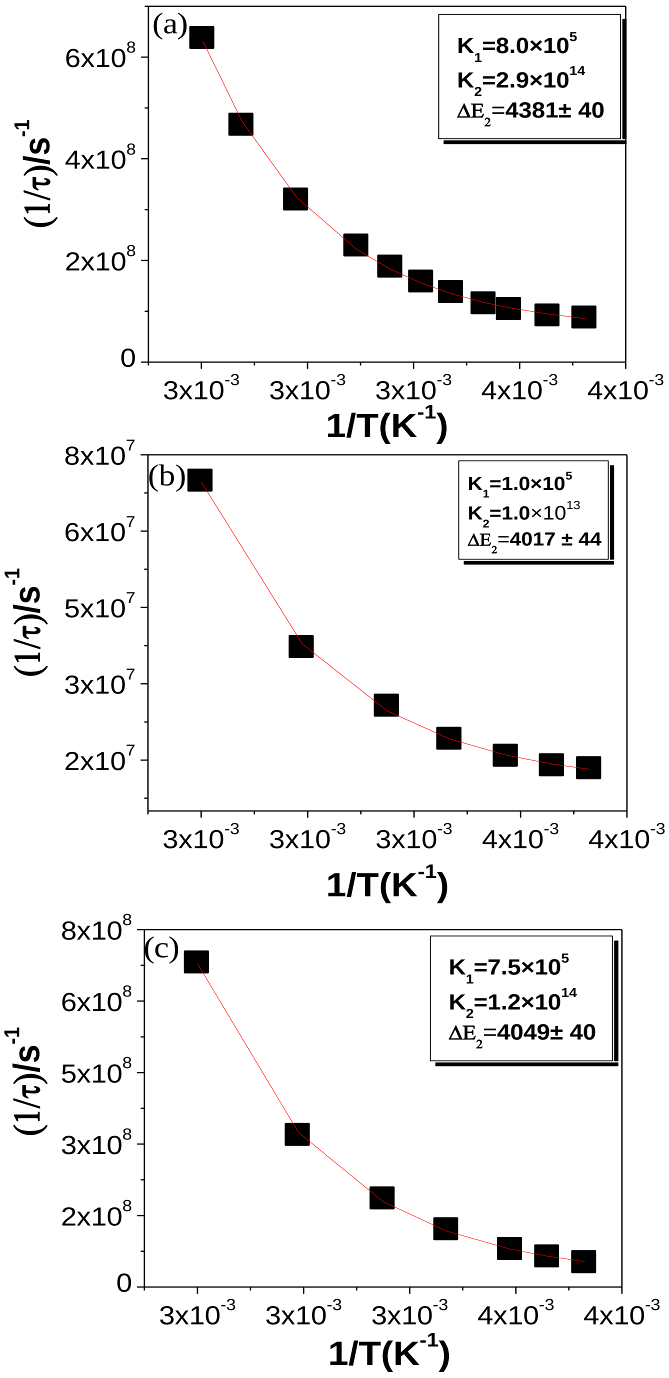

Figure 3.14. Different parameters obtained upon nonlinear fitting of $1/\tau$ vs. $1/T$ of complexes **1-3** in MeCN.

3.3.4 pH-Induced Switching of Absorption and Emission Spectral Characteristics. The imidazole NH proton(s) in tpy-HImzPh$_3$F$_2$ and H$_2$pbbzim motifs in the complexes turn into acidic upon coordination to Ru^{2+}. Inasmuch as the imidazole NH motifs turn into acidic, we investigated the effect of pH on the absorption, emission and lifetime of the complexes. The spectral titrations are performed in MeCN-H$_2$O (3:2 v/v) because the complexes are not fully soluble in pure H$_2$O. The Robinson-Britton buffer is employed to adjust the pH within the range of 2-12. As significant amount of organic solvent (MeCN) is used in the present study, we used the term “apparent pH” instead of pH only. We would also like to mention that the pH meter responded reproducibly to H$^+$ concentration of each solution. Similarly, the pK_a values calculated from absorption *vs.* pH titration data will be termed as treated as "apparent pK_a". Henceforth, the term “pH” and “pK_a” will be referred to as “apparent pH” and "apparent pK_a", respectively.

The complex **1** exhibits one-step change in its spectral profile within the pH range of 5.0-11.0 (Figure 3.15a-3.15b). Upon increase of pH, finite increase of band intensity is observed for the MLCT band at 496 nm, the valley at 405 nm and π-π* band at 315 nm, whereas decrease of intensity of the shoulder takes place at ~360 nm. Three isosbestic points at 380, 332 and 252 nm are observed during the process. Substantial quenching of emission without alteration of the band maximum at 655 nm takes place in the emission spectrum with the increase of pH.

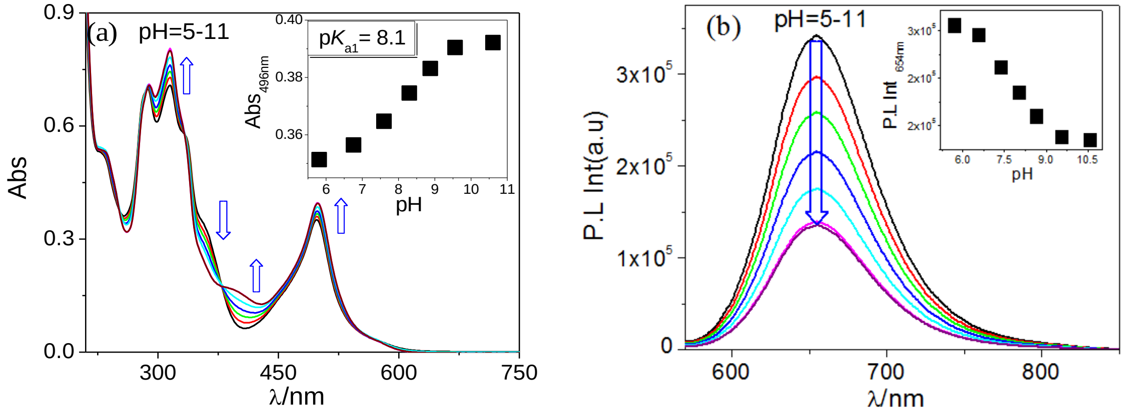

Figure 3.15. pH dependence absorption (a) and emission (λ_{ex} = 490 nm) (b) spectrum of **1** in MeCN-H$_2$O (3:2 v/v) buffer. The insets show the variation of absorbance (a) and emission intensity (b) with pH.

In contrast to **1**, two-step change is observed for **2** within the studied pH range (Figure 3.16a-3.16d). Upon increase of pH up to 7.0, the band at ~490 nm underwent small bathochromic-shift (up to 497 nm) along with diminution of the band intensity in the first step. The said band gets further shifted to 516 nm in the second step together with diminution of band intensity. A new band at higher wavelength also evolves and continues to increase in intensity till the solution pH reaches to 10. Isosbestic points are observed in each step. Interestingly, the color change from orange to deep violet is also noticed upon changing the pH from 3.0 to 10.0 which is also in-line with the bathochromic shift of the MLCT band. Upon increasing the pH, the emission maximum at ~675 nm is quenched substantially in the first step while keeping the emission maximum almost unaltered. During second step, complete emission quenching accompanied by dramatic shift of the emission maximum from ~675 nm to ~750 nm is

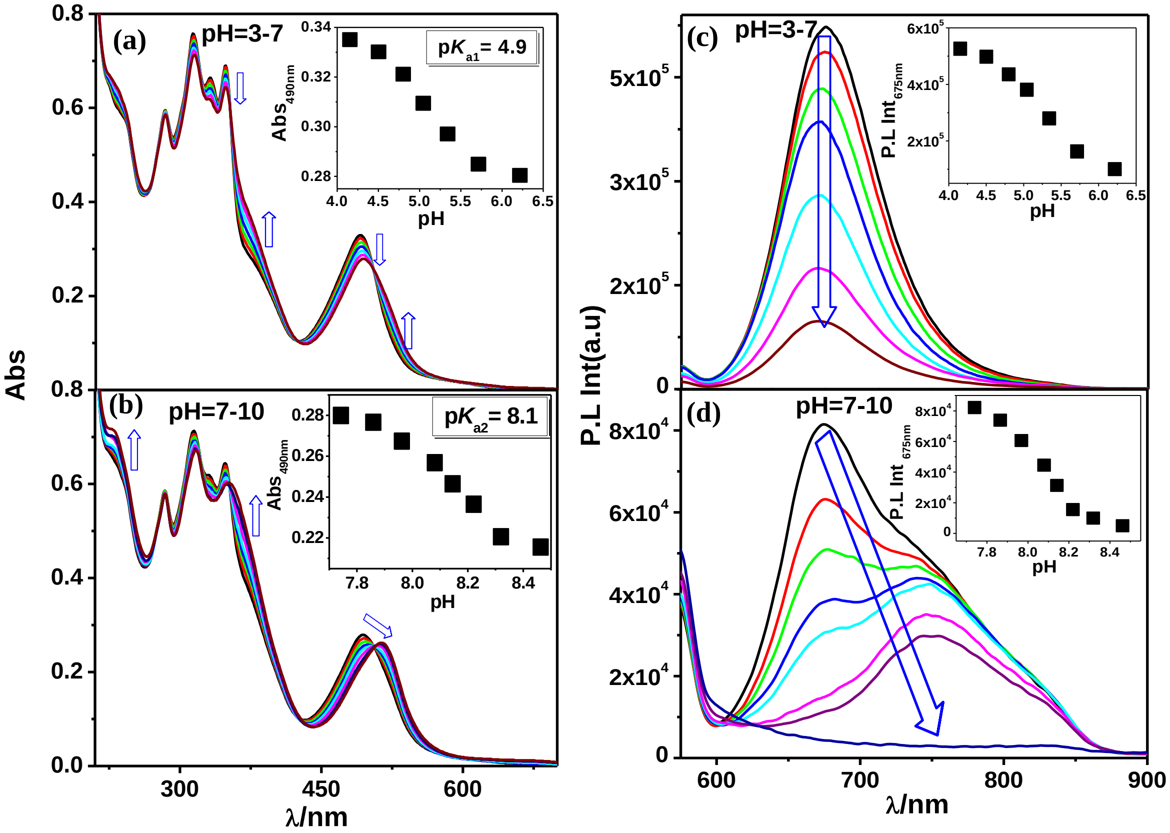

Figure 3.16. pH dependence absorption (a-b) and emission (λ_{ex} = 490 nm) (c-d) spectrum of **2** in MeCN-H_2O (3:2 v/v) buffer. The insets show the variation of absorbance (a-b) and emission intensity (c-d) with pH.

also observed. ^{1}H NMR spectral data indicate the NH protons associated with H_2pbbzim is more acidic than that of tpy-HImzPh$_3$F$_2$ fragment and the two-step change in the absorption and emission spectral profile in **2** is due to successive deprotonation of H_2pbbzim fragment as shown in Scheme 3.1.

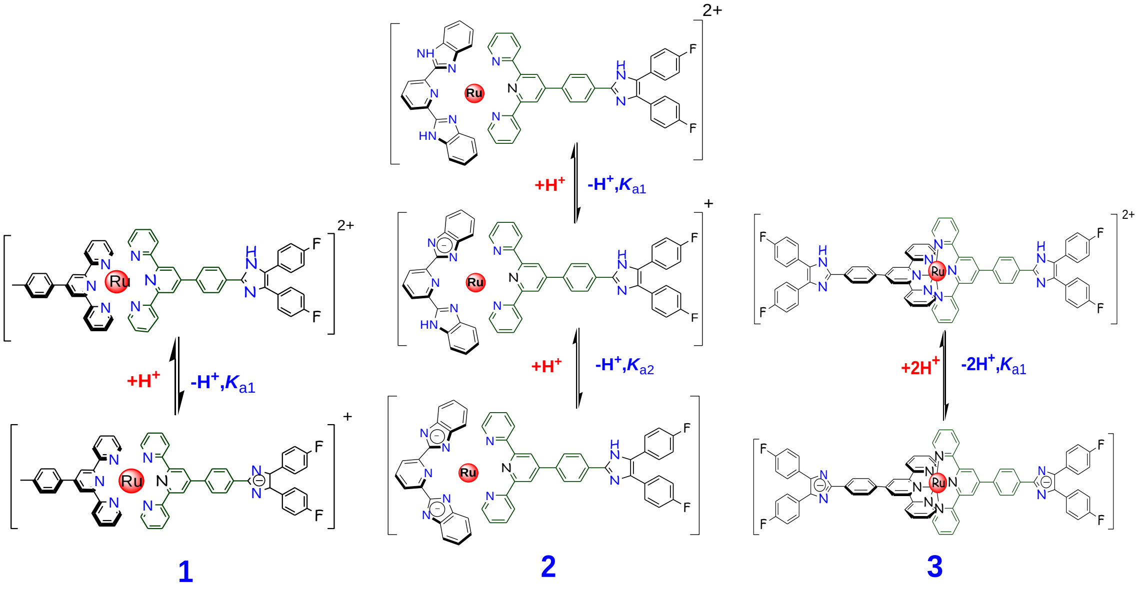

Scheme 3.1. Proposed acid-base equilibria in **1-3**.

Figure 3.17a and 3.17b displays a single step change in the absorption and emission spectrum of complex **3**, respectively as a function of pH. Gradual decrease in the MLCT band intensity at 497 nm is observed and at its expense a new band at ~550

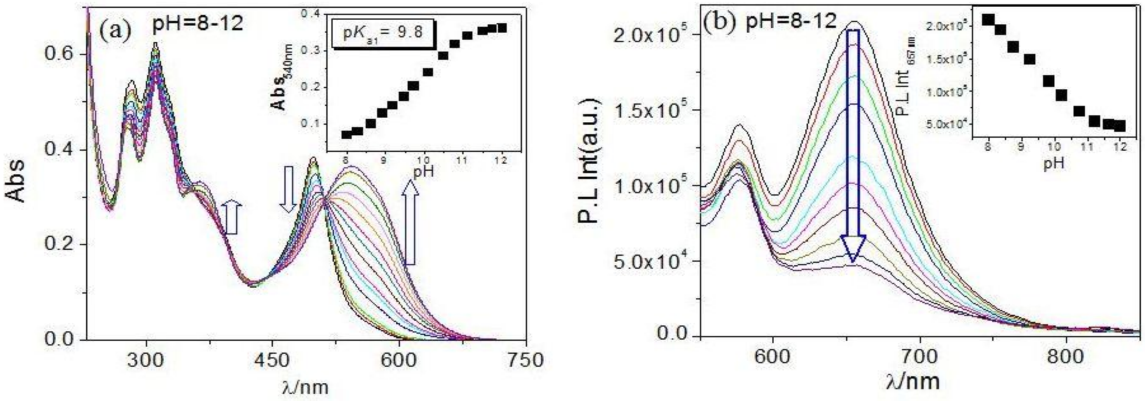

Figure 3.17. pH dependence absorption (a) and emission (λ_{ex} = 490 nm) (b) spectrum of **3** in MeCN-H_2O (3:2 v/v) buffer. The insets show the variation of absorbance (a) and emission intensity (b) with pH.

continues to intensify upon gradual increase in pH. The red-shift of MLCT band maximum upon increase of pH is also reflected in its visual color change from orange-yellow to blue. Substantial quenching of emission without alteration of the band maximum is observed upon increasing pH. The observed acid-base equilibria in the complexes is presented by Scheme 3.1.

The lifetimes of **1-3** are also acquired upon varying the pH of the solution and related decays and their lifetimes are presented in Figure 3.18-3.20. In conformity with their steady state emission, the lifetime also falls off with the increase of pH. In practice, change of pH induces remarkable alteration of the optical (color change) as well as emission spectral properties of all the three complexes. The complex **1** and **3** function as one-step whereas the complex **2** behaves as two-step “on-off” emission switch in the studied pH domain.

The bathochromic shift of the MLCT bands, albeit in different extent, is observed for all the three complexes upon increase of pH. The observed shift can be attributed to the pH-induced deprotonation of the NH motifs which enhances the electron density at

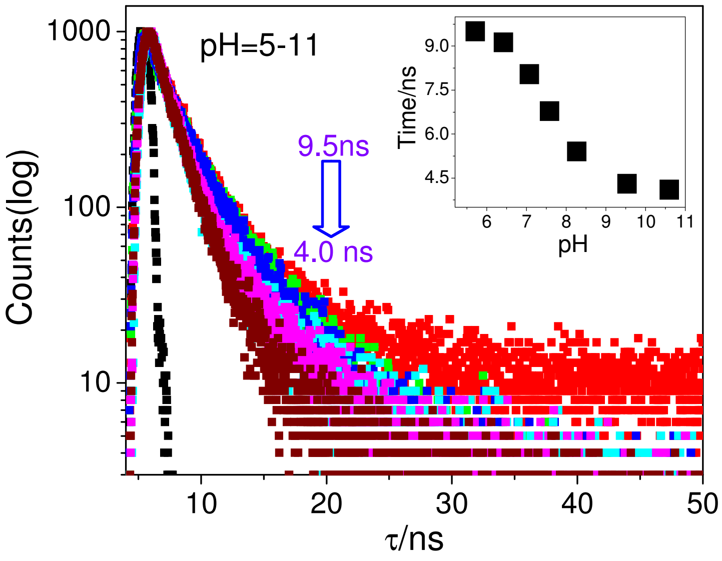

Figure 3.18. Change of luminescence decay profile of **1** with the variation of pH in 3:2 MeCN-H_2O buffer. Inset shows excited state lifetimes as a function of pH.

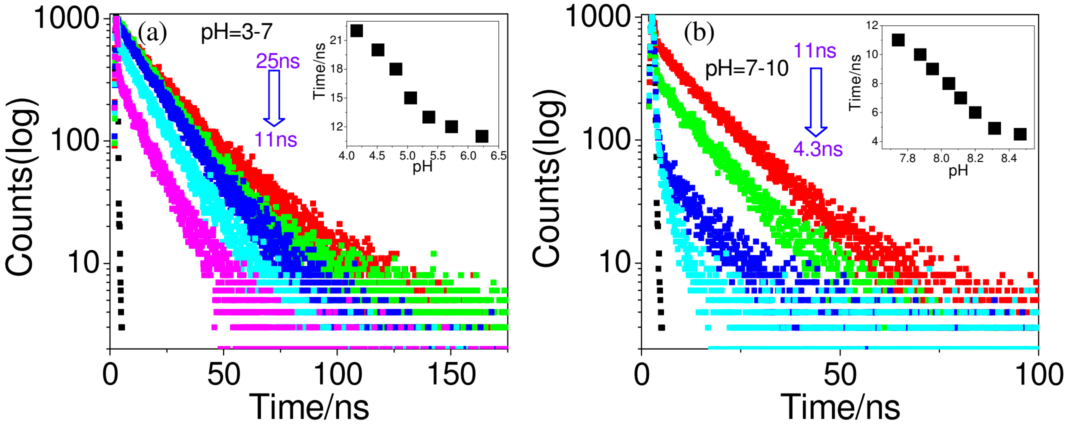

Figure 3.19. Change of luminescence decay profile (a-b) of **2** with the variation of pH in 3:2 MeCN-H_2O buffer. Inset shows excited state lifetimes as a function of pH.

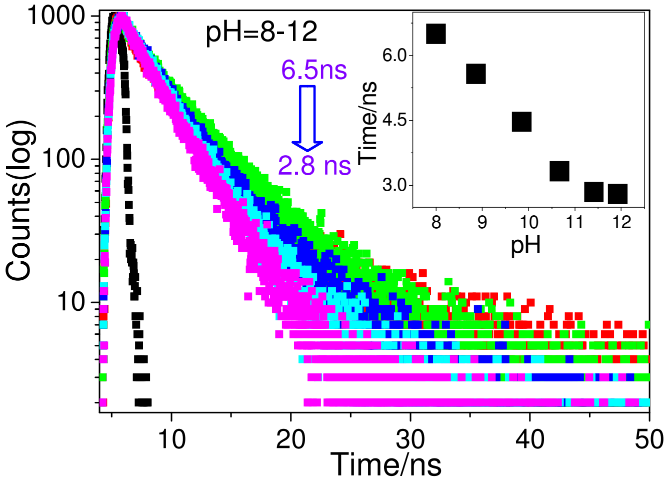

Figure 3.20. Change of luminescence decay profile of **3** with the variation of pH in 3:2 MeCN-H_2O buffer. Inset shows excited state lifetimes as a function of pH.

the Ru(II) center and facilitates Ru(dπ)→terpyridine (π^*) charge transfer process. In order to visualize the observed spectral shift upon the increase of pH, we also performed the TD-DFT as well as UKS calculations on the deprotonated states of the complexes. The details of the calculations are given in Tables 3.2-3.7 and Figures 3.6-3.10. The electrostatic surface potential (ESP) plots display the orientation of charge density among the complex architecture in both forms of the complexes (Figure 3.21). The green color designates the electron rich portion, whereas the blue color stands for electron

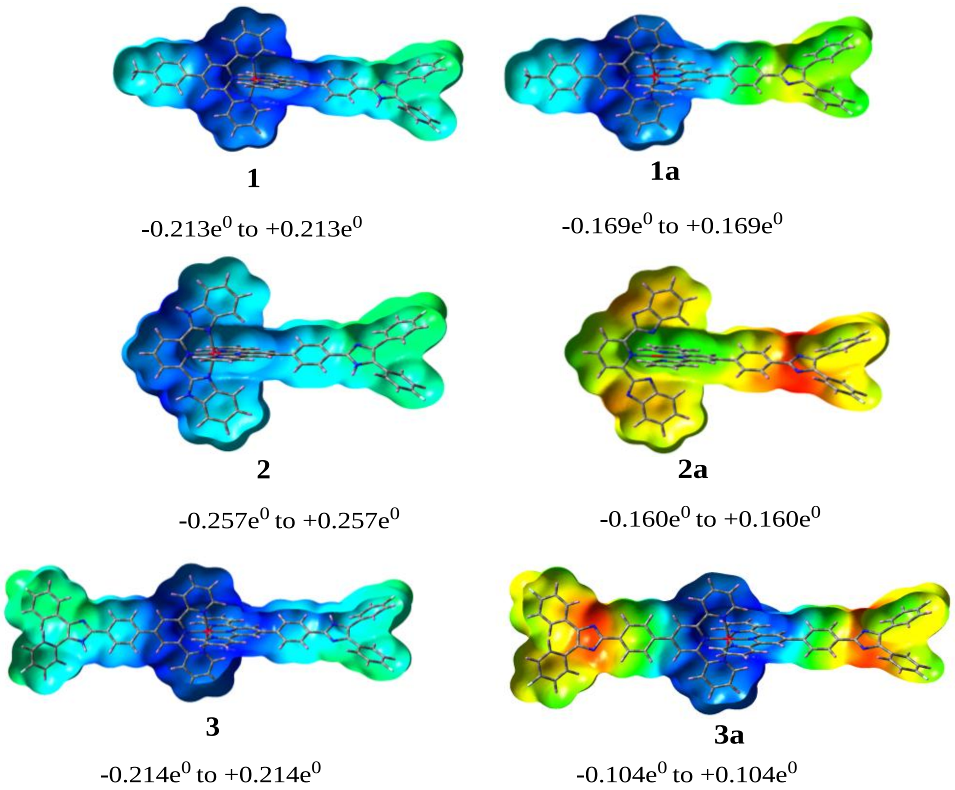

1

$-0.213e^{0}$ to $+0.213e^{0}$

1a

$-0.169e^{0}$ to $+0.169e^{0}$

2

$-0.257e^{0}$ to $+0.257e^{0}$

2a

$-0.160e^{0}$ to $+0.160e^{0}$

3

$-0.214e^{0}$ to $+0.214e^{0}$

3a

$-0.104e^{0}$ to $+0.104e^{0}$

Figure 3.21. The ESP plots of the complexes **1-3** and their deprotonated forms **1a-3a** in MeCN.

deficient region. The negative charge generated upon deprotonation is primarily localized over the phenyl-imidazole portion in the case of **1a** and **3a** whereas for **2a**, the charge is delocalized over the entire complex backbone. The frontier molecular orbitals that are involved in the lowest energy band in both forms of the complexes are presented in Figure 3.22. The HOMOs of the complexes get destabilized upon removal of the NH protons, whereas the LUMOs are less perturbed upon deprotonation. As a result, the lowest energy band gets red-shifted upon deprotonation of the imidazole moiety. Thus, the observed bathochromic shift of the lowest energy band in the complexes is reproduced by calculated results. EDDM and NTO plots for the lowest energy band of the deprotonated version (S_1 for **3a** and S_2 for **1a** and **2a**) of the complexes were also sketched which concluded the contribution of both the MLCT and ILCT characters in the aid band (Figures 3.9-3.10). The red-shift of emission energy, particularly for the

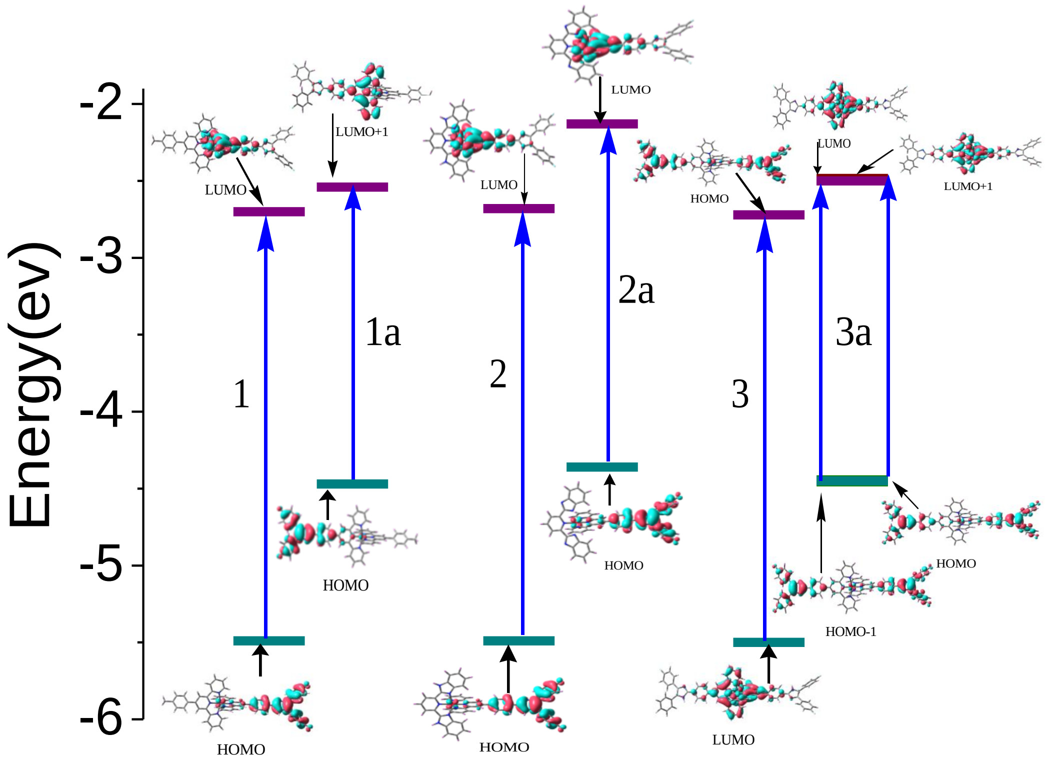

Figure 3.22. The calculated energy level diagram depicting major transitions that comprise the lowest-energy absorption band for the complexes in their free (**1-3**) and deprotonated (**1a-3a**) forms in MeCN.

complex **2**, upon deprotonation of the imidazole motifs is also reproduced by UKS calculations.

The apparent pK_a values of the complexes for each deprotonation step were estimated by using pH titration data via equation 3

$$\mathrm{pH} = \mathrm{p}K_a + \log (A-A_0)/(A_f-A_0) \qquad (3)$$

where A_0, A, and A_f corresponds to the absorbance at the initial, intermediate and final pH values, respectively at a particular wavelength. The pK_a values are provided in Table 3.9 The enhanced acidic character of the NH protons of H_2pbbzim moiety relative to tpy-HImzPh$_3$F$_2$ unit is also reflected in their pK_a values. The considerable increase in second pK_a value in **2** is due to increase in the negative charge in the complex backbone.

Table 3.9. Apparent pK_a values of **1-3** in 3:2 MeCN-H_2O Buffer

Compds	pK_{a1}	pK_{a2}
1	8.1±0.05	-
2	4.9±0.10	8.1±0.10
3	9.8±0.06	-

3.3.5.Electrochemical Behaviours and Proton-Coupled Electron-Transfer Reactions. The electrochemical behaviours of the complexes **1-3** were studied via cyclic and square wave voltammetry in acetonitrile-water (3:2) buffer medium. The voltammograms of the complexes are presented in Figure 3.23 and relevant redox data are provided in Table 3.10. A reversible oxidation wave corresponding to Ru^{3+}/Ru^{2+} process is observed for all the three complexes in the positive potential window. Several reversible and/or quasi-reversible waves are also observed in the negative potential range corresponding to the reductions of the tpy and H_2pbbzim units.

The oxidation potential of the complexes **1-3** were also measured within the pH range 2−12. It could be seen for **1** that up to pH 2, and greater than pH 10, the $E_{1/2}$ value remains unchanged. In between 2.5 < pH < 10, gradual drop of $E_{1/2}$ is observed with rise of pH. The slope of $E_{1/2}$ vs. pH plot is ~ 65 mV/pH, suggesting a $1e^-$-$1H^+$ transfer process. At pH > 10, the value of $E_{1/2}$ remains constant upon variation of pH indicating electron transfer process only. The electro-protic reactions could be represented by Scheme 3.2.

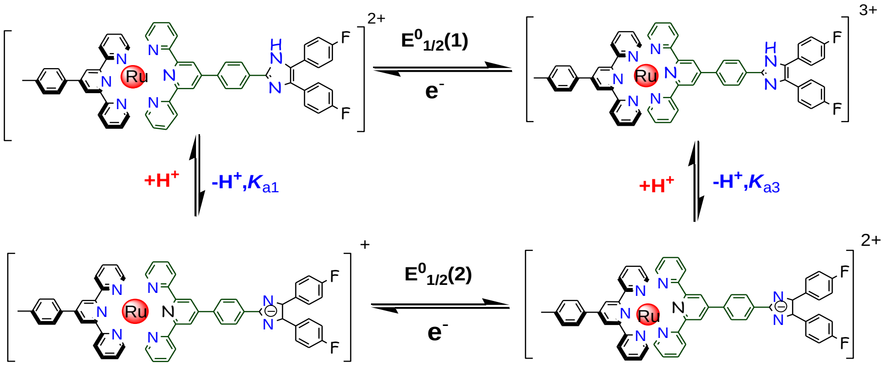

Scheme 3.2. Electro-protic equilibria involved in complex **1**.

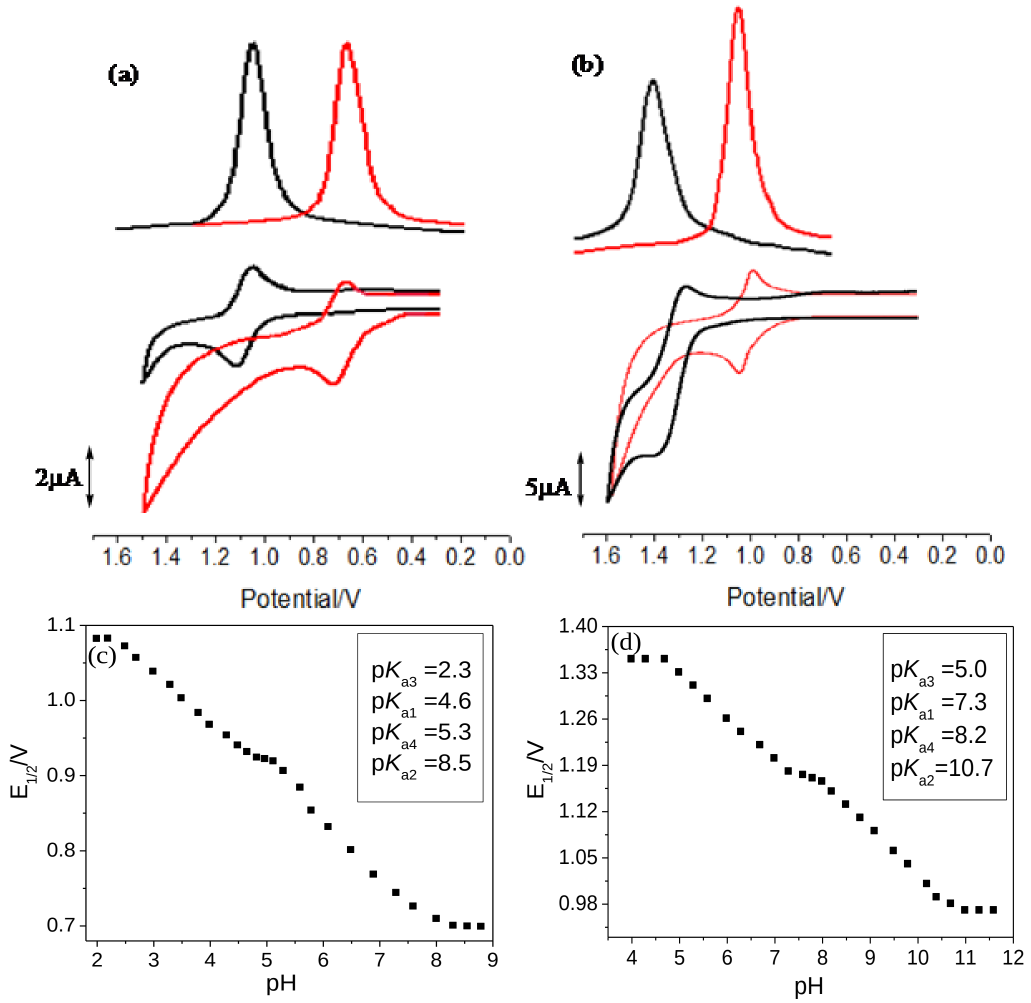

Figure 3.23. CV and SWV of **2** and **2a** (a), **3** and **3a** (b) in MeCN-H_2O (3:2, v/v) buffer. The black color represents the free form while the red color corresponds to the deprotonated forms of the complexes. The $E_{1/2}$ vs. pH plot for **2** and **3** are shown in figure (c) and (d), respectively.

Table 3.10. Electrochemical Data^a in MeCN-H_2O (3:2, v/v)

	Free (**1-3**)		Deprotonated (**1a-3a**)		
	Oxidation/V	Reduction /V		Oxidation /V	Reduction /V
1	1.28	-1.24,-1.46	**1a**	1.18	-1.13,-1.91
2	1.08	-1.29,-1.54	**2b**	0.70	-1.44,-1.60
3	1.35	-1.18,-1.39	**3c**	0.97	-1.16,-1.45

[a] All the potentials are referenced against Ag/AgCl electrode with $E_{1/2}$ = 0.36 V for Fc/Fc^+ couple.
[b] Reversible electron transfer process with a Pt working electrode. [c] $E_{1/2}$ values obtained from SWV using glassy carbon electrode

$E_{1/2}$ *vs.* pH profile for complex **2** is shown in Figure 3.23. The $E_{1/2}$ value remains unaltered up to pH 2 and greater than pH 9.0 indicating only the electron transfer process. In the pH range of 2.2-8.8, the $E_{1/2}$ value gradually decreases with the increase of pH with a slope of ~60 mV/pH suggesting two consecutive $1e^{-}$-$1H^{+}$ transfer process as presented in Scheme 3.3. The third deprotonation step does not take place within the studied pH window.

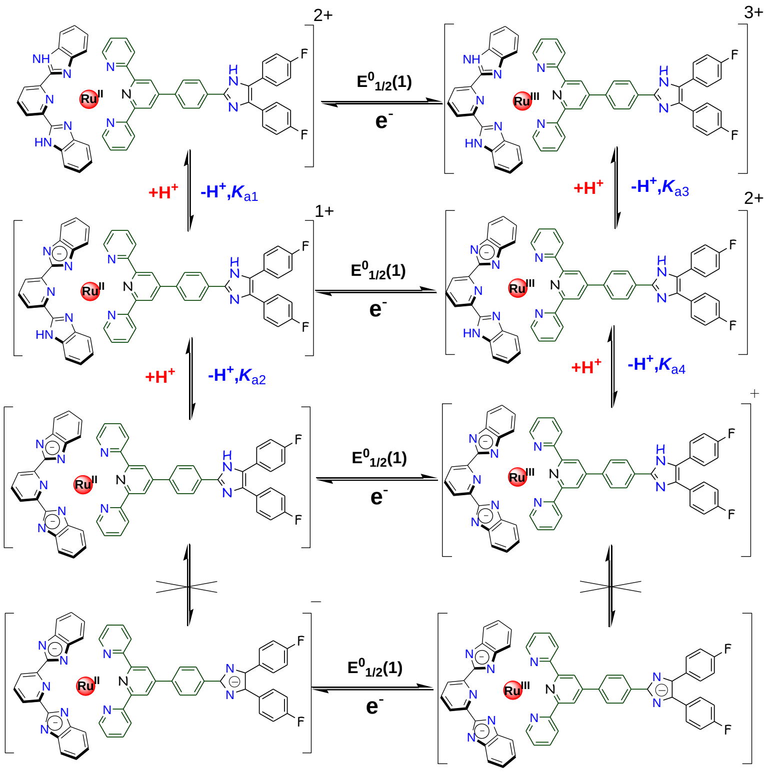

Scheme 3.3. Electro-protic equilibria involved in complex **2**.

Figure 3.23d presents the change of $E_{1/2}$ with the variation of pH for complex **3**. It may be observed that up to pH 2, and greater than pH 11, the $E_{1/2}$ values remain invariant. In between 2.5 < pH < 11, gradual decrease of $E_{1/2}$ with the increase of pH takes place in two consecutive steps with a plateau around pH 7.0 to 8.0. In both the regions, the slope of $E_{1/2}$ vs. pH plot is ~60 mV/pH suggesting two successive $1e^{-}$-$1H^{+}$ transfer processes (Scheme 3.4).

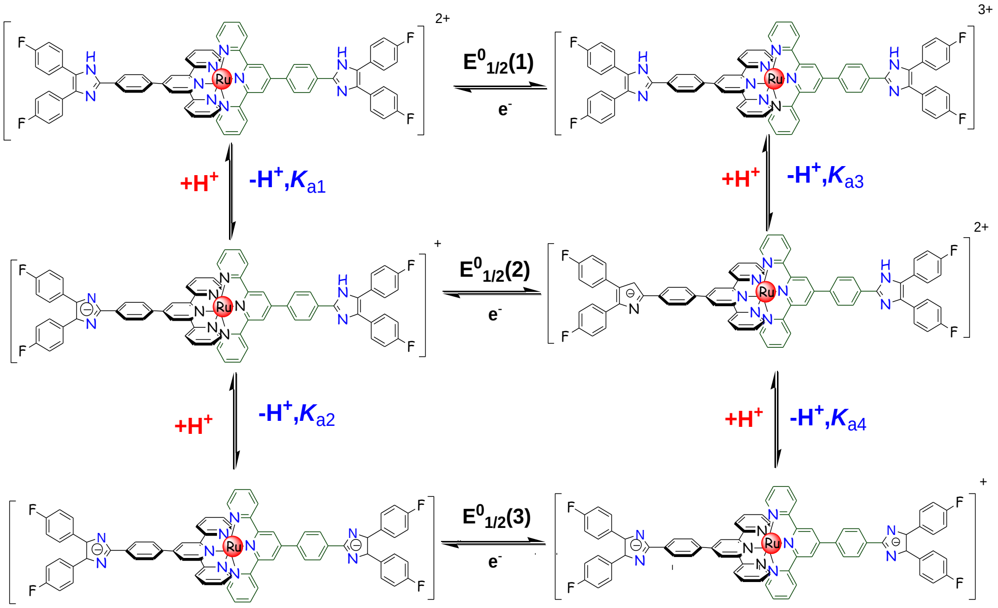

Scheme 3.4. Electro-protic equilibria involved in complex **3**.

Upon non-linear regression analysis of the experimental $E_{1/2}$ *versus* pH data through equation 4, all the pK_a values could be estimated. The estimated pK_a values are provided in Table 3.11.

$$\boldsymbol{E_{1/2} = E^0_{1/2} + 0.0591 \log \frac{[H^+]^2 + K_{a1}[H^+] + K_{a1}K_{a2}}{[H^+]^2 + K_{a3}[H^+] + K_{a3}K_{a4}}} \qquad (4)$$

$E^0_{1/2}$ corresponds to the standard redox potential at pH 0 for Ru^{3+}/Ru^{2+} couple. K_{a1} and K_{a2} correspond to the acid dissociation constants for the Ru^{2+} species, whereas K_{a3} and K_{a4} correspond to the Ru^{3+} species in the complexes. The acid dissociation constants for imidazole protons in the complexes are found to be greater when ruthenium is in Ru^{3+}

Table 3.11. Apparent pK_a Values of **1-3** in both of their Ru^{2+} and Ru^{3+} State in MeCN/H_2O (3:2) Buffer

comp	pKa_1	pKa_2	pKa_3	pKa_4
1	8.1 (8.1)[#]	-	5.1	-
2	4.6. (4.9)[#]	8.5 (8.1)[#]	2.3	5.3
3	7.3 (7.6)[#]	10.7 (10.3)[#]	5.0	8.2

[#]values obtained by spectrophotometric measuremenents state compared with the Ru^{2+} state. It is to be noted that the pK_{a1} and pK_{a2} values obtained by proton-coupled oxidative electrochemistry and spectrophotometry matches well with each other.

In all the three cases, we observed the expected decrease of $E_{1/2}$ with escalation of pH and the decrease of $E_{1/2}$ could be correlated with the bathochromic shift of the respective MLCT bands. The transformation of **1** into **1a** induces decrease of $E_{1/2}$ by 100 mV, while for the MLCT band energy the extent of decrease is 161 cm^{-1}. The corresponding change is 380 mV and 953 cm^{-1} for **2**, while 380 mV and 1684 cm^{-1} for **3**.

In PCET reactions, a single step hydrogen atom ($H\cdot \leftarrow H^+ + e^-$) transfer takes place from a particular species to the other in a concerted way.[83] The concurrent change in the oxidation state of Ru and the protonation state of the ligands can be represented schematically where the diagonal of the square represents hydrogen atom transfer (Scheme 3.5).[70]

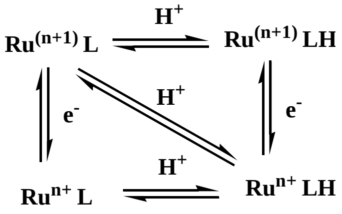

Scheme 3.5.

The horizontal arrows in scheme 3.5 indicate the pK_a values, while the vertical arrows represent the redox potential, $E°_{1/2}(n)$. The free energy change for the bond dissociation (BDFE) at 298 K can be estimated by using equation 5.[70]

$$\Delta G° = [1.37\mathrm{p}K_i + 23.1E°_{1/2}(n) + 54.9]\ \mathrm{kcalmol}^{-1} \qquad (5)$$

The $\Delta G°$ value for $H^+ + e^- \rightarrow H\cdot$ is 54.9 kcal mol^{-1} in MeCN. Although the proton-coupled oxidative electrochemistry is carried out in 3:2 MeCN-H_2O, the value in MeCN is utilized to estimate the $\Delta G°$ values of the complexes as the relative amount of MeCN is larger.

As the total enthalpy change in the said thermochemical cycle of the square scheme is zero, it is quite apparent that the $\Delta G°$ values evaluated for the diagonal arrows in the forward and backward directions should be equal. The $\Delta G°$ values involved in the square scheme of all three complexes **1-3** were calculated (Scheme 3.6) for the forward as well as the reverse processes and the values are summarized in Table 3.12. Again the calculated values are "apparent BDFEs" as the electrochemical investigations were performed in 3:2, MeCN-H_2O medium. The *G*° value for N–H bond dissociation for **1** is 90.95 kcalmol^{-1}. Two Δ*G*° values (82.45 and 82.71 kcal mol^{-1}) for **2** correspond to the dissociation of N-H bonds in H_2pbbzim unit, while for **3**, the values (91.92 and 92.00 kcalmol^{-1}) are due to the dissociation of N-H from the tpy-HImzPh$_3$F$_2$ motifs. The second N-H BDFE is little higher for both **2** and **3** as expected.

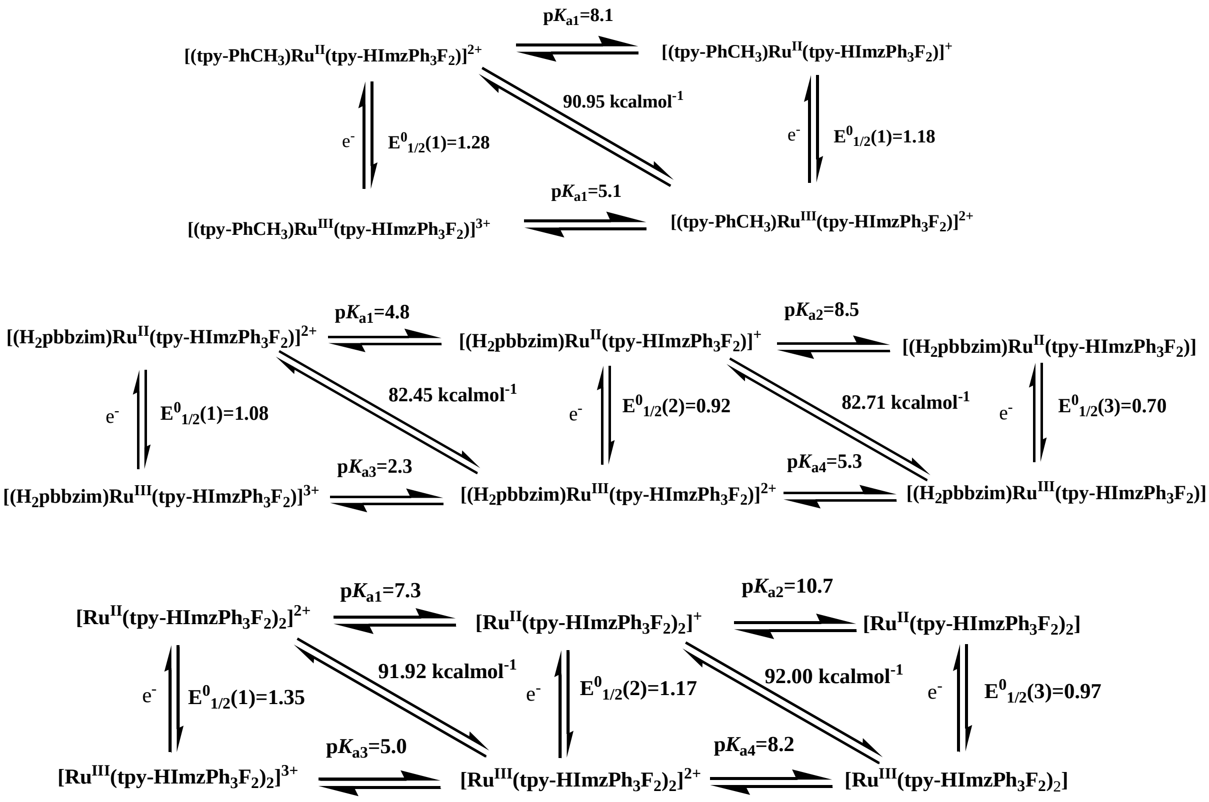

Scheme 3.6. The square schemes for the complexes **1-3** in MeCN-H_2O (3:2 v/v) buffer.

Table 3.12. Apparent Bond Dissociation Energy for the -NH Protons

compounds	ΔG^0 (1st -NH)/ Kcalmol^{-1}	ΔG^0 (2nd -NH)/ Kcalmol^{-1}
1	90.95	-
2	82.45	82.71
3	91.92	92.00

The CVs as well as the oxidation and reduction potentials of fully deprotonated forms of the complexes obtained at ~pH 10 are also presented Figure 3.23 and Table 3.10.

3.3.6. Fabrication of Logic Gates. In the preceding sections, we were able to modulate substantially the absorption, emission and redox potential of the complexes upon altering the pH of the solution. Emission quenching was made possible upon increase of either pH of solution or temperature. Restoration of the initial emission is also made possible by the decrease of pH or the temperature. Thus, the complexes exhibit successive "on-off" and "off-on" emission switching in presence of light and acid/base (pH) stimuli. We will now use their optical spectral responses as function of pH and temperature for the fabrication of two-input binary logic gates.

3.3.6.1. INHIBIT Gate. The term INHIBIT means the gate which creates a certain or fixed output whatever be the inputs or even the inputs are changed. An INHIBIT gate is actually an AND gate with an additional case. To construct the action of this gate, we have taken OH^- and H^+ as input 1 and input 2, respectively and the absorption intensity at 540 nm of complex **3** as the output (Figure 3.24a-3.24e). The truth table shows that only the addition of OH^- give rise to the ON state (1) (Figure 3.24b). Three other possible combinations of inputs originate the signal which lies below the threshold energy level, generating the OFF state (0) of this operation. In addition, the “off-on-off” cycle can be repeated several times upon successive addition of OH^- and H^+ ions (Figure 3.24e).

3.3.6.2. IMPLICATION Gate. An IMPLICATION consists of the functions of AND, OR, and NOT gates. If one input can implicit the other one then we can say that the function of an IMPLICATION gate is constructed. By picking up temperature (333K) and pH 2.0 as input 1 and input 2, respectively and the emission intensity at 655 nm as the output signal, we can mimic the function of this logic system (Figure 3.25a-3.25d). The truth table in Figure 3.25b shows that without the action of these two inputs, complex **1** exhibits intense emission at 655 nm representing the ON state (1) of the system. However, input 1 (333K) gives rise to a significant decrease in emission

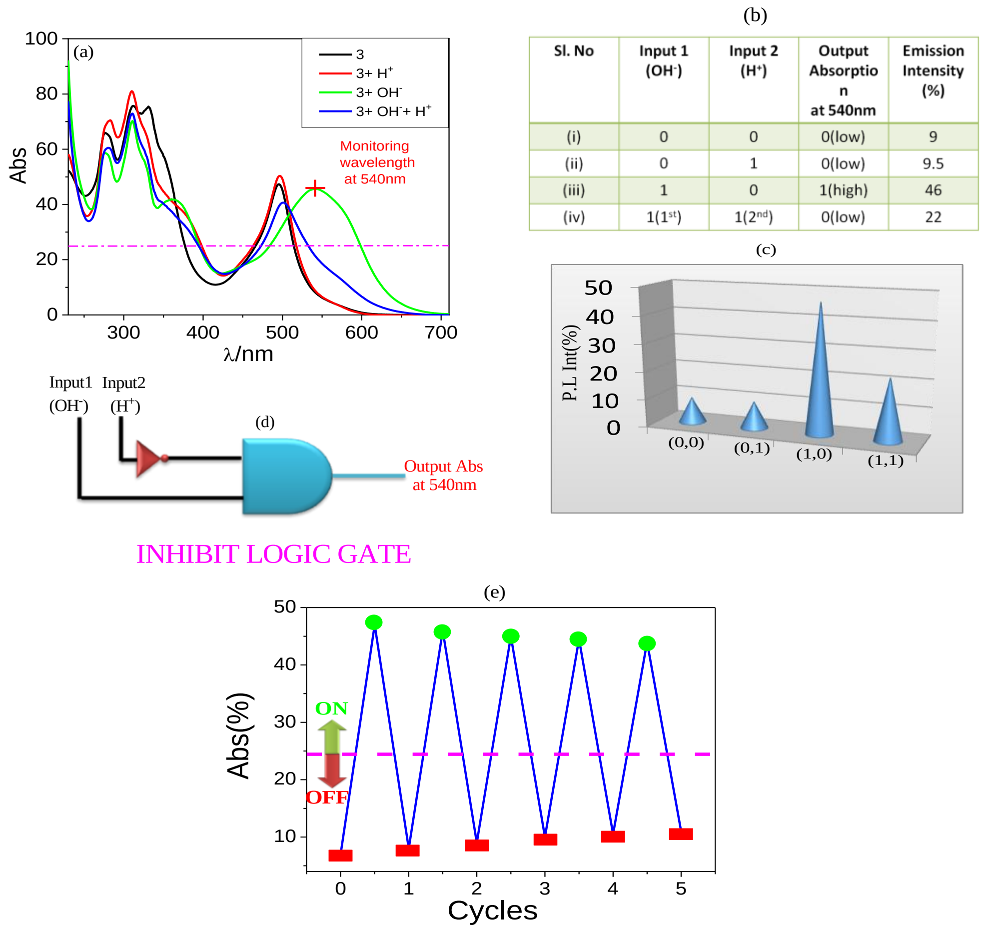

Sl. No	Input 1 (OH^-)	Input 2 (H^+)	Output Absorption at 540nm	Emission Intensity (%)
(i)	0	0	0(low)	9
(ii)	0	1	0(low)	9.5
(iii)	1	0	1(high)	46
(iv)	1(1st)	1(2nd)	0(low)	22

Figure 3.24. (a) The absorption spectral changes of complex **3** due to the addition of OH^- (input 1) and H^+ (input 2). (b) Corresponding truth table. (c) 3D representation of absorption intensities which change upon the action of different combinations of inputs. (d) Schematic presentation of an INHIBIT gate depending on the output absorption intensity at 540 nm. (e) Schematic presentation of the reversible cycles upon stepwise addition of acid and base.

intensity, indicating the OFF state (0). In addition, other three possible combinations of stimuli generate output values above the threshold level forming the ON state (1) of this system (Figure 3.25b). Thus, by observing the emission spectral intensity variation at 655 nm due to the action of these two inputs, an IMPLICATION can be constructed (Figure 3.25d).

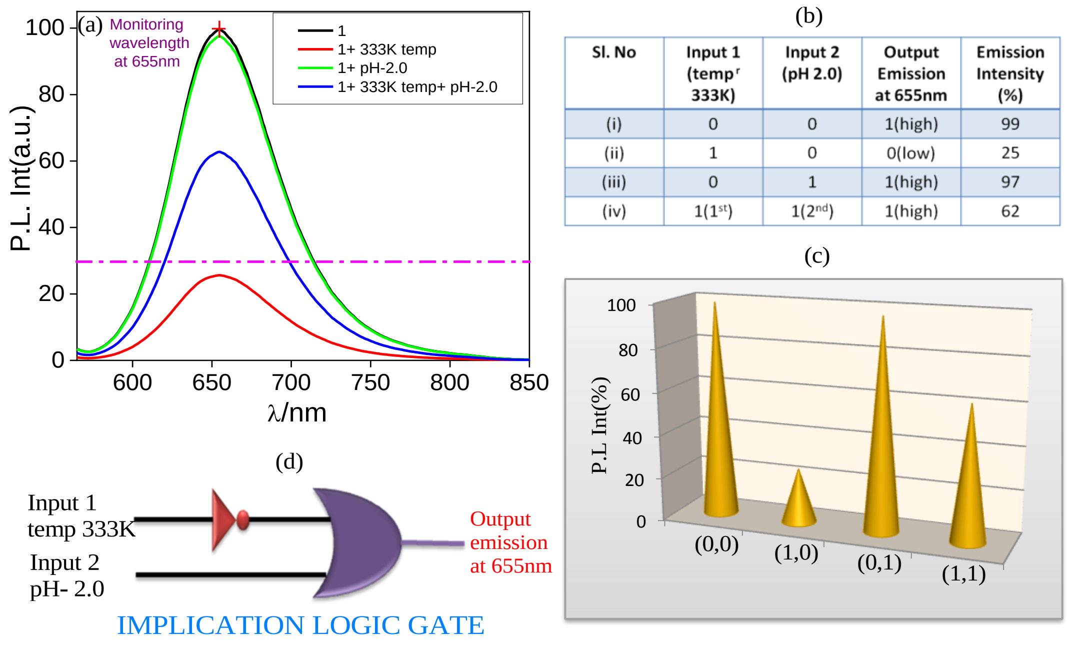

Sl. No	Input 1 (tempʳ 333K)	Input 2 (pH 2.0)	Output Emission at 655nm	Emission Intensity (%)
(i)	0	0	1(high)	99
(ii)	1	0	0(low)	25
(iii)	0	1	1(high)	97
(iv)	1(1st)	1(2nd)	1(high)	62

Figure 3.25. (a) The emission (λ_{ex}=490 nm) intensity changes of complex **1** as a function of temperature (333K) (input 1) and pH 2.0 (input 2). (b) Corresponding truth table. (c) 3D representation of emission intensity as a function of different combinations of inputs. (d) Schematic presentation of an IMPLICATION gate.

3.**3.6.3. NOR Gate.** NOR gate is a combination of two digital logic functions. By connecting an OR gate and an inverter or NOT gate together in a series, the function of NOR gate can be constructed. This gate is a complimentary form of inclusive OR gate and belongs to one of the universal logic gate. We have chosen OH^- ion and temperature at 333K as input 1 and input 2, respectively and the emission intensity at 684 nm for complex **2** as the monitoring output wavelength (Figure 3.26a-3.26d). The emission spectrum as well as the table in Figure 3.26a shows that without applying any inputs, complex **2** exhibits intense emission at 684 nm and gives rise to the ON state (1) of this operation. On the other hand, interaction with all the three other possible combinations of inputs gives rise to a value under the threshold energy barrier, designating the OFF state (0).

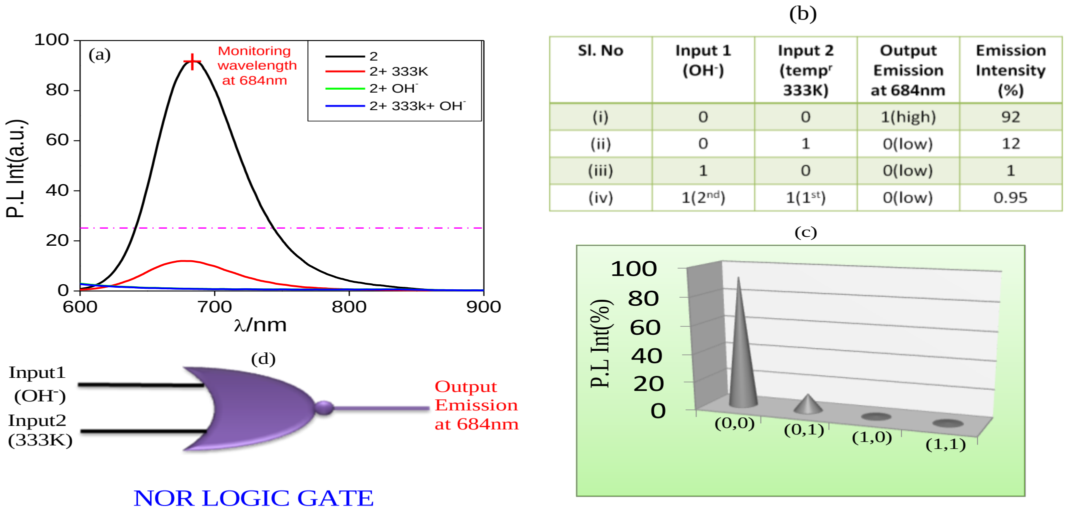

Sl. No	Input 1 (OH^-)	Input 2 ($temp^r$ 333K)	Output Emission at 684nm	Emission Intensity (%)
(i)	0	0	1(high)	92
(ii)	0	1	0(low)	12
(iii)	1	0	0(low)	1
(iv)	1(2^{nd})	1(1^{st})	0(low)	0.95

Figure 3.26. (a) The emission (λ_{ex}=490 nm) intensity changes of complex **2** upon varying **[**OH^-] (input 1) and temperature at 333K (input 2). (b) Corresponding truth table. (c) 3D representation of emission intensities which change upon the action of different combinations of inputs. (d) Schematic presentation of a NOR gate.

3.4. Conclusions

With regard to our desire to design stimuli-responsive molecular switches, we report herein three Ru(II) complexes based on a terpyridyl-imidazole ligand (tpy-$HImzPh_3F_2$) which exhibit luminescence at RT having lifetimes within 4.5-49.0 ns, depending on the auxiliary ligand and solvent used. The ^{3}MLCT-^{3}MC energy gap plays a crucial role on the luminescence behavior of these complexes and temperature plays an important role to tune the said energy gap. In this regard, we thoroughly studied the effect of temperature on the emission intensity and lifetime of the complexes in order to check the utility of these complexes to act as temperature-dependent molecular switches. In practice, "on-off" and "off-on" emission switching is feasible for all the complexes upon alternate heating and cooling the solution of the complexes through modulation of their ^{3}MLCT-^{3}MC energy gap.

The complexes also offer acidic imidazole protons in their outer coordination sphere which could be deprotonated upon increase of pH. In reality, the complexes undergo sequential deprotonation upon increase of pH with phenomenal alteration of their absorption, emission and redox properties. The bathochromic shift of ^{1}MLCT absorption and ^{3}MLCT emission band together with substantial quenching of emission is observed in all cases upon increase of pH. The spectral changes are fully reversible and restoration of their initial state can be feasible upon decreasing pH. The ground state pK_a values are also estimated from systematic alteration of absorption spectra of the complexes as a function of pH. In essence, the complexes have the potentiality to act as molecular switches based on remarkable alteration in their absorption, emission and redox behaviors as function of pH and temperature. In addition, their optical spectral responses as function of acid/base and temperature were utilized for the fabrication of two-input binary logic gates (IMPLICATION, NOR and INHIBIT).

3.5. References

1. Valeur, B. Molecular Fluorescence: Principles and Applications. *Wiley*. **2002**.
2. Prodi, L.; Bolletta, F.; Montalti, M.; Zaccheroni, N. Luminescent Chemosensors for Transition Metal Ions. *Coord. Chem. Rev*. **2000**, *205*, 59-83.
3. Hung, L. S.; Chen, C. H. Recent Progress of Molecular Organic Electroluminescent Materials and Devices**.** *Mater. Sci. Eng. R.* **2002**, *39*, 143-222.
4. Müllen, K.; Scherf, U. Organic Light Emitting Devices: Synthesis, Properties and Applications. *Wiley*. **2006**.
5. Zhang, J. F.; Zhou, Y.; Yoon, J.; Kim, J. S. Recent Progress in Fluorescent and Colorimetric Chemosensors for Detection of Precious Metal Ions (Silver, Gold and Platinum ions). *Chem. Soc. Rev*. **2011**, *40*, 3416-3429.
6. Kim, H. N.; Ren, W. X.; Kim, J. S.; Yoon, J. Fluorescent and Colorimetric Sensors for Detection of Lead, Cadmium, and Mercury ions. *Chem. Soc. Rev*. **2012**, *41*, 3210-3244.
7. Arm, K. J.; Williams, G. J. A. A Cross-Coupling Strategy for the Synthesis of Dimetallic Assemblies Containing Mixed Bipyridine-Terpyridine Bridging Ligands: Luminescence and Energy Transfer Properties. *Dalton Trans.* **2006**, *18*, 2172–2174.
8. McConnell, A. J.; Wood, C. S.; Neelakandan, P. P.; Nitschke, J. R. Stimuli-Responsive Metal-Ligand Assemblies**.** *Chem. Rev*. **2015**, *115*, 7729-7793.
9. John, Q. Li.; Ed. Intelligent Stimuli-Responsive Materials. *Wiley & Sons, Inc.: Hoboken, Nj*. **2013**.

10. Manez, R. M.; Sancenon, F. Fluorogenic and Chromogenic Chemosensors and Reagents for Anions**.** *Chem. Rev*. **2003**, *103*, 4419-4476.
11. de Silva, A. P.; Gunaratne, H. Q. N.; Gunnlaugsson, T.; Huxley, A. J. M.; McCoy, C. P.; Rademacher J. T.; Rice, T. E. Signaling Recognition Events with Fluorescent Sensors and Switches. *Chem. Rev.* **1997**, *97*, 1515-1566.
12. Kurihara, M.; Nishihara, H. Azo- and Quinone-Conjugated Redox Complexes-Photo- and Proton-Coupled Intramolecular Reactions Based on d–π Interaction. *Coord. Chem. Rev*. **2002**, *226*, 125-135.
13. Ko C.C.; Yam, V. W.W. Coordination Compounds with Photochromic Ligands: Ready Tunability and Visible Light-Sensitized Photochromism. *Acc. Chem. Res.* **2017**, *51*, 149-159.
14. Cui, B.B.; Zhong Y.W.; Yao, J. Three-State Near-Infrared Electrochromism at the Molecular Scale. *J. Am. Chem. Soc*. **2015**, *137*, 4058-4061.
15. Haga, M.; Ali, M. M.; Maegawa, H.; Nozaki, K.; Yoshimura A.; Ohno, T. Photoexcited States of Dinuclear Ru Complexes Bridged by Proton-Dissociable Benzimidazole Derivatives. *Coord. Chem. Rev.* **1994**, *132*, 99-104.
16. Ali, C.; Banaszak, M.; Astumian, R. D.; Stoddart J. F.; B. Grzybowski, A. Great Expectations: Can Artificial Molecular Machines Deliver on Their Promise? *Chem. Soc. Rev*. **2012**, *41*, 19-30.
17. Huynh M. H. V.; Meyer, T. J. Proton-Coupled Electron Transfer. *Chem. Rev.* **2007**, *107*, 5004-5064.
18. Costentin, C. Electrochemical Approach to the Mechanistic Study of Proton-Coupled Electron Transfer. *Chem. Rev.* **2008**, *108*, 2145-2179.
19. Licini, M.; Williams, G.J. A. Iridium (III) Bis-Terpyridine Complexes Displaying Long-Lived pH Sensitive Luminescence. *Chem. Commun.* **1999**, *19*, 1943–1944.
20. Miyazaki, S. Kojima, T.; Mayer J. M.; Fukuzumi, S. Proton-Coupled Electron Transfer of Ruthenium (III)-Pterin Complexes: A Mechanistic Insight. *J. Am. Chem. Soc.* **2009**, *131*, 11615-11624.
21. Manner V. W.; Mayer, J. M. Concerted Proton-Electron Transfer in a Ruthenium Terpyridyl-Benzoate System with a Large Separation Between the Redox and Basic Sites. *J. Am. Chem. Soc.* **2009**, *131*, 9874-9875.

22. Baitalik, S.; Florke, U.; Nag, K. Mononuclear and Binuclear Ruthenium(II) Complexes Containing 2,2'-Bipyridine or 1,10-Phenanthroline and Pyrazole-3,5-bis (benzimidazole). Synthesis, Structure, Isomerism, Spectroscopy, and Proton-Coupled Redox activity. *Inorg. Chem.* **1999**, *38*, 3296-3308.
23. Baitalik, S.; Dutta, S.; Biswas, P.; Florke, U.; Bothe E.; Nag, K. structural, Spectroscopic, and Proton-Coupled Electron-Transfer Behavior of Pyrazolyl-3,5-Bis (Benzimidazole)-Bridged Homo- and Heterochiral Ru^{II} Ru^{II}, Os^{II} Os^{II}, and Os^{II} Ru^{II} 2,2′-Bipyridine Complexes. *Eur. J. Inorg. Chem.* **2010**, *4*, 570-588.
24. Meng, T.T.; Wang, H.; Zheng, Z. B; Wang, K. Z. pH-Switchable "off-on-off" Near-Infrared Luminescence Based on a Dinuclear Ruthenium(II) Complex**.** *Inorg. Chem.* **2017**, *56*, 4775-4779.
25. Zheng, Z. B.; Kang, S. Y.; N Zhang, X. Yi.; Wang, K. Z. Off–on–off pH Luminescence Switching and DNA Binding Properties of a Free Terpyridine-Appended Ruthenium Complex. *J. of Inorg. Biochem.* **2014**, *141*, 70-78.
26. Maity, D.; Das, S.; Mardanya, S.; Baitalik, S. Synthesis, Structural Characterization, and Photophysical, Spectroelectrochemical and Anion-Sensing Studies of Heteroleptic Ruthenium (II) Complexes Derived from 4′-Polyaromatic-Substituted Terpyridine Derivatives and 2,6-Bis(Benzimidazol-2-yl)Pyridine. *Inorg. Chem.* **2013**, *52*, 6820-6838.
27. Bar, M.; Deb, S.; Paul A.; Baitalik, S. Stimuli-Responsive Luminescent Bis-Tridentate Ru (II) Complexes Toward the Design of Functional Materials *Inorg. Chem.* **2018,** *57*, 12010-12024.
28. Maity, D.; Mardanya, S.; Karmakar S.; Baitalik, S. pH-Induced Processes in Wire-like Multichromophoric Homo- and Heterotrimetallic Complexes of Fe(II), Ru(II), and Os(II) *Dalton Trans*. **2015**, *44*, 10048-10059.
29. Juris, A.; Balzani, V.; Barigelletti, F.; Campagna, S.; Beleser, P.; Zelewsky, A. V. Ru (II) Polypyridine Complexes: Photophysics, Photochemistry, Electrochemistry, and Chemiluminescence. *Coord. Chem. Rev.* **1988**, *84*, 85-277.
30. Balzani, V.; Juris, A.; Venturi, M.; Campagna S.; Serroni, S**.** Luminescent and Redox-Active Polynuclear Transition Metal Complexes. *Chem. Rev.* **1996**, *96*, 759-834.

31. Sauvage, J. P. ; Collin, J. P. J. ; Chambron, C. ; Guillerez, S. ; Coudret, C. ; Balzani, V.; Barigelletti, F.; De Cola, L. ; Flamigni, L. Ruthenium(II) and Osmium(II) Bis (Terpyridine) Complexes in Covalently-Linked Multicomponent Systems: Synthesis, Electrochemical Behavior, Absorption Spectra, and Photochemical and Photophysical Properties. *Chem. Rev*. **1994**, *94*, 993-1019.
32. Browne, W. R.; O'Boyle, N. M.; McGarvey, J. J.; Vos, J. G. Elucidating Excited State Electronic Structure and Intercomponent Interactions in Multicomponent and Supramolecular Systems. *Chem. Soc. Rev*. **2005**, *34*, 641- 663.
33. Williams, J. A. G. The Coordination Chemistry of Dipyridylbenzene: N-deficient Terpyridine or Panacea for Brightly Luminescent Metal Complexes. *Chem. Soc. Rev*. **2009**, *38*, 1783-1801.
34. Pal, A. K.; Hanan, G. S. Design, Synthesis and Excited-State Properties of Mononuclear Ru (II) Complexes of Tridentate Heterocyclic Ligands. *Chem. Soc. Rev*. **2014**, *43*, 6184-6197.
35. Medlycott, E. A.; Hanan, G. S. Synthesis and Properties of Mono and Oligo-Nuclear Ru (II) Complexes of Tridentate Ligands: the Quest for Long-Lived Excited States at Room Temperature. *Coord. Chem. Rev*. **2006**, *250*, 1763-1782.
36. Hofmeier, H.; Schubert, U. S. Recent Developments in the Supramolecular Chemistry of Terpyridine-Metal Complexes. *Chem. Soc. Rev*. **2004**, *33*, 373-399.
37. Constable, E. C. 2,2′:6′,2″-Terpyridines: from Chemical Obscurity to Common Supramolecular Motifs. *Chem. Soc. Rev*. **2007**, *33*, 246-253.
38. Harriman, A.; Ziessel, R. Making Photoactive, Molecular-scale Wires. *Chem. Commun*. **1996**, *15*, 1707-1716.
39. Breivogel, A.; Kreitner, C.; Heinze, K. Redox and Photochemistry of Bis (terpyridine) Ruthenium(II) Amino Acids and their Amide Conjugates-from Understanding to Applications. *Eur. J. Inorg. Chem*. **2014**, *32*, 5468-5490.
40. Winkler, J. R.; Netzel, T.; Creutz, C.; Sutin, N. Direct Observation of Metal-to-ligand Charge-transfer (MLCT) Excited States of Pentaammineruthenium (II) Complex. *J. Am. Chem. Soc*. **1987**, *109*, 2381-2392.
41. Wang, J.; Fang, Y. Q. ; Hanan, G. S. ; Loiseau F. ; Campagna, S. Synthesis and Properties of the Elusive Ruthenium(II) Complexes of 4'-cyano-2,2':6',2"-terpyridine. *Inorg. Chem*. **2005**, *44*, 5-7.

42. Kubel, J.; Schroot, R.; Wachtler, M.; Schubert, U. S.; Dietzek, B.; Jager, M. Photoredox-active Dyads Based on a Ru(II) Photosensitizer Equipped with Electron Donor or Acceptor Polymer Chains: a Spectroscopic Study of Light-induced Processes toward Efficient Charge Separation. *J. Phys. Chem. C*. **2015**, *119*, 4742-4751.
43. Maestri, M.; Armaroli, N.; Balzani, V.; Constable, E. C.; Thompson, A. M. W. C. Complexes of the Ruthenium (II)-2, 2':6',2''-Terpyridine Family. Effect of Electron-accepting and Donating Substituents on the Photophysical and Electrochemical Properties**.** *Inorg. Chem.* **1995**, *34*, 2759-2767.
44. Santoni, M.P.; Hanan, G. S.; Hasenknopf, B.; Proust, A.; Nastasi, F.; Serroni, S.; Campagna. S. Dinuclear Ru (II) Complexes of Bis-(dipyrid-2′-yl) Triazine (bis-dpt) Ligands as Efficient Electron Reservoirs**.** *Chem. Commun.* **2011**, *47*, 3586-3588.
45. Fang,Y. Q.; Taylor, N. J. ; Hanan, G. S.; Loiseau, F.; Passalacqua, R.; Campagna, S. ; Nierengarten, H.; Dorsselaer, A. V. A Strategy for Improving the Room-temperature Luminescence Properties of Ru (II) Complexes with Tridentate Ligands. *J. Am. Chem. Soc.* **2002**, *124*, 7912-7913.
46. Encinas, S.; Flamigni, L.; Barigelletti, F.; Constable, E. C.; Housecroft, C. E. ; Schofield, E. R.; Figgemeier, E.; Fenske, D.; Neuburger, M.; Vos, J. G., et al. Electronic Energy Transfer and Collection in Luminescent Molecular Rods Containing Ruthenium(II) and Osmium(II) 2,2′:6′,2″-Terpyridine Complexes Linked by Thiophene-2,5-diyl Spacers. *Chem. Eur. J.* **2002**, *8*, 137-150.
47. Duati, M.; Tasca, S.; Lynch, F. C.; Bohlen, H.; Vos, J. G.; Stagni, S.; Ward, M. D. Enhancement of Luminescence Lifetimes of Mononuclear Ruthenium(II)-Terpyridine Complexes by Manipulation of the Sigma-donor Strength of Ligands**.** *Inorg. Chem.* **2003**, *42*, 8377-8384.
48. Polson, M. I. J.; Loiseau, F.; Campagna, S.; Hanan.G. S. Bridging Ligand Planarity as a Route to Long-lived, Near Infrared Emitting Dinuclear Ruthenium (II) Complexes. *Chem. Commun*. **2006**, *12*, 1301-1303.
49. Loiseau, F.; Passalacqua, R.; Campagna, S.; Polson, M. I. J.; Fang, Y.Q.; Hanan, G. S. New Dinuclear Ru (II) Complexes Containing Free Chelating Polypyridine Sites within the Bridging Ligands: Absorption Spectra, Luminescence Properties,

Redox Behavior and Sensing Properties *Photochem. Photobiol. Sci.* **2002**, *1*, 982-990.

50. Yang, W.W., Zong, Y.W.; Yoshikawa, S.; Shao, J.Y.; Masaoka, Ken S.; Yao, J.; Haga.; M. Tuning of Redox Potentials by Introducing a Cyclometalated Bond to Bis-tridentate Ruthenium (II) Complexes Bearing Bis(N-methylbenzimazolyl) Benzene or- Pyrimidine Lignads. *Inorg. Chem*. **2012**, *51*, 890-899.
51. Zhang, Y.M.; Wu, S.H.; Yao, C.J.; Nie, H.J.; Zhong Y.W. A Bis(terpyridine) Ruthenium Complex with Three Redox-active Amine Sites: Electrochemical, Optical, and Computational Studies. *Inorg. Chem*. **2012**, *51*, 11387-11395.
52. Yao, C.J.; Nie, H.J.; Yang, W.W.; Yao, J.; Zhong Y.W. Combined Experimental and Computational Study of Pyren-2,7-diylbridged Diruthenium Complexes with Various Terminal Ligands .*Inorg. Chem.* **2015**, *54*, 4688-4698.
53. Shao, J.Y.; Yang, W.W.; Yao, J.; Zhong Y.W. Biscyclometalated Ruthenium Complexes Bridged by 3,3′,5,5′-Tetrakis(N-methylbenzimidazol-2-yl)biphenyl: Synthesis and Spectroscopic and Electronic Coupling Studies. *Inorg. Chem*. **2012**, *51*, 4343-4351.
54. Shao J.Y.; Zhong Y.W. pH Value-dependent Electronic Absorption and Ru(III/II) Potential of Bis-tridentate Pincer Ruthenium Complexes. *J. Organomet.Chem.* **2017**,*845,144-150*
55. Dietrich, J.; Thorenz, U.; Forster, C.; Heinze, K. Effects of Sequence, Connectivity, and Counter Ions in new Amide-linked Ru(tpy)$_2$-Re(bpy) Chromophores on Redox Chemistry and Photophysics. *Inorg. Chem*. **2013**, *52*, 1248-1264.
56. Wadman, S. H.; Lutz, M.; Tooke, D. M.; Spek, A. L.; Hartl, F.; Havenith, R.W. A.; van Klink G. P. M.; van Koten, G. Consequences of *N*,*C*,*N*′- and *C*,*N*,*N*′-Coordination Modes on Electronic and Photophysical Properties of Cyclometalated Aryl Ruthenium(II) Complexes. *Inorg. Chem*. **2009**, *48*, 1887-1900.
57. Kreitner, C.; Erdmann, E.; Seidel; W. W. Heinze, K. Understanding the Excited State Behavior of Cyclometalated Bis (Tridentate) Ruthenium (II) Complexes: a Combined Experimental and Theoretical Study. *Inorg. Chem*. **2015**, *54*, 11088.

58. Benniston, A. C.; Grosshenny, V.; Harriman, A.; Ziessel, R. Electron Delocalization in Ethynyl Bridged Binuclear Ruthenium(II) Polypyridine Complexes. *Angew. Chem. Int. Ed. Engl*. **1994**, *33*, 1884-1886.
59. Benniston, A. C.; Chapman, G.; Harriman, A.; Mehrabi, M.; Sams, C. A. Electron Delocalization in a Ruthenium(II) Bis (2,2′:6′,2″-Terpyridine) Complex. *Inorg. Chem*. **2004**, *43*, 4227-4233.
60. Mondal, D.; Bar, M.; Mukherjee, S.; Baitalik, S. Design of Ru (II) Complexes Based on Anthraimidazoledione-functionalized Terpyridine Ligand for Improvement of Room-temperature Luminescence Characteristics and Recognition of Selective Anions: Experimental and DFT/TD-DFT Study. *Inorg. Chem*. **2016**, *55*, 9707-9724.
61. Maity, D.; Bhaumik, C.; Mondal, D.; Baitalik, S. Ru (II) and Os(II) Complexes Based on Terpyridyl-imidazole Ligand Rigidly Linked to Pyrene: Synthesis, Structure, Photophysics, Electrochemistry, and Anion-sensing Studies. *Inorg. Chem*. **2013**, *52*, 13941-13955.
62. Maity, D.; Das, S.; Mardanya, S.; Baitalik, S. Synthesis, Structural Characterization, and Photophysical, Spectroelectrochemical and Anion-sensing Studies of Heteroleptic Ruthenium(II) Complexes Derived From 4′-polyaromatic-substituted Terpyridine Derivatives and 2,6-bis(benzimidazol-2-yl)pyridine. *Inorg. Chem*. **2013**, *52*, 6820-6838.
63. Bhaumik, C.; Saha, D.; Das, S.; Baitalik, S. Synthesis, Structural Characterization, Photophysical, Electrochemical and Anion-sensing Studies of Luminescent Homo- and Heteroleptic Ruthenium(II) and Osmium(II) Complexes Based on Terpyridyl-imidazole Ligand. *Inorg. Chem.* **2011**, *50*, 12586-12600.
64. Mondal, D.; Biswas, S.; Paul, A.; Baitalik, S. Luminescent Dinuclear Ruthenium Terpyridine Complexes with a Bis-phenylbenzimidazole Spacer. *Inorg. Chem.* **2017**, *56*, 7624-7641
65. Bhaumik, C.; Das, S.; Maity, D.; Baitalik, S. Luminescent Bis-tridentate Ruthenium (II) and Osmium (II) Complexes Based on Terpyridyl-imidazole Ligand: Synthesis, Structural Characterization, Photophysical, Electrochemical and Solvent Dependence Studies. *Dalton Trans.* **2012**, *41*, 2427-2438.

66. Deb, S.; Sahoo, A.; Pal, P.; Baitalik, S. Exploitation of the Second Coordination Sphere to Promote Significant Increase of Room-temperature Luminescence Lifetime and Anion Sensing in Ruthenium-terpyridine Complexes. *Inorg. Chem.* **2021**, *60*, 6836-6851.
67. Daisuke, M.; Kai, Y.; Hiroaki, O.; Makoto T.; Haga, M. Energy-storage Applications for a pH Gradient Between two Benzimidazole-ligated Ruthenium Complexes that Engage in Proton-coupled Electron-transfer Reactions in Solution. *Inorg. Chem.* **2017**, *56*, 6419-6428.
68. Yoshikawa, K.; Motoyama, D.; Hiruma, Y.; Ozawa, H.; Nagano S.; ; Haga, M. Proton-rocking-chair-type Redox Capacitors Based on Indium Tin Oxide Electrodes with Multilayer Films Containing Ru Complexes. *ACS Appl. Mater. Interfaces* **2018**, *10*, 26990-27000.
69. Haga, M.; Takasugi, T.; Tomie, A.; Ishizuya, M.; Yamada, T.; Hossain M. D.; Inoue, Miyao. Molecular Design of a Proton-induced Molecular Switch Based on Rod-shaped Ru Dinuclear Complexes with Bis-tridentate 2,6-bis(benzimidazol-2-yl)pyridine Derivatives. *Dalton Trans.* **2003**, *10*, 2069-2079.
70. Wu, A.; Masland, J.; Swartz, R. D.; Kaminsky, W.; Mayer, J. M. Synthesis and Characterization of Ruthenium Bis(β-diketonato) Pyridine-imidazole Complexes for Hydrogen Atom Transfer. *Inorg. Chem.* **2007**, *46*, 11190-11201.
71. Mo, H.J.; Niu, Y.L.; Zhang, M.; Qiao Z. P.; Ye, B.H. Photophysical, Electrochemical and Anion Sensing Properties of Ru(II) Bipyridine Complexes with 2,2'-Biimidazole-like Ligand. *Dalton Trans*. **2011**, *40*, 8218-8225.
72. Das, S.; Saha, D.; Karmakar, S.; Baitalik, S. Effect of pH on the Photophysical and Redox Properties of a Ruthenium(II) Mixed Chelate Derived from Imidazole-4,5- dicarboxylic Acid and 2,2′-Bipyridine: an Experimental and Theoretical Investigation. *J. Phys. Chem. A.* **2012**, *116*, 5216-5226.
73. Das, S.; Saha, D.; Mardanya, S.; Baitalik, S. A combined Experimental and DFT/TDDFT Investigation of Structural, Electronic, and pH-induced Tuning of Photophysical and Redox Properties of Osmium(ii) Mixed-chelates Derived from Imidazole-4,5-dicarboxylic Acid and 2,2′-Bipyridine. *Dalton Trans.* **2012**, *41*, 12296-12310

74. Karmakar, S.; Maity, D.; Mardanya, S.; Baitalik, S. Demonstration of Multiple Logic Operations in a Heteroditopic Pyrene-phenylimidazole-terpyridine Conjugate Based on Optical Responses by Selective Anions and Cations: an Experimental and Theoretical Investigation. *J. Phys. Chem. A* **2014**, *118*, 9397-9410.
75. De Silva, A. P.; Gunaratne, H.Q.N.; McCoy, C.P. A Molecular Photoionic AND Gate Based on Fluorescent Signaling. *Nature* 1993, *364*, 42-44.
76. De Silva, A. P.; Fox, D. P.; Huxley, A. J. M.; Moody, T. S. Combining Luminescence, Coordination and Electron Transfer for Signaling Purposes. *Coord. Chem. Rev*. **2000**, *205*, 41-57.
77. Katz (Ed.), E. Molecular and Supramolecular Information Porocessing: From Molecular Switches to Logic System, Wiley-VCH Weinheim, Germany, **2012**.
78. Guliyev, R.; Ozturk, S.; Kostereli, Z.; Akkaya, E. U. From Virtual to Physical: Integration of Chemical Logic Gates. *Angew. Chem Int. Ed*. **2011**, *50*, 9826-9831.
79. Karmakar, S.; Mardanya, S.; Das, S.; Baitalik, S. Efficient Deep-Blue Emittier and Molecular-Scale Memory Device Based on Dipyridyl-Phenylimidazole-Terpyridine Assembly. *J. Phys. Chem. C.* **2015**, *119*, 6793-6805.
80. Andreasson, J.; Pischel, U. Molecules with a Sense of Logic: a Progress Report *Chem. Soc. Rev*. **2015**, *44*, 1053-1069
81. Pott, K. T.; Usifer, D. A.; Abruna, H. D. 4-Vinyl-, 6-Vinyl-, and 4'-Vinyl-2,2':6',2"-Terpyridinyl Ligands: Their Synthesis and the Electrochemistry of Their Transition-Metal Coordination Complexes. *J. Am. Chem. Soc.* **1987**,*109*, 3961-3967
82. Haga, M.; Takasugi, T.; Tomie, A.; Ishizuya, M.; Yamada, T.; M. Hossain, D.; Inoue, M. Molecular Design of a Proton-Induced Molecular Switch Based on Rod-Shaped Ru Dinuclear Complexes with Bis-Tridentate 2,6-Bis(Benzimidazol-2-yl)Pyridine Derivatives. *Dalton Trans.* **2003**, *10*, 2069-2079.
83. Hynes, J. T.; Klinman, J. P.; Limbach H. H.; Schowen, R. L. (Eds.), *Hydrogen-Transfer Reactions*, Wiley-VCH, Weinheim, Germany, **2007**.

****

Chapter 4

Analysis and Prediction of Anion- and Temperature Responsive Behaviours of Luminescent Ru (II)-Terpyridine Complexes by Using Boolean, Fuzzy Logic, Artificial Neural Network and Adapted Neuro Fuzzy Inference Models

4.1. Introduction

The machine learning (ML) and diverse artificial intelligence (AI) implements have been extensively utilized in recent time in various areas in chemistry and biology.[1-10] One of the most emerging aspects of the current research is to fabricate smart materials and to investigate their varied physicochemical parameters (such as sensing) for diagnostic purposes. Comparatively little progress has been accomplished in other supplementary areas of AI, such as FL, ANNs, ANFIS and evolutionary computation.[10-20] Creation of dependable and exhaustive catalogue might enlarge the ML to a wide range of applications. Hence, tremendous efforts have now been paid to prosper the productive domain of AI having vague and imprecise inputs.

Our enthusiasm is targeted on the Ru(II) complexes based on polyheterocyclic ligands due to their remarkable photophysical and electrochemical properties and due to their involvement as active component in diverse areas of applications such as dye sensitized solar cells, sensors and switches.[21-27] In the present study, we prepared a terpyridine-based ligand {**(tpy-HImzPh$_3$(NMe$_2$)$_2$**} upon incorporating dimethylamino benzil group into the 4'-position of the tpy unit through phenyl-imidazole spacer. The said ligand is employed to synthesize both homo- and heteroleptic Ru(II) complexes as shown in **Chart 4.1**. The major advantage of using terpyridine-type ligand over their extensively studied bipyridine analogues is due to achiral nature of the resulting octahedral complex. But most of the terpyridine complexes of Ru(II) donot emit at room temperature (RT) and their excited state lifetime is quite short ($[Ru(tpy)_2]^{2+}$, $\tau = 0.25$ ns).[28-43] Herein, we introduced strongly electron-donating dimethylamino groups in the synthesis protocol of the ligand to augment the RT emission characteristics of the complexes by adjusting their ^{3}MLCT-^{3}MC energy barrier. As temperature plays a crucial role on the emission characteristics of the complexes through adjustment of their ^{3}MLCT-^{3}MC energy barrier, we performed temperature-dependent emission spectral measurements to explore the efficacy of the complexes as temperature-triggered molecular switches. Interestingly, substantial variation of emission intensity as well as lifetime is observed by altering the temperature.

The design protocol also provides several imidazole NH protons in the outer sphere of the complexes that can commune with anions through hydrogen bonding

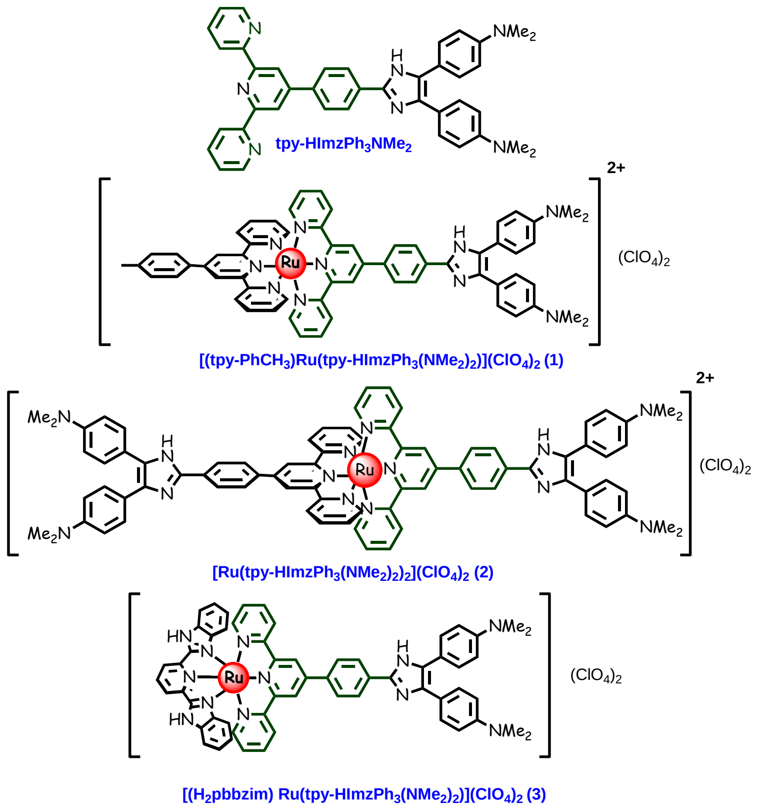

Chart 4.1. Chemical structures of the complexes.

association or through anion-triggered deprotonation. Hence, we thoroughly examined the influence of anions on their absorption and emission spectral properties. For fine tuning, we varied the number of NH protons; one (for **1**), two (for **2**), and (for **3**) (**Chart 1**). Essentially, the present complexes can mimic the function of molecular sensors and switches relying on substantial variation of their absorption and emission spectral outputs under the influence of temperature, anion, and acid.[44-51]

Previously, we reported a series of similar Ru(II) complexes derived from related terpyridyl-imidazole ligands differing by the terminal NMe$_2$ motifs and studied their photophysical characteristics as well as anion- and temperature responsive behaviours.[42-43,52] Acid-induced remarkable enhancement of RT emission lifetime (up to 80-fold) of our previously reported methyl-substituted terpyridyl-imidazole based Ru(II) complexes actually motivates us to investigate the present system. The enormous increase in lifetime was ascribed due to protonation of imidazole nitrogen(s) in the second coordination sphere of complexes which was facilitated by the electron donating Me-substituent. In order to achieve further enhancement of lifetime, we incorporated dimethylamino (-NMe_2) substituent in the ligand frame whose electron donating ability is much higher than Me group. Unfortunately, almost no acid-induced lifetime enhancement takes place for the present complexes and the photophysical as well as anion- and temperature responsive behaviours are only slightly differ from the previously reported systems. But the major focus of the present work is the implementation of ML and soft computing tools such as ANNs, FL and ANFIS to analyze and forecast the experimental anion- and temperature responsive behaviours of the complexes.

The spectral outputs of the complexes in response to different stimuli are also employed for construction of multiple BL as well as FL functions. In BL, the output signal varies between two extremes, "0" or "1".[52-63] But the practical systems often consist of innumerable number of intermediate states. To address the in-between states, the FL is an appropriate choice. Herein, we applied FL to provide an infinite-valued logic algorithm upon utilizing spectral output of the complexes in presence of the stimuli.

Performing very detailed sensing studies upon varying the analyte concentration within a wide domain is very tedious, time-consuming and expensive. In order to overcome the lacuna, we implemented soft computing tools such as ANNs, FL and ANFIS to predict the experimental anion- and temperature sensing data of the complexes.[1-9] An ANN is a network stimulated by the central nervous system of the animals (usually brain) and could be applied to guess functions that are dependent on massive number of unknown parameters. Among the two type of neural networks {recurrent (RNN) and feed-forward (FFN)}, we applied here the ANN-function fitting (ANN-FF) network due to the static nature of our systems and because of its efficiency in understanding and forecasting of a complicated system.[17-20]

It is evident that neural networks (NNs) posses efficient grasping ability from the data but not so efficient in terms of understanding the meaning of each neuron and its weight. In contrary to NNs, the FL-based model could better understand as it operates via linguistic languages and IF-THEN law. FLs, on the other hand, are unable to learn by itself. For learning and specifying via FLs, one needs to borrow the methodologies from other domains, viz. statistics, system identification etc. As the NNs are smart enough to learn, it is highly beneficial to merge FL and NN and the amalgamated methodology, called ANFIS is superior over the individual ones. The structure of ANFIS contains the same components as the fuzzy inference system (FIS) with the exception of NN block. In the present study, the outcomes of Fuzzy, ANN and ANFIS models were also compared with the experimental results for proper modeling of the anion sensing behavior of the complexes.

4.2. Experimental Section

4.2.1. Materials. Chemicals and solvents were purchased from local suppliers. 4-formyl-2,2':6',2"-terpyridine (tpy-PhCHO)[64] and 2,6-bis(benzimidazole-2-yl)pyridine (H_2pbbzim) were prepared following reported procedures.[46] [(tpy-$PhCH_3$)$RuCl_3$] and [(H_2pbbzim)$RuCl_3$] were synthesized by treating $RuCl_3 \cdot 3H_2O$ with tpy-$PhCH_3$ and H_2pbbzim, respectively in 1:1 molar ratio in refluxing EtOH.

4.2.2. Synthesis of the Ligand [(tpy-HImzPh$_3$(NMe$_2$)$_2$]. N,N dimethylamino benzil (1.5 g, 2.45 mmol), tpy-PhCHO (0.825g 2.45mmol) and NH_4OAc (2.3 g, 30 mmol) were dissolved in CH_3COOH (10 mL) and refluxed for 3h. After cool down to RT, the resulting solution was poured into crushed ice (300 mL) and upon stirring, a yellowish compound that deposited was filtered. The resulting solid was filtered and thoroughly washed with water. Purification of the compound was performed through column chromatography using $CHCl_3$ as the eluting solvent and finally through recrystallization from $CHCl_3$-MeOH (1:1) mixture Yield, 1.1 g, (73%). ^{1}H NMR (400 MHz, DMSO-d_6, δ/ppm): 12.25 (s, 1H, NH (imidazole)), 8.75 (s, 4H, $2H_{3'}$+$2H_6$), 8.67 (d, 2H, J=10.8 Hz, H_3), 8.26 (d, 2H, J=11.6 Hz, H_8), 8.00-8.06 (m, 2H, H_7), 7.50-7.54 (m, 2H, H_4), 7.38 (d, 6H, J=11.6 Hz, H_5+H_9), 6.71 (d, 4H, J=12 Hz, H_{10}), 2.48 (s,12H, Me). ESI-MS: m/z 614.34 ($[L+H]^+$). Anal. Calcd for $C_{40}H_{35}N_7$: C, 78.28; H, 5.75; N, 15.97. Found: C, 78.05; H, 5.82; N, 12.75.

4.2.3. Synthesis of Metal Complexes. [(tpy-PhCH$_3$)Ru(tpy-HImzPh$_3$(NMe$_2$)$_2$)] (ClO$_4$)$_2$·H$_2$O (1). Ru(tpy-$PhCH_3$)Cl_3 (80 mg, 0.15 mmol) and tpy-HImzPh$_3$(NMe$_2$)$_2$ (92 mg, 0.15 mmol) were added to 10 mL ethylene glycol and refluxed for 2h under Ar protection. The resulting solution was cooled to RT and upon spilling into an aqueous solution of $NaClO_4$ a red compound deposited. The compound was collected and purified by silica-gel column chromatography eluting with CH_3CN. Recrystallization from CH_3CN-MeOH (1:1, v/v) mixture results in the formation of a red microcrystalline compound. Yield: 97 mg (52%). ^{1}H NMR (400 MHz, DMSO-d_6, δ/ppm): 12.48 (s, 1H, NH (imidazole)), 9.51 (s, 2H, 2$H_{3'}$), 9.44 (s, 2H, $H_{3''}$), 9.09 (d, 4H, *J*=10.8 Hz, H_6+$H_{6'}$), 8.53 (d, 2H, *J*=6.8 Hz, H_8), 8.35 (d, 2H, *J*=10.8 Hz, H_7), 8.27 (d, 2H, *J*=11.6 Hz, $H_{8'}$), 8.01-8.08 (m, 4H, H_4+$H_{4'}$), 7.51-7.58 (m, 10H, H_3+$H_{3'}$+$H_{7'}$+H_9), 7.24-2.30 (m, 4H, H_5+$H_{5'}$), 6.90 (d, 4H, *J*=10.8 Hz, H_{10}), 2.48 (s, 12H, NMe_2)), 2.35 (s, 3H, Me). ESI-MS (positive, CH_3CN) *m/z* = 519.21 (100 %) $[(tpy\text{-}PhCH_3)Ru(tpy\text{-}HImzPh_3(NMe_2)_2)]^{2+}$. Anal. Calcd. for $C_{62}H_{54}N_{10}Cl_2O_9Ru$: C, 59.33; H, 4.34; N, 11.16. Found: C, 59.11; H, 4.21; N,11.02.

$[Ru(tpy\text{-}HImzPh_3(NMe_2)_2)_2](ClO_4)_2\cdot 2H_2O$(2) Synthetic protocol for **2** is basically similar to that of **1**. In this case $Ru(DMSO)_4Cl_2$ (72 mg, 0.15 mmol) and tpy-$HImzPh_3Me_2$ (184 mg, 0.30 mmol) were taken in 1:2 molar ratio in ethylene glycol and refluxed for 3h. The compound was purified successively by silica gel column chromatography as well as recrystallization from MeCN-MeOH (1:1, v/v) in weakly acidic condition Yield: 94 mg (40%). ^{1}H NMR (400 MHz, DMSO-d_6, δ/ppm): 12.71 (s, 1H, NH(imidazole)), 9.75 (s, 4H, $H_{3'}$), 9.10 (d, 4H, *J*=8.0 Hz H_6), 8.70 (d, 4H, *J*=11.6 Hz, H_8), 8.63 (d, 4H, *J*=8.0 Hz, H_7), 8.07 (t, 4H, *J*=10.0 Hz, H_4), 7.52 (d, 4H, *J*=8.0 Hz, H_3), 7.47 (d, 4H, *J*=8.0 Hz, H_9), 7.23 (t, 4H, *J*=10.6 Hz, H_5), 6.86 (d, 8H, *J*=12.0 Hz, H_{10}), 2.48 (s, 24H, NMe_2). ESI-MS(positive,CH_3CN) *m/z* = 664.25 (100%) $[Ru(tpy\text{-}HImzPh_3\ (NMe_2)_2)_2]^{2+}$. Anal. Calcd. for $C_{80}H_{74}N_{14}Cl_2O_{10}Ru$: C, 61.46; H, 4.77; N, 12.54. Found: C, 61.11; H, 4.23; N,12.75.

$[(H_2pbbzim)Ru(tpy\text{-}HImzPh_3(NMe_2)_2)](ClO_4)_2\cdot H_2O$ (3) Complex **3** was prepared by following the same procedure as **1**. In this case $[(H_2pbbzim)RuCl_3]$ (78 mg, 0.15 mmol) was used in place of $Ru(tpy\text{-}PhCH_3)Cl_3$ and recrystallization was carried out in CH_3CN-H_2O (2:1, v/v) mixture under weakly acidic condition. Yield: 90 mg (48%). ^{1}H NMR (400 MHz, DMSO-d_6, δ/ppm): 15.0 (s, 1H, NH(Py2,6)), 12.85 (s, 1H, NH(imidazole)), 9.62 (s, 2H, $H_{3'}$), 8.86 (d, 2H, *J*=10.8 Hz, H_6), 8.71 (d, 2H, *J*=11.2 Hz, H_8), 8.65-8.62 (m, 2H, H_{15}), 8.50-8.47 (m, 1H, H_{16}), 8.38 (d, 2H, *J*=11.6 Hz, H_7), 7.89-7.86 (m, 2H, H_4), 7.61 (d, 2H, *J*=10.8 Hz, H_{14}), 7.41 (d, 6H, *J*=11.8 Hz, H_3+H_9), 7.25-7.24 (m, 4H, H_5+H_{13}), 7.0 (t, 2H, *J*=10.4 Hz, H_{12}), 6.70 (d, 4H, *J*=11.2 Hz, H_{10}), 6.05 (d, 2H, *J*=10.8 Hz, H_{11}), 2.48 (s, 12H, NMe_2). ESI-MS (positive, CH_3CN) *m/z* = 513.21 (100

%) $[(H_2pbbzim)Ru(tpy\text{-}HImzPh_3(NMe_2)_2]^{2+}$. Anal. Calcd. for $C_{59}H_{50}N_{12}Cl_2O_9Ru$: C, 57.01; H, 4.05; N, 13.52. Found: C, 56.61; H, 3.83; N,13.85.

Caution! Perchlorate salts of the metal complexes are explosive and should be handled in small amount with extreme care

4.2.4. Physical Measurements. The details of different equipments used and experimental process to measure absorption and luminescence spectral behaviors, electrochemical investigations methods have been discussed in chapter 2.

4.2.5. Artificial Neural Networks (ANNs). An artificial neural network is a network stimulated by the central nervous system of the animals, primarily the brain. ANNs are often employed to guess functions which could rely on huge number of unknown inputs. Among the two principal categories of neural networks, viz. recurrent (RNN) and feed-forward (FFN), we employed FNN in the present study due to static nature of our system. FNN is the simplest and convenient category of network where the information passes into a particular direction, proceeds, from the input nodes, via the hidden notes, and finally to the output nodes. Additionally, due to its high efficiency in forecasting static system, we implemented advanced feed-forward back propagation network, namely, ANN-function fitting (ANN-FF) network for deeper understanding and forecasting of the system.

Artificial neural network model consisting of 2 inputs, 5 hidden layers and 1 output. In ANN-FF, the relation between the input and output is assumed to be a function, which is approximated using the experimental data. The network diagram of the ANN-FF for the system can be found in Figure 4.26. It can fit multidimensional mapping problems arbitrarily well when consistent data and enough neurons are designed in the hidden layer. For function fitting problem, a neural network is needed to map between a data set of numeric inputs and a set of numeric targets. Hence, each pattern is assigned a number (e.g., 1, 2, 3, 4, etc.).

In this study, a neural network for function fitting was coded in MATLAB 2018. The input data present the network, while the target data define the desired network output. Table 4.6 represents the emission intensity outputs upon the action of 40 different combinations of two inputs (input 1=H^+ and input 2=F^-). Thus, the 40×2 matrix represents the static input data of 40 samples involving 2 inputs, while 40×1 matrix represents the static output data (at 678 nm) of one element. Now, the 40 samples are divided into 3 sets of data. 70% of the data are conferred for the training and the network is corrected according to its error. Now the learning algorithm and the number of neurons in the hidden layer were optimized. 15% data are employed to compute the network generalization and to halt training. When generalization stops improving, the data validation takes place. The remaining 15% data give an independent estimate of the network performance during and after the training, called testing data (Figure 4.25).

4.2.6. Adaptive Neuro-Fuzzy Inference System (ANFIS). The network framework of the ANFIS is illustrated in Figure 4.28. It consists of five connected layers (excluding input layer) which is common for the two input dimensions, P and Q, both of which possess three fuzzy sets, viz. C1C2C3 for P, while D1D2D3 for Q input. We have chosen A number of inputs and B number of fuzzy set to represent each input which in turn implies A×B number of nodes in Layer 1. In Layer 2, all the nodes are interconnected with the membership function output of each input node, yielding a total of B^A node in Layer 2. Layer 3 and 4 possess the same number of nodes as that of Layer 2. Layer 5, on the other hand, possess only one node representing the output of the network. Upon considering each input as a node, the total number of nodes in the architecture will be A + A×B + 3×B^A + 1. In ANFIS, only the membership function parameters in Layer 1 and inputs weight in Layer 4 are to be predicted by training. Upon implication of the triangular membership function (*trimf*) which is represented by three parameters, we need to assess 3×B×A premise parameters in Layer 1 and A×B^A consequent weight parameters in Layer 4.

The structure of the ANFIS is automatically tuned by least-squares estimation and the back-propagation algorithm. A fuzzy set A of a universe of discourse X is represented by a collection of ordered pairs of generic elements and its membership function $\mu_A(x)$: X tends to [0 1], which associates a number $\mu A(x)$ to each element x of X. The fuzzy logic controller works on the basis of a set of control rules (called the fuzzy rules) among the linguistic variables. These fuzzy rules are represented in the form of conditional statements.

The basic structure of the pattern predictor model developed using ANFIS to predict the pattern of the flow regime consists of four important parts, namely, the fuzzification, knowledge base, artificial neural network, and defuzzification blocks, as shown in Scheme 1. The inputs to the ANFIS are the H^+ and F^-. These are fed to the fuzzification unit, which converts the binary data into linguistic variables. These in turn are given as inputs to the knowledge base block. The ANFIS tool in MATLAB 2018 developed 49 rules while training the neural network. The knowledge base block is connected to the artificial neural network block. A hybrid optimization algorithm is used to train the neural network and to select the proper set of rules for the knowledge base. To predict the emission intensity values at 678 nm, training is an important step in the selection of the proper rule base. Once the proper rule base is selected, the ANFIS model is ready to carry out prediction. The trained ANFIS was validated using 15% of the data. The output of the artificial neural network unit is given as input to the defuzzification unit, where the linguistic variables are converted back into numerical data in crisp form.

4.3. Results and Discussion

4.3.1. Synthesis and Characterization. Tpy-HImzPh$_3$(NMe$_2$)$_2$ is synthesized upon refluxing a 1:1 ratio of N,N-dimethyaminobenzil and tpy-PhCHO together with excess NH_4OAc in CH_3COOH. The heteroleptic complexes (**1** and **3**) are synthesized by refluxing 1:1 molar proportion of tpy-HImzPh$_3$(NMe$_2$)$_2$ with [(tpy-PhCH$_3$)RuCl$_3$] and [(H$_2$pbbzim)RuCl$_3$, respectively, whereas **2** is prepared by refluxing tpy-HImzPh$_3$ (NMe$_2$)$_2$ and Ru(DMSO)$_4$Cl$_2$ in 1:2 molar proportion in ethylene glycol. All complexes are precipitated as perchlorate salts with $NaClO_4$ and purified via chromatography and recrystallization techniques under mild acidic condition to keep the imidazole NH motifs intact. Characterizations of the compounds are performed through ESI-mass and NMR spectroscopy. Figure 4.1-4.3 display the ESI mass spectra of tpy-HImzPh$_3$(NMe$_2$)$_2$ and the complexes (**1-3**) in MeCN. The agreement among the simulated and experimental isotopic distribution is quite good. The abundant peak appears in the domain of 513.21-664.25 m/z and corresponds to di-positive cation of the complexes. ^{1}H NMR spectra of tpy-HImzPh$_3$(NMe$_2$)$_2$ and the complexes are displayed in Figure 4.4. All the peaks are tentatively assigned by using their ^{1}H-^{1}H COSY NMR spectra and by comparing the spectra of the structurally similar derivatives. All the complexes display a sharp peak at 2.48 ppm corresponding to their NMe$_2$ protons (12 for both **1** and **3** and 24 for **2**). **1** shows a singlet at 2.35 ppm integrating 3 protons due to -CH$_3$ unit in tpy-PhCH$_3$ moiety. The doublet at 6.05 ppm for **3** corresponds to H$_{11}$ in H$_2$pbbzim motif. **1** and **2** displays

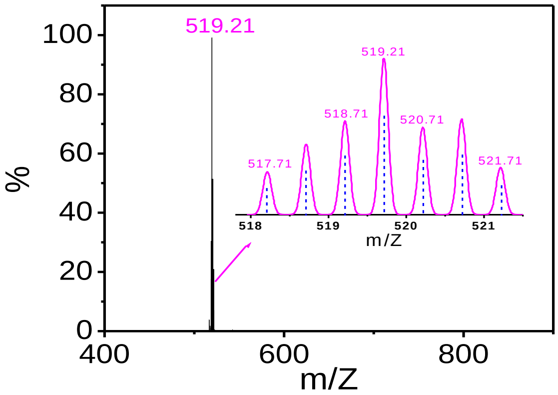

Figure 4.1. ESI (positive) mass spectrum for the complex cation of **1** [(tpy-PhCH$_3$) Ru(tpy-HImzPh$_3$(NMe$_2$)$_2$]$^{2+}$ (m/z = 519.21) in MeCN showing both observed and simulated isotopic distribution patterns.

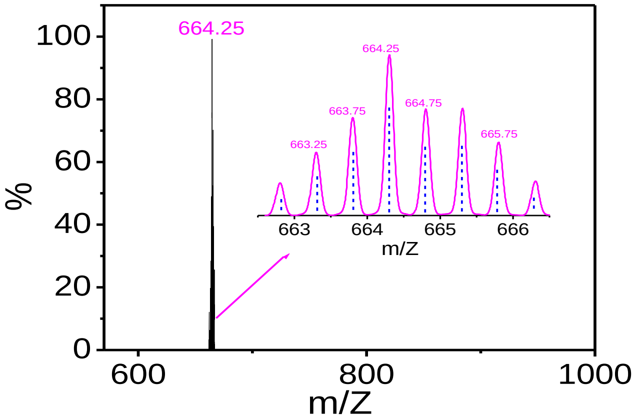

Figure 4.2. ESI (positive) mass spectrum for the complex cation of **2** [Ru(tpy-HImzPh$_3$ (NMe$_2$)$_2$)$_2$]$^{2+}$ (m/z = 664.25) in MeCN showing both observed and simulated isotopic distribution patterns.

one broad singlet at ~12.5 ppm due to imidazole NH proton, while **3** exhibits two NH resonances of unequal intensity at 12.85 and 15.00 ppm due to two types of NH protons. The peak at 12.85 ppm is due to NH of tpy-HImzPh$_3$(NMe$_2$)$_2$, whereas the signal at 15.00 ppm with double intensity corresponds to NH of H$_2$pbbzim. H$_{3'}$, H$_6$, H$_7$ and H$_8$ protons underwent a down-field shift, whereas the phenyl protons and H$_4$ of tpy-unit remain almost unaltered upon coordination to Ru^{2+}. H$_3$ of tpy unit underwent a remarkable up-field shift as it is underneath the ring current of a pyridine ring of another tpy ligand.

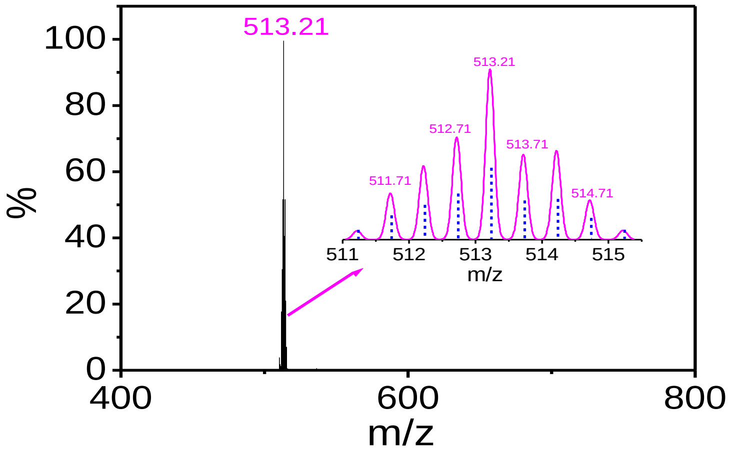

Figure 4.3. ESI (positive) mass spectrum for the complex cation of **3** [(H_2pbbzim)Ru (tpy-HImzPh$_3$(NMe$_2$)$_2$]$^{2+}$ (m/z=513.21) in MeCN showing both observed and simulated isotopic distribution patterns.

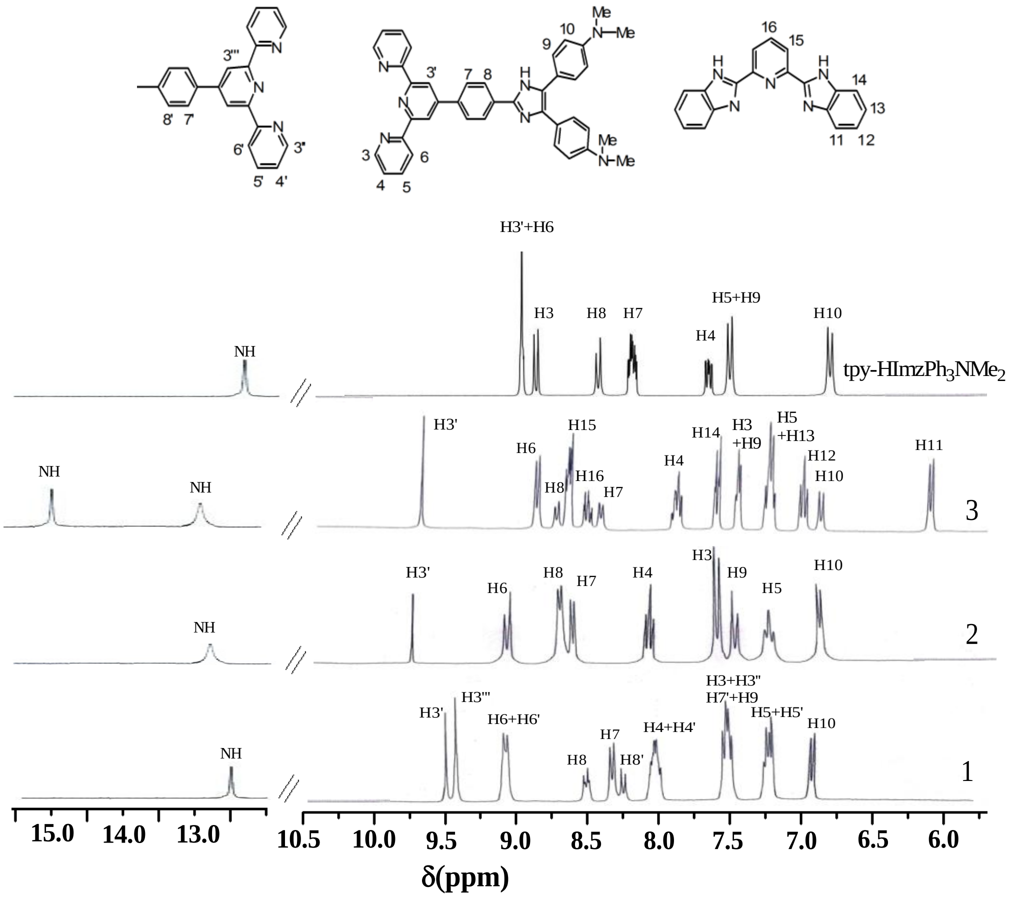

Figure 4.4. ^{1}H NMR spectra of the complexes in DMSO-d_6.

4.3.2. Absorption and Emission Spectra. The spectral data of the complexes, collected in MeCN, DMSO and H_2O, are summarized in Table 4.1. The representative spectra are displayed in Figure 4.5. By comparing the spectra of the structurally related complexes, the intense absorption peak within 488-512 nm can be assigned as Ru (II)→terpyridine charge transfer transition (MLCT), while the peaks within the domain of 330-350 nm as imidazole→tpy intra-ligand charge transfer (ILCT) transitions.[43,52] The very strong peaks at ~280 and ~315 nm is due to $\pi \rightarrow \pi^*$ electronic transition within the ligand framework.

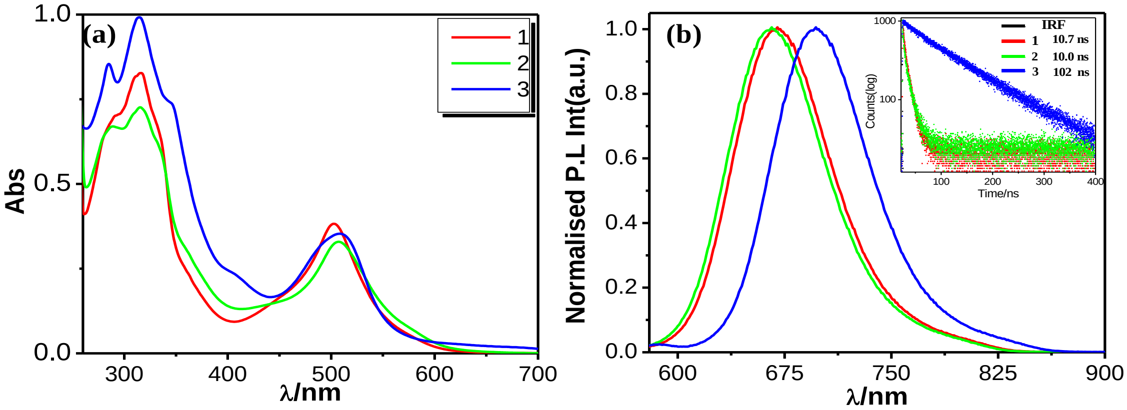

Figure 4.5. Normalized absorption (a) emission (b) (λ_{ex} = 490 nm) spectra of **1-3** in DMSO at RT. The decay profiles and corresponding lifetimes are presented in the inset of (b).

Excitation at the ^{1}MLCT absorption band leads to evolution of an emission band within the range of 658-696 nm. The MLCT absorption and emission band is red-shifted, albeit in small extent, on passing from MeCN to DMSO, probably because of the difference in the degree of NH proton dissociation in polar media. On moving from RT to 77K, a small hypsochromic shift of the emission band occurs together with substantial boost of intensity and quantum yield which is typical of ^{3}MLCT emitters. The noteworthy feature is the RT emissive characters of the complexes compared with their non-luminescent parents ($[Ru(tpy)_2]^{2+}$ or $[Ru(H_2pbbzim)_2]^{2+}$}. Time-correlated single photon counting measurements show that the RT lifetime of the complexes alter in the domain of 5.5 and 28.0 ns in MeCN, while between 12.0 and 18.6 μs at 77 K (Figure.4.6). Hence, the improvement of lifetime is essentially 2 orders of magnitudes greater compared with

Table 4.1. Photophysical Parameters of the Complexes in Various Solvents

Compounds		Absorption λ_{max}/ nm (ε,$M^{-1}cm^{-1}$)	Luminescence		
			λ_{max} / nm	τ/ns	Φ
1	MeCN(298K)	492(37100),327(sh)(62600),308(84600), 285(71800)	662	τ_1=1.6(15%) τ_2=6.0(85%)	1.2×10^{-3}
2		494(39000),330(sh) (73000),310(91800), 287(83200)	658	τ_1=1.2(6%) τ_2=5.5(94%)	0.9×10^{-3}
3		488(45300),345(82400), 328 (91300), 310(103900),284(81200),240(76400)	678	τ=28	2.5×10^{-3}
1	DMSO(298K)	503(38500),330(sh)(66900),315(82900), 290(69800)	670	τ_1=3.3(16%) τ_2=10.7(84%)	1.1×10^{-3}
2		508(33400),332(sh) (60400),314(72800), 288(67100)	665	τ_1=1.6(20%) τ_2=10.0(80%)	1.2×10^{-3}
3		508(35900),346(sh)(73700),314(99400), 285(85200)	696	τ=102	3.2×10^{-3}
1	Water (298K)	495(42300),327(sh)(75700),310(97500), 285(87200)	660	τ_1=0.5(25%) τ_2=9.0(75%)	0.7×10^{-3}
2		498(42500),328(sh)(81300),310(102800) ,286(98300)	658	τ_1=0.5(11%) τ_2=10.0(89%)	0.5×10^{-3}
3		512(40700),347(79300),316(109500), 285(94200)	683	τ_1=10(12%) τ_2=50(88%)	2.1×10^{-3}
1	EtOH-MeOH (4:1),(77K)		633	τ=18.6 μs	0.22
2			638	τ=18.0 μs	0.25
3			664	τ=12.0μs	0.32

$[Ru(tpy)_2]^{2+}$ (0.25 ns). The complexes demonstrate bi-exponential decay in MeCN at RT. The first short-lived exponent is presumably because of deactivation of the ^{3}MLCT state, whereas the second exponent is probably arising from equilibrated state of ^{3}MLCT and ^{3}ILCT. The zero-zero spectroscopic energy (E_{00}) is estimated from their 77K emission maxima. The 77K emission spectra demonstrate vibrational progression with separation of ~800 cm^{-1} recommending the association of ^{3}LC emission characteristics .

The excited-state deactivation of the Ru (II)-polypyridine complexes is frequently be represented by equation 1.[21,22]

$$k_{nr} = k_{nr}^{0} + k'_{nr} \qquad (1)$$

The radiation-less deactivation comprises of two terms. k_{nr}^{0} stands for the decay from the

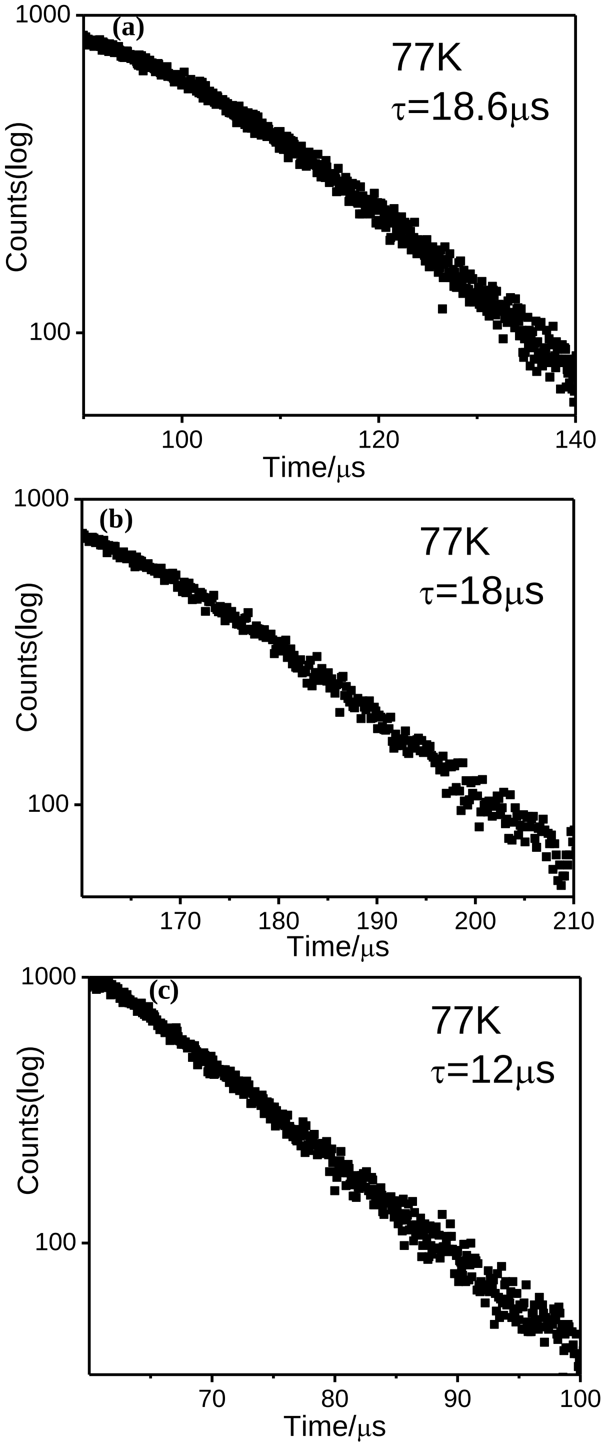

Figure 4.6. Excited state decay profiles together with the lifetime of **1** (a), **2** (b), and **3** (c) in EtOH-MeOH (4:1, v/v) glass at 77 K in MCS mode.

^{3}MLCT to the ground state, whereas k'_{nr} corresponds to surface crossing from ^{3}MLCT to the ^{3}MC state and banks on their energy difference (ΔE). k'_{nr} often plays a key role for Ru-tpy complexes due to their smaller ΔE values. We surmise that the position of ^{3}MC state remains practically constant, while the ^{3}MLCT state gets substantially stabilized because of the {tpy-HImzPh$_3$(NMe$_2$)$_2$} motif in the complexes which actually increases the MLCT-to-MC surface-crossing pathway.

4.3.3. Temperature-Trigged Emission Switching. We have already pointed out that the emission characteristics of the Ru(II)-terpyridine complexes are heavily dependent on ^{3}MLCT-^{3}MC energy gap which in turn is a delicate function of temperature (T). Hence, we use temperature stimulus to alter their emission characteristics. We acquired the emission spectra as well as lifetime within range of 268-330K and the outcomes are summarized in Figure 4.7-4.8 and Table 4.2. Lowering of temperature induces increase in emission intensity and lifetime (τ) indicating the “on-state”, while increase of T causes lowering of both intensity and τ demonstrating the “off- state”. Additionally, the "on-off" and "off-on" emission switching is completely reversible and can be recycled multiple times. For understanding the cause of emission switching upon variation of temperature as well as the to figure out the deactivation dynamics, we analyze the temperature dependent lifetime data of the complexes through the use of equation (2).[21,22]

$$(\tau(T))^{-1} = (k_1 + k_2 \exp[-\Delta E_2/RT])/(1+ \exp[-\Delta E_2/RT] \qquad (2)$$

k_1 stands for temperature-independent rate constant which is the aggregate of k_r and k_{nr} at 77K, while k_2 stands for temperature dependent rate constant which consider the population of ^{3}MC level from ^{3}MLCT state and ΔE_2 corresponds to the activation energy for this surface crossing path. Fitting of 1/τ *vs.* 1/T data gives rise to the values of k_2 and ΔE_2 (Figure 4.7-4.8 and Table 4.2).The estimated value of ΔE_2 is 3574±25, 3731±25, and 3876±72cm^{-1} for **1**, **2**, and **3**, respectively. k_1 varies between 5.5×10^4 and 8.3×10^4 s^{-1}, whereas k_2 alters in the domain of 2.0×10^{13}-2.6×10^{13} s^{-1}. Hence, the calculated ΔE_2 of the complexes are significantly greater relative to the parent, [Ru(tpy)$_2$]$^{2+}$ (ΔE_2=1500 cm^{-1}). The lowering of temperature leads to enhance the population on the emitting ^{3}MLCT state resulting in increase of the emission intensity and τ, whereas increase of temperature promotes thermal population on the ^{3}MC state and leads to quenching of emission intensity and τ. Hence, successive heating and cooling induces "off-on" and "on-off" emission switching upon regulating the population in ^{3}MLCT and ^{3}MC state.

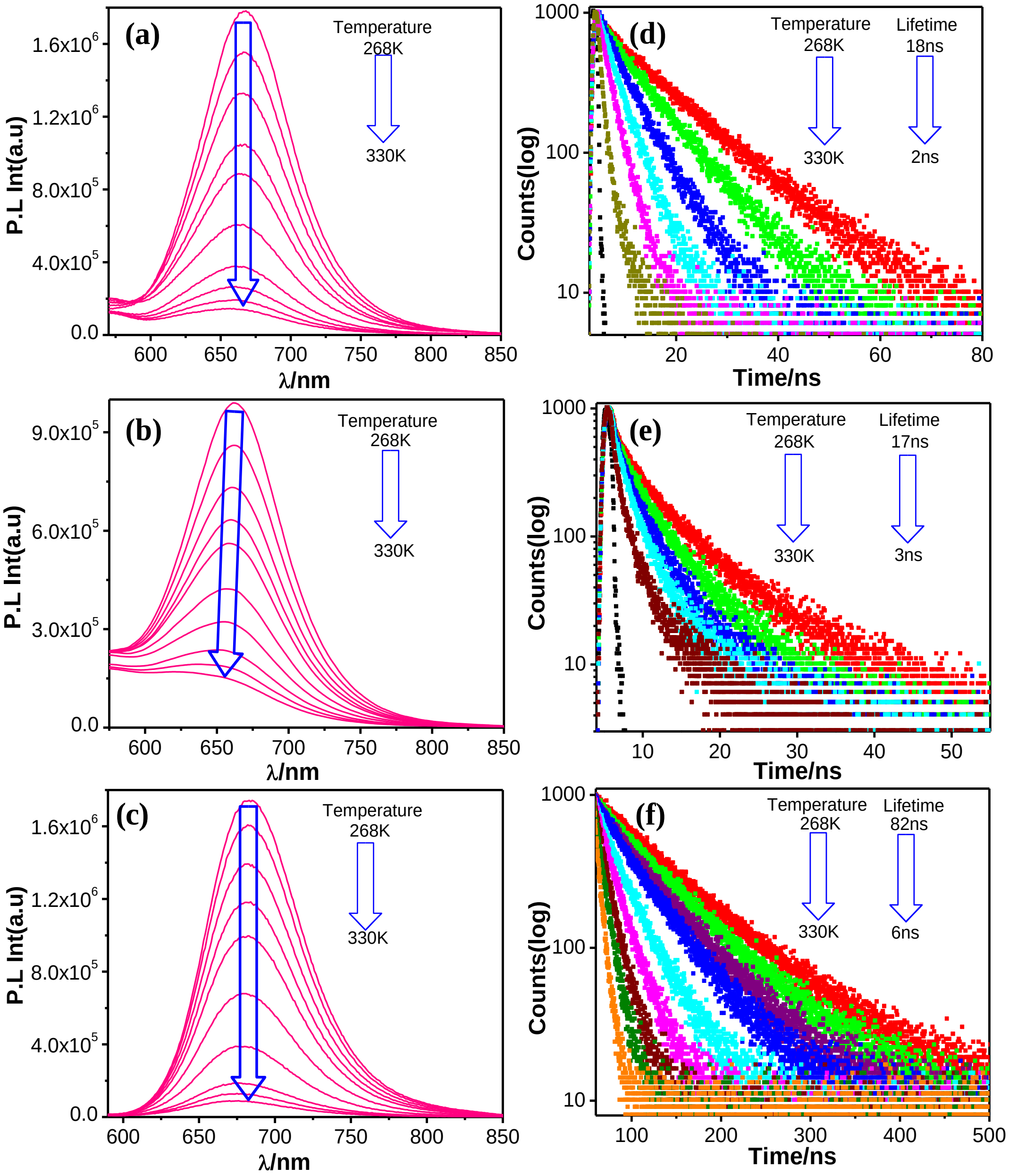

Figure 4.7. Variation of luminescence spectrum (a-c) and excited state decay profile (d-f) of **1**, **2** and **3** respectively, in MeCN as a function of temperature (T).

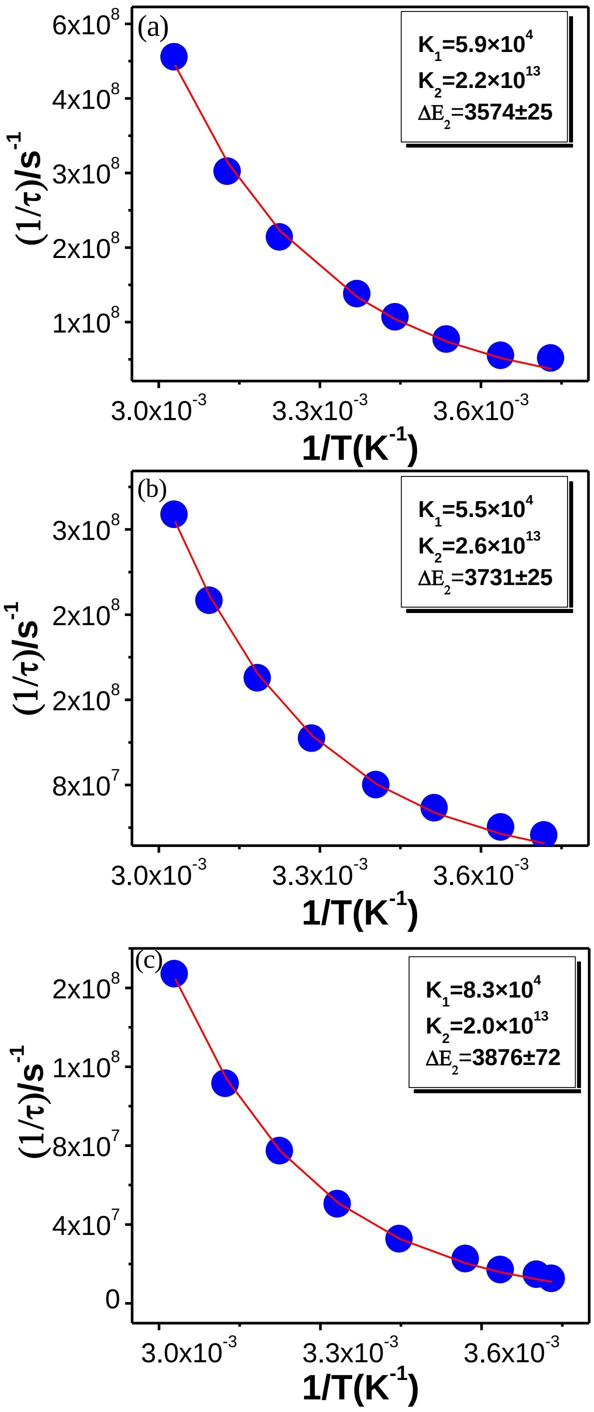

Figure 4.8. Nonlinear fits of 1/τ vs 1/T plot. Inset shows different temperature dependent parameters of the complexes of **1**(a), **2**(b) and **3**(c).

Table 4.2. Non linear fitting parameters of temperature dependent experiment of the complexes (**1-3**) in MeCN

Complex	k_1/s^{-1}	k_2/s^{-1}	ΔE_2/cm^{-1}
1	5.9×10^4	2.2×10^{13}	3574±25
2	5.5×10^4	2.6×10^{13}	3731±25
3	8.3×10^4	2.0×10^{13}	3876±72

4.3.4. Modulation of the Photophysical Behaviours in Presence of Anions. The complexes possess a number of acidic imidazole NH protons in their outer coordination sphere which are able to interact with anions. Hence, we investigated the influence of anions (tetrabutylammonium salts of F$^-$, Cl$^-$, Br$^-$, I$^-$, CN$^-$, AcO$^-$ and $H_2PO_4^-$) on the photophysical properties of the complexes (Figure 4.9-4.10). Appreciable change with respect to their color and spectral portrait are noticed for F$^-$, CN$^-$, AcO$^-$ and $H_2PO_4^-$ in MeCN compared with the rest of the anions. On the contrary, only CN$^-$ promotes small magnitude of change in H_2O. In the absorption spectra, bathochromic shift of the MLCT

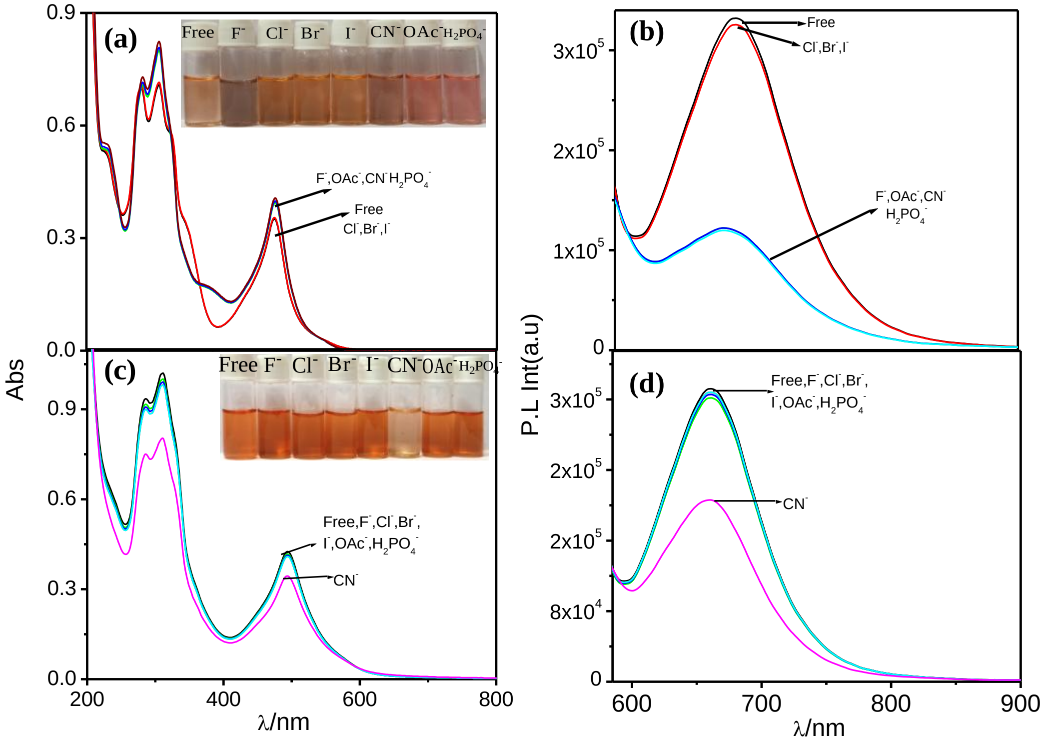

Figure 4.9. Alteration of absorption and emission spectra of **1** in MeCN (a and b, respectively) and water (c and d, respectively) in presence of different anions. Insets of (a) and (b) show the visual color changes.

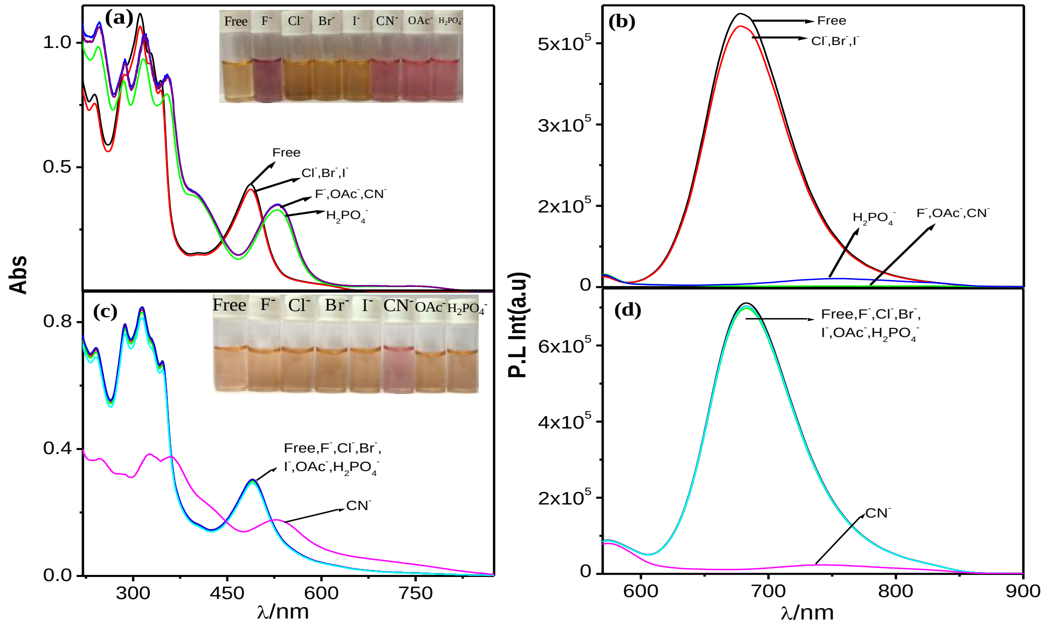

Figure 4.10. Alteration of absorption and emission spectra of **3** in MeCN (a and b, respectively) and water (c and d, respectively) in presence of different anions. Insets of (a) and (b) show the visual color changes.

bands is mostly observed. Emission quenching accompanied with red-shift of the maximum are seen. The magnitude of the change is critically dependent on the basicity of the anions as well as number of NH protons in the complexes. Interestingly, the complexes act as multi-channel sensors for CN^- in H_2O, whereas unselective for F^-, CN^- and AcO^- in MeCN. Selectivity towards CN^- is probably because of its smaller hydration energy ($\Delta G_h°$= -295 kJ/mol for CN^-) and higher basicity relative to F^- ($\Delta G_h°$= -465 kJ/mol) and AcO^- ($\Delta G_h°$= -365 kJ/mol). Greater $\Delta G_h°$ of remaining basic anions restrict them to get hydrated instead of interacting with polarized NH motifs in the complexes.[65]

Spectral titrations are executed for all three complexes in MeCN with different anions to get quantitative information about receptor-anion interplay (Figure 4.11-4.12). Clear-cut change in both the absorption and emission titration are observed upon gradual addition of the anions. One-step change for complex **1**, whereas two-step changes in both **2** and **3** is clearly visible in presence of F^-, CN^- and AcO^-. Spectral behaviour of the complexes induced by $H_2PO_4^-$ alters from the rest. Absorption titration profiles are also accompanied with well-defined isosbestic points in each step. Systematic emission

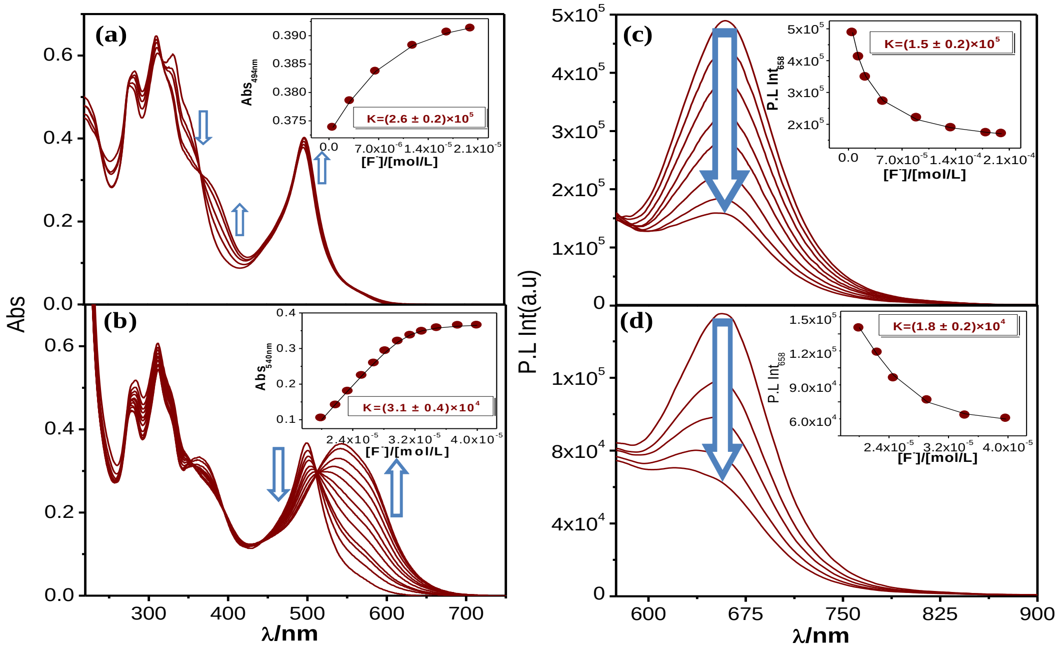

Figure 4.11. Absorption and emission spectral change of **2** in MeCN within 0-2 equiv (a and c, respectively) and within 2-4 equiv of F$^-$ (b and d, respectively). Insets show the fitting profile of the absorbance and emission spectral data along with its 1:1 binding constant.

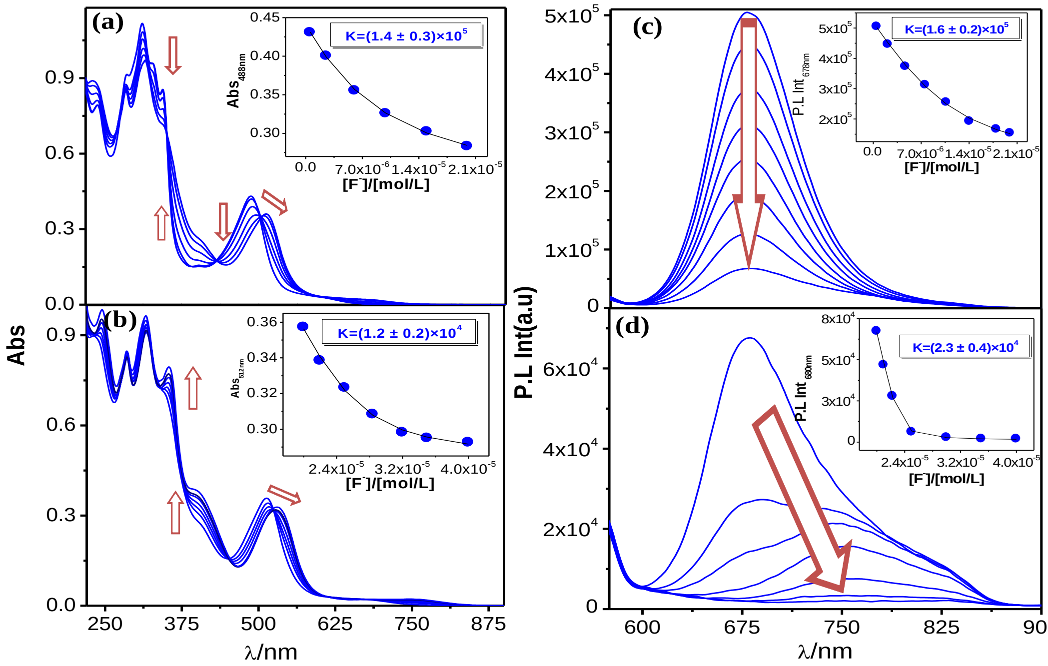

Figure 4.12. Absorption and emission spectral change of **3** in MeCN within 0-2 equiv (aand c, respectively) and within 2-4 equiv of F$^-$ (b and d, respectively). Insets show the fitting profile of the absorbance and emission spectral data along with its 1:1 binding constant.

quenching takes place for all cases, albeit the magnitude and mode of quenching critically relies on the nature of the complex and the basicity of the anions. No spectral-shift of the emission maximum takes place for **1** and **2**, whereas phenomenon quenching together with considerable red-shift of the band (678→682 nm for 1st step and 682→755 nm for 2nd step) occurs in **3**. The spectral portrait of the complexes with CN^- in H_2O resemble closely with MeCN with little change in peak position and intensity (Figure 4.13-4.14). CN^- causes depletion of emission intensity without changes in the peak maximum in both **1** and **2**. For **3**, two-step change takes place with CN^-. The shift of MLCT band maximum from 492 nm to 495 nm occurs in first step (up to 6 equiv) and finally shifted to 533 nm in the subsequent step with excess CN^-. In line with absorption spectra, the reduction of emission intensity in **3** also happens in two consecutive steps with small bathochromic-shift of the band maximum. The extent of change is little less in H_2O compared with MeCN for all three complexes. Emission lifetime of the complexes are acquired in MeCN and H_2O in presence of selected anions. **1** and **2** shows double-exponential decay, whereas **3** displays single-exponential decay in MeCN. F^- or CN^- leads to gradual decrease in lifetime for both components with reduction of overall lifetime of the complexes. The degree of lifetime shortening is greater for **3** (28 ns → 4.2 ns) relative to both **1** (6.0 ns → 1.5 ns) and **2** (5.5 ns →1.8 ns). In aqueous medium, only CN^- brings

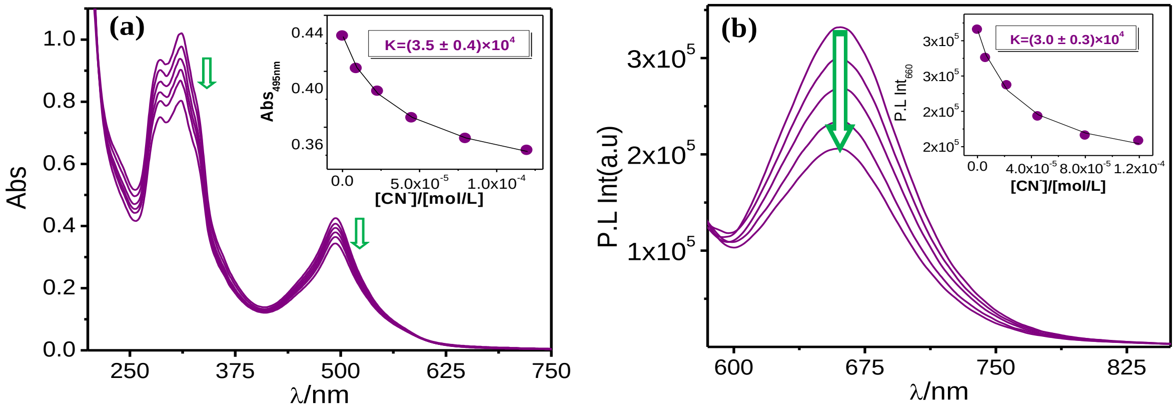

Figure 4.13. Change in UV-vis absorption (a) and luminescence (b) spectrum of **1** in water-HEPES buffer (pH = 7.4) upon incremental addition of CN^-. Insets show the fit of the experimental data to a 1:1 binding profile.

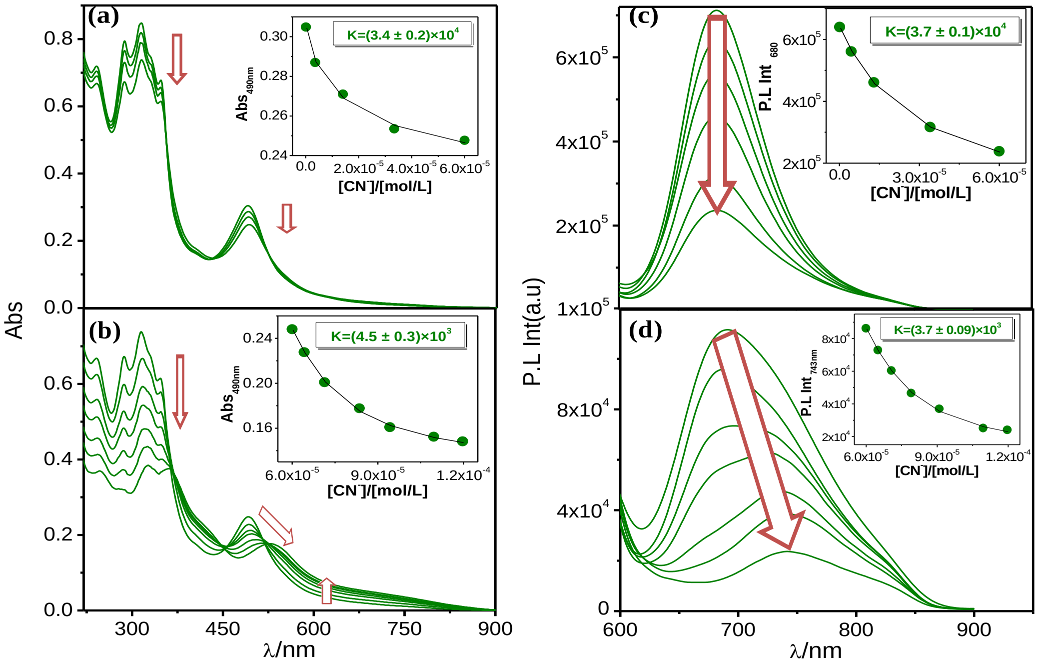

Figure. 4.14. Absorption and emission spectral change of **3** in water-HEPES buffer within 0-6 equiv (a and c, respectively) and within 6-10 equiv of CN^- (b and d, respectively). Insets show the fitting profile of the absorbance and emission spectral data along with its 1:1 binding constant.

about small decrease in lifetime and extent is again higher with **3** compared with **1** and **2**. A representative figure is provided in Figure 4.15. Hence, substantial variation of emission intensity as well as lifetime on the action of specific anions leads to recognize the anion sensing behaviours of the present complexes. The extent of interplay among the complexes and anions was estimated through the calculation of their equilibrium/binding constant by using the spectral titration data and the estimated values are in the order of 10^5 in MeCN and 10^4 in H_2O (Table 4.3). The limit of detection for CN^- in H_2O varies within the range of 2.3×10^{-8} M and 9.5×10^{-8} M (Table 4.4 and Figure 4.16-4.19). It is amazing that the values are below than that of the permissible level (0.2 ppm) for drinking water as recommended by Environment Protection Agency (EPA).[66] Good selectivity and sensitivity together with their chromogenic and fluorogenic conduct makes the complexes as useful for recognizing CN^- in water.

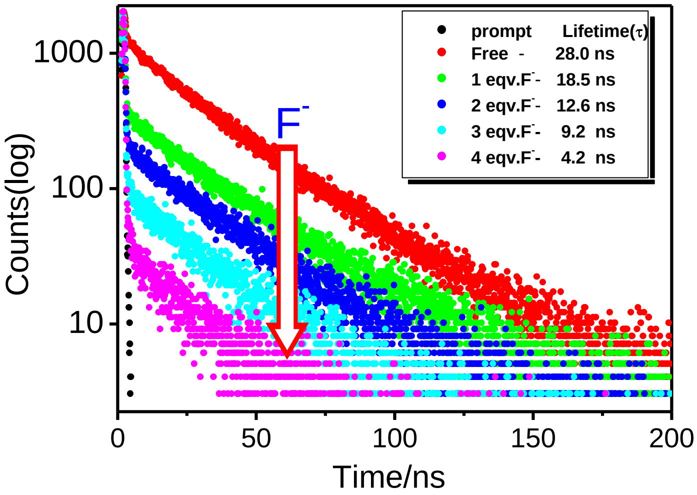

Figure 4.15. Change of excited state decay profile of **3** with the variation of F⁻ in MeCN medium. Inset shows the value of lifetime in presence of different equivalent of F⁻ added.

Table 4.3. Value of Binding Constants [a,b] (K) for **1-3** in MeCN and H_2O at RT

From Absorption spectra (acetonitrile medium)						
Anions	**1**		**2**		**3**	
	K_1	K_2	K_1	K_2	K_1	K_2
F⁻	1.7×10^5	-	2.6×10^5	3.1×10^4	1.4×10^5	1.2×10^4
	From Absorption spectra (aqueous medium)					
CN⁻	3.5×10^4		2.8×10^4	-	3.4×10^4	4.5×10^3
From Emission spectra (acetonitrile medium)						
Anions	**1**		**2**		**3**	
	K_1	K_2	K_1	K_2	K_1	K_2
F⁻	1.6×10^5	-	1.5×10^5	1.8×10^4	1.6×10^5	2.3×10^4
From Emission spectra (aqueous medium)						
CN⁻	3.0×10^4	-	3.8×10^4		3.7×10^4	3.7×10^3

[a] t-Butyl salts of the respective anions were used for the studies.

[b] Estimated errors were < 15 %.

Table 4.4. Detection Limit of **1-3** in MeCN and H_2O

Compounds	Detection Limit (M) in acetonitrile medium		Detection Limit (M) in aqueous medium	
	F^-		CN^-	
	Absorption	Emission	Absorption	Emission
1	2.3×10^{-8}	4.0×10^{-8}	7.5×10^{-8}	7.3×10^{-8}
2	6.3×10^{-8}	8.0×10^{-8}	7.9×10^{-8}	8.0×10^{-8}
3	4.0×10^{-8}	9.5×10^{-8}	7.5×10^{-8}	7.8×10^{-8}

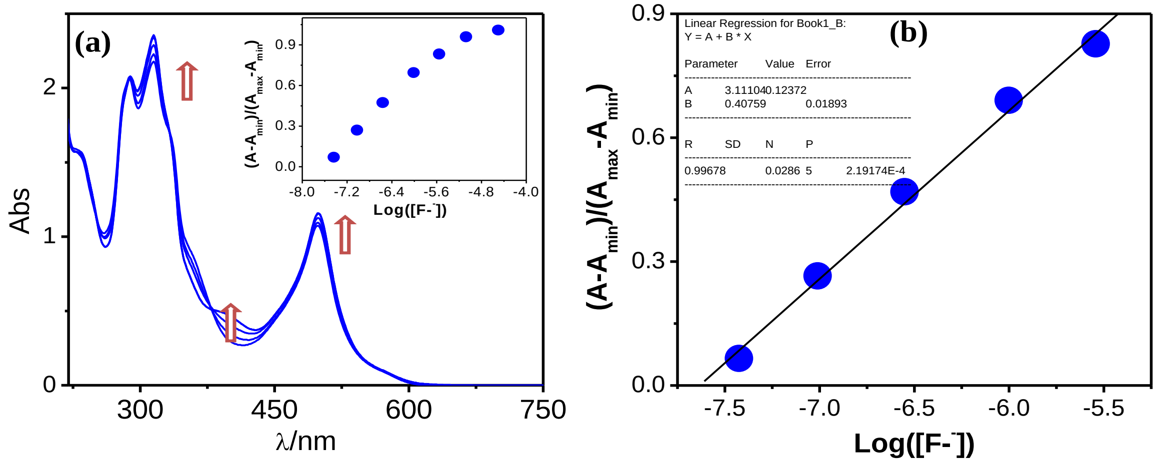

Figure 4.16. (a) Absorption spectral changes during the titration of the receptor **1** (1.0×10^{-5} M) with F^- in MeCN, inset: Normalized absorbance between the minimum absorbance and the maximum absorbance. (b) A plot of $(A-A_{min})/(A_{max}-A_{min})$ vs. Log ($[F^-]$), the calculated detection limit of receptor is 2.3×10^{-8} M.

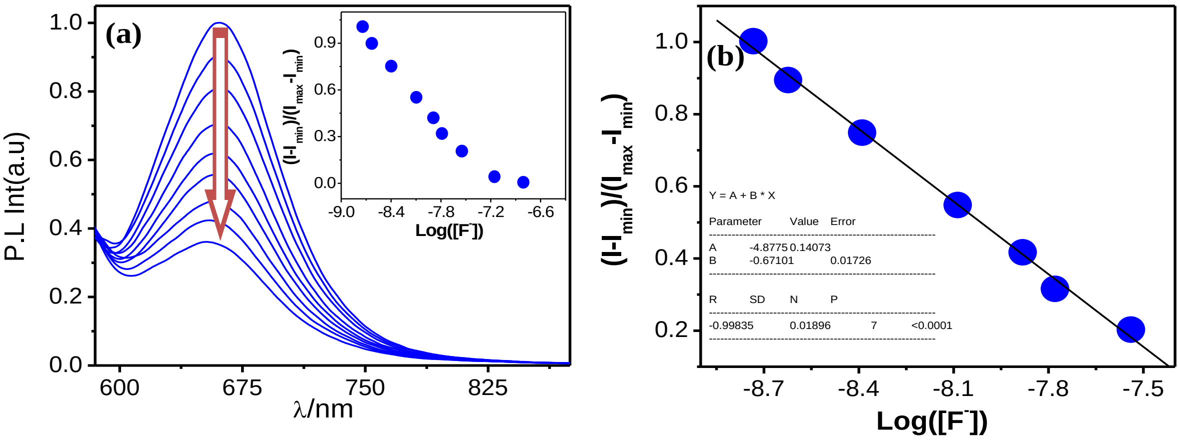

Figure 4.17. (a) Emission spectral changes during the titration of the receptor **1** (1.0×10^{-5} M) with F^- in MeCN, inset: Normalized intensity between the minimum intensity and the maximum intensity. (b) A plot of $(I-I_{min})/(I_{max}-I_{min})$ vs Log ($[F^-]$), the calculated detection limit of receptor is 4.0×10^{-8} M.

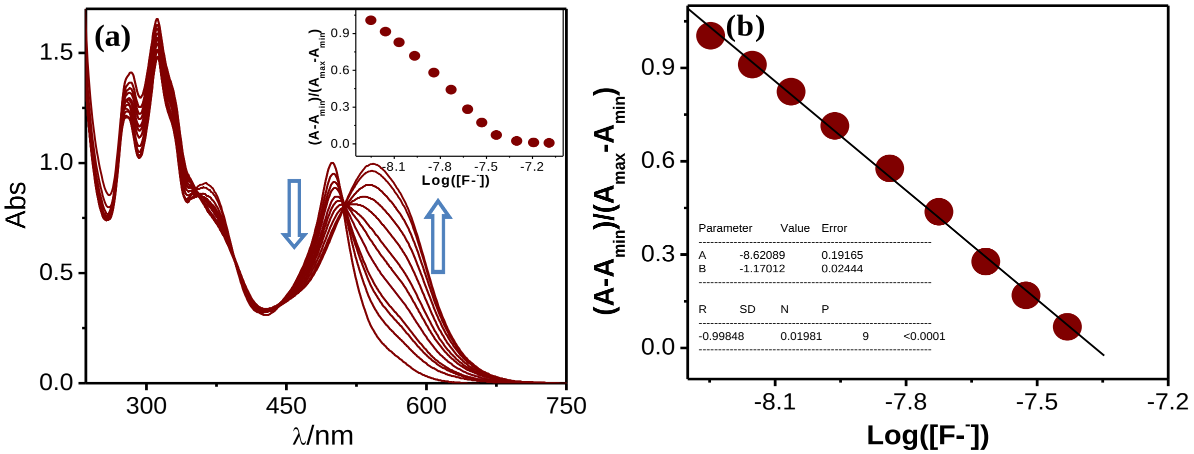

Parameter	Value	Error
A	-8.62089	0.19165
B	-1.17012	0.02444

R	SD	N	P
-0.99848	0.01981	9	<0.0001

Figure 4.18. (a) Absorption spectral changes during the titration of the receptor **2** (1.0×10^{-5} M) with F^- in MeCN, inset: Normalized absorbance between the minimum absorbance and the maximum absorbance. (b) A plot of $(A-A_{min})/(A_{max}-A_{min})$ vs. Log ($[F^-]$), the calculated detection limit of receptor is 6.3×10^{-8} M.

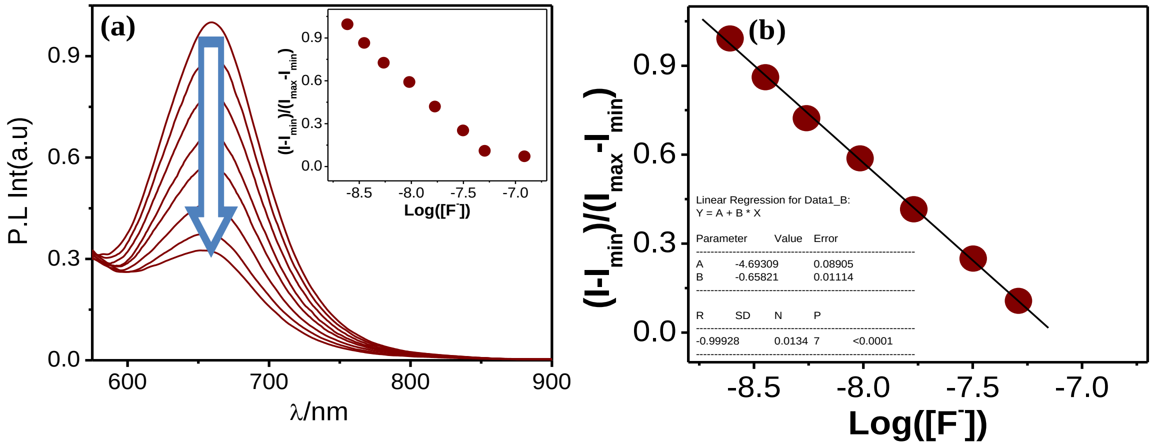

Linear Regression for Data1_B:
Y = A + B * X

Parameter	Value	Error
A	-4.69309	0.08905
B	-0.65821	0.01114

R	SD	N	P
-0.99928	0.0134	7	<0.0001

Figure. 4.19. (a) Emission spectral changes during the titration of the receptor **2** (1.0×10^{-5} M) with F^- in MeCN, inset: Normalized intensity between the minimum intensity and the maximum intensity. (b) A plot of $(I-I_{min})/(I_{max}-I_{min})$ vs Log ($[F^-]$), the calculated detection limit of receptor is 8.0×10^{-8} M.

4.3.5. Binary Logic Functions. In the previous sections, we convincingly demonstrated remarkable modification of the spectral behaviour of the complexes upon the influence of anions. In particular, the emission quenching was feasible in presence of anions or by increasing temperature and restoration of the initial state is attainable in presence of acid or by decreasing temperature. Hence, the complexes display alternate "on-off" and "off-on" emission switching upon proper manipulation of the stimuli. In this section, we will utilize their spectral responses for mimicking the functions of various Boolean and Fuzzy logic gates.

4.3.5.1. IMPLICATION Gate. It represents a conditional logical operation which is read as "If A, then B," and is designated as A⊃B or A→B. To execute the function of the IMPLICATION gate, we have chosen H^+ and F^- as inputs and the emission response at 678 nm as the output. On addition of F^-, the emission intensity gets quenched below the threshold level indicating the "OFF" state (0) (Figure 4.20). By contrast, other three plausible combinations of inputs generate the "ON" state (1).

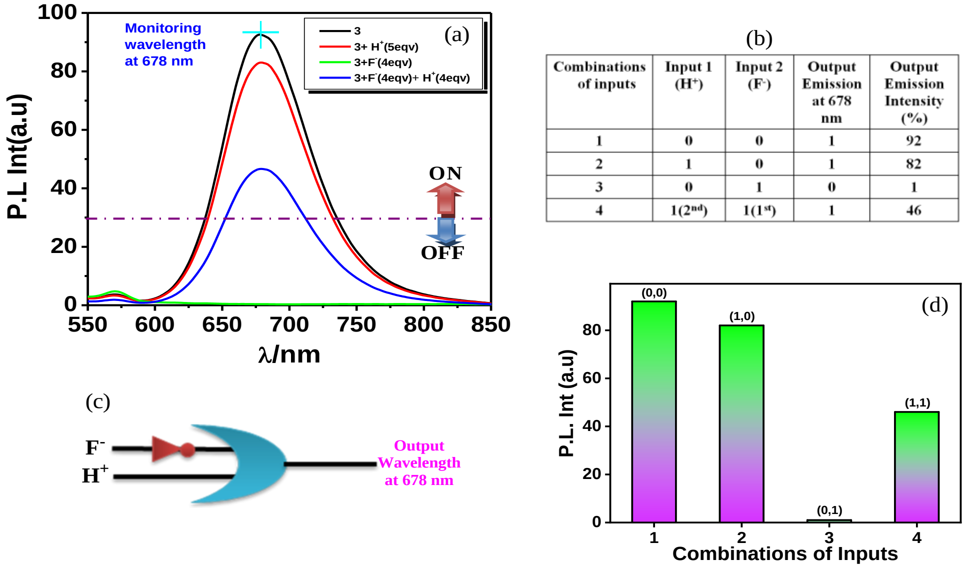

Combinations of inputs	Input 1 (H^+)	Input 2 (F^-)	Output Emission at 678 nm	Output Emission Intensity (%)
1	0	0	1	92
2	1	0	1	82
3	0	1	0	1
4	1(2nd)	1(1st)	1	46

Figure 4.20. (a) Emission spectrum of **3** in the presence of H^+ and F^-. (b) Truth table of the IMPLICATION gate. (c) Schematic diagram of this logic system. (d) Histogram of emission intensity in presence of different combinations of inputs.

4.3.5.2. Keypad Lock. Molecular level information could be secured through the use of keypad lock. Herein, we use F^- and H^+ as the inputs and the absorbance at 543 nm for **2** as the output. H^+ is assigned as "C", whereas F^- is designated as "A". "N" and "E" implies the "ON-" and "OFF state", respectively (Figure 4.21). The absorbance lies underneath the threshold in absence of both H^+ and F^- representing the "OFF" state. The sequential addition of "C" followed by "A" represents the "ON-state" and creates the password "CAN". Altering the sequence ("A" followed by "C"), on the other hand, generates the “OFF” state and creates the incorrect password, “ACE”. Thus, only the authorized user can access the secured information (Figure 4.21c).

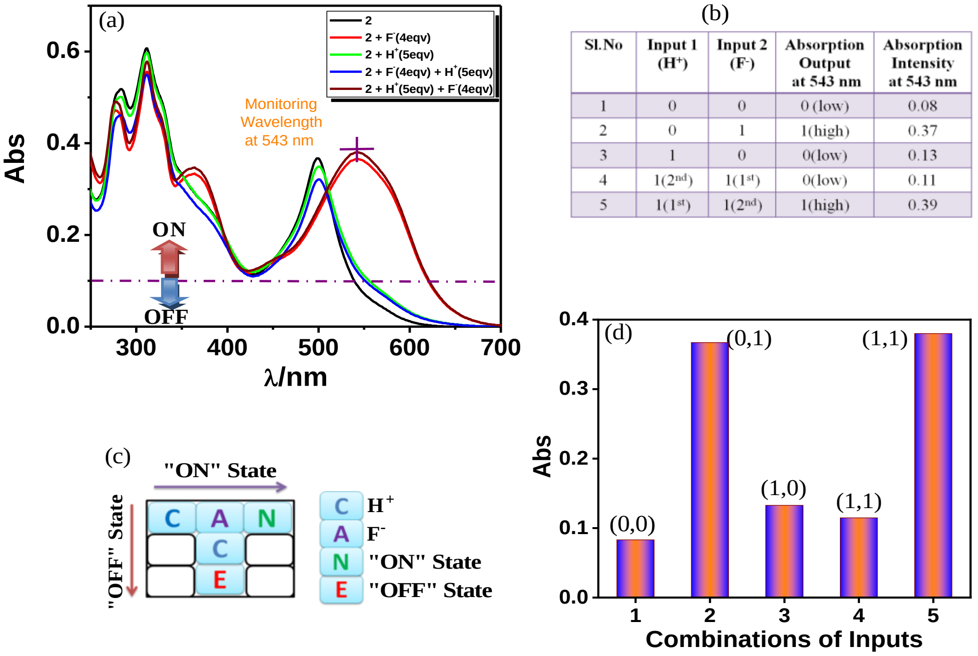

Sl.No	Input 1 (H^+)	Input 2 (F^-)	Absorption Output at 543 nm	Absorption Intensity at 543 nm
1	0	0	0 (low)	0.08
2	0	1	1(high)	0.37
3	1	0	0(low)	0.13
4	1(2nd)	1(1st)	0(low)	0.11
5	1(1st)	1(2nd)	1(high)	0.39

Figure 4.21. (a) Absorption spectrum of **2** in the presence of H^+ and F^-. (b) Truth table of the molecular level keypad lock. (c) Schematic diagram of this logic system. (d) Histogram of absorption intensity in presence of different combinations of inputs.

4.3.6. Fuzzy Logic Operations. FL is an expansion of classical set theory and is based on the hypothesis of fuzzy set theory proposed by Zadeh. BL can express only two crisp values at the two extreme (either zero or one) and unable to define the innumerable number of intermediate states. By contrast, FL offers the advantage of expressing the intermediate states. Thus, FL is a potential alternative to handle the inconclusive details of complicated chemical reactions. Figure 4.22 represents the alteration of emission intensity of **3** upon the action of F^- (input 1) and H^+ (input 2). Considering the unspecified character and great extent of change, the variables could be expressed in the form of lingual variables of the triangular membership functions (*trimf*) such as low, medium, and high. The influence of varying proportion of F^- and H^+ on the emission intensity of **3** can be presented in the form of fuzzy sets (Figure 4.23). A collection of

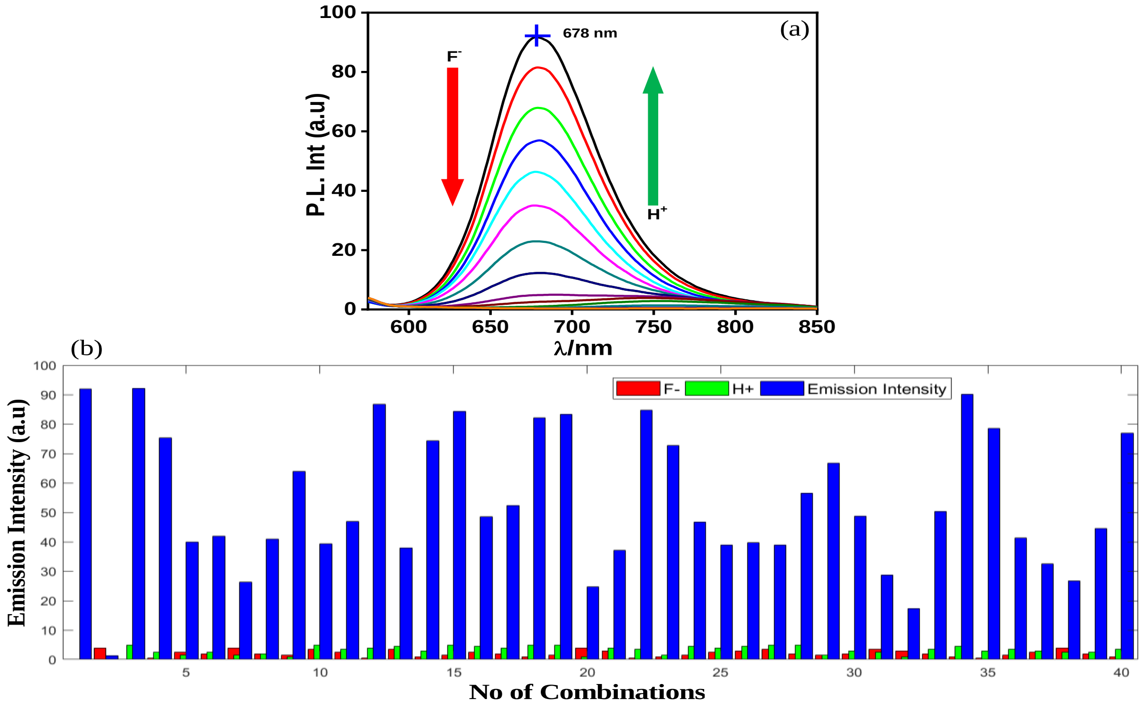

Figure 4.22. (a) Emission spectrum of **3** in the presence of F$^-$ and H$^+$. (b) Histogram of emission intensity in presence of 40 different combinations of inputs.

different IF-THEN rules encompassing the inference rules is presented in Table 4.5. IF-specifies to the predecessors, the THEN-part corresponds to the consequence. The decrease in emission intensity at 678 nm takes place in presence of F$^-$, while the reverse situation takes place if H$^+$ is added. Consequently, FL logic is applied to **3** as presented in Table 4.5. The possible combination of F$^-$ and H$^+$ yields 15 rules (Table 4.5 and Figure 4.24). Additionally, the alteration of emission response upon cooperative actions of F$^-$ and H$^+$ is sketched in a 3D plot (Figure 4.23).

4.3.7. Artificial Neural Network (ANN). As pointed out earlier, ANN is a suitable network where the information moves towards a definite direction, go ahead from the input nodes through the hidden notes, and eventually to the output nodes. Moreover, we applied ANN-function fitting (ANN-FF) array for proper understanding and better prediction of our static system. Levenberg-Marquardt algorithm is employed to train the data. Herein, the ANN-FF is coded in MATLAB 2018 [67] and the details of experimental procedure are already presented in Experimental Section. Input data is used to represent

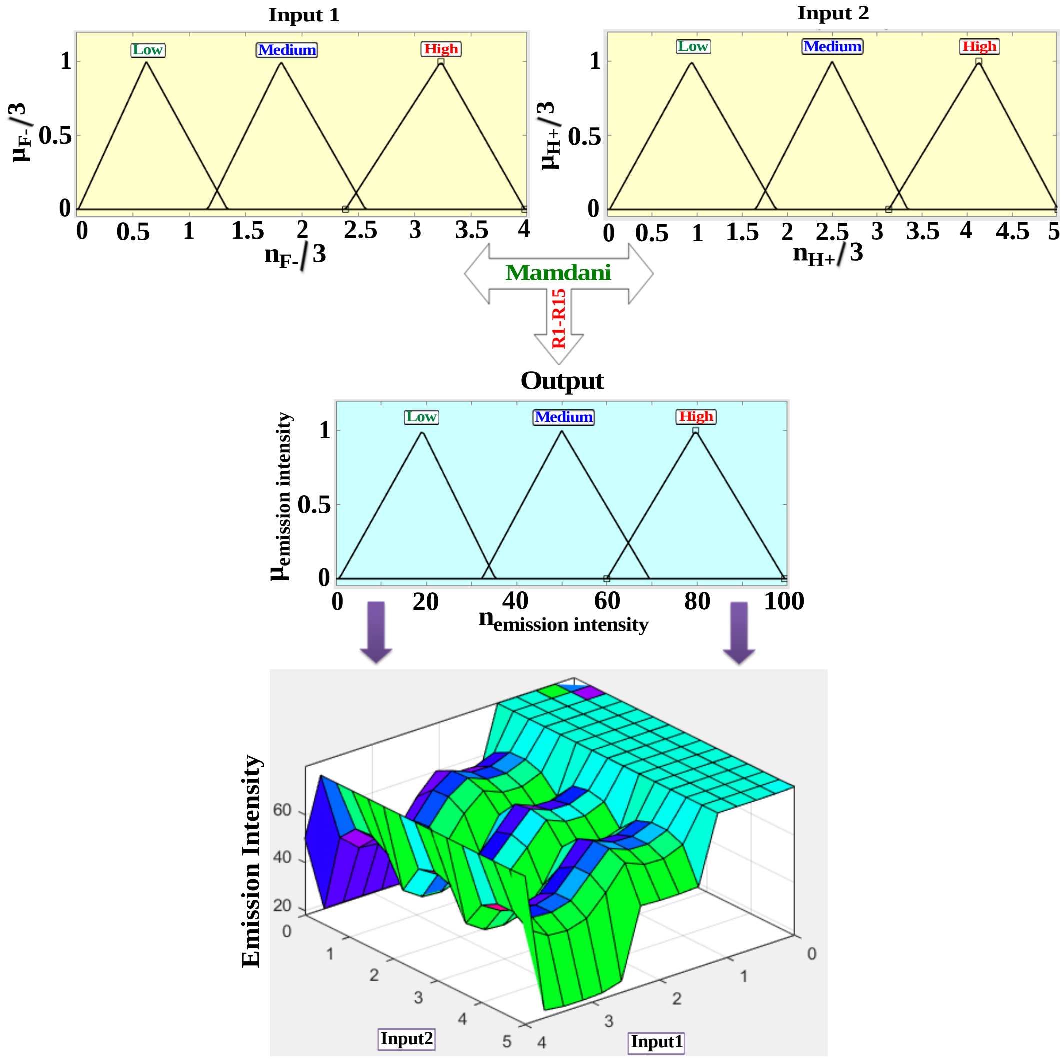

Figure 4.23. Schematic representation of FL system maintaining fuzzy inference rules upon observing emission response as a function of F^- and H^+. Fuzzy variables are fragmented in three triangular membership functions. (a) F^-: (1) low (trimf μ_{low}, [0.0127 0.616 1.33]); (2) medium (trimf μ_{medium}, [1.167 1.817 2.567]) (3) high (trimf μ_{high}, [2.39 3.236 3.98]). (b) H^+: (1) low (trimf μ_{low}, [0.02683 0.9368 1.877]); (2) medium (trimf μ_{medium}, [1.65 2.5 3.34]) (3) high (trimf μ_{high}, [3.129 4.13 5.06]). Emission response at 678 nm (Output): (1) low (trimf μ_{low}, [0.669 19.1 35.3]); (2) medium (trimf μ_{medium}, [32.3 50 69.45]); (3) high (trimf μ_{high}, [59.99 76.69 99.39]). 3D display of the dependence of emission response of **3** due to addition of F^- and H^+.

network and target data specifies proper network output. Table 4.6 shows the output emission response upon variation of 40 different combination of two different inputs (input 1=F^- and input 2=H^+). It is nicely indicated that the model validates best at epoch 6 with a performance of 86.019 (Figure 4.25). The increase of green colored line after

Table 4.5. Rules for the Fuzzy Logic System by Taking H^+ (Input 1) and F^- (Input 2) as the Inputs and Emission Intensity at 678 nm as the Outputs For **3**. The Rules Comprise of the Following Statements.

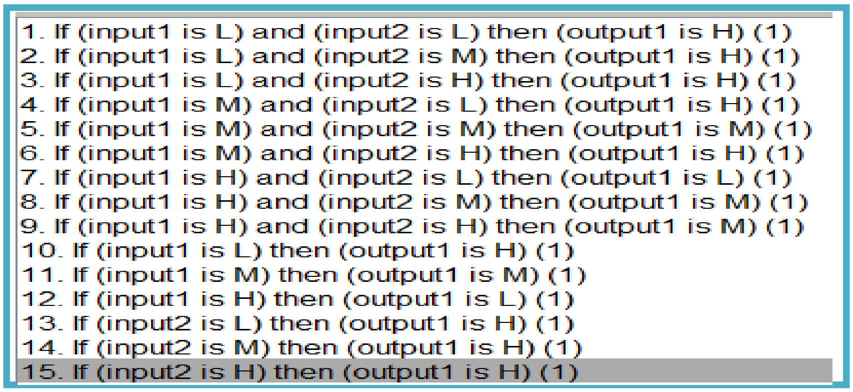

1. If (input1 is L) and (input2 is L) then (output1 is H) (1)
2. If (input1 is L) and (input2 is M) then (output1 is H) (1)
3. If (input1 is L) and (input2 is H) then (output1 is H) (1)
4. If (input1 is M) and (input2 is L) then (output1 is H) (1)
5. If (input1 is M) and (input2 is M) then (output1 is M) (1)
6. If (input1 is M) and (input2 is H) then (output1 is H) (1)
7. If (input1 is H) and (input2 is L) then (output1 is L) (1)
8. If (input1 is H) and (input2 is M) then (output1 is M) (1)
9. If (input1 is H) and (input2 is H) then (output1 is M) (1)
10. If (input1 is L) then (output1 is H) (1)
11. If (input1 is M) then (output1 is M) (1)
12. If (input1 is H) then (output1 is L) (1)
13. If (input2 is L) then (output1 is H) (1)
14. If (input2 is M) then (output1 is H) (1)
15. If (input2 is H) then (output1 is H) (1)

Table 4.6. Different Values of Emission Intensity as a Function of n_{H}^{+}/n_{1} and n_{F}^{-}/n_{1} for **3**

No of obs.	Equiv. of H^+	Equiv. of F^-	Emission Intensity at 678nm
1	0.0	0.0	92.00
2	4.0	0.0	1.34
3	0.0	5.0	92.05
4	0.5	2.5	75.32
5	2.5	1.5	40.00
6	2.0	2.5	42.00
7	4.0	1.5	26.30
8	2.0	2.0	41.00
9	1.5	1.0	64.00
10	3.5	5.0	39.33
11	2.5	3.5	47.00
12	0.5	4.0	86.78
13	3.5	4.5	37.89
14	1.0	3.0	74.34
15	1.5	5.0	84.23
16	2.5	4.5	48.45
17	2.0	4.0	52.34
18	1.0	5.0	82.15
19	1.5	5.0	83.24
20	4.0	1.0	24.76
21	3.0	4.0	37.05
22	0.5	3.5	84.67
23	1.0	1.5	72.78
24	1.5	4.5	46.78
25	2.5	4.0	38.90
26	3.0	4.5	39.65
27	3.5	5.0	38.95
28	2.0	5.0	56.46
29	1.5	1.5	66.76
30	2.0	3.0	48.76
31	3.5	2.5	28.76
32	3.0	1.0	17.30
33	2.0	3.5	50.32
34	1.0	4.5	90.10
35	0.5	3.0	78.56
36	1.5	3.5	41.23
37	2.5	3.0	32.45
38	4.0	2.5	26.78
39	2.0	2.5	44.56
40	1.0	3.5	76.89

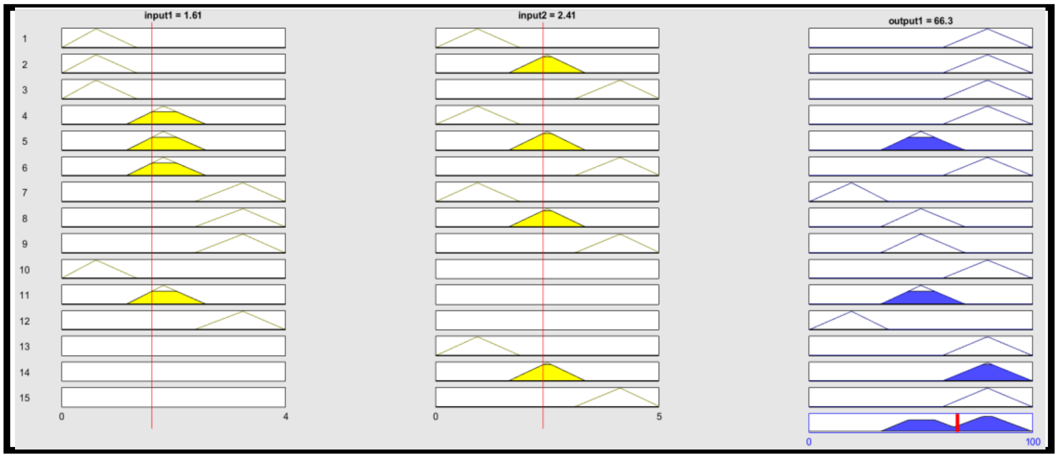

Figure 4.24. Mamdani rule view for **3.**

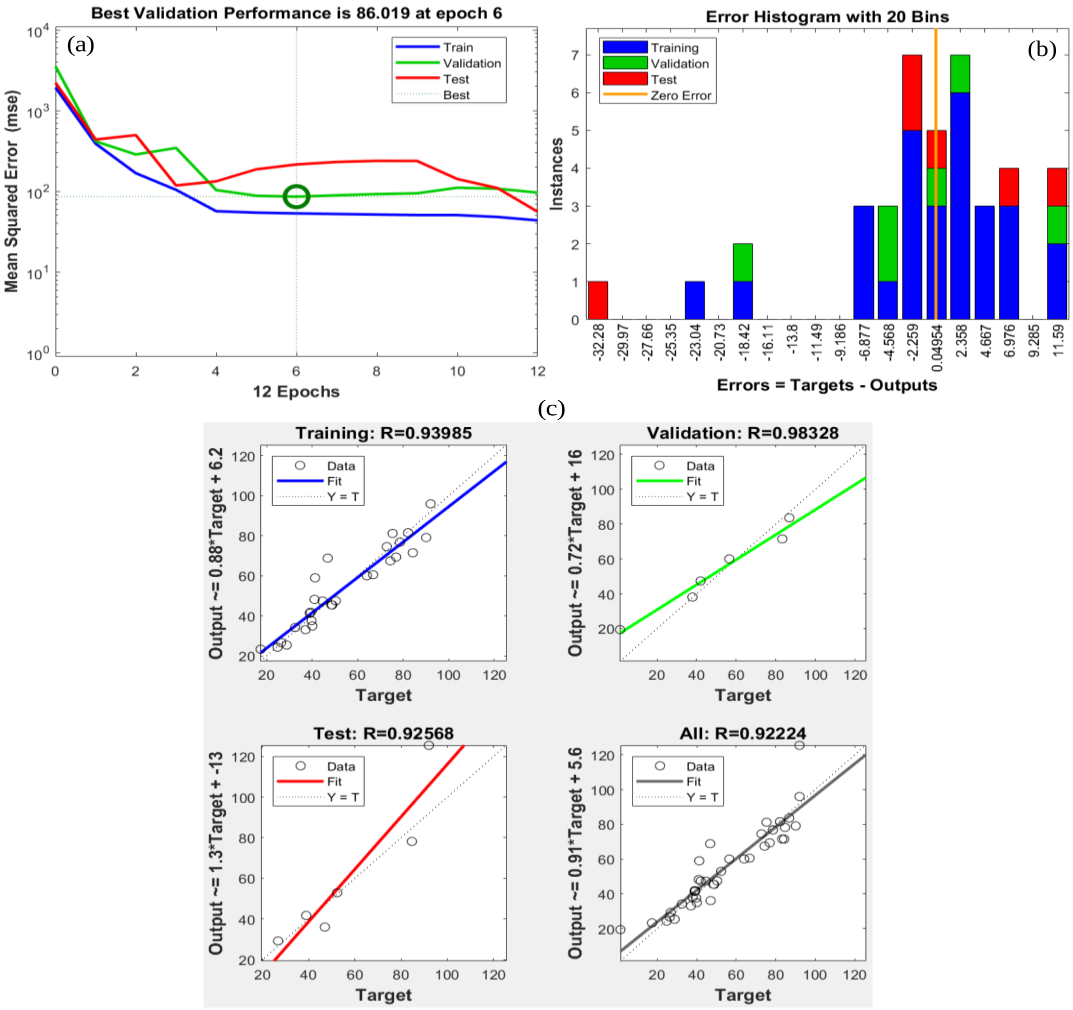

Figure 4.25. (a) The performance of the designed ANN model. (b) Error histogram of designed ANN model. (c) Comparison between linear regression and ANN model results plotted versus the observed values for training, validation and testing.

epoch 6 indicates the rise of the mean squared error (mse) and training is halted. Figure 4.25b shows the error histogram indicating the errors between the target and the forecasted values after training. Y-axis indicates the number of samples in the database that remains in a definite bin. The bins are equally spaced intervals which are utilized to sort data on the graph. The zero-error point is found to be located under the bin centre at 0.04954, whereas the total error of the array spans from -32.28 (leftmost bin) to 11.59 (rightmost bin) (Figure 4.25b). The regression values (R) estimate the correspondence between the outputs and targets. The value of R approaching to 1 indicates that the model is executed appropriately (Figure 4.25c). ANN model scheme consisting of two inputs, five hidden layers and one output also provided in Figure 4.26. The training state of the ANN network up to epoch 12 is portrayed in Figure 4.27.

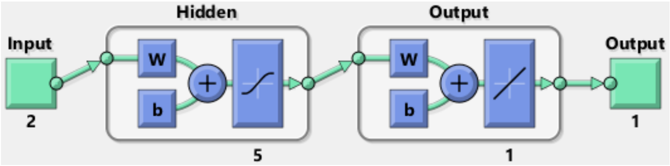

Figure 4.26. ANN model consisting of 2 inputs, 5 hidden layers and 1 output.

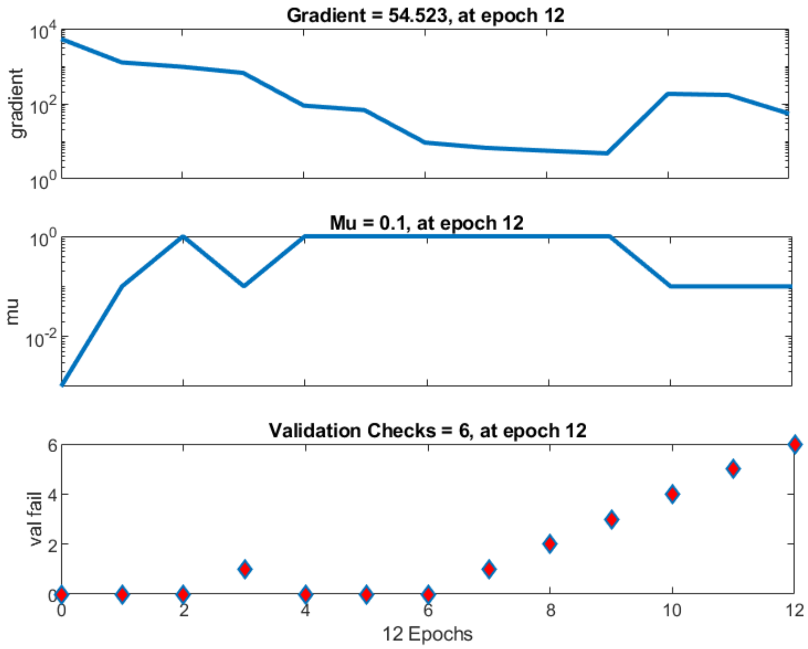

Figure 4.27. Training state of the ANN model of **3** (monitoring wavelength at 678 nm) up to epoch 12.

4.3.8. Adaptive Neuro-Fuzzy Inference System (ANFIS). Amalgamation of fuzzy and NN yield ANFIS network which eliminates the lacuna of individual ones and gives rise to better results.[68,69] A schematic sketch of the ANFIS network is displayed in Figure 4.28. Five layers (eliminating input layer) are joined together in this network. The sketch is typical for 2 input dimensions, P and Q, both of which consists of 3 fuzzy sets (C1C2C3 for P, whereas D1D2D3 for Q). The illustration of each layer is detailed in the Experiment Section. It is to be mentioned that the degree of freedom of ANFIS is quite less relative to analogous ANN network as ANFIS usually provides only a limited amount of trainable data. Only the membership function parameters in Layer 1 and inputs weight in Layer 4 could be anticipated by training in ANFIS network. The basic layout for predicting the emission intensity upon the influence of inputs (F^- and H^+) by ANFIS consists of 4 parts (fuzzification, knowledge base, ANN, and defuzzification layer) (**Scheme 4.1**).

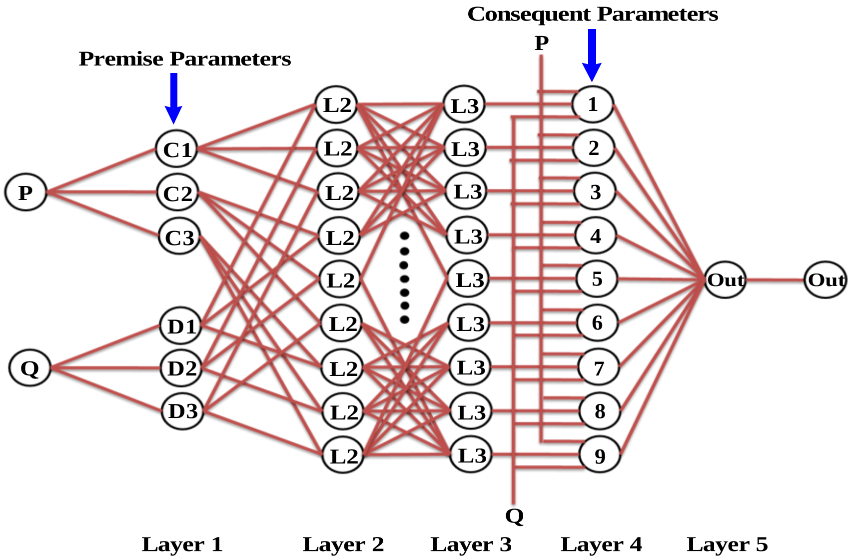

Figure 4.28. Schematic sketch of ANFIS network comprising of two inputs, five layers and one output.

To construct the system, 70% data are utilized for training with hybrid optimization technique and the remaining 30% for testing purpose. It is evident that training error is diminished in step by step manner up to 200 epochs suggesting that the system is learning in each step (Figure 4.29b). Because of the existence of 2 inputs and 7

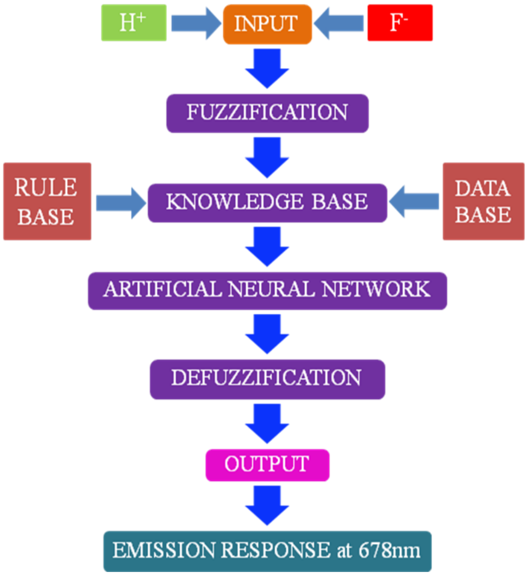

Scheme 4.1

membership functions each, the network will produce $7^2 = 49$ rules (Figure 4.30 and Table 4.7). The plausible combination of F^- and H^+ generates the output emission response at 678 nm, comprising of 49 rules on the basis of Sugeno's method (Figure 4.31).

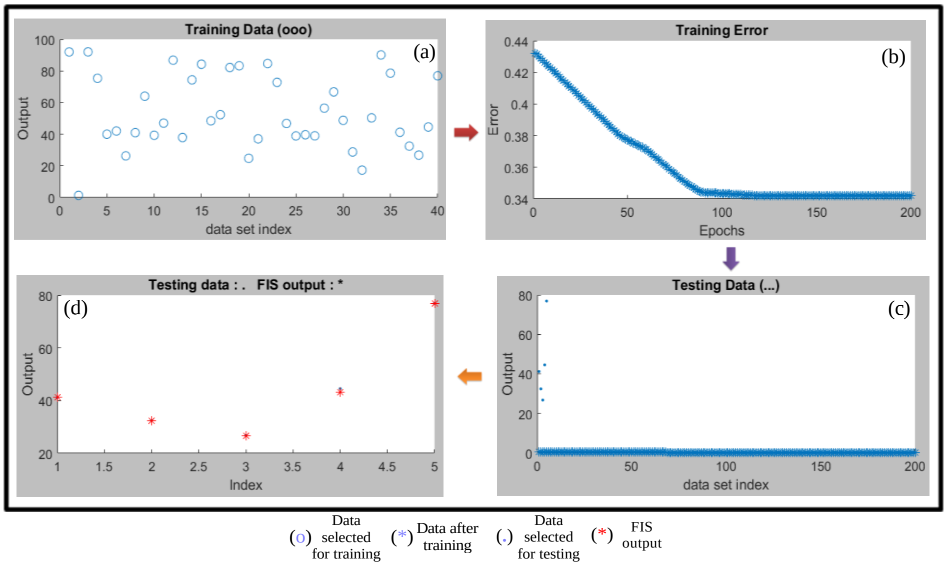

Figure 4.29 (a) Data set to train ANFIS network. (b) Root mean square error (RMSE) minimization up to 200 epochs. (c) Data for testing the accuracy of network output. (d) Combination of testing data and FIS output.

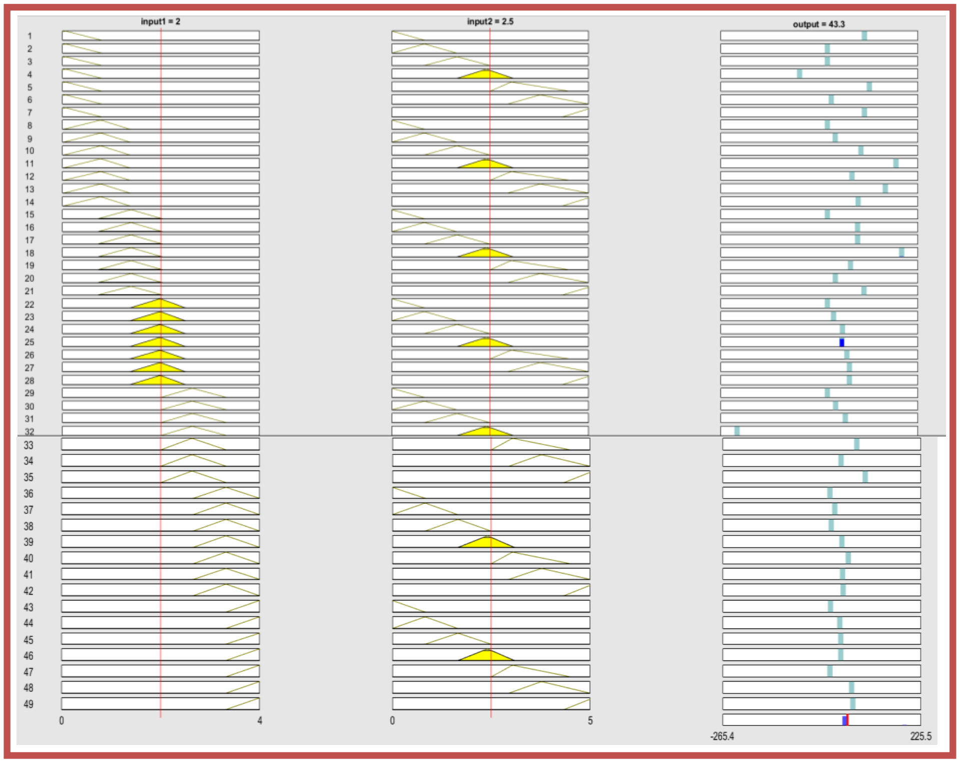

Figure 4.30. Sugeno rule view for **3** (monitoring wavelength at 678nm).

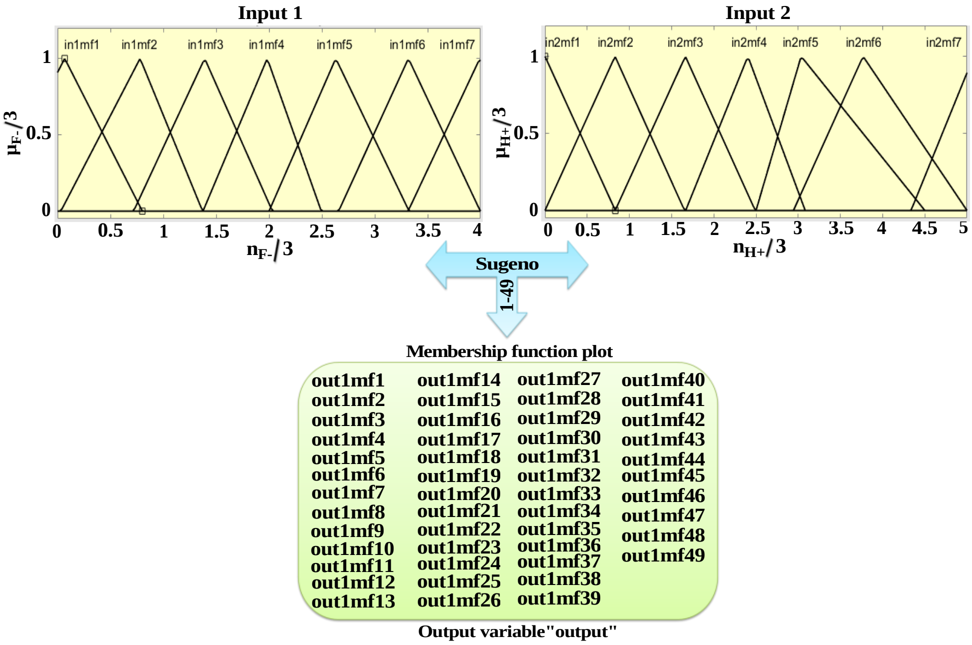

Figure 4.31. Schematic diagram of ANFIS on the basis of Sugeno's method (monitoring at 678 nm) maintaining 49 rules.

Table 4.7. Rules for the ANFIS (based on Sugeno's method) by Taking H^+ as Input 1 and F^- as Input 2, Whereas Emission Intensity at 678nm as the Output. The Rules Comprise of the Following Statements.

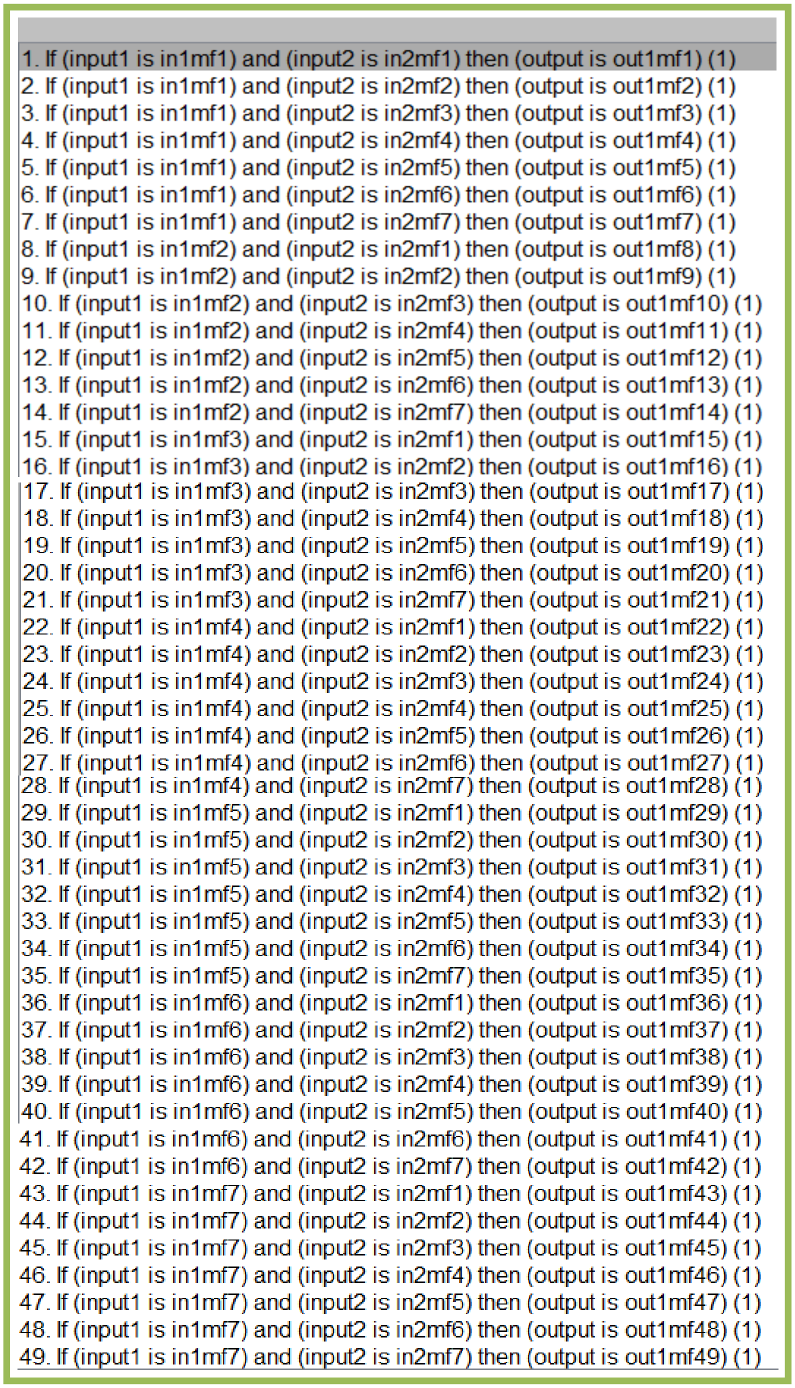

1. If (input1 is in1mf1) and (input2 is in2mf1) then (output is out1mf1) (1)
2. If (input1 is in1mf1) and (input2 is in2mf2) then (output is out1mf2) (1)
3. If (input1 is in1mf1) and (input2 is in2mf3) then (output is out1mf3) (1)
4. If (input1 is in1mf1) and (input2 is in2mf4) then (output is out1mf4) (1)
5. If (input1 is in1mf1) and (input2 is in2mf5) then (output is out1mf5) (1)
6. If (input1 is in1mf1) and (input2 is in2mf6) then (output is out1mf6) (1)
7. If (input1 is in1mf1) and (input2 is in2mf7) then (output is out1mf7) (1)
8. If (input1 is in1mf2) and (input2 is in2mf1) then (output is out1mf8) (1)
9. If (input1 is in1mf2) and (input2 is in2mf2) then (output is out1mf9) (1)
10. If (input1 is in1mf2) and (input2 is in2mf3) then (output is out1mf10) (1)
11. If (input1 is in1mf2) and (input2 is in2mf4) then (output is out1mf11) (1)
12. If (input1 is in1mf2) and (input2 is in2mf5) then (output is out1mf12) (1)
13. If (input1 is in1mf2) and (input2 is in2mf6) then (output is out1mf13) (1)
14. If (input1 is in1mf2) and (input2 is in2mf7) then (output is out1mf14) (1)
15. If (input1 is in1mf3) and (input2 is in2mf1) then (output is out1mf15) (1)
16. If (input1 is in1mf3) and (input2 is in2mf2) then (output is out1mf16) (1)
17. If (input1 is in1mf3) and (input2 is in2mf3) then (output is out1mf17) (1)
18. If (input1 is in1mf3) and (input2 is in2mf4) then (output is out1mf18) (1)
19. If (input1 is in1mf3) and (input2 is in2mf5) then (output is out1mf19) (1)
20. If (input1 is in1mf3) and (input2 is in2mf6) then (output is out1mf20) (1)
21. If (input1 is in1mf3) and (input2 is in2mf7) then (output is out1mf21) (1)
22. If (input1 is in1mf4) and (input2 is in2mf1) then (output is out1mf22) (1)
23. If (input1 is in1mf4) and (input2 is in2mf2) then (output is out1mf23) (1)
24. If (input1 is in1mf4) and (input2 is in2mf3) then (output is out1mf24) (1)
25. If (input1 is in1mf4) and (input2 is in2mf4) then (output is out1mf25) (1)
26. If (input1 is in1mf4) and (input2 is in2mf5) then (output is out1mf26) (1)
27. If (input1 is in1mf4) and (input2 is in2mf6) then (output is out1mf27) (1)
28. If (input1 is in1mf4) and (input2 is in2mf7) then (output is out1mf28) (1)
29. If (input1 is in1mf5) and (input2 is in2mf1) then (output is out1mf29) (1)
30. If (input1 is in1mf5) and (input2 is in2mf2) then (output is out1mf30) (1)
31. If (input1 is in1mf5) and (input2 is in2mf3) then (output is out1mf31) (1)
32. If (input1 is in1mf5) and (input2 is in2mf4) then (output is out1mf32) (1)
33. If (input1 is in1mf5) and (input2 is in2mf5) then (output is out1mf33) (1)
34. If (input1 is in1mf5) and (input2 is in2mf6) then (output is out1mf34) (1)
35. If (input1 is in1mf5) and (input2 is in2mf7) then (output is out1mf35) (1)
36. If (input1 is in1mf6) and (input2 is in2mf1) then (output is out1mf36) (1)
37. If (input1 is in1mf6) and (input2 is in2mf2) then (output is out1mf37) (1)
38. If (input1 is in1mf6) and (input2 is in2mf3) then (output is out1mf38) (1)
39. If (input1 is in1mf6) and (input2 is in2mf4) then (output is out1mf39) (1)
40. If (input1 is in1mf6) and (input2 is in2mf5) then (output is out1mf40) (1)
41. If (input1 is in1mf6) and (input2 is in2mf6) then (output is out1mf41) (1)
42. If (input1 is in1mf6) and (input2 is in2mf7) then (output is out1mf42) (1)
43. If (input1 is in1mf7) and (input2 is in2mf1) then (output is out1mf43) (1)
44. If (input1 is in1mf7) and (input2 is in2mf2) then (output is out1mf44) (1)
45. If (input1 is in1mf7) and (input2 is in2mf3) then (output is out1mf45) (1)
46. If (input1 is in1mf7) and (input2 is in2mf4) then (output is out1mf46) (1)
47. If (input1 is in1mf7) and (input2 is in2mf5) then (output is out1mf47) (1)
48. If (input1 is in1mf7) and (input2 is in2mf6) then (output is out1mf48) (1)
49. If (input1 is in1mf7) and (input2 is in2mf7) then (output is out1mf49) (1)

The ANFIS predicted results showing relationship between two inputs and the output are graphically presented in 3D plots (Figure 4.32). The generated ANFIS network

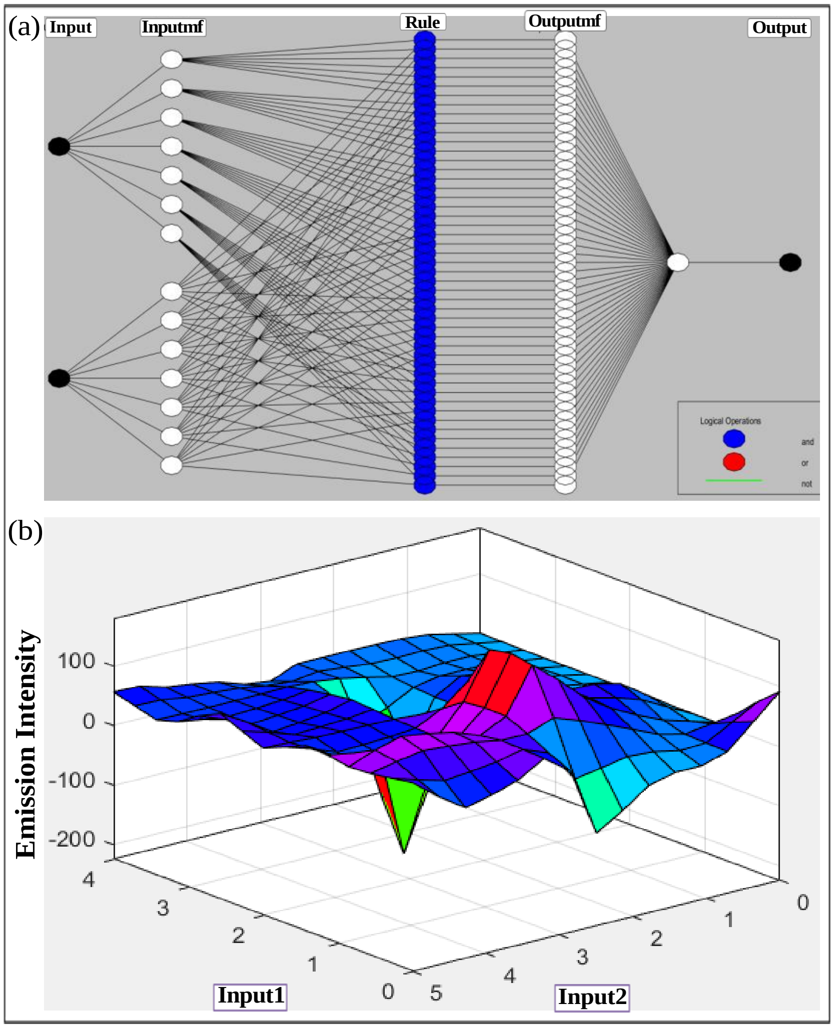

Figure 4.32. (a) Generated ANFIS structures for output. (b) Alteration of emission response upon combined effect of F^- and H^+ is displayed in a 3D plot.

architectures are also portrayed in Figure 4.32a on the basis of 49 rules. Upon incorporating the different values of inputs in the rule viewer of FL and the command segment of ANN model in MATLAB R2018a, we summarized the outputs values in Table 4.8. The output of ANN model is more in-line with that of the experimental data that that of the FL output. The efficacy of the ANFIS network is measured statically by the values of root mean squared error (RMSE). The testing RMSE value of 0.342149 clearly indicates that the system is functioning appropriately. The output of ANFIS is found to be closer to the experimental results than that of FL and NN. Hence, ANFIS is superior optimization system. A comparison of the experimental data to those of Fuzzy, ANN and ANFIS outputs is shown in Table 4.8 and Figure 4.33.

Table 4.8. Experimental, fuzzy, ANN and ANFIS generated outputs in presence of 5 different combinations of inputs.

F^-	H^+	Experimental Output	Fuzzy Output	ANN Output	ANFIS Output
3.5	5	39.33	51	41.78	39.1
1	1.5	72.78	79.7	74.50	72.8
2	2.5	44.56	50.6	47.36	43.3
1	4.5	90.1	79.6	79.08	90.1
0.5	3	78.56	79.7	76.77	78.7

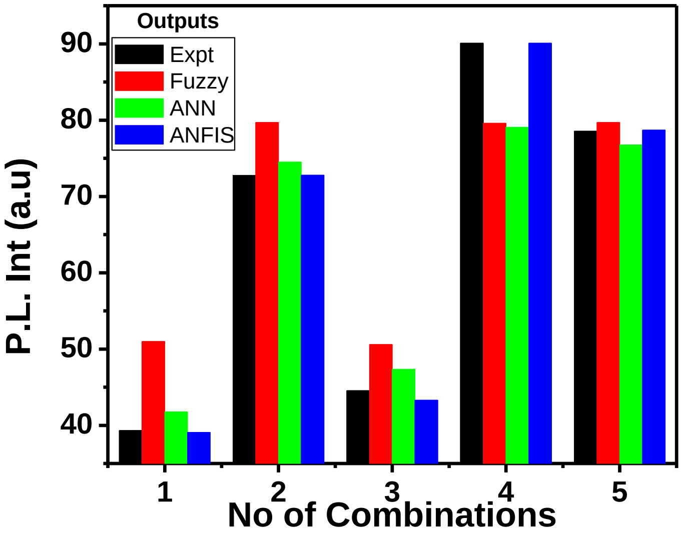

Figure 4.33. Deviation of the experimental data to those of Fuzzy, ANN and ANFIS outputs is presented in histograms.

4.4. Conclusions.

With regard to our sustained interest to investigate the possibility of exploring the computational work at the molecular level and implication of machine learning and other artificial intelligence tools in chemical systems, we designed in this work three Ru(II)-terpyridine complexes and thoroughly studied their stimuli-responsive photophysical behaviors. Taking advantage of imidazole protons in their outer coordination sphere, anion-promoted alteration of the photophysical characteristics of the complexes were thoroughly investigated via absorption, emission and time-correlated single photon counting measurements. In essence, the complexes act as anion- and temperature-responsive molecular switches. Additionally, the spectral signatures of the complexes upon the influence of anions, acid and temperature were employed to mimic multiple Boolean as well as Fuzzy logic functions. Performing very detailed sensing studies upon varying the analyte concentration within a wide domain is very tedious, time-consuming and expensive. In order to overcome the lacuna, we implemented ANNs and ANFIS networks to predict the experimental anion sensing behaviours of the complexes. In this study, we also compared the experimental output parameters of the complexes in presence of F^- and H^+ with those obtained from Fuzzy, ANN and ANFIS methods for appropriate modeling of their deprotonation-protonation behaviors. The statistical performance indicators (such as MSE and RMSE) clearly indicate that the predicted values of the anion sensing data by ANFIS network are best and comparable to the experimental data. Thus, the adopted soft computing and artificial intelligence based tools could be regarded as powerful methods for appropriate modelling for anion sensing behaviours of the present Ru (II)-terpyridine based metalloreceptors.

4.5. References

1. Artrith, N.; Butler, K. T.; Coudert, F. X.; Han, S.; Isayev, O.; Jain, A.; Walsh, A. Best Practices in Machine Learning for Chemistry. *Nat. Chem*. **2021**, *13*, 505-508.
2. Mater, A. C.; Coote, M. L. Deep Learning in Chemistry. *J. Chem. Inf. Model*. **2019**, *59*, 2545-2559.
3. Pflüger, P. M.; Glorius, F. Molecular Machine Learning: the Future of Synthetic Chemistry? *Angew. Chem. Int. Ed.* **2020**, *59*, 18860-18865.
4. He, L.; Bai, L.; Dionysiou, D. D.; Wei, Z.; Spinney, R.; Chu, C.; Xiao, R. Applications of Computational Chemistry, Artificial Intelligence, and Machine Learning in Aquatic Chemistry Research. *Chem. Eng. J.* **2021**, *426*, 131810.
5. Gentili, P. L. A Strategy to Face Complexity: The Development of Chemical Artificial Intelligence. In Advances in Artificial Life, Evolutionary Computation, and Systems Chemistry; Rossi, F., Piotto, S., Concilio, S., Eds.; *Springer: Cham*, Switzerland; New York, NY, USA. **2017**, *708*, 151-160.
6. Zadeh, L. A. Toward Human Level Machine Intelligence-is It Achievable? the Need for a Paradigm Shift. *IEEE Comput. Intell. Mag*. **2008**, *3*, 11-22.

7. Szaciłowski, K. Digital Information Processing in Molecular Systems. *Chem. Rev*. **2008**, *108*, 3481-3548.
8. Zadeh, L.A. Outline of a New Approach to the Analysis of Complex Systems and Decision Processes. *IEEE Trans. Syst. Man Cyb*. **1973**, *3,* 28-44.
9. Conrad, M. Molecular Computing. *Adv. Comput*. **1990**, *31*, 235-324.
10. Zadeh, L. A. Fuzzy sets. In Fuzzy Sets, Fuzzy Logic, and Fuzzy Systems: Selected Papers by Lotfi A Zadeh, pp. *394-432*. **1996.**
11. Gentili, P. L. Boolean and Fuzzy Logic Gates Based on The Interaction of Flindersine with Bovine Serum Albumin and Tryptophan. *J. Phys. Chem. A.* **2008**, *112,* 11992-11997.
12. Gentili, P. L. The Fuzziness of the Molecular World and Its Perspectives. *Molecules.* **2018**, *23,* 2074.
13. Gentili, P.L. The Fundamental Fuzzy Logic Operators and Some Complex Boolean Logic Circuits Implemented by the Chromogenism of a Spirooxazine. *Phys. Chem. Chem. Phys.* **2011**, *13*, 20335-20344.
14. Gentili, P.L.; Giubila, M.S.; Heron, B.M. Processing Binary and Fuzzy Logic by Chaotic Time Series Generated by a Hydrodynamic Photochemical Oscillator. *Chem Phys Chem.* **2017**, *18*, 1831-1841.
15. Gentili, P.L.; Giubila, M.S.; Germani, R.; Romani, A.; Nicoziani, A.; Spalletti, A.; Heron; B.M. Optical Communication Among Oscillatory Reactions and Photo-Excitable Systems: Uv and Visible Radiation Can Synchronize Artificial Neuron Models. *Angew. Chem. Int. Ed.* **2017**, *56*, 7535-7540.
16. Schumann, A.; Adamatzky, A. The Double-Slit Experiment with Physarum Polycephalum and P-adic Valued Probabilities and Fuzziness. *Int J Gen Syst.* **2015**, *44*, 392-408.
17. Giri Nandagopal, M. S.; Selvaraju, N. Prediction of Liquid-Liquid Flow Patterns in a Y-junction Circular Microchannel Using Advanced Neural Network Techniques. *Ind. Eng. Chem. Res.* **2016**, *55*, 11346-11362.
18. Bingöl, D.; Inal, M.; Çetintaş, S. Evaluation of Copper Biosorption Onto Date Palm (Phoenix Dactylifera L.) Seeds with MLR and ANFIS Models. *Ind. Eng. Chem.Res* **2013**, *52*, 4429-4435.

19. İnal, M. Predicting the Conversion Ratio for the Leaching of Celestite in Sodium Carbonate Solution Using An Adaptive Neuro-Fuzzy Inference System. *Ind. Eng. Chem.Res* **2014**, *53*, 4975-4980.
20. Sahoo, A.; Ahmed, T.; Deb, S.; Baitalik, S. Neuro-Fuzzification Architecture for Modeling of Electrochemical Ion-Sensing Data of Imidazole-Dicarboxylate-Based Ru(II)-Bipyridine Complex**.** *Inorg. Chem*. **2022**, *61*, 10242-10254.
21. Juris, A.; Balzani, V.; Barigelletti, F.; Campagna, S.; Beleser, P.; Zelewsky, A. V. Ru(II) Polypyridine Complexes: Photophysics, Photochemistry, Electrochemistry, and Chemiluminescence. *Coord. Chem. Rev*. **1988**, *84*, 85-277.
22. Balzani, V.; Juris, A.; Venturi, M.; Campagna S.; Serroni, S. Luminescent and Redox-Active Polynuclear Transition Metal Complexes. *Chem. Rev*. **1996**, *96*, 759-834.
23. Sauvage, J. P. ; Collin, J. P. J. ; Chambron, C. ; Guillerez, S. ; Coudret, C. ; Balzani, V.; Barigelletti, F.; De Cola, L. ; Flamigni, L. Ruthenium(II) and Osmium(II) Bis (Terpyridine) Complexes in Covalently-Linked Multicomponent Systems: Synthesis, Electrochemical Behavior, Absorption Spectra, and Photochemical and Photophysical Properties. *Chem. Rev.* **1994**, *94*, 993-1019.
24. Browne, W. R.; O'Boyle, N. M.; McGarvey, J. J.; Vos, J. G. Elucidating Excited State Electronic Structure and Intercomponent Interactions in Multicomponent and Supramolecular Systems. *Chem. Soc. Rev.* **2005**, *34*, 641- 663.
25. Williams, J. A. G. The Coordination Chemistry of Dipyridylbenzene: N-deficient Terpyridine or Panacea for Brightly Luminescent Metal Complexes. *Chem. Soc. Rev*. **2009**, *38*, 1783-1801.
26. Mondal, D.; Bar, M.; Mukherjee, S.; Baitalik, S. Design of Ru (II) Complexes Based on Anthraimidazoledione-functionalized Terpyridine Ligand for Improvement of Room-temperature Luminescence Characteristics and Recognition of Selective Anions: Experimental and DFT/TD-DFT Study. *Inorg. Chem*. **2016**, *55*, 9707-9724.
27. Bhaumik, C.; Saha, D.; Das, S.; Baitalik, S. Synthesis, Structural Characterization, Photophysical, Electrochemical and Anion-sensing Studies of

Luminescent Homo- and Heteroleptic Ruthenium(II) and Osmium(II) Complexes Based on Terpyridyl-imidazole Ligand. *Inorg. Chem.* **2011**, *50*, 12586-12600.

28. Mondal, D.; Biswas, S.; Paul, A.; Baitalik, S. Luminescent Dinuclear Ruthenium Terpyridine Complexes with a Bis-phenylbenzimidazole Spacer. *Inorg. Chem*. **2017**, *56*, 7624-7641.
29. Pal, A. K.; Hanan, G. S. Design, Synthesis and Excited-State Properties of Mononuclear Ru (II) Complexes of Tridentate Heterocyclic Ligands. *Chem. Soc. Rev*. **2014**, *43*, 6184-6197.
30. Medlycott, E. A.; Hanan, G. S. Synthesis and Properties of Mono and Oligo-Nuclear Ru (II) Complexes of Tridentate Ligands: the Quest for Long-Lived Excited States at Room Temperature. *Coord. Chem. Rev*. **2006**, *250*, 1763-1782.
31. Hofmeier, H.; Schubert, U. S. Recent Developments in the Supramolecular Chemistry of Terpyridine-Metal Complexes. *Chem. Soc. Rev*. **2004**, *33*, 373-399.
32. Constable, E. C. 2,2′:6′,2″-Terpyridines: from Chemical Obscurity to Common Supramolecular Motifs. *Chem. Soc. Rev.* **2007**, *33*, 246-253.
33. Harriman, A.; Ziessel, R. Making Photoactive, Molecular-scale Wires. *Chem. Commun*. **1996**, *15*, 1707-1716.
34. Breivogel, A.; Kreitner, C.; Heinze, K. Redox and Photochemistry of Bis (terpyridine) Ruthenium (II) Amino Acids and their Amide Conjugates-from Understanding to Applications. Eur. J. Inorg. Chem. **2014**, *32*, 5468-5490.
35. Winkler, J. R.; Netzel, T.; Creutz, C.; Sutin, N. Direct Observation of Metal-to-Ligand Charge-transfer (MLCT) Excited States of Pentaammineruthenium (II) Complex. *J. Am. Chem. Soc*. **1987**, *109*, 2381-2392.
36. Wang, J.; Fang, Y. Q. ; Hanan, G. S. ; Loiseau F. ; Campagna, S. Synthesis and Properties of the Elusive Ruthenium(II) Complexes of 4'-cyano-2,2':6',2''-Terpyridine. *Inorg. Chem.* **2005**, *44,* 5-7.
37. Maestri, M.; Armaroli, N.; Balzani, V.; Constable, E. C.; Thompson, A. M. W. C. Complexes of the Ruthenium (II)-2, 2’:6’, 2’’-Terpyridine Family. Effect of Electron-Accepting and Donating Substituents on the Photophysical and Electrochemical Properties. *Inorg. Chem.* **1995,** *34*, 2759-2767.

38. Fang,Y. Q.; Taylor, N. J. ; Hanan, G. S.; Loiseau, F.; Passalacqua, R.; Campagna, S. ; Nierengarten, H.; Dorsselaer, A. V. A Strategy for Improving the Room-temperature Luminescence Properties of Ru (II) Complexes with Tridentate Ligands. *J. Am. Chem. Soc.* **2002**, *124*, 7912-7913.
39. Encinas, S.; Flamigni, L.; Barigelletti, F.; Constable, E. C.; Housecroft, C. E. ; Schofield, E. R.; Figgemeier, E.; Fenske, D.; Neuburger, M.; Vos, J. G., et al. Electronic Energy Transfer and Collection in Luminescent Molecular Rods Containing Ruthenium (II) and Osmium (II) 2, 2′:6′,2″-Terpyridine Complexes Linked by Thiophene-2,5-diyl Spacers. *Chem. Eur. J.* **2002**, *8*, 137-150.
40. Duati, M.; Tasca, S.; Lynch, F. C.; Bohlen, H.; Vos, J. G.; Stagni, S.; Ward, M. D. Enhancement of Luminescence Lifetimes of Mononuclear Ruthenium(II)-Terpyridine Complexes by Manipulation of the Sigma-donor Strength of Ligands. *Inorg. Chem.* **2003**, *42*, 8377-8384.
41. Benniston, A. C.; Grosshenny, V.; Harriman, A.; Ziessel, R. Electron Delocalization in Ethynyl Bridged Binuclear Ruthenium (II) Polypyridine Complexes. Angew. *Chem. Int. Ed. Engl.* **1994**, *33*, 1884-1886.
42. Bhaumik, C.; Das, S.; Maity, D.; Baitalik, S. Luminescent Bis-tridentate Ruthenium (II) and Osmium (II) Complexes Based on Terpyridyl-imidazole Ligand: Synthesis, Structural Characterization, Photophysical, Electrochemical and Solvent Dependence Studies. *Dalton Trans*. **2012**, *41*, 2427-2438.
43. Deb, S.; Sahoo, A.; Pal, P.; Baitalik, S. Exploitation of the Second Coordination Sphere to Promote Significant Increase of Room-temperature Luminescence Lifetime and Anion Sensing in Ruthenium-terpyridine Complexes. *Inorg. Chem.* **2021**, *60*, 6836-6851.
44. Daisuke, M.; Kai, Y.; Hiroaki, O.; Makoto T.; Haga, M. Energy-storage Applications for a pH Gradient Between Two Benzimidazole-ligated Ruthenium Complexes that Engage in Proton-coupled Electron-transfer Reactions in Solution. *Inorg. Chem.* **2017**, *56*, 6419-6428.
45. Yoshikawa, K.; Motoyama, D.; Hiruma, Y.; Ozawa, H.; Nagano S.; Haga, M. Proton-rocking-chair-type Redox Capacitors Based on Indium Tin Oxide

Electrodes with Multilayer Films Containing Ru Complexes. *ACS Appl. Mater. Interfaces* **2018**, *10*, 26990-27000.

46. Haga, M.; Takasugi, T.; Tomie, A.; Ishizuya, M.; Yamada, T.; Hossain M. D.; Inoue, Miyao. Molecular Design of a Proton-induced Molecular Switch Based on Rod-shaped Ru Dinuclear Complexes with Bis-tridentate 2,6-bis(benzimidazol-2-yl)pyridine Derivatives. *Dalton Trans.* **2003**, *10,* 2069-2079.
47. Wu, A.; Masland, J.; Swartz, R. D.; Kaminsky, W.; Mayer, J. M. Synthesis and Characterization of Ruthenium Bis(β-diketonato) Pyridine-imidazole Complexes for Hydrogen Atom Transfer. *Inorg. Chem.* **2007**, *46*, 11190-11201.
48. Mo, H.J.; Niu, Y.L.; Zhang, M.; Qiao Z. P.; Ye, B.H. Photophysical, Electrochemical and Anion Sensing Properties of Ru(II) Bipyridine Complexes with 2,2'-Biimidazole-like Ligand. *Dalton Trans.* **2011**, *40*, 8218-8225.
49. Das, S.; Saha, D.; Karmakar, S.; Baitalik, S. Effect of pH on the Photophysical and Redox Properties of a Ruthenium(II) Mixed Chelate Derived from Imidazole-4,5- dicarboxylic Acid and 2,2′-Bipyridine: an Experimental and Theoretical Investigation. *J. Phys. Chem. A.* **2012**, *116*, 5216-5226.
50. Das, S.; Saha, D.; Mardanya, S.; Baitalik, S. A combined Experimental and DFT/TDDFT Investigation of Structural, Electronic, and pH-induced Tuning of Photophysical and Redox Properties of Osmium(ii) Mixed-chelates Derived from Imidazole-4,5-dicarboxylic Acid and 2,2′-Bipyridine. *Dalton Trans.* **2012**, *41*, 12296-12310.
51. Karmakar, S.; Maity, D.; Mardanya, S.; Baitalik, S. Demonstration of Multiple Logic Operations in a Heteroditopic Pyrene-phenylimidazole-terpyridine Conjugate Based on Optical Responses by Selective Anions and Cations: an Experimental and Theoretical Investigation. *J. Phys. Chem. A* **2014**, *118*, 9397-9410.
52. Deb, S.; Sahoo, A.; Ahmed, T.; Baitalik, S. Stimuli-Responsive Molecular Switches and Logic Devices Based on Ru (II)-Terpyridyl-Imidazole Coordination Motif. *J. Phys. Chem. B* **2021**, *125*, 8919-8931.

53. Mukherjee, S.; Sahoo, A.; Deb, S.; Baitalik, S. Light and Cation-Driven Optical Switch Based on a Stilbene-Appended Terpyridine System For The Design of Molecular-Scale Logic Devices. *J. Phys. Chem. A*. **2021**, *125*, 8261-8273.
54. Mondal, D.; Bar, M.; Maity, D.; Baitalik, S. Anthraimidazoledione-Terpyridine-Based Optical Chemosensor for Anions and Cations that Works as Molecular Half Subtractor, Key-Pad Lock, and memory device. *J. Phys. Chem. C*. **2015**, *119*, 25429-25441.
55. Omana, M.; Papasso, G.; Rossi, D.; Metra, C. A Model For Transient Fault Propagation in Combinatorial Logic. In *9th IEEE On-Line Testing Symposium*. **2003**. 111-115.
56. Zhang, Y.; Liu, W.; Zhang, W.; Yu, S.; Yue, X.; Zhu, W.; Wang, J. DNA-Mediated Gold Nanoparticle Signal Transducers For Combinatorial Logic Operations and Heavy Metal Ions Sensing. *Biosens. Bioelectron*. **2015**, *72*, 218-224.
57. Goldsworthy, V.; LaForce, G.; Abels, S.; Khisamutdinov, E. F. Fluorogenic RNA Aptamers: A Nano-Platform for Fabrication of Simple and Combinatorial logic Gates. *Nanomaterials.* **2018**, *8*, 984.
58. Magri, D. C.; Spiteri, J. C. Proof of Principle of A Three-Input AND–INHIBIT–OR Combinatorial Logic Gate Array. *Org. Biomol. Chem*. **2017**, *15*, 6706-6709.
59. Mardanya, S.; Mondal, D.; Karmakar, S.; Baitalik, S. Smart Ruthenium and Osmium Complexes Mimic the Complicated Functions of Traffic Signal and Memory Device. *Sens. Actuators B: Chem*. **2017**, *239*, 635-641.
60. Cui, B. B.; Tang, J. H.; Yao, J.; Zhong, Y. W. A Molecular Platform For Multistate Near-Infrared Electrochromism and Flip-Flop, Flip-Flap-Flop, and Ternary Memory. Angew. Chem. Int. Ed. **2015**, *54*, 9192-9197.
61. Shao, J. Y.; Yao, C. J.; Cui, B. B.; Gong, Z. L.; Zhong, Y. W. Electropolymerized Films of Redox-Active Ruthenium Complexes for Multistate Near-Infrared Electrochromism, Ion Sensing, and Information Storage. *Chin. Chem. Lett*. **2016**, *27*, 1105-1114.

62. Szaciłowski, K. Molecular Logic Gates Based on Pentacyanoferrate Complexes: From Simple Gates to Three-Dimensional Logic Systems. *Chem. Eur. J.* **2004**, *10,* 2520-2528.
63. Szaciłowski, K.; Wojciech, M.; Grażyna, S. Light-Driven OR and XOR Programmable Chemical Logic Gates. *J. Am. Chem. Soc.* **2006**, *128*, 4550-4551.
64. Pott, K. T.; Usifer, D. A.; Abruna, H. D. 4-Vinyl-, 6-Vinyl-, and 4'-Vinyl-2,2':6',2"-Terpyridinyl Ligands: Their Synthesis and the Electrochemistry of Their Transition-Metal Coordination Complexes. *J. Am. Chem. Soc.* **1987**,*109*, 3961-3967.
65. Marcus, Y. *J.* Thermodynamics of Solvation of Ions. *J. Chem. Soc. Faraday Trans*. **1991**, *87*, 2995-2999.
66. The US Environmental Protection Agency (EPA) Has Set the so Called Maximum Contaminant Level Goals For Cyanide in Drinking Water to 0.2 ppm, and Fluorideto be 2 ppm. http://ecfr.gpoaccess.gov (last Accessed 1st March, 2006).
67. MATLAB **2018a**, The MathWorks, Inc., Natick, Massachusetts, United States.
68. Jang, J. S. R.; Sun, C. T. Neuro-Fuzzy Modeling and Control. *Proc. IEEE.* **1995**, *83,* 378-405.
69. Sugeno, M.; Yasukhiro, T. A Fuzzy-Logic-Based Approach to Qualitative Modeling. *IEEE Trans. Fuzzy Syst.* **1993**, *1*, 7-31.

****

Chapter 5

Harnessing Deep Neural Networks to Analyze Multi-Channel Anion Sensing Characteristics of Ru(II)-Pyrazolyl-Bis(Benzimidazole) Complex

5.1. Introduction

Machine learning (ML) is now-a-days a very powerful tool in materials research. The technological progress of ML is now manifested in nearly all branches of science and technology.[1-11] Through proper handling of powerful computation and high-throughput experimentation, ML has expedited the scientific research and technological development.[12-31] Even though the adoption of data-guided growth of materials is inspiring to recognize the accurate potential of ML models, they should also have the potentiality over solely predictive ability. The prediction and inner execution of models must offer appropriate explanation to the human specialists. Enormous efforts are now committed to create a classification of interpretability and explainability modes of ML tools. Classical ML corresponds to the process of creating algorithms that are capable to learn from accessible data and take advantage of that learning to anticipate the output of new inputs. Deep learning (DL) method, on the other hand, relies on artificial neural networks (ANN) wherein manifold layers of processing are utilized to take out increasingly advanced level features from the data.

In this work, we employed one of our previously reported Ru(II) complex, $[(bpy)_2Ru(H_3pzbzim)](ClO_4)_2$ (**1**) as shown in **Chart 5.1**.[32] The reason of choosing of Ru(II) is due to their outstanding photophysical and redox properties along with their active participation in diverse light-induced applications such as dye sensitized solar cells as well as in optical sensors and switches.[33-52] The design protocol provides two imidazole and one pyrazole NH motifs in its outer sphere and taking advantage of which the anion sensing behaviors of the complex is comprehensively looked into in organic and aqueous media via absorption and emission spectroscopy as well as by square wave voltammetry (SWV). A wide range of anions is employed to fine tune the photo-redox behavior of the complex. Now to accomplish detailed sensing investigations by altering the anion concentration over a broad range is extremely tiresome, time-consuming and pricey. To get-rid of the inconvenience as well as to analyze and fully understand the anion sensing behavior of the complex, we applied herein neural network based deep learning methodologies (such as ANN and ANFIS).

In deep learning, ANN plays very crucial role and often yield satisfactory results. A subsection of ML, called deep learning (DL) allows computation for multilayer NNs.

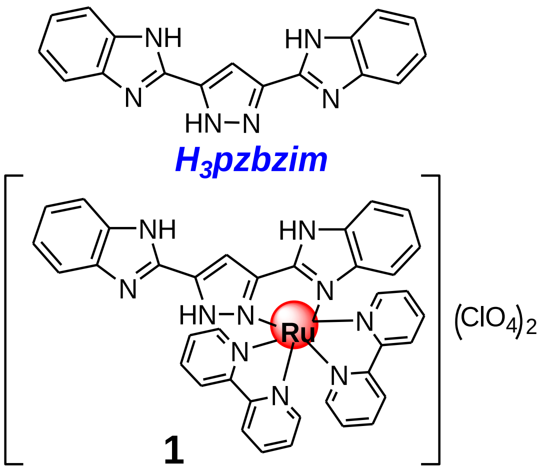

Chart 5.1. Chemdraw structure of the complex.

In disparity to AI's major objective of empowering machines to mimic human conduct, ML employs statistical methods to allow computers to grow over time. The key disparity amongst ML and DL is that in DL the pattern extraction and classification are accomplished automatically. But, with ML, the feature extraction is still required and the computer to do the jobs of cataloguing and prediction. An ANN is an intricate mathematical and computational model which relies on the widespread biological neural network in human brain. It might upsurge its performance upon learning from its mistakes, which is how an artificial neural network learns. It encompasses a network of functions and weights that function as artificial neurons. These are frequently used in AI applications that required them to examine tough and complicated problems. Different curve-fitting algorithms could be applied to run the ANNs. In this work, we will implement Levenberg-Marquardt (LM), Scaled Conjugate Gradient (SCG) and Bayesian Regularization (BR) algorithm for analysing our multi-channel anion sensing data. Furthermore, because of its elevated competence in predicting stationary organization, we applied advanced feed-forward back propagation network, viz., ANN-function fitting (ANN-FF) in each algorithm for superior grasping and prediction.[53,54] The detailed descriptions of the said algorithms are provided in the Experimental section.

Even though ANN is fairly proficient to grab the data but usually not so capable in terms of understanding the sense of each neuron and its weight. On the other hand, Fuzzy logic (FL)-derived models are sometimes better with regard to understanding as this operates via lingual language and IF-THEN rule.[55-59] However, the shortcomings of FL are its lack of ability to learn by itself. In order to learn via FL, one needs to borrow the methodologies from supplementary domains (statistics or system recognition). Since the NNs are competent in learning, it might be better to combine FL and NN and the combined methodology, termed as ANFIS, is sometimes superior above the individual ones.[60-61] The layout of ANFIS have the identical mechanism to that FL barring the NN block. Herein, the results of ANN and ANFIS models are also be compared among themselves together with the experimental outcomes for appropriate modeling of the anion sensing behavior of the complex.

5.2. Experimental Section

5.2.1. Materials. The chemicals and solvents were procured from Merck. $[Ru(bpy)_2Cl_2]\cdot 2H_2O$,[62] was prepared by the literature methods. Pyrazole-3,5-bis(benzimidazole) (H_3pzbzim) and the monometallic Ru(II) complex of composition, $[(bpy)_2Ru(H_3pzbzim)](ClO_4)_2$ (**1**) are synthesized following our previously reported procedure.[32]

5.2.2. Synthesis of the Ligand [H_3pzbzim]. A mixture of *o*-phenylenediamine (4.5g, 41.5 mmol) and pyrazole-3,5-dicarboxylic acid monohydrate (3.4 g, 20 mmol) and polyphosphoric acid (40 mL) was heated at 200°C for 4 h. The deep blue viscous solution that formed was poured into crushed ice. A blue precipitate thus obtained was filtered, washed with water, followed by dilute aqueous ammonia and again water. During this process the residue changed to light pink. This was dissolved in the minimum volume of hot (90°C) *N*,*N'*-dimethylformamide (DMF), treated with a small amount of activated charcoal, and filtered. To the filtrate water was slowly added when the product separated out as an off-white solid, which was recrystallized from DMF-H_2O; yield 2.7 g (40%), mp >250 °C (Found: C, 67.7; H, 3.95; N, 27.75. $C_{17}H_{12}N_6$ requires: C, 68.0; H, 4.0; N, 28.0%).ν/cm^{-1} (KBr): 3050, 2800, 1655, 1615, 1570, 1510, 1465, 1430, 1390, 1350, 1270, 1230, 1210, 1100, 1015, 960, 760, 750 cm^{-1}

5.2.3. Synthesis of Metal Complex. $[(bipy)_2Ru(H_3pzbzim)][ClO_4]_2.2H_2O$ (1). A mixture of $[Ru\text{-}(bpy)_2Cl_2].2H_2O$ (0.26 g, 0.5 mmol) and H_3pzbzim (0.3 g, 1 mmol) in 50 mL of ethanol-water (1:1 v/v) was heated under reflux with constant stirring for 24 h. After removal of the unreacted ligand, the orange-red filtrate was rotary-evaporated to *ca*.

20 mL and to it was then added an aqueous solution (5 mL) of $NaClO_4$ (1 g). The product that separated was filtered and recrystallized from methanol-water (3:1, v/v) containing a few drops of $HClO_4$ (10^{-5} M); yield 0.21 g (45%) (Found: C,46.6; H, 3.05; N, 14.65. $C_{37}H_{32}N_{10}Cl_2O_{10}Ru$ requires: C, 46.85; H, 3.15; N, 14.75%). *v*/cm^{-1}(KBr) 3400 (br), 3050, 1625, 1590,1460, 1440, 1415, 1280, 1100 (br), 770, 740, 730 and 620. ^{1}HNMR [$(CD_3)_2SO$]: *d* 4.30 (1H, br), 5.55 (1H, t), 6.94 (1H, t),7.24 (1H, t), 7.45 (4 h, m), 7.50 (1H, d), 7.57 (1H, t), 7.66 (2H, t),7.68 (2H, d), 7.73 (1H, d), 7.78 (1H, d), 7.82 (1H, s), 7.96 (1H, t), 8.03 (1H, t), 8.07 (2H, t), 8.20 (1H, t), 8.71 (1H, d), 8.75 (1H,d), 8.80 (2H, d), 14.23 (1H, br)

Caution! Perchlorate salts of the metal complexes are explosive and should be handled in small amount with extreme care

5.2.4. Physical Measurements. The details of different equipments used and experimental procedures to measure absorption and luminescence spectral characteristics as well as and electrochemical behaviors are already presented in chapter 2 and chapter 3.

5.2.5. X-ray Crystal Structure Determination. Crystals suitable for structure determination were obtained by diffusing toluene to a solution of **1** in MeCN-DCM (1:4, v/v). X–ray diffraction data for the crystal of **1** mounted on a glass fiber and coated with perfluoropolyether oil was collected on a Bruker-AXS SMART APEX II diffractometer at 296 K equipped with CCD detector using graphite–monochromated MoKα radiation (λ =0.71073 Å). Crystallographic data and details of structure determination are summarized in Table 5.1. The data were processed with SAINT and absorption corrections were made with SADABS.[63] The structures were solved by direct methods using SHELXT[64] program and refined by full matrix least-squares method based on F^2 by using SHELXL program through Olex-2.[65] The non hydrogen atoms were refined anisotropically, while the hydrogen atoms were placed with fixed thermal parameters at idealized positions. In the structure of **1**, two free water molecule remain in the crystal packing which were highly disordered and the structure was finally solved by removing the disordered water molecule by running the program SQUEEZE.[66-67] The electron density map also showed the presence of some unassignable peaks, which were removed by running the program

SQUEEZE. The crystallographic figures have been generated using Diamond 3.1e software.[68] CCDC reference number: 2195047 for **1**.

5.2.6. Artificial Neural Networks (ANNs). Execution details of ANNs have already been presented in the experimental section of chapter 4. Different training algorithms have been used for prediction of photophysical and electrochemical responses of **1** in presence of acid and base. In this project, feedforward back propagation neural network is utilized for comparison of three different training algorithms, i.e., Levenberg–Marquardt Algorithm (LM), Scaled Conjugate Gradient (SCG) and Bayesian Regularization (BR), as regards of their capability to predict the photophysical and electrochemical data. The advantages and disadvantages of these three curve fitting training algorithms are described below.

5.2.6.1. Levenberg-Marquardt Algorithm. This algorithm typically requires more memory but less time. Training automatically stops when generalization stops improving, as indicated by an increase in the mean square error of the validation samples. This method has been applied by researchers to challenging nonlinear least-squares problems in several different domains.

5.2.6.2. Scaled Conjugate Gradient. This algorithm requires less memory. Training automatically stops when generalization stops improving, as indicated by an increase in the mean square error of the validation samples.

5.2.6.3. Bayesian Regularization. This algorithm typically requires more time, but can result in good generalization for difficult, small or noisy datasets. Training stops according to adaptive weight minimization (regularization).

In this study, a neural network for function fitting was coded in MATLAB 2018. The input data present the network, while the target data define the desired network output. Current intensity outputs upon the action of 40 different combinations of two inputs (input 1= $F^-$and input 2= H^+). Thus, the 40×2 matrix represents the static input data of 40 samples involving 2 inputs, while 40×5 matrix represents the static output data of five elements. Now, the 40 samples are divided into 3 sets of data. For Levenberg-Marquardt and Scaled Conjugate Gradient algorithm assisted training process, 70% of the data are conferred for the training and the network is corrected according to its error. Now the learning algorithm and the number of neurons in the hidden layer were optimized.

15% data are employed to compute the network generalization and to halt training. When generalization stops improving, the data validation takes place. The remaining 15% data give an independent estimate of the network performance during and after the training, called testing data. But for Bayesian Regularization algorithm assisted training process, the previously taken 15% data for validation is not needed. In this case 70% data was taken for training purpose and rest 30% data was allotted for testing.

5.2.7. Adaptive Neuro-Fuzzy Inference System (ANFIS). The execution details of ANFIS model have already been presented in chapter 4.

5.3. Results and Discussion

5.3.1. Synthesis and Characterization. H_3pzbzim ligand was prepared upon refluxing a mixture of *o*-phenylenediamine and pyrazole-3,5-dicarboxylic acid monohydrate in 2:1 molar ratio in H_3PO_4 medium. The metal complex was obtained by refluxing 1:1 molar ration of $[Ru(bpy)_2Cl_2].2H_2O$ and H_3pzbzim in ethanol-water (1:1,v/v). The metal complex is precipitated as perchlorate salts with $NaClO_4$ and purified via chromatography and recrystallization techniques under mild acidic condition to keep the imidazole NH motifs intact. Characterizations of the compounds are performed through IR and NMR spectroscopy. We are also able to grow suitable single crystals of the complex. The structure of the complex cation (**1**$^{2+}$) is shown in Figure 5.1. The

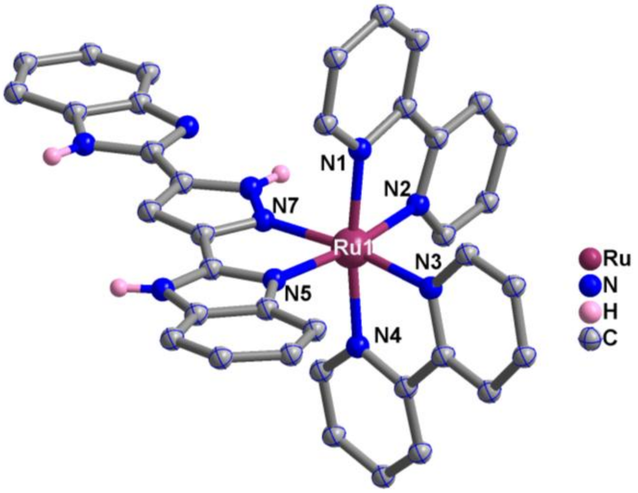

Figure 5.1. Perspective view of **1**$^{2+}$ showing 50% probability ellipsoid plots.

crystallographic parameters as well as selected bond lengths and angles are presented in Table 5.1-5.2. **1**$^{2+}$ crystallizes in the triclinic form having space group of $P2_1/c$. Three types of Ru-N distances are observed: the longest one [Ru1-N5, 2.094(3) Å] is associated with the benzimidazole nitrogen, the intermediate one [Ru1-N7, 2.063 (3) Å] is connected to the central pyrazole nitrogen, while the bpy offers the shortest Ru-N distances with their values within the range of 2.044 (4)–2.054 (5) Å.

Table 5.1 Crystallographic Data for $[(bpy)_2Ru(H_3pzbzim)](ClO_4)_2$ (**1**)

CCDC reference number	2195047
Compound	$[(bpy)_2Ru(H_3pzbzim)](ClO_4)_2$
Formula	$C_{37}H_{32}Cl_2N_{10}O_{10}Ru$
FW	948.70
T (K)	273.15K
Cryst. Syst.	Monoclinic
Space group	$P2_1/c$
a (Å)	12.2068(7)
b (Å)	17.1858(9)
c (Å)	19.5468(11)
α (deg)	90
β (deg)	106.362(3)
γ (deg)	90
V (Å3)	3934.5(4)
Dc(g cm-3)	1.595
Z	4
μ (mm-1)	0.606
F(000)	1928.0
2θ range (deg)	3.214 to 50.07
Data/restraints/parameters	6918/0/523
GOF on F^2	1.032
Final R indexes [I>=2σ (I)]	$R_1 = 0.0403$, $wR_2 = 0.1104$
Final R indexes [all data]	$R_1 = 0.0508$, $wR_2 = 0.1199$
Largest diff. peak/hole / e Å^{-3}	0.59/-0.46

5.3.2. Anion-Responsive Behavior. The complex possesses one pyrazole NH and two types of imidazole NH groups in its secondary coordination sphere which have the ability to interact with anions of varying basicity. To this end, we systematically looked into the anion sensing behavior of the complex in MeCN and H_2O. Tetrabutylammonium salts of F^-, Cl^-, Br^-, I^-, AcO^-, CN^-, SCN^- and $H_2PO_4^-$ ions are used here.

Table 5.2. Selected Experimental Bond Distances (Å) and Angles (deg) for **1**

Bond Distances (Å)	
Ru1-N1	2.048(3)
Ru1-N2	2.044(3)
Ru1-N3	2.051(3)
Ru1-N4	2.054(3)
Ru1-N5	2.094(3)
Ru1-N7	2.063(3)
Angles (deg)	
N4-Ru1-N5	89.76(11)
N4-Ru1-N7	96.26(11)
N3-Ru1-N5	94.99(11)
N3-Ru1-N4	78.60(11)
N3-Ru1-N7	171.04(11)
N2-Ru1-N5	171.60(11)
N2-Ru1-N4	95.87(11)
N2-Ru1-N3	92.24(11)
N2-Ru1-N1	79.01(11)
N2-Ru1-N7	95.61(11)
N1-Ru1-N5	96.00(11)
N1-Ru1-N4	172.20(11)
N1-Ru1-N3	95.60(11)
N1-Ru1-N7	90.14(10)
N7-Ru1-N5	77.54(11)

5.3.3. Absorption Spectral Monitoring. The absorption spectrum of the complex in presence of studied anions together with its visual color change is shown in Figure 5. 2. The photograph exhibits vivid color change with F^-, CN^- and AcO^- (for MeCN) and only with CN^- (in water). The complex displays several intense bands across the UV-vis region. Two overlapping absorption bands at 490 nm (ε=11500 M^{-1} cm^{-1}) and 440 nm (br) (ε=9300 M^{-1} cm^{-1}) in MeCN are due to Ru(dπ)→bpy and/or H_3pzbzim (π*)} charge transfer (MLCT) transitions, while the bands at 312 and 354 nm originated from H_3pzbzim-centered intra-ligand charge transfer (ILCT) transitions. Intense bands at 240 290 nm, on the other hand, are due to π–π* transition of the bipyridine motifs. The MLCT bands remain almost unaltered in presence of most of the studied anions except F^-, AcO^-, and CN^- which cause significant red-shift of the MLCT band maxima. The observation is in-line with the visual color change of the complex. The observed

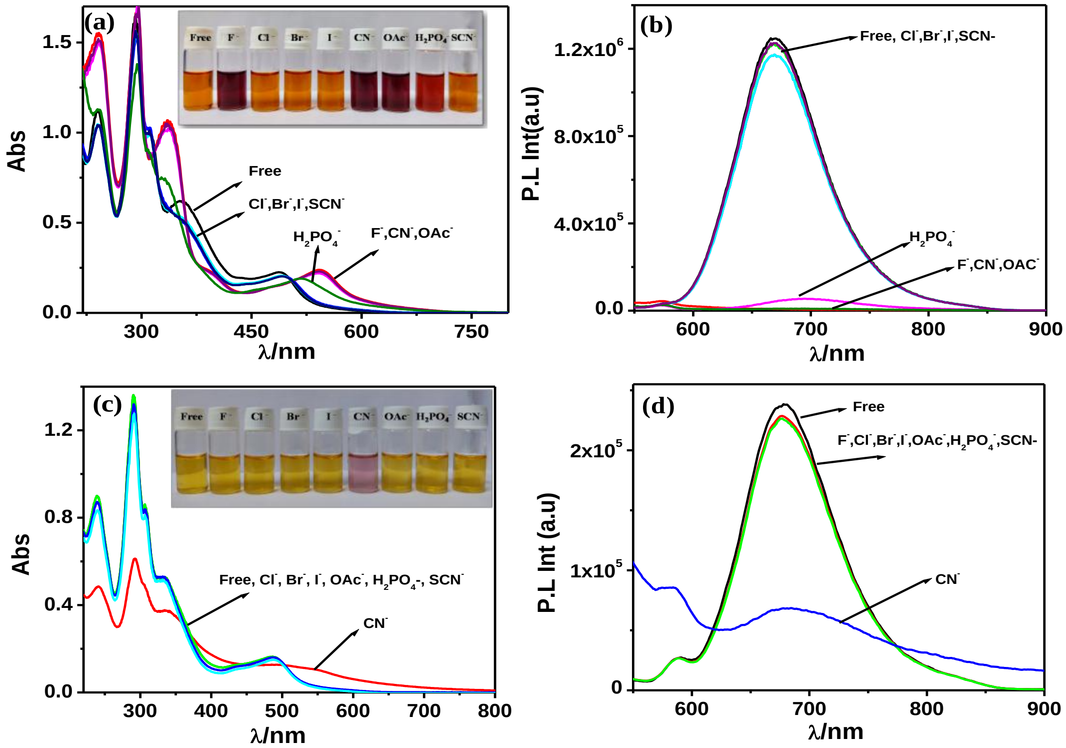

Figure 5.2. Absorption and emission spectral behavior of **1** in MeCN (a and b, respectively) and water (c and d, respectively) in presence of various anions.

bathochromic shift of the MLCT bands may be accredited to hydrogen-bonding interaction between NH motif and the anions followed by deprotonation with excess of the basic anions. The spectral behavior of complex towards anions differs dramatically in water relative to MeCN. In contrast to MeCN, only CN^- induces appreciable change in the spectral profile among the anions. In essence, the present complex functions as selective sensor for CN^- in H_2O, whereas unselective for F^-, CN^- and AcO^- in MeCN.

Absorption titration experiment is performed with various anions to get quantitative insight of receptor-anion interplay (Figure 5.3-5.4). Two-step changes are observed with F^-, CN^- and AcO^-, while a single step change takes place with $H_2PO_4^-$ in MeCN. Clear-cut isosbestic points are observed in each step of titration processes. Upon incremental addition of any one of F^-, CN^- and AcO^- ions, the MLCT bands maxima in the successive absorption curves undergo gradual-red shift and passes through three well-resolved isosbestic points (280, 342, and 494 nm) up to 2 equiv. Addition of anions beyond 2 equiv also induces additional red-shift of the MLCT band maxima and during

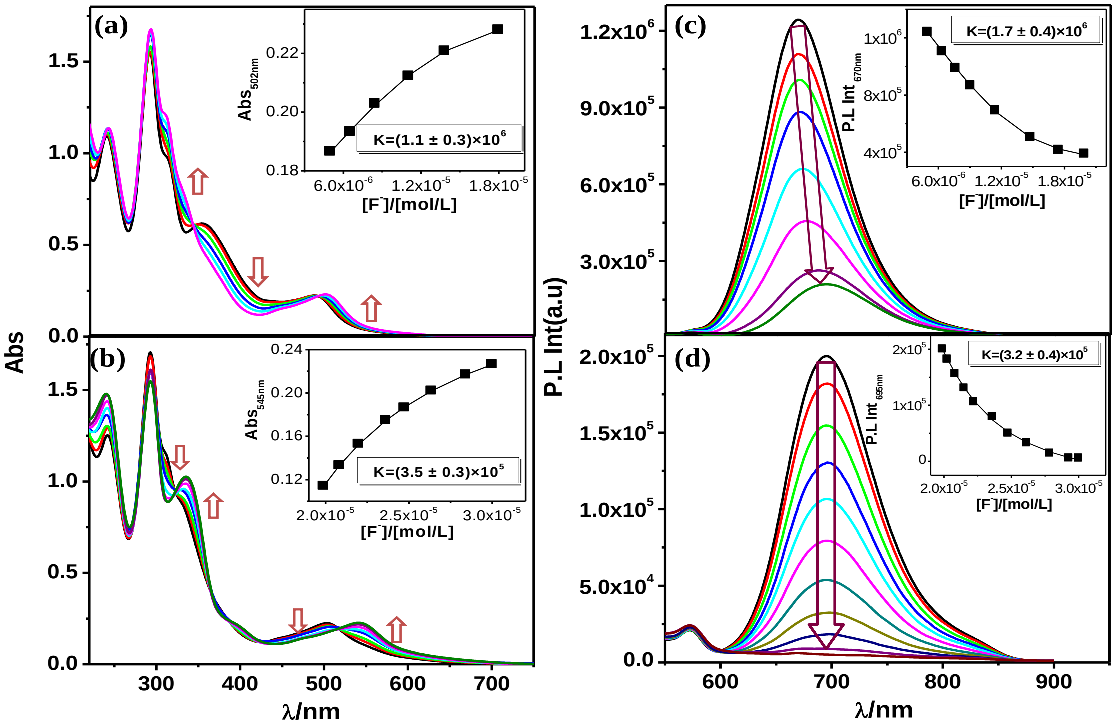

Figure 5.3. Change in absorption (a-b) and emission (c-d) spectral profile of **1** in MeCN with gradual addition of F$^-$. Insets show the binding profile.

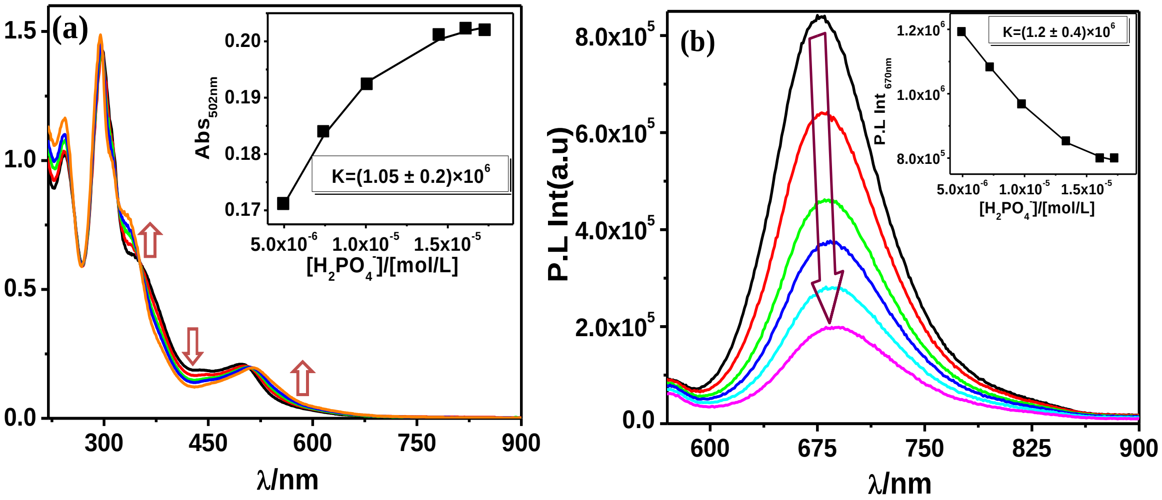

Figure 5.4. Change of absorption (a) and emission (b) spectral profile of complex in MeCN with gradual addition of $H_2PO_4^-$. Insets show the binding profile.

the process the absorption curves pass through a new set of isosbesic points (320, 365, and 518 nm) and saturation occurs with 3 equiv of the anions. The spectral behavior of the complex with AcO^- and CN^- is almost similar to that of F^-. The spectral behavior of the complex with $H_2PO_4^-$ differs from the rest as shown in Figure 5.4 and saturation takes place upon 3 equiv of $H_2PO_4^-$. The absorption titration data are utilized to estimate the equilibrium constant (*K*) for receptor-anion interaction process and the observed values are grossly of six orders of magnitudes (Table 5.3).

Table 5.3. Binding Constants [a,b] (*K*) for **1** in MeCN and H_2O

(MeCN medium)				
	From absorption spectra		From emission spectra	
Anion	K_1	K_2	K_1	K_2
F^-	1.1×10^6	3.5×10^5	1.7×10^6	3.2×10^5
$H_2PO_4^-$	1.0×10^6	-	1.2×10^6	-
(H_2O medium)				
	From absorption spectra		From emission spectra	
CN^-	2.8×10^5	4.7×10^4	1.8×10^5	4.8×10^4

[a] t-Butyl salts of the respective anions were used for the studies.

[b] Estimated errors were < 15 %.

5.3.4. Emission Spectral Monitoring. Upon excitation at the MLCT maxima, the complex exhibits an emission band with its maximum at 670 nm in MeCN at room temperature (RT). The quantum yield (Φ) of emission is estimated to be 0.014, while the lifetime (τ) is measured to be 66.0 ns by time-correlated single photon counting technique. By comparing the spectra of related polypyridine complexes of Ru(II), the origin of emission in the present complex is probably due to the radiative deactivation of its $^3MLCT_{Ru\rightarrow bpy}$ state.

The sensing behavior of the complex is also investigated via emission spectroscopy. The emission spectrum of the complex as a function of anions is displayed in Figure 5.2. It is observed that the emission intensity remains almost invariant in presence of Cl^-, Br^-, I^-, and SCN^-, moderately quenched with $H_2PO_4^-$, while almost completely quenched together with considerable red-shift in presence of F^-, AcO^- and CN^-. The observed trend in emission spectral behavior is in-line with those of the absorption spectral measurements. The emission titration experiments are also executed in order to acquire quantitative insights about the complex-anion interplay. For acquiring the emission spectra upon varying concentration of anions, we use the excitation light source at 494 nm which is the isosbestic point in absorption titration measurements. The spectral change as function of increasing concentration of the anions are presented in Figure 5.3-5.4. Two-step changes are also evident here with F^-, AcO^- and CN^-. The first-step change occurs up to the addition of 2 equiv of the said anions where quenching is accompanied with red-shift of emission-maximum. Continued addition up to 3 equiv induces further quenching without alteration of emission maximum in the second step. $H_2PO_4^-$ induces only one-step change in its spectral portrait (emission quenching with small red-shift). The emission spectral data are also utilized to determine the equilibrium constants of the complex-anion interplay. The insets to Figure 5.3-5.4 demonstrate the fit of the experimental emission data to a 1:1 binding profile and the values of the equilibrium/binding constants are found in the order of 10^6 which is in the same order as we observed with absorption spectroscopic measurements. (Table 5.3).

The variation of lifetime of the complex with anions is also measured. Typically, the lifetime changes upon addition of F^- is shown in Figure 5.5. The mono-exponential decay of the free complex is found to gradually converted into the bi-exponential one together with overall decrease of lifetime. Thus, it is anticipated the existence of at least two different luminescent species, comprising of the anion-bound form of the complex, whose lifetime is shorter, and free complex, the sum of which grades the observed overall decrease of lifetime as shown in Figure 5.5. Hence, the present complex could be regarded as a suitable lifetime-based sensor for selected anions.

It has already been pointed out that in aqueous medium the complex is very much selective towards CN^- among the anions. We perform the titration experiments in HEPES buffer medium at pH-7.3 in order to eliminate the interference of acid or base that may results because of the hydrolysis of TBA salts of the anions. The emission spectral profile as a function of CN^- is presented in Figure 5.6. Quenching of emission occurs in two consecutive steps similar to those observed in MeCN but the extent of shift as well as quenching is little less relative to MeCN. The degree of interaction amongst the complex and the anions in water is accessed via the calculation of equilibrium/binding constant by

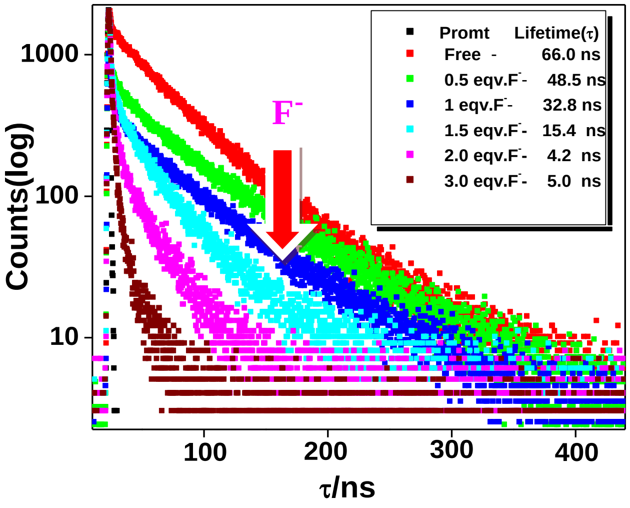

Figure 5.5 Change of excited state decay of **1** in MeCN with gradual addition of F^-. Inset shows the value of life time.

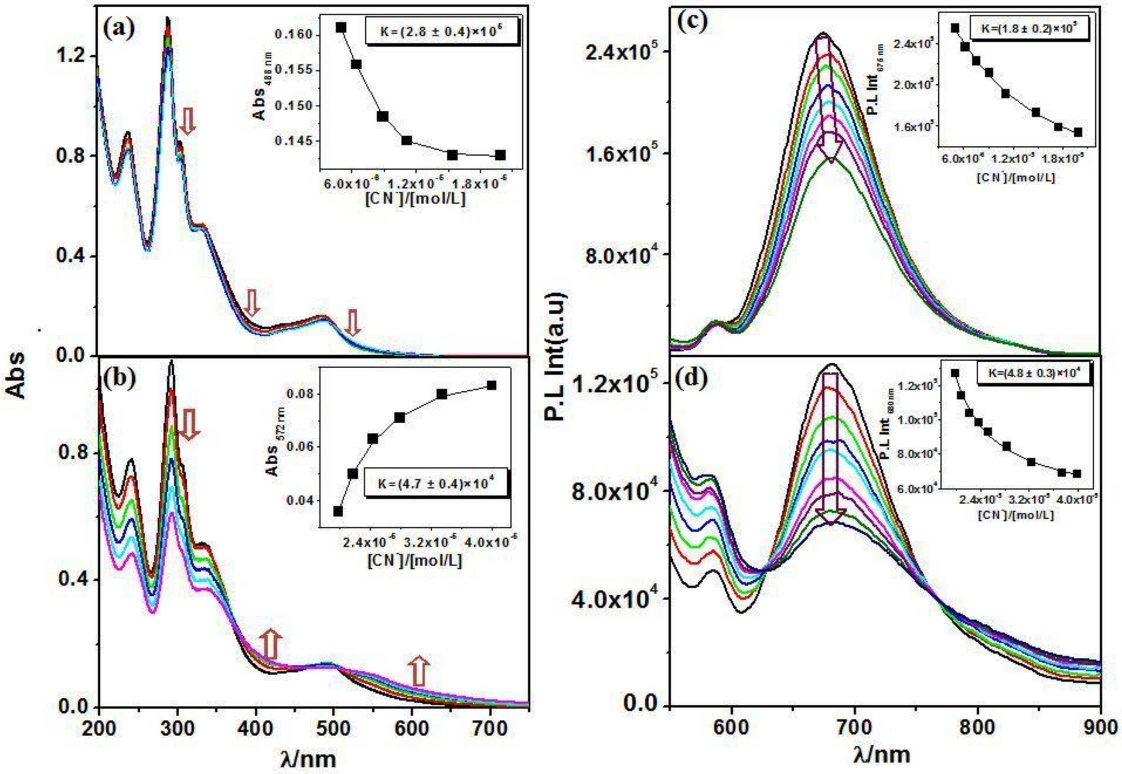

Figure 5.6. Change of absorption (a-b) and emission (c-d) spectral profile of complex **1** in water-HEPES buffer (pH = 7.3) with gradual addition of CN^-. Insets show the binding profile.

exploitation of the emission titration data and the assessed values are in the order of 10^4-10^5 (Table 5.3). The limit of detection for CN^- in H_2O is estimated to be ~1.2×10^{-8} M (Figure 5.7-5.8, Table 5.4). It is astonishing that the value is far less than the allowable

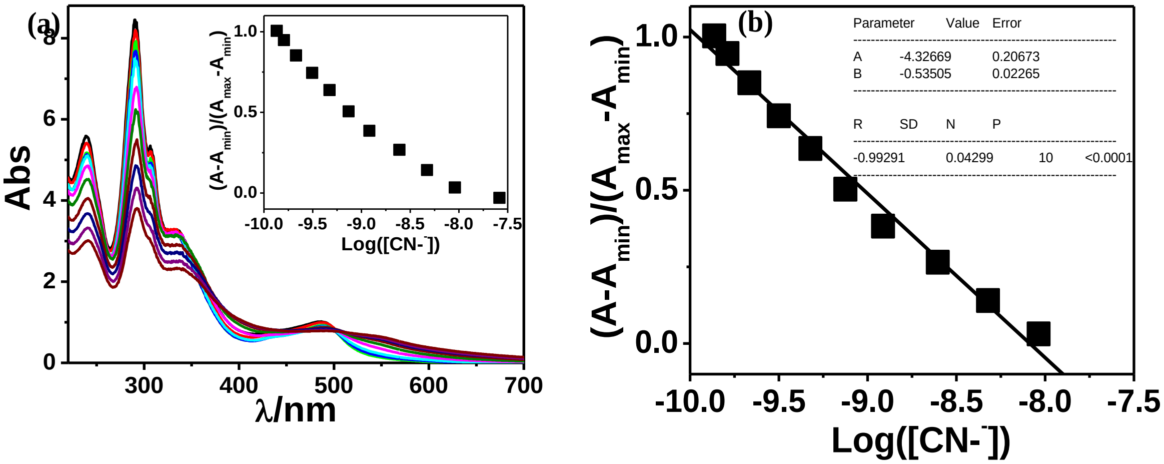

Figure 5.7. (a) Change of absorption spectra of the complex **1** (2.0×10^{-5} M) with CN^- water-HEPES buffer (pH = 7.3), inset: Normalized absorbance between the minimum absorbance and the maximum absorbance. (b) A plot of (A-A_{min})/ (A_{max}-A_{min}) vs. Log ([CN^-]), the calculated detection limit of receptor is 1.25×10^{-8} M.

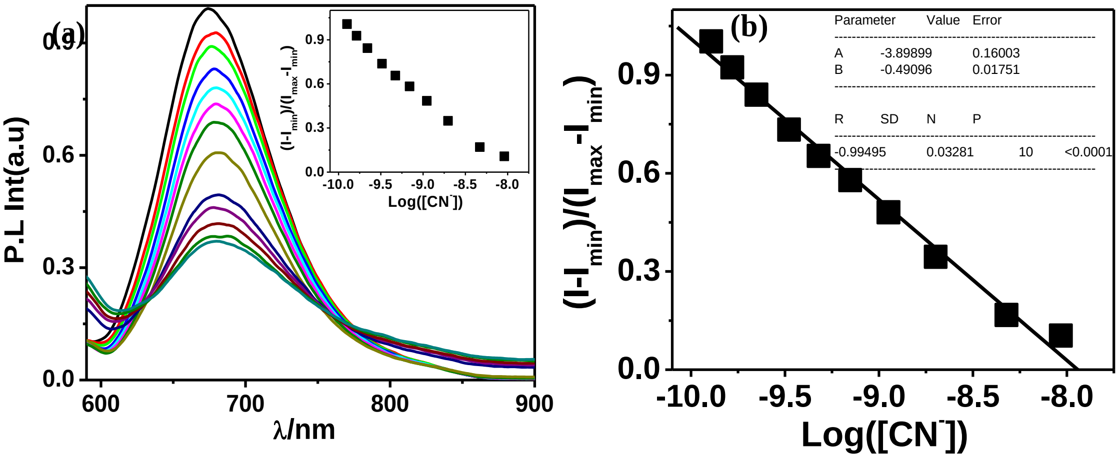

Figure 5.8. (a) Emission spectral changes during the titration of the complex **1** (2.0×10^{-5} M) with CN^- water-HEPES buffer (pH = 7.3), inset: Normalized intensity between the minimum intensity and the maximum intensity. (b) A plot of (I-I_{min})/(I_{max}-I_{min}) vs Log ([CN^-]), the calculated detection limit of receptor is 1.10×10^{-8} M.

Table 5.4 Value of Limit of Detection of **1** in H_2O

Detection Limit (M) in H_2O	
CN^-	
Absorption	Emission
1.25×10^{-8}	1.10×10^{-8}

limit (0.2 ppm) in drinking water as endorsed by Environment Protection Agency (EPA).[69] Decent selectivity and sensitivity in combination with its chromogenic and fluorogenic conduct makes the complex a suitable sensor for CN^- in water. Selectivity of the complex to CN^- is perhaps due of its lesser hydration energy ($\Delta G_h°$= -295 kJ/mol for CN^-) relative to F^- ($\Delta G_h°$= -465 kJ/mol) and AcO^- ($\Delta G_h°$= -365 kJ/mol).[70] Larger $\Delta G_h°$ of the other anions confine them to become hydrated instead of interacting with NH protons in the complex.

5.3.5. Electrochemical Monitoring. CV and SWV voltammetry are utilized to investigate the variation in the redox potential of the complex upon treating with the anions. The complex exhibits a reversible Ru^{II}/Ru^{III} couple with its $E_{1/2}$ = 0.93 V and two consecutive one-electron reversible reductions at -1.55 and -1.83 V due to reduction of two bpy motifs. The oxidative electrochemical behavior was monitored upon gradual addition of anions and the associated changes in SWV are displayed in Figure 5.9. The couple at 0.93 V gradually decreased in current intensity with concomitant evolution of a

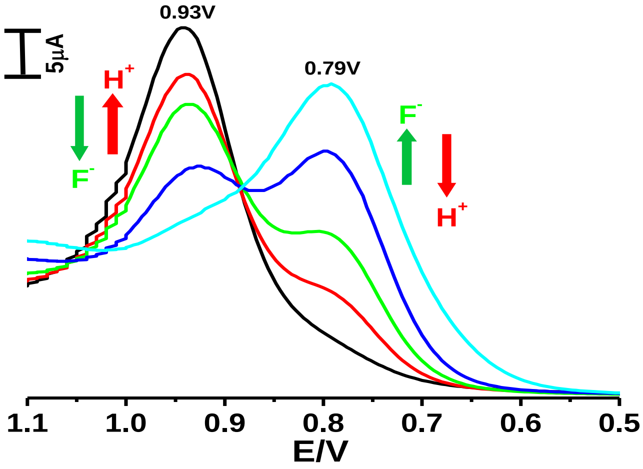

Figure 5.9. Change of SWVs of complex **1** in MeCN with gradual addition of F^- and H^+.

new peak at 0.79 V and eventually the original peak at 0.93 V is replaced by the peak at 0.79 V up to the addition of 2 equiv of F^-. Similar behavior is also observed with AcO^- and CN^- ions. In essence, the $E_{1/2}$ of the Ru^{3+}/Ru^{2+} couple is found to be substantially shifted towards lower potential in presence of strongly basic anions. The pyrazole and the imidazole NH protons connected with $Ru(bpy)_2$ motif are expected to be removed from the complex backbone and lower their net positive charge which in turn lowers the $E_{1/2}$ of Ru^{3+}/Ru^{2+}couple.

5.3.6. Mode of Receptor-Anion Interaction. We watched considerable variation of the absorption-, emission spectral as well as electrochemical properties of the complex upon treatment with F^-, AcO^-, and CN^-**.** The extent of variation with $H_2PO_4^-$ is comparatively little, whilst more or less insignificant by Cl^-, Br^-, I^- and SCN^-. Despite the occurrence of one pyrazole- and two imidazole NH motifs, two-tier changes are evident in the spectral portraits of the complex with F^-, AcO^-, and CN^-. We surmise consecutive dissociation of two NH motifs {most probably pyrazole- and imidazole unit coordinated to $Ru(bpy)_2$ unit}. To make sure of the practicability, absorption and emission titration experiments are accomplished with a strong base (TBAOH) (Figure 5.10). The spectral

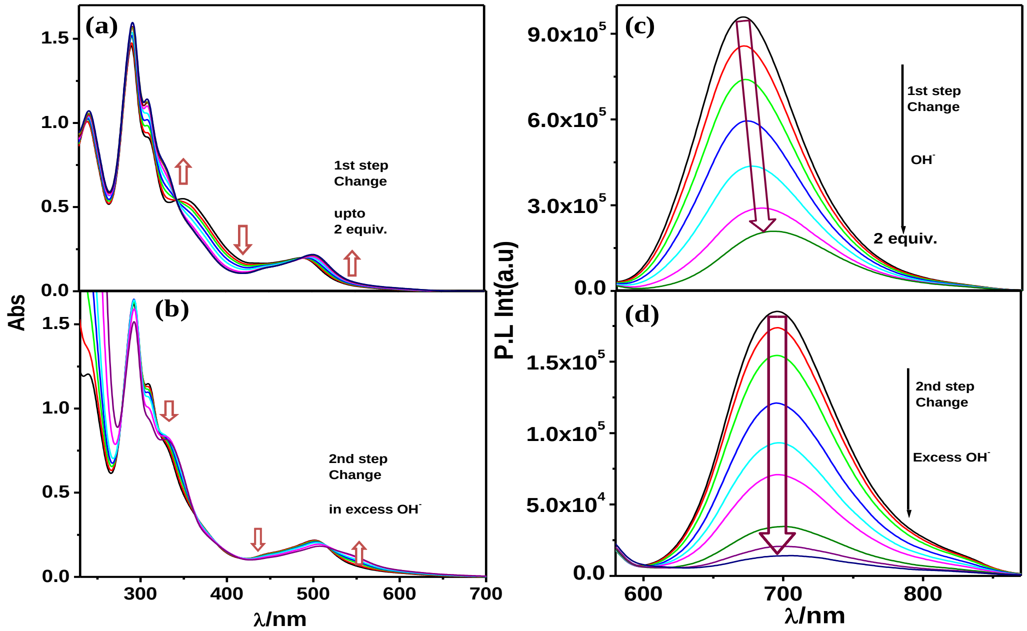

Figure 5.10. Change in absorption (a-b) and emission (c-d) spectral profile of **1** in MeCN with gradual addition of OH^-.

profiles taken as whole closely resemble to those acquired with F$^-$ and AcO$^-$. This points out that anion-prompted dissociation of the pyrazole and imidazole NH protons from the complex.

The overall sensing behavior of the complex through multiple channels is summed up in Figure 5.11. Interestingly, the initial state of the complex could be restored upon the action of acid. Additionally, deprotonation-induced alteration of the photo-redox

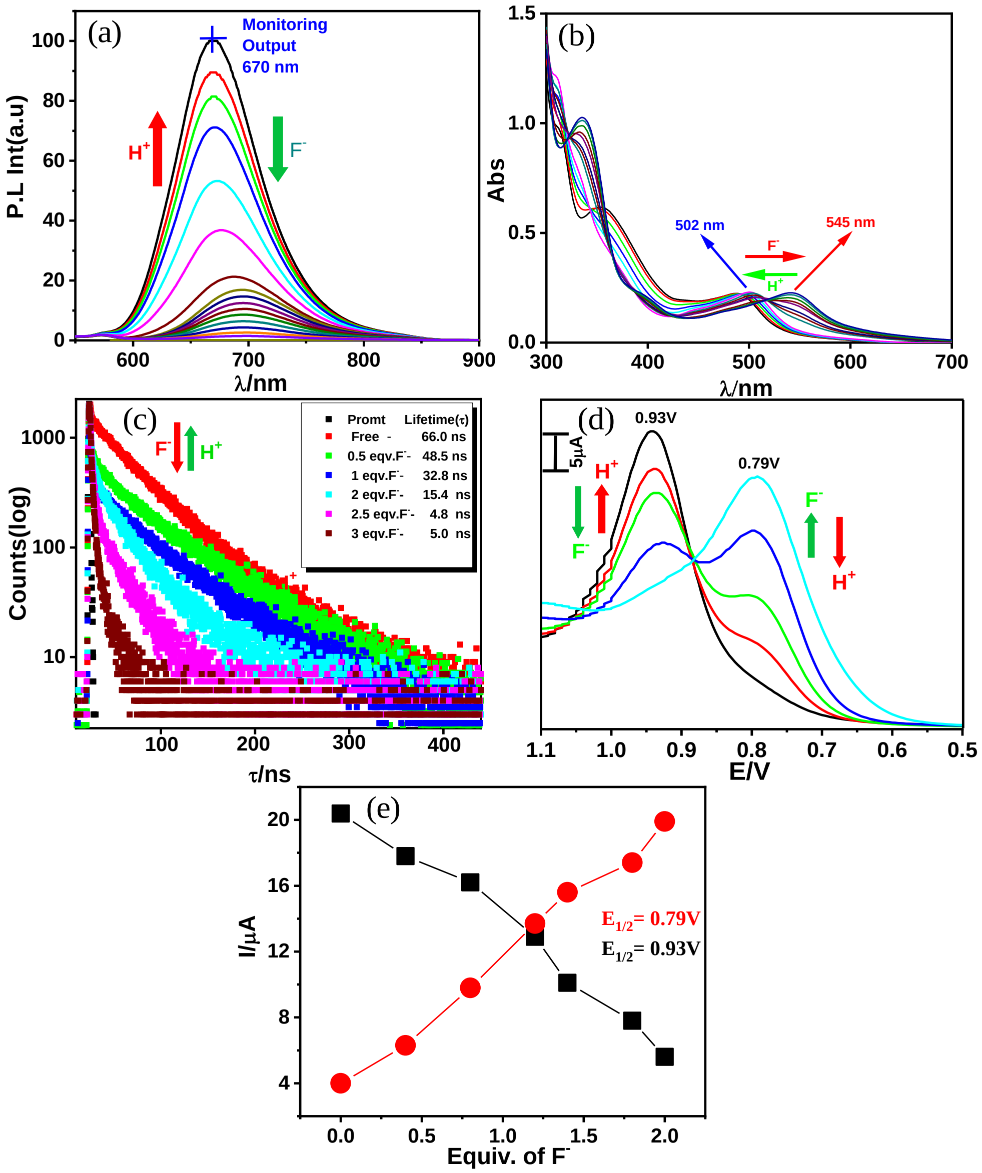

Figure 5.11. Alteration of emission- (a), absorption spectrum (b), luminescence decay together with lifetime (c), square wave voltammogram (d) and current intensity (e) of **1** on addition of F$^-$ and H$^+$.

behavior of the complex by anions followed by restoration of the initial state by acid is reversible and could be repeated many cycles. Now to accomplish detailed sensing investigations by altering the anion concentration over a broad range is extremely tiresome, time-consuming and pricey. To get-rid of the inconvenience as well as to analyze and fully understand the anion sensing behavior of the complex, we applied herein neural network based deep learning methodologies (such as ANN and ANFIS).

5.3.7. Artificial Neural Network (ANN). In order to analyze and forecast the multi-channel anion sensing behavior of the complex, we applied the ANN-function fitting (ANN-FF) tools. As already mentioned in the introduction, ANN is one of the very satisfactory models and operates via input nodes, hidden layer and output nodes. The experimental data are trained here through the use of three algorithms {Levenberg-Marquardt (LM), Scaled Conjugate Gradient (SCG) and Bayesian Regularization (BR)} encrypted via MATLAB 2018, [71] the procedure of which is narrated in Experimental Section. ANN comprises of 3 layers: input-, output-, and hidden layer. The nodes of input layer are associated with the nodes of hidden layer and each node of hidden layer is further linked to the nodes of the output layer. The inputs provided at the input layer will further conveyed to the neurons of the hidden layer. Thus, the hidden layer will receive the naive information from the input layer and then processes it. The gained value is then transmitted to the output layer which thereafter provides the output. In this project, feed forward back propagation neural network is used for comparison of three different training algorithms (LM, SCG and BR) to predict the photo-redox sensing data of the complex.

It is to be noted that LM algorithm typically necessitates higher memory but lesser time. SCG algorithm, on the other hand, often necessitates less memory. The training process stops automatically in both the algorithms once the generalization stops improving, as designated by an upsurge in the mean square error of the validation samples. BR algorithm typically needs more time but could yield good generalization for difficult, small or noisy datasets. In this case, the training process halts according to adaptive weight minimization (regularization). The significant results obtained upon execution of different algorithms are compared on the basis of following four criterions, viz. number of iterations, performance, error histogram, and regression.

The number of iterations plays crucial role in deciding the efficacy of the algorithm. It is evident that SCG requires least number of iterations (Figure 5.12b) while the BR (Figure 5.12c) needs highest number of iterations to accomplish the optimum solution of the experimental data set. After a larger number of training iterations, the

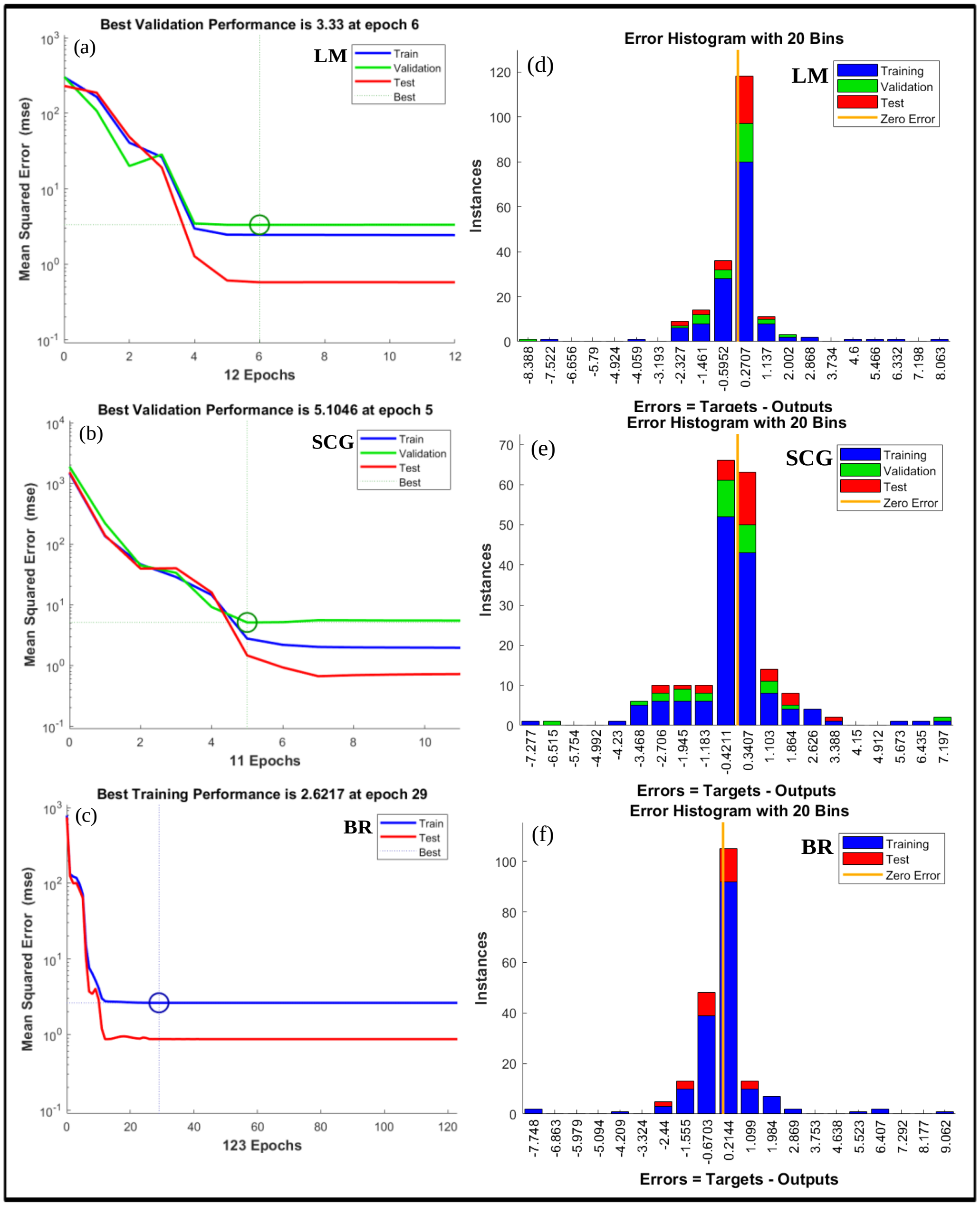

Figure 5.12. The performance (a-c) and error histogram (d-f) of LM, SCG and BR algorithms

error starts dropping. But the error could again start increasing as the over fitting of the training data starts in the validation phase. The iteration or epoch possessing minimum validation error is considered as the best performance. Figure 5.12b clearly indicates that in case of SCG algorithm, the iteration at which optimum mean square error reaches early and thus the number of iterations required are less. By contrast, in LM algorithm, the minimization of error takes place at the latter stage (Figure 5.12a). BR needs more data for training and thus requires many iterations to achieve the least mean square error iteration value (Figure 5.12c). Figure 5.12d-f denotes the histogram of the errors between the target and predicted values after training. The Y-axis characterizes the number of samples in the database that occurs in a definite bin. The bins are equally spread-out breaks that are exploited to category the data on the graph. The data derived during the training course of ANN models are summarized in Table 5.5. The performance of a model is also measured by its regression value (R) which measures the correlation between output and target. The R value close to unity implies good correspondence between output and target and also indicates that the model is performing very well (Figure 5.13). The training state of the ANN models are provided in Figure 5.14. The generated ANN-scheme comprising of 2 inputs, 5 hidden layer and 5 outputs is provided in Figure 5.15.

Table 5.5 Statistical Parameters of the Three Different ANN Models.

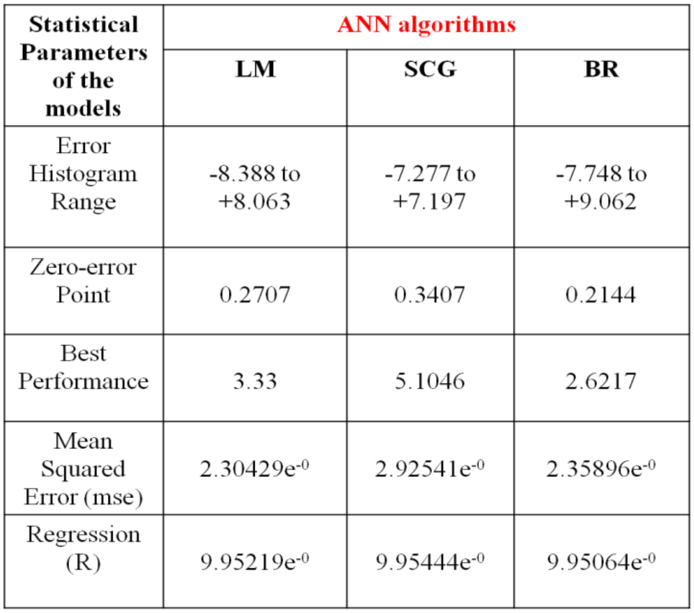

Statistical Parameters of the models	**ANN algorithms**		
	LM	**SCG**	**BR**
Error Histogram Range	-8.388 to +8.063	-7.277 to +7.197	-7.748 to +9.062
Zero-error Point	0.2707	0.3407	0.2144
Best Performance	3.33	5.1046	2.6217
Mean Squared Error (mse)	$2.30429e^{-0}$	$2.92541e^{-0}$	$2.35896e^{-0}$
Regression (R)	$9.95219e^{-0}$	$9.95444e^{-0}$	$9.95064e^{-0}$

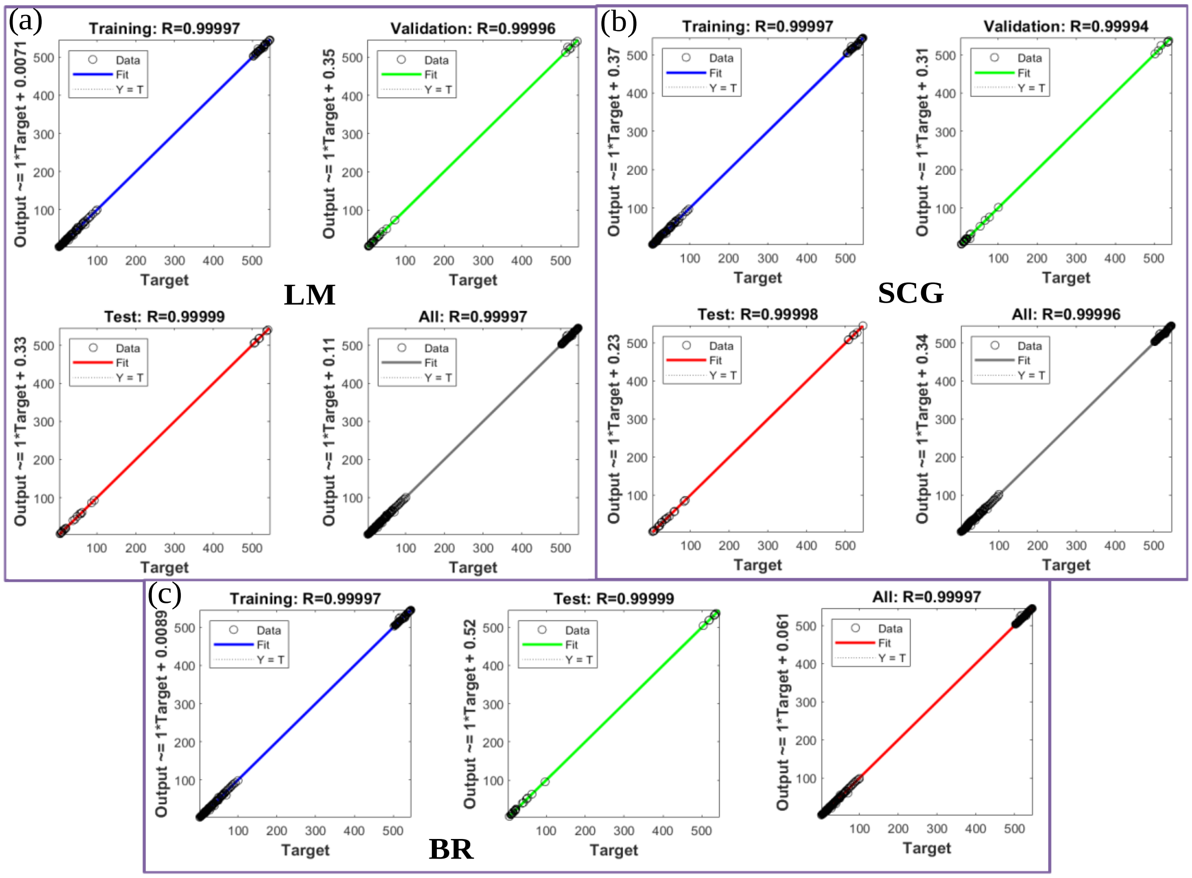

Figure 5.13. Regression plot of LM (a), SCG (b) and BR (c) algorithms.

Comparison of experimental data with different training algorithm-based ANN model outputs are provided in Table 5.6. Upon scrutinizing the results gained by three different algorithms on the basis of various criteria {number of iterations, performance plot, error histogram, mean squared error (mse) and regression}, it can be concluded that Levenberg Marquardt is best suited training algorithm among ANNs for analyzing and prediction of multi-channel anion sensing data of the present metalloreceptor.

5.3.8. Adaptive Neuro-Fuzzy Inference System (ANFIS) We previously said that the amalgamation of FL and NN generates ANFIS network that could remove the shortcoming of each one and often act as best predictive model.[72-75] ANFIS network could be schematically presented in Figure 5.16. 5 layers (excluding the input layer) are inter-connected in the network. The scheme is archetypal for 2 input size, P and Q, both of which are composed of 3 fuzzy sets (C1C2C3 for P, while D1D2D3 for Q). The detailing of each layer is narrated in the experimental section. The fundamental design for

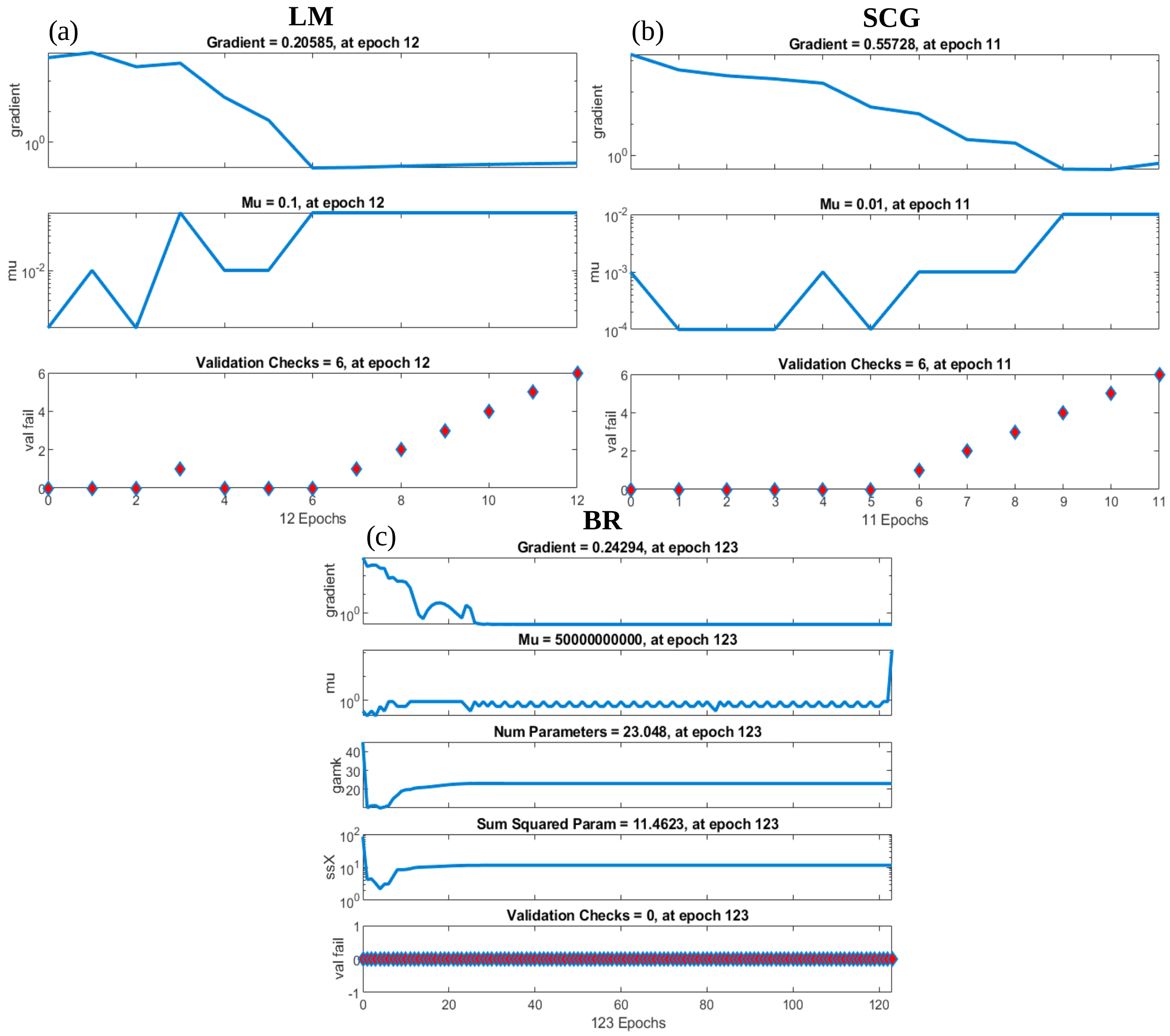

Figure 5.14. Training states of Levenberg-Marquardt (LM) {a}, Scaled Conjugate Gradient (SCG) {b} and Bayesian-Regularization (BR) {c} algorithms.

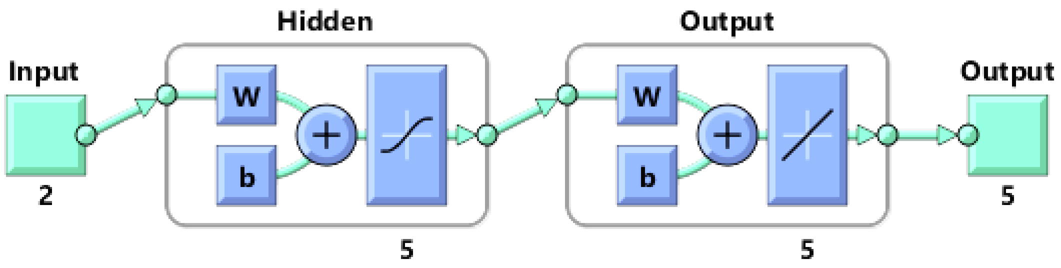

Figure 5.15. Schematic presentation of Artificial Neural Network consisting of 2 inputs, 5 hidden layer and 5 outputs.

Table 5.6. Comparison of Experimental Data with Different Training Algorithm-Based ANN Model Outputs in Presence of 5 Different Combinations of Inputs.

Input Combinations		Experimental Date					Levenberg-Marquardt (LM) Algorithm Based Predicted Data					Scaled Conjugate Gradient (SCG) Algorithm Based Predicted Data					Bayesian-Regularization (BR) Algorithm Based Predicted Data				
Input 1 (F^-)	Input 2 (H^+)	Emission Intensity	UV (nm)	Lifetime Value	Current Intensity at 0.79V	Current Intensity at 0.93V	Emission Intensity	UV (nm)	Lifetime Value (ns)	Current Intensity at 0.79V	Current Intensity at 0.93V	Emission Intensity	UV (nm)	Lifetime Value (ns)	Current Intensity at 0.79V	Current Intensity at 0.93V	Emission Intensity	UV (nm)	Lifetime Value (ns)	Current Intensity at 0.79V	Current Intensity at 0.93V
2.9	0.3	6.11	542.85	7.12	18.05	6.12	5.81	542.62	7.17	18.49	6.12	6.03	543.04	7.24	18.12	6.20	5.68	542.97	7.08	18.25	6.33
2.6	0.9	15.75	536.21	14.68	13.11	11.03	16.84	536.48	14.81	12.88	11.49	15.57	535.42	16.32	13.31	10.98	17.11	536.02	14.74	13.09	11.34
1.7	2.2	45.13	520.22	36.81	5.45	19.97	47.32	519.42	38.43	5.45	19.03	43.57	519.58	37.48	5.20	19.21	46.59	519.33	37.88	5.31	19.14
0.9	2.6	73.05	511.92	51.87	5.16	19.53	73.93	511.79	50.88	5.29	19.51	72.97	512.27	50.58	5.34	19.44	74.08	511.61	51.31	5.13	19.66
0.3	2.9	93.25	504.81	61.76	5.23	19.93	92.96	504.61	61.48	5.10	19.98	92.78	505.03	61.52	5.38	19.82	92.73	504.97	61.67	5.21	19.86

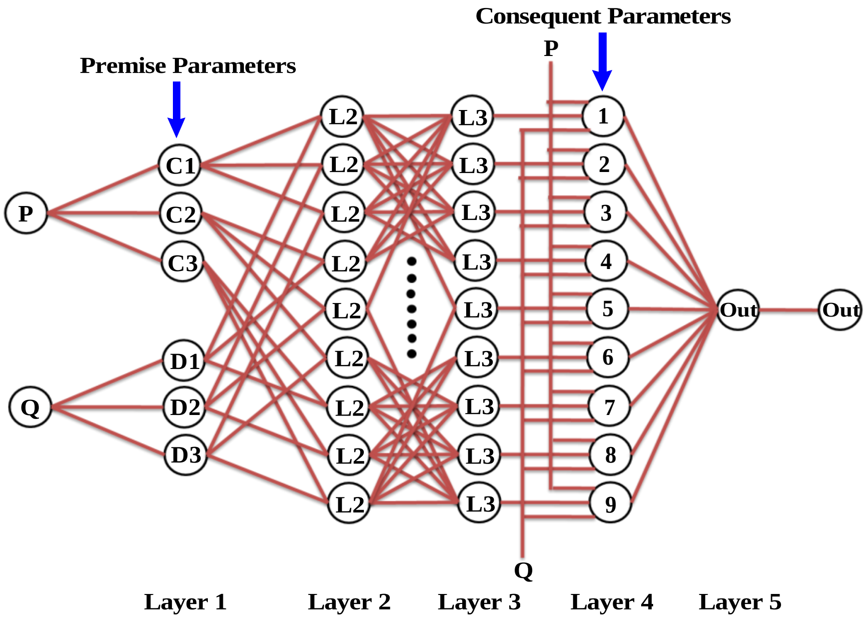

Figure 5.16. Schematic sketch of ANFIS network comprising of two inputs, five layers and one output.

forecasting the output characteristics in presence of F^- and H^+ by ANFIS comprises of 4 segments (fuzzification, knowledge base, ANN, and defuzzification layer) (**Scheme 5.1**).

To build up the scheme, 85% data are used for training while the rest 15% for testing. The training error is found to reduce gradually till 50 epochs signifying that the system learns in each individual step (Figure 5.17). For 2 inputs and 5 membership functions each, the network will create 5^2=25 rules for each output. The conceivable amalgamation of F^- and H^+ generates the output response which consists of 25 rules based on Sugeno’s method (Figure 5.18).

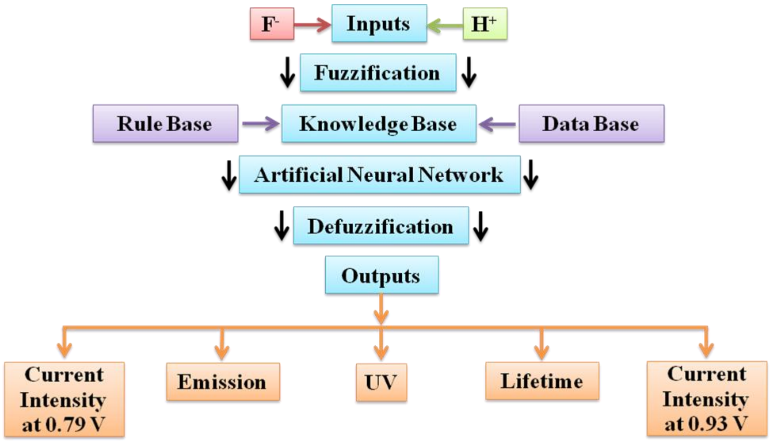

Scheme 5.1 Block diagram of the ANFIS for predicting the output in presence of inputs.

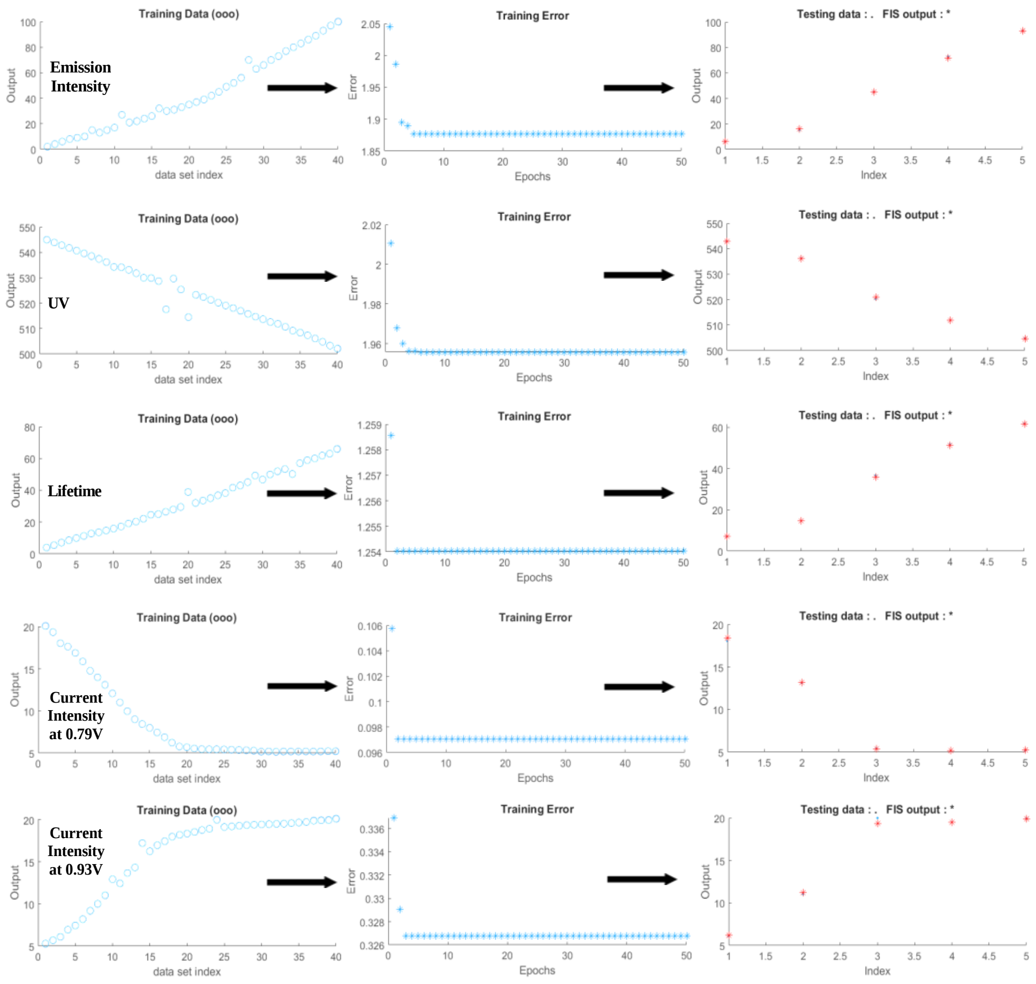

Figure 5.17 Data training process of ANFIS for two inputs and five outputs.

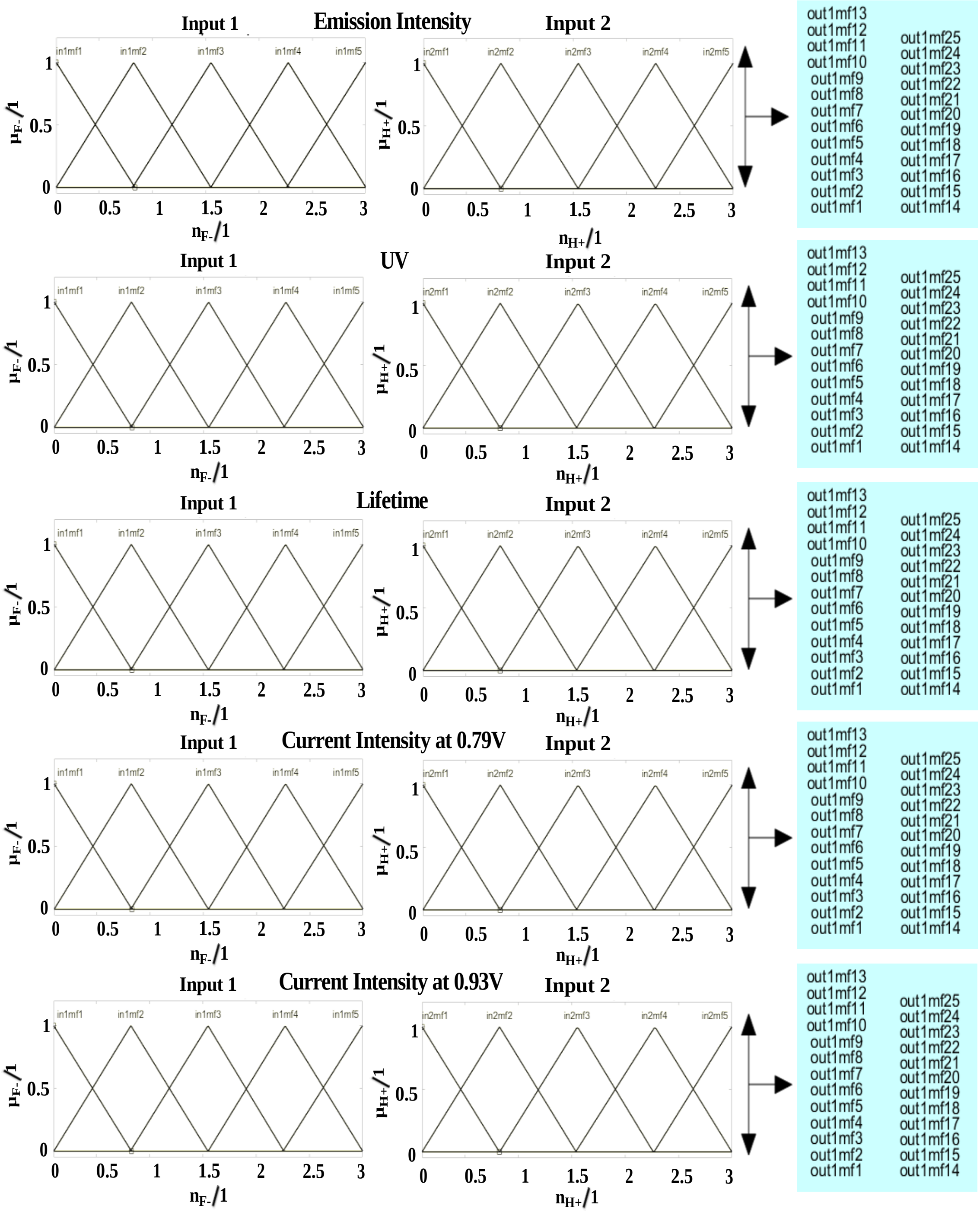

Figure 5.18. Schematic diagram of ANFIS on the basis of Sugeno's method (monitoring five outputs) maintaining 25 rules each.

The ANFIS predicted results for five outputs are displayed in 3D plots (Figure 5.19a-e), while the produced ANFIS structure is shown in Figure 5.19f on the basis of 25 rules. On providing the diverse values of inputs in the rule viewer of ANFIS, we sum-up the outputs in Table 5.7.

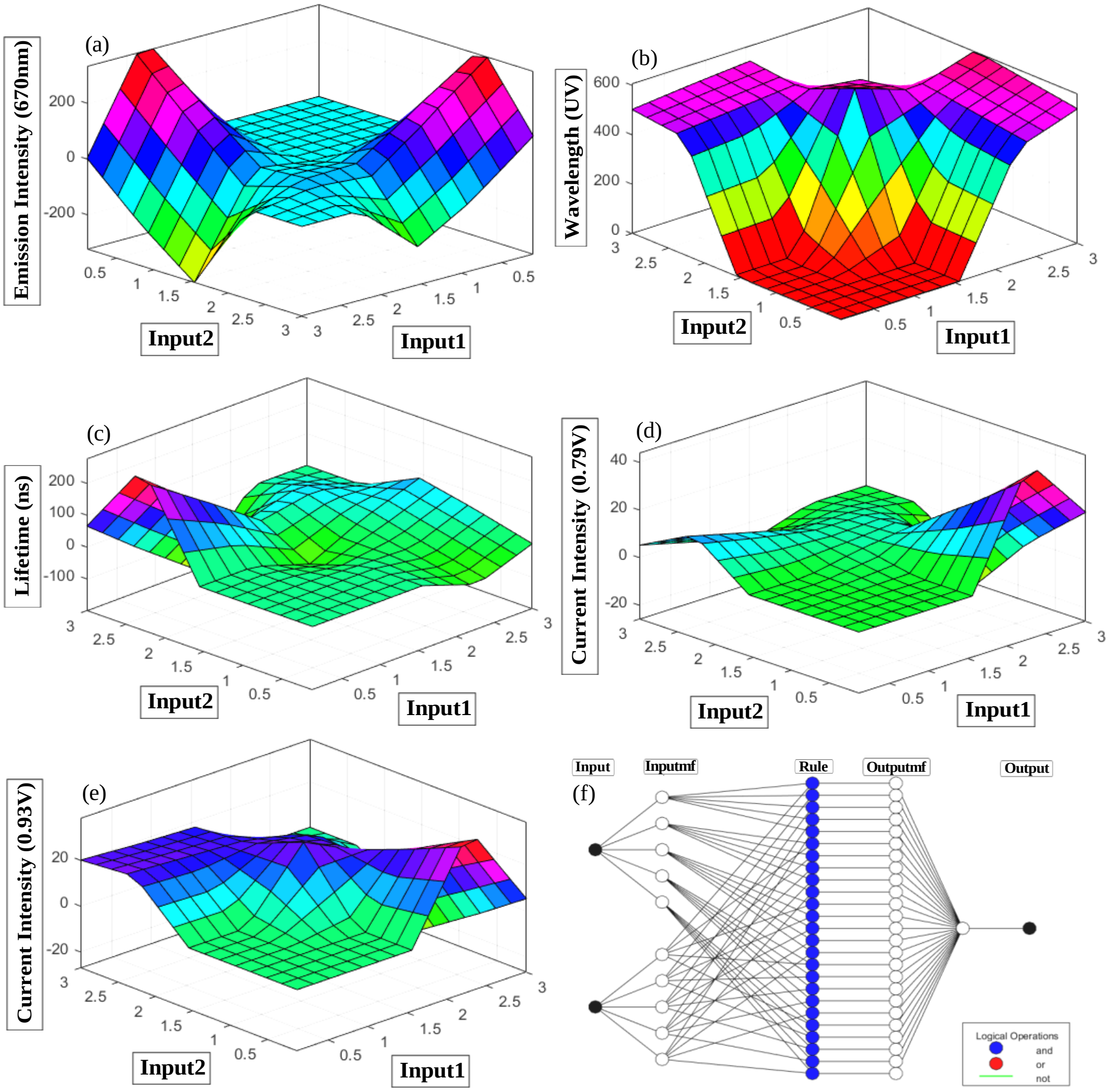

Figure 5.19. The variation of five outputs of **1** in presence of F$^-$ and H$^+$ (a-e). Generated ANFIS structure (f) consisting of two inputs (with five membership functions each) and one output.

Table 5.7. Comparison of experimental data with ANFIS predicted outputs.

Input Combinations		**Emission Intensity at 670 nm**		**UV (nm)**		**Lifetime (ns)**		**Current Intensity at 0.79 V**		**Current Intensity at 0.93 V**	
Input 1 (F$^-$)	Input 2 (H$^+$)	Expt. Data	ANFIS Output	Expt. Data	ANFIS Output	Expt. Data	ANFIS Output	Expt. Data	ANFIS Output	Expt. Data	ANFIS Output
2.9	0.3	6.11	5.99	542.85	543.12	7.12	7.14	18.05	18.41	6.12	6.21
2.6	0.9	15.75	15.91	536.21	536.07	14.68	14.81	13.11	13.24	11.03	11.23
1.7	2.2	45.13	44.92	520.22	521.21	36.81	35.92	5.45	5.37	19.97	19.38
0.9	2.6	73.05	71.52	511.92	512.08	51.87	51.42	5.16	5.15	19.53	19.52
0.3	2.9	93.25	92.81	504.81	505.15	61.76	61.79	5.23	5.24	19.93	19.87

The effectiveness of the ANFIS network is deliberated statistically upon considering their root mean squared errors (RMSE) (Table 5.8). The testing RMSE value of training dataset 4 (RMSE = 0.097041) and 5 (RMSE = 0.326787) is indicative of proper functionality of the system. But the RMSE of the rest three training datasets are greater than unity indicating that the data set is badly over-fitted (i.e., created model tests well in sample but has little predictive value when tested out of sample) (Table 5.8).

Table 5.8. RMSE values derived from ANFIS model for five training data sets.

Training Dataset No.	**ANFIS model for**	**Root Mean Squared Error (RMSE)**
1	Emission Intensity at 670 nm	1.876387
2	UV (nm)	1.955814
3	Lifetime (ns)	1.254030
4	Current Intensity at 0.79 V	0.097041
5	Current Intensity at 0.93 V	0.326787

Thus, taking into consideration the performance indicators of different algorithms in both ANN and ANFIS models, it appears that the Levenberg-Marquardt algorithm in ANN network is effective for analyzing and predicting all the five-anion sensing dataset, while the ANFIS network is very much efficient only for two electrochemical anion sensing datasets of the receptor.

5.4. Conclusions

With regard to our ongoing interest in implementing machine learning tools in chemistry, we thoroughly investigated anion sensing characteristics of a monometallic Ru(II)-bipyridine complex containing pyrazole-3,5-bis (benzimidazole) moiety through multiple optical channels as well as by square wave voltammetry. The design strategy furnishes one pyrazole- and two imidazole NH motifs in the secondary coordination sphere of the complex which have the ability to commune with anions through hydrogen bonding interaction or by anion-induced deprotonation. Anion-responsive behavior of the complex is convincingly demonstrated in both organic and aqueous media through absorption, emission as well as by CV and SWV. In practice, remarkable alteration of the photo-redox behavior of the complex takes place in presence of anions. In absence of anion, the complex displays emission and corresponds to the “on-state”, whereas inclusion of anions induces almost complete emission quenching and represents the “off-state”. The restoration of the initial state of the complex is also made possible by acid. Essentially, the complex acts as anion- and acid-responsive molecular switch.

To execute detailed sensing investigations by varying the anion concentration within a broad range is extremely tiresome, time-consuming and pricey. To get-rid of the inconvenience, we applied herein several soft computing methodologies to analyze and fully understand the anion sensing behavior of the complex. Thus, the major focus of the study is the implementation of neural network based deep learning methodologies such as Artificial Neural Networks (ANNs) and Adaptive Neuro-Fuzzy Inference System (ANFIS) to analyze and fully understand the multi-channel anion sensing behavior of the complex. We also compared the outputs of the both models with those of the experimentally observed values. Upon considering the performance indicators of different algorithms, it is evident that the Levenberg-Marquardt algorithm in ANN network is effective for analyzing and predicting all the five-anion sensing dataset, while the ANFIS network is very much efficient only for two electrochemical anion sensing datasets of the receptor.

5.5. References

1. Artrith, N.; Butler, K. T.; Coudert, F. X.; Han, S.; Isayev, O.; Jain, A.; Walsh, A. Best Practices in Machine Learning for Chemistry. *Nat. Chem.* **2021**, *13*, 505-508.
2. Mater, A. C.; Coote, M. L. Deep Learning in Chemistry. *J. Chem. Inf. Model.* **2019**, *59*, 2545-2559.

3. Pflüger, P. M.; Glorius, F. Molecular Machine Learning: The Future of Synthetic Chemistry? *Angew. Chem. Int. Ed.* **2020**, *59*, 18860-18865.
4. He, L.; Bai, L.; Dionysiou, D. D.; Wei, Z.; Spinney, R.; Chu, C.; Xiao, R. Applications of Computational Chemistry, Artificial Intelligence, and Machine Learning in Aquatic Chemistry Research. *Chem. Eng. J.* **2021**, *426*, 131810.
5. Gentili, P. L. A Strategy to Face Complexity: The Development of Chemical Artificial Intelligence. In Advances in Artificial Life, Evolutionary Computation, and Systems Chemistry; Rossi, F., Piotto, S., Concilio, S., Eds.; Springer: Cham, Switzerland; New York, NY, USA. **2017**, 708, 151-160.
6. Zadeh, L. A. Toward human level machine intelligence-is it achievable? the need for a paradigm shift. *IEEE Comput. Intell. Mag.* **2008**, *3*, 11-22.
7. Szaciłowski, K. Digital Information Processing in Molecular Systems. *Chem. Rev.* **2008**, *108*, 3481-3548.
8. Zadeh, L.A. Outline of a New Approach to the Analysis of Complex Systems and Decision Processes. *IEEE Trans. Syst. Man Cyb.* **1973**, *3*, 28-44.
9. Conrad, M. Molecular Computing. *Adv. Comput***.** **1990**, 31, 235-324.
10. Wlaźlak, E.; Przyczyna, D.; Gutierrez, R.; Cuniberti, G.; Szaciłowski, K. Towards Synthetic Neural Networks: Can Artificial Electrochemical Neurons be Coupled with Artificial Memristive Synapses? *Jpn. J. Appl. Phys.* **2020,** *59*, SI0801(1-16).
11. Pilarczyk, K.; Daly, B.; Podborska, A.; Kwolek, P., Silverson, V.A.D.; de Silva A. P.; Szaciłowski, K. Coordination Chemistry for Information Acquisition and Processing. *Coord. Chem. Rev.* **2016,** *325*, 135-160.
12. Vo, A. H.; Vleet, T. R.V.; Gupta, R. R.; Liguori, M. J.; Rao, M. S. An Overview of Machine Learning and Big Data for Drug Toxicity Evaluation. *Chem. Res. Toxicol.* **2020**, *33*, 20-37.
13. Korshunova, M.; Ginsburg, B.; Tropsha, A.; Isayev, O. Open Chem: A Deep Learning Toolkit for Computational Chemistry and Drug Design. *J. Chem. Inf. Model.* **2021**, *61*, 7-13.
14. Lu, J.; Zhang Y. Unified Deep Learning Model for Multitask Reaction Predictions with Explanation. *J. Chem. Inf. Model.* **2022**, *62*, 1376-1387.

15. Singh, K.; Munchmeyer, J.; Weber, L.; Leser, U.; Bande A. Graph Neural Networks for Learning Molecular Excitation Spectra. *J. Chem. Theory Comput.* **2022**, *18*, 4408-4417.
16. Yao, K.; Herr, J. E. Brown, S. N.; Parkhill, J. Intrinsic Bond Energies From a Bonds-In-Molecules Neural Network. *J. Phys. Chem. Lett.* **2017**, *8*, 2689-2694.
17. Cho, E. H.; Deng, X.; Zou, C.; Lin, L. C. Machine Learning-Aided Computational Study of Metal-Organic Frameworks for Sour Gas Sweetening. *J. Phys. Chem. C* **2020**, *124*, 27580-27591.
18. Shiratori, K.; Bishop, L. D. C.; Ostovar, B.; Baiyasi, R.; Cai, Y.Y.; Rossky, P. J.; Landes, C. F.; Link, S. Machine-Learned Decision Trees for Predicting Gold Nanorod Sizes From Spectra. *J. Phys. Chem. C* **2021**, *125*, 19353-19361.
19. Zhu, L.; Zhou, J.; Sun, Z. Materials Data Toward Machine Learning: Advances and Challenges. *J. Phys. Chem. Lett.* **2022**, *13*, 3965-3977.
20. Takahashi, K.; Takahashi, L.; Creating Machine Learning-Driven Material Recipes Based on Crystal Structure. *J. Phys. Chem. Lett.* **2019**, 10, 283-288.
21. Brown, K. A.; Brittman, S.; Maccaferri, N.; Jariwala, D.; Celano U. Machine Learning in Nanoscience: Big Data at Small Scales. *Nano Lett.* **2020**, *20*, 2-10.
22. Cui, F.; Yue, Y.; Zhang, Y.; Zhang, Z.; Zhou, H. S. Advancing Biosensors with Machine Learning. *ACS Sens.* **2020**, *5*, 3346-3364.
23. Ayyappan, V.; Chang, A.; Zhang, C.; Paidi, S. K.; Bordett, R.; Liang, T.; Barman, I.; Pandey, R. Identification and Staging of B-Cell Acute Lymphoblastic Leukemia Using Quantitative Phase Imaging and Machine Learning. *ACS Sens.* **2020**, *5*, 3281-3289.
24. Kang, M.; Cho, I.; Park, J.; Jeong, J.; Lee, K.; Lee, B.; Henriquez, D. D. O.; Yoon, K.; Park, I. High Accuracy Real-Time Multi-Gas Identification by a Batch-Uniform Gas Sensor Array and Deep Learning Algorithm. *ACS Sens.* **2022**, *7*, 430-440.
25. Coliaie, P.; Prajapati, A.; Ali, R.; Korde, A.; Kelkar, M. S.; Nere, N. K.; Singh, M. R. Machine Learning-Driven, Sensor-Integrated Microfluidic Device for Monitoring and Control of Supersaturation for Automated Screening of Crystalline Materials. *ACS Sens.* **2022**, *7*, 797-805.

26. Ma, P.; Xu, W.; Teng, Z.; Luo, Y.; Gong, C.; Wang, Qin. An integrated Food Freshness Sensor Array System Augmented by a Metal-Organic Framework Mixed-Matrix Membrane and Deep L:earning. *ACS Sens.* **2022**, *7*, 1847-1854.
27. Jin, Y.; Du, N.; Huang, Y.; Shen, W.; Tan, Y.; Chen, Y. Z.; Dou, W.T.; He, X. P.; Yang, Z.; Xu, N.; Tan, C. Fluorescence Analysis of Circulating Exosomes for Breast Cancer Diagnosis Using a Sensor Array and Deep Learning. *ACS Sens.* **2022**, *7*, 1524-1532.
28. Li, D.; Liu, W.; Zhu, B.; Qu, M.; Zhang, Q.; Fu, Y.Q.; Xie, Jin. Machine Learning-Assisted Multifunctional Environmental Sensing Based on a Piezoelectric Cantilever. *ACS Sens.* **2022**, *7*, 2767-2777.
29. Dias, G. G.; Rodrigues, M. O.; Paz, E. R. S.; Nunes, M. P.; Araujo, M. H.; Rodembusch, F. S.; da Silva Júnior, E. N. Aryl-Phenanthro[9,10‑*d*]Imidazole: A Versatile Scaffold for the Design of Optical-Based Sensors. *ACS Sens.* **2022**, *7*, 10, 2865-2919.
30. Cao, Y.; Yu, H.; Abbott, N. L.; Zavala, V .M. Machine Learning Algorithms for Liquid Crystal-Based Sensors. *ACS Sens.* **2018**, *3*, 2237-2245.
31. Schroeder, V.; Evans, E. D.; Wu, Y.C.M.; Voll, C.C.A.; McDonald, B. R.; Savagatrup, S.; a Swager, T. M. Chemiresistive Sensor Array and Machine Learning Classification of Food. *ACS Sens.* **2019**, *4*, 2101-2108.
32. Baitalik, S.; Flörke, U.; Nag, K. Synthesis, Structure, Redox Activity and Spectroscopic Properties of Ruthenium(II) Complexes with 3,5-Bis(Benzothiazol-2-yl)Pyrazole, 3,5-Bis(Benzimidazol-2-yl)Pyrazole and 2,2-Bipyridine as Co-Ligands. *Dalton Trans.*, **1999**, 719-727.
33. Balzani, V.; Juris, A.; Venturi, M.; Campagna S.; Serroni, S. Luminescent and Redox-Active Polynuclear Transition Metal Complexes. *Chem. Rev*. **1996**, *96*, 759-834.
34. Sauvage, J. P. ; Collin, J. P. J. ; Chambron, C. ; Guillerez, S. ; Coudret, C. ; Balzani, V.; Barigelletti, F.; De Cola, L. ; Flamigni, L. Ruthenium(II) and Osmium(II) Bis (Terpyridine) Complexes in Covalently-Linked Multicomponent Systems: Synthesis, Electrochemical Behavior, Absorption Spectra, and Photochemical and Photophysical Properties. *Chem. Rev.* **1994**, *94*, 993-1019.

35. Santoni, M.P.; Hanan, G. S.; Hasenknopf, B.; Proust, A.; Nastasi, F.; Serroni, S.; Campagna. S. Dinuclear Ru (II) Complexes of Bis-(Dipyrid-2′-yl) Triazine (Bis-dpt) Ligands as Efficient Electron Reservoirs. *Chem. Commun*. **2011**, *47*, 3586-3588.
36. Fang,Y. Q.; Taylor, N. J. ; Hanan, G. S.; Loiseau, F.; Passalacqua, R.; Campagna, S. ; Nierengarten, H.; Dorsselaer, A. V. A Strategy for Improving the Room-Temperature Luminescence Properties of Ru (II) Complexes with Tridentate Ligands. *J. Am. Chem. Soc.* **2002**, *124*, 7912-7913.
37. Deb, S.; Sahoo, A.; Pal, P.; Baitalik, S. Exploitation of the Second Coordination Sphere to Promote Significant Increase of Room-Temperature Luminescence Lifetime and Anion Sensing in Ruthenium-Terpyridine Complexes. *Inorg. Chem.* **2021**, *60*, 6836-6851.
38. Williams, J. A. G. The Coordination Chemistry of Dipyridylbenzene: N-Deficient Terpyridine or Panacea for Brightly Luminescent Metal Complexes. *Chem. Soc. Rev.* **2009**, *38*, 1783-1801.
39. Harriman, A.; Ziessel, R. Making Photoactive, Molecular-Scale Wires. *Chem. Commun*. **1996**, *15*, 1707-1716.
40. Shao, J. Y; Zhong, Y. W. Stabilization of a Cyclometalated Ruthenium Sensitizer on Nanocrystalline TiO_2 by an Electrodeposited Covalent Layer. *Inorg. Chem.* **2019,** *58*, 3509-3517.
41. Nie, H. J.; Yang, W. W.; Shao, J. Y.; Zhong, Y. W. Ruthenium-Tris(Bipyridine) Complexes with Multiple Redox-Active Amine Substituents: Tuning of Spin Density Distribution and Deep-Red to NIR Electrochromism and Electrofluorochromism. *Dalton Trans.*, **2016**, *45*, 10136-10140.
42. Shao, J. Y.; Wu, S. H.; Ma, J.; Gong, Z. L.; Sun, T. G.; Jin, Y.; Yang, R.; Sun, B.; Zhong, Y. W. Ratiometric Detection of Amyloid-β Aggregation by a Dual-Emissive Tris-Heteroleptic Ruthenium Complex. *Chem. Commun*. **2020**, *56*, 2087-2090.
43. Balgley, R.; Drees, M.; Bendikov, T.; Lahav, M.; Facchetti, A.; van der Boom M. E. Polypyridyl Complexes as Electron Transporting Materials for Inverted Bulk

Heterojunction Solar Cells: The Metal Center Effect. *J. Mater. Chem. C*, **2016**, *4*, 4634-4639.

44. Motiei, L.; Kaminker, R.; Sassi, M.; van der Boom, M. E. Molecule and Electron Transfer Through Coordination-Based Molecular Assemblies. *J. Am. Chem. Soc.* **2011**, *133*, 14264-14266.
45. Lahav, M.; van der Boom M. E. Polypyridyl Metallo-Organic Assemblies for Electrochromic Applications. *Adv. Mater.* **2018**, *30*, 1706641(1-7).
46. Baitalik, S.; Dutta, B.; Nag, K. Spectroscopic and Redox Properties of Rh^{III} Ru^{II} and Ru^{II} Ru^{II} Complexes Derived From 2,2′-Bipyridine, Pyrazole-3,5-Bis(benzimidazole) and 1,2,4-Triazole-3,5-Dicarboxylic Acid as Bridging Ligands. *Polyhedron*. **2004**, *23*. 913-919.
47. Karmakar, S.; Maity, D.; Mardanya, S.; Baitalik, S. Multichromophoric Bimetallic Ru(II) Terpyridine Complexes Based on Pyrenyl-Bis-Phenylimidazole Spacer: Synthesis, Photophysics, Spectroelectrochemistry, and TD-DFT Calculations. *Inorg. Chem.* **2014**, *53*, 12036-12049.
48. Mondal, D.; Bar, M.; Mukherjee, S.; Baitalik, S. Design of Ru(II) Complexes Based on Anthraimidazoledione-Functionalized Terpyridine Ligand for Improvement of Room-Temperature Luminescence Characteristics and Recognition of Selective Anions: Experimental and DFT/TD-DFT Study. *Inorg. Chem.* **2016**, *55*, 9707-9724.
49. Pal, P.; Ganguly, T.; Das, S.; Baitalik S. pH-Responsive Colorimetric, Emission and Redox Switches Based on Ru(II)-Terpyridine Complexes. *Dalton Trans.*, **2021**, *50*, 186-196.
50. Khatua, S.; Schmittel, M. A Single Molecular Light-Up Sensor for Quantification of Hg^{2+} and Ag^{+} in Aqueous Medium: High Selectivity towards Hg^{2+} Over Ag^{+} in a Mixture. *Org.Lett.* **2013,** *12*, 4422-4425.
51. Natarajan, P.; Schmittel, M. On-off Luminescence Signaling of Organic-Inorganic Hybrids Switches, *Inorg. Chem.* **2013,** 52, 8579-8590.
52. Khatua, S.; Samanta, D.; Bats, J. W.; Schmittel, M. Rapid and Highly Sensitive Dual-Channel Detection of Cyanide by Bis-Heteroleptic Ruthenium (II) Complexes. *Inorg. Chem.* **2012,** 51, 7075-7086.

53. Gentili, P.L.; Giubila, M.S.; Germani, R.; Romani, A.; Nicoziani, A.; Spalletti, A.; Heron; B.M. Optical Communication Among Oscillatory Reactions and Photo-Excitable Systems: Uv and Visible Radiation Can Synchronize Artificial Neuron Models. *Angew. Chem. Int. Ed.* **2017**, *56*, 7535-7540.
54. Giri Nandagopal, M. S.; Selvaraju, N. Prediction of Liquid-Liquid Flow Patterns in a Y-Junction Circular Microchannel Using Advanced Neural Network Techniques. *Ind. Eng. Chem. Res.* **2016**, *55*,11346-11362.
55. Zadeh, L. A. Fuzzy sets. In Fuzzy sets, Fuzzy logic, and Fuzzy Systems: Selected Papers by Lotfi A Zadeh, pp. *394-432*. **1996.**
56. Gentili, P. L. Boolean and Fuzzy Logic Gates Based on the Interaction of Flindersine with Bovine Serum Albumin and Tryptophan. *J. Phys. Chem. A.* **2008**, *112*, 11992-11997.
57. Gentili, P. L. The Fuzziness of the Molecular World and Its Perspectives. *Molecules.* **2018**, *23*, 2074.
58. Gentili, P.L. The Fundamental Fuzzy Logic Operators and Some Complex Boolean Logic Circuits Implemented by the Chromogenism of a Spirooxazine. *Phys. Chem. Chem. Phys.* **2011**, *13*, 20335-20344.
59. Gentili, P.L.; Giubila, M.S.; Heron, B.M. Processing Binary and Fuzzy Logic by Chaotic Time Series Generated by a Hydrodynamic Photochemical Oscillator. *Chem Phys Chem.* **2017**, *18*, 1831-1841.
60. Bingöl, D.; Inal, M.; Çetintaş, S. Evaluation of Copper Biosorption Onto Date Palm (phoenix dactylifera L.) Seeds with MLR and ANFIS models. *Ind. Eng. Chem.Res* **2013**, *52*, 4429-4435.
61. İnal, M. Predicting the Conversion ratio for the Leaching of Celestite in Sodium Carbonate Solution Using an Adaptive Neuro-Fuzzy Inference System. *Ind. Eng. Chem.Res* **2014**, *53*, 4975-4980.
62. Sullivan, B. P.; Salmon, D. J.; Meyer, T. J. Mixed Phosphine 2,2'-Bipyridine Complexes of Ruthenium. *Inorg. Chem.* **1978,** *17*, 3334-3341.
63. SAINT (version 6.02), SADABS (version 2.03); Bruker AXS Inc.: Madison, WI, **2002.**

64. Sheldrick, G. M. ***SHELXT***-Integrated Space-Group and Crystal-Structure Determination. *Acta Cryst. A*, **2015**, *71*, 3-8.
65. Dolomanov, O. V.; Bourhis, L. J.; Gildea, R. J.; Howard, J. A. K. and Puschmann, H. *J. Appl. Crystallogr*. **2009**, *42*, 339–341.
66. Spek, A. L. Single-Crystal Structure Validation with the Program PLATON. *J. Appl. Cryst.* **2003**, *36*, 7-13.
67. Spek, A. L. Single-Crystal Structure Validation with the Program PLATON. *J. Appl. Cryst.* **2003**, *36*, 7-13.
68. Bradenburg, K. Diamond, version 3.1 e, Crystal Impact GbR: Bonn, Germany, **2005**.
69. The US Environmental Protection Agency (EPA) has set the so called Maximum Contaminant Level Goals for Cyanide in Drinking Water to 0.2 ppm, and Fluoride to be 2 ppm. http://ecfr.gpoaccess.gov (last Accessed 1st March, 2006).
70. Marcus, Y. *J*. Thermodynamics of Solvation of Ions. *J. Chem. Soc. Faraday Trans*. **1991**, *87*, 2995-2999.
71. MATLAB **2018a**, The MathWorks, Inc., Natick, Massachusetts, United States.
72. Jang, J. S. R.; Sun, C. T. Neuro-Fuzzy Modeling and Control. *Proc. IEEE.* **1995**, *83,* 378-405.
73. Sugeno, M.; Yasukhiro, T. A Fuzzy-Logic-Based Approach to Qualitative Modeling. *IEEE Trans. Fuzzy Syst.* **1993**, *1*, 7-31.
74. Sahoo, A.; Ahmed, T.; Deb, S.; Baitalik, S. Neuro-Fuzzification Architecture for Modeling of Electrochemical Ion-Sensing Data of Imidazole-Dicarboxylate-Based Ru(II)-Bipyridine Complex. *Inorg. Chem*. **2022**, *61*, 10242-10254.
75. Deb, S.; Sahoo, A.; Mondal, P.; Baitalik, S.; Analysis and Prediction of Anion- and Temperature Responsive Behaviours of Luminescent Ru (II)-Terpyridine Complexes by Using Boolean, Fuzzy Logic, Artificial Neural Network and Adapted Neuro Fuzzy Inference Models. *Dalton Trans.,* **2022**, *51*, 15601-15613.

****

Chapter 6

Multi-Channel Anion Sensing Behaviour of a Ru(II)-Bipyridine Complex Based on Benzothiazolyl Pyrazole Ligand: Experimental and Implication of Machine Learning Tools for Data Prediction

6.1. Introduction

Accomplishing computational exertion at the molecular level is currently an important task for the scientists and enormous efforts are being paid to manufacture powerful computers with very small size that are otherwise not obtainable by conventional silicon-based skill.[1-4] Molecular level computational may be achieved through the creation of suitable logic gates that could merge the simple logics to complicated combinational circuits.[5-12] Quite a sizeable number of molecular arrays were designed to this end that could mimic varied binary logic operations in presence of external stimuli.[13-27] While going through the literature, it appears that systems derived from the metal complexes are less compared with their organic counterparts.[28-33] Herein, we used one of our reported Ru(II) complexes, [(bpy)$_2$Ru (Hpzbzth)](ClO$_4$)$_2$ (**1**) for this purpose as presented in **Chart 6.1.**[34] We picked up polyheterocyclic complexes of Ru(II) as they possess remarkable photo-redox behaviours which in turn can be modulated by external stimuli and could take part in varied light-promoted applications such as dye sensitized solar cells as well as in molecular sensors and switches.[35-46] The design strategy offers one pyrazole NH motifs in its second coordination environment. We thoroughly investigated the anion sensing aspect of the complex via various optical channels and spectroscopic techniques through the intermediary of pyrazole NH motif. Anions of varying basicity are used to fine tune the photo-redox behaviour of the complex. The spectral outputs of the complex upon the action of selected anions are employed to mimic various BL operations such as those of combinational logic and key pad lock.[10-12,16,18,28,30]

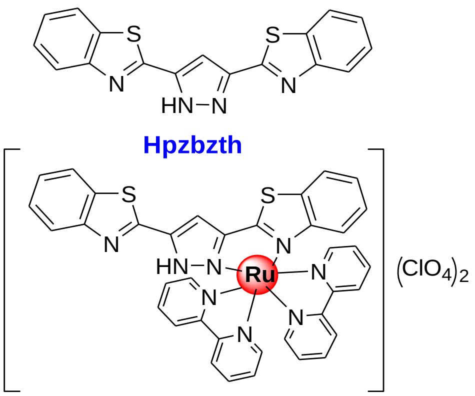

Hpzbzth

[(bpy)$_2$Ru(Hpzbzth)](ClO$_4$)$_2$ (1)

Chart 6.1. Chemdraw structure of the complex used in the present work.

The action of Boolean logic trusts on changing the output signal among the two extremes ("0" or "1"). Nevertheless, the real systems are quite complex and composed of countless number of in-between states. For addressing the huge number of intermediate states, FLS could be a suitable choice.[47-54] FLS express the conversion of the non-linear input vectors to the scalar outputs.[47-50] Herein, FL is applied on the emission behaviour of the complex upon the action of F^- and H^+.

Performing very extensive sensing analysis by varying the anion concentration within a large domain is awfully tiresome, laborious and pricey. To overcome the shortcomings, we implemented herein neural network-based machine learning tools such as ANN and ANFIS to understand as well as to forecast the anion-responsive characteristic of the complex. ANN are designed by the inspiration of the functioning of human brain and frequently applied to speculate functions that may depend on enormous numbers of unidentified inputs. Amongst the two types {recurrent (RNN) and feed-forward (FFN)}, we used herein FNN because of the static nature of our system.[55-56] In FNN, the information moves to a definite track (from the input nodes to the output nodes through the intermediacy of the hidden notes).

While ANN is pretty capable to perceive data but not so capable with regard to realize the significance of every neuron and its load. By contrast, the FL-based method is better with regard to understand as it operates via linguistic language and IF-THEN regulation. But the shortcoming of FL is their incapability to understand by its own. To understand via FL, one has to hire the techniques from different domain (statistics or system recognition). Taking advantage of the better efficiency in learning, it would be good to couple FL and NN and the combined tool, named as ANFIS, is far more superior over the discrete ones.[57-58] The layout of ANFIS possess the same skeleton to that of the FL with the exclusion of NN block. Herein, we applied both ANN and ANFIS networks for proper modelling of anion sensing characteristics of the complex.

6.2. Experimental Section

6.2.1. Materials. $[Ru(bpy)_2 Cl_2]\cdot 2H_2O$,[59] was prepared by the literature methods. Pyrazole-3,5-bis(benzothiazole) (Hpzbzth) and the monometallic Ru(II) complex of composition, $[(bpy)_2Ru(Hpzbzth)](ClO_4)_2$ (**1**) are synthesized following our previously reported procedure.[34]

6.2.2. Synthesis of the Ligand [Hpzbzth]. A mixture of pyrazole-3,5-dicarboxylic acid monohydrate (3.4g, 20 mmol) and *o*-aminothiophenol (5.0 g, 40 mmol) in syrupy phosphoric acid (40 mL) was heated at 140°C for 3h under nitrogen atmosphere. The resulting light yellow liquid was poured into crushed ice and the mixture was carefully neutralized with a KOH solution (3 mol dm^{-3}). A greenish yellow precipitate thus obtained was filtered off, washed several times with water and dried over P_2O_5 under vacuum. The product on recrystallization from acetone gave yellowish green platelets; yield 2.0 g (30%), mp >250°C (Found: C, 61.2; H, 3.1; N, 16.7. $C_{17}H_{10}N_4S_2$ requires : C, 61.1; H, 3.0; N, 16.75%). ν/cm^{-1}(KBr) : 3100, 1600, 1560, 1480, 1450, 1430, 1320, 1240, 1200, 1180, 950, 930, 810, 750, 720, 700 cm^{-1}

6.2.3. Synthesis of Metal Complex. $[(bpy)_2Ru(Hpzbzth)][ClO4]_2.2H_2O$ (1). The complex is prepared by stirring a mixture of $[(bpy)_2RuCl_2]$ (0.52 g, 1 mmol) and $AgClO_4$ (0.42 g, 2 mmol) in ethanol (50 mL) at room temperature under argon protection for 2 h, followed by removal of AgCl precipitated. To the filtrate, solid Hpzbzth (0.41 g, 1.25 mmol) and 0.5 cm^3 of $HClO_4$ (1 mmol dm^{-3}) were added. The mixture was stirred and heated under reflux for 10h, after which it was cooled to room temperature and the unreacted ligand was removed by filtration. The filtrate was concentrated to *ca.* 20 mL and kept overnight in a refrigerator. The orange crystals that deposited were filtered and recrystallized from methanol-water (5:1) containing two drops of $HClO_4$ (1 mmol dm^{-3}); yield 0.6 g (60%) (Found: C, 44.3; H, 2.9; N,11.1. $C_{37}H_{32}Cl_2N_8O_{11}RuS_2$ requires : C, 44.4; H, 3.2; N, 11.2%). ν/cm^{-1} (KBr) 3400(br), 1605, 1540, 1470, 1450, 1425, 1320,1100(br), 975, 760, 730 and 625 $cm^{-1.}$

Caution! Perchlorate salts of the metal complexes are explosive and should be handled in small amount with extreme care

5.2.4. Physical Measurements. The details of different equipments used and experimental process to measure absorption and luminescence spectral behaviors, electrochemical investigations methods have been discussed in chapter 2 and 3.

The detailed description of single crystal X-ray structure determination has been presented in chapter 5. Crystallographic data and details of structure determination are summarized in Table 6.3-6.4. CCDC reference number: 2212695.

Procedure of carrying out the soft computing techniques such as ANN and ANFIS have been discussed in chapter 4.

6.3. Results and Discussion

6.3.1. Synthesis and Characterization. Hpzbzth was prepared upon refluxing a mixture of *o*-aminothiophenol and pyrazole-3,5-dicarboxylic acid monohydrate (2:1 molar ratio) in H_3PO_4. The metal complex was obtained by refluxing $[Ru(bpy)_2Cl_2].2H_2O$ and Hpzbzth (1:1) in ethanol-water mixture. The metal complex is precipitated as perchlorate salts with $NaClO_4$ and purified via chromatography and recrystallization techniques under mild acidic condition to keep the imidazole NH motifs intact. Characterizations of the compounds are performed through IR and NMR spectroscopy, already mentioned in the Experimental Section.

6.3.2. Solvent Dependent Absorption and Emission Spectral Behaviour The absorption and emission spectrum of the complex is acquired in a few selected solvents and associated spectral parameters are provided in Table 6.1. Figure 6.1 shows the normalized emission spectrum and lifetime decay in the studied solvents. The complex shows multiple strong absorption peaks in the UV-vis domain. The position of the lowest energy peak in the visible region varies between 490 and 508 nm, while the next higher energy bands within 443-453 nm and can be attributed to Ru(d)→bpy and/or Hpzbzth (π*)} charge transfer (MLCT) transitions. The peak within 332-368 arises because of intra-ligand charge transfer (ILCT) transition within Hpzbzth moiety, while the bands at ~310 and ~290 nm are bpy-centred π–π* transitions. Excitation at the MLCT maxima of the complex leads to evolution of an intense emission band at RT, the maximum of which varies between 676 and 722 nm, dependent upon the nature of solvents. The emission quantum yield (Φ) varies within the range of 9.0×10^{-4}-8.0×10^{-3}, whereas the lifetime (τ) of the complex alters between 37 and 137 ns. Comparing the emission spectra of structurally similar polyheterocyclic Ru(II) complexes, it appears that the

Table 6.1. Photophysical Parameter in Different Solvents

Solvent	Absorption	Luminescence		
	λ_{max}/ nm (ε,$M^{-1}cm^{-1}$)	λ_{max}/ nm	τ/ns	Φ
DCM	498(19300),453(br)(13900) 368(br)(56400),312(77100), 294(145000)	676	137	8.0×10^{-3}
MeCN	492(24500), 448(br) (18700) 365(br)(57500),312(117700), 292(192000)	685	72	2.4×10^{-3}
Water	490(13000),445(br) (9000) 334(br)(35000),308(57000), 292(90000)	690	37	9.0×10^{-4}
EtOH	501 (17500), 443(br)(12700) 332(br)(59200),309(96300), 294(147000)	700	38	1.1×10^{-3}
DMSO	508 (19300), 453(br)(12700) 337(br)(61000), 312(100000), 297(150000)	710	45	1.9×10^{-3}
DMF	508 (20000), 450(19000) 334(br)(70000),312(111200), 295(164000)	722	90	1.5×10^{-3}

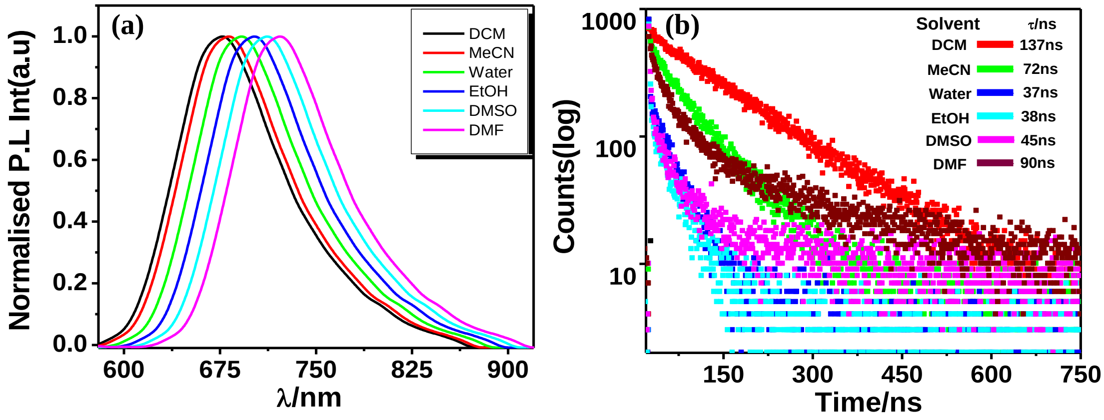

Figure 6.1. (a) Normalised emission profiles (b) Excited state decay profile of **1** in different solvents.

observed emission in the complex arises because of radiative deactivation of its ^{3}MLCT$_{\mathrm{Ru}\rightarrow\mathrm{bpy}}$ state. The MLCT absorption and emission peaks in the complex get red-shifted with increase in polarity of the solvent. The extent of red-shift is found to be maximum in case of DMF and DMSO which have the ability to be associated via hydrogen bonding interaction with the pyrazole NH proton.

6.3.3. Anion Sensing Properties. We carried out the anion sensing characteristics of the complex in acetonitrile via manifold optical channels and spectroscopic tools. We used herein the tetrabutylammonium salts of F^-, Cl^-, Br^-, I^-, AcO^-, CN^-, SCN^- and $H_2PO_4^-$. The absorption and emission spectrum of the complex upon addition of different anions along with its visual colour change is shown in Figure 6. 2. Substantial red-shift of the MLCT bands take place in

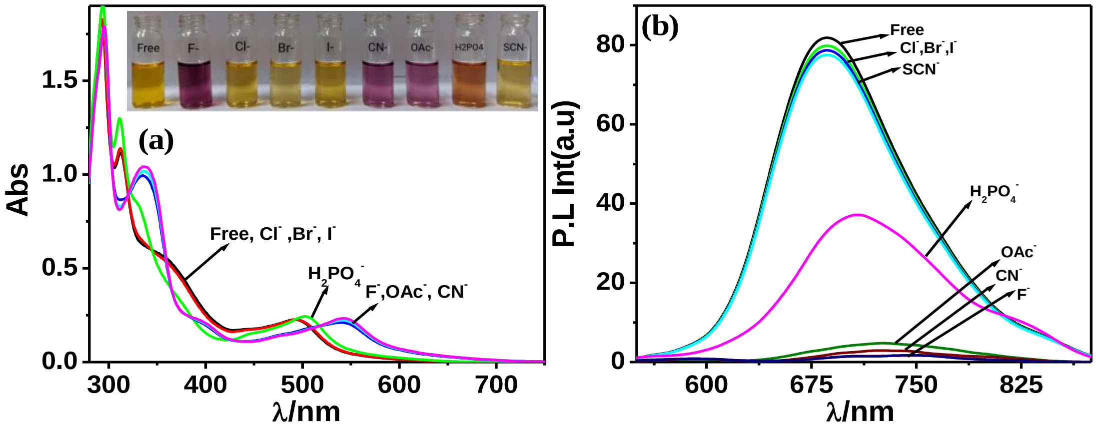

Figure 6. 2. UV-vis absorption (a) and emission (λ_{ex} = 490 nm) (b) spectral behaviour of **1** in MeCN in presence of various anions. Inset shows the visual colour change.

presence of basic anions (F$^-$, AcO$^-$, and CN$^-$), while the band position remains almost unaltered with other anions. Essentially, the receptor acts as sensor for F$^-$, CN$^-$ and AcO$^-$ without much selectivity. The observed red-shift in the MLCT bands is ascribed due to incipient hydrogen-bonding communication among NH proton and the anions followed by deprotonation in presence of excess of the anions which is also in agreement with its visual colour change. In-line with the trend in the absorption spectra, the emission intensity remains practically unaltered in presence of Cl$^-$, Br$^-$, I$^-$, and SCN$^-$, moderately quenched with $H_2PO_4^-$, whereas nearly fully quenched accompanied with large red-shift of the emission maximum in presence of F$^-$, AcO$^-$ and CN$^-$.

Absorption and emission titration measurements are executed with anions to acquire quantifiable perception of complex-anion interaction (Figure 6.3-6.4). Two-steps changes are clearly observed with basic anions (such as F$^-$, CN$^-$ and AcO$^-$), while one-step change with $H_2PO_4^-$ in the spectral profile of the complex. The initial change occurs up to the addition of 1 equiv of the anions and the extent of change is relatively small, while extent of change in the second step is quite large and saturation occurs with 2 equiv of anions.

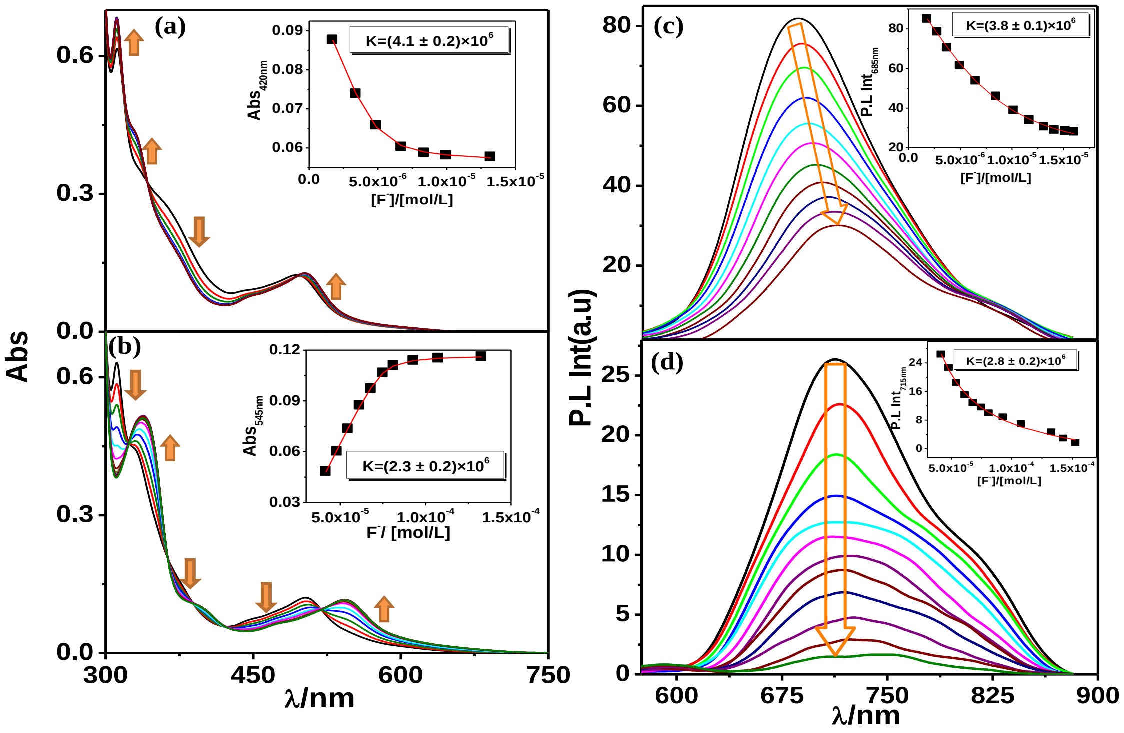

Figure 6.3. Change in UV-vis absorption (a-b) and emission (λ_{ex} = 490 nm) (c-d) spectral profile of **1** upon stepwise addition of F$^-$ in MeCN. Insets show the 1:1 binding profile.

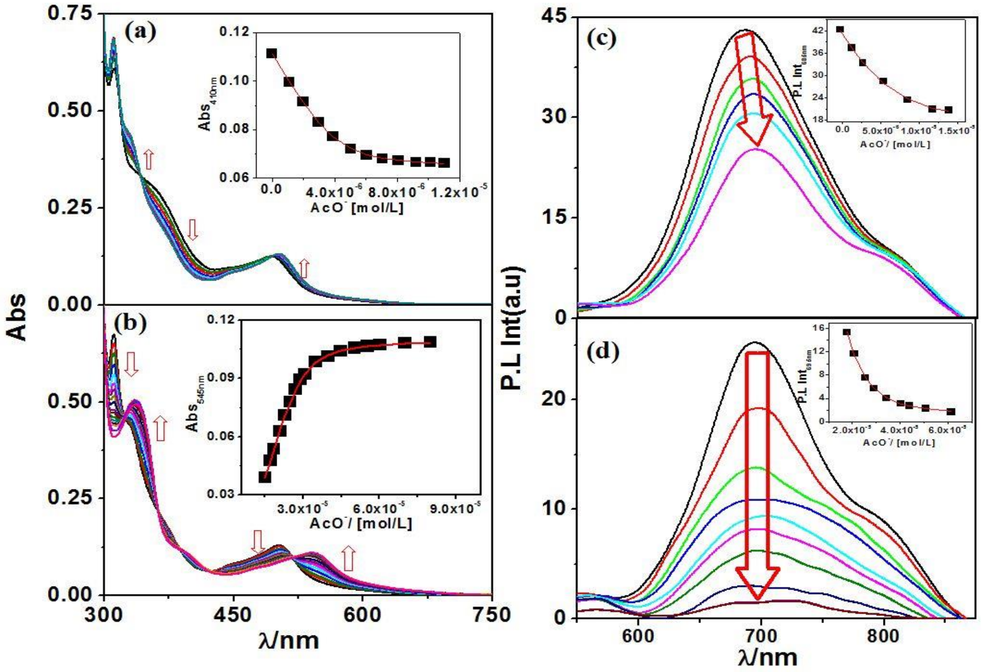

Figure 6.4. Absorption (a and b) and emission (λ_{ex} = 490 nm) (c and d) spectral changes of **1** with gradual addition of AcO^-. The insets show the change of absorption and emission intensity vs. equivalent of AcO^- added.

In absorption spectra, increasing amount of the anions induces red-shift of the MLCT peak maxima in the second step and consecutive absorption spectrum goes via several clear-cut isosbestic points (323, 362, and 518 nm). The spectral characteristics of the complex in presence of $H_2PO_4^-$ diverges from the rest of the anions and the extent of change is relatively small compared with the said anions (Figure 6.5). The titration figures are exploited to evaluate the equilibrium/binding constant (K) for complex-anion interplay the calculated values are of the six orders of magnitudes (Table 6.2). The emission spectral profile upon step-by-step addition of anions ions are displayed in (Figure 6.3c-6.3d and Figure 6.4c-6.4d).

Systematic quenching of emission intensity accompanied with considerable red-shift of emission maximum takes place in the initial step up to 1 equiv of the anions. In the subsequent step, further quenching without alteration of emission maximum occurs upon addition of excess anions. With $H_2PO_4^-$ small quenching without shifting of emission maximum takes place in a single step (Figure 6.5b). Equilibrium/binding constants among the complex and anion were also estimated from the emission titration data which are also in the order of 10^6 and tallied reasonably well with those obtained from absorption spectroscopy (Table 6.2).

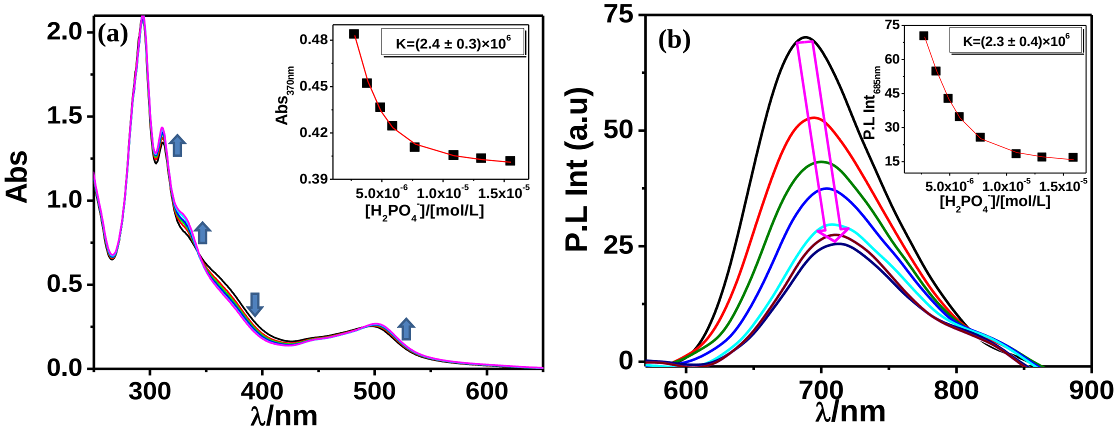

Figure 6.5. UV-vis absorption (a) and emission (λ_{ex} = 490 nm) (b) spectrum of **1** upon stepwise addition of $H_2PO_4^-$ in MeCN. Insets show the 1:1 binding profile.

Table 6.2. Equilibrium/Binding Constants (***K***) for **1** in MeCN at 298 K

From absorption spectra		
Anion	**1**	
	***K*₁** K_1	K_2
F^-	4.1×10^6	2.3×10^6
$H_2PO_4^-$	2.4×10^6	
From emission spectra		
F^-	3.8×10^6	2.8×10^6
$H_2PO_4^-$	2.3×10^6	

The modulation of lifetime in presence of selected anions is also investigated. Lifetime of the complex upon step-by-step addition of F^- are acquired and the result is presented in Figure 6.6. The single-exponential decay of the free complex is changed to bi- exponential in presence of the anions accompanied with reduction of total lifetime. Therefore, existence of at least two luminescent species is suspected. The anion-bound or the deprotonated form is expected to be short-lived compared with its initial form resulting in overall reduction of lifetime. In essence, the complex can function as a suitable lifetime-based sensor for selected anions which could be more beneficial over the conventional intensity-based sensor.

6.3.4. Electrochemical Monitoring. The CV and SWV voltammogram of the complex display a reversible Ru^{II}/Ru^{III} oxidation at $E_{1/2}$ = 0.94 V and two successive reversible waves at -1.46 and -1.78 V due to reduction of two bpy motifs. The oxidative redox behaviour was checked upon step-by-step addition of anions and observed changes are presented in Figure 6.7.

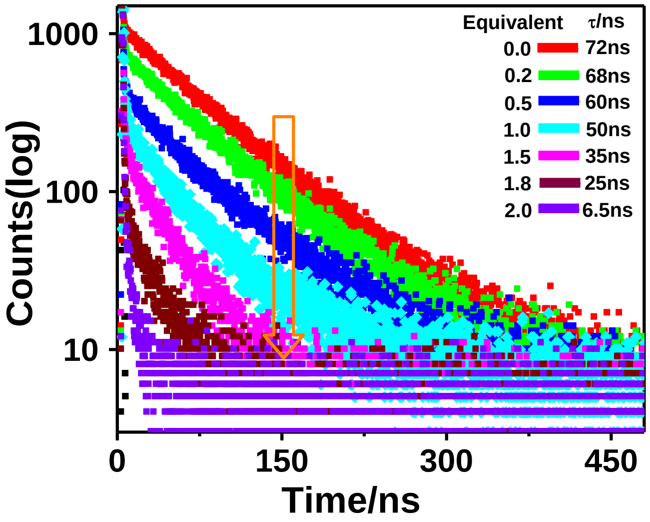

Figure 6.6. Change in excited-state decay profile (λ_{ex}=450 nm) of **1** upon stepwise addition of F^- in MeCN. Inset shows the lifetime values.

The peak at 0.94 V progressively reduced in current intensity with concomitant growth of a new peak at 0.80 V and ultimately the initial peak at 0.94 V is substituted by the peak at 0.80 V during addition of 2 equiv of F^-. Essentially, the $E_{1/2}$ of the Ru^{3+}/Ru^{2+} couple is dramatically shifted to lesser potential in presence of strongly basic anions. The pyrazole NH proton is expected to be deprotonated from the complex moiety and reduces its net positive charge that eventually drops the $E_{1/2}$ of Ru^{3+}/Ru^{2+}couple.

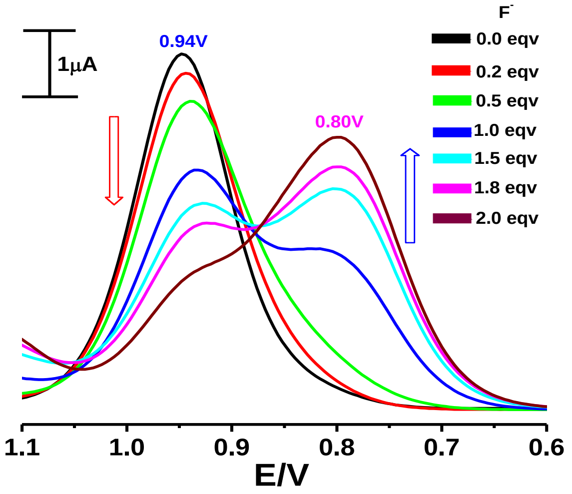

Figure 6.7. Change of SWVs of **1** in MeCN upon stepwise addition of F^- .

6.3.5. Mode of Interaction Among the Complex and Anions. In the previous section, we noticed substantial alteration of the spectral and electrochemical characteristics of the complex upon interaction with F^-, AcO^-, and CN^-. The extent of interaction with $H_2PO_4^-$ is relatively small, while almost negligible with Cl^-, Br^-, I^- and SCN^-. In spite of the presence of one pyrazole NH proton, two-step changes are observed in both absorption and emission spectral profiles of the receptor in presence of basic anions such as F^-, AcO^-, and CN^-. Thus, presence of two dissociable protons in the complex backbone is a finite possibility. We surmise that one of two thiazole moieties gets protonated during the process of recrystallization of the complex in presence of $HClO_4$ and these protons are successively deprotonated in presence of the basic anions. To check the possibility, spectral titrations are also executed with a strong base, viz. tetrabutylammonium hydroxide (TBAOH) (Figure 6.8). The overall spectral pattern of the complex resembles closely with those obtained with F^- and AcO^- ions. This implies that anion-induced dissociation of the pyrazole and thiazole NH protons probably take place from the complex backbone.

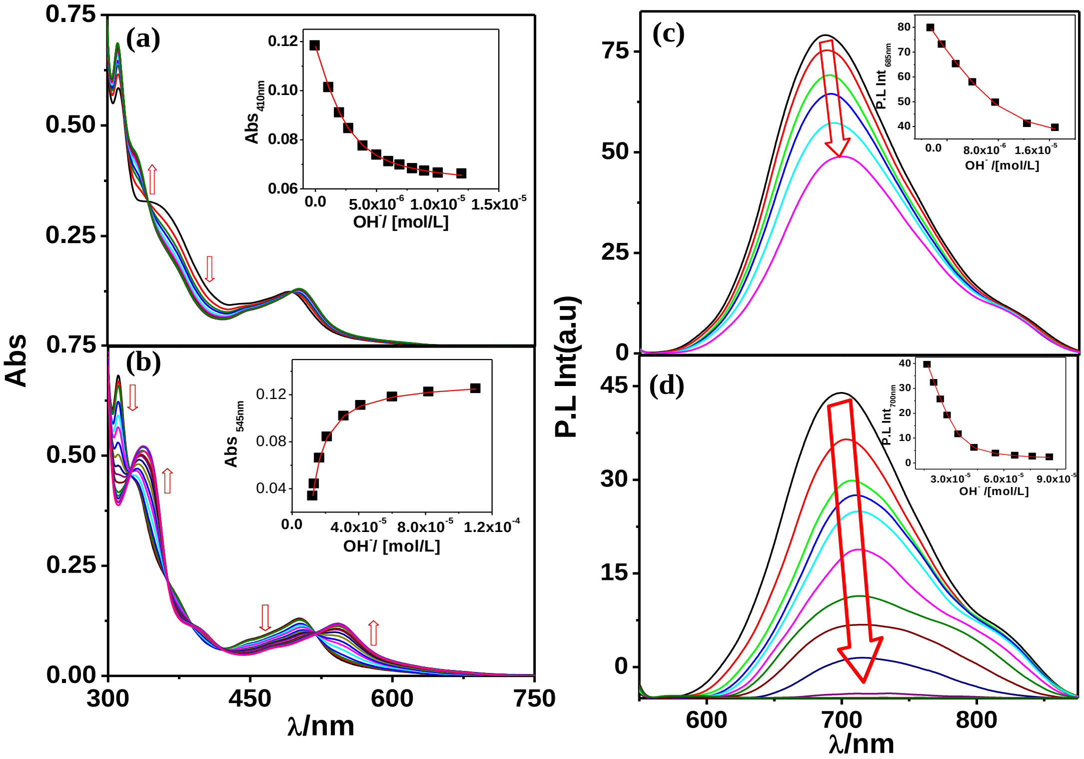

Figure 6.8. Absorption (a and b) and emission (λ_{ex} = 490 nm) (c and d) spectral changes of **1** with gradual addition of OH^-. The insets show the change of absorption and emission intensity vs. equivalent of OH^- added.

In order to obtain a concrete proof of interaction among the receptor and the anions, we tried to grow single crystals of the complex by diffusing $PhCH_3$ to its MeCN-DCM (2:1 v/v) solution in presence of excess TBAF. Fortunately, we succeed after several attempts and the crystal structure of the resulting compound is presented in Figure 6.9. The crystal structure clearly shows that excess F^- abstracts the pyrazole NH proton providing the deprotonated form of the complex. Crystallographic parameters along with selected bond distances and angles of the deprotonated form of the complex are presented in Table 6.3-6.4.

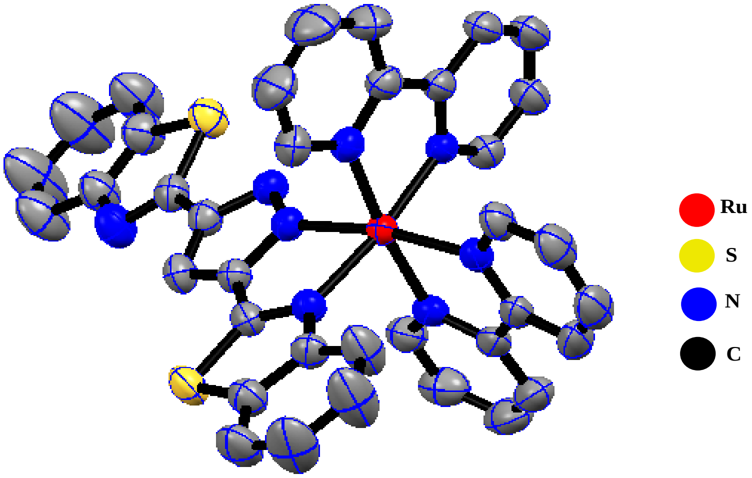

Figure 6.9. Perspective view of **1**$^+$ showing 50% probability ellipsoid plots.

6.3.6. Logic Operations. In the previous section, we observed quite a large degree of change in the absorption and emission spectral as well as in the electrochemical behavior of the complex in presence of specific anions. The restoration of the initial form of the complex is also possible upon treating with acid. Furthermore, deprotonation-induced modification of the photo-redox conduct of the receptor by anions followed by refurbishment of the original form by acid is fully reversible and can be recycled many times. Herein, we will utilize spectral and electrochemical output of the complex upon successive addition of anions and acid for fabrication of multiple logic functions. The complex is capable to show complex Boolean and FL operations by using its absorption, emission and electrochemical responses upon the action of appropriate combination of inputs.

Table 6.3. Crystallographic Data For [(bpy)$_2$Ru(pzbzth)](ClO$_4$)(**1**)

CCDC reference number	2212695
Compound	[(bpy)$_2$Ru(pzbzth)](ClO$_4$)
Formula	$C_{37}H_{25}ClN_8O_4RuS_2$
FW	846.29
T (K)	293K
Cryst. Syst.	Triclinic
Space group	P-1
a (Å)	10.277(5)
b (Å)	13.114(5)
c (Å)	13.275(5)
α (deg)	84.471(5)
β (deg)	82.781(5)
γ (deg)	89.431(5)
V (Å3)	1766.7(13)
Dc(g cm-3)	1.591
Z	2
μ (mm-1)	0.692
F(000)	856.0
2θ range (deg)	3.1 to 50
Data/restraints/parameters	6210/0/478
GOF on F^2	0.974
Final R indexes [I>=2σ (I)]	R_1 = 0.0322, wR_2 = 0.1055
Final R indexes [all data]	R_1 = 0.0371, wR_2 = 0.1150
Largest diff. peak/hole / e Å^{-3}	0.53/-0.43

Table 6.4. Selected Experiment Bond Distance (Å) and Angles (deg) of **1**

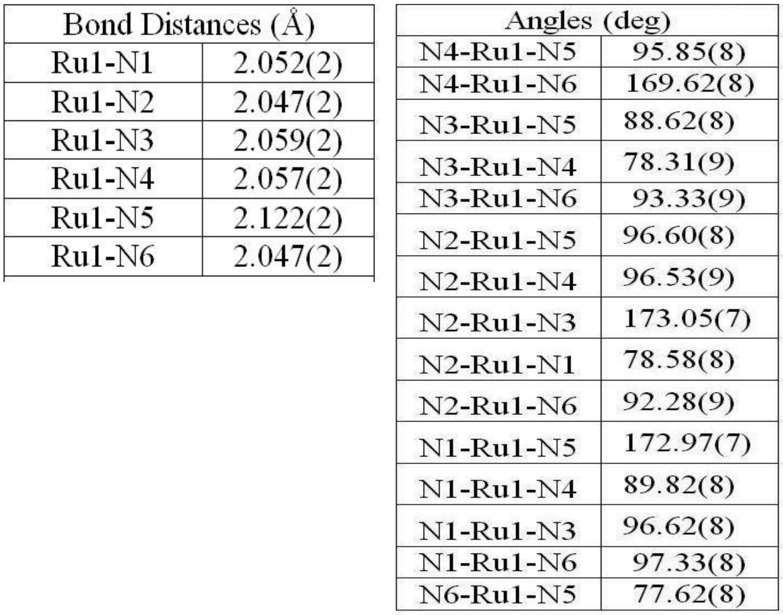

Bond Distances (Å)	
Ru1-N1	2.052(2)
Ru1-N2	2.047(2)
Ru1-N3	2.059(2)
Ru1-N4	2.057(2)
Ru1-N5	2.122(2)
Ru1-N6	2.047(2)

Angles (deg)	
N4-Ru1-N5	95.85(8)
N4-Ru1-N6	169.62(8)
N3-Ru1-N5	88.62(8)
N3-Ru1-N4	78.31(9)
N3-Ru1-N6	93.33(9)
N2-Ru1-N5	96.60(8)
N2-Ru1-N4	96.53(9)
N2-Ru1-N3	173.05(7)
N2-Ru1-N1	78.58(8)
N2-Ru1-N6	92.28(9)
N1-Ru1-N5	172.97(7)
N1-Ru1-N4	89.82(8)
N1-Ru1-N3	96.62(8)
N1-Ru1-N6	97.33(8)
N6-Ru1-N5	77.62(8)

6.3.6.1. Combinational Logic and Keypad Lock. Combinational logic is accomplished by basic Boolean operators ("OR," "AND," and "NOT"). Herein, the luminescence response at 685 nm and absorbance at 545 nm are treated as the outputs in presence of H^+ (input 1) and F^- (input 2). Emission quenching below the threshold and absorbance enhancement above the threshold takes place under the influence of F^-, suggesting the "OFF" state (0) and "ON" state (1), respectively. The emission and absorption maxima at their respective wavelengths upon chronological addition of inputs (F^- and thereafter H^+) leads to creation of a combination of IMPLICATION and INHIBIT gate (Figure 6.10c and 6.10e).

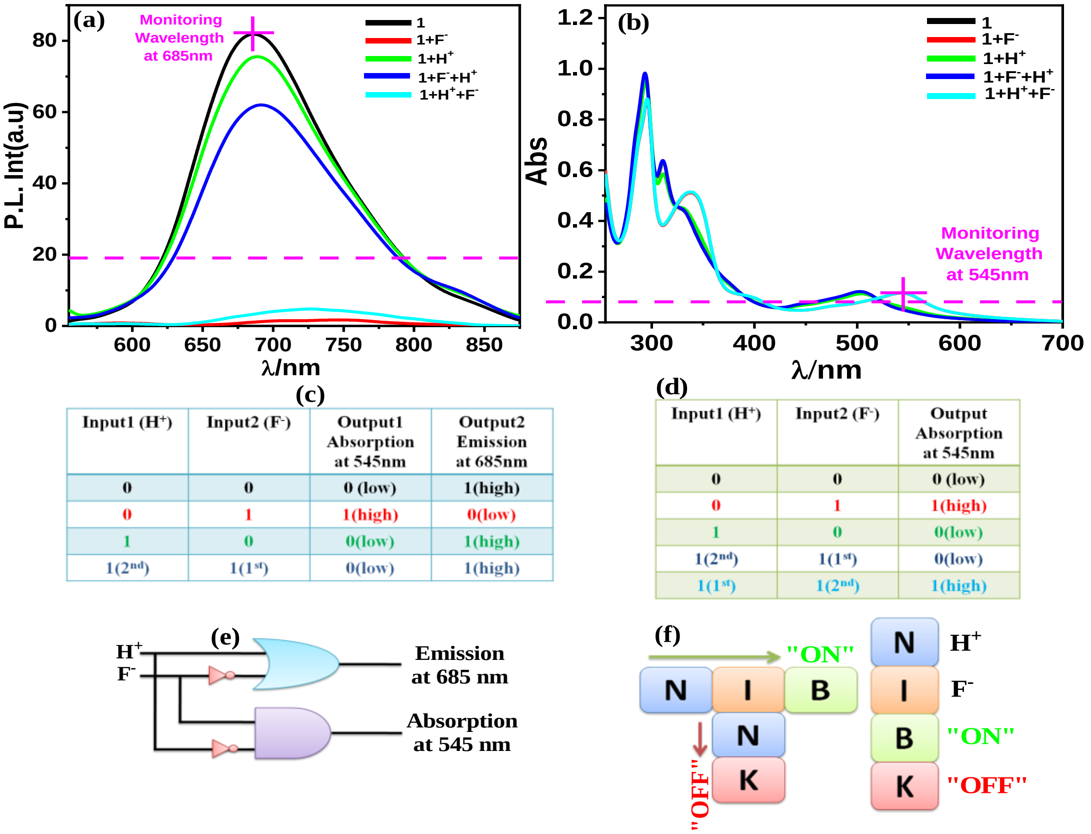

(c)

Input1 (H^+)	Input2 (F^-)	Output1 Absorption at 545nm	Output2 Emission at 685nm
0	0	0 (low)	1(high)
0	1	1(high)	0(low)
1	0	0(low)	1(high)
1(2nd)	1(1st)	0(low)	1(high)

(d)

Input1 (H^+)	Input2 (F^-)	Output Absorption at 545nm
0	0	0 (low)
0	1	1(high)
1	0	0(low)
1(2nd)	1(1st)	0(low)
1(1st)	1(2nd)	1(high)

Figure 6.10. (a) Emission and (b) absorption spectrum of **1** due to sequential addition of H^+ and F^-. (c) and (d) corresponds to the Truth table of combinational logic and keypad lock, respectively. (e) and (f) represents the respective schematic diagram of these logic operations.

To secure valuable data at the molecular level, we fabricated a keypad lock device. The absorption spectral output at 545 nm with H^+ and F^- is utilized for this purpose (Figure 6.10b). H^+ (input 1) and F^- (input 2) is allocated as "N" and "I", respectively, whereas the "ON" and "OFF" state is designated as "B" and "K", respectively (Figure 6.10f). Plausible amalgamations of the inputs wherever either in presence of F^- or incorporation of F^- after H^+ induces the "ON" state (1) and creates the secret password “NIB”. Reversal of the sequence (addition of H^+ after F^-), on the contrary, leads to the “OFF” state (0) and generates the incorrect password “INK”. Hence, only the authorized person who knows the actual password will be able to unlock the secured information.

6.3.7. Fuzzy Logic Operations. As already pointed out in the introduction that the action of BL trusts on changing the output signal among the two extremes ("0" or "1"). Nevertheless, the real systems are quite complex and composed of countless number of in-between states. For addressing the huge number of intermediate states, FLS could be a suitable choice. FLS express the conversion of the non-linear input vectors to the scalar outputs. Herein, FL is applied on the emission spectral behavior of the complex upon the action of F^- and H^+. The emission spectrum of **1** varies to a huge degree in presence of F^- (input 1) and H^+ (input 2) (Figure 6.11). Bearing in mind the large degree of change together with lack of accurate values, the variation may be articulated via a small number of lingual parameters of the triangular molecular functions (*trimf*) such as low, medium, and high. Figure 6.12 shows that the spectral change could be expressed in respect of fuzzy sets. An album of diverse IF-THEN comments encompassing the inference laws is tabulated in Table 6.5. The IF-part designates to the antecedent, while the THEN-portion corresponds to the result. Systematic emission quenching at 685 nm occurs with F^-, whereas the restoration happens with H^+. Hence, FL is implemented in the present system upon inspecting the emission characteristics upon cumulative action of F^- and H^+ ions. The practicable compilation of F^- and H^+ generates 15 rules (Table 6.5 and Figure 6.13). The alteration in emission intensity upon co-addition of F^- and H^+ is also displayed in a three-dimensional plot (Figure 6.12d).

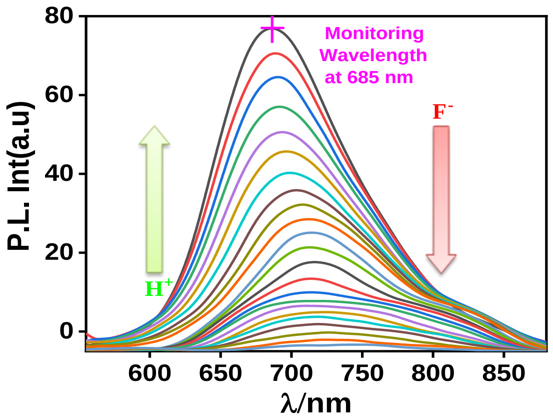

Figure 6.11. Emission spectral change of **1** due to step by step addition of F^- and H^+.

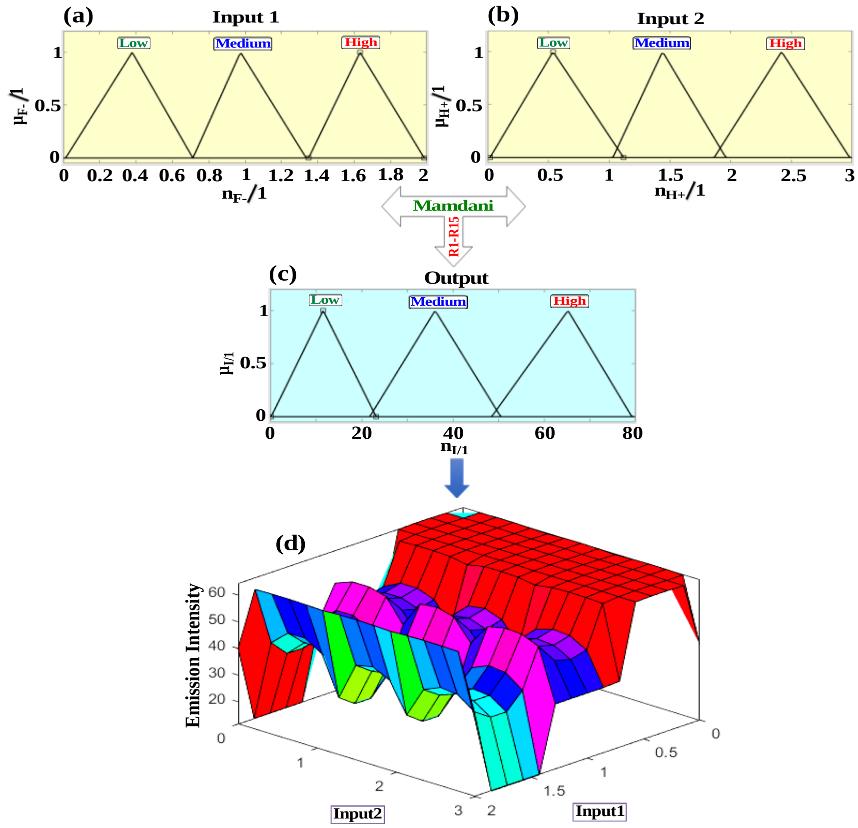

Figure 6.12. Sketch of FLS on the basis of fuzzy inference rules upon scanning the emission response of **1** in presence of F^- and H^+. The variables are disintegrated into 3 fuzzy sets. (a) F^-: (1) low (trimf μ_{low}, [0.0124 0.3786 0.7126]); (2) medium (trimf μ_{medium}, [0.7129 0.9749 1.336]) (3) high (trimf μ_{high}, [1.349 1.632 1.985]). (b) H^+: (1) low (trimf μ_{low}, [0.0184 0.5379 1.118]); (2) medium (trimf μ_{medium}, [1.031 1.439 1.961]) (3) high (trimf μ_{high}, [1.865 2.421 2.981]). (c) Emission intensity at 685 nm (Output): (1) low (trimf μ_{low}, [0.1986 11.61 23.21]); (2) medium (trimf μ_{medium}, [21.81 36.13 50.51]); (3) high (trimf μ_{high}, [48.52 65.24 79.24]).

Table 6.5. Rules for the Fuzzy Logic System by Taking Input 1 (F^-) and Input 2 (H^+) as the Inputs and Emission Intensity at 685 nm as the Output. The Rules Consist of the Following Statements.

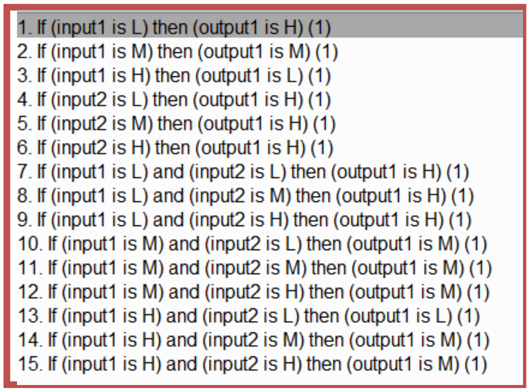
1. If (input1 is L) then (output1 is H) (1)
2. If (input1 is M) then (output1 is M) (1)
3. If (input1 is H) then (output1 is L) (1)
4. If (input2 is L) then (output1 is H) (1)
5. If (input2 is M) then (output1 is H) (1)
6. If (input2 is H) then (output1 is H) (1)
7. If (input1 is L) and (input2 is L) then (output1 is H) (1)
8. If (input1 is L) and (input2 is M) then (output1 is H) (1)
9. If (input1 is L) and (input2 is H) then (output1 is H) (1)
10. If (input1 is M) and (input2 is L) then (output1 is M) (1)
11. If (input1 is M) and (input2 is M) then (output1 is M) (1)
12. If (input1 is M) and (input2 is H) then (output1 is M) (1)
13. If (input1 is H) and (input2 is L) then (output1 is L) (1)
14. If (input1 is H) and (input2 is M) then (output1 is M) (1)
15. If (input1 is H) and (input2 is H) then (output1 is M) (1)

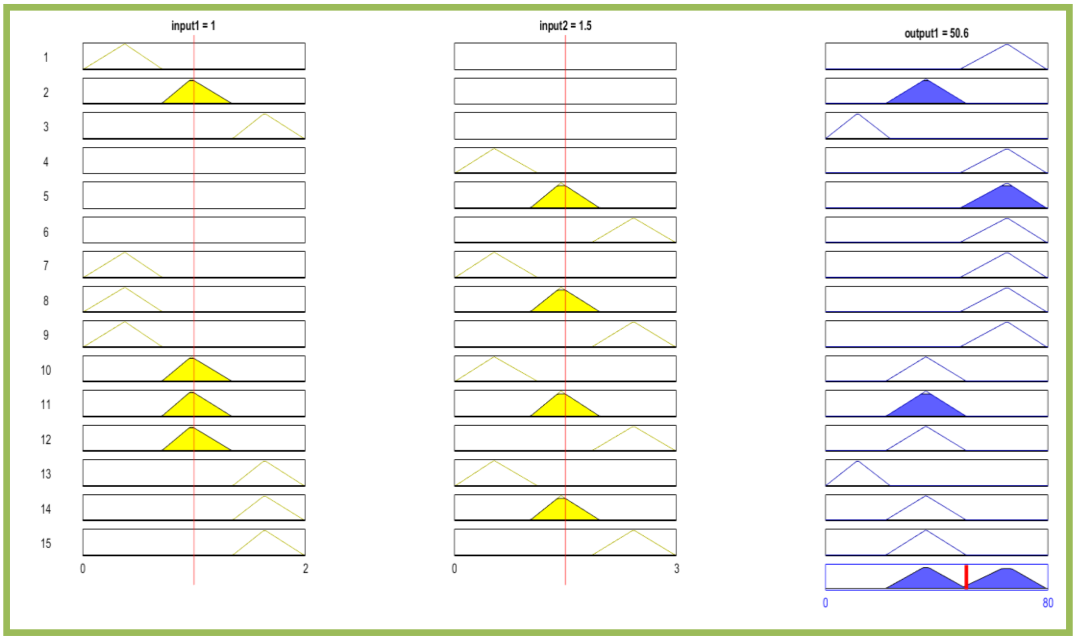

Figure 6.13 . Mamdani rule view for **1.**

6.3.8. Artificial Neural Network (ANN). ANN is the easiest and one of the most suitable type of organizations where the information flows to a definite direction. Moreover, taking into consideration its elevated competence in predicting the static system, we employed herein ANN-function fitting (ANN-FF) array for appropriate grasping and predicting the system. We employ herein Levenberg-Marquardt method for training. The ANN-FF is coded in MATLAB 2018 [60] and Table 6.6 represents the emission intensity outputs upon the action of 39 different combinations of two inputs (input 1=F^- and input 2=H^+). The full operational details are already provided in the Experimental Section. It is evident that the model's most excellent validation activity is 0.028672 up to epoch 5 (Figure 6.14a). The augmentation of green colored line after epoch 5 indicates that the growth of the mean squared error (mse) and training gets halted. Figure 6.14b expresses the error histogram among the target and predicted values after the training process. Y-axis symbolizes the quantity of samples in the dataset which retains in a specific bin. The bins are evenly arranged intervals that are used to segregate the data on the graph. The zero-error point is positioned beneath the bin centered at -0.04061 and +0.02199 for 685 nm, while the total error spans from -0.6041 (leftmost bin) to +0.5854 (rightmost bin). The R value nearing to unity indicates satisfactory coherence among the target and output and is also indicative of model's good performance (Figure 6.14c). The training status of ANN network up to epoch 11 is shown in Figure 6.15.

Table 6.6. Values of Emission Intensity as a Function of n_{F}^{-}/n_1 and n_{H}^{+}/n_1.

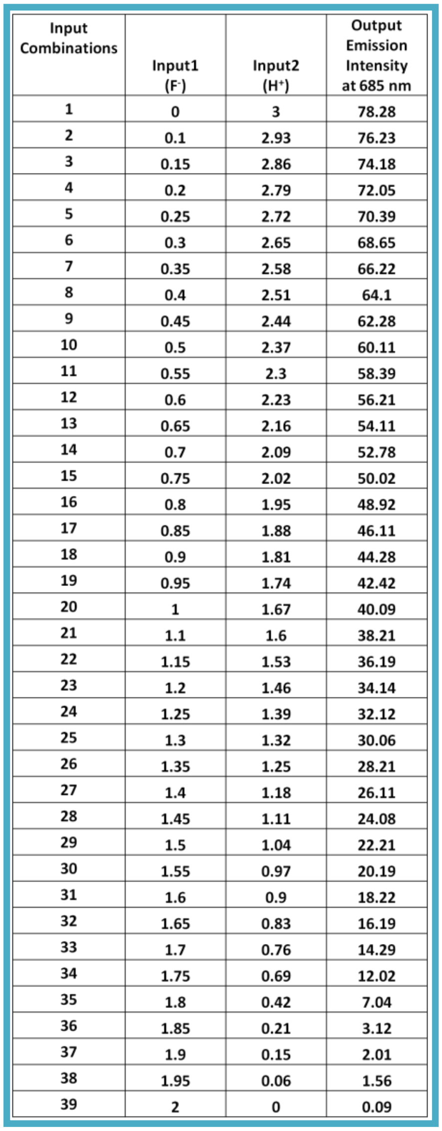

Input Combinations	Input1 (F$^-$)	Input2 (H$^+$)	Output Emission Intensity at 685 nm
1	0	3	78.28
2	0.1	2.93	76.23
3	0.15	2.86	74.18
4	0.2	2.79	72.05
5	0.25	2.72	70.39
6	0.3	2.65	68.65
7	0.35	2.58	66.22
8	0.4	2.51	64.1
9	0.45	2.44	62.28
10	0.5	2.37	60.11
11	0.55	2.3	58.39
12	0.6	2.23	56.21
13	0.65	2.16	54.11
14	0.7	2.09	52.78
15	0.75	2.02	50.02
16	0.8	1.95	48.92
17	0.85	1.88	46.11
18	0.9	1.81	44.28
19	0.95	1.74	42.42
20	1	1.67	40.09
21	1.1	1.6	38.21
22	1.15	1.53	36.19
23	1.2	1.46	34.14
24	1.25	1.39	32.12
25	1.3	1.32	30.06
26	1.35	1.25	28.21
27	1.4	1.18	26.11
28	1.45	1.11	24.08
29	1.5	1.04	22.21
30	1.55	0.97	20.19
31	1.6	0.9	18.22
32	1.65	0.83	16.19
33	1.7	0.76	14.29
34	1.75	0.69	12.02
35	1.8	0.42	7.04
36	1.85	0.21	3.12
37	1.9	0.15	2.01
38	1.95	0.06	1.56
39	2	0	0.09

6.3.9. Adaptive Neuro-Fuzzy Inference System (ANFIS).The merging of FL and NN generates ANFIS network that could remove the shortcoming of each one and often produces superior results. [61-62] ANFIS network could be schematically presented in Figure 6.16. 5 layers (excluding the input layer) are inter-connected in the network. The scheme is archetypal for 2 input size, P and Q, both of which are composed of 3 fuzzy sets (C1C2C3 for P, while D1D2D3 for Q). The detailing of each layer is narrated in the Experimental Section. The fundamental design for forecasting the emission characteristics in presence of F$^-$ and H$^+$ by ANFIS comprises of 4 segments (fuzzification, knowledge base, ANN, and defuzzification layer) (Figure 6.17). To build up the scheme, 70% data are used for training while the rest 30% for testing. The training

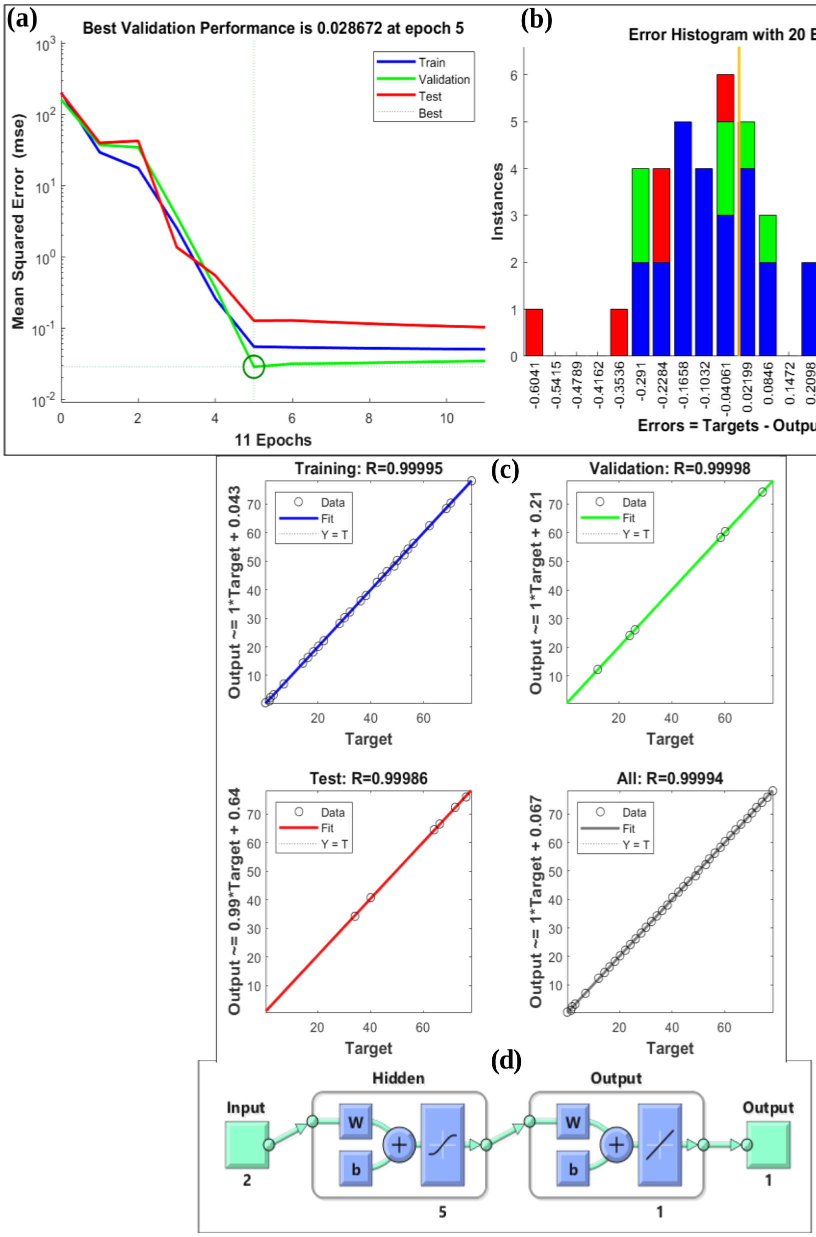

Figure 6.14. (a) Minimization of mse up to epoch 5. (b) Error histogram. (c) Comparison of the outputs obtained by linear regression and ANN model. (d) Generated ANN scheme

error is found to reduce gradually till 50 epochs signifying that the system learns in each individual step (Figure 6.18). For 2 inputs and 3 membership functions each, the network will create 3^2= 9 rules (Figurer 6.19 and Table 6.7). The conceivable amalgamation of F^- and H^+ generates the output emission response which consists of 9 rules based on Sugeno’s method (Figure 6.20c). The ANFIS predicted results are displayed in 3D plots (Figure 6.20e), while the produced ANFIS structure is shown in Figure 6.20d on the basis of 9 rules. On providing the diverse values of inputs in the rule viewer of FL and the command part of ANN in MATLAB

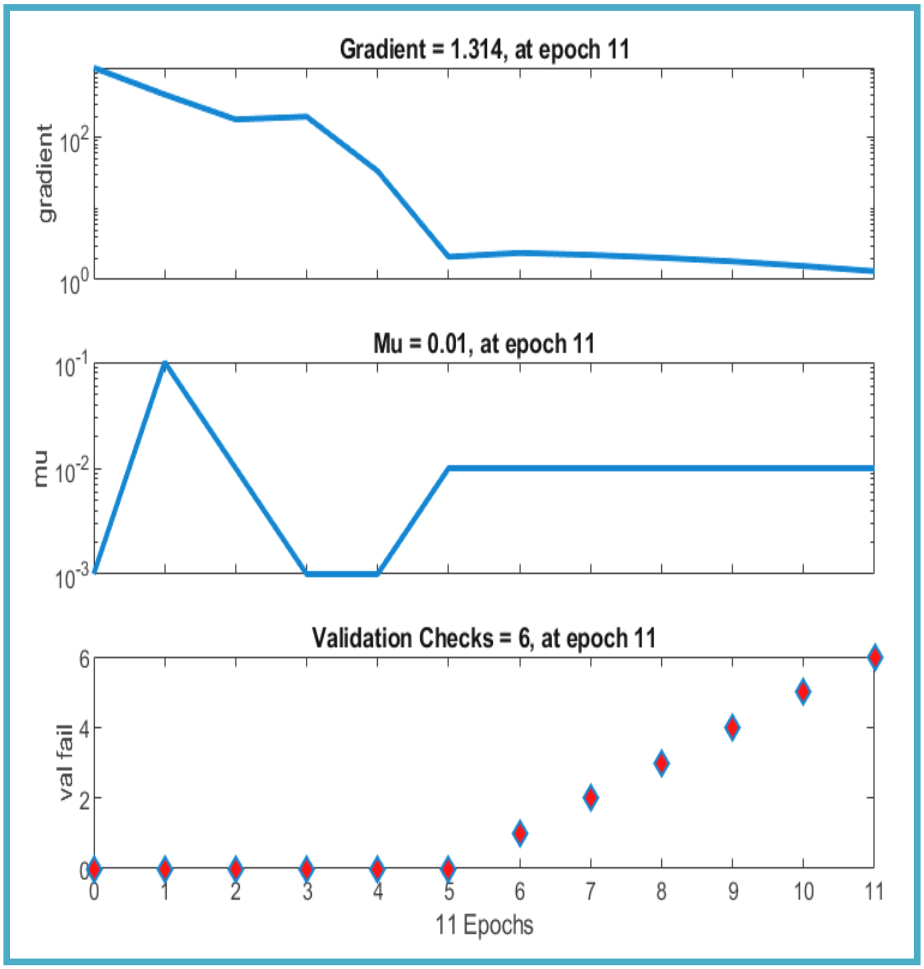

Figure 6.15. Training state of the ANN model of **1** at 685 nm up to epoch 11.

R2018a, we sum-up the outputs in Table 6.8. The effectiveness of the ANFIS network is deliberated statically upon considering their root mean squared error (RMSE) values. The testing RMSE value of 0.195691 is indicative of proper functionality of the system. The output obtained from ANFIS is very close to that of the experimental results compared with FL and NN. Table 6.8 compares the outputs of Fuzzy, ANN and ANFIS models together with the experimental results. In essence, ANFIS is found to be the best optimization system.

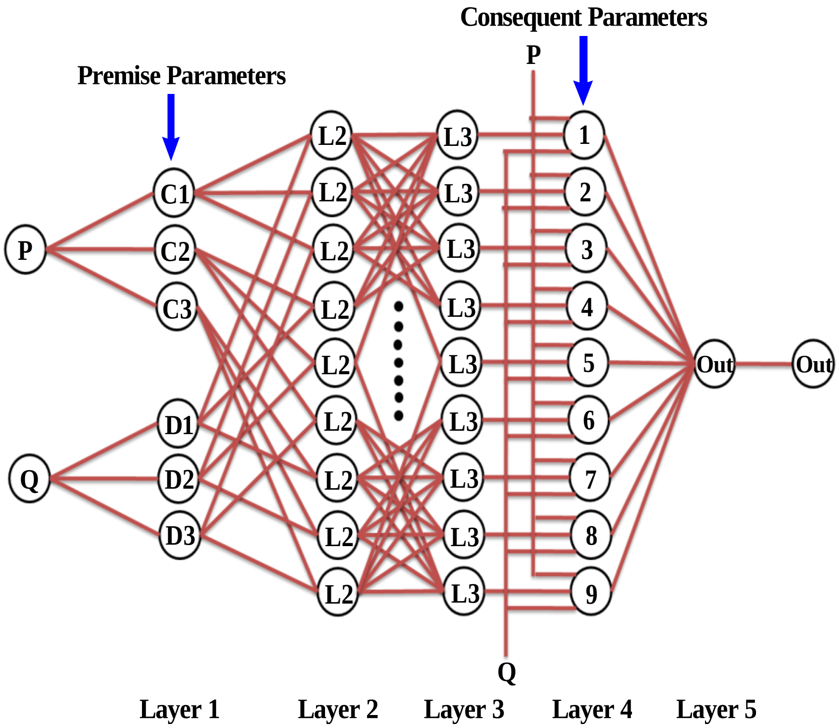

Figure 6.16. Schematic sketch of ANFIS network comprising of two inputs, five layers and one output.

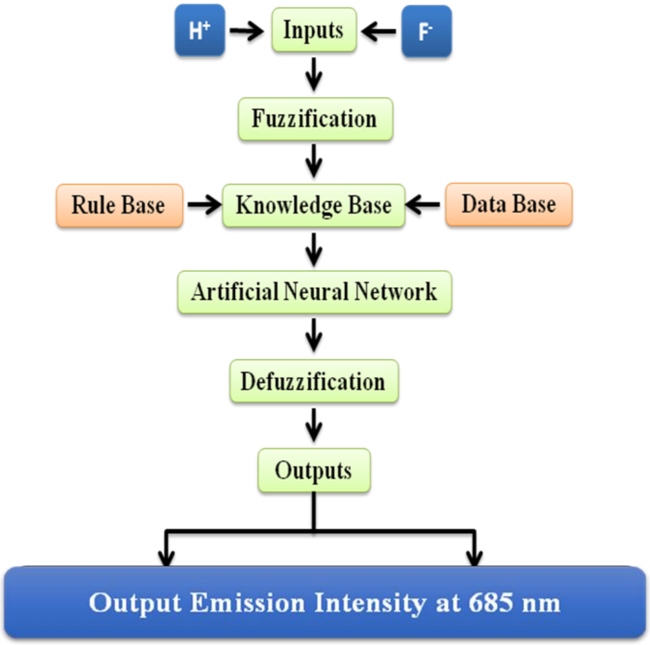

Figure 6.17. Schematic presentation of ANFIS based on Sugeno's method (monitoring wavelength at 685 nm) maintaining 9 rules.

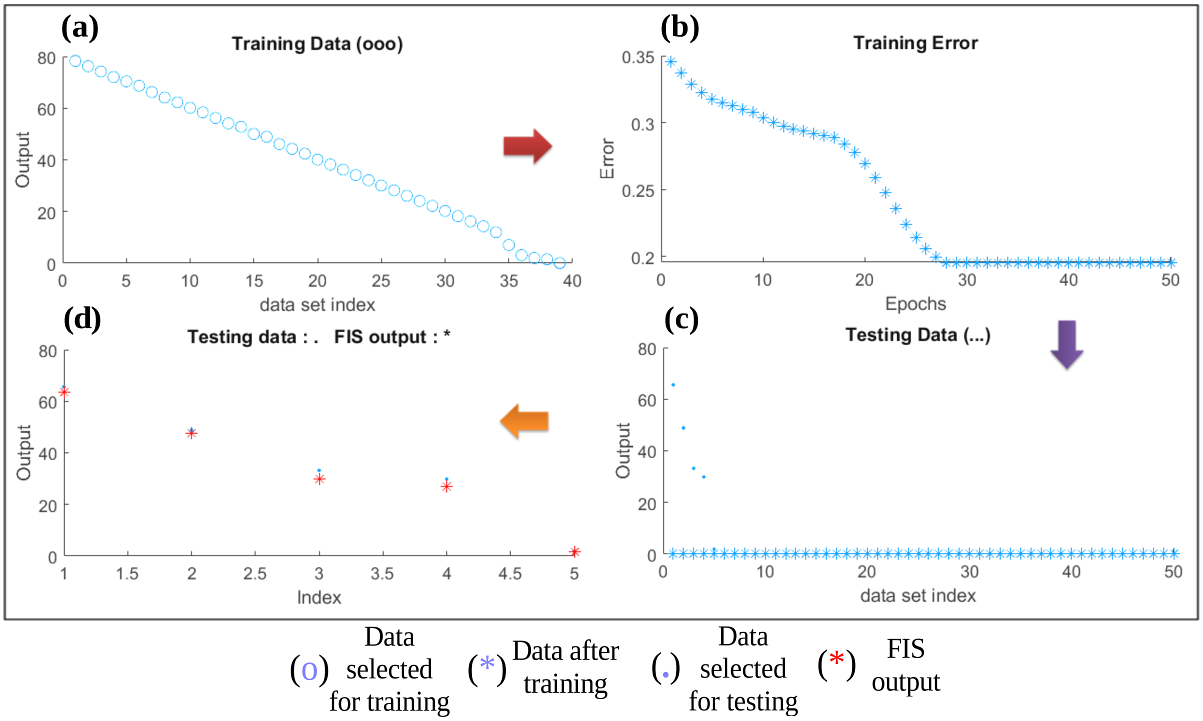

Figure 6.18. (a) ANFIS training data set. (b) Statistical performance indicator (rmse) up to 50 epochs. (c) Testing dataset to measure the accuracy of the network. (d) Comparison of testing data with ANFIS network outputs.

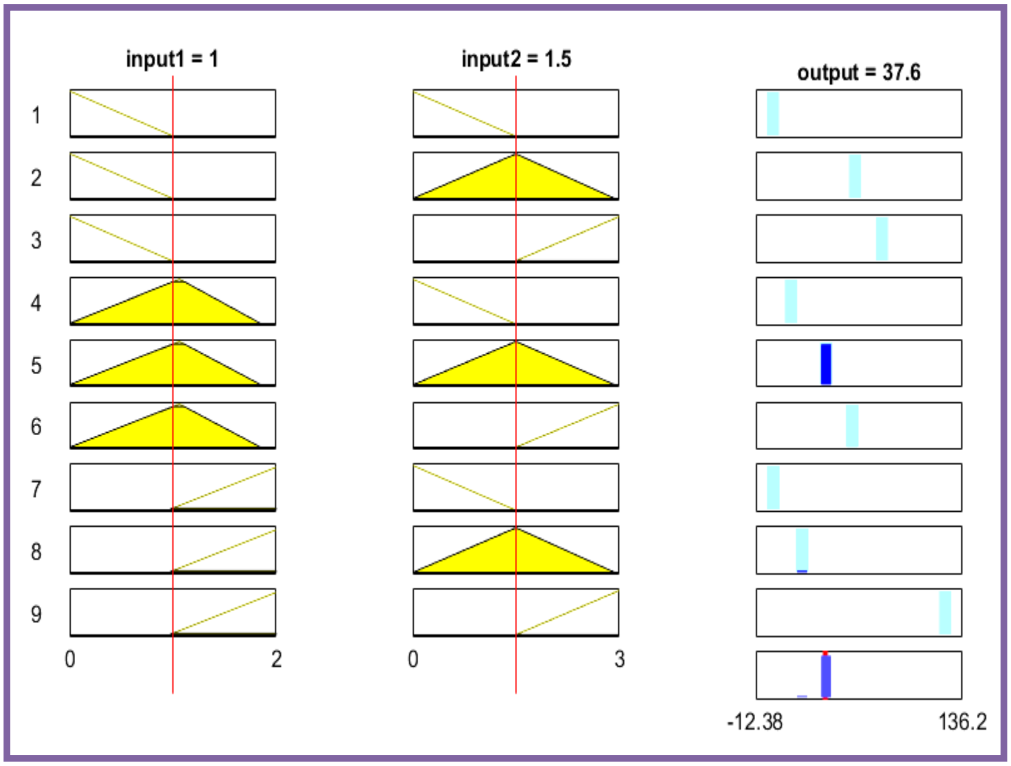

Figure 6.19. Sugeno rule view (output at 685 nm) for **1**.

Table 6.7. Rules for the Fuzzy Logic System (based on Sugeno's Method) by Taking F^- as Input 1 and H^+ as Input 2, Whereas Emission Intensity at 685 nm as the Output. The Rules Consist of the Following Statements.

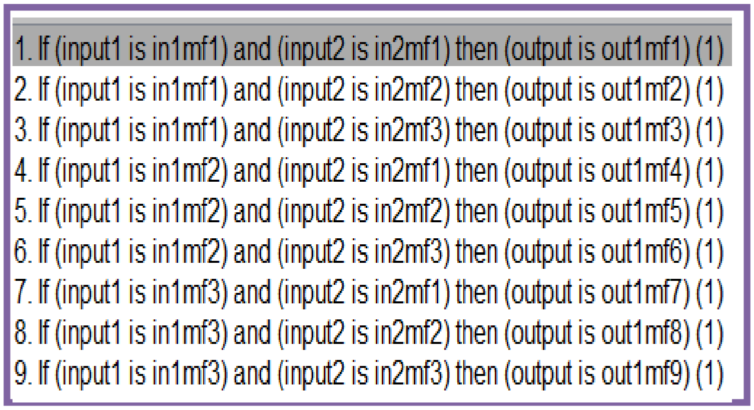

1. If (input1 is in1mf1) and (input2 is in2mf1) then (output is out1mf1) (1)
2. If (input1 is in1mf1) and (input2 is in2mf2) then (output is out1mf2) (1)
3. If (input1 is in1mf1) and (input2 is in2mf3) then (output is out1mf3) (1)
4. If (input1 is in1mf2) and (input2 is in2mf1) then (output is out1mf4) (1)
5. If (input1 is in1mf2) and (input2 is in2mf2) then (output is out1mf5) (1)
6. If (input1 is in1mf2) and (input2 is in2mf3) then (output is out1mf6) (1)
7. If (input1 is in1mf3) and (input2 is in2mf1) then (output is out1mf7) (1)
8. If (input1 is in1mf3) and (input2 is in2mf2) then (output is out1mf8) (1)
9. If (input1 is in1mf3) and (input2 is in2mf3) then (output is out1mf9) (1)

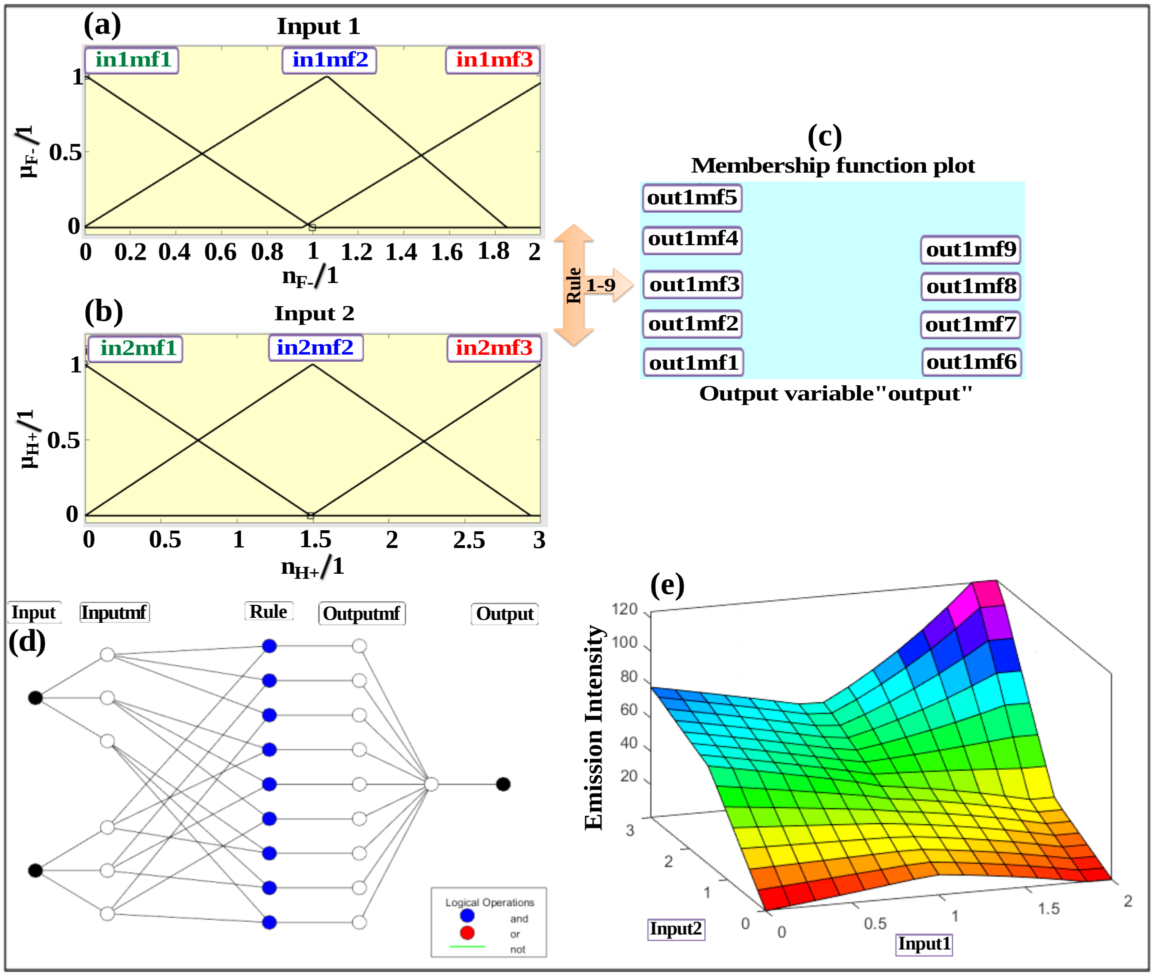

Figure 6.20. (a, b, c) Schematic presentation of ANFIS maintaining 9 rules. (d) Corresponding ANFIS structure. (e) Alteration of emission intensity due to addition of F^- and H^+.

Table 6.8. Comparison of Experimental Data with Fuzzy, ANN and ANFIS Outputs.

Input Combinations	Input1 (F^-)	Input2 (H^+)	Expt. Output	Fuzzy Output	ANN Output	ANFIS Output
1	0.43	2.51	65.56	64.31	63.81	63.51
2	0.84	1.95	48.87	44.22	47.66	47.52
3	1.33	1.34	33.21	63.43	29.88	30
4	1.42	1.25	29.88	45.41	26.73	26.9
5	1.97	0.11	1.881	10.81	1.821	1.77

6.4. Conclusions

In continuation of our ongoing activities in the promising area of molecular computing as well as in implementing the machine learning tools in chemistry, we employed a mononuclear Ru(II)-bipyridine complex possessing 3,5-bis(benzthiazol-2-yl) pyrazole motif. The complex offers one pyrazole NH group in its outer coordination sphere which can interact with anions via hydrogen bonding or by anion-promoted deprotonation. Anion sensing property of the receptor is thoroughly investigated in MeCN via absorption and emission spectroscopy as well as by SWV. Substantial modulation of photophysical and electrochemical properties of the complex occurs under the influence of selected anions. The anion-induced deprotonation of the complex is also convincingly demonstrated through single crystal X-ray crystallography. In absence of anions, the complex exhibits emission and designates the “on-state”, while presence of anions causes complete emission quenching and corresponds to the “off-state”. The reinstatement of the initial state of the complex could be feasible in presence of acid. Practically, the complex can function as anion- and acid-induced molecular switch. Another fascinating feature of the present work is that the absorption and emission spectral outputs of the complex upon the action of specific anions and acid are used to demonstrate many Boolean and FL functions. To perform very extensive sensing experiments by varying the anion concentration within a wide range is awfully tiresome, laborious and pricey. To overcome the shortcomings, several machine learning tools such as FL, ANN, and ANFIS have also implicated to predict the full anion sensing characteristics of the complex. The outcomes of the three ML tools are compared among themselves as well as with that of the experimentally obtained results. Interestingly, the ANFIS model is found to be superior decision making and learning tool over FL and ANN models.

6.5. References

1. de silva, A.P.; Gunaratne, H. Q. N.; McCoy, C.P. A Molecular Photoionic AND Gate Based on Fluorescent Signalling. *Nature*. **1993**. *364*. 42-44.
2. Ling, J.; Naren, Kelly, G. J.; Fox, D. B.; de Silva, A. P. Small Molecular Logic Systems Can Draw the Outlines of Objects *via* Edge Visualization. *Chem. Sci.* **2015** *6*, 4472-4478.
3. Ling, J.; Daly, B.; Silverson, V. A. D.; de Silva, A. P. Taking Baby Steps in Molecular Logic-Based Computation. *Chem. Com.* **2015.** *51*. 8403-8409.
4. Ling, J.; Kelly, G. J. Moody, T. S.; de Silva, A. P. Building pH Sensors into Paper-Based Small-Molecular Logic Systems for Very Simple Detection of Edges of Objects. *J.Am.Chem.Soc.* **2015.** *137*, 3763-3766.
5. Szaciłowski, K. Digital Information Processing in Molecular Systems. *Chem. Rev.* **2008**, *108*, 3481-3548.
6. Adamatzky, A.; Costello, B. D. L. Experimental Logical Gates in a Reaction-Diffusion Medium: The XOR Gate and Beyond. *Phys. Rev. E* **2002**, *66*, 046112.
7. Adamatzky, A.; Tegelaar, M.; Wosten, H. A.; Powell, A. L.; Beasley, A. E.; Mayne, R. On Boolean Gates in Fungal Colony. *Biosystems*. **2020**, *193*, 104138.
8. de Silva, A. P.; McClenaghan, N. D. Molecular-Scale Logic Gates. *Chem. Eur. J.* **2004.** *10*. 574-586.
9. Pflüger, P. M.; Glorius, F. Molecular Machine Learning: The Future of Synthetic Chemistry? *Angew. Chem. Int. Ed.* **2020**, *59*, 18860-18865.
10. Zhang, Y.; Liu, W.; Zhang, W.; Yu, S.; Yue, X.; Zhu, W.; Wang, J. DNA-Mediated Gold Nanoparticle Signal Transducers For Combinatorial Logic Operations and Heavy Metal Ions Sensing. *Biosens. Bioelectron.* **2015**, *72*, 218-224.
11. Goldsworthy, V.; LaForce, G.; Abels, S.; Khisamutdinov, E. F. Fluorogenic RNA Aptamers: A Nano-Platform for Fabrication of Simple and Combinatorial Logic Gates. *Nanomaterials*. **2018**, *8*, 984.
12. Mardanya, S.; Mondal, D.; Karmakar, S.; Baitalik, S. Smart Ruthenium and Osmium Complexes Mimic the Complicated Functions of Traffic Signal and Memory Device. *Sens. Actuators B: Chem.* **2017**, *239*, 635-641.

13. Schmittel, M.; Mal, P.; de los Rios, A. Multiport Logic Operations Triggered by Protonation a Trisphenanthroline as a 3-input AND-NOR-OR Circuit. *Chem. Commun.* **2010**, *46*, 2031-2033.

14. Biswas, P. K.; Saha, S.; Gaikwad, S.; Schmittel, M. Reversible Multicomponent AND Gate Triggered by Stoichiometric Chemical Pulses Commands the Self-Assembly and Actuation of Catalytic Machinery. *J. Am. Chem. Soc.* **2020**, 142 7889- 7897.

15. E. Katz, (Ed.) Molecular and Supramolecular Information Processing: From Molecular Switches to Logic Systems, *Wiley-VCH, Weinheim,* Germany, **2012**.

16. Karmakar, S.; Mardanya, S.; Das, S.; Baitalik, S. Efficient Deep-Blue Emittier and Molecular-Scale Memory Device Based on Dipyridyl-Phenylimidazole-Terpyridine Assembly. *J. Phys. Chem. C* **2015**, *119*, 6793-6805.

17. Mukherjee, S.; Sahoo, A.; Deb, S.; Baitalik, S. Light and Cation-Driven Optical Switch based on a Stilbene-Appended Terpyridine System for the Design of Molecular-Scale Logic Devices. *J. Phys. Chem. A.* **2021**, *125, 8261*-8273.

18. Mondal, D.; Bar, M.; Maity, D.; Baitalik, S. Anthraimidazoledione-Terpyridine-Based Optical Chemosensor for Anions and Cations That Works As Molecular Half-Subtractor, Key-Pad Lock, and Memory Device. *J. Phys. Chem. C.* **2015** ,*119* , 25429-25441

19. Omana, M. Papasso, G.; Rossi, D.; Metra, C. A. In 9th IEEE On-line Testing Symposium. **2003**,111-115.

20. Andréasson, J.; Pischel, U. Smart Molecules at Work Mimicking Advanced Logic Operations. *Chem. Soc. Rev*. **2010**, *39*, 174-188.

21. Andréasson, J.; Pischel, U.; Straight, S. D.; Moore, T. A; Moore, A. L.; Gust, D. All-Photonic Multifunctional Molecular Logic Device. *J. Am. Chem. Soc.* **2011**, *133*, 11641-11648.

22. Magri, D. C.; Fava, M. C.; Mallia, C. J. A Sodium-Enabled ‘Pourbaix Sensor’: A Three-Input AND Logic Gate as a ‘Lab-On-A-Molecule’ for Monitoring Na^+, pH and pE. *Chem. Comm.* **2014**, *50*, 1009-1011.

23. Mardanya, S.; Karmakar, S.; Das, S.; Baitalik, Anion and Cation Triggered Modulation of Optical Properties of a Pyridyl-Imidazole Receptor Rigidly Linked to Pyrene and Construction of INHIBIT, OR and XOR Molecular Logic Gates: A Combined Experimental and DFT/TD-DFT Investigation. S. *Sens. Actuators B: Chem.* **2015**, *206*.701-713.

24. Magri, D. C. A Fluorescent AND Logic Gate Driven by Electrons and Protons. *New J .Chem.* **2009**, *33*, 457-461.
25. Georgiev, N. I.; Dimitrova, M. D.; Todorova, Y. D.; Bojinov, V. B. Synthesis, Chemosensing Properties and Logic Behaviour of a Novel Ratiometric 1,8-Naphthalimide Probe Based on ICT and PET. *Dyes and Pigments*. **2016**, *131*. 9-17.
26. Marinova, N. V.; Georgiev, N. I.; Bojinov, V. B. Facile Synthesis, Sensor Activity and Logic Behaviour of 4-Aryloxy Substituted 1,8-Naphthalimide. *J. Photochem. Photobio. A* 2013 *254*. 54-61.
27. Said, A. I.; Georgiev, N. I; Bojinov, V. B. Synthesis of a Single 1,8-Naphthalimide Fluorophore as a Molecular Logic Lab for Simultaneously Detecting of Fe^{3+}, Hg^{2+} and Cu^{2+} .*Spectrochim. Acta A Mol. Biomol. Spectrosc*. **2018**, *196* .76-82.
28. Magri, D. C.; Spiteri, J. C. Proof of Principle of a Three-Input AND-INHIBIT-OR Combinatorial Logic Gate Array. *Org. Biomol. Chem.* **2017**, *15*, 6706-6709.
29. Deb, S.; Sahoo, A.; Ahmed, T.; Baitalik, S. Stimuli-Responsive Molecular Switches and Logic Devices Based on Ru (II)-Terpyridyl-Imidazole Coordination Motif. *J. Phys. Chem. B* 2021, *125*, 8919-8931.
30. Sahoo, A.; Ahmed, T.; Deb, S.; Baitalik, S. Neuro-Fuzzification Architecture for Modeling of Electrochemical Ion-Sensing Data of Imidazole-Dicarboxylate-Based Ru(II)-Bipyridine Complex. *Inorg. Chem.* **2022,** *61*, 10242-10254.
31. Cui, B. B.; Tang, J. H.; Yao, J.; Zhong, Y. W. A Molecular Platform for Multistate Near-Infrared Electrochromism and Flip-Flop, Flip-Flap-Flop, and Ternary Memory *Angew. Chem. Int. Ed.* **2015,** *54*, 9192-9197.
32. Dash, N.; Malakar, A.; Kumar, M.; Mondal, B. B.; Krishnamoorthy, G. Metal Ion Dependent “ON” Intramolecular Charge Transfer (ICT) and “OFF” Normal Switching of the Fluorescence: Sensing of Zn^{2+} by ICT Emission in Living Cells .*Sens. Actuators B: Chem*. **2014** ,*202* ,1154-1163.
33. Chen, K.; Schmittel, M. An Iridium (III) Complex as a Versatile Platform for Molecular Logic Gates: An Integrated Full Subtractor and 1:2 Demultiplexer. *Anal. Bioanal. Chem.* **2016**, **408**, 7077-7083.
34. Baitalik, S.; Flörke, U.; Nag, K. Synthesis, Structure, Redox Activity and Spectroscopic Properties of Ruthenium(II) Complexes with 3,5-Bis(Benzothiazol-2-yl)Pyrazole, 3,5-

Bis(Benzimidazol-2-yl)Pyrazole and 2,2'-bipyridine as co-ligands. *Dalton Trans.* **1999**, 719-727.

35. Beer, P.D.; Szemes, F.; Balzani, V.; Salà, C.M.; Drew, M.G.B.; Dent, S.W.; Maestri, M. Anion Selective Recognition and Sensing by Novel Macrocyclic Transition Metal Receptor Systems. ^{1}H NMR, Electrochemical, and Photophysical Investigations. *J. Am. Chem. Soc.* **1997**,*119*, 11864-11875.
36. Mo, H. J.; Niu, Y.L.; Zhang, M.; Qiao, Z.P.; Ye, B.H. Photophysical, Electrochemical and Anion Sensing Properties of Ru(II) Bipyridine Complexes with 2,2′-Biimidazole-Like Ligand. *Dalton trans.* **2011**, *40*, 8218-8225.
37. Cui, Y.; Niu, Y.L.; Cao, M.L.; Wang, K.; Mo, H.J.; Zhong, Y.R.; Ye, B.H. Ruthenium(II) 2,2′-Bibenzimidazole Complex as a Second-Sphere Receptor for Anions Interaction and Colorimeter. *Inorg. Chem.* **2008**, *47*, 5616-5624.
38. Mo, H. J.; Shen, Y.; Ye, B.H. Selective Recognition of Cyanide Anion via Formation of Multipoint NH and Phenyl CH Hydrogen Bonding with Acyclic Ruthenium Bipyridine Imidazole Receptors in Water. *Inorg. Chem.* **2012**, 51,7174-7184.
39. Cui, Y.; Mo, H.J.; Chen, J.C.; Niu, Y.L.; Zhong, Y.R.; Zheng, K.C.; Ye, B.H. Anion-Selective Interaction and Colorimeter by an Optical Metalloreceptor Based on Ruthenium(II) 2,2‘-Biimidazole: Hydrogen Bonding and Proton Transfer. *Inorg. Chem.* **2007**, *46*, 6427-6436.
40. Sauvage, J. P. ; Collin, J. P. J. ; Chambron, C. ; Guillerez, S. ; Coudret, C. ; Balzani, V.; Barigelletti, F.; De Cola, L. ; Flamigni, L. Ruthenium(II) and Osmium(II) Bis (Terpyridine) Complexes in Covalently-Linked Multicomponent Systems: Synthesis, Electrochemical Behavior, Absorption Spectra, and Photochemical and Photophysical Properties. *Chem. Rev.* **1994**, *94*, 993-1019.
41. Santoni, M.P.; Hanan, G. S.; Hasenknopf, B.; Proust, A.; Nastasi, F.; Serroni, S.; Campagna. S. Dinuclear Ru (II) Complexes of Bis-(Dipyrid-2′-yl) Triazine (Bis-Dpt) Ligands as Efficient Electron Reservoirs. *Chem. Commun.* **2011**, *47*, 3586-3588.
42. Harriman, A.; Ziessel, R. Making Photoactive, Molecular-Scale Wires. *Chem. Commun.* **1996**, *15*, 1707-1716.
43. Baitalik, S.; Dutta, B.; Nag, K. Spectroscopic and Redox Properties of Rh^{III} Ru^{II} and Ru^{II} Ru^{II} Complexes Derived From 2,2$'$-Bipyridine, Pyrazole-3,5-Bis(benzimidazole) and

1,2,4-Triazole-3,5-Dicarboxylic Acid as Bridging Ligands. *Polyhedron*. **2004**, *23*, 913-919.

44. Karmakar, S.; Maity, D.; Mardanya, S.; Baitalik, S. Multichromophoric Bimetallic Ru (II) Terpyridine Complexes Based on Pyrenyl-Bis-Phenylimidazole Spacer: Synthesis, Photophysics, Spectroelectrochemistry, and TD-DFT Calculations. *Inorg. Chem.* **2014**, *53*, 12036-12049.
45. Mondal, D.; Bar, M.; Mukherjee, S.; Baitalik, S. Design of Ru (II) Complexes Based on Anthraimidazoledione-Functionalized Terpyridine Ligand for Improvement of Room-Temperature Luminescence Characteristics and Recognition of Selective Anions: Experimental and DFT/TD-DFT Study. *Inorg. Chem.* **2016**, *55*, 9707-9724.
46. Bhaumik, C.; Maity, D.; Das, S.; Baitalik, S. Anion Sensing studies of Luminescent Bis-tridentate Ruthenium(II) and Osmium(II) Complexes Based on Terpyridyl-Imidazole Ligand Through Different Channels. *Polyhedron.* **2013**, *52*, 890-899.
47. Zadeh, L. A. Toward Human Level Machine Intelligence-Is It Achievable? The Need For a Paradigm Shift. *IEEE Comput. Intell. Mag.* **2008**, *3*, 11-22.
48. Zadeh, L.A. Outline of A New Approach to the Analysis of Complex Systems and Decision Processes. *IEEE Trans. Syst. Man Cyb.* **1973**, *3*, 28-44.
49. Zadeh, L. A. Fuzzy sets. In Fuzzy Sets, Fuzzy Logic, and Fuzzy Systems: Selected Papers by Lotfi A Zadeh, pp. *394-432*. **1996.**
50. Gentili, P. L. Boolean and Fuzzy Logic Gates Based on The Interaction of Flindersine With Bovine Serum Albumin and Tryptophan. *J. Phys. Chem. A.* **2008**, *112*, 11992-11997.
51. Gentili, P. L. The Fuzziness of the Molecular World and Its Perspectives. *Molecules.* **2018**, *23*, 2074.
52. Gentili, P.L. The Fundamental Fuzzy Logic Operators and Some Complex Boolean Logic Circuits Implemented by the Chromogenism of a Spirooxazine. *Phys. Chem. Chem. Phys.* **2011**, *13*, 20335-20344.
53. Sahu, S.; Sil, T. B.; Das, M.; Krishnamoorthy, G. A Single Fluorophore to Address Multiple Logic Gates. *Analyst.* **2015,** *140*, 6114-6123.
54. Gentili, P.L.; Giubila, M.S.; Heron, B.M. Processing Binary and Fuzzy Logic by Chaotic Time Series Generated by a Hydrodynamic Photochemical Oscillator. *Chem Phys Chem.* **2017**, *18*, 1831-1841.

55. Gentili, P.L.; Giubila, M.S.; Germani, R.; Romani, A.; Nicoziani, A.; Spalletti, A.; Heron; B.M. Optical Communication Among Oscillatory Reactions and Photo-Excitable Systems: Uv and Visible Radiation Can Synchronize Artificial Neuron Models. *Angew. Chem. Int. Ed.* **2017**, *56*, 7535-7540.
56. Giri Nandagopal, M. S.; Selvaraju, N. Prediction of Liquid-Liquid Flow Patterns in a Y-Junction Circular Microchannel Using Advanced Neural Network Techniques. *Ind. Eng. Chem. Res.* **2016**, *55*,11346-11362.
57. Bingöl, D.; Inal, M.; Çetintaş, S. Evaluation of Copper Biosorption Onto Date Palm (Phoenix Dactylifera L.) Seeds with MLR and ANFIS Models. *Ind. Eng. Chem.Res* **2013**, *52*, 4429-4435.
58. İnal, M. Predicting the Conversion Ratio for the Leaching of Celestite in Sodium Carbonate Solution Using An Adaptive Neuro-Fuzzy Inference System. *Ind. Eng. Chem.Res* **2014**, *53*, 4975-4980.
59. Sullivan, B. P.; Salmon, D. J.; Meyer, T. J. Mixed Phosphine 2,2'-Bipyridine Complexes of Ruthenium. *Inorg. Chem.* **1978,** *17*, 3334-3341.
60. MATLAB **2018a**, The MathWorks, Inc., Natick, Massachusetts, United States.
61. Jang, J. S. R.; Sun, C. T. Neuro-Fuzzy Modeling and Control. *Proc. IEEE.* **1995**, *83*, 378-405.
62. Sugeno, M.; Yasukhiro, T. A Fuzzy-Logic-Based Approach to Qualitative Modeling. *IEEE Trans. Fuzzy Syst.* **1993**, *1*, 7-31.

****

List of Publications

1. **Deb, S**.; Sahoo, A.; Mondal, P.; Baitalik, S*. "Analysis and Prediction of Anion- and Temperature Responsive Behaviours of Luminescent Ru(II)-Terpyridine Complexes by Using Boolean, Fuzzy Logic, Artificial Neural Network and Adapted Neuro Fuzzy Inference Models". ***Dalton Trans*. 2022,** *51*, 15601-15613.
2. **Deb, S**.; Sahoo, A.; Pal, P.; Baitalik, S*. "Exploitation of the Second Coordination Sphere to Promote Significant Increase of Room-Temperature Luminescence Lifetime and Anion Sensing in Ruthenium-Terpyridine Complexes". ***Inorg. Chem.*** **2021,** *60*, 6836-6851.
3. **Deb, S**.; Sahoo, A.; Ahmed, T.; Baitalik, S*. "Stimuli-Responsive Molecular Switches and Logic Devices Based on Ru (II)-Terpyridyl-Imidazole Coordination Motif"'. ***J. Phys. Chem. B*** **2021**, *125*, 8919-8931.
4. **Deb, S**.; Sahoo, A.; Baitalik, S*. "Harnessing Deep Neural Networks to Analyze Multi-Channel Anion Sensing Characteristics of Ru(II)-Pyrazolyl-Bis(Benzimidazole) complex". (Communicated in ***Phys. Chem. Chem. Phys.***)
5. **Deb, S**.; Sahoo, A.; Karmakar, S.; Baitalik, S*. "Multi-Channel Anion Sensing Behaviour of a Ru(II)-Bipyridine Complex Based on Benzothiazolyl Pyrazole Ligand: Experimental and Implication of Machine Learning Tools for Data Prediction". (Communicated in ***Inorganica Chim. Acta***)
6. Sahoo, A.; Ahmed, T.; **Deb, S**.; Baitalik, S*. "Neuro-Fuzzification Architecture for Modeling of Electrochemical Ion-Sensing Data of Imidazole-Dicarboxylate-Based Ru(II)-Bipyridine Complex". ***Inorg. Chem. 2022,*** *61*, 10242-10254.
7. Mukerjee, S.; Sahoo, A.; **Deb, S**.; Baitalik, S*. "Light and Cation-Driven Optical Switch based on a Stilbene-Appended Terpyridine System for the Design of Molecular-Scale Logic Devices". ***J. Phys. Chem. A*** **2021**, *125*, 8261-8273.
8. Paul, A.; Bar, M.; **Deb, S**.; Baitalik, S*. "Long-Lived Trimetallic Complexes of Fe(II), Ru(II), and Os(II) Based on a Heteroditopic Bipyridine-Terpyridine Bridge: Synthesis, Photophysics and Electronic Energy Transfer". ***Inorg. Chem. 2019,*** *58*, 10065-10077.

9. Dutta, A.; Behera, R. K.; **Deb, S**.; Baitalik, S*.; Pradhan, N.* “Doping Mn(II) in All Inorganic Ruddlesden-Popper Phase of Tetragonal $Cs_2PbCl_2I_2$ Perovskite Nanoplatelets”. ***J. Phys. Chem. Lett.*** **2019**, *10*, 1954-1959
10. Bar, M.; **Deb, S.;** Mukherjee, S.; Baitalik, S.* “Stimuli-Responsive Near-Infrared Emissive Os (II)-Terpyridine Complexes with a Sense of Logic”**.** ***ACS Omega,*** **2019**, *4*, 2241-2255.
11. Bar, M.; **Deb, S**.; Paul, A.; Baitalik, S.* “Stimuli-Responsive Luminescent Bis-Tri dentate Ru (II) Complexes toward the Design of Functional Materials”. ***Inorg. Chem*. 2018**, *57*, 12010-12024.
12. Bar, M.; Maity, D.; **Deb, S**.; Das, S.; Baitalik, S.* “Ru-Os Dyads Based on a Mixed Bipyridine Terpyridine Bridging Ligand: Modulation of the Rate of Energy Transfer and pH-Induced Luminescence switching in the Infrared Domain”. ***Dalton Trans*. 2017**, *46*, 12950-12963.

Publications 1-5 are included in the thesis

****